NASA Conference Publication 2446

14th Space Simulation Conference

Testing For A Permanent Presence In Space

Sponsored by
National Aeronautics and Space Administration
Institute of Environmental Sciences
The American Institute for Aeronautics and Astronautics
The American Society for Testing and Materials

Proceedings of a symposium held at
Sheraton Inner Harbor Hotel, Baltimore, Maryland
November 3-6, 1986

NASA

National Aeronautics
and Space Administration

Scientific and Technical
Information Branch

1986

PREFACE

The Fourteenth Space Simulation Conference held at the Sheraton Inner Harbor Hotel in Baltimore, Maryland, November 3-6, 1986 was sponsored by the Institute of Environmental Sciences (IES) and supported by the National Aeronautics and Space Administration (NASA), the American Institute of Aeronautics and Astronautics (AIAA), and the American Society of Testing and Materials (ASTM). Additionally, NASA provides publication of these proceedings.

The Conference addressed subjects of continued interest such as facilities, thermal testing, and contamination as they relate to space simulation. Welcome was more involvement by the European Space Community. Future trends, acoustics, and heat pipes sessions rounded out the technical program.

Featured guest speaker, Mr. Raymond P. Villard, Media Service Coordinator for the Space Telescope Science Institute and an excellent tour by the Goddard Space Flight Center added the variety needed for the conference.

Success of the conference and the quality of these proceedings are the results of extraordinary performance by the Technical Chairman, Al Lunde and his technical programs committee, IES Meeting Manager, John P. Campbell, Facilities Chairman, R. T. (Tom) Hollingsworth, IES Executive Director, Janet A. Ehmann, and Publication Chairman Joseph L. Stecher III of NASA Goddard Space Flight Center.

R. P. Parrish
General Chairman

PRECEDING PAGE BLANK NOT FILMED

COMMITTEES FOR

14TH SPACE SIMULATION CONFERENCE

MEETING MANAGEMENT COMMITTEE

General Chairman:	Robert P. Parrish, Jr., Martin Marietta Corp.
Technical Program:	Albert R. Lunde, Boeing Aerospace Company
IES Meeting Manager:	John D. Campbell, Consultant
Publication Chairman:	Joseph L. Stecher III, NASA Goddard Space Flight Center
Facilities Chairman:	Russell T. Hollingsworth, Consultant
IES Executive Director:	Janet A. Ehman, Institute of Environmental Sciences

TECHNICAL PROGRAM COMMITTEE

Eugene N. Borson, The Aerospace Corporation
Peter W. Brinkman, ESA/ESTEC
Richard Hartenbaum, RCA Corporation
John W. Harrell, Jet Propulsion Laboratory
Steven W. Liu, TRW Electronics & Defense
Raymond D. Rempt, Boeing Aerospace Company
Emile S. J. Wang, McDonnell Douglas Corporation
George F. Wright, Jr., Sandia National Laboratories

JOINT POLICY COMMITTEE

IES

John D. Campbell, Consultant
George Frankel, Grumman Aerospace

ASTM

Eugene N. Borson, The Aerospace Corporation
George F. Wright, Jr., Sandia National Laboratories

AIAA

Albert R. Lunde, The Boeing Company

CONTENTS

SESSION X: ACOUSTICS

Chairman: John W. Harrell, Jet Propulsion Laboratory

INFRA-RED LAMP PANEL STUDY AND ASSESSMENT APPLICATION TO THERMAL VACUUM TESTING OF SIGMA TELESCOPE

Jacques MAUDUYT
CENTRE NATIONAL D'ETUDES SPATIALES

Joseph MERLET and Christiane POUX
INTESPACE, FRANCE

ABSTRACT

A Research and Development Program on the Infra-Red Test has been conducted by the CNES (French Space Agency) and developped by INTESPACE (a Subsidiary of CNES). A choice, after characterization, among several possibilities has been made on the type of methods and facilites for the I.R. test. An application to the Thermal Vacuum Test of SIGMA Telescope is described.

INTRODUCTION

The CNES (French Space Agency) built in 1970 a large space simulation in its TOULOUSE Center. This facility is managed by INTESPACE, a subsidiary of CNES.
Yet, the new launchers, Space Shuttle and Ariane, allow to design spacecraft with highermasses and dimensions. So, two actions are developped :

- the increase of performance of the space simulator,
- the study of test technique for I.R. Thermal vacuum test.

The new capabilities of the space simulator are :

- a collimated solar beam of 3,8 m diameter,
- a gimbal of 2 degrees of freedom with 2,5 tons capacity,
- a control and command system which limits the test team for the facility at 3 people for shift.
- a measurement system with 450 T.C. Channels and 200 electric Channels.

A Research and Developpement Program has been decided by CNES and developped in cooperation with INTESPACE on the I.R Test method and test facilities. This method has several advantages.

- to utilize the maximum dimension of T.V. Facility (our large chamber is 6.2 m diameter and 5.7 m height),

- to allow different fluxes on the faces of the test specimen, for example :

  - Earth albedo,
  - Emitted or reflected flux by Space Shuttle Cargo Bay.

Theses possibilities has been studied for some cases.
The object of this paper is the presentation of results of this study and its application for the test of SIGMA Satellite.

CHOICE OF I.R. FACILITIES

I.1 : SOURCES

Two types of I.R. lamps have been tested : 500 W and 112-125 V :

Research Inc. type 5236-5
Philips type IRK C 536/98.

A set of 10 lamps have been characterized in the same conditions. The irradiance has been measured at 300 mm from the tube. The axis of the radiometer was normal to the tube and passing through its middle point. The results are :

	UNIT	PHILIPS	RESEARCH
Averaged irradiance	mW/cm2	76,5	117,7
Estimed dispersion	%	6,05	12,8

Table 1 : irradiance of I.R. lamp

The research lamps have a metallic reflector, set behind the lamp. But for the Philips lamp, the reflector is a ceramic coating, on the quartz tube. This difference explains the different measured irradiance.

We have choosen Philips lamps for :

- the peak of irradiance in front of the lamp is less due to the type of refector, so a good homogeneity is easier to obtain on a plane,
- the least dispersion of characteristics,
- its cheapest cost.

I.2 : CHARACTERISTICS OF SOURCES

I.2.1 : Irradiated spectrum.
A survey of facilities for this type of measurement has been made. But no

industrial hardware have been found for spectrum 0,4µm and 5µm wavelength. A French laboratory will perform these measurements this year for several color temperatures of the lamp.

1.2.2 : Spatial irradiance

Preliminary measurement have been made, but the requirements for the software dedicated for design of I.R. panels are measurements :

- at a fixed distance, in front of the lamp,
- along angle in the plane normal to the filament of the lamp,
- along in the plane of the filament normal to the reflector,
- versus input voltage.

The values are given in Table 2.

φ/θ	$f(\theta)$	$f(\varphi)$
0	1	1
10	0,9978	1,016
20	0,9632	1,023
30	0,8858	1,005
40	0,7679	0,9776
50	0,6080	0,9733
60	0,4306	0,9772
70	0,2587	0,952
80	0,103	0,850
90	0,014	0,588

Spatial flux intensity distribution, table 2

I.3 : POWER SUPPLY

We have tested two types of power supplied :

- distributed zero cross over firing circuit power supply,
- direct current power supply.

We have checked if they satisfy to the MIL-STD-1542 which is related to EMC-EMI. The first power supply does not meet the requirements it is due to the system which controls the zero cross over. But the Direct current power supply, has a defect in conducted mode for frequency below 500 Hz, but is good in radiated mode.

Although the first type is less in dimensions and cost, we have choosen the second type SODILEC SDR 150/10 which is or has :

- more safe to use,
- clear display of function parameters,

- IEEE programmable,
- very easy measurement of electric power supplied to the lamp,
- no variation of thermal flux on the specimen,
- good behaviour from a EMI-EMC point of view.

I - 4 : FLUX MEASUREMENTS

We have tested several radiometers :

- a Hy CAL radiometer type P 8400 water-cooled with a removable quartz window. But the sensitivity we have measured is 8 % greater than those given by the manufacturer. Our measures have been confirmed by the Intitut National of metrologie (French Bureau of Standards),

- a Medtherm radiometer type 64-02-16 no cooled without window.
  We have noted a discrepancy of 4 %, also confirmed. But the lack of thermal regulation does not allow its use in vacuum,

- a Medtherm radiometer type 64-02-20 water-cooled without window.
  Our measurement of sensitivity was in accordance with the manufacturer (2 % of error). We have noted that its response versus incident angle, is not good below with 60° where we have already 4% of error whith the cosine law. The measured time constant is 3,1 s so the time to perform a measurement with an error less than 5% is 9,3 s minimum.

So to have good measurement of flux we have choosen this last type. But we think that it is not very interesting to generalize flux measurement in vacuum chamber like cartography because :

- the difficulty of this type of measurement (discrepancy between laboratory),

- the need of radiometer with thermal control (risk of water leak),

- response time is long,

- influence of the incident angle.

I - 5 : DESIGN OF LAMPS PANNEL

One problem is the design of lamps pannel to meet requirements on :

- flux intensity level,
- fluctuation of flux intensity level over the surface.

Europeen Space Agency has developped a softwave which can give a solution to this given problem. The IRSIM program computes (ref 2) the flux on the surface of the specimen and on the sensors when the user gives :

- a description of the test specimen by a set of surfaces,
- a set of infrared lamps,

- a system of baffles,
- a set of sensors.

We can adjust the level and the homogeinity of the flux by changing the lamp operating voltage and the position of the lamps.
The incident flux is calculated from the next data :

- the flux delivered by the lamp at 1 m distance directly in front of the lamp at the operating voltage,

- the distance from thelamp to the incident point,

- the spatial distribution of the flux intensity delivered by the lamp,

- the information if the incident point is or is not shadowed from the lamp and if the lamp is or is not baffled from a surface, the flux is calculated, with the assumption the intensity varies as the squared distance inverse.

ESA has given a copy of this sofware to the CNES so we made an evaluation.

The software is efficient but some additional possibilities would be useful :

- spherical surface for test specimen modeling,

- graphical output such flux curves along choosen axis or cartography of flux relative to an average flux.

The actual version is nevertheless very useful and we applied it to the design of the panel for the SIGMA test.

APPLICATION TO SIGMA TELESCOPE T/V TEST

2 - 1 : CONTEXT AND DESIGN GOALS

SIGMA is a Gamma Telescope (Ø≃1.2 m, Hn* ≃3.5 m, M≃1000 Kg), placed on an eccentric orbit (2000/200000 KM), 3 axis stabilized with telescope axis normal to Sun direction.

Thermal control is achieved with MLI all over the structure, and internal equipments thermally coupled with external VCHP radiator at opposite of Sun direction.

T/V tests could not be performed with solar simulator (unavailability of facility) and had to take place in Simdia facility (Ø 3 m, L = 3 m).
Telescope tube height had to be reduced from 3.5 m to 2.5 m, and solar fluxes simulated by I.R. means.

R.D. works in progress at that moment and SIGMA requirements gave the opportunity to evaluate I.R. simulation capabilities in a "real" case.

In accordance with SIGMA project management it was decided to build an I.R. simulator to achieve temperature field simulation on MLI surface. Development of this I.R. simulator had 3 steps :

- I.R. flux calibration in ambient air conditions (flux map),
- T/V qualification of I.R. simulator,
- T/V SIGMA telescope test.

2 - 2 : I.R. SIMULATOR SPECIFICATIONS

- To generate a well defined temperature field, as similar as possible to in-flight one,in view to have representative heat balance through MLI.

- To authorize various environment configuration (Hot case, cold case, no flux case...)

- To guarantee an error less than 10 % between measured and calculated flux density on a 90 % cyclindrical sector, and between measured and the vertical (k.cos θ) angular distribution.

- Not to illuminate shadowed surfaces.

- To be compatible with test facility mechanically (dimensions/fixation), thermally (no significant disturbances of heat sink temperature) and electrically (electrical power)
- To authorize precise and stable positionning of lamps with respect to illuminated surface.

* Hn≃2,5 m for STM model

2 - 3 : I.R. SIMULATOR DESCRIPTION

(See photo Fig. 1)

Mechanical structure is an aluminum grid with teflon isolating spacers for lamp fixation. A set of 49 "500 W Philips" lamps (cf. § I.1) is distributed (7 columns and 7 rows) on a 90° cylindrical surface at 30 cm distance from Ø 1200 telescope cylinder (see fig. 2).

Due to symetry it was natural to have one electrical power source for two lamps.

This power source was at regulated voltage (DC 0/120 V) (cf. § I.3) and voltage setting commanded by computer.

2 - 4 : AMBIENT AIR TEST

Ambient air tests were performed by means of a flux map device equipped with water cooled Medtherm radiometer (cf. § I.4) and connected with data acquisition/recording system. Voltage setting of each lamp couple was calculated by taking into account individual characteristics (couples determined after individual calibration).

Measurements gave us two flux map related to two typical flux values (1200 W/m2 and 750 W/m2).

Results were studied on graphs (Flux variation along columns and along rows) and compared with IRSIM program results (See fig. 3 and 4).

Table N° 3 and 4 gives calculation/measurement discrepancies. We note that 10 % flux specification is achieved excepted in particular points and that errors are quite always underestimations in flux calculation.

Cosine law is respected in row distribution up to $\pm$ 37° with an error less than 3 % and flux homogeneïty along centry column is better than 8 % as for as 300 mm from ends.

2 - 5 : T/V QUALIFICATION OF I.R. SIMULATOR

(See photo fig. 5)

T/V qualification tests were performed in Simdia Chamber with a very simple model. This model had the same geometrical shape and thermal coating (Aluminized Kapton e = 25 μm) that SIGMA telescope.
This model was equipped with about 80 thermocouples.

Electrical configurations have been the same that these defined during Ambient Air Testing plus a "maximum hot case" to simulate a worst case (maximum coating aging) and other various "sensitivity" configurations (voltage variations on a lamp, a row, a column).

2 - 6 : T/V TELESCOPE TEST

Structural and Thermal Model (STM) was tested in Simdia Chamber with the two configurations ("cold case", "maximum hot case") defined during T/V Qualification tests of I.R. Simulator, and with a third configuration (zero I.R. flux).

Tests were performed in good accordance with procedure and previsions, without any problem related to I.R. simulation.

Temperature discrepancies which could have been noted, were induced by geometrical differency between first model (I.R. Qualification) and telescope STM (polygonal section instead of cylindrical, MLI thickness, cone angle between Ø 1200 - Ø 800 cylinders).

Test results made SIGMA thermal people able to evaluate temperature influence on MLI effectiveness, and to bring test temperature levels and test thermal exchanges nearer to "flight" estimations. So, if we consider alternate solution without any flux simulation, we obtain a reduction of differences between test heat leaks and flight heat leaks through MLI in the ratio of 4 (or more). In other respects temperature level differences (Flight-Tests) were reduced from 15° C to less 4° C.

CONCLUSION

Gradual approach was advisable and made the telescope tests performed without any major problem while we used a complete I.R. simulation set for the first time at INTESPACE and in a "R and D./Project joint venture".

During preparation and execution of these tests, encountered problems were :

. Variation ($k.\frac{1}{d2}$) of incident power for a surface at a distance (d) from source

  makes source/surface positionning has to be very precise.

. Dispersion of lamp characteristics requires individual calibration.

. Influence of power voltage on emitted spectrum (and consequently on receiver absorption coefficient) induces on uncertainty.

. Dues to the first problem hereover, geometrical irregularities and appendices have to be carefully evaluated.

. Global efficiency (useful flux/electrical power) is rather low (25 %) for this type of cylindrical structure (with two different diameters). We need large electrical power and we have large heat load to evacuate through heat sink.

At this step of R. an D. action, we envisage to improve our knowledge of spectrum related to voltage and associated absorption coefficient for typical coatings. By another way we intend to develop automatic control and command of power supply.

REFERENCES

1) IRSIM : A Program for the calculation of infrared flux intensity incident spacecraf inside a test chamber, R.P. ROGERS ESA. SP - 100 (Intl. Symposium on Environmental and Thermal System for Space Vehicles. Toulouse, France, 4, 7 Oct. 1983).

△ %	G6 (14°)	G7 (28°)	G8 (42°)	60°	70°
R1	0 %	- 0, 7 %	- 10, 7		
R2	+ 7, 3 %	- 0, 7 %	- 10, 6		
R3	- 0, 6 %	- 3, 8 %	- 14, 4	- 45, 7	- 74, 6
R4	- 2, 7 %	- 5, 9 %	- 17		
R5	+ 0, 6 %	- 2, 9 %	- 12, 9		
R6	+ 1, 9 %	- 2, 9 %	- 11, 3		
R7	- 1, 6 %	- 1, 7 %	- 12, 6	- 24, 2	- 55, 6

Table 3 - Verification of cosine law
Comparison measured/theoretical flux

△ %	G5	G6	G7	G8
R1	- 8, 8 %	- 9 %	- 8, 5 %	- 4, 8 %
M12	- 7 %			
R 2	- 9, 9 %		- 7, 7 %	- 5, 4 %
M23	- 6, 2 %			
R3	- 5, 8 %	- 7, 2 %	- 8 %	- 5, 8 %
M34	+ 1, 4 %			
R4	- 2 %	- 2, 4 %	- 3, 1 %	0

Table 4 - Comparison measured/
computed flux by IRSIM

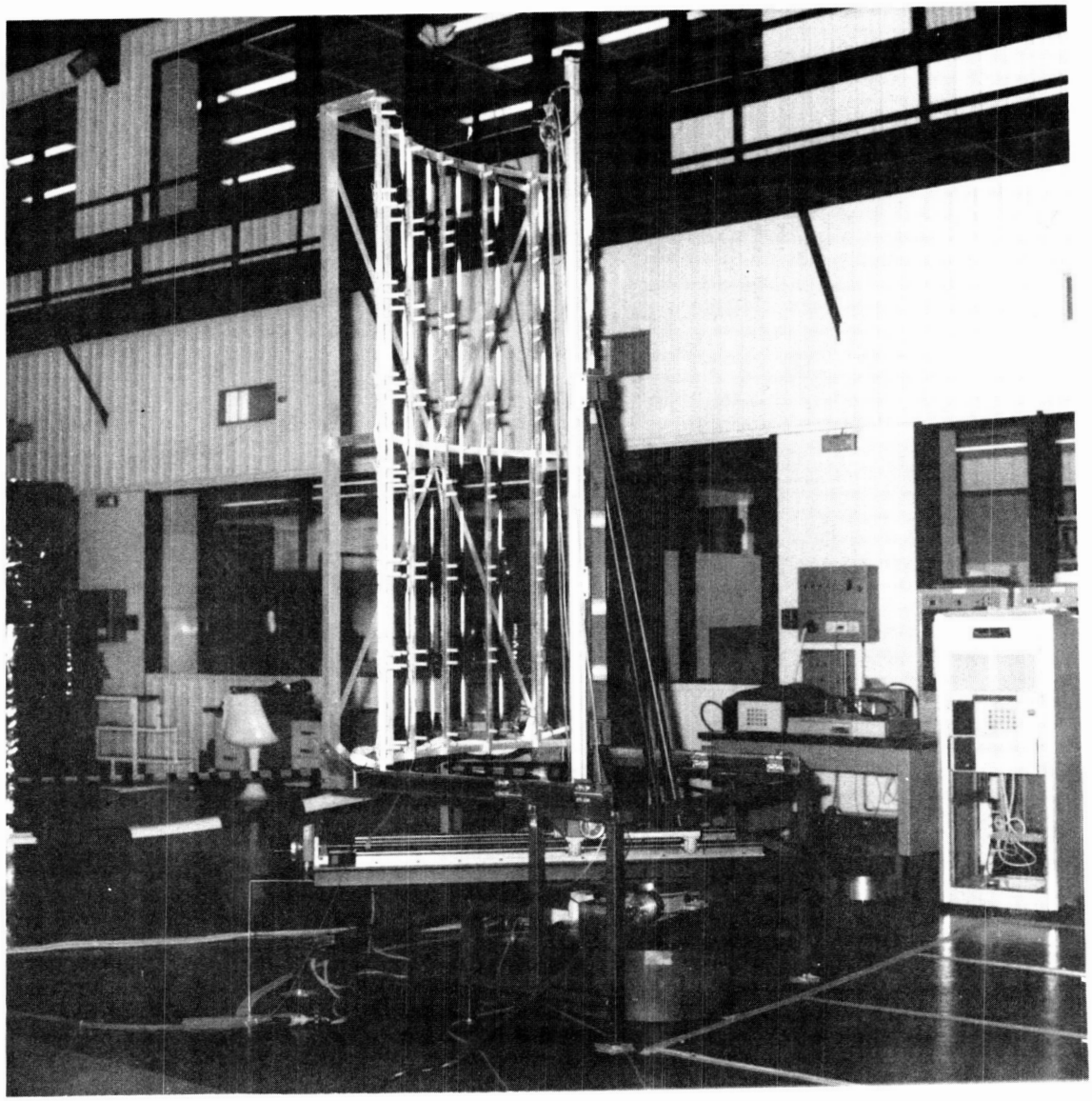

Fig. 1

I.R. Panel for Sigma Telescope
during flux cartography measurement

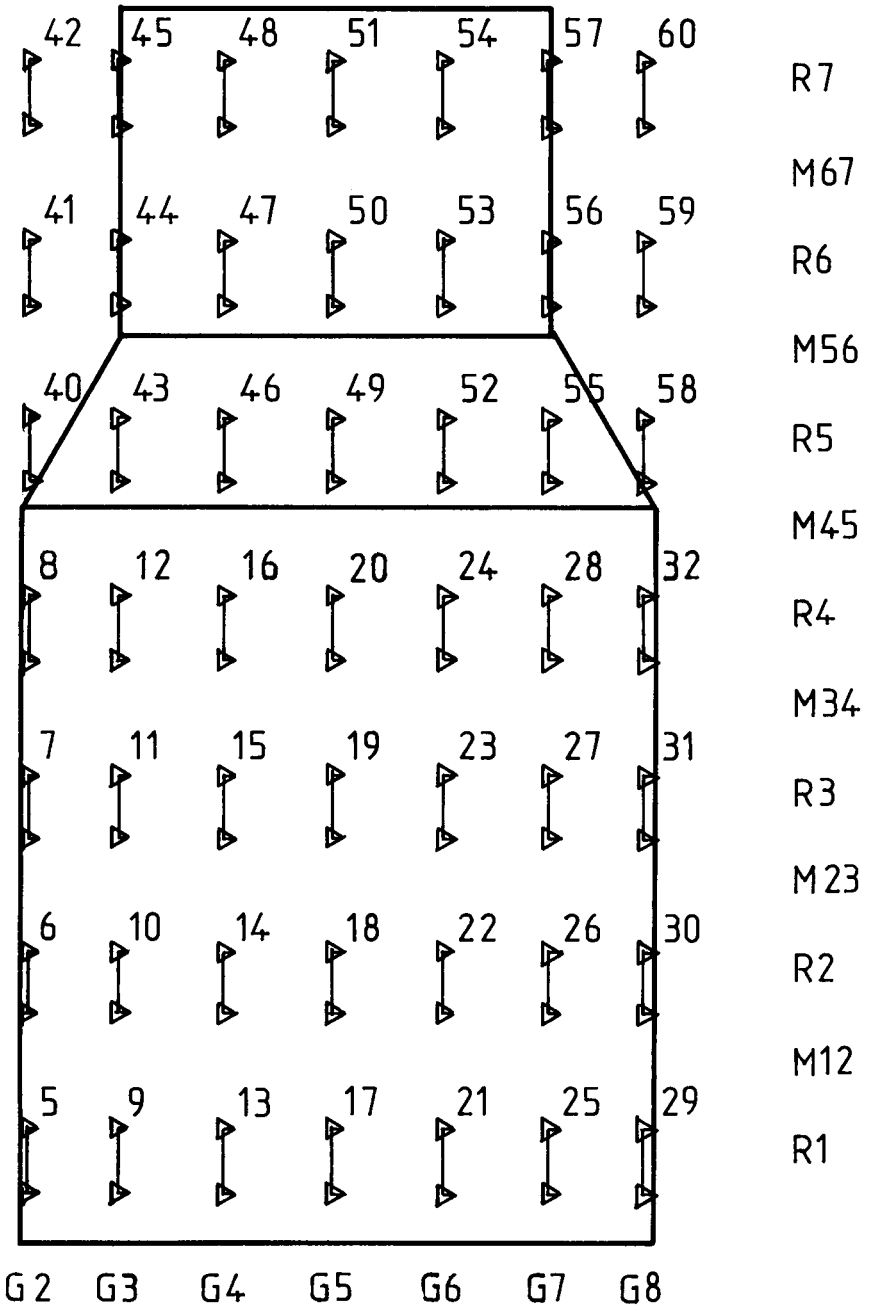

Fig. 2 : Set-up of I.R. lamps for the SIGMA Test

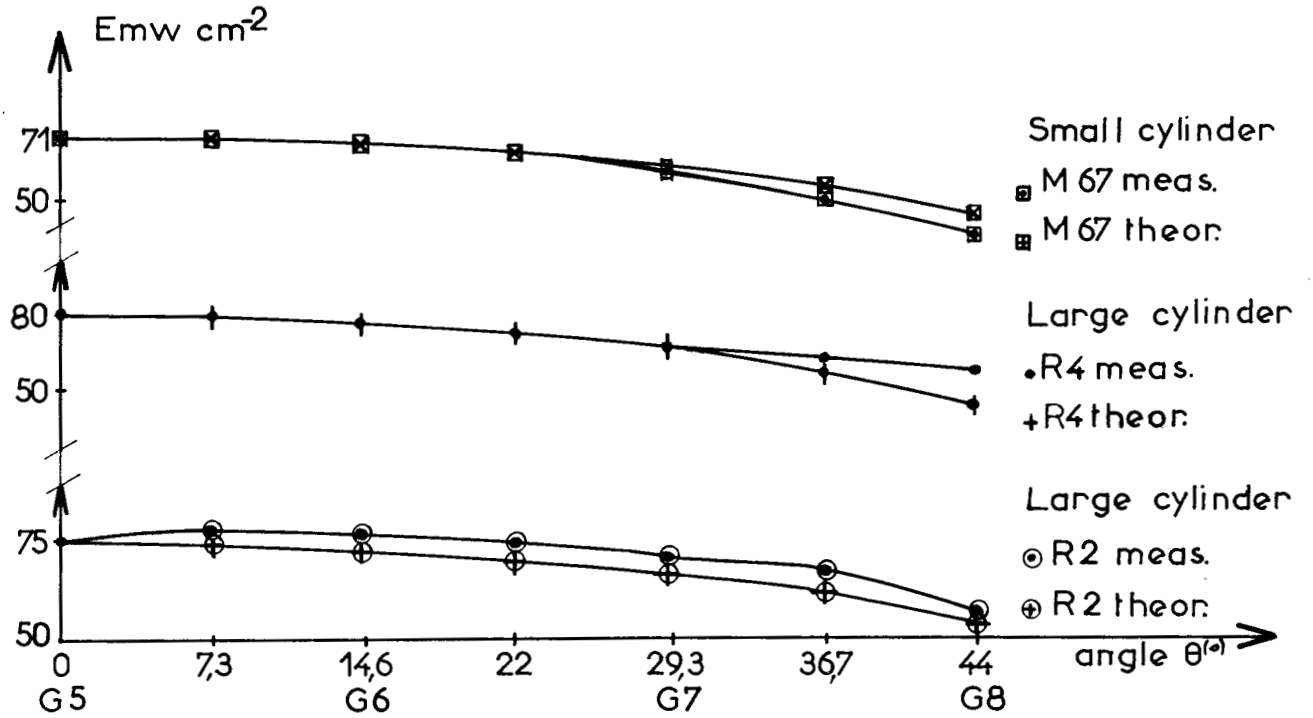

Fig. 3 : Verification of cosine-law (case 750 $W.m^{-2}$)

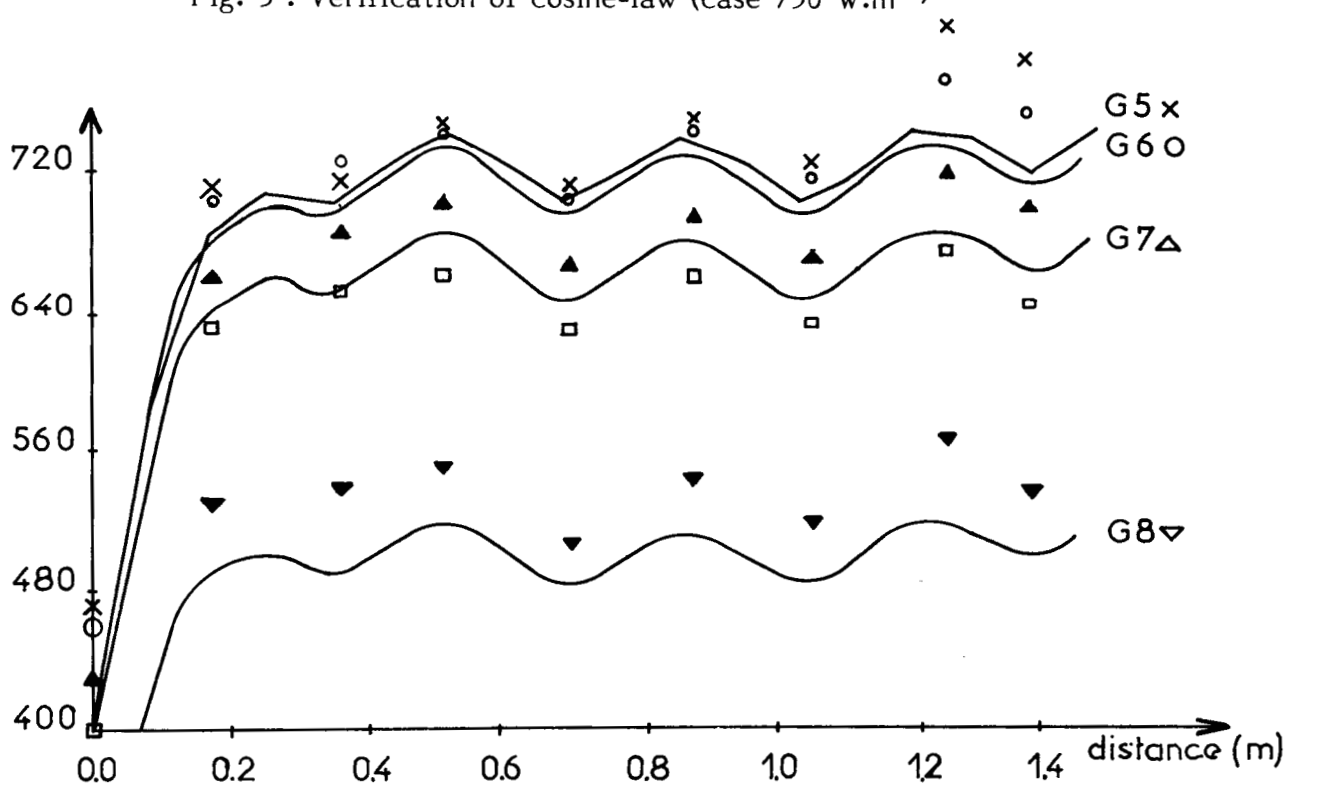

Fig. 4 : Comparison predicted/measured flux (case 750 $W.m^{-2}$)

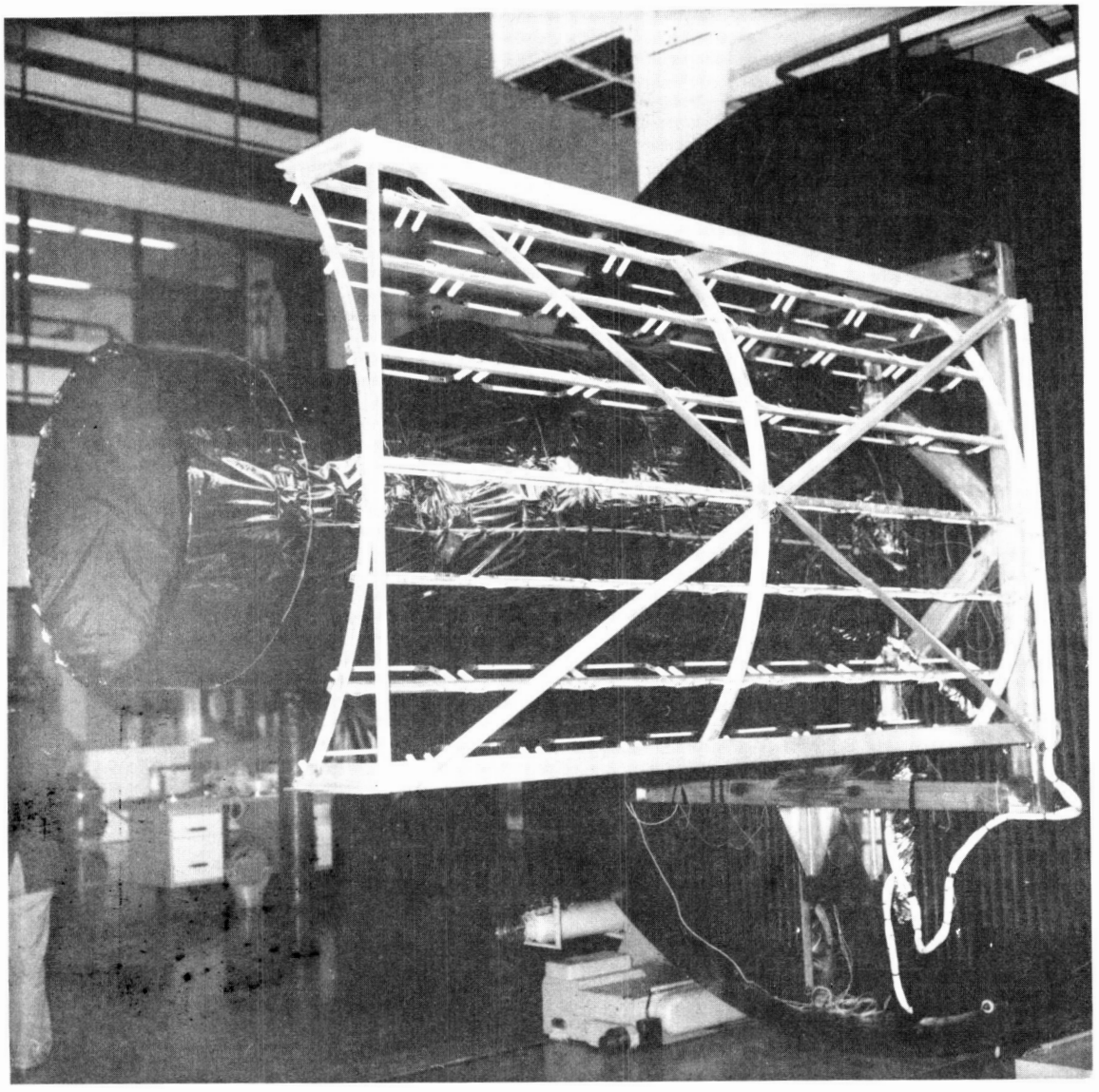

Fig. 5

I.R. lamp testing fixed on the door of
SIMDIA Thermal Vacuum Facility

MONITORED BACKGROUND RADIOMETER*

by

C. Ruel, M. Larouche, and M. Donato

Spar Aerospace Limited,
Ste-Anne-de-Bellevue, Quebec, Canada.

INTRODUCTION

The infrared (IR) testing of the Olympus thermal model at the David Florida Laboratory in Ottawa has provided Spar Aerospace Ltd a capability to perform cost-effective thermal balance testing of satellites and satellite components.

One of the requirements of the IR test technique is to accurately measure the radiant flux absorbed by the spacecraft surfaces. Most of the commercially available radiometers did not meet the high accuracy and quick time response required, or were too complex to implement in the test set up because of the presence of fluid loops or power supplies. To overcome this obstacle, a high-accuracy, monitored background radiometer (MBR) was developed at Spar Aerospace Ltd for the measurement of absorbed radiation heat flux encountered during IR thermal vacuum testing of spacecraft (S/C). This paper describes the design, development, calibration of this radiometer.

BACKGROUND AND DESCRIPTION

Various radiometer designs have been used for IR testing. Flat plate calorimeters, which represent one class of radiometer, consist of a control surface with a thermocouple and insulation on its backside (1,2). Many attempts have been made to optimize its design but the major drawbacks of this type of sensor remain the inadequate time response, and the accuracy in conditions different from the calibration conditions due to heat leaks from the sensor plate to the background environment.

* This work was supported in part by the Canadian federal government's Department of Communictions, contract no. 1ST84-00275.

Thermopile type devices have also been used but they require fluid loops or an external power source and therefore increase the complexity of the test set up (3).

A third type of radiometer currently available is the controlled background radiometer. It consist of a sensor surface mounted to a body which is kept at a constant temperature via a heater and control circuit. This type of radiometer also requires an external power source.

As an extension to the above concepts, the MBR was developed to account for heat transfer from the back surface of the sensor plate. This is accomplished by monitoring the temperatures of both the sensor plate and body.

The MBR consists of an aluminum sensor plate (SP) and body. Aluminum was chosen because its high thermal diffusivity ensures uniform temperatures and quick time responses. The SP is attached to the body with insulating teflon stand-offs to limit heat flow, and its outside surface is covered with the same material as the surface whose absorbed flux is to be measured.

To accommodate the various coatings with which the sensor is to be covered, two basic versions of the MBR are currently in use as shown in Figure 1. Rectangular control materials like second surface mirrors, kevlar or graphite fiber epoxy (GFEC) samples can be bonded to rectangular MBR's, and paint or kapton films can be applied to the cylindrical MBR's. Except for their shape, the construction of the two types of MBR is identical.

A flexible foil heater is bonded to the inner surface of the SP to supply the heat input required for calibration, and an aluminized mylar sheet covers the exposed surface of the heater to limit radiation heat loss from the back of the SP to the body.

A very important aspect of the MBR design was to insulate the back of the SP as well as possible from the body and the environment to ensure that the ratio of the radiation heat transfer from the top SP surface to the heat transfer from the back of the SP was large. At the same time, to accurately account for heat transfer from the back of the SP, it was necessary design the MBR in a way that the heat transfer from the back of the SP was mainly to the body with little or no heat loss to the environment. This was done by bonding all the sensor plate leads to the body before they were fed through the body wall. The length of the leads bonded to the body was determined by analysis to prevent any conductive heat loss from the sensor plate to the environment.

Black paint is applied on the inside surface of the body to limit the reflection of incident radiation passing through the gap between the SP and body as shown in Figure 2.

Two high accuracy thermocouples, respectively soldered to the SP and the body, are used to monitor temperatures.

PRINCIPLE OF OPERATION

In a conventional flat plate calorimeter the flux absorbed by the sensing surface equals the flux radiated and conducted to the surrounding environment. The sensing surface reaches an equilibrium temperature, from which the absorbed flux can be computed through a calibration curve. For the computation to be valid the radiometer must be used in conditions equivalent to the calibration conditions. Otherwise, the heat leaks to the environment implicitly included in the calibration curve cause an error to be introduced in the computation. Another peculiarity of a conventional flat plate calorimeter is that the flux measurements can be made only when the temperature of the sensing plate has reached steady state.

The MBR can be classified as a flat plate radiometer but differs from the conventional type in that a second thermocouple is used to measure the background temperature. With this information, both the heat leaks to the background environment and the energy stored in the SP can be evaluated. These values are then used in the heat balance equation of the sensor plate to determine the heat flux absorbed. Because of this the sensor can be accurately used in a wide ranging temperature environment and the absorbed heat flux can be calculated even when the sensor plate temperature has not reached steady state.

A heat balance performed on the sensor plate yields:

$$Qcap + Qcond + Qrad/in + Qrad/out + Qabs = 0 \qquad (1)$$

where Qcap represents the energy stored in the sensor plate, Qcond the SP-to-body conductive heat transfer through the leads and stand-offs, Qrad/in the radiative heat exchange between the sensor and body, Qrad/out the radiative heat loss from the SP to the environment, and Qabs the radiant energy absorbed by the sensor plate.

To characterize the thermal behavior of the radiometer the MBR was mathematically modelled with two nodes. One of the node represents the sensor plate and the second one the body. A two-node model representation was chosen based on the simplifying assumption that temperatures are uniform along the SP and body. The assumption that material properties (specific heat, conductivity and surface emissivity) are constant with temperature was also made. Thus,

equation 1 can be rearranged:

$$F1\ dT/dt + F2(Ts-Tb) + \sigma F3(Ts^4+Tb^4) + \sigma As\ \varepsilon_s(Ts^4) - Qabs = 0 \quad (2)$$

where Ts and Tb are the sensor and body temperatures respectively. F1, F2, and F3 are calibration factors which are experimentally determined by measuring Qabs and the resulting Ts and Tb for different Qabs values.

CALIBRATION

The purpose of the calibration activity was to evaluate factors F1, F2 and F3 of equation 2.

The calibration tests were performed in a thermal vacuum (TVAC) chamber with LN2 cooled shrouds. For each MBR, five different power levels were supplied to the SP calibration heater to simulate the heat absorbed by the sensor plate, and the SP and the body temperatures were recorded as a function of time.

For the calibration process the heat absorbed by the sensor plate Qabs can be expressed to account for heat radiation from the chamber wall:

$$Qabs = Qm + \sigma As \varepsilon_s\ Tw^4 \quad (3)$$

where Qm is the measured heater power and Tw the chamber wall temperature, and Qabs here is the simulated absorbed flux.

Equation 2 can then be rewritten:

$$Qcalc - Qabs = 0 \quad (4)$$

where:

$$Qcalc = F1\ dT/dt + F2\ (Ts-Tb) + \sigma F3\ (Ts^4-Tb^4) + \sigma As\ \varepsilon_s\ Ts^4 \quad (5)$$

and Qcalc is the heat flux value calculated from the SP and body temperatures.

For each MBR the difference between the measured absorbed flux

(equation 3) and the calculated flux (equation 5) at time i is defined:

$$\phi_i = Qabsi - Qcalci \tag{6}$$

Function Φ is the summation of the square of the ϕ_i's .

$$\Phi = \sum_{i=1}^{n} (\phi_i)^2 \tag{7}$$

where n is the number of selected data points for each MBR.

F1, F2, and F3 were computed by minimizing Φ with the constraint that upper and lower bounds were defined for F1, F2, and F3. These bounds were centered about nominal values which were physically representative of the SP capacitance, conductive conductance and radiative conductance from the SP to the body. These bounds were necessary, because a least square minimization without constraints on the independent variables can result in calibration factor values with no physical significance.

The minimization of function Φ was performed using a simplex optimization code (4).

ERROR ANALYSIS

The total uncertainty of the MBR arises from the calibration uncertainty and the uncertainty for usage outside the calibration conditions.

CALIBRATION UNCERTAINTIES

The total calibration uncertainty of the MBR can be expressed as the sum of the RMS deviation of the calculated flux from the measured absorbed flux, and the uncertainties in the absorbed flux measurement.

DEVIATION OF THE CALCULATED FLUX

The goal of the calibration was to obtain an expression which could be used to calculate the flux absorbed by the sensor plate by measuring the SP and body temperatures.

The deviation of the calculated flux was defined as the RMS value of the difference between the calculated and the measured absorbed flux. This deviation can be attributed to the thermocouple uncertainty, the optimization process tolerance, and the simplifying assumptions of the MBR mathematical model.

The typical RMS deviation of an MBR was found to be less than 1% when calibrated with quasi-steady state data ($dT/dt \leq 0.5$ C).

UNCERTAINTY IN THE ABSORBED FLUX MEASUREMENT

The uncertainty in the measured absorbed flux is due to inaccuracies in measuring the heater power and the sensor plate surface area.

The measured absorbed flux consists of the heater power and the test chamber wall radiation (equation 3). The absorbed heat flux density is calculated from:

$$qabs = Qabs/As \tag{8}$$

where As is the sensor plate surface area.

The inaccuracy in the absorbed flux density can be calculated from:

$$\Delta qabs/qabs = \Delta Qabs/Qabs + \Delta As/As \tag{9}$$

where (from equation 3)

$$\Delta Qabs/Qabs = (\Delta Qm + 4\,\sigma\, As\, \varepsilon_s Tw^3 \Delta Tw)/Qabs \tag{10}$$

The contribution of the Tw inaccuracy to the measured absorbed flux inaccuracy can be neglected, and equation 10 is rewritten:

$$\Delta Qabs/Qabs \simeq \Delta Qm/Qm \tag{11}$$

The power dissipated by the heater is measured from the voltage drop across the heater V1 and across a shunt resistance V2 such that:

$$Qm = V1*V2/R \tag{12}$$

where R is the shunt resistance value. The error in R is $\leq$ 1%, in V1 << 0.1%, and in V2 $\leq$ 1%. Thus the total error in Qm is

$$\Delta Qm/Qm = \Delta V1/V1 + \Delta V2/V2 + \Delta R/R \tag{13}$$

$$\simeq 2\%$$

The error on the sensor area was estimated to be $\Delta As/As = 0.5\%$ such that the uncertainty on the absorbed flux density due to the heater power and sensor area measurement uncertainties is 2.5%.

The total calibration uncertainty is the sum of the measured flux inaccuracy (2.5%) and the deviation of the calculated flux from the measured (< 1%). This results in a total calibration uncertainty of less than 3.5% for the MBR.

UNCERTAINTIES FOR USAGE OUTSIDE CALIBRATION CONDITIONS

An additional source of error during the usage of the MBR is the heat transfer between the sensor plate and the environment via the gap between the SP and body. This error was shown to be < 0.1% by analysis.

During the usage of the MBR the temperature difference Ts-Tb varies between 0°C and 30°C, which is less than the temperature difference in calibration, where Ts-Tb varied from 100°C in rapidly changing conditions to 40°C at steady state. Larger Ts-Tb values in calibration result in higher accuracies of the calibration factors F2 and F3. However, as can be seen from equation 1, for the limiting case when the Ts-Tb values approach 0 the contribution of factors F2 and F3 is decreased, in which case the absorbed heat flux value can be calculated from:

$$qabs = \sigma \varepsilon_s Ts^4 \qquad (14)$$

The total error is then given by:

$$\Delta qabs/qabs = \Delta \varepsilon_s / \varepsilon_s + 4\,\Delta Ts/Ts, \qquad (15)$$

Therefore an uncertainty of $\pm$ 1% in ε_s, and of $\pm$ 0.2°C in Ts results in a total error of $\pm$ 1.2% for Ts = 130°C and $\pm$ 1.5 % for Ts = -100°C. Usually during testing, Ts-Tb varied from 0 to 30°C at steady state resulting in a total error between $\pm$ 3.5% and $\pm$ 1.5%.

RESULTS

Results of a typical MBR calibration are presented in Table 1. It shows that the RMS error between the calculated and measured flux is 0.85 % for a range of flux values varying from 8 % to 100 % of a solar constant (absorbed).

Results from an actual test where the MBR was used to measure the absorbed flux radiated from IR lamps are presented in Figure 3. It shows the time response of the MBR to a step change of 320 W/m**2

in the incident flux intensity. For curve 1 the capacitance term F1 was included in the flux calculation process, and for curve 2 it was omitted. At the first data point available, after 5 minutes, the flux prediction was 2.8% off for curve 1 from the final stabilized value of 700 W/m**2, and it was 17% off for curve 2 where the flux prediction was made without the capacitance term.

CONCLUSION

This paper has presented the design, development and calibration of a simple , light and accurate radiometer. This radiometer can be used in infrared or solar illumination testing of spacecraft, and requires no fluid loops or power supplies. Results highlighting the quick time response of the device to step heat inputs and the accuracy over a wide range of incident flux were presented.

The monitored background raiometer design was shown to be adequate and reliable during the infrared testing of the Olympus (5) satellite thermal model where 80 MBR's were used to measure the flux absorbed by spacecraft surfaces.

SYMBOLS

As	sensor plate surface area (m**2)
F1	capacitance calibration factor
F2	conduction calibration factor
F3	radiation calibration factor
q	power density (watts/m**2)
Q	power (watts)
T	temperature (Kelvin)

Greek Symbols:

ε	surface emissivity
σ	Stefan-Boltzman constant

Subscripts:

abs	absorbed
b	body
calc	calculated
cap	capacitance
cond	conductive
m	measured
rad	radiative
s	sensor plate
w	test chamber wall

REFERENCES

1. Bachtel, F.D. and Loose, J.D., "Design and Control of an Orbital Heating Simulator", AIAA paper 71-432, AIAA 6th Thermophysics Conference, April 1971.

2. Gilcrest, A.S. and Mon, G.R., "A Calorimeter for Determining Thermal Radiation Fluxes in Space Simulation Chambers", Proc. Inst. of Environmental Sciences, 1963, p. 369.

3. Redman, R.S. and Wolff, C.M., "Development of a Multipurpose Radiometer", Vol 16, #5, Journal of Spacecraft and Rockets, Sept./Oct. 1979, p. 350.

4. Siddall, J.N., " 'OPTISEP' Designers' Optimization Subroutines ME/71/DSN/REP1", Faculty of Engineering, McMaster University, Canada, 1970, pp. 28-32.

5. Donato, M. et al., "Design of an Orbital Heating Simulator Using IR techniques", Fourteenth AIAA-NASA/ASTM/IES Space Simulation Conference, NASA CP- ,1986.

Qm/As (W/m)	93	166	538	897	1220	COMBINED FOR ALL DATA
N	7	11	13	26	11	68
RMSe	2.1	0.59	0.75	0.67	0.4	0.85

NOTES:
1) Qm/As is the measured flux in the calibration heater divided by the sensor surface area

2) N is the number of data points at each power level

3) RMSe is the RMS error in per cent between Qm and Qcalc

Table 1 - Typical Calibration Results Versus Power Level

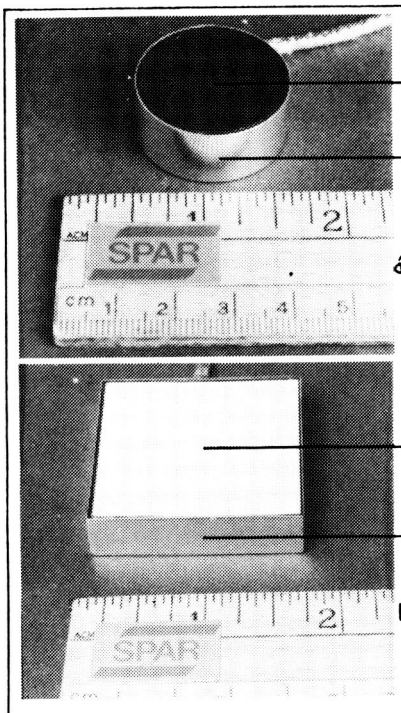

Figure 1 - MBR Types

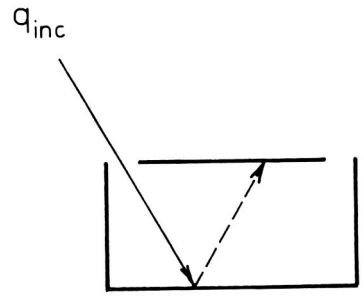

Figure 2 - Reflected Incident Radiation

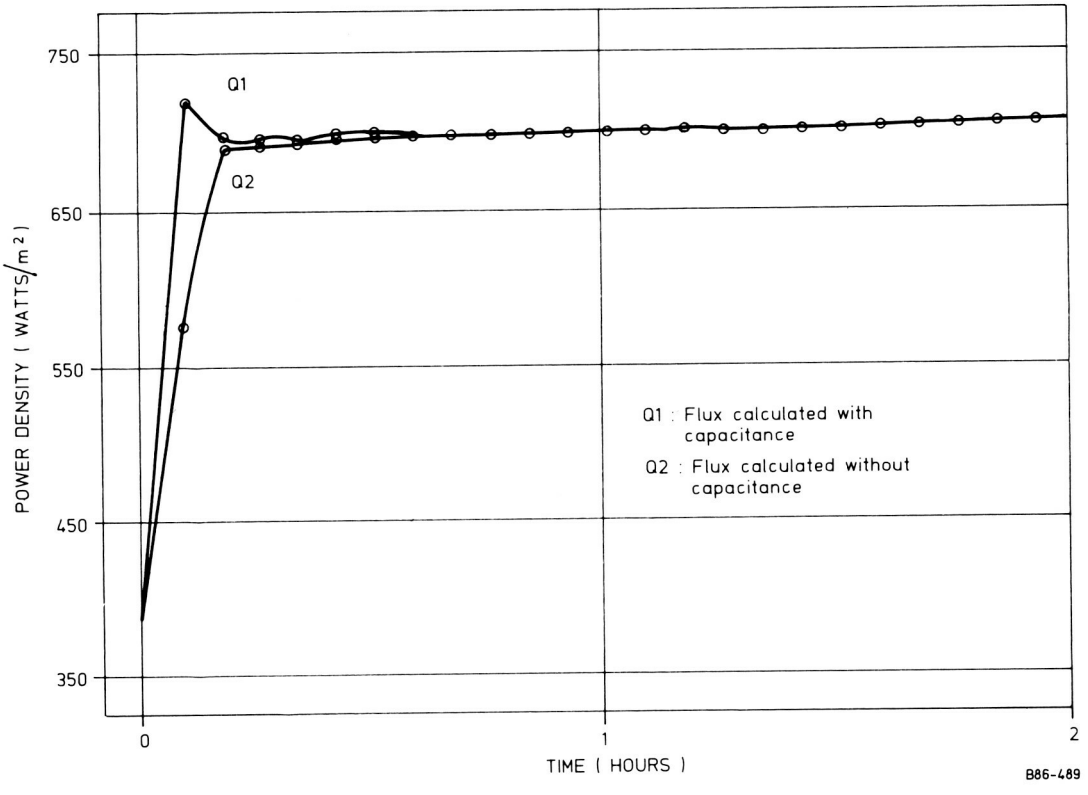

Figure 3 - Response to Infrared Lamp Step Heat Input

ROCKET NOZZLE THERMAL SHOCK TESTS IN AN ARC HEATER FACILITY

James H. Painter and Ronald A. Williamson
McDonnell Douglas Astronautics Company

BSTRACT

The McDonnell Douglas Astronautics Company (MDAC) has developed a rocket motor ozzle thermal-structural test technique that utilizes arc heated nitrogen to imulate a motor burn. The technique was used to test four heavily instrumented full-cale Star 48 rocket motor 2D carbon/carbon nozzle segments at conditions simulating ne predicted thermal-structural environment. All four nozzles survived the tests ithout catastrophic or other structural failures. The test technique demonstrated romise as a low cost, controllable alternative to a rocket motor firing. The echnique includes the unique capability of rapid termination in the event of failure nat allows post-test analysis.

NTRODUCTION

In February 1984 the McDonnell Douglas Astronautics Company (MDAC) Payload sist Module (PAM) failed to boost two communications satellites into their proper ansfer orbits. As part of the failure investigation, the MDAC Aero and Thermo-namics Laboratory was requested to develop a nozzle thermal-structural test chnique that utilized the High Impact Pressure (HIP) Arc Heater Facility.[1] After tensive development testing and environment calibrations, full scale truncated nical segments of 2D carbon/carbon nozzles were tested at conditions which mulated the thermal structural conditions which exist in an actual motor firing.

The objectives of these tests were to simulate the thermal structural envir-ment encountered by a carbon/carbon rocket motor nozzle during the first 8 s of burn d to rapidly terminate if any problems developed. The nozzle was instrumented to ovide analytical correlation, identify failure regions, mechanisms and sensitivity density variations with the carbon/carbon exit cone. The test technique utilized high power electric arc heater[2] operating on pure nitrogen at stagnation pressures om 0.9 to 1.4 MPa and stagnation temperatures from 5000 to 6700 K. The heated trogen was expanded to Mach 2 through a narrow annulus formed by a conical personic flow guide (SSFG) and a full scale truncated conical segment of the nozzle be tested. The expansion was designed to yield close simulation of the local ating rates and pressures encountered by the nozzle in an actual firing.

The test phase consisted of four carbon/carbon nozzle assemblies. The first st established the baseline thermal response characteristics using a standard zzle. The second nozzle had low density variations (DV's) identified using mputed Tompography (CT) inspection techniques. The third nozzle tested included personic flow guide modifications to more closely simulate flight conditions. The 's in the third nozzle were more severe than the second. The fourth nozzle which d passed stringent CT screening tests, was subjected to the same environment as mber three to ascertain its behavior in the same environment.

ANALYTICAL CONSIDERATIONS

The investigation had shown the most probable time of failure was 3 to 5 s after ignition. A maximum test duration of 8 s was established. The goal of these tests was to provide the heat flux and pressure required to simulate the temperature and temperature gradients which exist in the first 8 s of an actual motor firing. These conditions were established by extracting the temperature, heat flux and pressure from the detailed analytical model used for thermal structural response during a motor firing and then analytically determining what test conditions were required to provide an equivalent environment with the test hardware. The conditions used to establish the test specifications are shown in Figures 1 and 2.

In order to meet the thermal-structural environment specifications in the HIP arc heater facility with a 12 MW arc power limitation, it was necessary to confine the arc heated gas to the nozzle wall region. That confinement required a conical flow guide inside the 2D carbon/carbon nozzle, as shown in Figure 3, to reduce the gas flow requirement to the order of 0.5 kg/s. The flow guide outer contour (Figure 3) became a major design consideration since it controlled the gas expansion and thereby the local pressures and, to a large degree, the local heat transfer coefficients. An extensive boundary layer analysis resulted in four contours being tested in the course of this program. Only two of these contours were used in nozzle firings.

SUBSONIC FLOW GUIDES

Subsonic flow guides were designed to maintain subsonic flow to near node 56, provide a smooth flow transition from the exit of the arc heater to the annular throat and minimize the heating to the side walls. Figure 3 shows the geometry of the flow guides and their relative position during the calibration and nozzle tests. Flow from the arc heater is subsonic (Mach = 0.33) and remains subsonic (flow area increasing) until it approaches the throat region. Near the throat the area decreases to an equivalent throat diameter of approximately 2.5 cm and then increases allowing the flow to expand to supersonic velocity and lower local pressures. Pressure data indicated that the blunt nose shown in Figure 3 provided a smooth flow transition from the heater exit to the throat region. An earlier sharper nose choked the flow upstream of the intended throat and created significant pressure losses. The blunt nose also provided a significant reduction in heating to the front end.

SUPERSONIC FLOW GUIDE

The annular flow channel between the nozzle and the supersonic flow guide was designed to produce local pressures and surface temperatures to meet the nozzle thermal requirements. This was accomplished by contouring the conical section to a specified gap height.

The initial heat transfer calculations were made using the MINIVER code[3] and its cone flow option. These calculations used air properties and the surface emissivities were varied from zero to unity bracketing the required stagnation conditions. The supersonic flow guide was a severe heat sink in close proximity to the nozzle. Since the nozzle liner was 2D carbon/carbon and the initial flow guide was graphite there was a significant difference in temperature response for a short test. Consequently, it was necessary to use gas stagnation temperatures that were significantly higher than the rocket motor combustion products stagnation tempera-

ture (3550 K) in order to compensate for radiation from the nozzle to the flow guide. Subsequent calculations improved on the MINIVER predictions by using nitrogen gas properties, better conduction models, and closer approximations of the surface emissivities. These calculations indicated higher required stagnation temperatures.

Nominal nitrogen gas stagnation conditions were selected after completing arc heater calibrations to define the stagnation pressure, mass flow rate, current, voltage and stagnation enthalpy using an effective throat diameter of 3.18 cm. Combining these results with heating rate calculations, the following conditions were selected to meet the nozzle requirements: Stagnation pressure = 1.2 MPa, stagnation enthalpy = 7.9 MJ/kg, mass flow = 0.36 kg/s, and arc current = 1700 A.

The location of the annular throat was selected to yield the desired local pressures with the above stagnation conditions. The resultant throat was approximately 0.64 cm upstream of the carbon/carbon nozzle leading edge (Figure 3). The flow is nearly conic from this location to the exit of the skirt.

The inviscid flow area required to produce the desired pressure distribution along the nozzle was calculated for nitrogen gas expanding from the stagnation conditions described above. At this condition the ratio of specific heats for nitrogen is approximately 1.22. The inviscid flow area was calculated at approximately 1.27 cm axial intervals along the nozzle.

To prevent velocity and pressure decrement in the channel, the viscous boundary layer displacement thickness was calculated and added to the channel height. The calculations were performed by MDAC-HB using a boundary layer code that compares well with experimental data. Figure 4 presents the inviscid and viscous thicknesses along the channel. The displacement thickness (viscous value) must be multiplied by two to account for the boundary layer growth on both the guide wall and nozzle.

APPARATUS

The Star 48 nozzle thermal shock tests were conducted in the MDAC Arc Heater Facility.[1] The MDC-200 arc heater was used to heat nitrogen at pressures from 0.9 to 1.4 MPa to temperatures from 5000 to 6700 K. The heated gas was then expanded through hardware designed and fabricated specifically for this test program. The MDC-200 arc heater has been described previously[2] and no major modifications were made to it for these tests. The arc heater nozzle throat that controls the gas mass flow-pressure-enthalpy relationship was formed by the new flow guides with the equivalent diameter ranging from 2.54 to 3.18 cm.

ARC HEATER

The nitrogen stagnation temperature and pressure available for these thermal shock tests was determined through two series of arc heater calibrations. The first series used four power units in a series parallel arrangement. The upper arc current limit was approximately 1800 A. The second series of tests used three parallel power units in series with two parallel higher current units yielding an upper arc current limit of approximately 3000 A for periods of less than 10 s. The nozzle throat diameters for these calibrations were 2.54 and 3.18 cm.

Figure 5 shows the performance of the MDC-200 arc heater operating on nitrogen over the complete range of calibration. Data are included for two forward electrode lengths (68 and 91 cm). In general, a higher gas temperature can be achieved with the

shorter electrode and the smaller nozzle throat. Higher enthalpies can be achieved at higher arc current. As dissociation of the nitrogen begins, the gas temperature increase does not follow the rate of enthalpy increase (lower gas specific heat).

One critical test requirement was rapid stabilization. Simulation of a rocket motor firing required full flow conditions within 0.5 s of start-up. The gas flow control system and the arc current controllers in the HIP facility were modified to attempt to meet this requirement. Rapid action regulators were installed in the main gas flow lines to the arc heater and their opening rates were adjusted to achieve minimum start time without arc extinction (blow-out). Meter relays were used to sense arc current and trigger the regulator loading via solenoid valves. The arc current controllers were set to yield maximum demand on start-up and then switched to a pre-set level shortly thereafter. In later tests, a third controller was used to yield current reductions during a test. The arc heater starting characteristics shown in Figure 6 are typical of the rapid response achieved in the actual nozzle tests. The 10 to 90% rise time to full heating for the Phase I tests was 0.5 s. It was slightly longer for the Phase II tests (0.8 s) due to the higher arc current requirement.

SUPERSONIC FLOW GUIDE

Eight supersonic flow guides were fabricated with four different external contours for these tests. The first SSFG assembly was used for only one calibration test and then discarded when a crack developed in the vertical forward face of the ATJ graphite. The second configuration determined that the local pressures and heating rates were too low requiring modifications to the subsonic nose region. In the third configuration, the ATJ-S nose and centering plug were combined into a single piece and the contour was blunted significantly to avoid pressure degradations from premature accelerations. This SSFG was used to test the first nozzle. During that test, thermal stress cracks were encountered in the sonic region of the ATJ cone. The sonic region was strengthened in the fourth and fifth configurations by using ATJ-S graphite. The ATJ-S sonic region was bonded to the ATJ cone using graphite cement. This configuration was used to test the second nozzle. Again thermal stress cracks developed in the sonic region but this time there was no significant separation of the pieces. A sixth SSFG was identical to the fourth for over-test calibrations.

Subsequent thermal analysis indicated the nozzle heat flux distribution needed improvement. A new contour was specified that was aimed at reducing the heat flux in the near sonic region, holding the same flux in the mid-region and increasing the flux at the exit. This was accomplished primarily by moving the sonic point upstream 1.27 cm and decreasing the gap width over the entire flowfield. In addition to the contour change, the material of the sonic region was changed from ATJ-S to 3D carbon/carbon. Figure 7 shows the design selected to improve the thermal strength.

The seventh SSFG shown in Figure 7 was used to test the third nozzle. After 4.5 s at the higher current condition, the ATJ aft skirt failed through the three pressure ports where stainless steel fittings were used. The 3D carbon/carbon was undamaged.

The eighth and final SSFG was identical to the previous design except that graphanol pressure fittings were used and an accelerometer was added. The accelerometer was protected by RTV insulation as shown in Figure 7. This configuration was used to test the fourth nozzle for 8 s. The SSFG was in excellent condition post-test.

CALIBRATION MODULE

Calibration modules (Figure 8) were used to define the thermal environment of the nozzle. Water-cooled calorimeters and pressure taps were used in conjunction with the SSFG instrumentation to document the cold wall heating rates, local pressures and thus local heat transfer coefficients from the sonic point to the nozzle exit. The instruments were located at stations defined by thermal model nodes as numbered by the original nozzle analysis. Node 56 was the entrance to the nozzle segment, node 121 was located 6.35 cm downstream, node 151 was 10.92 cm downstream and node 186 was 16.51 cm downstream. Node 186 was essentially the end of the SSFG and node 56 was very near the sonic point in the initial tests. Node 121 was used in the early design work as the nominal target point and node 151 was a convenient distribution point between node 121 and the exit.

The first calibration module was used in nine tests to define the flowfield for Phase I nozzle tests (Figure 9). This module failed in Test 1811 after 6.4 s at the intersection of the cylindrical body and the conical skirt just downstream of the flange. The entire cone separated banging against the SSFG causing a trapazoidal segment to break loose from the main body.

The second calibration module differed from the first in two ways. First, the failure region was beefed-up by machining a large radius at the conical blend (Figure 8) and second the calorimeters were relocated to nine locations. Three calorimeters were located at node 56, three at node 121 and three at node 186. The four pressure taps were also located at nodes 56, 121 (two). and 186. This module was used to calibrate the flowfield using two different supersonic flow guides in 16 tests and remains operational.

CALIBRATION TESTS

A total of 32 calibration tests were made to define the flowfield adjacent to the nozzle segment and improve the simulation of flight conditions. The first calibration series (Tests 1802-1811) optimized the heating rates at arc currents less than 1800 A and reduced mechanical deflections of the supersonic flow guide and arc heater. The second calibration series (Tests 1824-1830) established the heating rates at arc currents to 2900 A and reduced the thermal distortion from sting heating. The third calibration series (Tests 1831-1839) documented the high current heating rates using a modified contour on the supersonic flow guide and provided data on the effects of arc current variations during a test.

CALIBRATION DATA - SERIES I

The calibration data acquired in Series I, tests 1809 to 1811, were measured with the supersonic flow guide positioned to yield an annular throat area of 6.45 cm^2. The nitrogen flow rate was 0.36 kg/s. The measured pressures agreed favorably with the predicted values and thus the nozzle design values. Figure 9 compares the local static pressures at four locations to the nozzle design pressures. These data indicate less boundary layer growth than predicted and hence slightly lower static pressures at nodes 151 and 186 than predicted. The measured cold wall heating rates were higher than desired at node 91, very close to design values at node 121 and lower than desired at nodes 151 and 186 as shown in Figure 9.

Heat transfer coefficients were derived from the cold wall heating rates, local pressures and local enthalpies. The local enthalpies were estimated from measured stagnation enthalpies and estimated wall losses upstream of the point in question. The calculated heat transfer coefficients for tests 1806 through 1811 could be correlated as proportional to the local pressure to the 0.8 power from 65 to 350 kPa.

The local heat transfer coefficients were then used to estimate the hot wall heat flux as a function of time at nodes 56 and 121. The predicted hot wall heating rates are shown in Figures 10 and 11 where they are compared to the original predictions for the nozzle to be tested. The calibration data indicates an over-test at node 56 and a good match at node 121.

CALIBRATION DATA - SERIES II

The second series of calibration tests was conducted to determine the facility over-test capability (higher heating rate). The power supplies were reconfigured to allow arc currents to 3400 A. The calorimeters were relocated in the new module to yield better axial and circumferential distributions and two more calorimeters were added. This yielded three calorimeters at node 56, three at node 121, and three at node 186. They were aligned along three rays 120° apart with rows at 22°, 142° and 262° from top center. The pressure taps were located at nodes 56, 121, 151 and 186.

Tests 1825 through 1828 were conducted at constant nitrogen flow rates and constant effective throat area while the arc current was increased from 1480 to 2750 A. The averaged local heating rates increased 33% at node 56, 43% at node 121 and 30% at node 186 as a result of the 86% increase in arc current. The nitrogen stagnation enthalpy increased 46% but due to dissociation the temperature increased only 20%. The stagnation pressure increased 15% due to the hotter gas and constant mass flow rate. The expected heat flux improvement based on the increased heat transfer coefficient the increased gas temperature and the assumption that no recombination occurs in the boundary layer would be a 31% increase. Thus increased arc current does yield predictably higher heating rates but dissociation limits the increase.

CALIBRATION DATA - SERIES III

The third calibration series provided flowfield definition for the final two nozzles tested and perfected the technique of arc current variation during a test. The supersonic flow guide contour was modified to move the sonic point 1.27 cm upstream and thus decrease the heat flux at node 56, hold the same level at node 121 and increase the flux at node 186.

The new SSFG contour improved the heat flux distribution. A comparison of the data from Series II and III shows a 10% reduction in heat flux at node 56, no change at node 121 and a 68% increase at node 186. The reduction at node 56 was not as desired but the contour was judged to be acceptable for nozzle testing.

ROCKET MOTOR NOZZLE THERMAL SHOCK TESTS

Four full-scale nozzles were subjected to the environments summarized in Table 1, simulating a rocket motor firing. These nozzles were truncated conical segments of Star 48 rocket motors fabricated using production materials processes and tooling. The objectives of these tests were to validate thermal/structural response predictions, to determine the sensitivity of these nozzles to low density regions in the 2D carbon/carbon exit cone, and to identify any failure regions and/or mechanisms.

The four nozzles tested were delivered by Morton-Thiokol with thermocouples, strain gauges and pressure transducers installed. The exit cones used in the first and fourth nozzles passed the CT screening criteria, the second and third nozzles contained exit cones which had low density regions (DV's) identified by Computed Tomography (CT) inspection techniques.

Figure 12 illustrates a typical nozzle segment. It consists of a 2D carbon/carbon truncated conical liner, a two-piece carbon/phenolic insulator, a titanium closure and a titanium adaptor ring. Two layers of carbon felt were wrapped around the outside of the downstream end. The minimum inside diameter of the 2D carbon/carbon liner was 12.2 cm and the exit inside diameter was 30.5 cm. The cone half-angle was 24°. Thermocouples, strain gauges, pressure taps and accelerometers instrumented the nozzle tests. The instrumentation was completely outboard of the 2D carbon/carbon liner. The strain gauges were outboard of the carbon phenolic insulator and the accelerometers were outboard of the titanium closure. Two pyrometers were focused on the nozzle near the SSFG exit during all four tests.

In addition to the nozzle instrumentation, each test included standard arc heater facility instruments, the SSFG instruments and displacement or deflection instruments. The standard arc heater over-pressure interlock was the primary test terminator in the event of a catastrophic nozzle failure. Three motion picture cameras were also used to record each test. The top and side cameras normally used color film. The bottom camera normally used black and white film for fast developing. The frame rates varied from 400 to 800 fps.

PHASE I - THERMAL SHOCK TESTS

The first nozzle was tested at a nitrogen stagnation temperature of 5670 K. The stagnation pressure and enthalpy are shown in Table 1. Ten thermocouples were in contact with the 2D carbon/carbon liner along two rows 180° apart. Nine thermocouples were located in the carbon phenolic insulator along two rows 180° apart and 2.5 cm circumferentially away from the liner rows. One thermocouple was located in the bottom of the locking pin hole and one near a strain gauge. Six strain gauges were bonded to the carbon phenolic insulator.

Figure 12 shows the nozzle in place prior to Test 1812. The supersonic flow guide is retracted showing its surface as well as the inside nozzle surface. The SSFG mounting sting had not yet been covered with the cylindrical heat shield in order to illustrate the mounting and alignment apparatus. The alignment of the SSFG with the nozzle was critical and great care was taken to precisely align the two cones.

In the first nozzle test the steady-state conditions were reached in 0.75 s and 90% of the full pressure in 0.50 s. The stagnation pressure increased at about 100 kPa/s during the test as the energy losses to the flow guides decreased. At 6 s into the test, there was an abrupt pressure increase. At 6.34 s, a SSFG thermocouple rapidly increased in output indicating internal gas flow. At 7.09 s the over-pressure interlock terminated the test. The pre-set test time was 8 s.

Post-test inspection revealed the ATJ graphite SSFG had failed circumferentially in the near sonic region (maximum heat flux) and a section of the guide had partially blocked the flow creating the over-pressure termination at 7.09 s. The interior of the nozzle was coated with a white deposit of zinc chromate from the nozzle region between the 2D carbon/carbon liner and the carbon phenolic "dixie cup" insulator. The asymmetric pattern was caused by a combination of SSFG deflection and

fracture. Two sections from the sonic region separated from the SSFG and wedged against the 2D carbon/carbon liner.

The test data was reviewed and an excellent temperature correlation was found for selected points. There were several obviously bad contact thermocouples. The optical pyrometer data correlated well with the analysis. Carbon phenolic temperatures reached as high as 1000 K during post-test soak.

Figure 13 compares the predicted flight surface temperatures to those derived from an analysis that included actual calibration data for and stagnation gas properties from the first nozzle test. The comparison in Figure 13 shows higher than desired temperatures at node 56, a reasonable simulation at node 121 and lower than desired temperatures at node 186.

The sonic region material of the SSFG was changed to ATJ-S graphite in an attempt to strengthen the assembly and test the full 8 s on the second nozzle. A copper spray ring was attached to the titanium closure to bathe the carbon felt in cool gaseous nitrogen and prevent post-test combustion.

The stagnation pressure was essentially constant at 1.1 MPa throughout Test 1813. The stagnation enthalpy was 7.7 MJ/kg. The slightly lower pressure resulted in slightly lower heating rates on the second nozzle than on the first. Following the test, the carbon felt was removed immediately and the SSFG was retracted much faster than the first test. As a result, the peak temperatures post-test were lower in the carbon phenolic. A low nitrogen flow rate purged the flow field post-test which also helped to reduce post-test heat soak and preserved the model for examination.

In general, the interface temperature data correlated reasonably well with the analysis (Figure 14). It was apparent that the second nozzle test ended with an asymmetric flowfield. The oxide patterns on the nozzle and the SSFG surfaces were the first indication of asymmetry and the temperaure measurements confirmed it. Additional thermal protection was incorporated on the sting and sting holder for Phase II to reduce the SSFG deflections that cause asymmetric flow.

Conclusions drawn from the Phase I tests were: (1) the test facility was capable of providing a good simulation of node 121 temperatures and pressures, (2) SSFG and/or nozzle deflections resulted in asymmetric heating, (3) temperature data indicated the desired temperature gradient was achieved in the critical area, and (4) there was no catastrophic failure of either nozzle.

PHASE II - THERMAL SHOCK TESTS

The contour of the SSFG was changed to reduce the heating rate at node 56 relative to node 121 and the stagnation temperature and pressure were increased to raise the heating rates at node 186. The increased gas temperature was achieved through significantly increased arc current and a shorter arc heater cathode. Nitrogen dissociation limited the temperature rise. An arc current of 3000 A was required to achieve a 6670 K stagnation temperature.

Twenty-two thermocouples were located along six conical rays. Four of the rows each contained four thermocouples at the carbon/carbon outside surface to yield a direct symmetry check. Five thermocouples measured carbon phenolic temperatures and one was located at the bottom of the locking pin hole. Two transducers were added to sense the venting pressure between the liner and insulator 5 cm upstream of the insulator exit and 180° apart.

The Phase II SSFG was designed to incorporate a 3D carbon/carbon sonic region. This significantly enhanced the high temperature strength of the flow guide in the high heat flux region. The contour of the SSFG was modified to move the sonic point forward of the previous location and to reduce the gaps on the entire flowfield.

In the test of the third nozzle, a stagnation pressure of 1.3 MPa was achieved in 1 s and the pressure then rose linearly to 1.4 MPa at 3.25 s followed by a decrease to 1.3 MPa at 4 s. The gas enthalpy reached 10.9 MJ/kg in 3.25 s and then was decreased to 8.1 MJ/kg for the remainder of the test. At 4.5 s into the test, the SSFG graphite aft skirt fractured and the test was manually terminated at 5.1 s.

Post-test inspection of the 2D carbon/carbon nozzle liner revealed ten delaminations on the inside surface in the high heat flux region. Two additional delaminations were just starting. The worst delamination was 5 mm deep. The effluent appeared quite symmetrical and this was verified by both temperature and pressure data. The ATJ graphite aft skirt of the SSFG fractured into several pieces. The 3D carbon/carbon sonic region held up well with only a few fibers missing from the surface. The fractures of the SSFG aft skirt were attributed to differential thermal expansion between the node 121 pressure tap fittings, which were stainless steel, and the graphite. The stainless steel fittings thermally expanded inside what was already a stress concentration at four times the graphite expansion rate causing fracture initiation. Subsequent tests used graphite fittings with aluminum oxide interior sleeves to reduce leakage.

Even though the stagnation conditions were higher than planned, the larger flowfield gap apparently resulted in lower temperatures than predicted. Figure 15 compares the predicted flight surface temperatures of the 2D carbon/carbon nozzle to those derived from an analysis that included actual calibration data for and gas state properties from the third nozzle test. The comparison in Figure 15 shows a distinct improvement in simulation over the first two nozzle tests. The temperatures are lower than desired at 5 s but higher than flight at 3 s.

Three general conclusions were reached regarding the third nozzle test: (1) the flow was symmetrical, (2) a good simulation of the surface temperature profile was produced, and (3) the temperature gradient through the carbon/carbon was in good agreement with flight predictions.

Several improvements were made in the instrumentation for the final nozzle test. Another 14-channel tape recorder was added to yield higher frequency data. Six strain gauges, three SSFG pressures, two displacement measurements, one vent pressure, one microphone and a time code were recorded on the new unit. An accelerometer was mounted inside the SSFG with elaborate heat shielding (see Figure 7). Linear potentiometer displacement transducers were attached to the nozzle to measure vertical and lateral movement.

The test plan was to achieve a stagnation pressure of 1.4 MPa and a stagnation enthalpy of 10.5 MJ/kg at 3.25 s then decrease the pressure to 1.2 MPa and enthalpy to 7.8 MJ/kg. The desired test time was 8 s. The objective was to provide a test environment as close to flight (and the third nozzle test) as possible for a nozzle that passed all acceptance criteria. The actual test conditions came very close to the planned conditions. The total test time was 8.03 s. The test conditions were virtually identical to those for the third nozzle.

There were five nozzle surface delaminations plus one just starting in the high heat flux region. They were shallow and visible only with a high intensity light. All delaminations appeared to be at the feathered end of the 2D carbon/carbon layers.

There was a significant improvement in the quality of the thermocouple data primarily due to the improved installation technique. The temperatures measured at the insulator-liner interface near the knuckle region were in reasonable agreement with the predictions. The external temperature aft of the closure was also in reasonable agreement with predictions. Temperatures measured at the downstream interface were higher than predicted but the optical pyrometer data obtained on the inner surface near that location were in good agreement with predictions.

Figure 16 compares the predicted flight surface temperatures of the 2D carbon/carbon nozzle to those derived from an analysis that included actual calibration data for and gas state properties from the fourth nozzle test. This comparison shows the best flight simulation achieved to date.

SUMMARY

The MDAC-STL Aero and Thermodynamics Laboratory developed a Rocket Motor Nozzle Thermal-Structural Test Technique utilzing the High Impact Pressure (HIP) Arc Heater Facility. The technique was then used to test four Star 48 rocket motor truncated conical nozzle segments at conditions simulating the predicted nozzle environment. Two of the nozzles had passed the new CT screening criteria and two had not. A very good simulation of the predicted thermal pulse at the forward end of the motor exit cone through 8 s of motor burn was achieved.

Significant problems with this test technique included high thermal stress on the supersonic flow guide (SSFG), deflection and thermal distortion of the SSFG sting assembly, and post-test nozzle thermal soak caused by the presence of the hot SSFG. SSFG thermocouple and pressure fitting problems also plagued the tests.

The technique developed and used in these tests has demonstrated considerable promise as a low cost alternative to a rocket motor firing for investigation of failures, screening of materials, development of new designs and batch qualification of production hardware. Further development of the technique should include advanced materials for the SSFG aft section, an improved pedestal for the SSFG to further avoid deflections, improved instrumentation inside the SSFG, and additional terminators in the event of failures.

REFERENCES

1. Rinehart, W. A., Painter, J. H., Williamson, R. A., et al, High Impact Pressure (HIP) Arc Heater Facility, 17th Anual Technical Meeting of the Institute of Environmental Sciences, Los Angles, CA 1971.

2. Painter, J. H. and Ehmsen, R. J., A 12 MW, 200 atm Arc Heater for Reentry Testing, AIAA J. 9, 2307 (1971).

3. Hender, D. A., A Miniature Version of the JA70 Aerodynamic Heating Computer Program, H800 (MINIVER), McDonnell Douglas Report MDC G0462, June 1970 (revised January 1972).

Table 1
Star 48 rocket motor nozzle segment tests

11–6269

TEST NO.	DATE	NOZZLE NO.	STAGNATION PRESSURE (MPa)	STAGNATION ENTHALPY (MJ/kg)	TEST TIME (s)	RESULTS	THERMAL STRUCTURE SIMULATION
1812	10 MAY 84	1	1.2 – 1.3	8.1	7.09	NO EXIT CONE DAMAGE.	UNDER FLIGHT PREDICTIONS.
1813	15 MAY 84	2	1.0 – 1.1	7.7	8.03	ONE SLIGHT DELAMINATION	UNDER FLIGHT PREDICTIONS.
1840	19 JUNE 84	3	1.3 – 1.4	8.1 – 10.9	5.09	TWELVE DELAMINATIONS	FLIGHT PREDICTIONS.
1841	09 JULY 84	4	1.3 – 1.4	7.7 – 10.9	8.00	SIX DELAMINATIONS	FLIGHT PREDICTIONS.

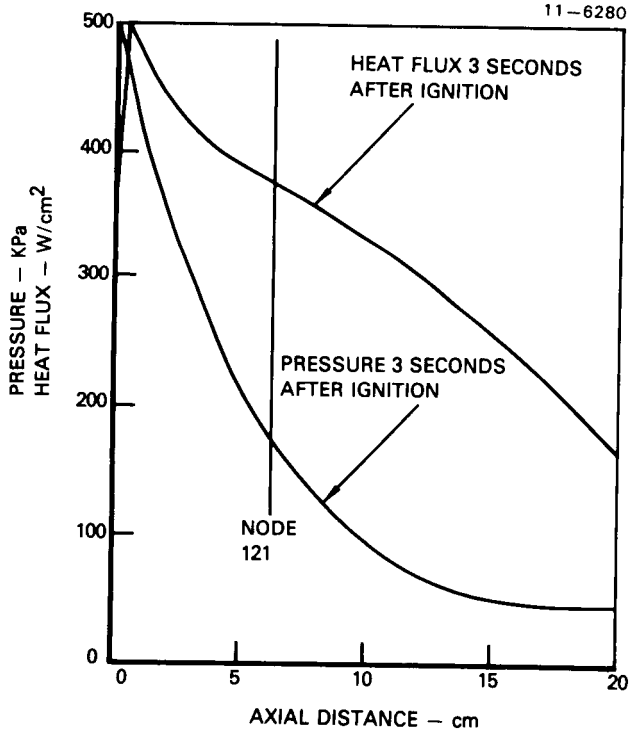

Figure 1. Nozzle surface heat flux specifications

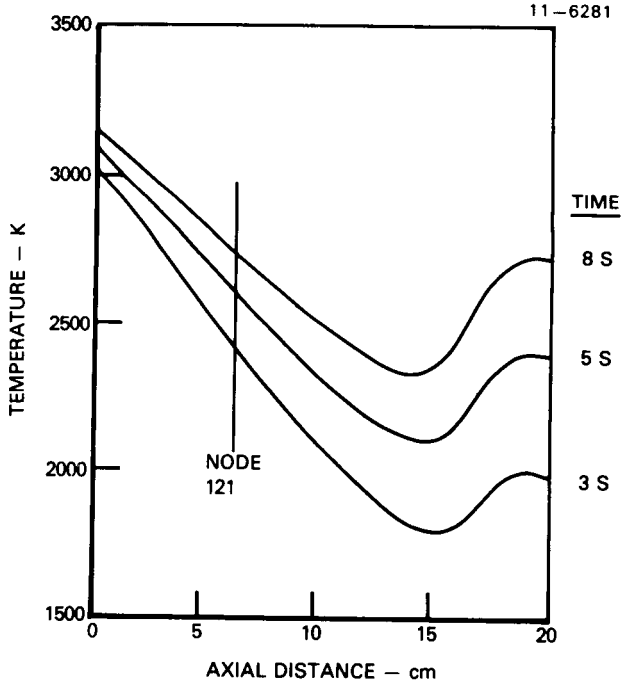

Figure 2. Nozzle surface temperature specifications

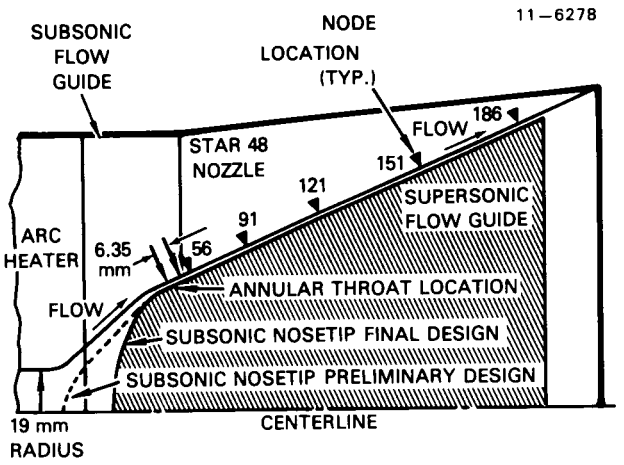

Figure 3. Schematic diagram of rocket nozzle test technique

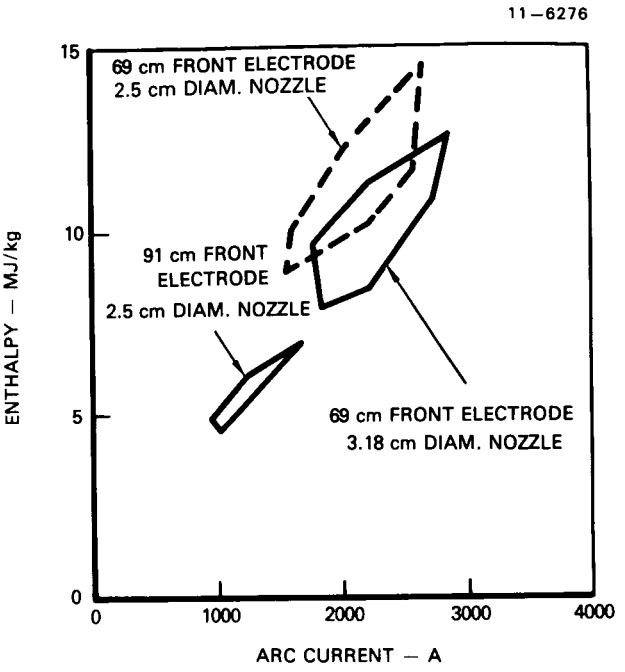

Figure 5. Arc heater calibrated enthalpy range for nozzle tests

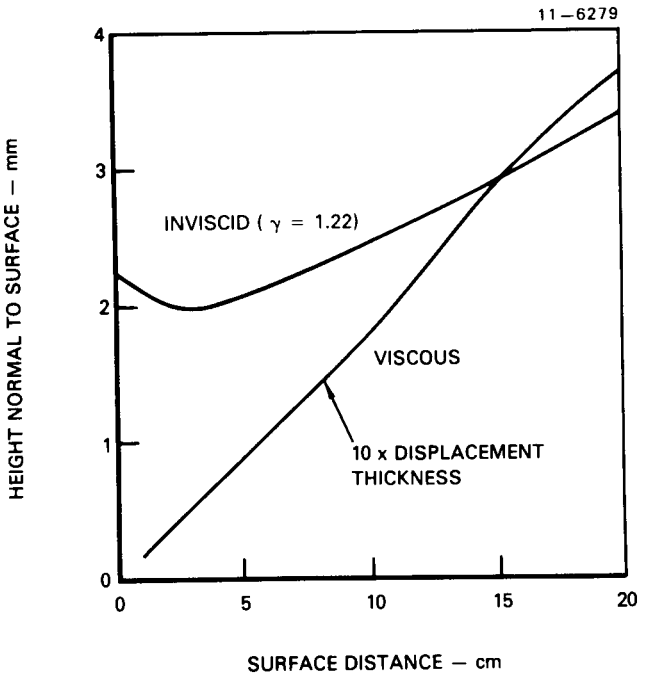

Figure 4. Flow channel height derivation

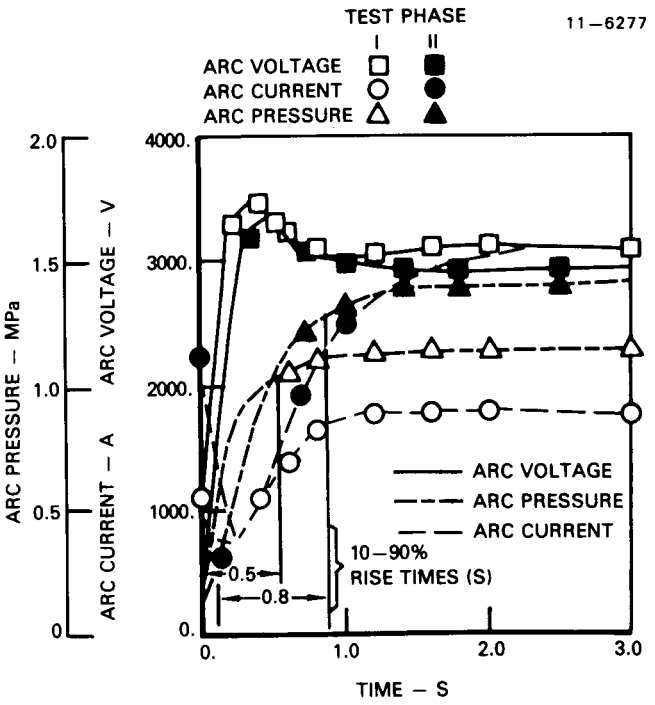

Figure 6. Arc heater start characteristics

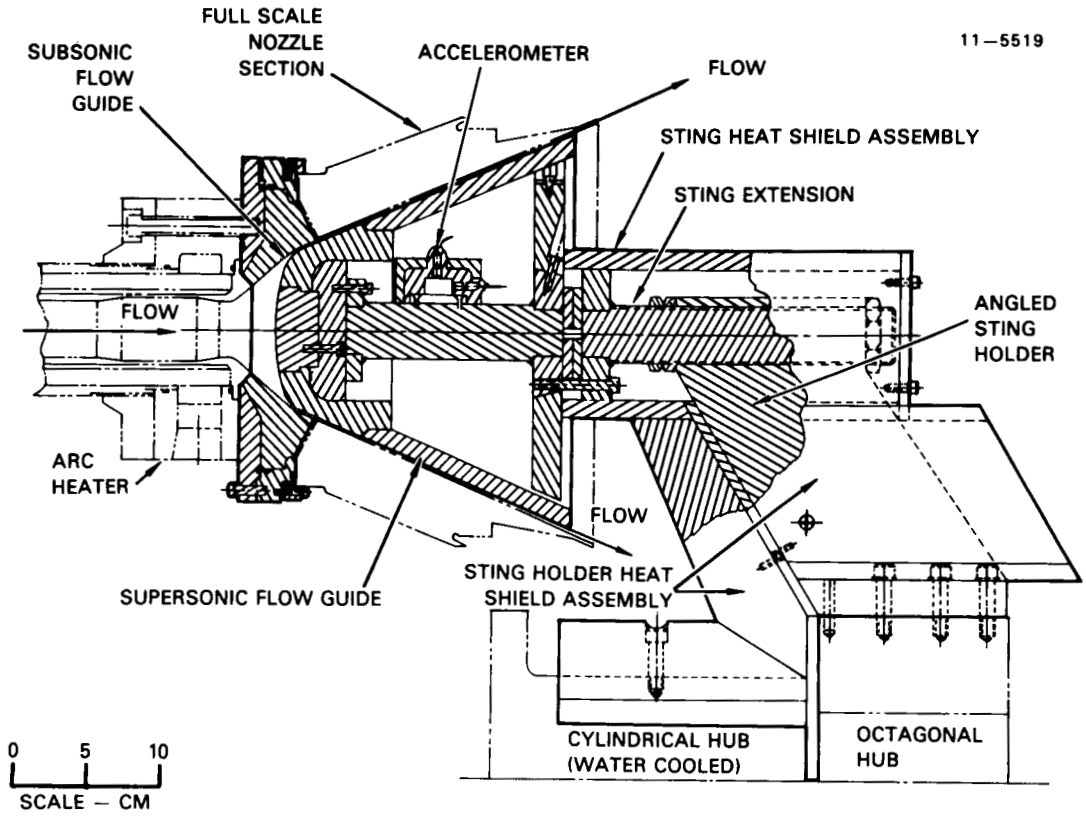

Figure 7. Flow guide assembly for phase II nozzle tests

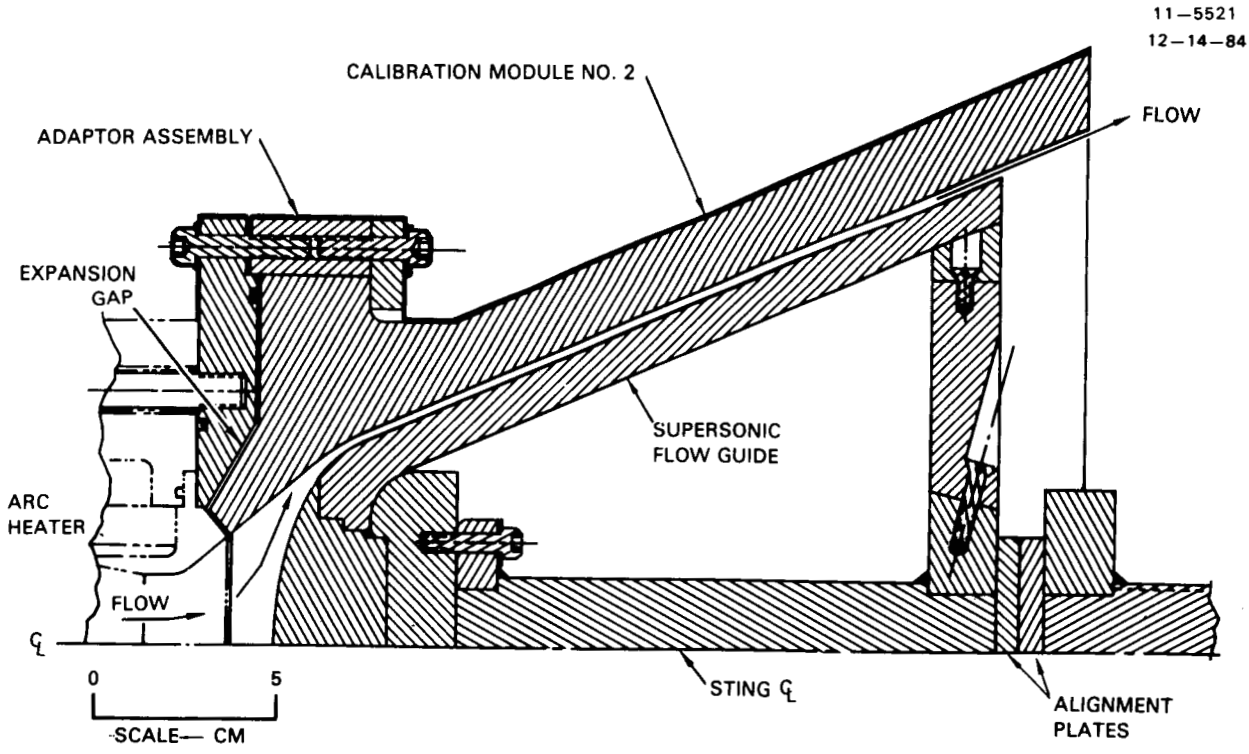

Figure 8. Nozzle environment calibration module

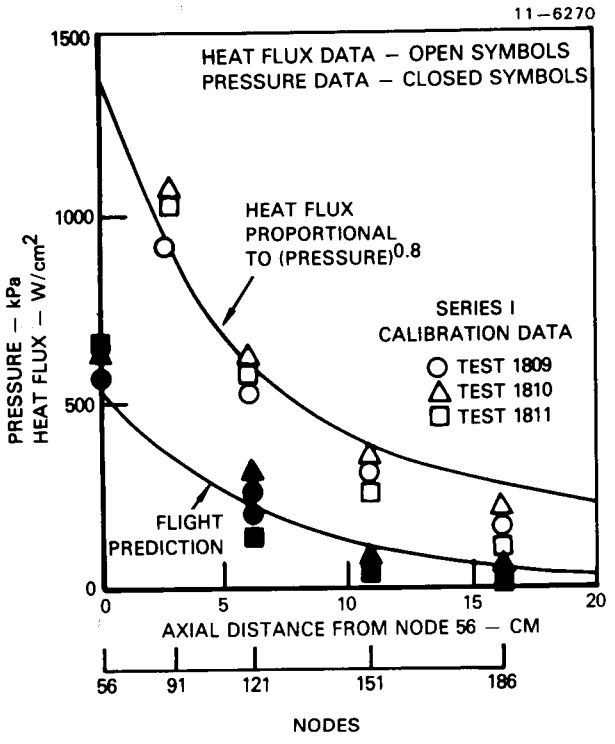

Figure 9. Heat flux profiles from calibration series I

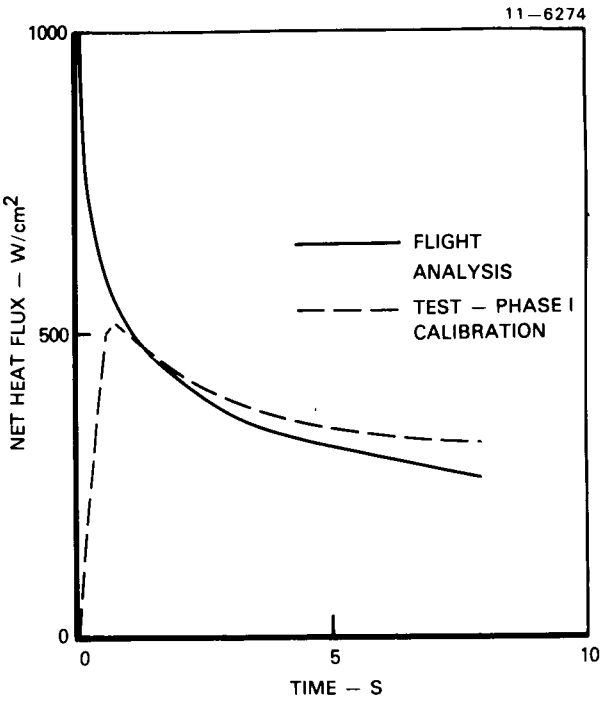

Figure 11. Comparison of flight and test heat flux predictions at node 121

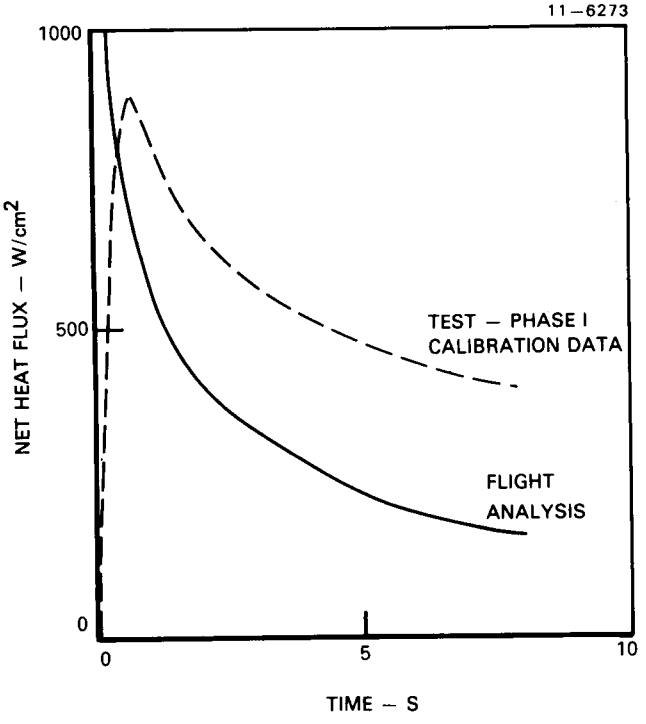

Figure 10. Comparison of flight and test heat flux at node 56

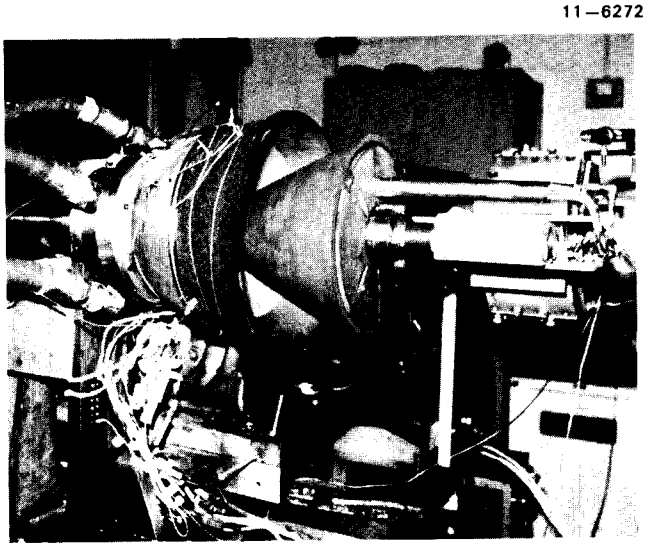

Figure 12. Nozzle test assembly

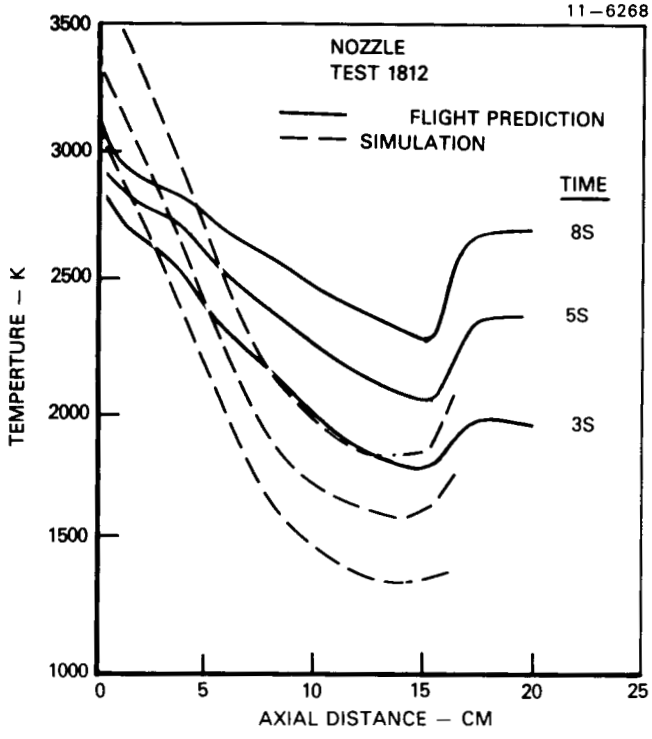

Figure 13. Comparison of nozzle surface flight temperature predictions to test 1812 simulation

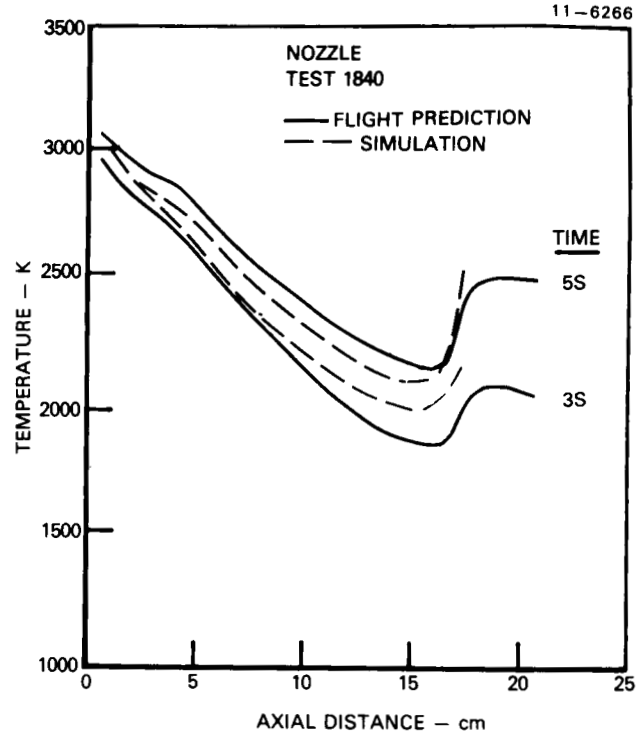

Figure 15. Comparison of nozzle surface flight temperature predictions to test 1840 simulation

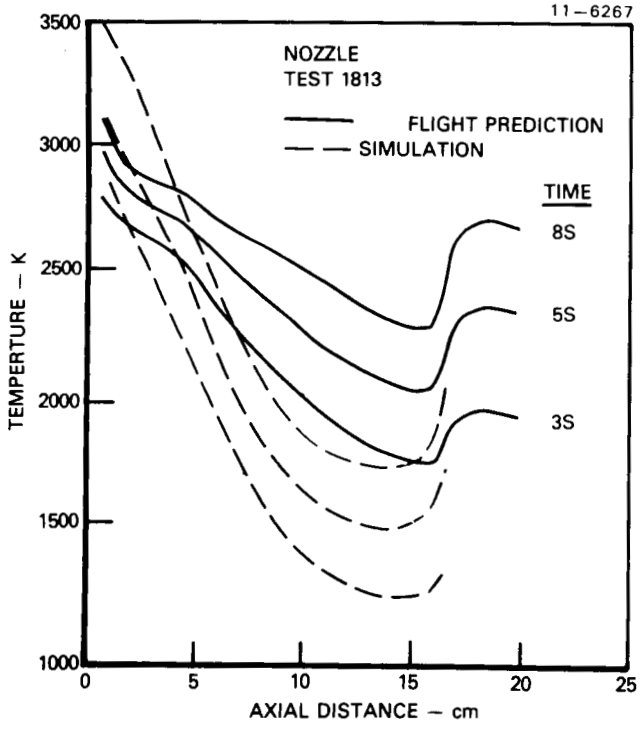

Figure 14. Comparison of nozzle surface flight temperature predictions to test 1813 simulation

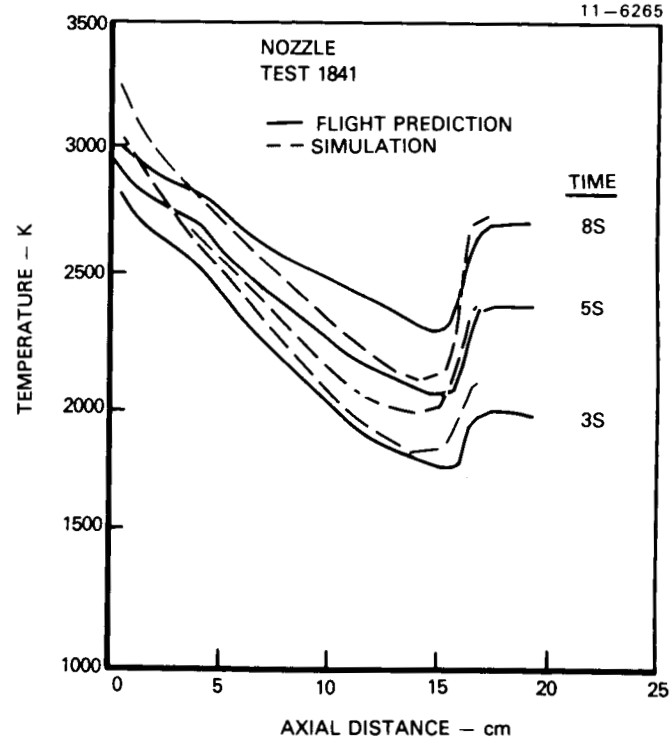

Figure 16. Comparison of nozzle surface flight temperature predictions to test 1841 simulation

RADIATIVE AND FREE-CONVECTIVE HEAT TRANSFER FROM A FINITE HORIZONTAL PLATE INSIDE AN ENCLOSURE*

Peter Hrycak and D. J. Sandman

New Jersey Institute of Technology
Newark, New Jersey 07102

ABSTRACT

An experimental and analytical investigation of heat transfer from a horizontal, thin, square plate inside of an enclosure has been carried out. Experimental results have been obtained from both the upward-facing and the downward-facing sides of the heated plate. Starting with the integrated momentum and energy equations, approximate solutions have been obtained for heat transfer in the laminar and the turbulent regime that correlate well with own experimental data and the results of other investigators. Radiative heat transfer correction was given a special attention. Effects of the enclosure-related recirculation of the test fluid, as well as effects of simultaneous heat transfer on both sides of the plate, caused an early transition, and indicated a high level of internal turbulence.

INTRODUCTION

Heat transfer from horizontal, heated plates by far has not received the attention accorded to other geometries. There appears still to exist a general scarcity of representative experimental data, in particular in the turbulent regime. As heat transfer by free convection, for moderate temperature differentials, is of the same order of magnitude as that by radiation, the need for radiation correction during experimentation cannot be disregarded. Therefore, the experimental results below have been carefully checked for the effects of radiation. Also, equations of the boundary-layer type are set up, describing free convection on both sides of a horizontal plate of finite dimensions, heated electrically. Similarity is assumed for both the velocity and temperature profiles. These assumptions are then justified by a close agreement between the results of the analysis and the experimental findings and the literature on the subject. The solutions obtained apply for laminar as well as for turbulent free convection. Due to highly sheltered conditions inside the chamber where the present experiments were carried out, undesirable disturbances like uncontrollable small air movements were eliminated. Ample space between the walls of the chamber and the test plate should have made the resulting free convective flow essentially undisturbed by the presence of the confining walls.

SYMBOLS

A_1 area of specimen, m^2

a thermal diffusivity, m^2/s

$\underline{a}$ constant in reference velocity equations, s^{-1}

* This work has been partially supported under NSF Grant No. MEA- 81-19471

c_p	specific heat at constant pressure, J/(K kg)
Gr_L, Gr^*	Grashof number, $g\beta L^3(T_w - T_\infty)/\nu^2$, Gr_L/L^3, m^{-3}
h	heat transfer coefficient, $W/(m^2K)$
k, $\underline{k}$	thermal conductivity, W/(m K); empirical constant in expression for $\underline{a}$
K	numerical constant in expressions for the Rayleigh number
P	pressure, N/m^2
Pr	Prandtl number, ν/a
q, Q	heat flux density, W/m^2; heat flow rate, W
r, R	coordinate, radial direction, m; radius of test plate, m
$\underline{R}$	gas constant, J/(kg K)
Re_r	Reynolds number, Ur/ν
Ra	Rayleigh number, Gr Pr
T	thermodynamic temperature, K
u, U	dr/dt, velocity ; reference velocity, r-direction, m/s
v	specific volume, m^3/kg
w, W	dz/dt, velocity ; reference velocity, z-direction (perp. to plate), m/s
z	coordinate perpendicular to plate, m
Nu_L	Nusselt number, hL/k
β	cubic expansion coefficient, K^{-1}
δ	boundary-layer thickness, m
ϵ_1	emissivity of specimen
ν	kinematic viscosity, m^2/s
ρ	mass density, kg/m^3
σ	Stefan-Boltzmann constant, $W/(K^4 m^2)$
θ	reduced temperature, $T - T_\infty$, K

In turbulent regime, u, U, w, and W represent mean-flow velocities

Subscripts:

m condition where maximum velocity occurs in the polynomial expression

w " at the wall of plate

∞ " far away from wall

EXPERIMENTAL TEST SET-UP

In order to make the intended free-convective experiments reasonably accurate, it was decided to test the specimens, that were to be used as the horizontal plates in the tests, independently for emissivity under high-vacuum conditions. Therefore, a high-vacuum chamber was built first, that could contain pressures as low as 10^{-4} mm Hg, with the mean free path of molecules inside long enough to eliminate convection, and to leave only radiation as the mode of heat transfer. Conduction along the specimen support wire, and the heater and the thermocouple wires was calculated to be less than 1% of the total heater input. For free-convective measurements, atmospheric pressure inside of chamber was reestablished.

As the total area of specimens, A_1, represented only 2.1% of the wall area of the vacuum chamber (Fig.1), the required emissivity could be calculated from the formula

$$Q = \epsilon_1 \sigma A_1 (T_1^4 - T_2^4) \tag{1}$$

The emissivities measured with this set-up are seen in Fig.2. They all appear to be of the right order of magnitude, when compared with results from the literature, and appear to be adequate for making radiative-loss corrections in free-convective measurements more realistic.

BASIC EQUATIONS OF THE PROBLEM

Let's now consider natural convection flow of a Newtonian, single species fluid over a horizontal surface in an axisymmetric flow, with the coordinates r and z. The flow is in the steady state, the velocity field consists of $u = dr/dt$ and $w = dz/dt$, and the corresponding temperature field is $T = T(r,z)$. The acting surface force is the pressure, and the body force is the gravitational force, g, all acting on a horizontal plate 86.0 mm in diameter which, in turn, gives rise to convective flow considered positive in the direction towards the center of plate; at edge of plate, $r = 0$. We assume that this flow is amenable to analytical treatment using the boundary-layer theory approach, together with Boussinesq approximation towards the treatment of the variable physical properties. Also, there is assumed similarity of velocity and temperature profiles. Then the continuity, momentum, and the energy equations assume the form

$$\frac{\partial (ru)}{\partial r} + \frac{\partial (rw)}{\partial z} = 0 \tag{2}$$

$$u \frac{\partial u}{\partial r} + w \frac{\partial u}{\partial z} = -\frac{1}{\rho} \frac{\partial P}{\partial r} + \nu \frac{\partial^2 u}{\partial z^2} \tag{3}$$

$$0 = -\frac{1}{\rho} \frac{\partial P}{\partial z} + g\beta (T - T_\infty) \tag{4}$$

$$u \frac{\partial T}{\partial r} + w \frac{\partial T}{\partial z} = a \frac{\partial^2 T}{\partial z^2} \tag{5}$$

with the boundary conditions:

at $z = 0$, $u = w = 0$; $T = T_w = \text{const}$; at the edge of plate, $r = 0$, and $u = 0$ (6)

at $z = \delta$, $u = 0$, $T = T_\infty$; $\partial u/\partial z = \partial T/\partial z = 0$ (7)

On differentiating eq. (4) with respect to r, and integrating it with respect to z, we have

$$-\frac{1}{\rho}\frac{\partial P}{\partial r} = g\beta \int_z^\delta \frac{\partial}{\partial r}(T - T_\infty)\, dz \tag{8}$$

This approach to free convection on a horizontal plate, apparently first outlined by Stewartson [1], for two-dimensional flow, is applied here to three-dimensional, axisymmetric flow. Thus, from the continuity equation, we have

$$w = -\int_o^z \left(\frac{\partial u}{\partial r} + \frac{u}{r}\right) dz \tag{9}$$

Equations (8) and (9), on substitution in eq. (3), after partial integration, yield

$$\frac{1}{r}\frac{d}{dr}\left(r \int_o^\delta u^2\, dz\right) = g\beta \int_o^\delta \left[\int_z^\delta \frac{\partial}{\partial r}(T - T_\infty) dz\right] dz - \nu \left(\frac{\partial u}{\partial z}\right)_w \tag{10}$$

Equation (5) may be transformed in a similar fashion after a partial integration. Letting $\theta = T - T_\infty$, and assuming that δ (hydrodynamic) $\approx \delta$ (thermal), there results

$$c_p \rho \frac{1}{r}\frac{d}{dr}\left(r \int_o^\delta u\theta\, dz\right) = -k \left(\frac{\partial \theta}{\partial z}\right)_w \tag{11}$$

Additionally, letting the velocity and temperature profiles be

$$u = U\,(z/\delta)(1 - z/\delta)^2; \quad \theta = \theta_w (1 - z/\delta)^2 \tag{12}$$

as proposed, for example, by Eckert and Drake for a related problem [2], and letting

$$U = C_1 r^m \quad ; \quad \delta = C_2 r^n \tag{13}$$

a speedy solution of eqs. (10) and (11) is obtained. With $\beta = 1/T_\infty$, we get

$$\frac{1}{r}\frac{d}{dr}\left(rU^2\delta\right) = 17.5\, g\beta\, \theta\delta\, d\delta/dr - 105\, \nu(U/\delta), \quad \text{and} \tag{14}$$

$$\frac{1}{r}\frac{d}{dr}\left(rU\theta_w\delta\right) = 60\, a\theta_w/\delta \tag{15}$$

which, after eq. (13) has been substituted, yield

$$(2m + n + 1)C_1^2 C_2\, r^{2m+n-1} = 17.5\, g\beta\, \theta_w n\, C_2^2\, r^{2n-1} - 105\,(C_1/C_2)\, r^{m-n}\nu \quad \text{and} \tag{16}$$

$$(m + n + 1)\, C_1 C_2\, r^{m+n-1} = 60\, a\, r^{-n}/C_2 \tag{17}$$

For similarity solutions, both sides of these equations must be independent of r; this is true if $m = 1/5$ and $n = 2/5$ for the present geometry. Then eqs. (16) and (17) yield, with $Gr^* = Gr/L^3$

$$C_1 = 2.978\, a\, Pr^{4/5}(9/14 + Pr)^{-2/5}\, (Gr^*)^{2/5} \quad \text{and}$$

$$C_2 = 3.548\, Pr^{-2/5}(9/14 + Pr)^{1/5}\, (Gr^*)^{-1/5}$$

from which, together with eq. (13) is calculated the local heat transfer coefficient

$$h_r = q_w/\theta_w \tag{18}$$

while the average heat transfer coefficient becomes

$$h_R = 0.705\ k\ Pr^{2/5}(0.643 + Pr)^{-1/5}(Gr^*)^{1/5}R^{-2/5} \tag{19}$$

In order to obtain a formula for the average heat transfer coefficient based on the side L of an equivalent square plate, we let $L^2 = \pi R^2$, such that L (equivalent) $= \pi^{\frac{1}{2}}R$, $h_R = \pi^{-1/5}$, and $Nu_L = h_L L/k$, or

$$Nu_L = 0.886\ Pr^{2/5}\ (0.643 + Pr)^{-1/5}\ Gr_L^{1/5} \tag{20}$$

For air (Pr = 0.72), this generates the Rayleigh number, $Ra_L = Gr_L Pr$, based on L, or

$$Nu_L = 0.780\ Ra_L^{1/5} \tag{21}$$

for a horizontal square plate heated on the top side only. With the present choice of coordinates, $\delta = 0$ at the edge of plate. In the case of a horizontal plate, heated at both sides, $\delta \neq 0$ at the edges. According to the literature on this subject (cf. reference 3, for example), a horizontal plate heated on both sides has its heat transfer on the upper side appreciably increased by formation of a warm air "bubble" on its lower side. It appears in the present case that increasing the area of plate by about one fifth generates an "effective area" that shows realistically the effect of heating of the bottom side of plate on heat transfer on the upper side in the form of an "effective radius", R_{eff}

$$R_{eff} = 1.095\ R_{actual} \tag{22}$$

to be used as the upper limit in the evaluation of the average heat transfer coefficient

$$h_{R,eff} = 0.816\ k\ Pr^{2/5}\ (0.643 + Pr)^{-1/5}\ Gr^{1/5}/R \tag{23}$$

which, for example, for Pr = 0.72, results in

$$Nu_L = 0.902\ Ra_L^{1/5} \tag{24}$$

The velocity and temperature profiles applicable here as per eqs.(6) and (7) satisfy the physical conditions of the problem at hand, eqs.(2) - (5), and reduce to zero for $z > \delta$. They are also for $z < \delta$ qualitatively what can be reasonably expected in free convective flow under conditions of conservation of mass and energy, regardless of orientation of flow, with exception of a small area near the plate's center, where an upward-pointing jet is generated, as has been already observed by Stewartson [1]. This effect will be accounted for below in a separate discussion. Other velocity and temperature profiles have been considered. It may be seen from the comparison with the experimental results (cf. discussion below) that eqs. (21) and (24) come already reasonably close to physical reality. This is perhaps the best justification of the methods used above, and for the particular u and θ used.

Experience teaches us that in free convection inside an enclosure (cf. McAdams [5], p. 182) turbulence may develop already at relatively low Grashof numbers. For the case of heated, horizontal plates, this is explainable by the destabilizing ef-

fect of the upward-directed buoyant force on the boundary-like layer formed by the fluid flowing in the direction tangential to the plate. For developed turbulent flow, the last term in eq. (10) may be replaced by the semi-empirical expression

$$0.0228\ U^2\ (\nu/U\delta)^p(\delta/\delta_m)^p\ J^{2-p} \tag{25}$$

and the right-hand side of eq. (11) may be defined as

$$0.0228\ c_p\rho\ U\theta_w\ (\nu/U\delta)^p\ Pr^{-2/3}(\delta/\delta_m)^p\ J^{1-p} \tag{26}$$

while the velocity and temperature distribution may be written (cf. Eckert and Jackson [4], and reference 2, p. 324) as

$$u = UJ\ (z/\delta)^{1/q}(1 - z/\delta)^s \quad ; \quad \theta = \theta_w[1 - (z/\delta)^{1/t}] \tag{27}$$

with the exponents q, s, and t determined later.

Since eqs. (25) and (26) were originally based on the maximum velocity in the boundary layer, occurring here at $z = \delta_m$, a normalizing scale factor is introduced in eq. (27), assuring that $u/U = 1.0$ when $z = \delta_m$ applies. It may be shown that u peaks out when $z = \delta_m = \delta/(q \cdot s + 1)$, while the nominal length δ itself signifies to what extent the effect of heating from the plate penetrated the fluid above. The numerical constant in eq. (25) may be approximated by the formula

$$C(p,q) = 1.013\ (0.92\ q + 2.30)^{-pq} \tag{28}$$

based on results of Wieghardt (cf. Schlichting [6], p. 601). With $p = \frac{1}{4}$, eq. (25) becomes the Blasius formula, linked to $q = 7$ in eqs. (27) and (28); when $p = 1/5$, $q = 9$ applies. It is felt that with these changes, eqs. (25) to (28) will be representative of turbulent flow in general, regardless of orientation. Furthermore, eqs. (27) and (28) satisfy the boundary conditions for u and θ at $z = 0$ and $z = \delta$ in a satisfactory manner; with these substitutions, with the required integrations carried out, eqs. (10) and (11) yield the relations

$$J^2\ I_1(1/r)\frac{d}{dr}(rU^2\delta) = I_2\ g\beta\ \theta_w\delta d\delta/dr - K_3U^2(\nu/U\delta)^pJ^{2-p} \quad \text{and} \tag{29}$$

$$J\ I_3(1/r)\ \frac{d}{dr}(rU\delta)\ = K_5\ U(\nu/U\delta)^p\ Pr^{-2/3}\ J^{1-p} \tag{30}$$

Assuming again validity of eq. (13), eqs. (29) and (30) yield after a few transformations the expression for the local Nusselt number, for $m = 1/(2+3p)$, and $n = 2m$,

$$Nu_r = JK_5\ (K_2/K_1)^m(K_5/K_4)^{m(1-3p)}Pr^{-m(1-3p)}(1 + Pr^{2/3}K_4/K_1)^{-m}Ra_r^{\ m} \tag{31}$$

and the average Nusselt number for an equivalent square plate with side L,

$$Nu_L = JK_5(K_2/K_1)^m(K_5/K_4)^{m(1-3p)}Pr^{-m(1-3p)}(1 + Pr^{2/3}K_4/K_1)^{-m}\ \frac{2}{1+3m}^{-\frac{1}{2}m(1-3p)}Ra_L^{\ m} \tag{31a}$$

In eqs. (31) and (31a), the use of J should be considered entirely empirical; the constants K_n below stand for the integrals based on eqs. (27) and (28):

$$K_3 = K_5 = C(p,q)\ (\delta/\delta_m)^p$$

$$K_1 = (2m + n + 1)/(U^2\delta)\int_0^\delta u^2\ dz = (2m + n + 1)\ I_1$$

$$K_2 = n/(\theta_w \delta d\delta/dr) \cdot \int_o^\delta (\int_z^\delta \frac{\partial}{\partial r}\theta \, dz) \, dz = n \, I_2 = n/(2t + 1)$$

$$K_4 = (m + n + 1)/(U\theta_w) \cdot \int_o^\delta u\theta \, dz = (m + n + 1) \, I_3$$

With the use of the Blasius formula for wall shear stress and heat transfer, and s = 8 and t = 4 in eq. (27) results have been obtained that for $5x10^5 < Ra < 10^6$ deviate for less than ± 1.5% from the least-squares fit curve representing the present experimental data, or with m = 4/11 ≈ 0.364, and Pr = 0.72,

$$Nu_L = 0.104 \, Ra_L^{0.364} \tag{32}$$

Here, m = 0.364 is somewhat lower than the experimental value of m = 0.384. The experimental value of m was closely approximated with m = 0.385, when p = 1/5, q = 9, s = 8 and t = 1 in eqs. (27) and (28) was used, but the constant in eq. (31a) was 6% too low vis-à-vis experimental data. In order to get the commonly cited in the literature value of m = 1/3 for the turbulent, free-convective heat transfer from the upward-pointing, horizontal plate by the present method, p = 1/3, q = 5, s = 3, and t = 5 would have been required in eqs. (25) to (28), to yield

$$Nu_L = 0.150 \, Ra_L^{1/3} \tag{32a}$$

Equation (32a) seems to fit experimental data of others, for free convection without recirculation, reasonably well.

The analysis outlined above has been carried out along the lines suggested in references 2 and 4, but modified in several respects to fit the physical requirements of a horizontal plate of finite dimensions, heated and pointing upward. As is stated in reference 4, the exponent of Ra, m = 2/5, fitted very well experimental data for turbulent heat transfer, for free convection on vertical plates and a vertical cylinder. It is seen that semi-empirical approaches can be used to advantage where the exact analysis still fails to give answers of practical significance.

EFFECTS OF FREE CONVECTION ON HEAT TRANSFER AT CENTER OF A HORIZONTAL PLATE

It is obvious from the consideration of the continuity equation alone that free convective flow, for the present geometry, will generate near the center of plate a vertical jet, known as the thermal plume. For purposes of the analysis below, we assume that temperature distribution within the plume is still given by eq. (12), but velocity follows the profile $u = U(z/\delta_m)$, $z \leq \delta_m$, $u = U$, $z > \delta_m$, and

$$U = -\underline{a} \, r \quad ; \quad W = 2^i \underline{a} \, z \quad (r = z = 0 \text{ at center of plate}) \tag{33}$$

where i = 1, axisymmetric flow, and i = 0, plane flow. U and W in eq. (33) satisfy identically the continuity equation. By considering a volume element $(2\pi \, r)^i dr\delta$ and the heat fluxes in and out by convection, as well as by conduction at the bottom through the area element $(2\pi r)^i dr$, after the substitutions for u and θ have been made, there results the expression

$$r^{-i}(\rho c_p \frac{d}{dr} r^i \int_o^\delta u\theta \, dz) = k(\frac{\partial \theta}{\partial z})_w \tag{34}$$

Taking θ from eq. (12) and U as stated above, the integral in eq. (34) may be written, for $\delta_m/\delta \ll 1$, as $I = -ar^2\delta/3$. It yields for δ (which is actually the height of the present thermal plume), the expression

$$\delta = (3a/\underline{a})^{\frac{1}{2}} \tag{35}$$

Using eq. (18), we may write $Nu_r = 2R/\delta$. The still required expression for $\underline{a}$ in eq. (33) is now to be derived. If differential pressure at the center of the plate is proportional to $\underline{k}^4 g\rho\beta\theta_w z/R$, working through a distance dz, that accelerates a fluid element from velocity 0 to W (here $\underline{k}^4$ is the constant of proportionality), one gets $\rho\, \underline{k}^4 \frac{dA}{R} \int_o^z \beta g \theta_w z\, dz = \rho\, dA \int_o^W w\, (dw/dz)\, dz$, on assumption of inviscid flow there, the simple result

$$W = (\beta g \theta_w \underline{k}^4/R)^{\frac{1}{2}}\, z \tag{36}$$

From comparison with eq. (33), eq. (36) yields

$$\underline{a} = (\beta g \theta_w \underline{k}^4/R)^{\frac{1}{2}}/2 = (\underline{k}^4\, Gr\nu^2/R^4)^{\frac{1}{2}}/2, \text{ and} \tag{37}$$

$$Nu_R = (2/3)^{\frac{1}{2}}\, \underline{k}\, Pr^{\frac{1}{2}}\, Gr_R^{\frac{1}{4}} \tag{38}$$

For air with Pr = 0.72, and $L = \pi^{\frac{1}{2}}R$, there results

$$Nu_L = 0.864\, \underline{k}\, Ra_L^{\frac{1}{4}} \tag{39}$$

Integral methods generate useful results that still depend on the approximating polynomials needed to represent u and θ. Thus, if in the present case we use eq. (12) for both u and θ, but with the reasonable constraint that, at $z = \delta_m$, $u = U$, so that eq. (33) is satisfied, we obtain from eqs. (34) and (37)

$$Nu_L = 0.710\, \underline{k}\, Ra_L^{\frac{1}{4}} \tag{39a}$$

Application of the same procedure to the case of an infinite strip (i = 0 in eqs. (33) and (34), u and θ according to eq. (12), and scale factor J = 27/4 applied to u), yields for a strip of the width 2b

$$Nu_b = 0.62\, \underline{k}\, Ra_b^{\frac{1}{4}} \tag{40}$$

It is to be emphasized that eq. (34), obtained from a direct summing up of the convective and conductive contributions to the control volume, differs in sign from eq. (11), obtained from the exact integration of the energy equation, as the chosen coordinate system is different. Also, as the hydrodynamic information on δ is not required, the momentum equation is not at all involved. This greatly simplifies the problem. The use of scale factor J here is needed to satisfy the continuity, eqs. (33).

RELATIONS FOR A HORIZONTAL DOWNWARD-FACING PLATE

It appears that for this geometry the conventional boundary-layer approach is not possible (cf. reference (3), for example). In the present case, the only reason for the movement of fluid is its thermal expansion, due to the contact with the wall at T_w. Therefore, the resulting flow is similar to that occurring in forced, axisymmetric stagnation flow, for which an exact solution of the Navier-Stokes equations exists (reference 6, p. 100). One can expect the fluid temperature near r = 0

to vary, on the average, at some distance below the plate's center, as

$$\theta = (\theta_w/2)\,(1 - r^2/R^2) \tag{41}$$

while simultaneously the velocity terms for the potential flow related to the present problem follow the relations satisfying identically the continuity equation:

$$U = \underline{a}r \quad ; \quad W = -2^{i}\underline{a}z \tag{42}$$

that applies to any incompressible flow, to any geometry. If the fluid in question is perfect gas, the term $\partial P/\partial r$ in eq. (2) may be now transformed as (with $Pv = \underline{R}T$)

$$-\frac{\partial P}{\partial r} = -\left(\frac{\partial P}{\partial T}\right)_v\left(\frac{\partial T}{\partial r}\right) = \rho\underline{R}\,\theta_w r/R^2, \text{ or } -\frac{\partial P}{\partial r} = \frac{P}{T_\infty}\,\frac{\theta_w r}{R^2}$$

using eq. (41) for $T = \theta + T_\infty$. In quiescent gas, $P = g/v$ times an element of length assumed here to be proportional to R. As $\underline{a}$ is still a free constant, we may assume $\underline{k}^4$ to be that constant of proportionality, without the loss of generality. Then,

$-\frac{\partial P}{\partial r} = \underline{k}^4\,\beta g\theta_w r/(Rv) = \underline{k}^4\,Gr^*\nu^2 r(Rv)^{-1}$; letting $\underline{a}^2 = \underline{k}^4\,Gr^*\nu^2/R$, there results

$$-\frac{\partial P}{\partial r} = \rho\,\underline{a}^2 r \tag{43}$$

With the present definition of $\underline{a}$, the pressure-gradient related term in the momentum equation is linked to the acting temperature differential, θ_w. Writing $u = r f'(z)$, and $w = -2 f(z)$, and using a new variable $\eta = (\underline{a}/\nu)^{\frac{1}{2}}z$, eq. (3) above is readily solved. This solution is considered as good for the complete Navier-Stokes equation (reference 6, p. 100). The corresponding solution of the energy equation is available (cf. references 7 and 8). For Pr near unity, we have

$$Nu_r = 0.763\,Pr^{0.4}\,Re_r^{\frac{1}{2}} \tag{44}$$

This is a boundary-layer type solution, based on a exact solution of the Navier-Stokes equations. As here $Re_r = Ur/\nu$, with $\underline{a}$ from eq. (43), we get $Re_r = \underline{k}^2 \cdot (Gr_r\, r/R)^{1/2}$. With Pr = 0.72, and $L = \pi^{\frac{1}{2}}R$, there results for air

$$Nu_L = 0.630\,\underline{k}\,Ra_L^{\frac{1}{4}} \tag{45}$$

where $\underline{k}$ is an experimental constant with a value $\underline{k} \approx 0.5$, in view of the constant K = 0.27 and m = 1/4 in the original correlation due to Saunders and Fishenden, for example [9]. It must be stressed that the present approach is valid only in the region where eqs. (41) and (42) continue to apply, that is, near the center of a circular plate (i = 1), and near the center of a long strip, where r is the distance away from that center, (i = 0). It is of some interest to note that a solution can also be obtained through a direct integration of eq. (11) here, for the same velocity and temperature distributions as in eq. (12), but using a normalizing factor J = 27/4, such that eq. (42) is satisfied. Then from $\delta = (a/\underline{a})^{1/2} \cdot 2.11$, and Pr = 0.72 we have the formula

$$Nu_L = 1.00\,\underline{k}'\,Ra_L^{\frac{1}{4}} \tag{46}$$

The term $\underline{k}'$ expresses the effect of geometry at hand as well as that of the approximating polynomials used. $\underline{k}' = 0.25$ yields K that comes close to the above Saunders and Fishenden result.

It is seen from the discussion above that methods, based both on the exact solution of the Navier-Stokes equations, and on the integrated energy equation method, lead to results that are experimentally verifiable. The relations for streamline

and temperature distribution, calculated by Miyamoto et al. [10] agree qualitatively with our eqs. (41) and (42) and are also suggested by the scheme shown in Fig. 3. In reference 10 are also reported results of Sugawara and Michiochi [11], where K = 0.264 and m = 1/4, that are based on the boundary-layer approximation.

In addition to our eqs. (45) and (46), and to solutions reported in references 10 and 11, there exist also several approximate analytical solutions for the present geometry with m = 1/5 proposed (cf. references 12 and 13). As an explanation for this one should consider that as the exact solution of the governing momentum equation is only valid near r = 0, and with m = 1/4 applicable for the associated heat transfer problem, the flow starting far away from the stagnation point, at the edge of the plate, would result in a quasi-boundary layer flow for which, at least initially, m = 1/5 would be entirely appropriate. The real flow must be actually nonsimilar for a good portion of $0 < r < R$.

DISCUSSION OF EXPERIMENTAL RESULTS

It is interesting to note that the present experimental results show that transition to turbulent flow has already occured as early as at $Gr = 5 \times 10^5$, in agreement with the discussion by McAdams [5], p.182, as the side effect of the confinement in the relatively small vacuum chamber. Our own experimental results on free convection on an upward-facing, horizontal heated plate are shown in Fig. 4. It is seen from Fig. 4 that, for $Ra < 6 \times 10^5$, the experimental data show a reasonable agreement with eq. (24) here, but the number of experimental points for what is considered laminar free convection on a typical upward-pointing, horizontal plate, heated on both sides, is not sufficient for a definitive finding. For comparison, let's consider the formula proposed by Lewandowski and Kubski [14] for a horizontal plate 100 x 60 mm, heated on one side only,

$$Nu = 0.66\, Ra^{1/5} \tag{47}$$

valid for $10^4 < Ra < 10^7$, with a ± 10% error margin, based on experiments with distilled water, glycerine, and soybean oil. Equation (47) is very close to our eq. (21) above. On the other hand, Yousef et al. [15], using Mach-Zehnder interferometer, and for $10^4 < Ra < 10^7$, in air, obtained

$$Nu = 0.622\, Ra^{1/4} \tag{48}$$

for square plates with L = 100, 200, and 400 mm. A similar exponent of Ra has been also obtained by a number of other investigators, for air and for the same geometry: Fishenden and Saunders [16], Bosworth [17], Al Arabi and El-Riedi [18], for example, with K = 0.54, 0.71, 0.70, respectively, all of them for laminar flow. The experimental constants K come very close to that in our eq. (39a) with $\underline{k} = 1.0$, but the range of Ra is similar. The details are shown in Fig. 5. This discussion applies to the average Nusselt numbers only. It is seen that eqs. (21) (horizontal plate heated on one side only), and (24) (horizontal plate heated on both sides), this paper, fall unquestionably into the range of the experimental results reported in the recent literature, although there are differences in the power of the Rayleigh number: m = 1/5 is recommended in reference 14 and in this paper (depending on the flow situation), and in reference 14, while references 15 to 18 report m = 1/4. Also, in this paper, expressions for m = 1/4 and m = 1/3 have been derived.

For turbulent convection results shown in Fig. 4, the least squares fit equa-

tion is

$$Nu_L = 0.0799\ Ra_L^{0.384} \tag{49}$$

that agrees reasonably well with the calculated formula, eq. (32) here, while in reference 14 the experimental result

$$Nu = 0.173\ Ra^{1/3} \tag{50}$$

is proposed, valid for $10^5 < Ra < 10^8$. This result is typical of other experimental findings shown in Fig.5, where, in addition, references 14 to 21 are included. From the review of the above it is seen that $m = 1/3$ is very common for the situations where turbulent free convection takes place on horizontal plates, heated on one side only. For thin plates, of finite size, heated on both sides in finite enclosures, m increases somewhat, due apparently to flow instabilities generated by heat transfer at the bottom of the plate.

To produce the exponent $m = 1/3$ for turbulent, free convective flow in the present case, $p = 1/3$ would have been necessary in eq. (25). It is interesting to see that most of the experimental results for the upward-pointing, heated plate show a remarkable similarity with the results for the vertical walls; the finding of Eckert and Jackson in reference 4 of $m = 2/5$ is worth noting, as it is derived from a semi-empirical theory, as exemplified here by eqs. (25) and (26), and is also backed up by experimental data. It appears that this similarity in free convective heat transfer, in comparing results for horizontal with those for the vertical geometry, lies in the effect of the thermal jet generated at the point where the boundary flow meets head-on and a thermal plume is formed - something like the reverse of the situation depicted in Fig. 3. This aspect has also been analyzed above separately for laminar flow. It is mentioned also by Bosworth in reference 17.

For a horizontal plate facing downward, the controversy concerning the validity of the exponents $m = 1/5$ vs. $m = 1/4$ can be resolved with the analysis of the flow situation, represented here schematically as Fig. 3. The flow on a downward-facing, heated horizontal plate is visualized. It is seen that near the stagnation point a thin boundary-layer-like region exists. Then, farther away, the "boundary-layer" becomes at first thicker, but that thickness is gradually diminishing, as the edge of plate is approached. In this fashion, two kinds of existing analytical solutions, and the corresponding existing dual experimental correlations could be reconciled, as either of the flow modes may predominate in the given experimental set-up.

Our own experimental data are shown in Fig.6. It is seen from Fig.6 that the flow regime there must have been already turbulent for Ra as low as 6×10^5. There is a considerable scatter of the data, indicating a highly unstable flow. Heat transfer intensity, as represented by the corresponding Nusselt numbers, is roughly 50 % of that existing on the upward-facing side of plate, which is also to be found in the literature (cf. reference 19). The results shown in Fig. 6 may be correlated by either of the two equations below. Equation (51) represents the least squares fit

$$Nu_L = 0.0017\ Ra_L^{0.596} \tag{51}$$

while eq. (52) represents the limiting case of flow corresponding to $p = 0$ in eq. (25), or

$$Nu_L = 0.0064\ Ra_L^{0.5} \tag{52}$$

The relatively large exponents of the Rayleigh number in the present case indicate that some recirculation of the air in the test chamber was actually taking place, as the result of simultaneous heating of the bottom and the top of the test plate, thus representing a kind of synergistic effect. Few other data for the present configuration are available for the turbulent regime, for the sake of comparison, except those in reference 19, correlated by a formula that represents simply one-half of the results obtained with the heated flat plate facing upward, with m = 1/3, within ± 10%, as

$$Nu = 0.06\ Ra^{1/3} \tag{53}$$

Obviously, more data for this configuration are still required, and our objective has been to fill this need at least partially. Additional cases for this geometry are discussed in reference 3. A general comparison of results of various investigators is shown in Fig. 7. It is seen from the discussion above that for laminar free convection, on both sides of the horizontal plate, many investigators still use correlations of the type $Nu = K\ Ra^{\frac{1}{4}}$ while some prefer the supposedly more "theoretical" version of $Nu = K\ Ra^{1/5}$. A plausible explanation was given for this discrepancy. In reference 17, K occurring in eq. (53) is given as 0.08, without details.

It is worth noting that Mangler's transformation changes relations valid for two-dimensional flow over a wedge into expressions valid also in three-dimensional (stagnation) flow, without the change of power of Re, for forced convection. A similar phenomenon, by analogy, may be also expected for free convection, with the Reynolds number replaced by its physical equivalent, the Grashof number to one half power. Moreover, the precise values of K would depend on experimental conditions and refinements observed while taking measurements, on geometry, boundary conditions on edges and the details of how the plates were heated. It should also be kept in mind that the left-hand side of the integrated energy equation is the same for both forced and free convection, regardless of the flow regime. The right-hand side of that equation must be changed to an empirical formula when the flow is turbulent, however.

CONCLUDING REMARKS

For turbulent, free-convective heat transfer, characterized by an exponent $m > 0.25$, most investigators propose $m = 1/3$. It is conceivable, however, that for cases of really well-developed, rough, non-isotropic turbulence, that exponent may get as high as 0.384 and perhaps even higher than 0.5, as is indicated by the present experiments, for the significantly unstable flow at the bottom of a heated, flat horizontal plate, heated on both sides. This uncertainty is also due to the fact that experimental results for turbulent free convection for that particular geometry are still very scarce, and additional data are needed. Because of relatively low convective heat transfer coefficient here, the effect of radiation correction becomes very important. Cases have been found in our experimentation where this correction for some specimens amounted to more than 50 % of the total heat transferred. Because of its emphasis on the radiation aspects in this case, and since both sides of plate were heated, the present investigation may be considered the first of its kind. The maximum total experimental error is calculated as ± 15 %.

A general comparison of the various experimental and analytical correlations is shown in Figs. 5 and 7, to stress the degree to which the results from the lit-

erature still differ from each other. It is also believed that, for the space environment, the present experiment shows that radiation cooling of electronics is more promising than free-convective cooling, where characteristic velocities are proportional to one half power of the Grashof number. With weak gravitational acceleration, Grashof numbers will be small, and effects of convective cooling negligible.

REFERENCES

1. Stewartson, K.: On Free Convection from a Horizontal Plate. ZAMP, vol.IXa, 1958, pp. 276-282.

2. Eckert, E. R. G., and Drake, R. M., Jr.: Heat and Mass Transfer. McGraw-Hill, 1959.

3. Bandrowski, J., and Rybski, W.: Analysis of Heat Transfer in Free Convection on Horizontal Plates. Chemical Engineering, vol. 3, 1975, pp. 3 - 16,(in Polish).

4. Eckert, E. R. G., and Jackson, T. W.: Analysis of Turbulent Free-Convection Boundary-Layer on a Flat Plate. NACA Report 1015, 1951.

5. McAdams, W. H.: Heat Transmission, 3rd ed. McGraw-Hill, 1954.

6. Schlichting, H.: Boundary-Layer Theory, 7th ed. McGraw-Hill, 1979.

7. Sibulkin, M.: Heat Transfer Near the Forward Stagnation Point of a Body of Revolution. J. of Aeronautical Sciences, vol. 19, 1952, pp. 570 - 571.

8. Hrycak, P.: Heat Transfer from Impinging Jets to a Flat Plate with Conical and Ring Protuberances. Int. J. Heat Mass Transfer, vol. 27, 1984, pp. 2145-2154.

9. Saunders, O., and Fishenden, M.: Some Measurements of Convection by an Optical Method. Engineering, May 1935, pp. 483-485.

10. Miaymoto, M., et al.: Free Convection Heat Transfer from Vertical and Horizontal Short Plates. Int. J. Heat Mass Transfer, vol. 28, 1985, pp. 1733-1745.

11. Sugawara, S., and Michioyshi, I.: Heat Transfer from a Horizontal Flat Plate by Natural Convection. Trans. Jap. Soc. Mech. Engrs., vol. 21, no. 109, 1955, pp. 651-657, (in Japanese).

12. Schulenberg, T.: Natural Convection Heat Transfer to Liquid Metals Below Downward-Facing Horizontal Surfaces. Int. J. Heat Mass Transfer, vol. 27, 1984, pp. 433-441.

13. Singh, S. M., Birkebak, R. C., and Drake, R. M., Jr.: Laminar Free Convection Heat Transfer from Downward-Facing Horizontal Surfaces of Finite Dimensions. Progress in Heat and Mass Transfer, vol. 2, 1969, pp. 87-98.

14. Lewandowski, W. M., and Kubski, P.: Effect of the Use of the Balance and the Gradient Methods... Natural Convection... Wärme und Stoffübertragung, vol. 18, 1984, pp. 247-256.

15. Yousef, W.W., Tarasuk, J.D., and McKean, W.J.: Free Convection Heat Transfer from Upward-Facing Isothermal Horizontal Surfaces. J. of Heat Transfer, vol. 104, 1982, pp. 493-500.

16. Fishenden, M., and Saunders, O. A.: An Introduction to Heat Transfer, Clarendon Press, 1952.

17. Bosworth, R. L. C.: Heat Transfer Phenomena. Wiley, 1952.

18. Al Arabi, M., and El-Riedy, M. K.: Natural Convection Heat Transfer from Isothermal Horizontal Plates ... Int. J. Heat Mass Transfer, vol. 19, 1976, pp. 1399-1404.

19. Hassan, K. E., and Mohamed, S. A.: Natural Convection from Isothermal Flat Surfaces. Ibid., vol. 13, 1970, pp. 1873-1886.

20. Fujii, T., and Imura, H.: Natural Convection from Plate with Arbitrary Inclination. Ibid., vol. 15, 1972, pp. 755-767.

21. Ishiguro, R., et al.: Heat Transfer .. Flow Instability ... Nat. Conv. .. Horizontal Surfaces. Proceedings, 6th Int. Heat Transfer Conf., vol. 2, Toronto, Canada, 1978, pp. 229-234.

22. Aihara, R., et al.: Free Convection along the Downward-Facing Surface of a Heated Horizontal Plate. Int. J. Heat Mass Transfer, vol. 15, 1972, pp. 2535-2549.

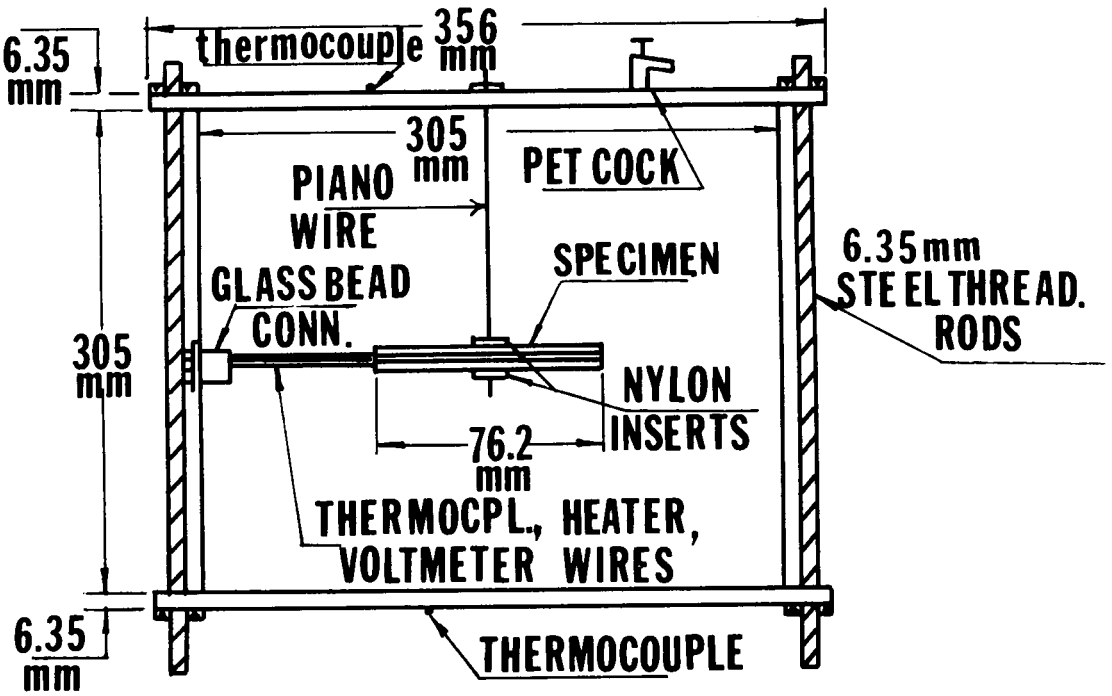

Figure 1. Experimental test set-up.

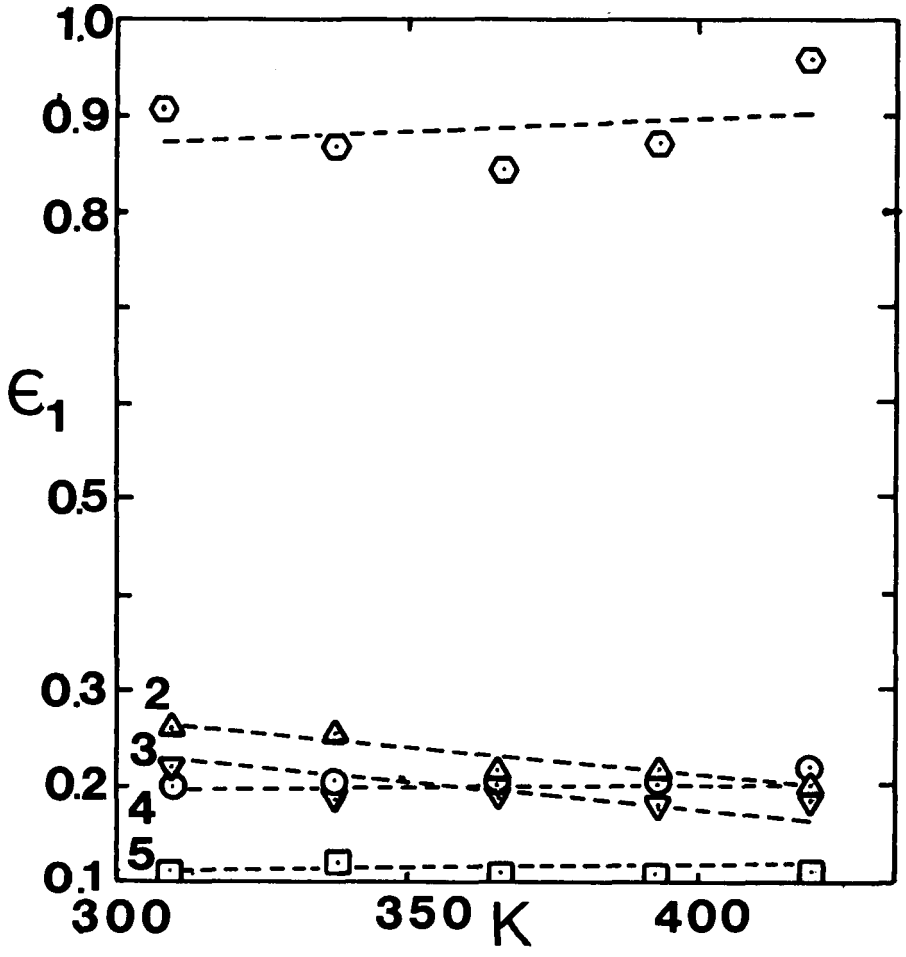

Figure 2. Emissivities of all samples tested. 1 - oxydized aluminum with Parson's black coating; 2 - oxydized aluminum with finger prints; 3 - oxydized aluminum, clean; 4 - oxydized aluminum, burnished; 5 - polished copper (all results by least squares fitting method; error margin: less than $\pm$ 6.5%).

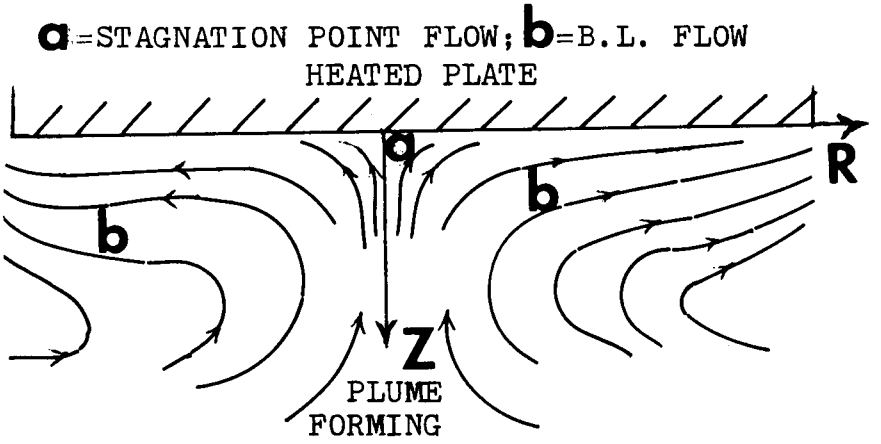

Figure 3. Schematic representation of natural convection near the center of a downward-facing, heated plate of finite dimensions.

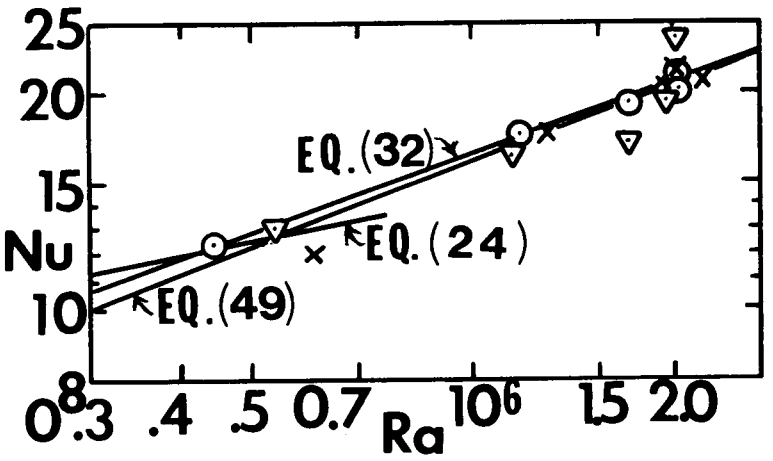

Figure 4. Average Nusselt number vs. Raleigh number for three specimens on horizontal, heated plate facing upward (maximum error ± 15%).

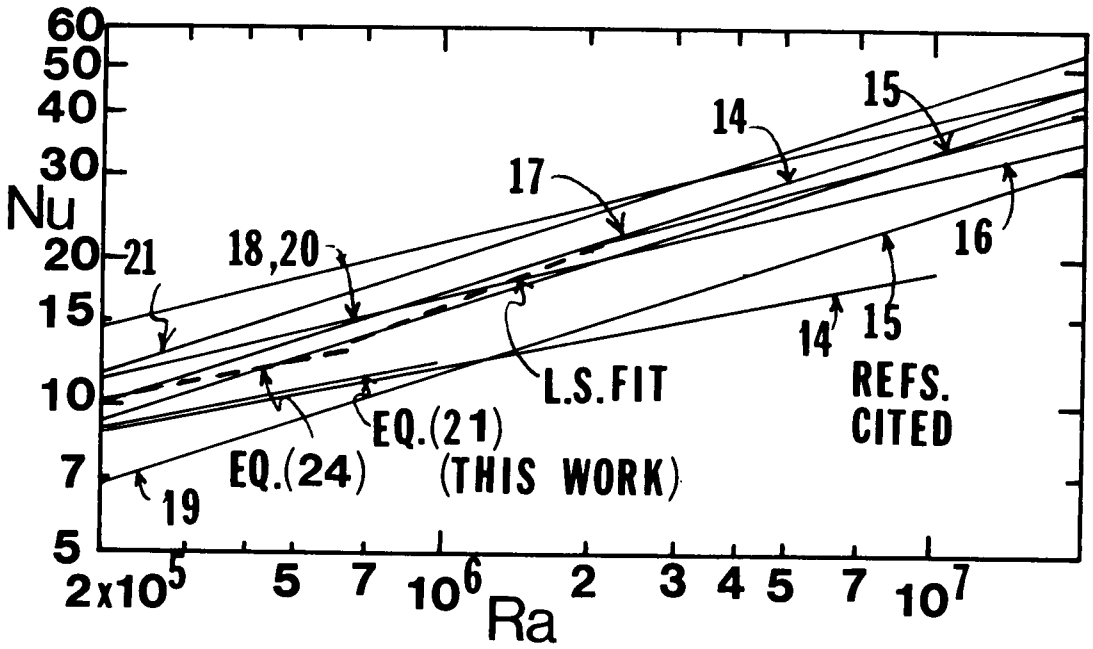

Figure 5. Comparison of results of various investigators, for a heated, upward-facing horizontal plate.

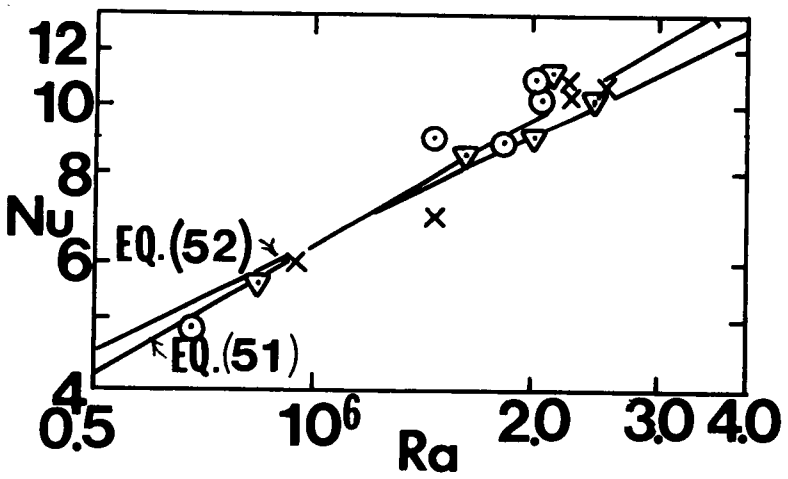

Figure 6. Average Nusselt number vs. Raleigh number for three specimens on horizontal, heated plate facing downward (maximum error: ± 15%).

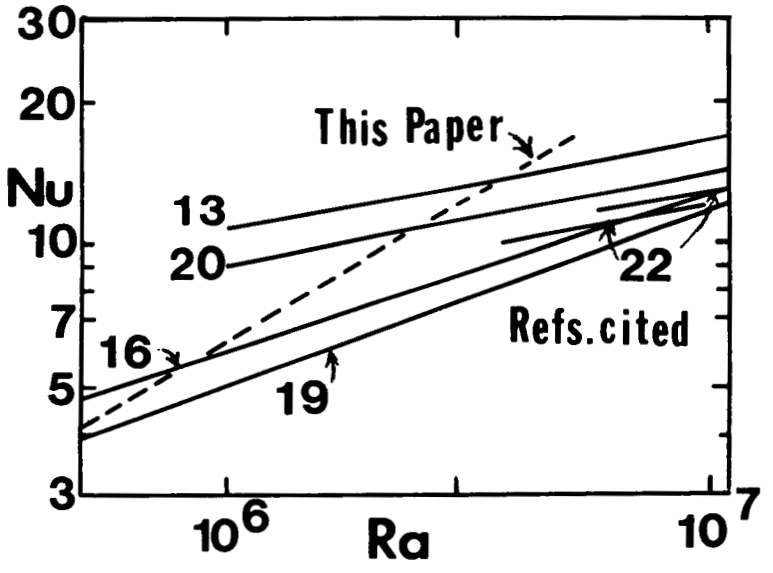

Figure 7. Comparison of results of several investigators, for a heated, downward-facing, horizontal plate.

CONTAMINATION CONTROL OF THE SPACE SHUTTLE ORBITER CREW COMPARTMENT

Donald W. Bartelson
Lockheed Space Operations Company

ABSTRACT

The crew compartment of the Space Shuttle Orbiter is a unique environment where contamination control is critical to the performance of orbiter systems and astronauts alike.

A balance must be established between materials used in the crew compartment (both flight and ground support)/system design/personnel activities and nominal system equipment functioning/crew safety. Materials selected must meet programmatic requirements such as flammability, non-shedding and chemmical off-gasing specifications. A "debris-filtering" system consisting of screens for electronic equipment and conditioning breathing air for life support must be in top performance at all times. Another very important aspect for the achievement and maintenance of strict cleanliness levels in the crew compartment is the development and effective practice of contamination control procedures by both astronauts and ground personnel.

With the advent of the Space Shuttle Transportation System and the ensuing reality of the Space Station, a compatible environment for personnel and sophisticated equipment must be further enhanced and fine tuned to state-of-the-art standards.

To facilitate the accomplishment of this goal, several studies in contamination control science involving the crew compartment are in progress. These studies include:

1) Ground Processing contamination control improvements,

2) Analysis and source identification of crew compartment debris,

3) Screen design effectiveness and air flow patterns,

4) Air ionization techniques and

5) Proposal improvements for flight materials, system operations and personnel activities/dress.

An effective ground processing contamination control program is an essential building block to a successful shuttle mission. Personnel are required to don cleanroom-grade clothing ensembles before entering the crew compartment and follow cleanroom rules and regulations. Prior to crew compartment entry, materials and equipment must be checked by an orbiter integrity clerk stationed outside the white-room entrance for compliance to program requirements.

Facility ground processing equipment (GSE) improvements have recently been made to upgrade crew compartment cleanliness. A totally new designed white room entry-way for crew compartment access was built. This

improvement allowed personnel and GSE cleaner access conditions to the crew compartment. A positive pressure gradient from the crew compartment to the whiteroom to the facility ambient environment was achieved.

Other improvements are forth coming as a direct result of contamination control studies (described herein) and SPC/NASA concern for the ''cleanest'' zero-G environment possible.

Analysis and source identification of crew compartment debris studies have been on-going for approximately 2 years. The objective of these studies is to determine and identify particulate generating materials and activities in the crew compartment. Visual inspections are performed and samples of debris are collected for analysis. The results show a wide spectrum of many different types of materials; food particles, hair, paint products, aluminum, etc. The contaminants are studied closely as to probable identity and source. Analysis results are then compared to a list of approved flight and GSE materials. When a source identification is made, corrective action is implemented to minimize or curtail further contaminant generation.

Another very critical area for nominal orbiter system functioning and life support systems are the equipment screens installed in the avionics, computer, air recirculation, etc., units in the crew compartment. The overall effectiveness and in-flight ease-of-maintenance of this ''air-flow filtering'' system is an area where further improvements and modifications would provide a ''cleaner'', more trouble-free environment for flight. A dilemma exists in the design of the equipment screens and air flow system; adequate air flow rates vs. effective contaminant capture where co-existence is necessary for system balance and operation.

A fourth category of study is effective air ionization techniques to allow dissipation of charged particles deposited on surfaces in the crew compartment. Preliminary investigations involving this technique to determine effectiveness and applicability is introductory. Although, studies to date reveal beneficial results.

To summarize, effective contamination control as applied to manned space flight environments is a discipline characterized and controlled by many parameters. This introductory paper on Orbiter Crew Compartment contamination control will present the referenced studies and results to-date. It is the hope of the SPC, by means of investigative/analysis and system enhancement to upgrade the cleanliness level of the crew compartment to the best extent technologically possible.

USE OF A 35mm CAMERA FOR REMOTE SURFACE CLEANLINESS VERIFICATION

E. R. Crutcher
Boeing Company

ABSTRACT

Non-contact or remote monitoring of surfaces for both particle and molecular contaminants is required for verification of surface cleanliness on many program subsystems. The capability of a 35mm camera to satisfy this need is presented here. The many limmitations imposed by standard available lens systems are compared to actual required sensitivies. Methods of optimizing camera systems for specific applications and descriptions of support systems for extending the range of usefulness of the recorded data are also provided. Although this general concept is not new significant improvements in the technique involving the use of polarized light and diffraction effects have resulted in a more efficient utilization of information recorded on the film.

S7-72
10284
9

N88-10836

AN INVESTIGATION OF THE BEHAVIOR OF OUTGASSED MOLECULES IN THERMAL VACUUMS

W. Mahone
Lockheed-EMSCO

R. Kays
Lockheed-EMSCO

S. Koontz
NASA Laboratories Test Office

NC45421

ABSTRACT

Personnel at the White Sands Test Facility (WSTF) are currently developing a method to evaluate the amount of outgassing from active surfaces in individual Shuttle payload items that may condense on functional surfaces. To develop a viable method of assessing the extent to which materials can contaminate surfaces in space vehicles, an experimental apparatus has been designed in which space-simulation studies are being conducted. The objective of these studies is to understand how surfaces outgas and how the outgassed substances subsequently condense on other surfaces.

There are two techniques for evaluating the mass flux from a surface. The Langmuir technique measures directly the mass flux from a surface (Langmuir 1913). The Knudsen technique (Knudsen 1909), on the other hand, measures the mass flux through an orifice. This method measures the mass flux from the surface indirectly since it will be equal to the mass flux through the orifice at equilibrium.

A device used to measure partial pressure is necessary to evaluate experimentally the mass flux through the orifice. Two instruments have been incorporated into the design of the experimental apparatus that will not only allow the determination of the partial pressure in the inner chamber, but will also provide direct information about the relationship between outgassing and condensation for various materials. One of these instruments, a mass spectrometer, measure the partial pressure directly. The other instrument, a thermally controlled quartz crystal microbalance (TQCM), evaluates the partial pressure of condensable materials by measuring the condensation rate.

The advantage of the Knudsen technique becomes obvious when the following expression for the rate of mass flux through the orifice is considered:

$$dm/dt = Ap\,(Vu*Du - V1*D1)/4 \qquad (1)$$

Here Ap is the area of the exit orifice; Vu is the average molecular velocity of the gas in the inner chamber (where the sample is located); V1 is the average molecular velocity in the outer chamber; Du and D1 are the gas densities in the inner and outer chambers, respectively. When ideal gas conditions are satisfied, the density of the ith gaseous species Di is related to the partial pressure by the following equation:

$$Di = Pi*Mi/R*T \qquad (2)$$

where Mi is the molecular weight of the ith species; R is the universal gas constant; and T is the absolute temperature of the gas. These equations show that by monitoring the equilibrium partial pressure of an outgassed species in an inner chamber, the rate at which outgassing is occurring for all the surfaces in the chamber can be determined.

If it is assumed that every outgassed molecule that strikes a surface, such as a TQCM crystal, becomes an adsorbed molecule, the following relationship between the condensation rate and the partial pressure will hold:

$$Pi = B*(R*T/Mi)*ri \quad (3)$$

where ri is the condensation rate of the ith gaseous species on a surface and B is a constant. Partial pressures can be calcualted from TQCM condensation rates using equation (3). The partial pressures can then be substituted into equation (2) to calculate densities. Those densities can then be substituted into equation (1) to calculate semi-empirical outgassing rates for single-component samples (sublimation rates). These outgassing rates can be integrated over the test time to generate calculated total mass losses.

Preliminary tests conducted at WSTF produced calculated mass losses that were found to be in reasonable agreement with mass losses determined by weighing the sample before and after testing on analytical balances. However, tests using materials with various molecular properties showed characteristic variations in the ratios of calculated total mass loss to experimental loss. These variations indicate that for some molecules energetic barriers to adsorption and desorption can exist between outgassed molecules and the surfaces on which they condense.

REDISTRIBUTION OF PARTICULATES IN SHUTTLE BAY DURING LAUNCH

John J. Scialdone
Goddard Space Flight Center

ABSTRACT

The dislodgement, venting, and redeposition of particles on a surface in the shuttle bay by the vibroacoustic, gravitational, and aerodynamic forces present during shuttle ascent have been investigated (ref. 1). The particles of different sizes which are displaced, vented, and redistributed have been calculated; and an estimate of the increased number of particles on certain surfaces and the decrease on others has been indicated. The average sizes, velocities, and length of time for certain particles to leave the bay following initial shuttle doors opening and thermal tests have been calculated based on indirect data obtained during several shuttle flights. Suggestions for future measurements and observations to characterize the particulate environment and the techniques to limit the in-orbit particulate contamination of surfaces and environment have been offered.

ANALYSIS RESULTS AND CONCLUSIONS

Particulate contaminants on shuttle bay surfaces and on surfaces of payloads carried by the shuttle will be resuspended during shuttle ascent by vibroacoustic, gravitational, and aerodynamic loadings.

Random mechanical accelerations of about 13 g rms in the frequency range of 20 to 2000 Hz experienced during ascent by surfaces and systems are expected to release from surfaces all the particles in excess of 80-90 μm diameter and only 1-2 percent of particles less than 10 μm. These particles--depending on the direction of the releasing surface with respect to the acceleration vector--will fall back on the surface, fall on another surface properly positioned with respect to the velocity vector, or be transported to the vent filters. Also, if they have sufficient falling kinetic energy, they may bounce from surface to surface until they either deposit on a surface or are entrained by the outgassing molecules in the bay acquiring the energy of the outgassing molecules which will be colliding with them. The particles not deposited will be moving randomly in this relatively tenous gas only rarely hitting a surface.

Two periods of releasing and resetting of particles are envisioned. During these two periods, the random acceleration forces have magnitudes of about 13 g rms including some peak magnitudes of about 39 g.

An initial number of particles will be released during the initial 2 minutes of ascent while venting of the bay volume is occurring. During the transonic region of flight with maximum mechanical disturbance at the surfaces

and maximum vent velocity in the bay, released particles of less than about 58 μm, will be entrained by the gas flow. Most of them may be directed to the vents where they are trapped if greater than about 35 μm. Others entrapped in a turbulent flow will remain in random motion in the bay.

Released particles greater than 58 μm will resettle on the surface of origin if the surface is normal and facing the velocity vector. Those released from surfaces parallel and/or not facing the velocity vector will drop on surfaces facing the vector by virtue of the shuttle acceleration.

During the second stage of the ascent, which terminates about 9 minutes after launch, additional particles are released and resettled. Aerodynamic drag in the bay is no longer effective in moving particles; and those released either will be accommodated on the surface by the shuttle acceleration or will be floating about in the bay in a zero g environment.

The following particle redistributions may be expected during launch in the shuttle or in an instrument:

- A surface facing opposite the acceleration vector at a prelaunch cleanliness level of 750 as per MIL-STD 1246A will lose particles as it cleans up (fig. 1).

  In orbit, that surface will have slightly less particles in the size range up to 36 μm and considerably less particles of larger size than it had at launch. No particle greater than about 90 μm will be left on that surface.

- A surface looking into the velocity vector and located toward the rear recovers its own acceleration released particles and collects particles released from other surfaces which are accelerated toward the rear of the shuttle or of the instrument (fig. 2). The increased number of particles on these surfaces are mainly those of diameter greater than 58 μm. The number of particles per unit area may double for this range if there is a one-to-one view factor between the rejecting and accepting surfaces. If the area of the surfaces releasing particles is K times the area of those surfaces receiving particles, then the accommodation is approximately K times the one for the one-to-one view factor. For the shuttle bay, the distribution per unit area on the aft surface of the bay may be approximately 18 times that for the double distribution obtained for the one-to-one view factor.

- A relatively clean surface (less than Level 500) will be contaminated with particles from other surfaces greater than 58 μm, and with few particles with diameters between 58 and 5 μm (fig. 3).

- The redistribution of particles on surfaces assumed to have an initial distribution of particles corresponding to Level 750, with a surface correspondence of a one-to-one, has been indicated. These assumptions can be changed since the losses and gains of particles are provided in terms of the percentage of particles per unit area in the specific particle size range. The gain on a unit surface can be estimated by

modifying the results for a one-to-one relation by the area ratio of the surface losing to the one gaining particulates.

- Some small particles <58 μm, which did not enter the vents or were released during the second phase of acceleration, are entrained in the outgassing molecules and move randomly in the bay where the outgassing mean free path is a few tens of cm. After about 2 hours in orbit when the bay doors are opened, those particles which have mean diameters of 10-15 μm leave the bay with average velocities of about 1×10^{-2} cm/s. Outside of the bay, these particles are decelerated with respect to the orbiter by drag forces and will be moving away from the velocity vector. The camera-photometer observing these particles at various distances from the bay will see the particle moving at about 1.5 m/s if the particle is 20 m away and about 0.33 m/s if at 1 m away. These bay released particles lose energy with respect to the shuttle and enter a different orbit.

- Particles of mean diameter of about 36 μm which had deposited on surfaces and/or did not leave the bay will be made to leave the bay at velocities of 1.5×10^{-3} cm/s by thermally induced effects. Thermal shock, differential thermal expansions, friction between surfaces, photodesorption, thermophoresis, desorption from surfaces, and other mechanisms can be the cause of these additional emissions, which have been observed by the camera photometer in one of the shuttle flights.

RECOMMENDATIONS

1. Clean the bay surfaces and payloads to optimum level of cleanliness before launch. Protect the clean surfaces whenever possible.

2. Surfaces normal to the acceleration vector should be as clean as possible, since they will receive additional particles from other surfaces above them not facing the acceleration vector.

3. The bay doors should be opened as soon as possible to allow particles floating in the bay to exit. This will limit the settling of those particles on surfaces.

4. Provide particulate shields, covers, and doors on surfaces normal to acceleration. The covers should firmly enclose the protected surface preventing particles carried by turbulent venting flow from entering the spacing between cover and surface.

5. Optical observations out of the bay should be carried out after the source of particles leaving the bay is depleted. The time constant (1/e drop in number) is about 10-15 hours. The time to wait for the number of particles leaving the bay to be a few percent of the initials is therefore 40-50 hours after bay opening. This delay in observation may also be necessary after an initial thermo-shock of the shuttle bay.

6. Suggested measurements and data collections which may provide additional understanding of the release and redistribution of particles in the bay are:

   a. Photomicrograph control surfaces located on bulkhead and aft of the bay, before launch, after rocket boosters' separation (2 min), after tank separation. Analyze these photos for particles redistributions as a function of ascent stages.

   b. Analyze the particulates on a filter vent before launch and in orbit. The sample filter could be replaced in orbit and returned to ground in a protected enclosure.

   c. Inspect and check visually for particulate deposits in the aft bay and bulkhead after shuttle flights to note gross differences in deposits.

   d. Use particle deposition instruments located at strategic locations in the bay and timed to operate at specific periods of the ascent to provide particulate density data in the bay at various times.

   e. Use QCMs with sticky surfaces to collect particulates at various bay locations during ascent.

   f. Use optical systems to get data on particulate density in the bay as a function of time while bay doors are closed and when opened.

REFERENCES

1. Scialdone, J. J.: Particulate Contaminant Relocation During shuttle Ascent, NASA TM-87794, June 1986.

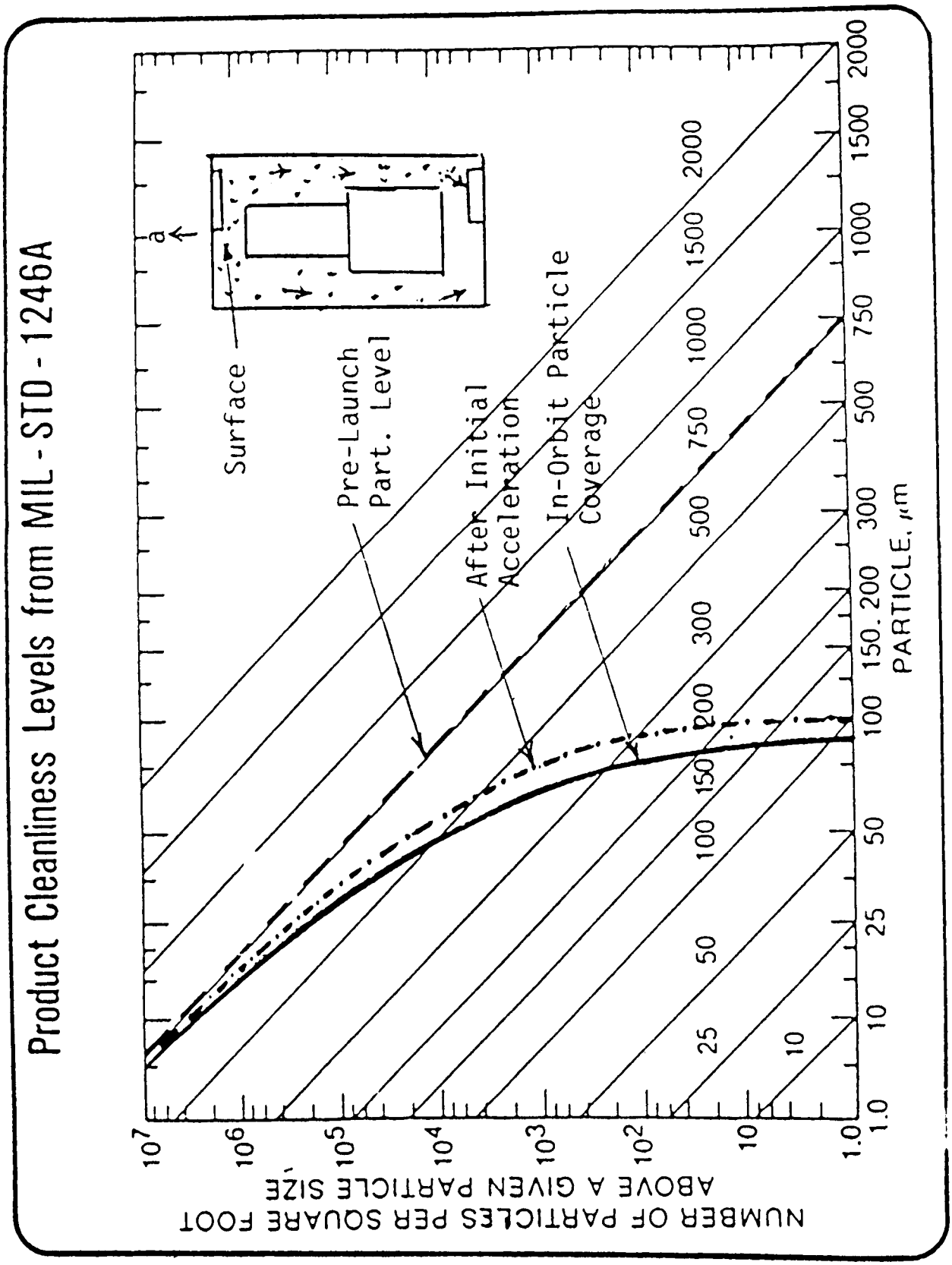

Figure 1. Particles depletion during shuttle ascent from a surface not facing the acceleration vector, contaminated to A Lv 750 of MIL-STD-1246A

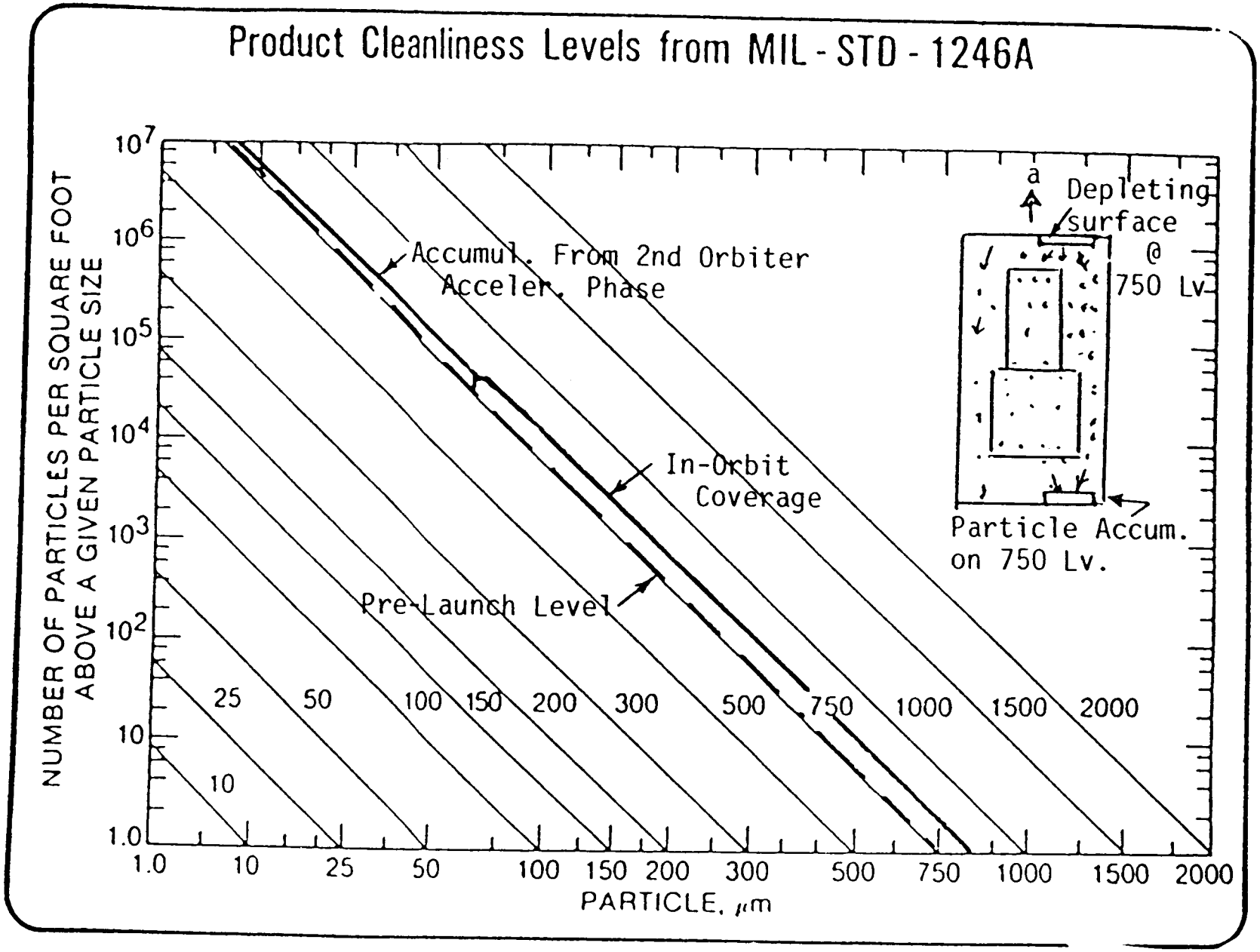

Figure 2. Particles accumulation during shuttle ascent on a surface facing the acceleration vector at a pre-launch Lv 750 from a depleting surface also at 750 Lv with a one-to-one field of view

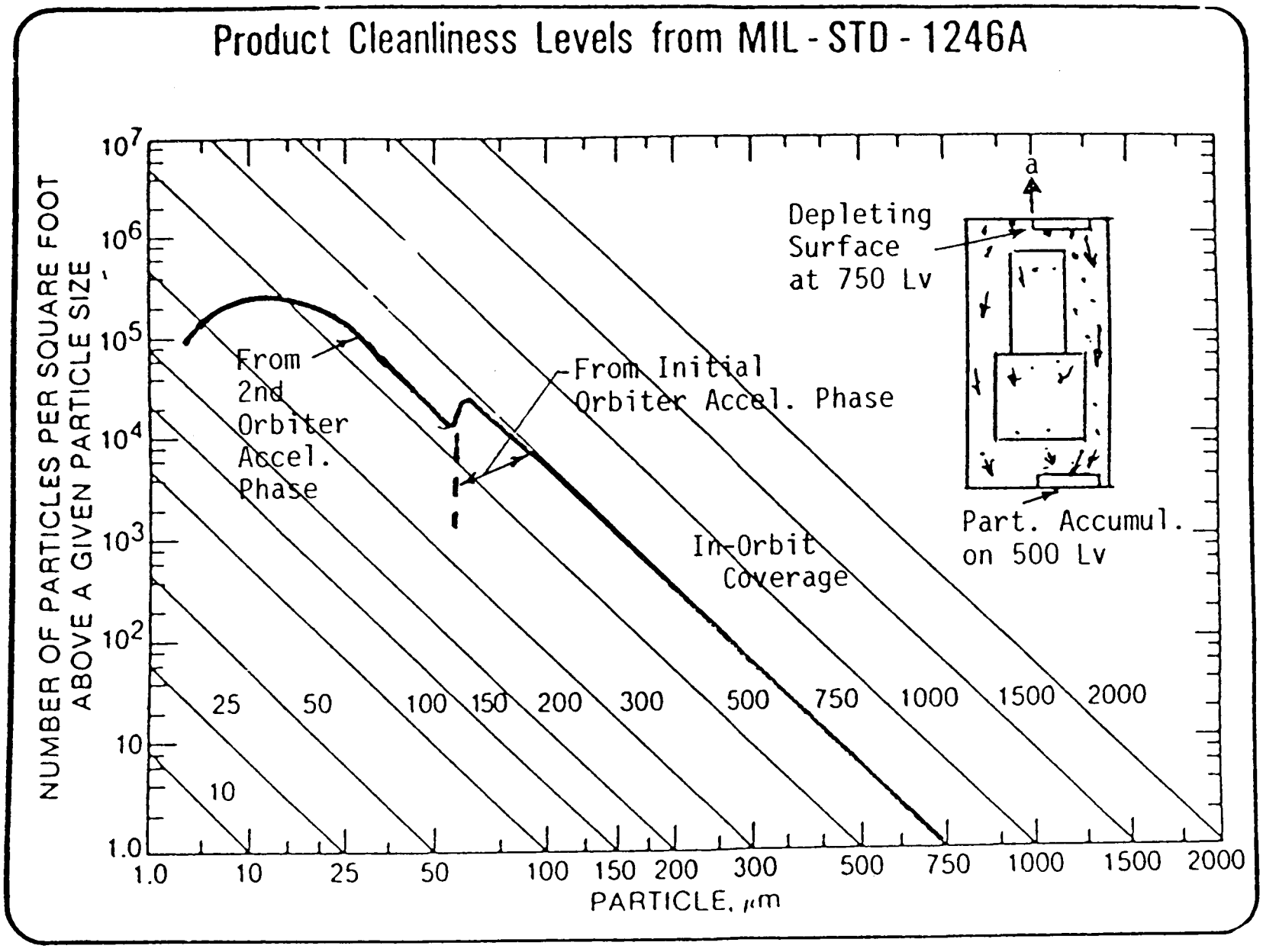

Figure 3. Particles accumulation during shuttle ascent on a clean surface (pre-launch Lv 500) facing acceleration from a depleting surface at Lv 750 with a one-to-one field of view

SHEAR STRESS™ CLEANING FOR SURFACE DEPARTICULATION

R. P. Musselman and T. W. Yarbrough

Quadrex HPS Inc.
Gainesville, Florida

ABSTRACT

A cleaning technique widely used by the nuclear utility industry for removal of radioactive surface contamination has proven effective at removing non-hazardous contaminant particles as small as 0.1 micrometer (μm). The process employs a controlled high-velocity liquid spray inside a vapor containment enclosure to remove particles from a surface. The viscous drag force generated by the cleaning fluid applies a shear stress greater than the adhesion force that holds small particles to a substrate. Fluid mechanics and field tests indicate general cleaning parameters.

INTRODUCTION

Microminiaturization of electronic devices and increasing performance requirements of precision mechanical systems, optical elements, and clean room equipment have lowered the tolerance limits for particulate surface contamination to unprecedented levels. The primary goal of the extensive contamination control effort is to attain and maintain desired levels of cleanliness on surfaces of items during production and/or use. Particle induced failures and low product yields attest to the fact that contamination avoidance is not always possible. A number of techniques have been developed to remove particles from contaminated surfaces. Traditional gross cleaning methods such as solvent immersion, low-pressure spray in the range of 3.4×10^{-2} to 2.8×10^{-1} MPa (5 to 40 psig), vapor degreasing and ultrasonics remove visible solids but do not adequately address particles

smaller than about 25 μm [1,2]. For smaller particles, the relative forces of adhesion are so large that the only effective method of removing them is to apply a direct mechanical force. Wiping, while effective, is labor intensive, especially for complex surfaces [3-5].

Alternatively, a shear stress sufficient to overcome small particle adhesive forces may be applied by the viscous drag force generated by a high velocity fluid.

In the late 1970's, a general technology called shear stress cleaning evolved which incorporates the use of pressurized (6.9×10^5 to 1.5×10^7 MPa [100 to 2200 psig]), high-velocity, (140m/s [450 fps]), fluid sprays for removal of surface contamination. Simultaneous independent development led to systems specialized for different applications. ERDA-sponsored research [1] at Lawrence Livermore Laboratory produced a cleaning system for optics used in high energy lasers for fusion research. Commercial applications [6] allowed generators of radioactive or toxic wastes to decontaminate items to levels allowing unrestricted release of materials for reuse, thereby reducing the volume of waste requiring shallow land disposal and minimizing the risk of personnel exposure and environmental contamination.

The dynamics of shear stress cleaning are the same for all applications requiring highly efficient removal of particles, oils, and process chemicals, whether the contaminants pose a health hazard or lower product yield and reliability. This article describes the mechanics of surface cleaning by shear stress and discusses results obtained from tests and field applications of the technology.

EFFORT REQUIRED TO REMOVE PARTICLES

Numerous studies have been conducted [7-10] to determine the relative magnitude of adhesion forces of small particles to surfaces. Such a broad array of forces and conditional parameters affect the force of adhesion that accurate a prior prediction of the force necessary to remove particles in real world situations is impossible. (Forces of adhesion include gravitational, electrostatic, intermolecular, capillary and sedimentary; conditional parameters

include particle size, shape, ability to deform, tendency to agglomerate and surface topography). However, some useful generalizations can be made that indicate techniques to improve cleaning effectiveness.

Where intermolecular attraction forces dominate, the net attractive force on a particle increases proportionally [9] as particle size (diameter) increases. However, cleaning techniques are less effective on smaller particles because the ability of the method to impart a force to a particle decreases with diameter more rapidly than does the force holding the contaminant to the surface. Techniques that clean by centrifugal or impulse forces depend on particle mass, which decreases with effective diameter cubed. As will be shown, the drag force produced by shear stress cleaning depends on the particles projected frontal area and decreases more slowly, with the square of particle diameter.

A common practice is to compare adhesion forces holding a particle on a surface to the force exerted by gravity on the particle. While the intermolecular forces on a 1000μm (0.04 in) particle are comparable to one time the force of gravity (1 g), the force on a 5μm particle is more than 2 million g's and relative adhesion forces of hundreds of millions of g's have been postulated [10,11] for submicron particles. Although cleaning solvents may reduce these forces by orders of magnitude, sufficient attraction will remain to require vigorous mechanical action to effect the removal of small particles.

DRAG FORCE ON PARTICLES

A stationary particle in a moving fluid stream will experience a drag force (F_d) due to the pressure exerted by the moving fluid and the friction between fluid molecules and the particle skin as they flow around the particle. The magnitude of the force may be determined from the equation

$$F_d = C\rho \frac{V^2}{2} A,$$

where C is the drag coefficient dependent upon particle shape, particle surface roughness and other factors; ρ is the fluid density; V is the local

fluid velocity around the particle; and A is the projected frontal area of the particle.

The objective of Shear Stress cleaning is to increase the value of drag force to the point that it exceeds the force of adhesion, thereby detaching the particle from the surface. There are only two apparent controllable parameters available to optimize cleaning effectiveness. In general, the higher the fluid density and local velocity, the more effective particle removal becomes. Density may be selected by an appropriate choice of cleaning fluid. For example, liquids are much more effective than gases, and of the common cleaning fluids, fluorocarbon solvents such as trichlorotrifluoroethane (CCl_2F-$CClF_2$, Fluorocarbon-113) lend themselves well to spray cleaning applications due to their selective solvency, high density, low toxicity and, as will be explained, low viscosity. Increasing the fluid velocity at the particle is more complicated and requires further discussion.

THE LAW OF THE WALL AND PARTICLE HIDEOUT

When a fluid passes over a surface, the velocity approaches zero immediately at the surface but increases to a maximum, known as the free stream velocity (u_s), at some distance above the surface. The universal dimensionless profile relating velocity to distance from a surface is known as the "law of the wall".

Considering flow of fluid along a flat plate as a model, fluid molecules at the plate surface are brought to rest, and those for a short distance above the plate are slowed because of viscous shear in the fluid. This region of retarded flow is called the "boundary layer" and for practical purposes extends to the point at which fluid velocity equals 99% of the free stream velocity. For most high velocity spray applications, the flow within this boundary layer can be considered turbulent over the entire surface. A thin laminar sublayer will exist between the plate surface and the turbulent portion of the boundary layer. Within this sublayer, velocities decrease rapidly to zero.

The manner in which fluid velocity varies with distance above the surface depends on whether the point of reference lies within the free stream, the turbulent boundary layer or the laminar sublayer. Once this has been established, the velocity as a function of distance may be determined from known empirical relationships.[12,13]

The thickness of this low-velocity sublayer determines to a large extent the effectiveness of spray cleaning at removing very small particles. If the sublayer is thick compared to particle dimensions, the particles can "hide out" in the sublayer. Since they will be affected only by the lower velocities, the drag forces exerted may be too small to detach them from the surface.

This effect of "particle hideout" is illustrated in Figure 1 for typical low velocity sprays (such as encountered in vapor degreaser spray wands) and a relatively large particle. The effect of particle hideout is more obvious if micron size particles are of concern.

Examining the parameters that affect the sublayer thickness, and therefore fluid velocity incident on the particle, discloses effective methods for exposing particles to higher velocities, preventing particle hideout. It will be shown that the predominant adjustable factors in making the local fluid velocities at the particle higher are increasing the free stream velocity (u_s) and reducing fluid viscosity (μ).

VELOCITY PROFILES

A mathematical model has been derived[13] from classical fluid mechanics to determine the relative velocities at any point downstream from the point of spray impact on a smooth surface (x coordinate) and above the surface (y coordinate) [Figure 2]. A computer model was developed to generate isovelocity profiles for any fluid, given density (ρ), dynamic viscosity ($\nu = \mu/\rho$), and free stream velocity (u_s). This report extends the study to predict approximate values of drag force over a range of particle sizes and spray pressures.

Figures 3 and 4 illustrate velocity profiles of two cleaning fluids (water and Fluorocarbon-113 respectively), each having a free stream velocity of 100 m/s (328 fps). Note that by raising the free stream velocity, the local velocity near the surface is much higher than in the example illustrated by Figure 1. Further, the velocities produced by the fluorocarbon solvent near the surface are higher than those for water, due primarily to the fluorocarbon's lower viscosity. This takes on added significance considering the fact that drag force (F_d) depends on the square of the local velocity. A numerical listing of some of the values obtained in generating these profiles is given in Tables 1 and 2.

DRAG FORCE

Since the local velocity may vary significantly from the substrate surface up to a distance equal to a small particle's diameter, a model was developed to account for this in calculating drag force (F_d). The model is illustrated by Figure 5.

Here a one micron particle is approximated as a sphere and divided into ten segments. The drag force on a segment is calculated using the local velocity at a distance from the substrate surface corresponding to the mid-point of that segment. Each segment's projected frontal area is also considered. As illustrated, the maximum drag force occurs well above the particle midpoint, due to the higher fluid velocities experienced by these segments. Similar calculations were used to generate Table 3. Data from this table is graphed in Figures 6 and 7.

The data show a near linear relationship between drag force (F_d) and spray nozzle pressure. At a given spray pressure (and therefore free stream velocity), the drag force depends predominantly on the particle's projected frontal area (A) and thus on particle diameter squared.

Superimposed on Figure 7 are results of experiment[9] and calculations[10] conducted to determine the value of the average adhesion force on particles of various sizes. It is seen that extrapolation to the submicron

region indicates quite high pressures may be required to detach these particles. The adhesion force lines are for particles attached to a substrate in air. The need for excessively high spray pressures may be mitigated somewhat by the fact that the adhesion force will be reduced when the substrate and particles are immersed in a liquid [7,10]. Counteracting this to a degree, however, is the fact that all particles of the same size do not have the same value of adhesion force. A monodisperse collection of particles will have a distribution of adhesion force values that may span several orders of magnitude. Cleaning applications that require extremely low particle counts must target the removal of the most tenacious particles, rather than the average.

Though the absolute values predicted by the model may not be precise, the relative trends should allow some general predictions. For example, once the drag force required to remove a given particle (with diameter D) from a substrate is determined experimentally (e.g.) point A on Figure 7), a line parallel to that calculated [10] for intermolecular attraction ($F_d \propto D$) may be drawn to estimate the minimum particle size removed at a different pressure (point B). Similar curves can be calculated at intermediate pressures. A rule of thumb that allows order of magnitude predictions is that the pressure required to detach a particle (P_{det}) is roughly inversely proportional to the particle size (D).

$$P_{det} \propto \frac{1}{D}$$

The object of this exercise has not been to produce a means of determining with absolute accuracy the exact spray pressure required to remove a particle of a given size. Rather, it has been to show that drag forces generated by liquid fluorocarbon sprays are of a magnitude that makes removal of submicron particles feasible. The practicality of this technique must be determined experimentally on a case-by-case basis. The next section describes such a case study.

PERFORMANCE EVALUATION

A chromium-plated glass test coupon was artificially contaminated with A/C Test Dust by spraying a suspension of the dust in methyl ethyl ketone (MEK) onto a rapidly spinning plate. The prepared surface had approximately 6000 particles/cm^2 in the 0.1-5μm size range. The coupon was sprayed for 10 seconds with trichlorotrifluoroethane (fluorocarbon-113) at a nozzle pressure of 14.8 MPa (2150 psig). The free stream velocity (u_s) of the fluid was 134 m/s (440 fps) and the velocity profile similar to that depicted for u_s = 100 m/s in Figure 3. Coupons were analyzed by light scattering surface scanner and scanning electron microscope. Typical before and after results are shown in Figure 8. Average final particle count was less than 0.3 particles per square centimeter, giving a particle removal efficiency of 99.995%.

A number of field tests have been done, though not under highly controlled conditions, using a variety of substrates and contaminants. The results of these tests are summarized in Table 4. Final contamination levels vary greatly and depend heavily on the analysis technique employed.

SUMMARY

A fluid dynamics model has been used to predict the magnitude of drag force applied to small particles by a high velocity spray of liquid fluorocarbon solvent. Comparison with theoretical and experimental particle adhesion force data indicates sufficient force will be generated to remove particles extending down into the submicron range. Tests have verified removal of particles as small as 0.1μm.

With the stringent demands for surface cleanliness placed on manufacturers of electronic devices, optics, precision mechanical equipment, and clean room process lines, the advent of shear stress cleaning technology is expected to play an increasingly important role in achieving compliance with surface departiculation requirements.

REFERENCES

1. Stowers IF, "Advances in Cleaning Metal and Glass Surfaces to Micron-level Cleanliness", Journal of Vacuum Science & Technology, 15(2): 751, 1978.

2. Beeson RD, "Hardware Cleaning and Sampling for Cleanliness Verification", presented to the 29th Annual Technical Meeting of the Institute of Environmental Sciences, Los Angeles, 1983.

3. Kwan SC, Mason KD, and Wieckowski, JM, "Precision Cleaning of Large Complex Structures", presented to the 29th Annual Technical Meeting of the Institute of Environmental Sciences, Los Angeles, 1983.

4. Kwan SC, Tomer RS, and Mason KD, "Precision Cleaning of Large Complex Structures - II", The Journal of Environmental Sciences, 28(4): 27, 1984.

5. Chidester MH, Kwan SC, Bush JM, and Mason KD, "Precision Cleaning of Large Complex Structures - III", presented to the 9th Contamination Control Working Group Meeting of the Inertial Guidance and Navigation Community, Los Angeles, 1985.

6. McVey, JT, Campuzano C, and Fowler DE, "Tools and Equipment: From Nuclear Waste to Reusable Items", Nuclear and Chemical Waste Management, 2: 197, 1981.

7. Zimon, AD, Adhesion of Dust and Powder, Consultants Bureau, New York, Second Edition, 1982.

8. Corn, M, "The Adhesion of Solid Particles to Solid Surfaces I", Journal of the Air Pollution Control Association, 11: 523, 1961.

9. Corn, M, "The Adhesion of Solid Particles to Solid Surfaces II", Journal of the Air Pollution Control Association 11: 566, 1961.

10. Brandreth DA, and Johnson RE, "Removal of Particulates from Optical Lenses", The Optical Index's Journal of Opthalmic Dispensing, January, 1979.

11. Tolliver DL, and Schroeder HG, "Particle Control in Semiconductor Process Streams", Microcontamination, June/July: 34, 1983.

12. Olson RM, Essentials of Engineering Fluid Mechanics, Intext Educational Publishers, New York, Third Edition.

13. Musselman RP, and Yarbrough, TW, "Shear Stress Removal of Submicron Particles from Surfaces", presented to the 9th Contamination Control Working Group Meeting of the Inertial Guidance and Navigation Community, Los Angeles, 1985.

TABLE 1. PHYSICAL PARAMETERS OF FREON® SPRAY AT 70°F

Nozzle Pressure (psi)	Nozzle Pressure (Mpa)	Free Stream Nozzle) Velocity (m/s)	Velocity Profile: Local Velocity (m/s)	Velocity Profile: at Distance Above Surface (microns)
1	6.9×10^{-3}	3.0	0.004	0.1
			0.041	1.0
			0.42	10.0
			1.9	100.0
3	2.1×10^{-2}	5.1	0.012	0.1
(Typical for open top vapor degreaser)			0.12	1.0
			1.2	10.0
			3.6	100.00
40	2.8×10^{-1}	18.7	0.17	0.1
(Typical for in-line vapor degreaser)			1.7	1.0
			10.0	10.0
			16.0	100.0
100	6.9×10^{-1}	29.5	0.42	0.1
			4.1	1.0
			19.0	10.0
			27.0	100.0
2000	13.8	132	8.3	0.1
(Typical for high pressure spray system)			61.0	1.0
			107	10.0
			132	100.0

TABLE 2

FREE STREAM VELOCITY AND BOUNDARY LAYER THICKNESS AT DIFFERENT PRESSURES

Nozzle Pressure (PSIG)	Nozzle Pressure (MPA)	Free Stream Velocity (M/S)	Turbulent Boundary Layer Thickness (Microns)	Laminar Sublayer Thickness (Microns)
1	6.9×10^{-3}	2.95	2000	16
10	6.9×10^{-2}	9.34	630	5.2
100	6.9×10^{-1}	29.5	200	1.6
1000	6.9×10^{0}	93.4	63	0.52
10000	6.9×10^{1}	295	20	0.16

Free Stream Velocity and Layer Thicknesses are Proportional to the Square Root of the Nozzle Pressure.

TABLE 3

DRAG FORCE VS. PRESSURE FOR
DIFFERENT PARTICLE SIZES

Nozzle Pressure (PSIG)	DRAG FORCE (DYNES) FOR PARTICLE SIZE LISTED				
	0.1 Micron	1 Micron	10 Micron	100 Microns	1000 Microns
1	1.36×10^{-7}	1.36×10^{-5}	1.96×10^{-3}	8.25×10^{-1}	1.41×10^{2}
10	1.36×10^{-6}	1.43×10^{-4}	4.34×10^{-2}	1.05×10^{1}	1.90×10^{3}
100	1.36×10^{-5}	1.96×10^{-3}	8.25×10^{-1}	1.41×10^{2}	2.11×10^{4}
1000	1.43×10^{-4}	4.34×10^{-2}	1.05×10^{1}	1.90×10^{3}	2.16×10^{5}
10000	1.96×10^{-3}	8.25×10^{-1}	1.41×10^{2}	2.11×10^{4}	2.17×10^{6}

Small Particle Limit (within laminar sublayer):

$$F_d \propto V_{local} \propto (V_{free\ stream})^2 \propto P_{nozzle}$$

Large Particle Limit (outside turbulent boundary):

$$F_d \propto (V_{free\ stream})^2 \propto P_{nozzle}$$

TABLE 4. TEST RESULTS

Substrate	Contaminant	Contaminant Size Range (μm)	Post-Cleaning Analysis Technique	Final Contamination Level (particles/cm^2)
Cr plated onto glass	A/C Test Dust	0.1 - 5	Scattered light surface scanner and scanning electron microscope	<0.3
Stainless Steel	Metal particles	≥10	50 psi flush, filter effluent and count particles on filter	0.0045
Cast Steel	Metal particles	0.5-20	Tape lift/200x magnification	<12
Rolled Cu	Lycopodium powder	25-30	Visual inspection/10x	0.8
Sintered Tungsten	Metal oxide	Unknown	Tape lift and 1x visual inspection under intense light	----*
Polypropylene	Metal particles	≥10	50 psi flush, filter effluent and count particles on filter	0.0015
Polyvinylidine Fluoride	PVDF	5-50	Tape lift/100x magnification	1-2
Mylar	Lycopodium powder	25-30	Visual inspection/10x magnification	----*
Polycarbonate	Unknown	≥5	Visual inspection/100x magnification	<0.05

*Below detection limits.

25μm Particle Sprayed with Freon® TF at 10 m/s Free Stream Velocity (Turbulent)

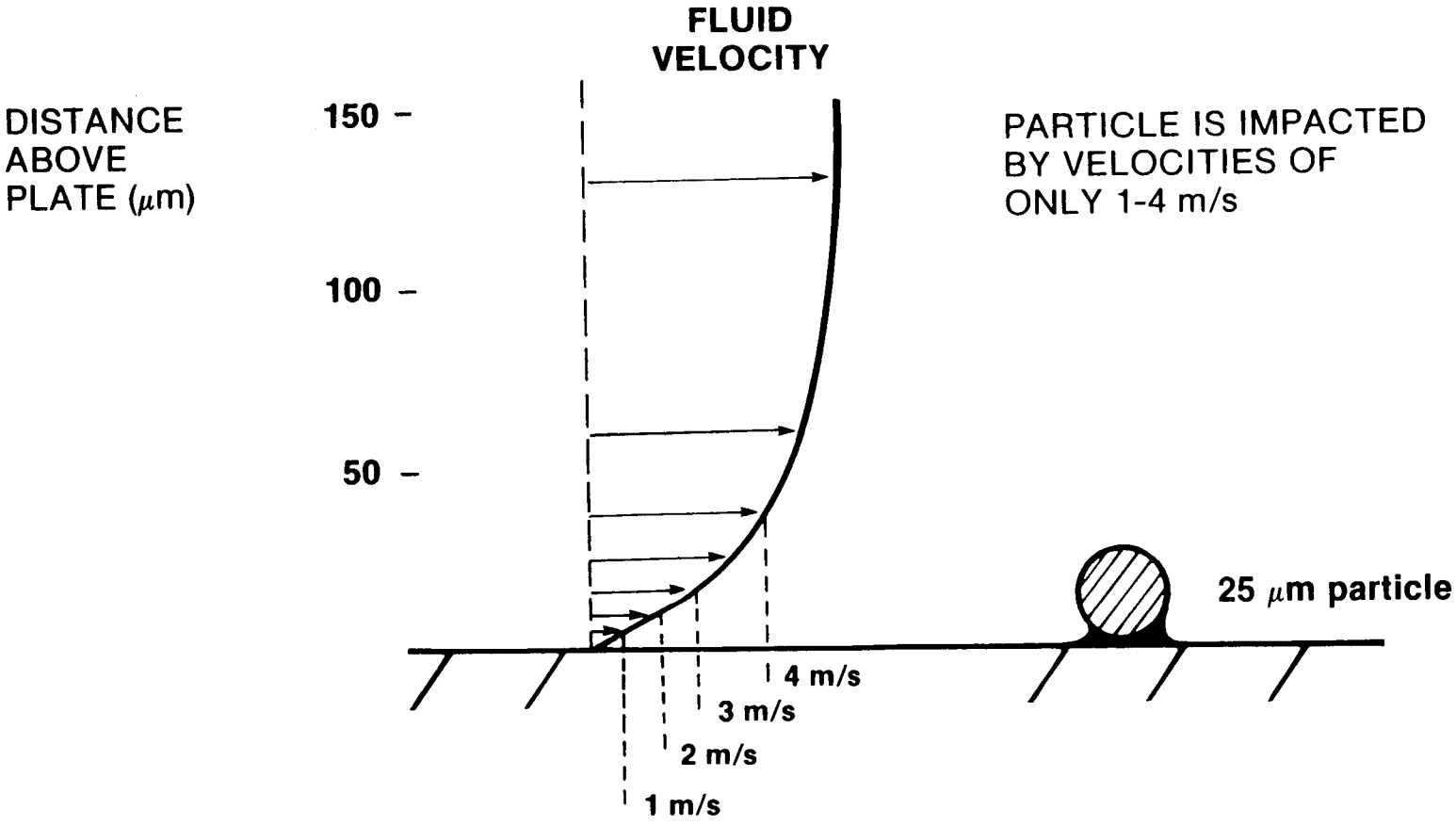

Figure 1. Particle hideout

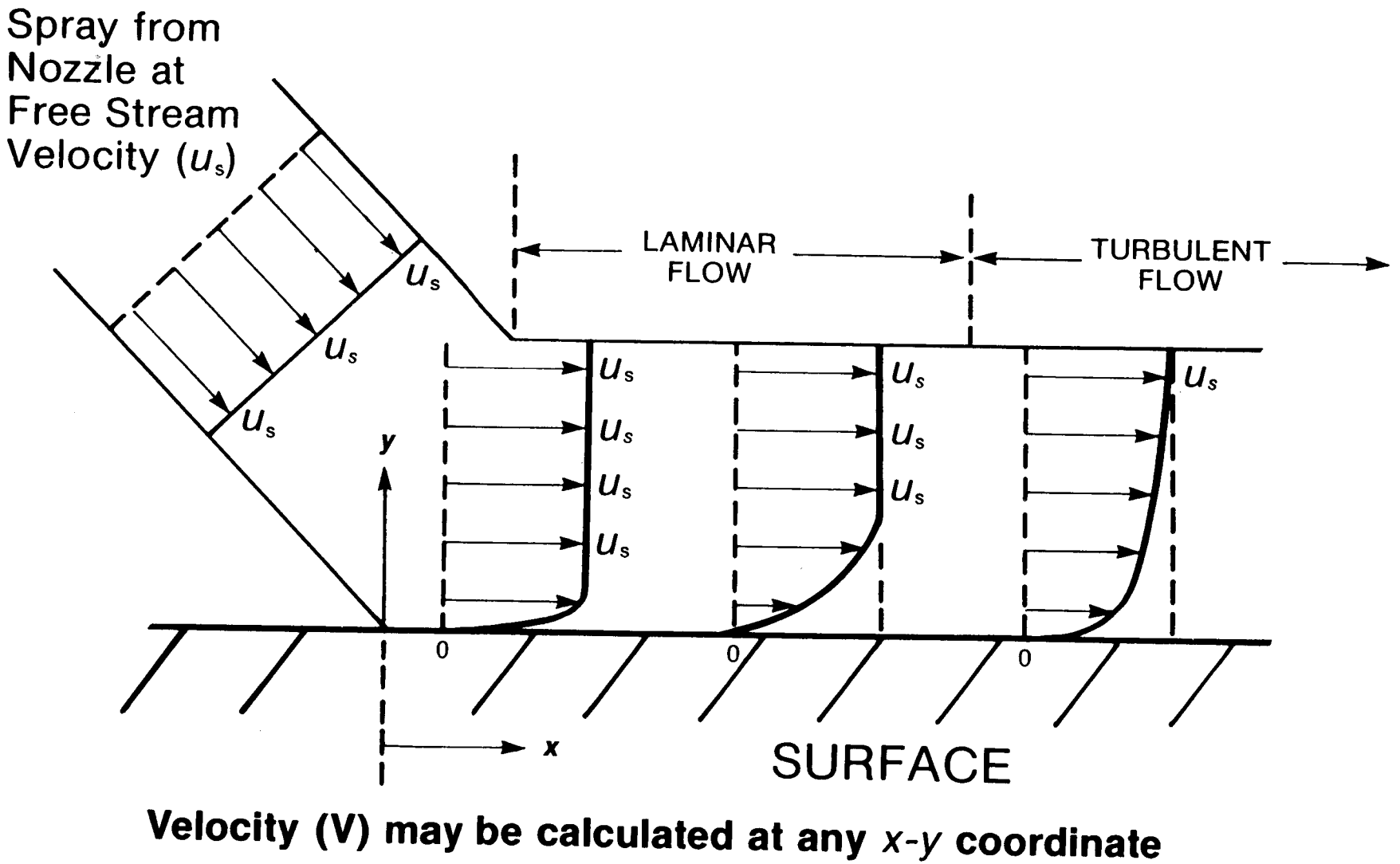

Figure 2. Velocity profiles of spray flow

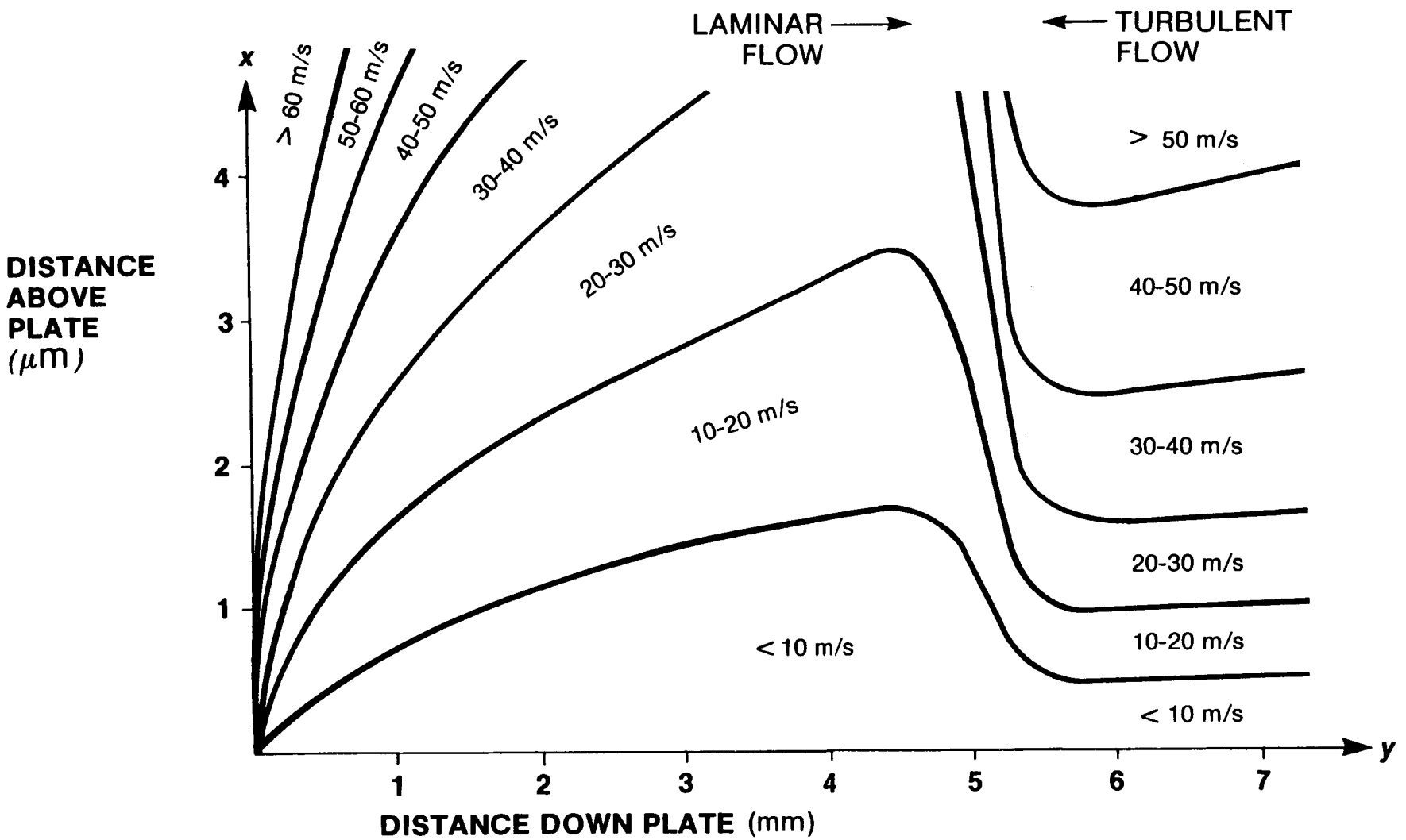

Figure 3. Isovelocity profiles along plate water @ 70°F, free stream velocity = 100 m/s

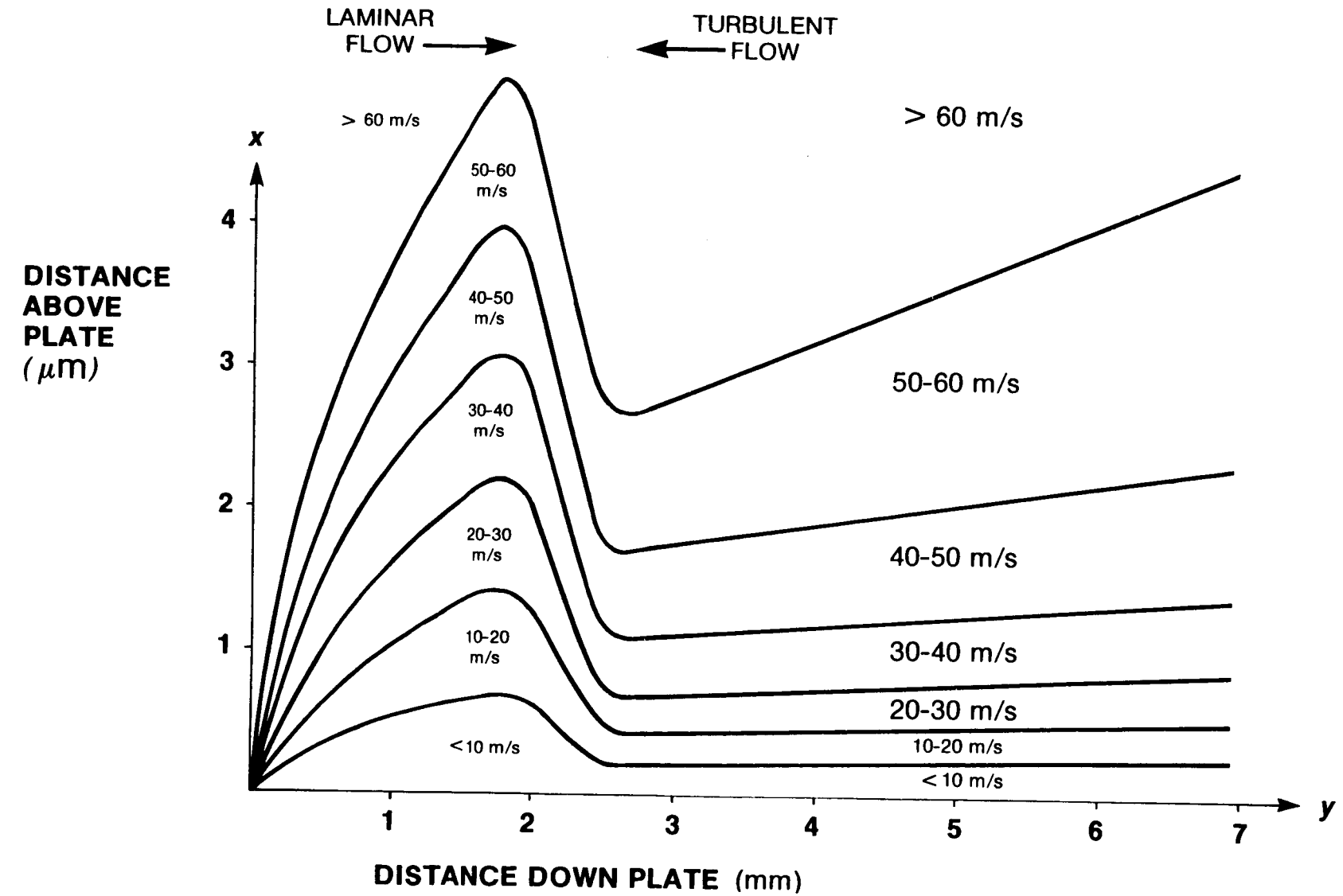

Figure 4. Isovelocity profiles along plate freon® TF at 70°F, free stream velocity = 100 m/s

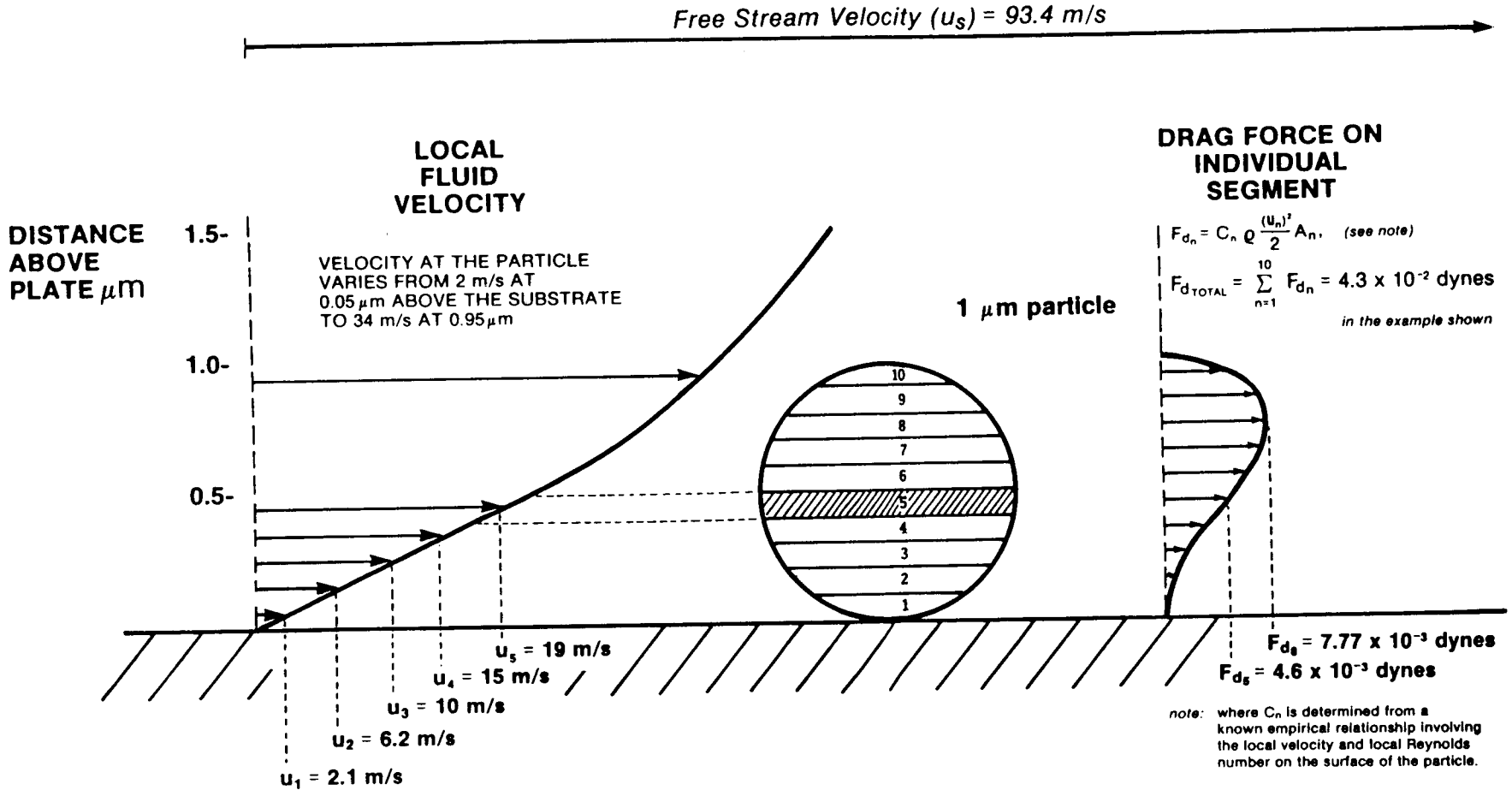

Figure 5. Drag force calculation

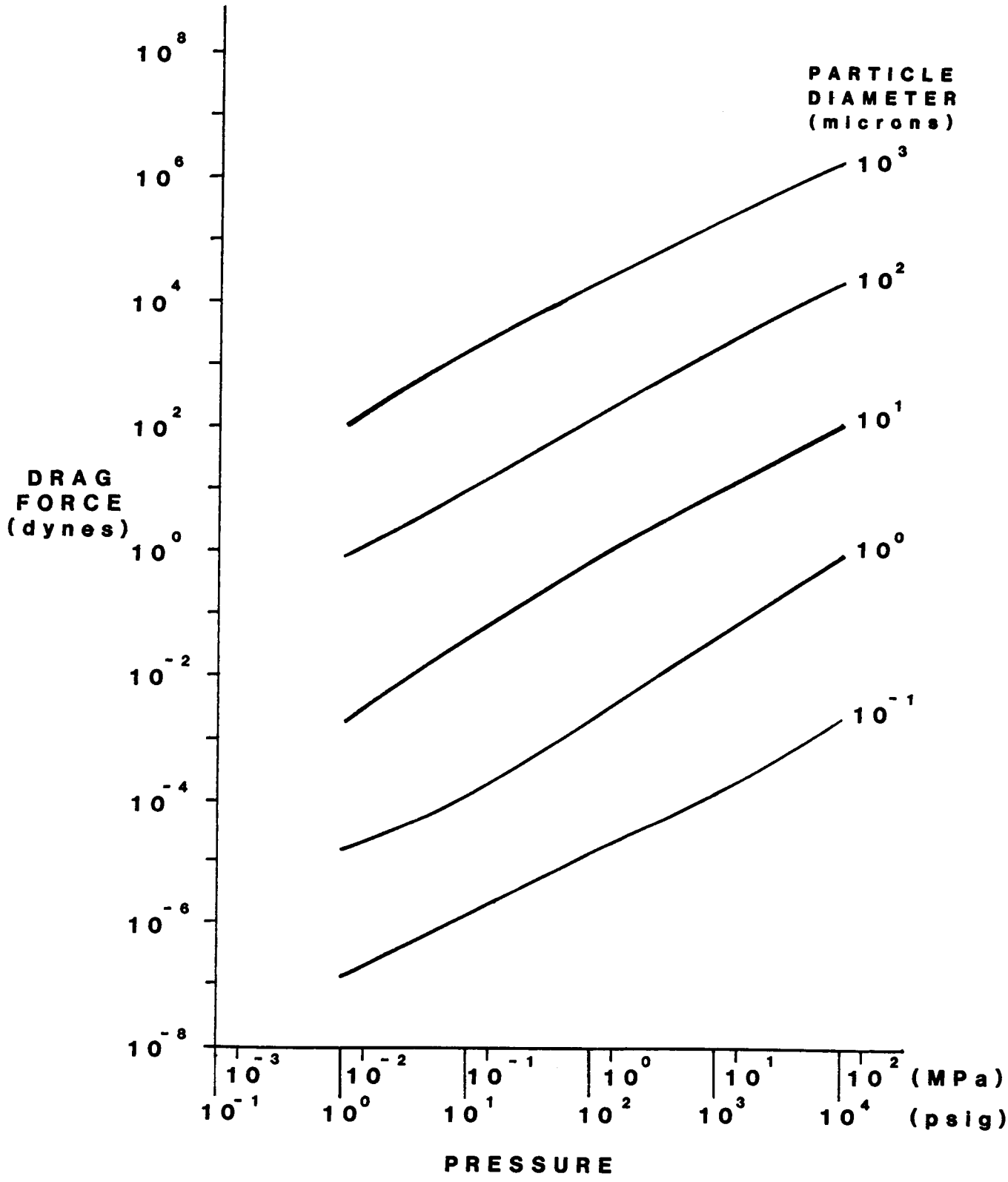
DRAG FORCE (dynes)
10^{8}
10^{6}
10^{4}
10^{2}
10^{0}
10^{-2}
10^{-4}
10^{-6}
10^{-8}
PARTICLE DIAMETER (microns)
10^{3}
10^{2}
10^{1}
10^{0}
10^{-1}
10^{-3} 10^{-2} 10^{-1} 10^{0} 10^{1} 10^{2} (MPa)
10^{-1} 10^{0} 10^{1} 10^{2} 10^{3} 10^{4} (psig)
PRESSURE

Figure 6

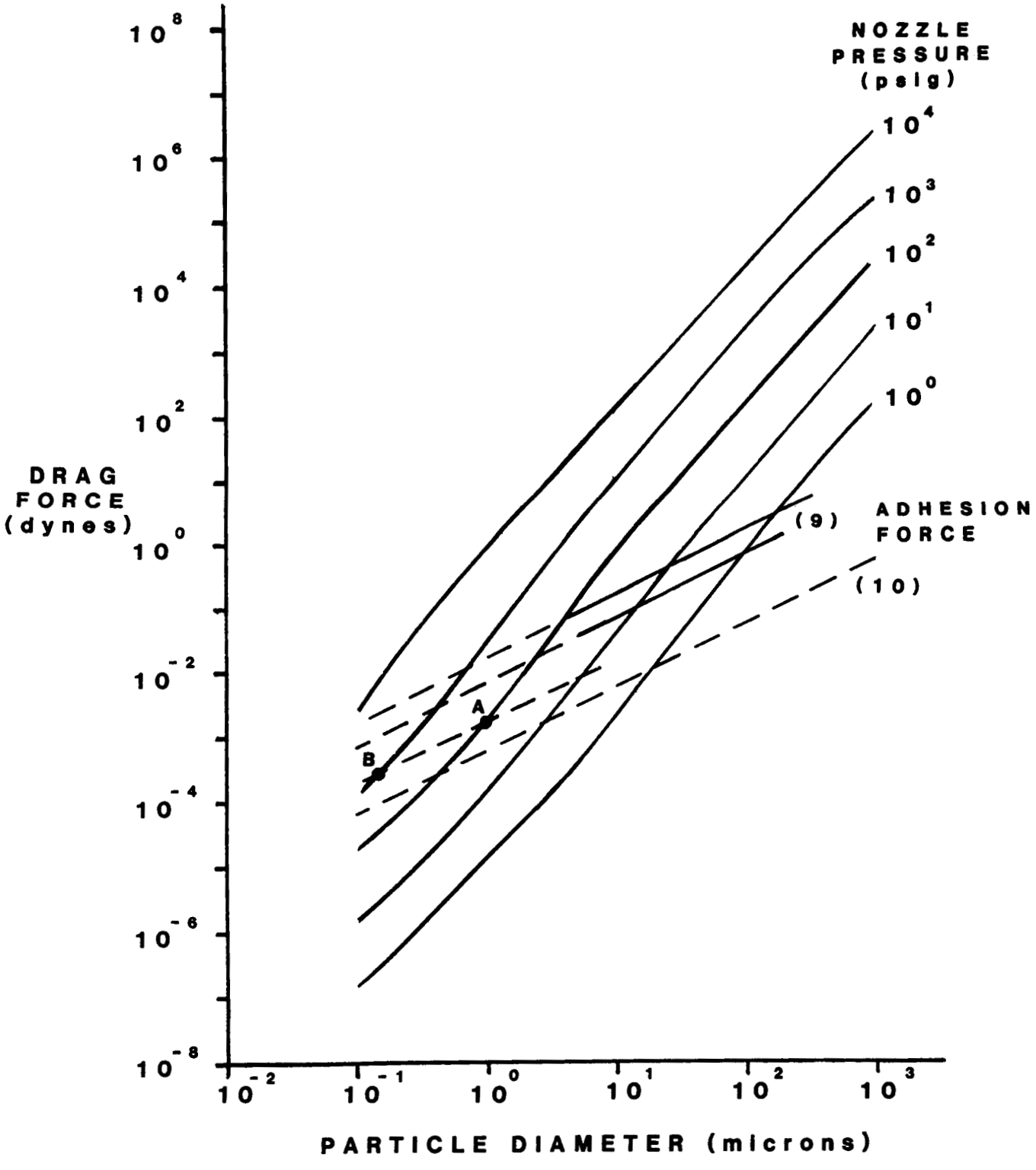
NOZZLE
PRESSURE
(psig)
10^4
10^3
10^2
10^1
10^0
DRAG
FORCE
(dynes)
10^8
10^6
10^4
10^2
10^0
10^{-2}
10^{-4}
10^{-6}
10^{-8}
(9)
ADHESION
FORCE
(10)
A
B
10^{-2}
10^{-1}
10^0
10^1
10^2
10^3
PARTICLE DIAMETER (microns)

Figure 7

Figure 8a. 2000x SEM photomicrograph of a test coupon artificially contaminated to 6000 particles/cm^2 with 0.1-5μm A/C test dust particles in methyl ethyl ketone.

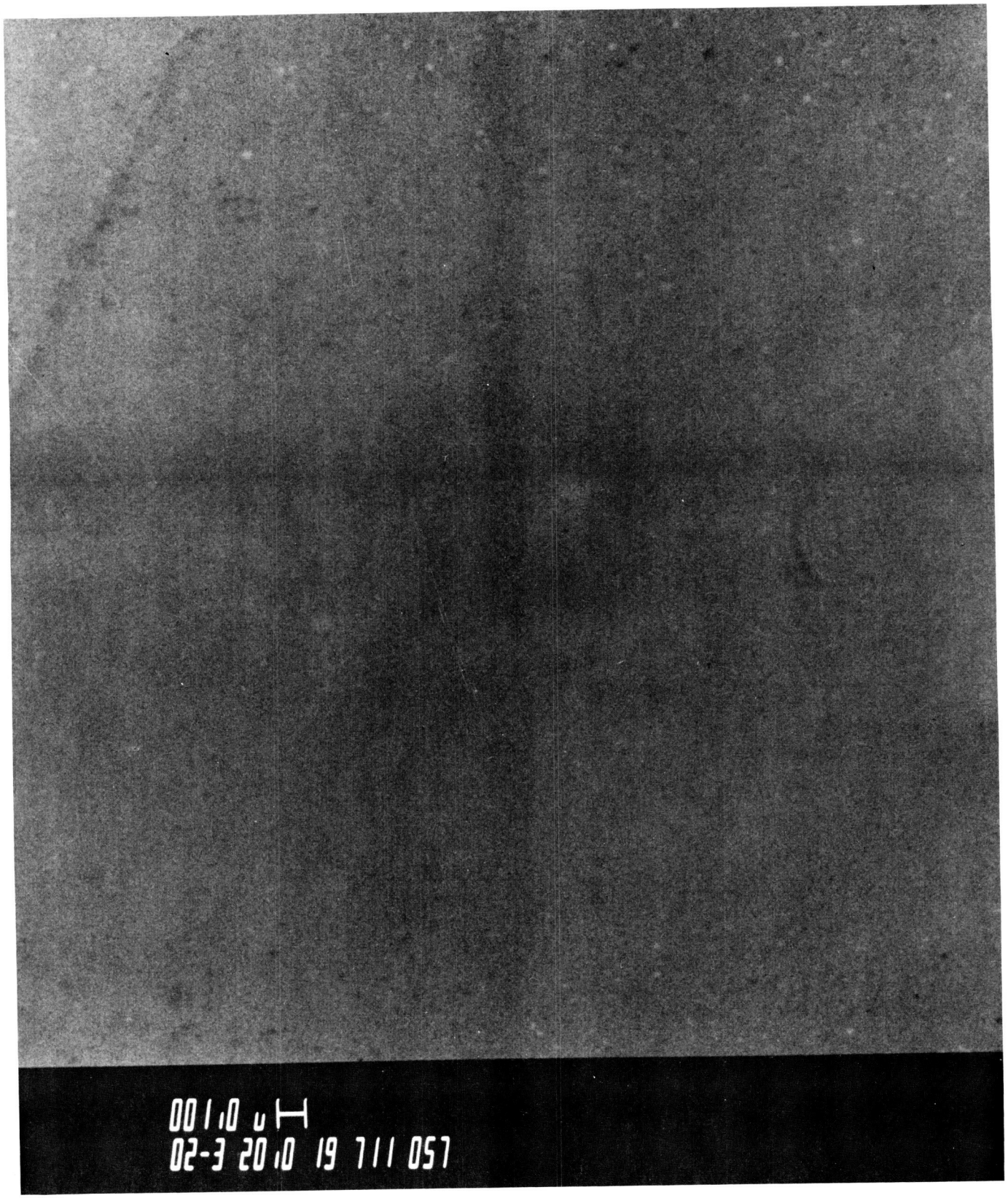

Figure 8b. After spraying for 10 seconds with fluorocarbon-113 at a free stream velocity of 137 m/s, the typical surface is featureless. Final contamination levels of <0.3 particles/cm^2 were observed, indicating a particle removal efficiency of 99.995%.

VACUUM PUMPS AND SYSTEMS:

A REVIEW OF CURRENT PRACTICE

STUART GILES

HELIUM LEAK TESTING, INC.

ABSTRACT

A review of the fundamental characteristics of the many types of vacuum pumps and vacuum pumping systems may provide helpful perspective for the designer and user. The optimum operating range, relative cost, performance limitations, maintenance problems, system operating costs and similar subjects are discussed. Experiences from the thin film deposition, chemical processing, material handling, food processing and other industries as well as space simulation are used to support the conclusion and recommendations. Large space simulation systems have been and are discussed in detail by others at this, and other conferences and are therefore omitted from this paper.

INTRODUCTION

There is no one "best way" to design and build a space or altitude simulation vacuum pumping system but, as in any design project, an unbiased approach will provide optimum, cost effective results. This paper is only a brief summary of the characteristics of vacuum pumps and systems with some field experience examples and the full knowledge that it may over simplify the problems.

Vacuum pumps are grouped under DISPLACEMENT PUMPS AND ENTRAINMENT PUMPS to clarify the operating mode of each type. The former can run continuously as they compress the pumped gas and discharge it to atmosphere or to a backing pump. The latter traps and holds the pumped gas within the structure and therefore requires occasional regeneration or replacement of the gas trapping elements.

DISPLACEMENT PUMPS

OIL SEALED ROTARY TYPES (Fig. 1 & 2)

Vane and rotary piston sealed vacuum pumps are the most commonly used. Most pumps provide nearly constant throughput within their operating range.

Advantages include simplicity, reliability, and economy. Oil vapor discharge out the vent, particularly at high pressure and oil vapor backstreaming can be problems. Special configurations of this type of pump are available for corrosive gas pumping, high water vapor loads and operation at continuously high inlet pressures which will overload the common oil sealed pump designed to blank off in 10^{-2} Pascal range or below.

ROOTS BLOWERS (Fig. 5)

Lobe type blowers (Roots) are useful as mechanical boosters when backed by an oil sealed pump. The blower is bypassed until a pressure between 3 and 50 Pascal (depending on design) is reached at which time the blower becomes a booster. Single stage units have good throughput to 100 Pascal range and blank-off in the low 0.1 range.

Staging can produce lower pressures. Lubrication is external to the vacuum pumping portion of the pump so that the Roots blower is not a source of backstreaming.

Roots blowers provide the increased pumping speed often required in the .1 to 40 Pascal range. They are a rugged, simple machine, reasonably resistant to dust and moisture. Backstreaming contamination is not usually a problem but can be if the oil sealed backing pump and the Roots blower are allowed to reach the molecular flow pressure range and the blower lobes become coated with oil from the backing pump. This can be prevented by automatically purging the backing pump with a dry gas to maintain viscous flow pressure level in the backing pump or by limiting the pressure by other means.

TURBOMOLECULAR PUMPS (Fig. 6)

This type of vacuum pump is also a booster pump requiring a backing pump. Modern design permits this pump to be mounted with the inlet downward which reduces the chance of particulate matter entering and damaging the high speed turbine blades. Backstreaming possibility from this type of pump is very remote, contamination of oil from the backing pump, as discussed under Roots blowers, can produce backstreaming. Normal maintenance involves relubrication of the bearings after 5,000 to 10,000 hours of operation. Another advantage of the turbo pump is that overloading (high pressure suction) simply slows the pump; Roots pumps overheat and diffusion pumps backstream excessively if overloaded in this way.

The available sizes of this type of pump are limited so that they are not suitable for large vacuum system gas loads. Backstreaming of the mechanical backing pump oil can be reduced by a properly installed fore-line trap. The problem of syphoning oil from the backing pump after shut down into the turbo pump can be protected against by installing an automatic up-to-air valve.

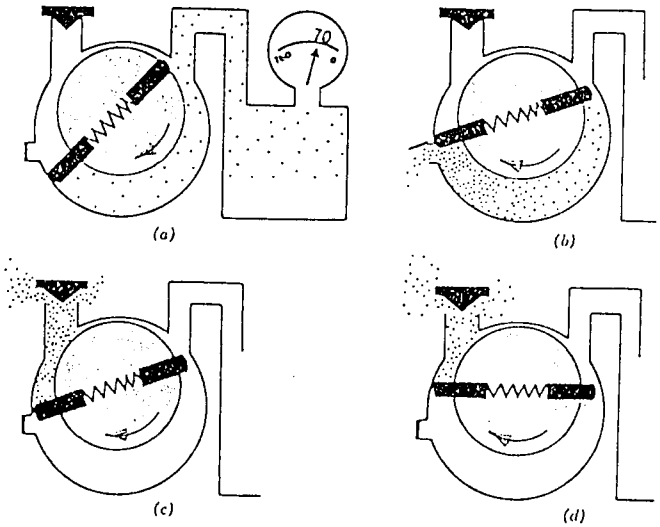

ROTARY VANE PUMP
with gas-ballast FIG. 1

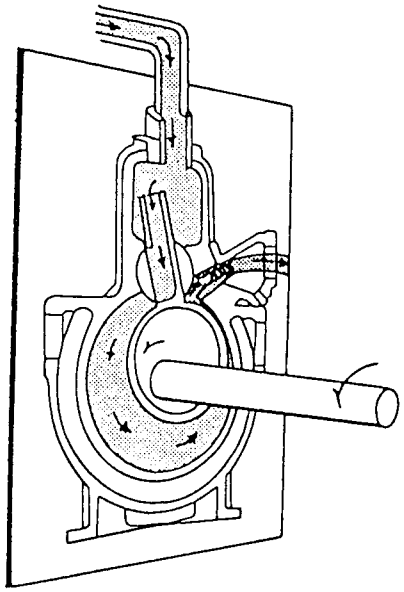

ROTARY PISTON PUMP
FIG. 2

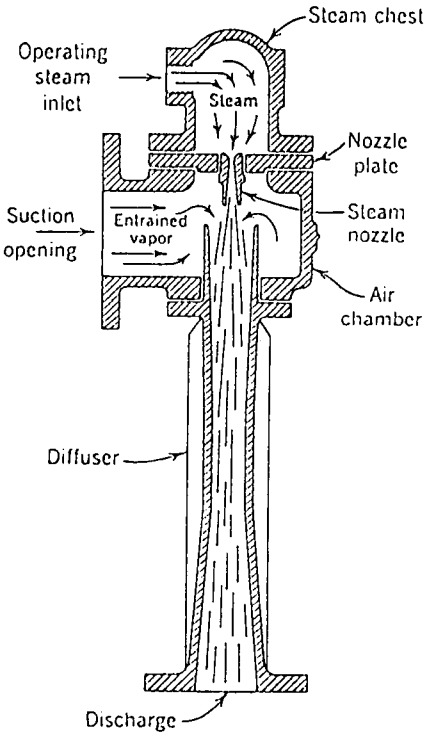

STEAM JET EJECTOR PUMP
FIG. 3

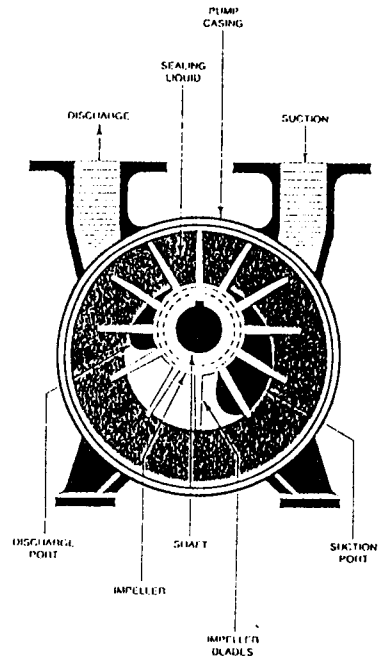

LIQUID RING PUMP
FIG. 4

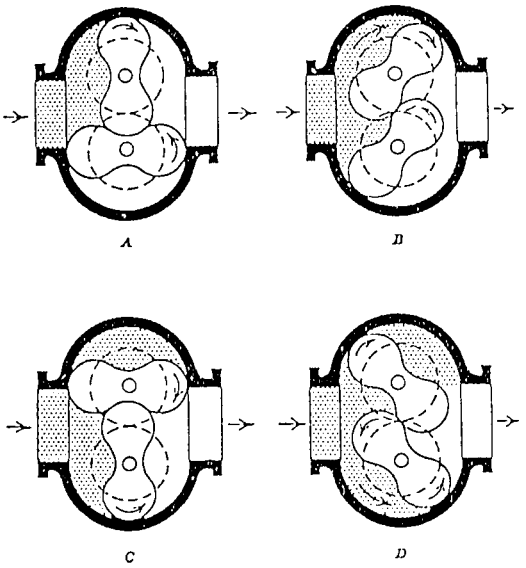

ROOTS TYPE BLOWER
FIG. 5

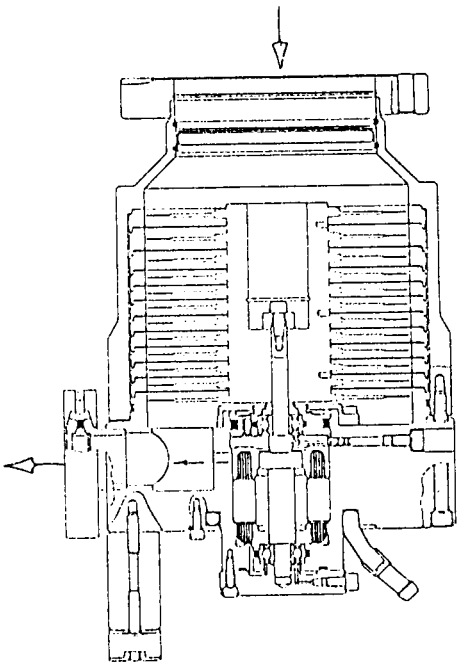

TURBOMOLECULAR PUMP
FIG. 6

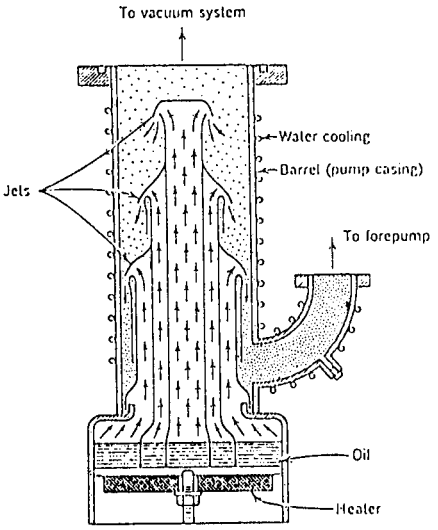

DIFFUSION PUMP
FIG. 7

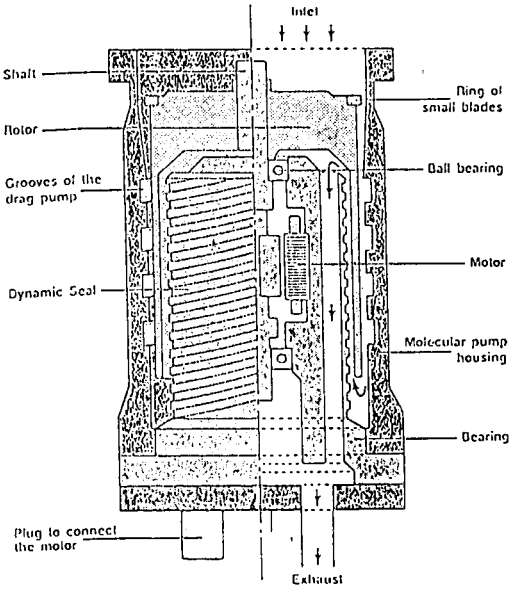

MOLECULAR DRAG PUMP
FIG. 8

DIFFUSION PUMPS (Fig. 7)

Oil diffusion pumps are most commonly used for industrial processing in the 10 to 10^{-5} Pascal range. This type of pumping system is the lowest first cost for its pressure range, but cryogenic cold trapping must be used for processes sensitive to backstreamed oil. Diffusion pumps are available in a wide range of sizes.

Diffusion pumps are boosters and therefore require backing pumps which must be protected against backstreaming or syphoning the lubrication oil into the diffusion pump: this is the same problem as discussed under Roots pumps, except that the fore-line (discharge) pressure must be maintained below its tolerable level or the diffusion pump backstreaming will be excessive. It is advisable to use the same oil in the diffusion pump and backing pump if practical.

ENTRAINMENT PUMPS

CRYOGENIC PUMPS (Fig. 9)

Cryo vacuum pumping is accomplished by a condenser and adsorber at cryogenic temperatures within or connected to the vacuum system. This type of pump is available in medium to large capacity sizes for most high vacuum applications. Because of its lack of contamination backstreaming and high pumping speed, it is popular for space simulation, manufacturing of thin film electronic devices and other sensative processes. Regeneration is required and the possibility of power failure during operation should be considered in application design.

IONIZATION PUMPS (Fig. 11)

The ionization pump uses the Penning gage principle to collect gas within the pump structure by ionization and gettering. These work best below the 10^{-2} Pascal range as pump life is relatively short at higher pressures. They find use in materials research and microminiature circuitry fabrication as well as space simulation. A primary advantage is that they provide a "dry vacuum environment" as there is no oil or other contaminant in the system. The roughing system may include a turbo or cryo pump and a well trapped two stage mechanical pump or an adsorption pump. Blank-off in the 10^{-9} Pascal range is practical. The lack of traps and baffles, low power requiremens and lack of need for LN_2 are operating advantages particularly for long term life tests. A turbo or cryo pump may be necessary to pump the non-getterable gases in some applications.

The ion pump has a finite capacity and is relatively costly to rebuild when saturated; it cannot be regenerated as can a cryo or adsorption pump. Start-up pressure is critical and a used pump, if started at too high a pressure, may go into a glow discharge mode and release previous pumped gasses which can contaminate the chamber and the product under test or production.

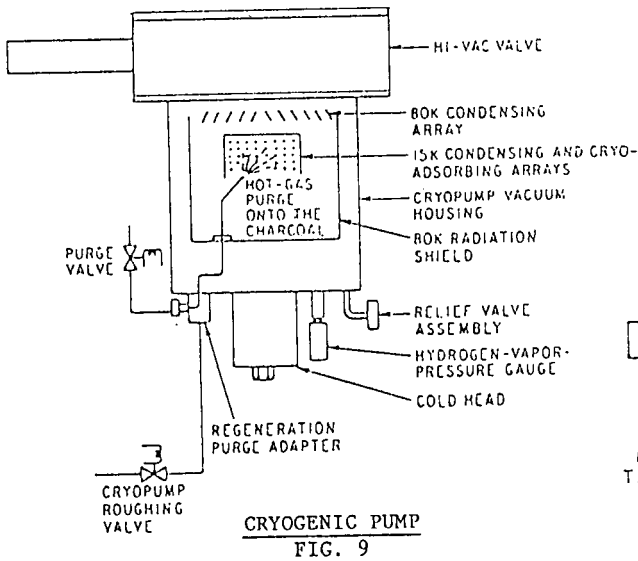

CRYOGENIC PUMP
FIG. 9

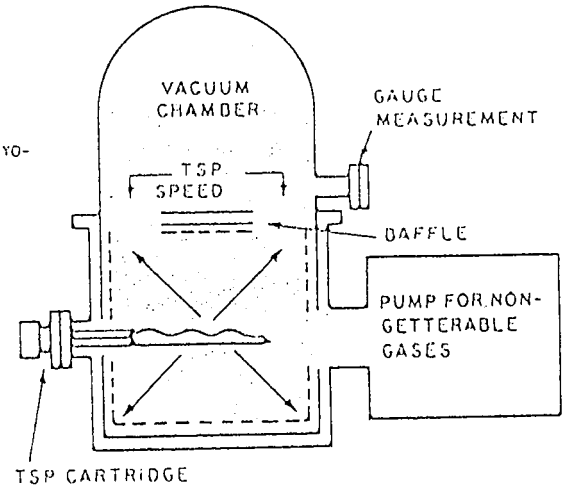

TITANIUM SUBLIMATION SYSTEM
FIG. 10

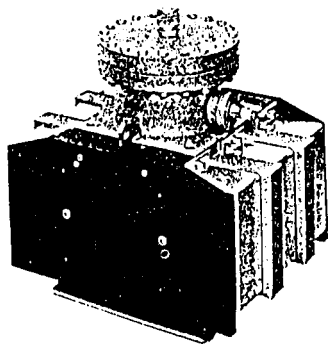

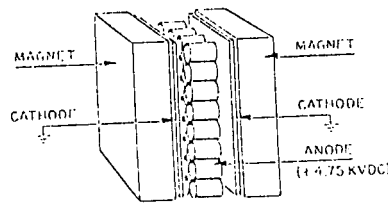

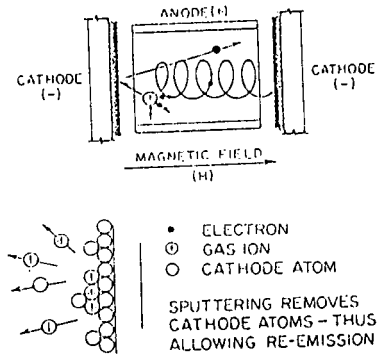

IONIZATION PUMP
FIG. 11

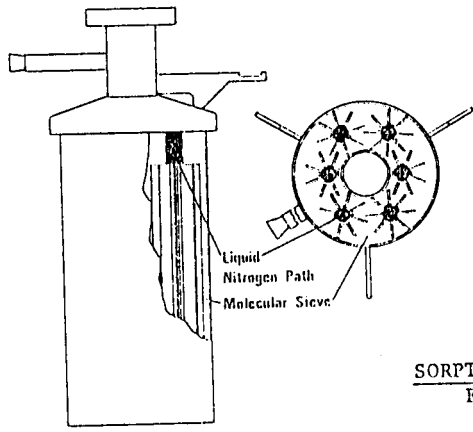

SORPTION PUMP
FIG. 12

TITANIUM SUBLIMATION PUMP (Fig. 10)

Sublimation of titanium (or other active metal) onto a surface will getter some gases providing high pumping speeds. This technique suppliments other pumping methods. The titanium source is replaceable and the reacted deposits may be mechanically removed. Combined with an ionization pump and the advantage of requiring no backing pump make it a completely closed system. A small turbo pump may be desireable to remove traces of non-getterable gases. No contamination occurs on power failure and only a small pressure rise takes place in a well-built system.

SORPTION PUMP (Fig. 12)

Silica gel and other gas sorption materials, may be used to evacuate a chamber by chilling with liquid nitrogen or other refrigerant when the risk of backstreaming from a mechanical pump must be avoided. They are only practical for small systems, when cycle time is not a problem. Regeneration is frequently required and time consuming.

OTHER TYPES OF VACUUM PUMPS

Centrifugal, diaphragm and reciprocating vacuum pumps are used for some industrial processes but not applicable to high vacuum work.

Liquid ring pumps are commonly used for dewatering and deaerating chemicals when solvents may be pumped. (Fig. 4). The required water supply and disposal may be a problem and the ultimate pressure is limited by the water vapor pressure.

The steam jet ejector (Fig. 3) is one of the oldest devices for producing vacuum in industrial applications. Staging of steam jets can produce ultimate pressures in the low 10^{-3} Pascal range. Their primary application is for large degassing operations at 100 to 1.0 Pascal. The principal advantage is rugged simplicity: The most practical vacuum pump for pumping acids and caustics since they can be fabricated from almost any metal or even ceramics. Costs are very reasonable if "free" steam is available. If the steam generator, condenser, cooling water and accessory equipment are considered, costs are comparable to mechanical booster systems. This type is not safe for some applications as steam flashback is possible.

The molecular drag pump (Fig. 8) uses a rotating helical seal to produce the pumping action in shear instead of impingement as in the turbo pump. Now available in a small size, it may be something for the future.

VACUUM PUMPING SYSTEMS

The performance of a vacuum pumping system depends not only on the pumps employed but also on the piping design, the valving, the gauging and the controls. The following discussion is designed to introduce the designer and user to some of the criteria which should be considered for the various types of vacuum pumping systems. Each application of a system imposes special considerations and requirements.

VACUUM PUMPING SYSTEM CASH FLOW ANALYSIS (Fig. 13 & 14)

The cumulative cash flow analysis curves show the net costs of owning and operating four types of vacuum systems over a period of 10 years. The capital investment, installation cost, utilities, maintenance, and operating costs, depreciation and taxes are included. The required pumps and controls for a typical 1000 liter/second pumping stack without a vacuum chamber, roughing pumps and gauging were used to estimate the purchase cost. Inflation was assumed at 5% per year, straight line depreciation over the 10 years to zero value is included, 40% tax rate and expensed installation cost are also included.

This type of cash flow is the net cost of ownership after taxes and depreciation. The curves will vary from one installation to another as different experience, type of operation and accounting methods dictate but shows the trends for the diffusion, cryo, turbo and ion pump systems.

The ion pump is most favorable because it is only used below the 10^{-2} Pascal range. This and the fact that they are limited in pumping speed make their application limited. The limited size of turbo pumps makes them impractical for large systems.

The cost difference between the cryo pump and diffusion pump helps explain the popularity of the cryo system in addition to its availability with very high pumping speeds.

When operating on a continuous basis (7 day, 3 shift) maintenance cost per hour of operation is reduced due to less wear and tear during start-up. Continuous operation yields 4.35 times the production per year compared to a standard 40 hour week. Because of the reduced maintenance, net cost will increase only 4 times for diffusion, 1.5 times for ion, etc. This shows the advantage of operating a production system on a continuous basis.

The popularity of the cryo pump is due to the net cost saving as well as performance advantages despite the higher initial capital cost. The cost savings shown for the cryo pump over the diffusion with mechanical refrigeration over the 10 year period on a continuous basis yields a 236% return on the additional $2,205 cryo system cost. The Internal Rate of Return Method was employed in this calculation.

DIFFUSION PUMP SYSTEMS

Figure 15 is a 20 port manufacturing system for evacuating, purging, baking, backfilling, pinch-off and leak testing glass plasma display devices. These devices are extremely sensative to contamination of any sort and reflect the effect of impriorities by poor color and shortened life. The liquid nitrogen cold trapped diffusion pump used in this system has proven to be very satisfactory by increasing the excellarated life test of the devices from 500 hours to 1200 hours when compared to the previously employed vacuum processing system.

Various system features contribute to the cleanliness of this system:

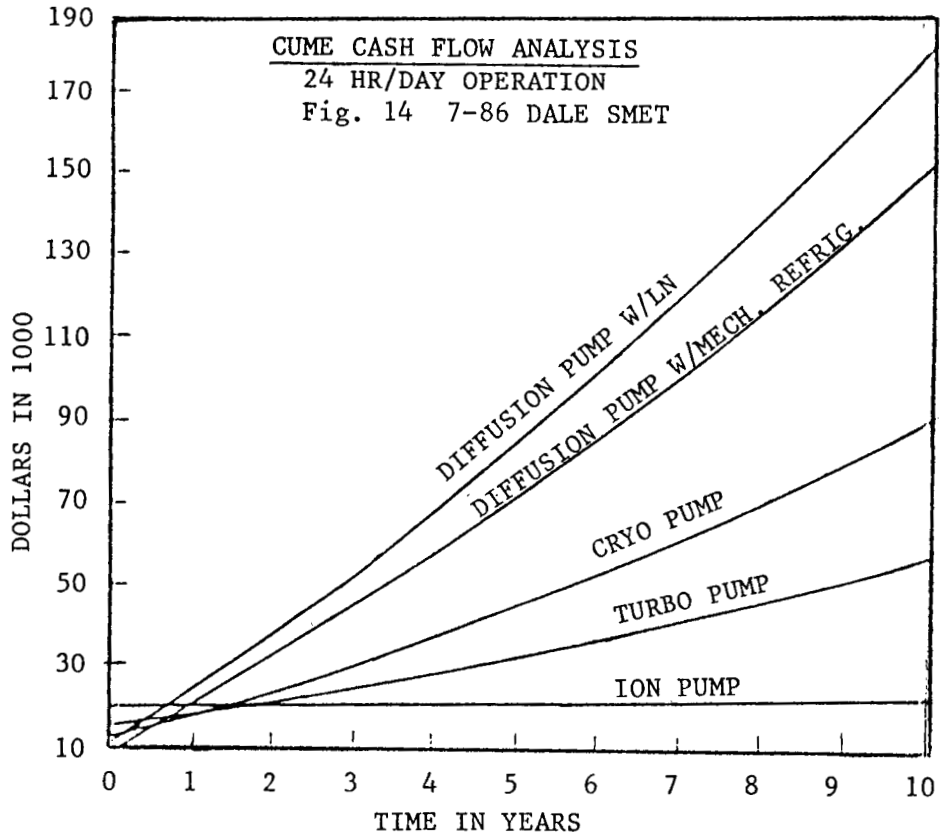
CUME CASH FLOW ANALYSIS
24 HR/DAY OPERATION
Fig. 14 7-86 DALE SMET
DOLLARS IN 1000
190
170
150
130
110
90
70
50
30
10
0 1 2 3 4 5 6 7 8 9 10
TIME IN YEARS
DIFFUSION PUMP W/LN
DIFFUSION PUMP W/MECH. REFRIG.
CRYO PUMP
TURBO PUMP
ION PUMP

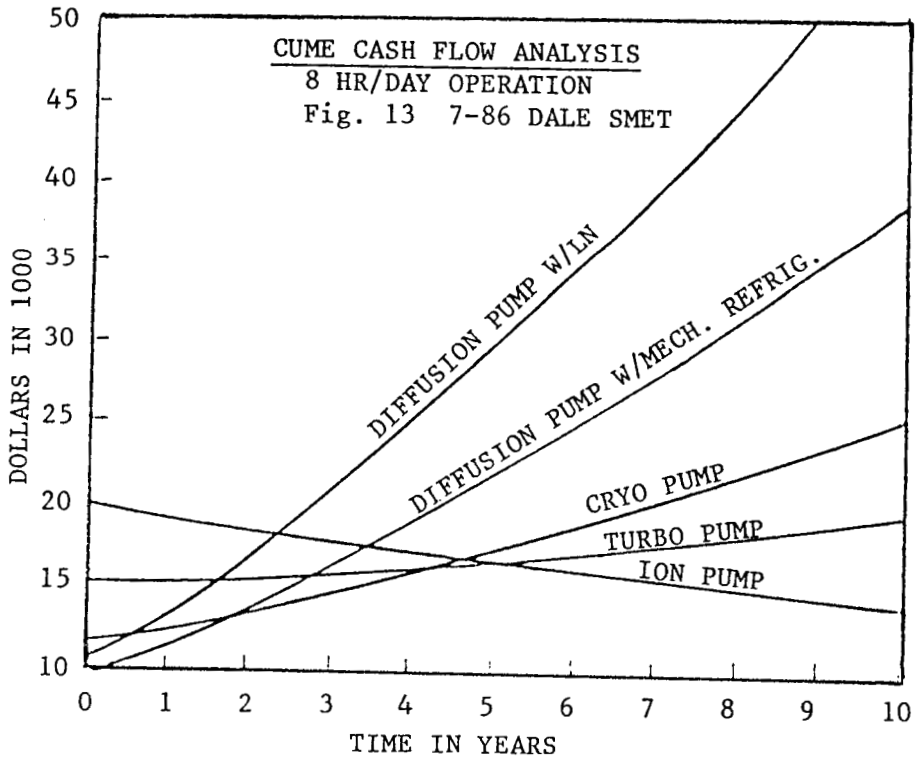
CUME CASH FLOW ANALYSIS
8 HR/DAY OPERATION
Fig. 13 7-86 DALE SMET
DOLLARS IN 1000
50
45
40
35
30
25
20
15
10
0 1 2 3 4 5 6 7 8 9 10
TIME IN YEARS
DIFFUSION PUMP W/LN
DIFFUSION PUMP W/MECH. REFRIG.
CRYO PUMP
TURBO PUMP
ION PUMP

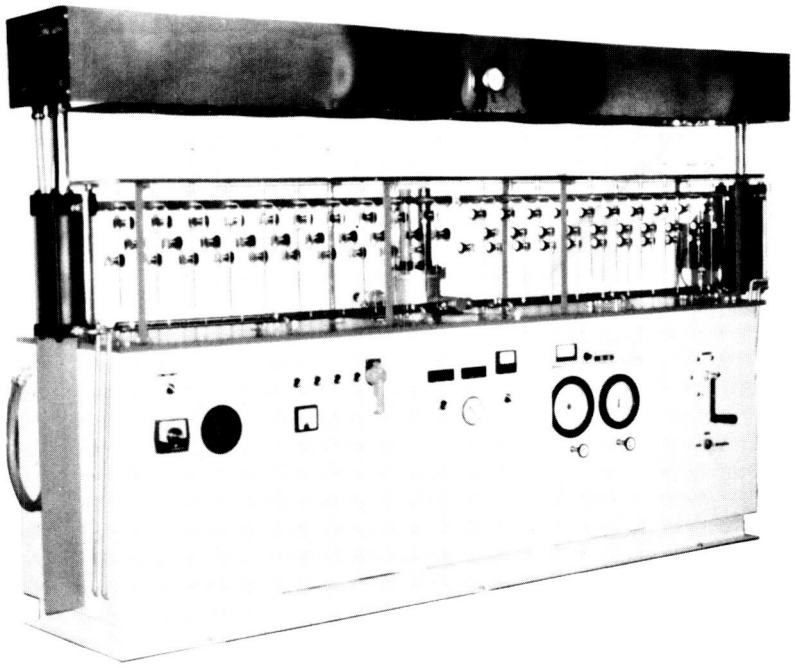

OPERATOR SIDE WITH OVEN RAISED

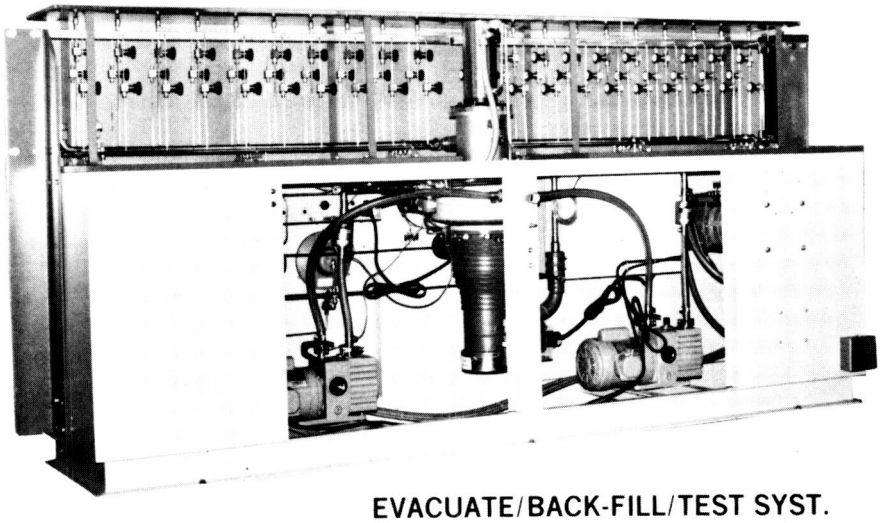

SERVICE SIDE SHOWING DIFFUSION PUMP,
LN COLD TRAP, ROUGHING & BACKING PUMPS

FIG. 15 PROCESSING SYSTEM FOR GLASS
PLASMA DISPLAY DEVICES

The devices are repetatively evacuated to 1 x 10^{-4} Pascal and back-filled with an inert gas. The evacuation of this inert gas purges the piping, cold trap and vacuum pumps maintaining the oils in good condition. Each device is evacuated through an 8 mm diameter tube and control valve which provides a relatively high gas velocity during initial evacuation.

The 300 degrees C oven is hydraulically raised and lowered so that it can be raised slowly after the heat cycle and not shock the hot devices with cold room air. The baking process, while evacuating and purging, has been proven in many processes to be the best way and sometimes the only way to assure complete cleanliness of a device.

The diffusion pump and mechanical pumps in this system use the same type of oil. This assures that no cross contamination of the pump oils. The user of this system has banned all silicon oils and greases from his facility as they have been found to be an impossible to remove contaminant.

A roughing pump and a backing pump are included in this system. Using one pump for these two functions can cause excessive backstreaming of the diffusion pump during the period when the foreline valve is closed and the mechanical pump is used to rough the system.

Figure 16 shows a completely automated sputtering system for high production of 5" x 5" substrates. The vacuum pump systems, one at each end of the 9 foot long sputtering chamber, roughs out the entry and exit air locks and maintains the sputtering chamber argon environment in the low 10^{-1} Pascal range. Oil sealed rotary vane type pumps (not shown) and the two diffusion pumps are connected to mechanically refrigerated cold traps. The diffusion pumps are maintained in the 10^{-4} Pascal range by throttling vanes in the suction.

Diffusion pumps are not considered good practice for this application and yet three of these systems produced completely satisfactory titanium thin films for many years on a 3 shift basis. The diffusion pump oil wasn't changed for the first six years of operation and even then it showed little degradation!

This example is given to illustrate that a well designed system, properly operated can give many years of service at low cost. The fact that these pumps were constantly purged with argon probably explains this outstanding performance record which contradicts the cost analysis previously presented.

CRYOGENIC PUMPING SYSTEM

Figure 17 illustrates a large portable cryo pumping system with a rotary vane pump and Roots blower for roughing. This system was designed to evacuate a group of 34,000 liter chemical reactor chambers to 1 x 10^{-3} Pascal in less than one hour through 30 feet of 10" pipe without hydrocarbon backstreaming. The system is moved from one reactor to another with a motorized pallet jack and connected to the reactor 10" suction line with a ring clamped, O-ring sealed flange. Pump exhaust, nitrogen and compressed air supplies, power, and central control room computer connections are all made with quick disconnect type fittings. No cooling water is required.

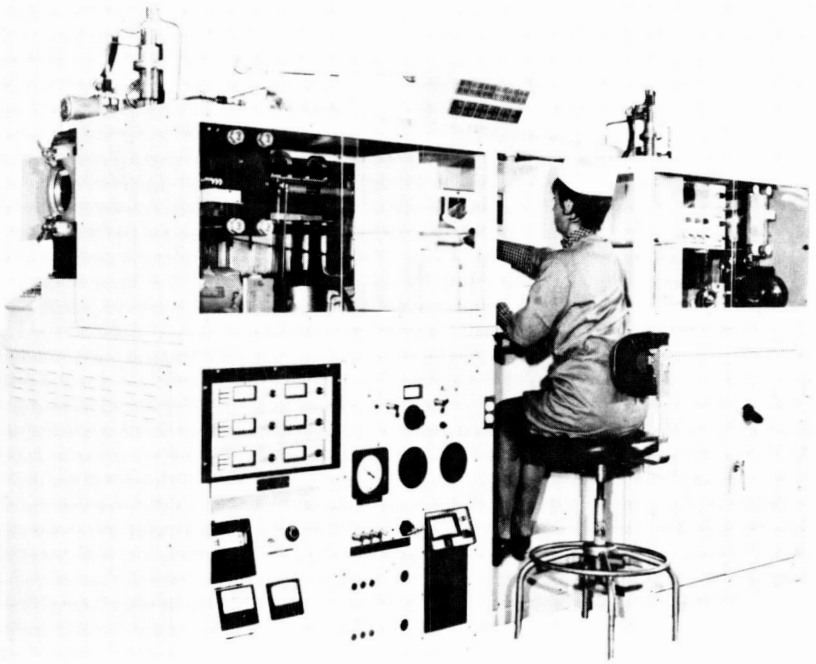

FRONT VIEW: OPERATOR LOADS AND UNLOADS SUBSTRATES

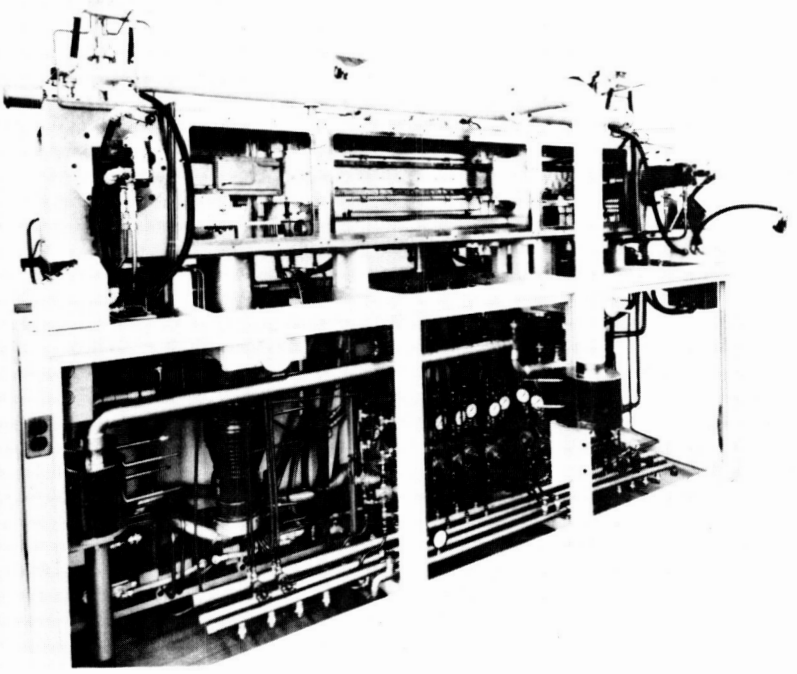

REAR VIEW WITH ACCESS PANELS REMOVED

FIG. 16 DIFFUSION PUMPED SPUTTERING SYSTEM

SYSTEM ASSEMBLY

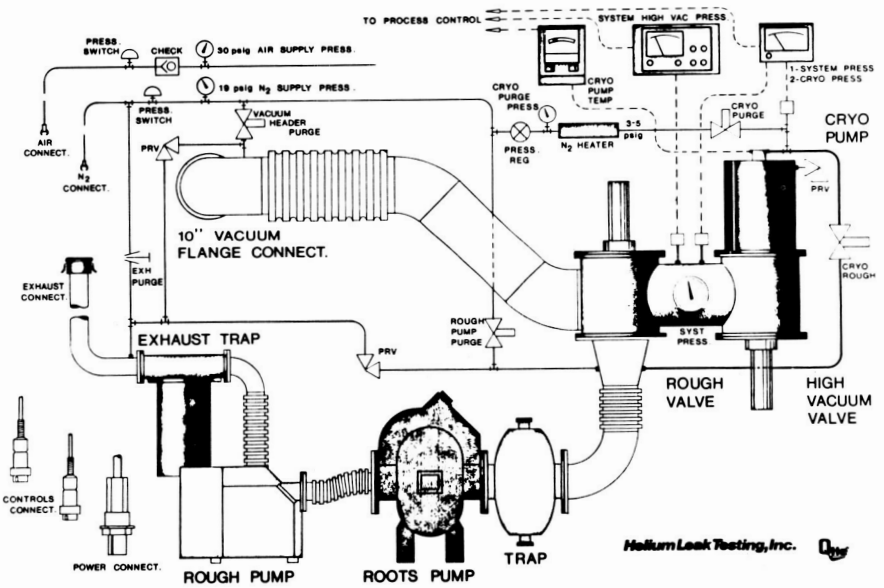

FIG. 17 A CRYO, ROOTS & OIL SEALED PORTABLE PUMPING SYSTEM

The 3" diameter rough pump and 6" diameter Roots pump connections assure that viscous flow is maintained during pump down and a nitrogen purge into the Roots pump suction after blank-off prevents backstreaming. An alumina ball filled trap is added insurance against backstreaming and protects the mechanical pump against the remote possibility that abrasive dust may be evacuated from the reactor. The trap also protects the cryo pump against possible hydrocarbon contamination during regeneration evacuation. This type of trap is usually filled with silica gel but because of its large size, the more shock resistant alumina was used. Silica gel would shatter, settle, and create dust and small particles which might damage the pumps and the settling would provide a bypass channel.

This cryo system is the 2nd generation for the same application; the previous four smaller systems are used to evacuate 1800 liter reactors. A cryo pump system design must protect the cryogenically cooled surfaces against the in-rust of warm air at too high a cross-over pressure which would warm the cold condensing shrouds. If this is allowed to happen, the shrouds will release the previously condensed gases as the refrigeration capacity is small, require a long time to recover pumping speed. The system shown in Figure 17 is able to cross-over at 15 Pascal because it is connected to the large reactor by a conductance limiting suction line (10" diameter x 30'). If the cryo system were directly connected to the chamber, the required cross-over pressure would be much lower.

OIL SEALED ROTARY PUMP SYSTEMS

There are probably more oil sealed pump systems in operation than all other types combined when we consider the automated material handling, vacuum packaging and degassing, vacuum hold down, hospital and laboratory, and other commercial and industrial applications. (Don't forget your dentist).

Figure 18 ROTARY OIL SEALED VACUUM PUMP WITH DROP-OUT TANK

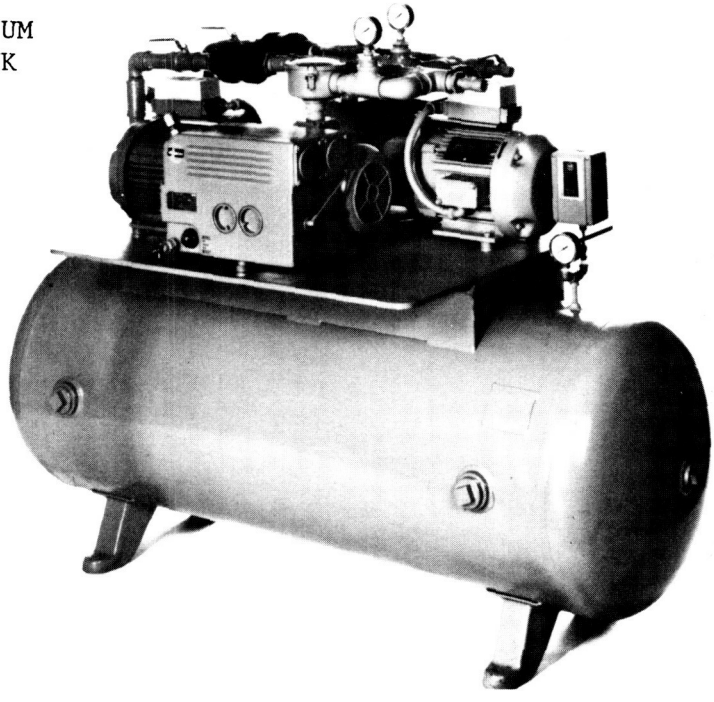

Figure 18 shows a relatively simple method of protecting a vacuum pump in many of these types of applications. The vacuum tank acts not only as a surge tank but also as a drop-out tank for liquids and solid particles which may cause pump maintenance problems. Machine shops using vacuum chucks induct cutting oils and chips into the vacuum suction lines, the hospital operating room is another problem, the electronic circuit board de-soldering and many other applications find this type of vacuum system to be cost effective.

These types of central system applications impose other problems for the standard vacuum pumps. The suction pressure in the system must often be limited to 20" Hg for which specially designed oil sealed pumps are available. Critical applications such as hospitals require redundant pumps and emergency power for reliability. Some applications employ a vacuum pressure switch on the tank or automatic air bleed valves to control the tank at the desired system operating pressure. Time delay of on-off control must be provided to prevent fast cycling the pump.

ROOTS PUMP SYSTEM

Figure 19 and 20 show an application of a rotary piston and Roots blower for freeze drying (lyophilization) of food products. This is a severe application as the pumps will be exposed to water vapor, food acid, caustics and oils; the refrigerated condensors are not 100% effective. In spite of this, the system shown has been in operation for 15 years on a one 10 hour run, 5 day per week basis. Each of the two rotary piston pumps and Roots blowers are overhauled approximately every 15 months. A spare of each type is kept on hand so that production is not interrupted during the pump overhaul.

As this system sublimes up to 125 Kilograms of water per run, the problem of condensed moisture in the oil sealed pumps is severe. After trying oil filtration and other methods, it was found cost effective to change the oil after each run. The rotary piston pump is the best choice for this application as it is most tolerant to dust, acid, water vapor and other contaminants.

CONCLUDING REMARKS

This discussion of vacuum pumps and vacuum systems is only a brief introduction to the subject. The designer and the user must make an in-depth study of the many types of pumps and systems which are available to determine the most effective and efficient for the process to be performed. As indicated by the cash flow analysis, the lowest first cost system may not be the best investment. It may be necessary to conduct process tests on a pilot basis to help select the best pumping system. There is no substitute for field experience to determine process criteria. A search for experience reports in the same or similar industries will frequently provide valuable data but do not accept "we have done it this way for 20 years and therefore, it is the best way". Vacuum technology is moving ahead and better ways may be available.

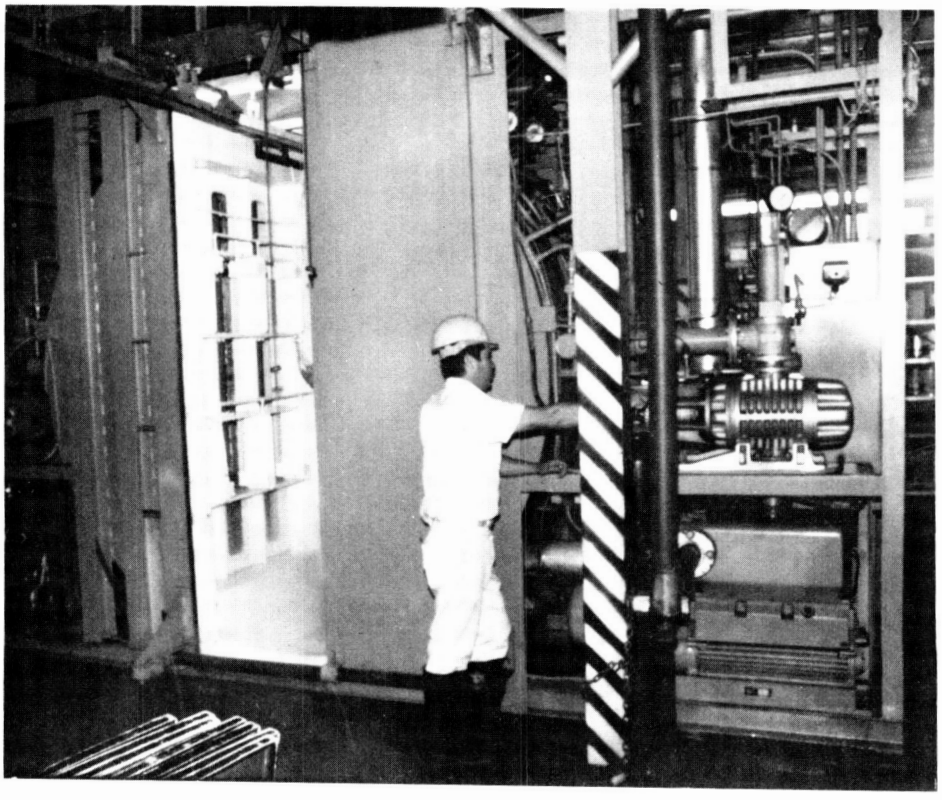

FIG. 19 FRONT VIEW SHOWING CHAMBER ACCESS AND ONE ONE SET OF PUMPS

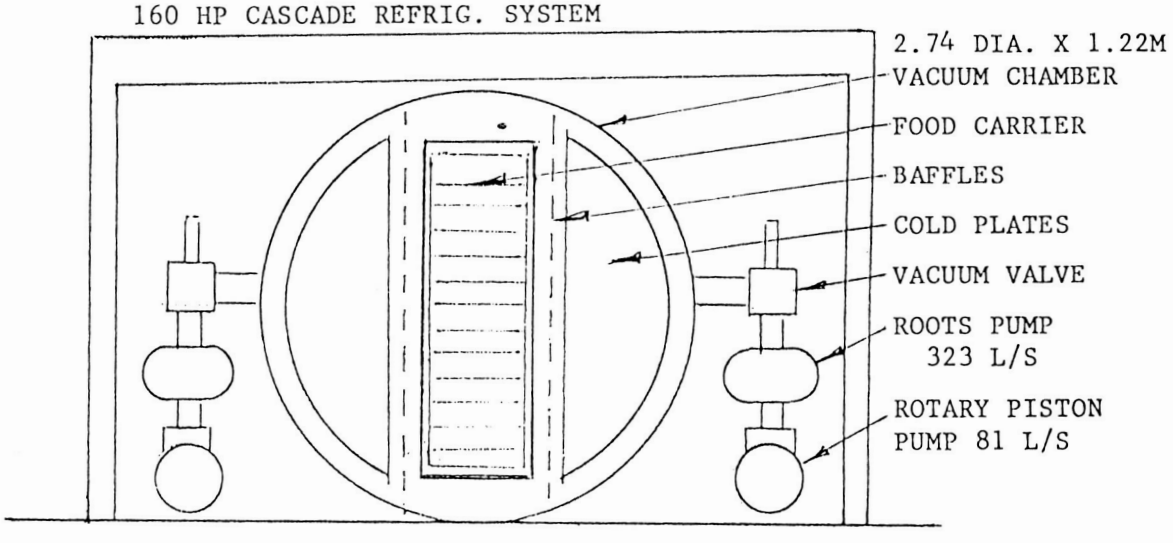

FIG. 20 FOOD FREEZE DRYING SYSTEM SCHEMATIC

PICTURE CREDITS

The author wishes to thank the following publishers and manufacturers for use of their drawings and photographs.

Fig. 1, 2, & 3	Dushman, Saul and Lafferty, J. H., Editor, Scientific Foundations of Vacuum Technique, John Wiley & Sons, Inc., New York 2nd Edition, 1962
Fig. 4	Kinney Vacuum Unit of General Signal, Canton, MA, Liquid Ring Vacuum Pumps, Bulletin 4105
Fig. 5 & 7	Guthrie, Andrew, Vacuum Technology, John Wiley & Sons, Inc., New York, 1965
Fig. 6	Leybold-Heraeus, Inc., Export, PA, Product and Vacuum Technology Reference Book
Fig. 8	Alcatel Vacuum Products, Inc., Hingham, MA, New Products Introduction, 1986
Fig. 9	CTI-Cryogenics, Helix Technology Corp., Waltham, MA, Cryo Pump Regeneration - Simplified, 1980
Fig. 10	Varian Industrial Components Div., Santa Clara, CA, Titanium Sublimation Pumps Bulletin, 1982
Fig. 11 & 12	Perkin-Elmer Vacuum Products Div., Ion and Sorption Pumps Bulletins
Fig. 13 & 14	Smet, Dale, Cash Flow Analysis, Helium Leak Testing, Inc., Northridge, CA, 1986
Fig. 15, 17, & 18	Helium Leak Testing, Inc., Northridge, CA, Specially designed and manufactured systems.
Fig. 16	Vacuum Atmospheres Co., Hawthorne, CA, Specially designed and manufactured system.
Fig. 19 & 20	Brewster Foods, Inc., Reseda, CA, Specially designed system for in-house use.

MEETING TODAY'S REQUIREMENTS

FOR LARGE THERMAL VACUUM TEST FACILITIES

R. L. Corinth - Pitt-Des Moines, Inc.
J. A. Rouse - CVI, Inc.

ABSTRACT

The Lockheed Thermal Vacuum Facility at Sunnyvale, California, completed late 1986, is one of the largest multi-program facilities constructed to date. The horizontal 12.2 m (40 ft.) diameter by 24.4 m (80 ft.) long chamber has removable heads at each end and houses a thermal shroud providing a test volume 10.4 m (34 ft.) diameter by 24.4 m (80 ft.) long. The chamber and thermal shroud are configurated to permit the insertion of a 6.1 m (20') wide x 24.4 m (80') long vibration isolated optical bench.

The pumping system incorporates an internal cryopumping array, turbomolecular pumps and cryopumps to handle multi-program needs and ranges of gas loads. The high vacuum system is capable of achieving clean, dry and empty pressures below 1.3×10^{-6} Pa (10^{-8} torr).

The thermal shroud is a closed loop LN_2 circulation system incorporating a subcooled heat exchanger. A GN_2 warm-up system is utilized to return the thermal shroud to ambient temperature.

The facility also includes the following systems:

- Chamber Air/GN_2 Repressurization
- Chamber Purge and Air Handling System
- Internal Heat Flux Simulator
- Communications System
- Closed Circuit TV System
- Ambient Thermal Control System

The facility is controlled from a remote control console. Sufficient local control is provided for local checkout and maintenance.

INTRODUCTION

The most advanced state-of-the-art thermal vacuum chamber facility for full scale satellite and systems integration testing by LMSC is in the final stage of completion.

LMSC initiated the Delta Chamber project by soliciting proposals to a performance specification with an early 1985 start and project completion date in late 1986.

The Delta Chamber designed and built by PDM/CVI is a second generation multi-purpose, quick turnaround, full space environment facility capable of pumping large gas loads.

The test volume is 10.4 m (34') diameter x 24.4 m (80') long with a flat floor section removable from either end of the chamber.

The chamber is unique because a full length thermally stable vibration isolated optical bench may be installed through either end and operated under vacuum at ambient or cryogenic temperatures.

The specifications required the facility to have:

(1) 30-day test period

(2) Four hour pumpdown to .7 Pa (5 microns)

(3) Six hour shroud cooldown

(4) Sustain a 700 KW heat load with shroud temperatures less than 110°K

(5) Pumping for .44 PaL/S (.0033 TL/S) helium, 110000 PaL/S (825 TL/S) nitrogen, and 856000 PaL/S (6420 TL/S) water gas loads.

(6) Plus or minus 1°K shroud temperature control at ambient temperature.

The Delta chamber is a multi-purpose chamber designed and constructed as a turnkey fixed price facility.

CHAMBER

The chamber as shown in Figure 1 is 12.2 m (40') dia. x 24.4 m (80') long with side moving top supported heads at each end giving unobstructed high bay access from sides and top of chamber opening. Chamber stiffening will support a 22700 Kg (50 kip) monorail load inside the chamber while under vacuum.

Both IR heating cage and test article are capable of being supported from top or bottom. The monorail contains a swing in place section outside the chamber at each end to interface with high bay handling structures. Bottom support of test article and IR cage allows movement to and away from chamber on air transporters. The upper three-fourths of the IR cage may remain in the chamber.

Movement in and out of the chamber of the flat shroud platform is on air transporters as is the insertion of an optical bench.

The chamber shell is Type 304 stainless steel polished to give an emissivity of less than .2. All external structures are carbon steel.

A distribution duct runs the length of the chamber along each side for repressurization and ventilation distribution.

All inside surfaces are accessible for cleaning and will be washed and given a black light inspection and NVR test followed by a bakeout and TCQM analysis to demonstrate the residual internal cleanliness.

Instrumentation ports for program use are located along both sides of the chamber at two elevations (See Figure 2) which are accessible from both internal and external platforms.

LN_2 connections to the bottom removable shroud are flanged with aluminum seals. Connections to the chamber head shroud sections employ hairpin pipe sections with bayonnet connections on each end of the hairpin for ease of assembly.

VACUUM SYSTEMS

The high vacuum pumping system in this chamber includes an internal cryopumping array, external cryopumps, and turbomolecular pumps. While these can be used simultaneously, the size and capacity of each of them are not simultaneously determined by any single test condition. The LN_2 shroud acts as an infinite water vapor pump when at cryogenic temperature. Figure 2 shows the arrangement of the high vacuum pumping systems and the test volume.

The shroud is required for thermal control and is the primary contributor to water pumping speed at LN_2 temperature. The internal cryopumping array is required to handle a large nitrogen gas load. Testing at high vacuum with the shrouds at room temperature requires the external cryopumps, while extended testing with the large helium gas loads is accommodated by the turbomolecular pumps.

ROUGHING PUMPS

The chamber roughing pumps are in two separate skids manifolded together to provide 22700 m^3/h (13368 cfm), designed to start at atmospheric pressure and to reach .7 Pa (5 microns) in four hours with the passive nitrogen gas load of 167 PaL/S (1.25 TL/S).

Both skids have valved connections to the roughing line which contains an LN_2 trap.

Each Leybold-Heraeus skid contains a 11360 m^3h (6684 cfm) lead blower followed by 4360 m^3/h (2567 cfm) and 2350 m^3/h (1383 cfm) blowers backed by a 808 m^3/h (475 cfm) mechanical pump.

The pumpdown time to .7 Pa (5 microns) is extendable to 24 hours by a roughing line valve and a programmable controller.

CRYOPUMPS

The high vacuum pumping system utilizes five (5) CVI TM 1200, 1.22 m (48 inch) cryopumps. The pumping capacity required from this source is determined by the test pressure requirements associated with tests to be conducted with the thermal shroud at ambient temperature. Determination of the net pumping speed of these pumps, interior to the shroud, involves use of a Monte Carlo analysis of the combination of an ambient baffle, LN_2 baffle, and nozzle with 1.32 m (52 inch) GNB gate valve.

The following speeds have been determined:

	Warm Shroud	Cold Shroud
Nitrogen	200,800	116,000 liter/sec
Water	456,250	--- liter/sec
Hydrogen	142,500	82,500 liter/sec
Helium	100,000	57,500 liter/sec

TURBOMOLECULAR PUMPS

The high vacuum system also utilizes four (4) Balzer turbomolecular pumps with .762 m (30 inch) GNB gate valves. The turbos provide the pumping speed to handle the large long term helium gas loads. A Monte Carlo analysis has also been used to determine the pumping speeds of the baffle/nozzle/elbow/valve and two baffle combination of the turbomolecular pump mountings. The following speeds have been determined:

	Warm Shroud	Cold Shroud
Nitrogen	20,000	11,600 liter/sec.
Water	20,560	--- liter/sec.
Hydrogen	22,240	12,840 liter/sec.
Helium	21,721	12,560 liter/sec.

INTERNAL CRYOPUMPING ARRAY

An internal, flat panel cryopumping array has been incorporated into the chamber shroud system to maintain the specified chamber pressure during periods of high active GN_2 gas loads (825 TL/S). The nitrogen pumping portions of this array are maintained at 20°K with a 1,000 watt helium refrigerator designed and supplied by CVI. Our experience with cryopumping arrays of this type indicates the capture probability is limited to about 0.22. With a total cryopumping array surface area of 139 m^2 (1500 sq. ft.), the nitrogen speed will be 2,100,000 liter/sec.

LN_2 SHROUD

The chamber shroud is maintained at LN_2 temperatures with a subcooled refrigeration system that will be described later. This shroud acts as an infinite pump for water. The effective water speed will be:

2.85×10^8 liter/sec. based on 1022 m^2 (11000 sq. ft.) of shroud surface

VACUUM GAUGING

Vacuum gauging instrumentation in the chamber consists of five Granville Phillips 303 Vacuum Process Controllers, each reading both a convectron and an ion gauge, at two chamber locations (a total of ten locations, each with both gauge types). The convectron gauges are used for chamber pressures down to .13 Pa (1 micron), and the ion gauges are used below that point.

All the convectron gauges are located in the annular space between the thermal shrouds and the chamber walls, while all but one of the ion gauges are located interior to the thermal shrouds. The other ion gauge is located in the annular space. All interior ion gauges are mounted on flanges, off removable shroud panels, facilitating gauge removal either from the annular space or from the interior of the shroud without disturbing the chamber penetration vacuum integrity.

TEST ENVIRONMENT AND CONTROL

TEST REGIMES

Table 1 presents the test regimes as divided between operation with a cold shroud and warm shroud, and with and without an optical bench inside the chamber. The chamber pressures shown at the bottom of Table 1 are nominal and will vary with actual conditions and chamber history.

Each item of the high vacuum pumping system is an element in a particular regime. For example, the most efficient means of pumping the large nitrogen active gas load is with an internal helium array, whereas cryopumps are the ideal choice under warm shroud conditions.

Passive gas loads are present during all phases of vacuum, whereas the active gas loads are intermittent and may have an accumulative total of 45.4 Kg (100 pounds) of water and 9.1 Kg (20 pounds) of nitrogen during a typical test cycle.

With an optical bench in the chamber, several new sources of gas loads are present - vibration isolator leakage, outgassing from a warm shroud, outgassing from multi-layered insulation, and outgassing from the optical bench and its internals.

Both roughing and chamber repressurization are extendable to eliminate air current disturbances particularly with use of an optic bench. Vacuum performance in the different regimes is shown by the nominal pressure listed in Table 1.

LN_2 SHROUD SYSTEM

The shroud is fabricated of flat 1100F aluminum extrusion incorporating the LN_2 tube. These extrusions are shop fabricated into flat panels 1.22 m (4 ft.) wide by 7.62 m (25 ft.) long and painted with 3M's ECP-2200 solar absorber coating. The cylinder and end closeouts of the shroud are fabricated from the same basic 1.22 m (4 ft.) wide panel. See Fig. 3.

Thermal control is maintained with a pressurized recirculating subcooled LN_2 system. This approach was selected to maintain thermal uniformity with the high design heat loads on the shrouds. The total shroud is divided into ten thermal control zones. Flow rates can be modulated through each of the zones.

In addition to the specified heat load from the test article, the shroud will also see the radiation heat load from the chamber walls which adds 25 kw to the total heat load.

With the specified 700 kw heat load, the total shroud heat load will be 725 kw, or 223 BTU/hr/sq. ft.

Under full design heat loads, the maximum allowable temperature at any point on the shroud is 110°K. The LN_2 will be supplied to the shroud at 82.8°K (-311°F), or lower, and its temperature is allowed to increase by 13.9°K (25°F) as it passes through the shroud. Half way between two LN_2 tubes, where the fluid is leaving the shroud, the temperature will be 102.2K (-275.4°F).

A schematic of the LN_2 circuit is presented on Figure 4. State points are shown for the circuit operating at most critical conditions with full design heat load applied to the shroud system.

The minimum pressure point is critical because the fluid must remain in the liquid state throughout the system. At the minimum pressure point, 755 kPa (109.5 psia), this state is maintained, since the maximum temperature will be 96.7°K and nitrogen will be in the liquid state at any pressure above 614 kPa (89 psia).

The subcooling coil submerged in the LN_2 of the LN_2 Storage Tank is designed to produce a 11.1°K (20° Rankin) temperature drop with an LN_2 flow of 111 m^3/h (490 gpm).

The LN_2 makeup venturi is designed to provide a mimimum LN_2 pump suction pressure of 418 kPa (60.6 psig) when the LN_2 level in the storage tank is at its minimum (just covering the subcooling coil). The tank static head plus tank vapor pressure, coupled with the geometry of the venturi and pressure losses betwen the venturi and the pump inlet, establish the minimum suction pressure.

The total LN_2 flow will be supplied through any two of the three cryogenic pumps provided on the circulation skid and connected in parallel. Each of these is a 5.08 cm x 10.16 cm x 19.05 cm (2" x 4" x 7.5") CVI centrifugal pump with 19.05 cm (7.5 inch) impeller and 14.9kW (20 HP) motor.

Two of these pumps will be supplying 55.7 m^3/h (245 gpm) of LN_2 each, while operating at 13.3 kW (17.8 BHP). The third cryogenic pump is a reliability backup.

AMBIENT BAFFLE TEMPERATURE CONTROL

During testing with the shroud at ambient temperature, all surfaces forming the test volume must remain at a constant temperature. The shroud baffle in front of the cryopumps must be shielded from the cold surfaces of the cryopumps. This is accomplished by electrically heating a secondary baffle located between the shroud baffle and the cryopumps. The shroud baffle is to be maintained within 1°K of the temperature of the rest of the shroud.

Following a radiation heat transfer analysis of the cryopumps and baffle systems, the distributed electric heater power has been sized for satisfaction of the temperature control requirements.

Control will be achieved by proportionally controlling the electric heater power to minimize the temperature difference between the secondary baffle and the nominal chamber wall.

SPECIMEN HEATING

Thermal balance testing is accomplished through use of the LN_2 shroud as a "heat sink" and infrared (IR) lamp as a heat source.

The IR lamps are mounted on a cylindrical framework with end closeouts providing a heat source from all view angles of the test specimen. The IR cage with lamps and wiring is designed for minimum shadowing of the cryogenic heat sink.

The IR lamps are divided into 100 zones, each zone controlled by a motor operated transformer. The system is capable of being varied from zero to 80 volts, 110 volts, or 220 volts by stepper motors. Under emergency conditions, one of the two emergency generators is dedicated to supply IR power, and an uninterruptable power supply will maintain program control during power switchover. Manual control of each of the 100 autotransformers is also provided should the need arise.

WARMUP WITHOUT CONDENSATION

An electrically heated recirculating GN_2 warmup system is used to return the shrouds to room temperature, following tests. The shrouds can be warmed from LN_2 temperature to room temperature in eight (8) hours. See Fig. 5. Warmup of the helium cooled internal cryoarray is expedited with a thaw heater, included as part of the helium refrigeration system.

An LN_2 cooled scavenger panel is maintained in its cold state as all the rest of the chamber equipment is warmed up. All condensible materials will therefore be accumulated at this scavenger panel rather than dispersed throughout the chamber area.

TEST FIXTURES

The monorail along the top centerline of the chamber has a double set of trolley flanges. The top set supports an IR cage which can be rolled in or out of the chamber independent of the test article supported from the bottom flange. Test article support at the monorail is by two trucks 8 feet apart. The close out disc and test article may be removed and inserted from either end of the chamber. The monorail contains a "swing in place" section outside the chamber, at each end, to interface with high bay handling structures.

Both test article and IR heating cage may be supported from underneath. Rails running the full length of the chamber will support the bottom 1/4 of the cage. The upper 3/4 of the cylindrical IR cage is supported on separate tracks from the lower quarter section and may remain in the chamber during insertion and removal of the bottom 1/4 section.

Support of the test article cradle support is integral with the bottom 1/4 shroud section which, when outside the chamber, may be moved to and from the chamber on air transporters. Use of an optical bench as a work platform requires removal of the flat shroud platform.

Horizontal surfaces flush with the outside high bay floor (see Fig. 2) allow the bottom shroud platform and optic bench to be moved in and out of the chamber on air transporters.

With an optic bench 4.57 m wide x 18.3 m (15 ft. wide x 60 ft.) long in place, two 3.05 m (10 foot) long shroud platform sections may be installed at each end. The pneumatic vibration isolators along each side are captive to the optic bench when moved and provide isolation of the optic bench outside the chamber in the high bay at either end. The table with a clear height of 9.45 m (31 feet) above the table may be moved in and out of the chamber fully loaded. Loads of 1816 kg (4000 pounds) may be supported on each platform section at ambient and vacuum conditions.

WORK PLATFORM STABILITY

Initial requirements were to provide an optic bench capable of functioning in both a controlled ambient temperature environment and a cryogenic temperature environment.

An optic bench is not currently supplied due to changed program requirements. However, design has been completed on an optic bench system and all supporting equipment has been installed.

The optic bench system is designed to provide a work platform inside the chamber capable of alignment stability of less than 20 nanoradians on the work surface. Performance is based on finite element modeling of the structure considering ground and machinery inputs, building attachments, chamber attachments, uncorrelated inputs, plus thermal stability effects on the optic bench.

The chamber support girders and supporting grade beam with piles act as a composite structure providing an end to end slope error of .2 to .3 nanoradians at the isolator support surface.

Where the thermal environment at the optic bench top surface is at LN_2 temperatures, a multilayered insulation blanket system designed to reduce the temperature related end to end deformation to about 1/2 nanoradian for short duration. For longer durations of 30 days, alignment deformations are held to less than 25 microradians.

Work platform stability is provided by an optic bench in both a controlled ambient temperature environment and cryogenic environment.

SPECIMEN OBSERVATION

Two TV cameras are mounted in the test volume with monitors and pan and tilt controls located in the control console. The cameras are the type successfuly used on space flights. They are sealed and require a continuous flow of GN_2 cooling gas. Lighting is provided by 12 - 150 watt lamps containing debris shields.

REPRESSURIZATION

Normal repressurization is accomplished with dry nitrogen gas supplied through a gas fired, LN_2 vaporizer. Provisions are also included for repressurization with air from the high bay room in front of the chamber.

PROCESS CONTROL & DATA ACQUISITION

CONSOLE

A high degree of flexiblity of operations is maintained in this facility by utilizing manual remote controls for all systems in the central control console. All subsystems can be started, controlled, and shut down from the remote control console. Programmed logic controllers are used to automatically maintain many of the process systems on test set points.

A photo of the console is shown in Figure 6.

DATA ACQUISITON

The complete data acquisition system is provided by the customer. The supplied equipment provides the necessary interfaces for that data system.

SAFETY

Personnel safety was of prime importance in developing an interlock system for chamber pumpdown and the repressurization with nitrogen.

With the chamber heads in place, four access doors contain Kirk key lock systems that require master keys to be inserted in the console before chamber pumpdown may commence. The console has two alarms: (1) "Man in chamber" alarm should an emergency stop button inside the chamber be pressed after start of pumpdown, (2) "Chamber not safe to enter" alarm which is a fault condition resulting from any one of 13 safety related items not being satisfied. The reverse of the "Fault condition" is a "Chamber safe to enter" light which includes a positive lock out on the nitrogen supply to the chamber repressurization system.

EMERGENCY POWER AND REDUNDANCY

Emergency electrical power is provided by (2) 500 kW diesel generator sets. They are connected to (2) main load busses, one for equipment and the other primarily for IR power. Automatic transfer switches are on each line. One generator can be committed to both busses should one generator fail to start. The operator must monitor loads brought back on line to stay within the one generator's capacity. The purpose is to maintain a safe thermal balance for the test article.

A secondary power feeder, to a locally mounted power transformer, can be brought into use by manual transfer switches should a fault occur in the principal feed line.

Key elements of the cooling water system are two units each containing circulating pumps and water coolers. Both units are required for initial pumpdown, whereas one unit will handle the steadystate heat load.

Multiple cryopumps and turbopumps provide redundancy. The 1.0 kW helium refrigerator contains two expander turbines. The second turbine is maintained cold and can be brought into service from the control console.

A third LN_2 pump provides backup where two are required for normal flow of 111 m^3/h (490 gpm).

Identical backing pumps for the turbo and cryo pumps provide redundant flexibility once the cryopumps are at operating temperature.

Ten nude ion gauges penetrate the shroud into the test volume to provide flexibility and redundancy.

SUMMARY

The Delta chamber is a turnkey thermal vacuum facility designed for multiple program use with large operational gas loads.

The chamber is full sized, double ended, and capable of receiving a full length vibration isolated and thermally stable optical bench.

Completion of the facility will be on schedule in late 1986.

Table 1
Test Regimes
(SI Units)*

	WITHOUT OPTIC BENCH			WITH OPTIC BENCH	
	CD & E	PASSIVE GAS LOADS	ACTIVE GAS LOADS	SHROUD COLD	SHROUD WARM
Roughing	.67 Pa in 4 Hrs			Extendable to 24 Hrs	
Gas Loads, Pa L/S	Outgas	GN_2 208 H_e .44	GN_2 110,000 H_2O 856,000	GN_2 216 H_2O 56 H^e .44 H_2 .06	GN_2 216 H_2O 63 H^e .44 H_2 .06
Shroud Temperature	90°K	90°K	90°K	90°K	Ambient Temp. Controlled to ± 1° K
High Vacuum Pumps	Internal H_2 Array Cryopumps Turbomolecular Pumps Shroud				Cryopumps Turbopumps
Nominal Vacuum Pressure, Pascal	1.3×10^{-6}	1.1×10^{-4}	5.3×10^{-2}	1.3×10^{-4}	1.1×10^{-3}
Chamber Warmup and Repress.	Air in 1 Hr, or GN_2 Extendable to 12 Hrs.				

*See Table 1A for US Customary Units

Table 1A
Test Regimes
(US Customary Units)

	WITHOUT OPTIC BENCH			WITH OPTIC BENCH	
	CD & E	PASSIVE GAS LOADS	ACTIVE GAS LOADS	SHROUD COLD	SHROUD WARM
Roughing	5 Microns in 4 Hrs			Extendable to 24 Hrs	
Gas Loads, TL/S	Outgas	GN_2 1.25 H_e .0033	GN_2 825 H_2O 6400	GN_2 1.62 H_2O .42 H^2 .0033 H^e_2 .00047	GN_2 1.62 H_2O .47 H^2 .0033 H^e_2 .00047
Shroud Temperature	90°K	90°K	90°K	90°K	Ambient Temp. Controlled to ± 1° K
High Vacuum Pumps	Internal H_2 Array Cryopumps Turbomolecular Pumps Shroud				Cryopumps Turbopumps
Nominal Vacuum Pressure, Torr	$1x10^{-8}$	$8.3x10^{-7}$	$4x10^{-4}$	$1x10^{-6}$	$8x10^{-6}$
Chamber Warmup and Repress.	Air in 1 Hr, or GN_2 Extendable to 12 Hrs.				

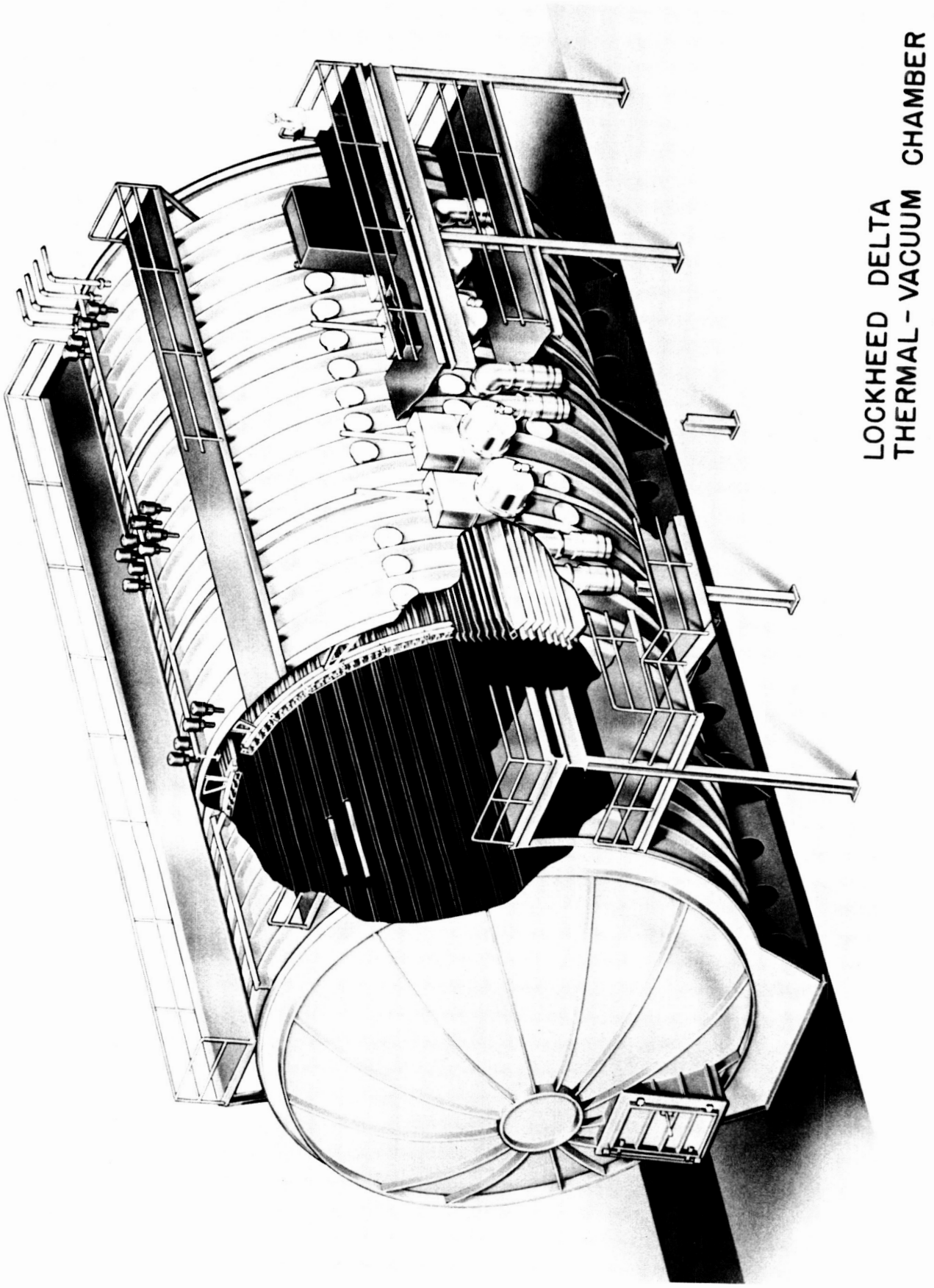

Figure 1. Lockheed delta thermal-vacuum chamber

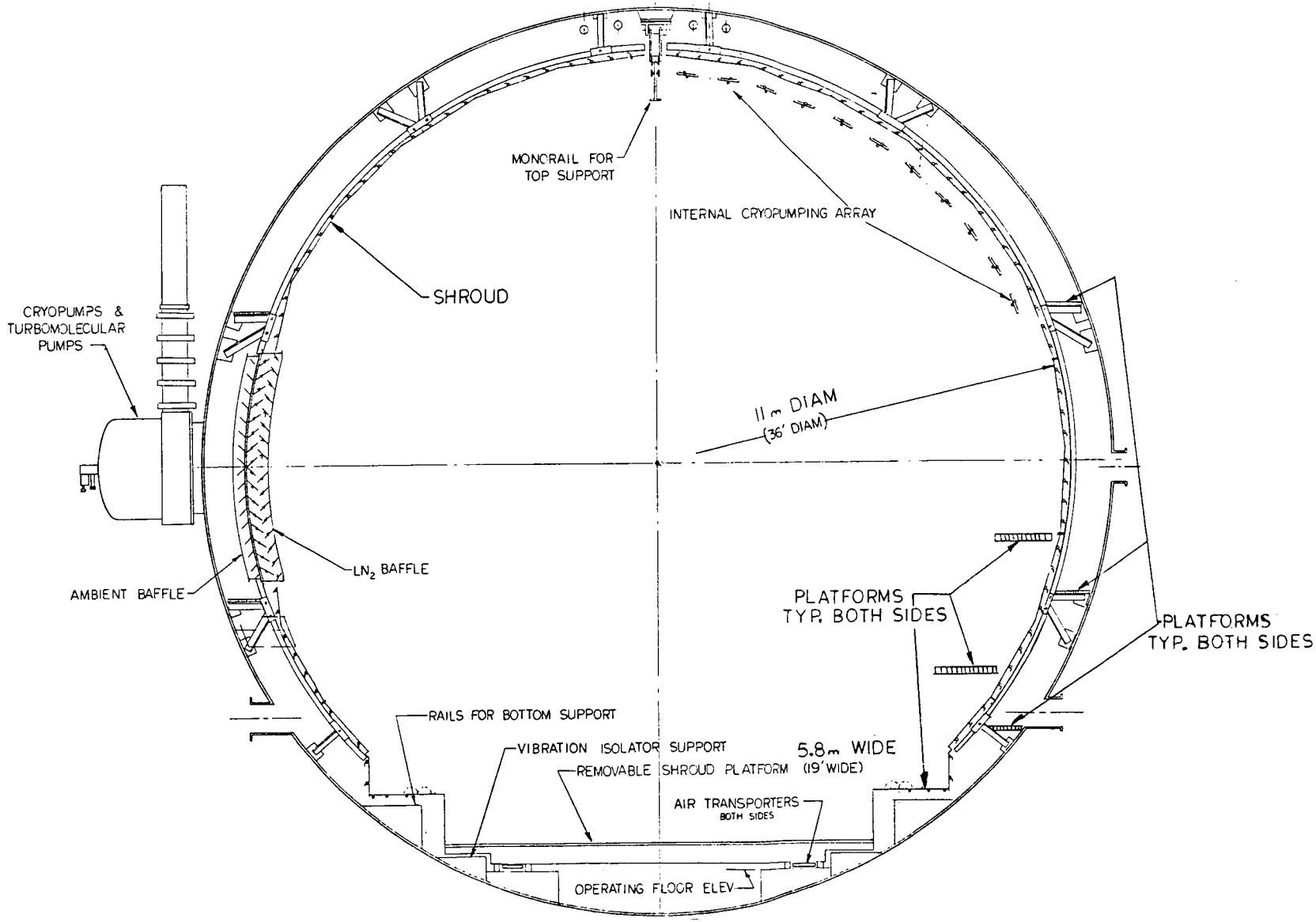

Figure 2. Chamber features

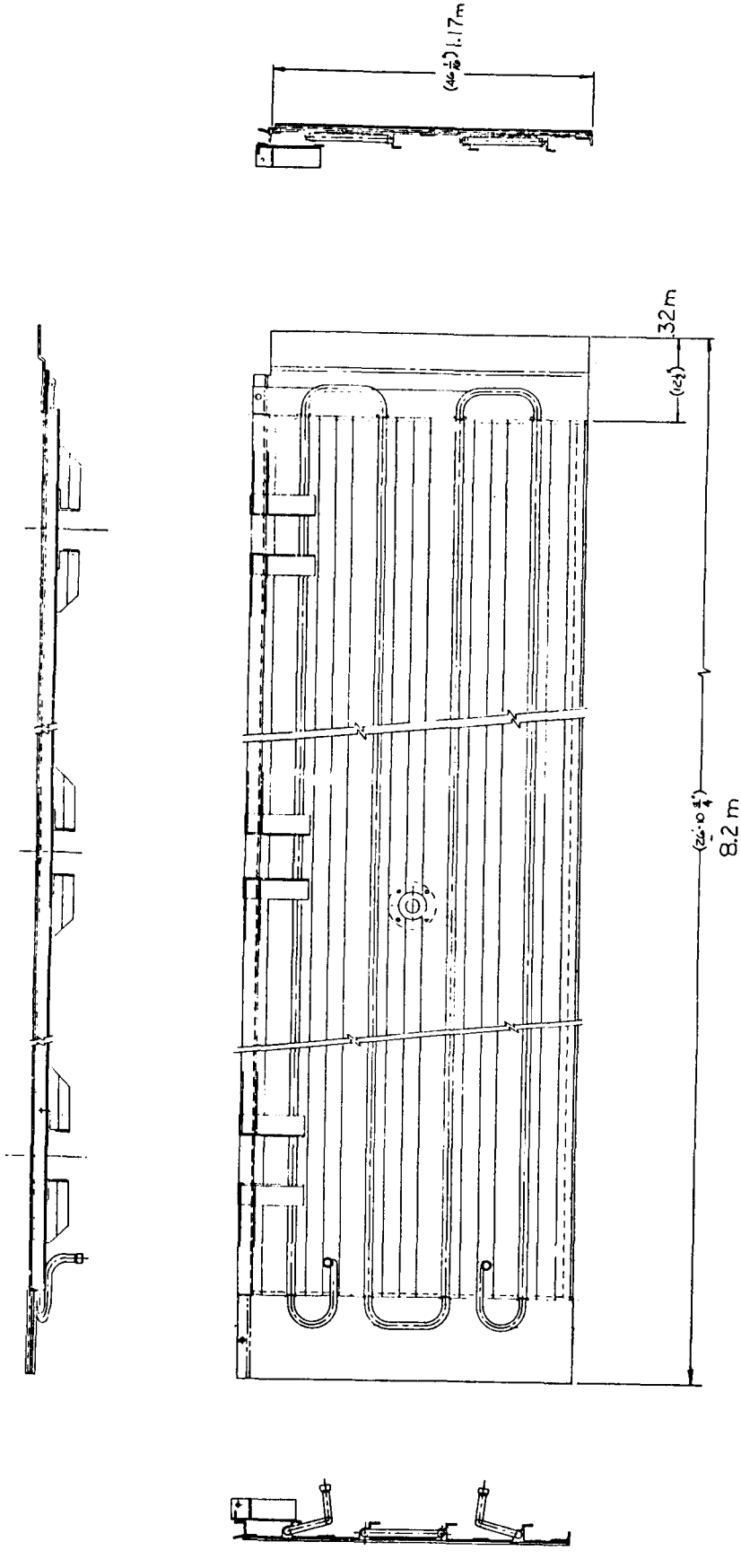

Figure 3. Typical shroud panel

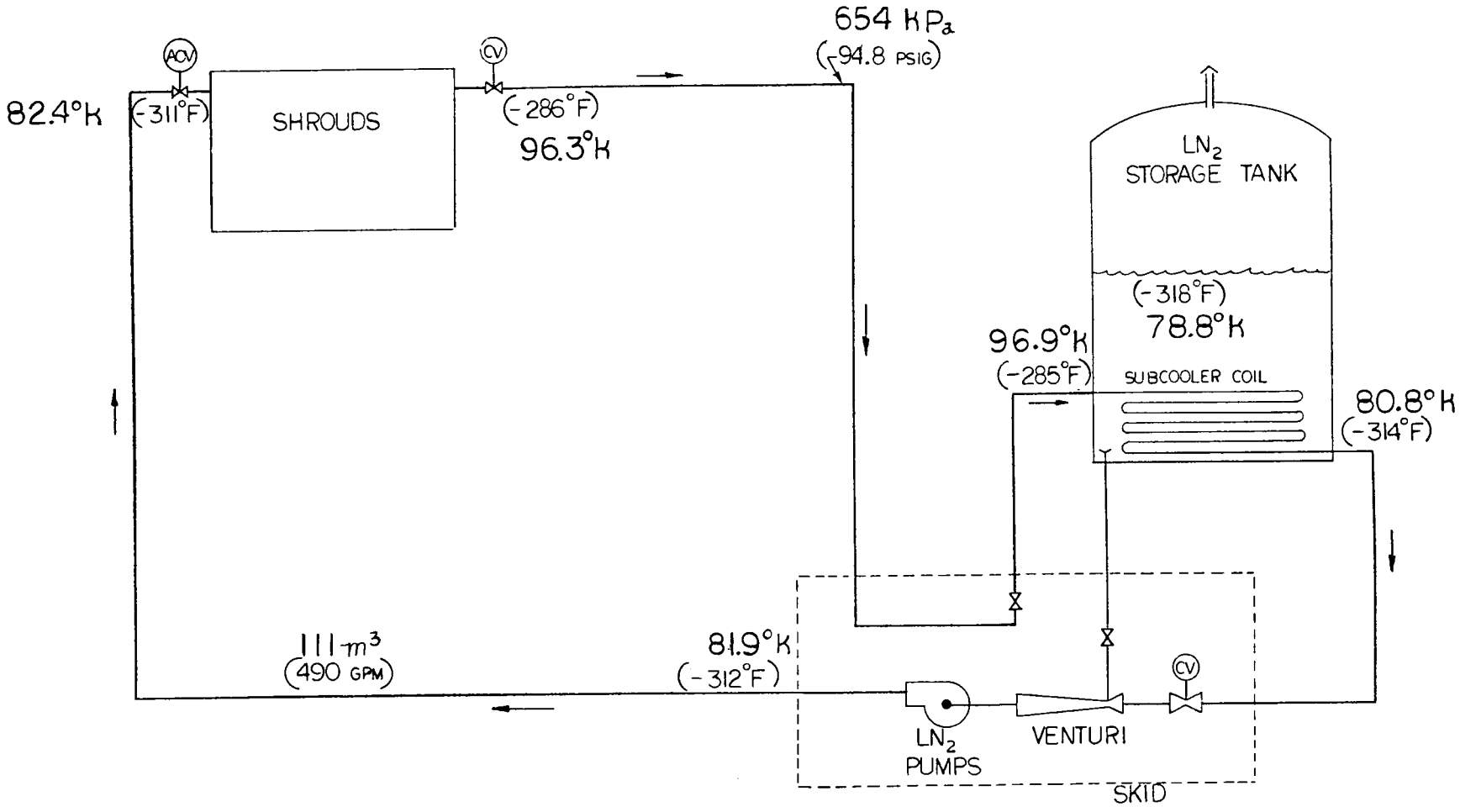

Figure 4. LN_2 system at design conditions

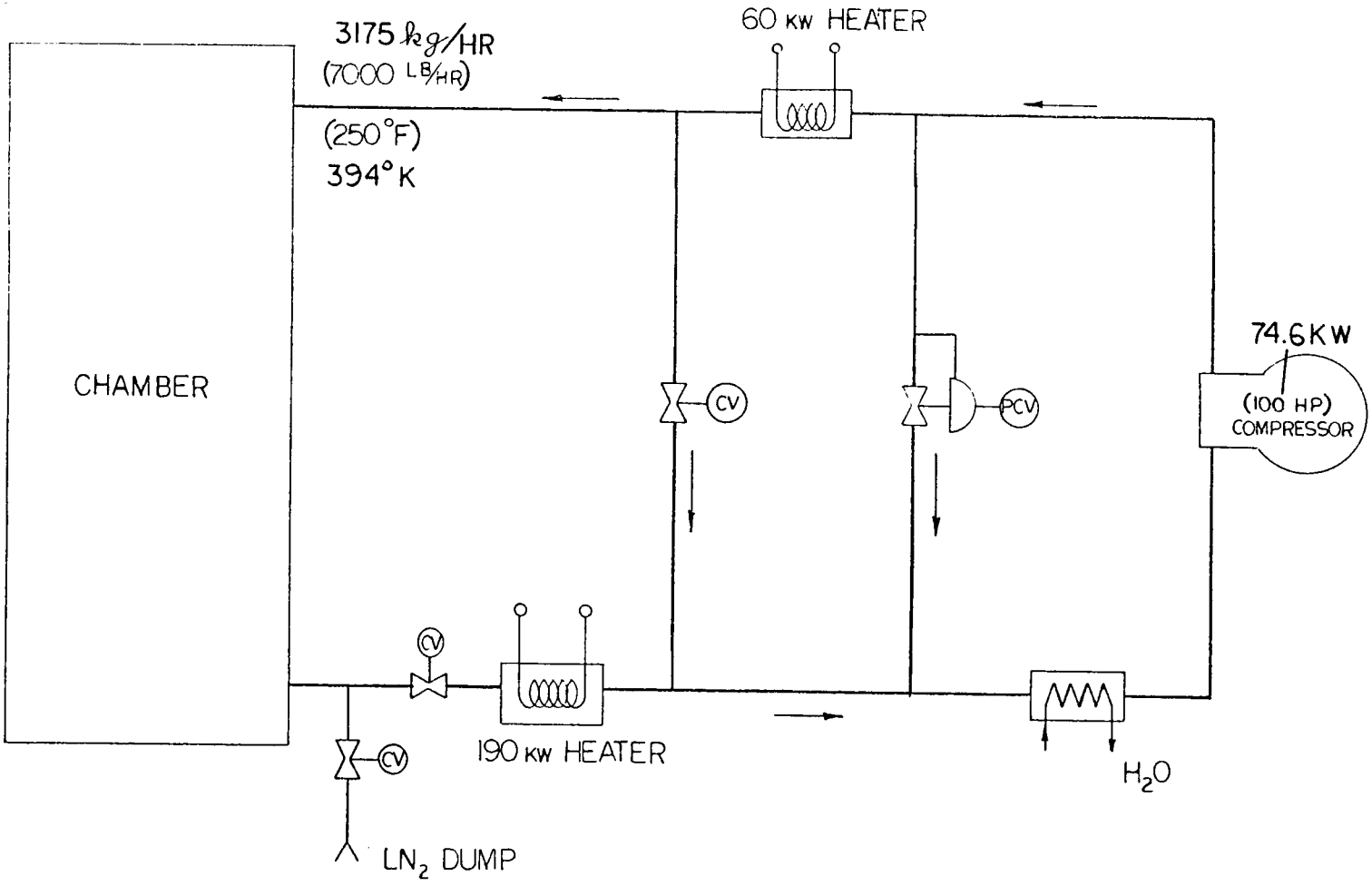

Figure 5. GN_2 warmup unit

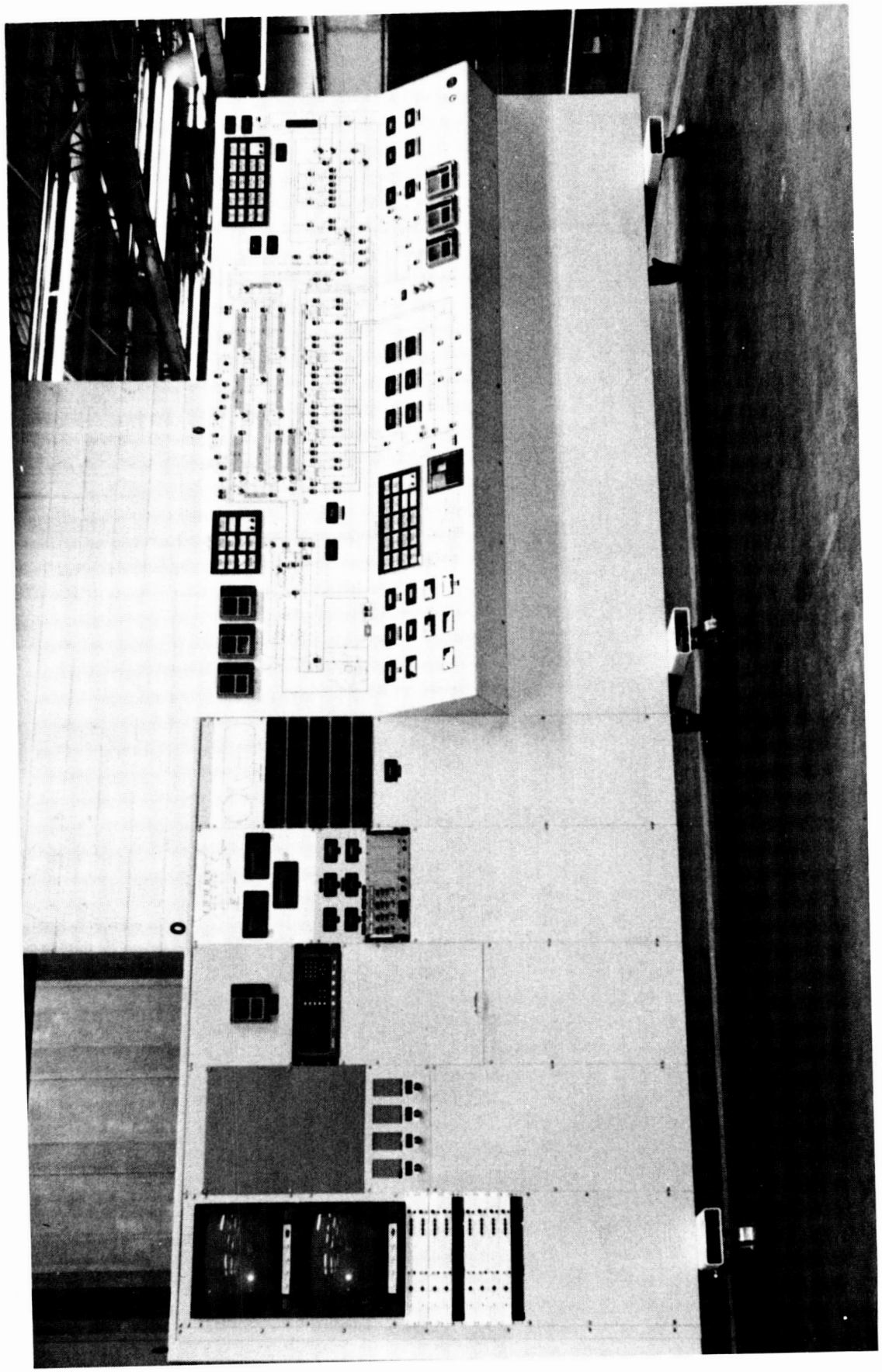

Figure 6. Chamber control console

A MODERN SPACE SIMULATION FACILITY TO ACCOMMODATE HIGH PRODUCTION ACCEPTANCE TESTING

J. D. Glover
Rockwell International Corporation

ABSTRACT

Rockwell International's Satellite Systems Division has designed and activated a space simulation laboratory that supports acceptance testing of spacecraft and associated subsystems at throughput rates as high as nine per year. The Laboratory includes a computer operated 27Ø′ x 30′ space simulation, a 20′ x 20′ x 20′ thermal cycle chamber and an eight station thermal cycle/thermal vacuum test system.

The design philosophy and unique features of each system are discussed. The development of operating procedures, test team requirements, test team integration, and other peripheral activation details is described. A discussion of special accommodations for the efficient utilization of the systems in support of high rate production is presented. A description of the Laboratories' technical capabilities and potential for the future supplements the text.

S13-18
102847
11P

N88-10842

COLUMBUS PRESSURIZED MODULE VERIFICATION

Piero Messidoro and Emanuele Comandatore
Aeritalia S.A.I.p.A. - Space System Group

ABSTRACT

The baseline verification approach of the COLUMBUS Pressurized Module has been defined during A and B1 project phases. Peculiarities of the verification programme are the testing requirements derived from the permanent manned presence in space. The model philosophy and the test programme have been developed in line with the overall verification concept. Critical areas as meteoroid protections, heat pipe radiators and module seals are investigated and tested. Verification problem areas are identified and recommendations for the next development are proposed.

INTRODUCTION

The european space station programme COLUMBUS is now starting the B2 design and development phase. It foresees several elements (Pressurized Module, Platform, Service Vehicle, Resource Module) which will be time phased to form different on-orbit configurations with indefinite life/operation. AERITALIA has system responsibility for the Pressurized Module element which is designed to be part of COLUMBUS scenario together with the other elements, the US Space Station, the Space Transportation System and associated TDRSS, the launchers, etc. ...

The COLUMBUS Pressurized Module is a manned laboratory derived from Spacelab with the capability of being a free flyer, to have periodical upgrading of its features, to receive different payloads (life science/material science) and to be capable of joining the space station. The life requirements of the Space Station dictate that all the components with limited life are considered interchangeable units and will be replaced on orbit as required, the structure and the service parts are considered not changeable.

Redundancy criteria are strongly affected not only by reliability but also by above requirements. The baseline verification approach for the Pressurized Module has been established on the basis of previous consideration and taking into account the testing requirements imposed by the permanent presence in space. The proposed philosophy foresees development/qualification models at unit/subsystem level and two complete models (Engineering and Flight) at element level. The overall system qualification campaign is carried out on the

Engineering Model, which will be maintained for ground simulation after launch, while the flight model undergoes acceptance tests only.

Environmental qualification is performed at subsystem/unit level because of the dimensional constraints of Pressurized Module. Dedicated pre-development technological programmes investigate and test the critical areas of meteoroid protections, heat pipe radiators, and module seals. The paper presents the status of above Pressurized Module verification activities including problem areas and recommendations.

COLUMBUS PRESSURIZED MODULE (PM)

CONFIGURATION

When the invitation came from the USA government to participate in the Space Station, it seemed likely that, with some modifications, the Spacelab module could be used as the primary building block for the COLUMBUS PM. Being modular in concept, not only to accommodate various combinations of experiments, but also to give flexibility for later growth, studies had been carried out to find ways of extending the time Spacelab could stay in orbit, increasing its power and cooling capabilities, and increasing the volume (in terms of length) of the module.

Starting from the Spacelab experience, ESA, together with AERITALIA as its COLUMBUS PM Phase B1 contractor, began to consider the utilization and operational scenarios which would lead to a set of preliminary requirements from which design concepts could be developed. At the time of writing the Phase B2 proposal has been presented (see ref. 1) and it is based on a programme which foresees:

- a four (Spacelab) Segment Laboratory Module attached to the US Space Station, which should be ready for the first operational use of the Space Station (described by the acronym IOC - Initial Operational Capability), planned by NASA for January 1994.

- Two segment PM, together with a Resource Module (RM), in a combination called the Man-Tended Free Flyer (MTFF) that can be updated, reloaded, serviced etc., at the US Space Station but can then be detached and operated in an unmanned mode for extended periods while formation-flying (co-orbiting) with the Station. Its major characteristic is its very low gravity environment, currently anticipated to be one order of magnitude lower than that of the core station (in parallel, other, unpressurized elements such as a polar, and a co-orbiting platform, a service vehicle and a man-tended servicing unit are under study). The PM within its COLUMBUS scenario is shown on figure 1.

- The layout and facilities offered in the PM should provide a number of user friendly features:
  - Earth-like working conditions i.e. one-g layout (floor and ceiling),
  - standard rack spaces for payloads,
  - racks which can be configured as experiment carriers, work benches, or storage areas,
  - power, cooling and data interfaces allowing maximum flexibility for users,
  - racks themselves and payload inserts to be replaceable (Orbital Replaceable Units - ORU's),
  - module and hatches allowing passage of crew and ORU's,
  - modern ergonomic features.

To comply with above requirements the PM consists of the following subsystems: Primary and Secondary Structures, Thermal Control, Environmental Control and Life Support, Data Management, Electrical Power Distribution, Communications, Docking/Berthing Mechanisms and appendices like Scientific Airlock/Window and Viewports.

REQUIREMENTS

In terms of requirements, the ground rule of the Space Station applies: design for indefinite life by means of on-orbit maintenance, re-configuration and growth. As part of the maintenance concept, a problem has arisen in allowing for interior and exterior access to the module shell for inspection/repair. The aim is to use European subsystem equipment and infrastructures to the maximum extent feasible. This also includes achieving compatibility with Ariane 5, Hermes and the European Data Relay Satellite. The induced microgravity environment gets particular attention from the designers, as experiments requiring such conditions could be a major part of the payloads.

It is mainly for this reason that the MTFF would be detachable from the Station since the crew movements, various docking/undocking manoeuvres, service activities etc. will cause considerable disturbance to the microgravity environment. Therefore, for critical experiments/production processes a free-flyer with a minimum of mechanical movements on board is preferable. Detailed COLUMBUS requirements are listed on ref. 2 and PM specific requirements on ref. 3. Many technical trade-offs have been performed during the phase B1 in order to optimize the design is light of the above requirements. All subsystems in the various COLUMBUS elements are being scrutinised and where possible cost saving common items and systems are being incorporated. Major trade-results were:

Basic PM physical skeleton

Spacelab isostatic scheme and trunnions, four 2.7 m Spacelab segments, US Space Station common separate interconnect elements.

Operations and verification

Empty launch, transportation of integrated PM, Engineering Model philosophy, segmented integration approach, internal pressure.

Payload and crew size

Mixed laboratory payloads (material + life), 8.5 crew for PM experiment conduction.

Avionic and software architecture

Data exchange via system local Network, standard acquisition unit to interface with the network, software architecture and requirements.

Detail configuration

Meteoroid and debris protection, radiation analysis, Spacelab location for Window/Viewport, Airlock and Grapple Fixture.

VERIFICATION APPROACH

OVERALL CONCEPT

The COLUMBUS PM verification approach has been established through the following steps:

- investigation of the mission to define the sequence of events, the environments present or induced during occurrence of these events and the related element/subsystem functions;

- definition of the project requirements to be verified and their subdivision in categories (interfaces, performance, design, etc.);

- identification of the qualification status of the subsystem candidates (considering the existing Spacelab and EURECA hardware to the maximum extent) with respect to the COLUMBUS requirements and applicable environments;

- preparation of a verification matrix showing the method (test / analysis / similarity / inspection / demonstration / review of design) and the level of verification (Unit/Subsystem /Element) for each identified requirement.

The verification philosophy will be implemented in the following programme phases using the standard verification logic based on the Verification Control Document (VCD) as shown on figure 2. In agreement with the above overall concept, the PM model philosophy and test programme have been established in light of the following guidelines:

- minimum model philosophy taking into account spacelab experience.
- No environmental tests at element level (except EMC), only at equipment & subsystem level.
- All flight equipment & spares to be subjected only to acceptance tests.
- Qualification testing to be performed at the lowest practical hardware level, at the earliest opportunity in the verification programme.
- Optimization of the number of tests, simulators and support equipment and their utilization.
- Element level tests verify and demonstrate element functional performance, prove compatibility of the subsystems and verify the functional and dimensional interfaces to standard payloads and external elements.
- The verification programme must, in principle, demonstrate compliance with all requirements, and should therefore not rely on "on-orbit" verification.
- Verification of all element external interfaces should be included in the element verification programme.
- Validation of operational software as well.

MODEL PHILOSOPHY

For the model philosophy a prototype approach has been selected which foresees two system models: Engineering Model (EM) and Flight Model (FM). The EM will be used for the functional performance qualification of the PM element and will have the following characteristics: full flight design, no redundancy, whenever possible (cost saving), limited flight standard hardware (no hi-rel parts). The FM will be accepted for the flight and will present full flight design and full flight standard hardware (hi-rel parts included). A development fixture (DM) is foreseen at element level, with the major objectives of interface assessment, operation/maintenance preliminary verification, training of integration team and procedures. The EM will be maintained after launch for ground simulation activities.

At subsystem/unit level development hardware (breadboard, test bad, etc.) is foreseen only for items of new design. A Qualification Model (flight standard) will be used for the qualification test campaign of the hardware not qualified or requiring a delta qualification. These qualification units, after partial refurbishment will become integration spares for the element activities. EM and FM units/subsystems will then be accepted and delivered for the element Integration and test campaign. Spare model (SP) is also foreseen as required by on-orbit maintenance and operations. Figure 3 summarizes the proposed model philosophy.

TEST PROGRAMME

The verification of PM requirements by testing is performed, on the basis of the defined model philosophy, through the following test programme:

Development Model

Development activity on development fixture (a three segment demonstration mock-up has been already manufactured and utilized in phase B1 - see fig. 4).

Engineering Model

Element functional qualification: subsystem functional performance, Integrated System Test (IST), interface test (Payloads, STS, US Space Station, PM), support equipment demonstration, interchangeability (ORU's etc.), ground operation demonstration, audible noise, offgassing, crew habitability demonstration, maintainability demonstration, mission simulation, physical properties, electromagnetic compatibility (EMC), pressure decay, ground simulation of flight operation.

Flight Model

Element flight acceptance: subsystem functional performance, IST, interface tests, support equipment demonstration, interchangeability, crew habitability demonstration, physical properties, system leak, EMC.

COLUMBUS programme characteristics and PM configuration impose some constraints on the test programme and on its feasibility. For example the PM dimensions necessitated performing thermal testing at subsystem level, and spacelab main structure reuse to avoid dedicated acoustic testing on the overall PM. However erious difficulties will remain in performing the EMC test (many COLUMBUS parts will meet for the first time in orbit), interface verifications (the several elements must be properly simulated together with the other external interfaces), maintainability demonstration (man interfaces, airborne support equipment and check-out procedures must be suitably addressed), software validation (complete and represen- tative validation facility will be necessary to offer the opportunity to intervene on the software in real time).

The environmental qualification test campaign will be performed mainly at subsystem/unit level within dedicated subsystem programmes. Significative activities will be:

- Radiator system functional qualification in vacuum with a parametric verification of radiator performance within the LSS ESTEC chamber.
- Active thermal control loop breadboard test in line with similar Spacelab activity performed in AERITALIA (see ref. 4).
- Cabin/Avionic loop functional performance at power using a suitable test bed.

- Latching performance verification of docking/berthing mechanism with SENER provided interface rig including a three dimensions simulation table.

Concerning the PM payloads, they will be installed inside the racks in order to satisfy the PM modularity and on-orbit exchangeability requirements. The PM interface to payload will be verified by means of standard payload simulators, while the payload verification programme will see environmental qualification at equipment and payload level. The various payloads will be installed inside the standard PM racks and then subjected to functional verification, interface test with PM, IST and mission sequence test. A two model philosophy is foreseen for qualification and acceptance activities.

TECHNOLOGICAL DEVELOPMENT

As complement to the main programme activities and to support the new technologies necessary to comply with COLUMBUS requirement, dedicated Preparatory Programmes have already been commissioned by ESA to the european industries and are now in progress. The areas involved are: Thermal Control components and software tools, Power Generation components and EMC mathematical model, Energy Storage batteries and rotors, Attitude and Orbit Control design, Communication High data rate terminal, Structure meteoroid protections and seals/welding, Environment & Life Support components, Power Management Switches, Data Management optical fibre devices, Rendez-vous and Docking operation test bed, In-orbit Propulsion engine and plume dynamic interactions, Robotics, Telemanipulation test bed and servicing interfaces. Within the PM oriented technological development AERITALIA is involved as described herein.

METEOROID/DEBRIS PROTECTION

The reason for the technology improvement is that the impact of meteoroids and space debris on primary structure could produce puncture and consequent depressurization. The environment specification (see ref.'s 5 and 6) and the COLUMBUS requirements (see ref. 2 and 3), with the help of previous studies and applications on the subject (see ref. 7 and 8) are pushing towards a solution of dual shield concept especially to cover the range of velocity around 10 km/sec.

The meteoroid is allowed to perforate the first alluminum shield, there it usually evaporizes, the debris cloud expands and it is stopped by the second shield kevlar-form sandwich plate. The phenomenum has been computer simulated (see ref. 9) and confirmed by a series of test that AERITALIA is performing at the Ernst-Mach Institut

of Freiburg investigation different parametric condition of meteoroid diameter, impact speed and protection configuration. Figure 5 shows the computer simulation and the hypervelocity impact facility used.

MODULE SEALING AND WELDING

The reason for the technology support programme for seals and welding are respectively: to minimize maintenance and improve Spacelab joint reliability in relation to the uncertainty about sealing material behaviour in space environment for indefinite life, to improve welding quality and minimize joint distortion and residual stress in the whole assembly. Trade-offs have been performed between several solutions to improve Spacelab joints and the result suggested a minimization of the number of joints (welding almost all 4 m diameter joints) and, for the remainder using a back-up seal to be inserted in orbit. A specific leakage test will be carried out on a 4 m diameter seal to demonstrate that the concept is working and that the amount of leakage during the seal substitution (1 m^3 of module air) will be an acceptable leak.

The welding process will be improved from the Spacelab TIG method to the Variable Polarity Plasma are one. The variable polarity approach will have the advantage of cleaning the welding, resulting in a well balanced coupling. The process is now under investigation (cooling system, support hardware, etc.) and will be completed by performing static and fracture mechanics tests on samples. Figure 6 shows the proposed welding set-up.

HYBRID RADIATOR

The standard fluid radiator (i.e. TDM/EURECA concept, see ref. 10) would imply high maintenance activity with increased risk of contamination in case of perforation due to high freon leakage. The standard heat pipe radiator (i.e. OLYMPUS concept, see ref. 11 are not adequate in terms of heat rejection capability). For this reason a hybrid radiator concept is required allowing autonomous heat dissipation (essential in MTFF mode) with high life and minimum maintenance.

The hybrid radiator proposed design consists of heat pipe assemblies coupled to a liquid, or two phase loop heat exchanger which interfaces with a central heat transportation system. Micrometeoroid protection is also included (see figure 7). Qualification testing in the Aerospatiale thermal vacuum chamber is planned, with performance verification during hot, cold, steady state, and transient conditions, at different flow rates and inlet temperatures, including the demonstration of the capability to recover from heat pipe freezing.

CONCLUSIONS AND RECOMMENDATIONS

The PM verification approach has been defined on the basIs of COLUMBUS programme requirements for a manned space station permanently present in space. Starting from the Spacelab qualification status a two system models philosophy has been established with functional qualification on EM and flight acceptance on FM. Subsystem/Unit development and qualification test campaigns will be performed on dedicated hardware including major environmental tests. Pre-development support programmes in the new technology areas offer the availability of early results.

The B2 phase activities which are starting now will refine the technical content of the design together with the operations and verification philosophies in view of the starting of C/D phase presently planned for January 1988. The major areas to be furtherly investigated are the development and qualification activities at subsystem/unit level on which the impact of new technologies and risk assessment is direct. Particular care will be devoted to investigate the following:

- telescopic flexible fluid lines for Docking mechanisms
- leak detection and isolation within the active loop
- cabin pressure regulator, CO_2 storage, hand wash and microbial control equipment of Environmental subsystem
- ORU connectors and high power gauges crimp joints
- computer chips, magnetic and optical disks, space qualified comale, within the Data Management hardware
- communication interface requirements.

In summary, the COLUMBUS PM is being engineered to make best use of Spacelab hardware/experience, allowing experimenters to reuse their Spacelab equipment with minimum changes. On the other hand, total system requirements dictated by the U.S. Space Station and the long term European scenarios is being incorporated. Both aspects will be achieved within a tight development budget, with the aim being to minimize operational and verification costs.

REFERENCES

1. Proposal for COLUMBUS PM Phase B2 - SG-PP-AI-052 - AERITALIA - July 1986

2. System Requirements Document (SRD) - COL-RQ-ESA-001 - ESA - July 1986

3. Design Definition Report - COL-RP-AI-009 Sect. D - AERITALIA - May 1986

4. P. Messidoro & Al.: Spacelab Active Thermal Control Subsystem Breadboard Test - AERITALIA - Proceedings of ICIASF IEEE Publication 79CH1500-8 AES - Monterey - Sept. 1979

5. Space Station Natural Environment - NASA-JSC-30000 NASA/JSC - March 1986

6. D.J. Kessler: Orbital Debris Environment for Space Station - NASA-JSC-2001 NASA/JSC - Sept. 1984

7. H.F. Swift & Al.: Designing Dual Plate Meteoroid Shields - A new Analysis - NASA-JPL-82-39 - NASA/JPL - March 1982

8. F. Felici: Giotto Hypervelocity Impacts Tests Report - ESA WIP. 1311 - ESA - Oct. 1981

9. F. Arnandeau & Al.: Numerical Analysis of the Giotto Spacecraft Shield under Micrometeoroid Impacts - ESI Inv. paper to the "Finite Element Methods" Congress - Interlaken - Sept. 1984

10. P. Messidoro & Al.: Functional Test Performance of TDM Advanced Heat Rejection System in Vacuum - AERITALIA Proceedings of 14th ICES - SAE Publ. 840962 - S. Diego - July 1984

11. P. Messidoro & Al.: Thermovision and Heat Pipe Simulation Techniques to test on ground Heat Pipe Radiators and Thermal Model of OLYMPUS - AERITALIA Proceedings of 5th IMPC - Tsukuba - May 1984.

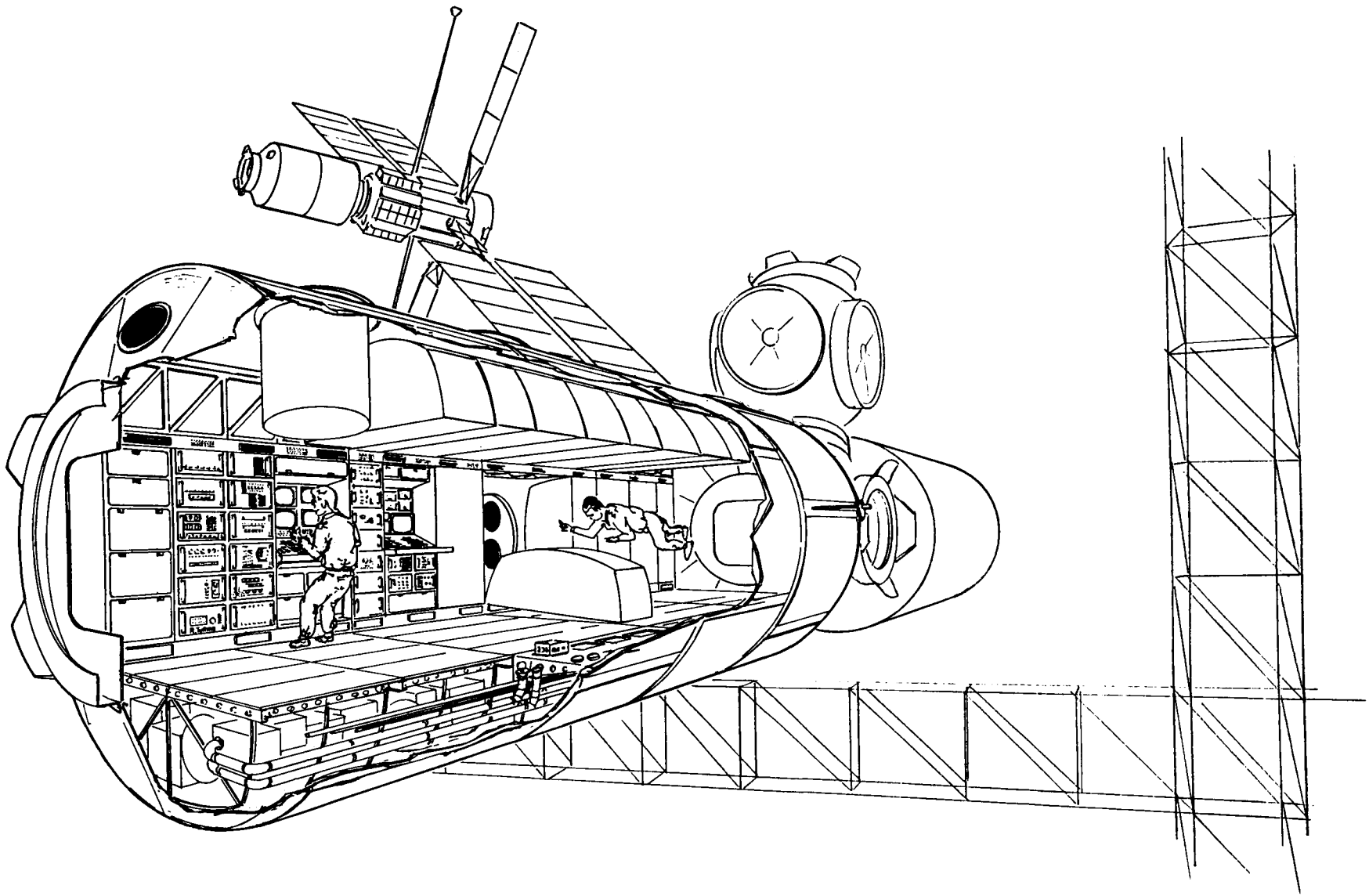

Figure 1. Pressurized module and columbus scenario

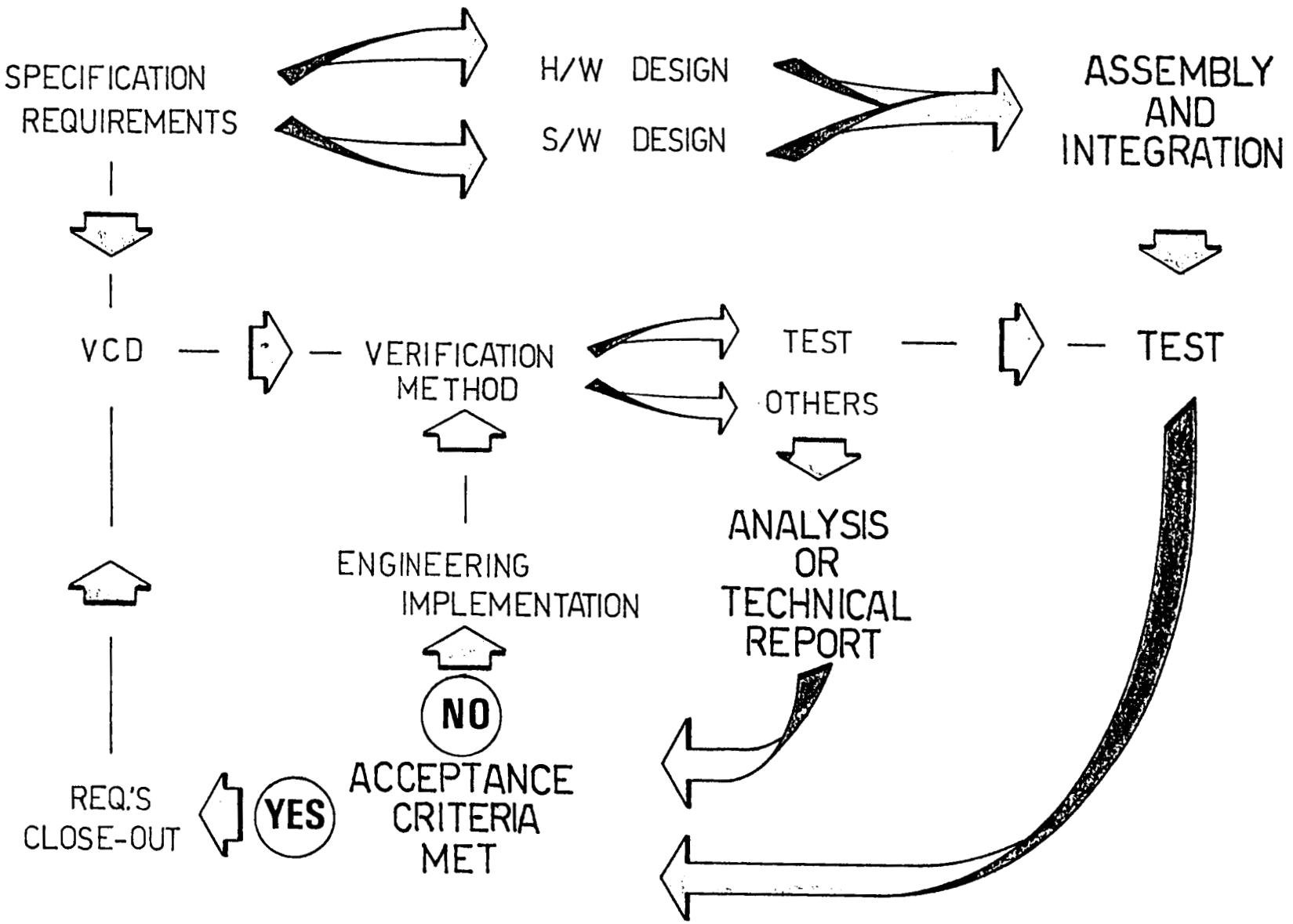

Figure 2. Verification logic

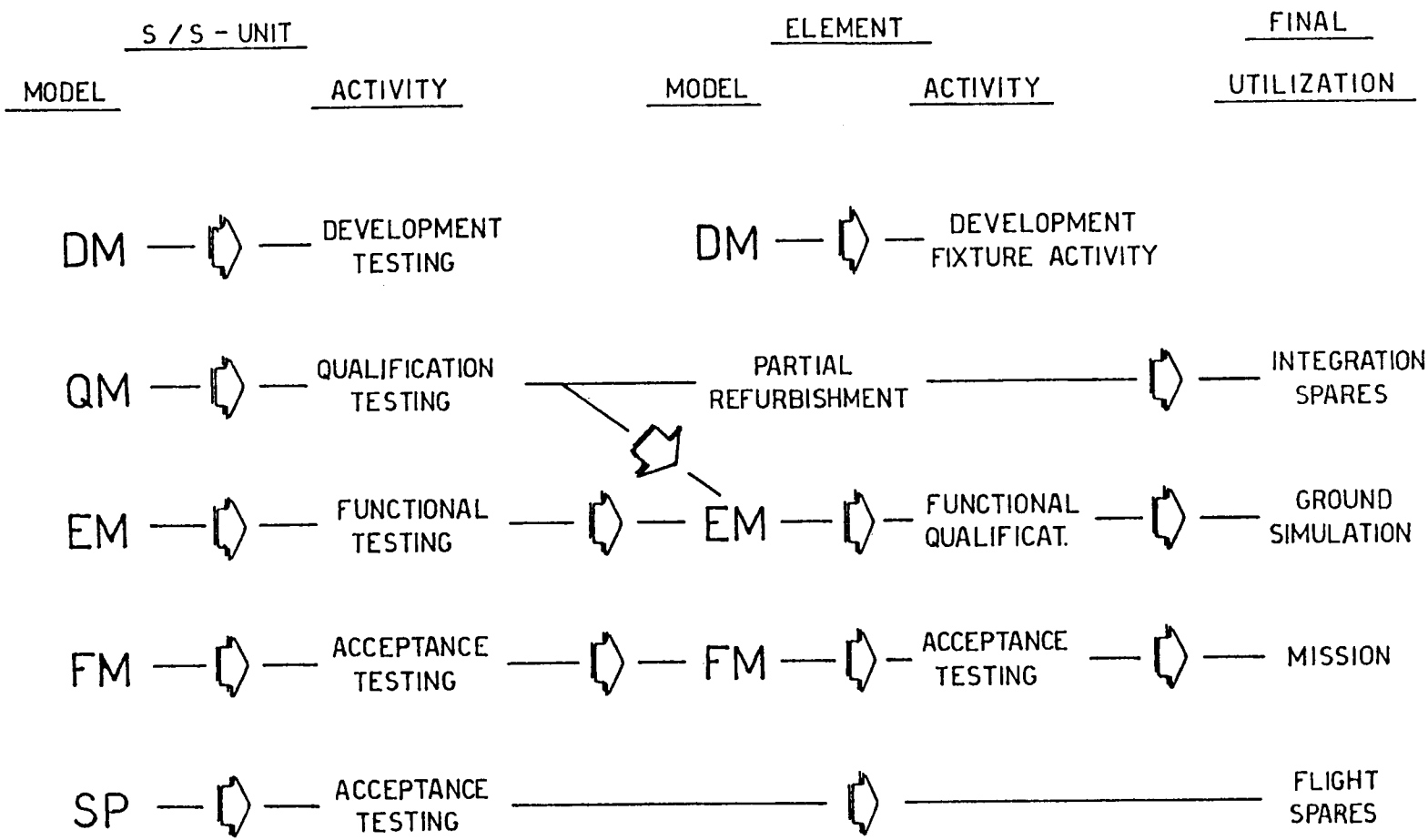

Figure 3. Proposed model philosophy

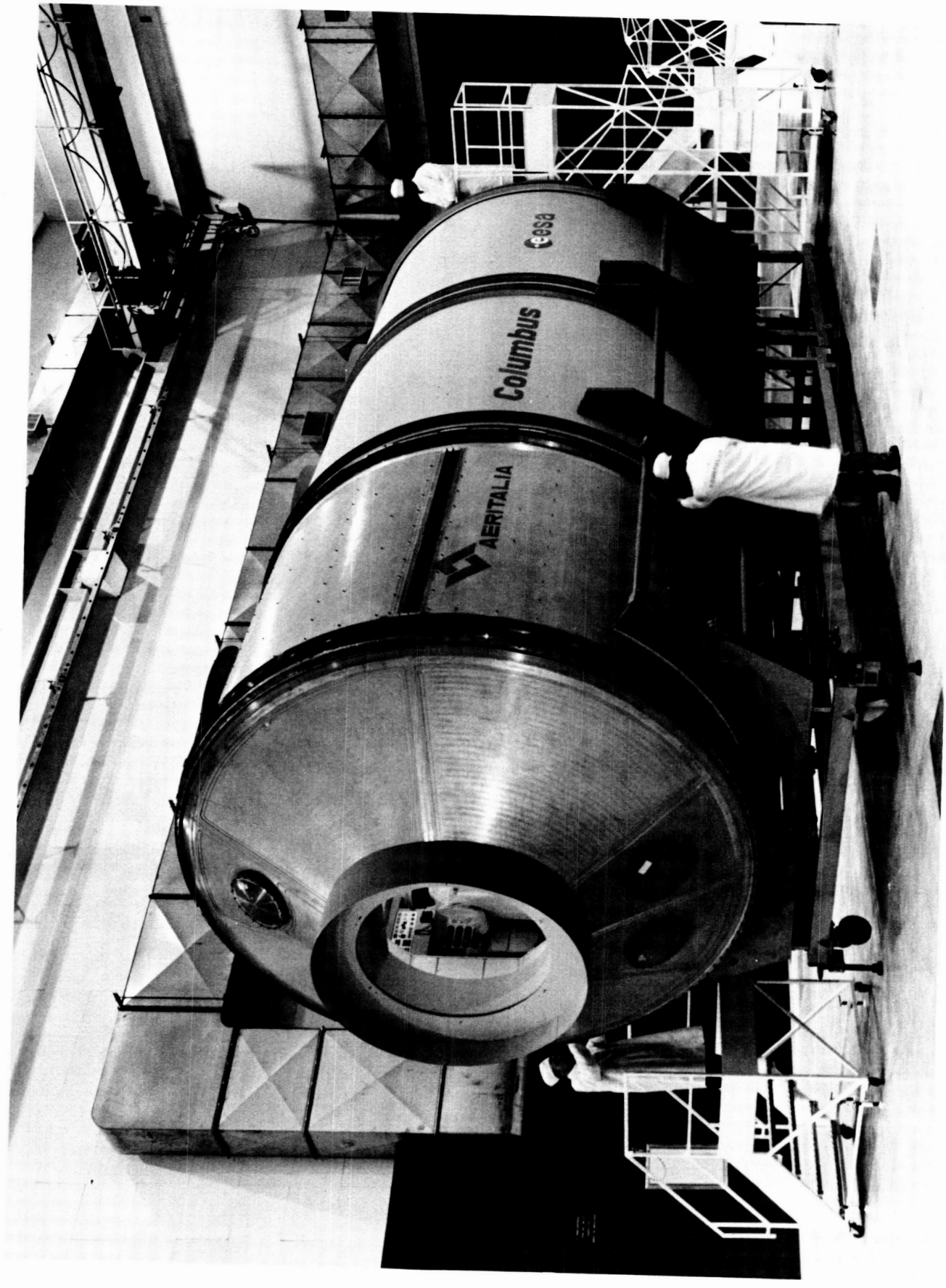

Figure 4. PM phase B1 mock up

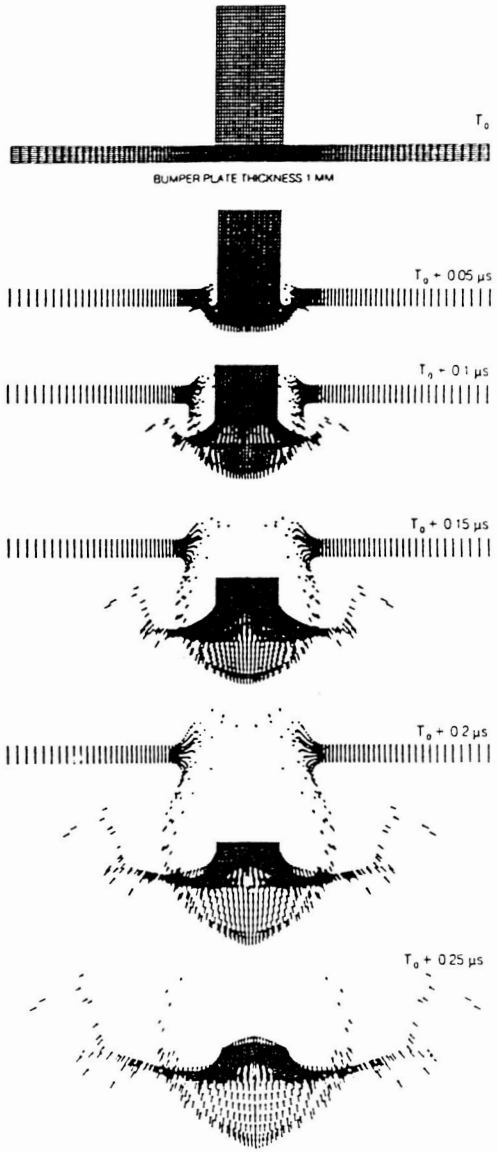

Perforation sequence (velocity vectors) predicted by the Lagrangian code (HEMP/ /ESI) for a foamed silica meteoroid (4 mm in diameter, 100 mg in weight) impacting on an aluminum alloy bumper shield at 68 km/sec

Impact vacum facility, having gun gas hydrogen, (for projectiles caliber 4.5 mm, 100 mg in weight, velocity up 10 km/sec) equipped with two shadow graph stations at X-Ray and optical laser system for velocity measurement. Impact tank reaches a vacum 10^{-7} torr

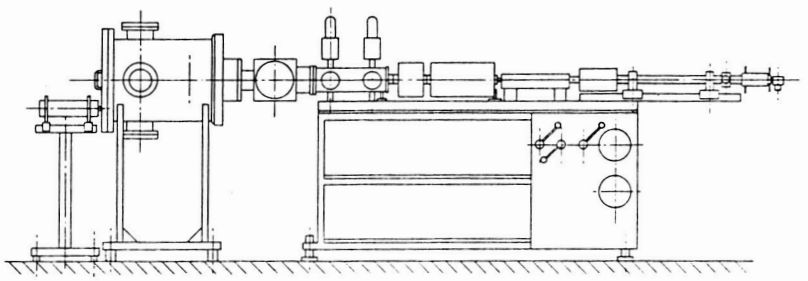

Figure 5. Meteoroid impact computer simulation and test facility

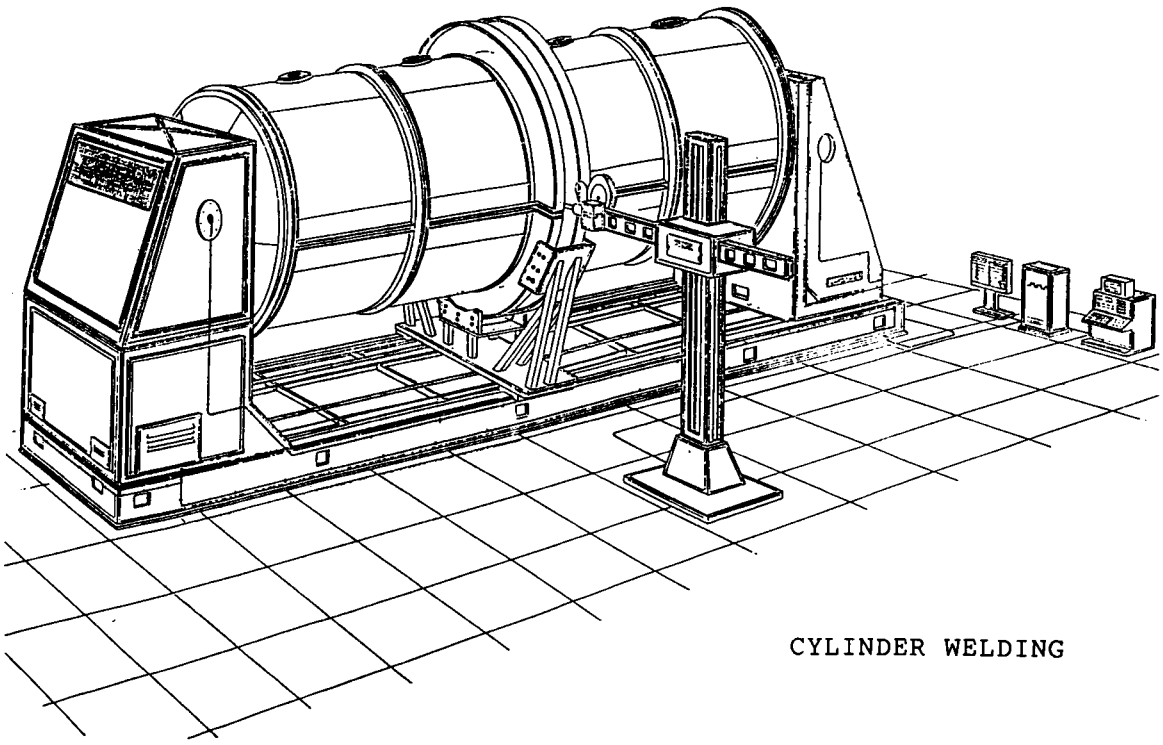

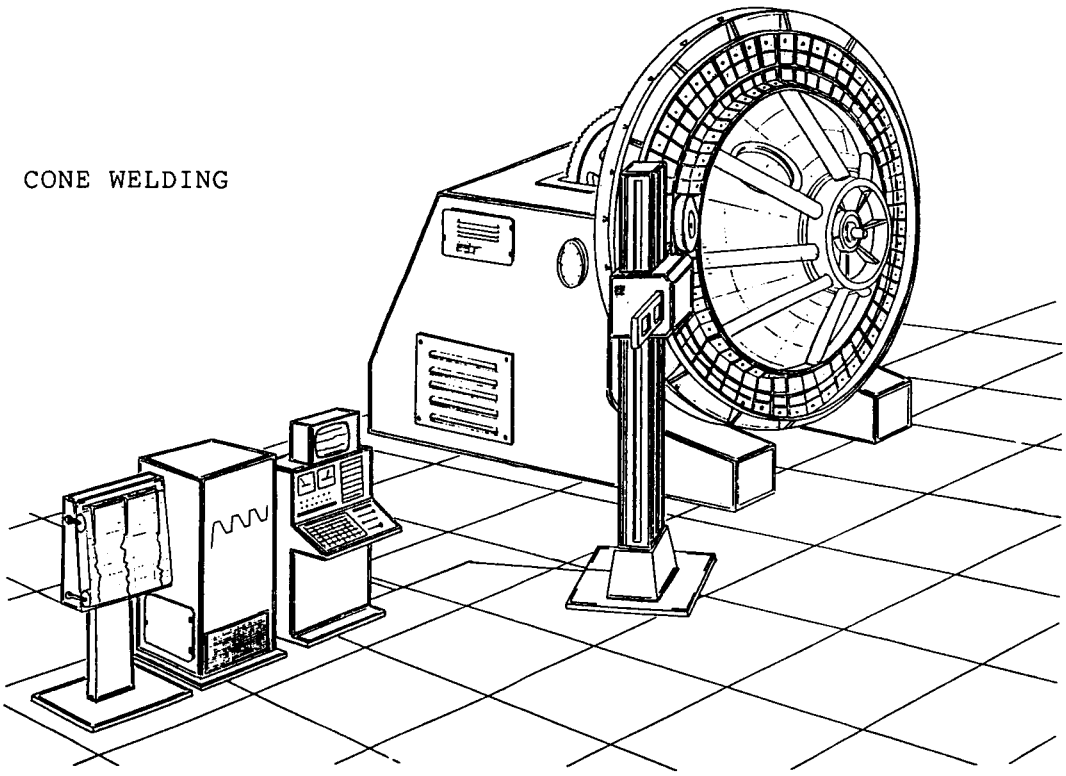

Figure 6. Module welding set-up

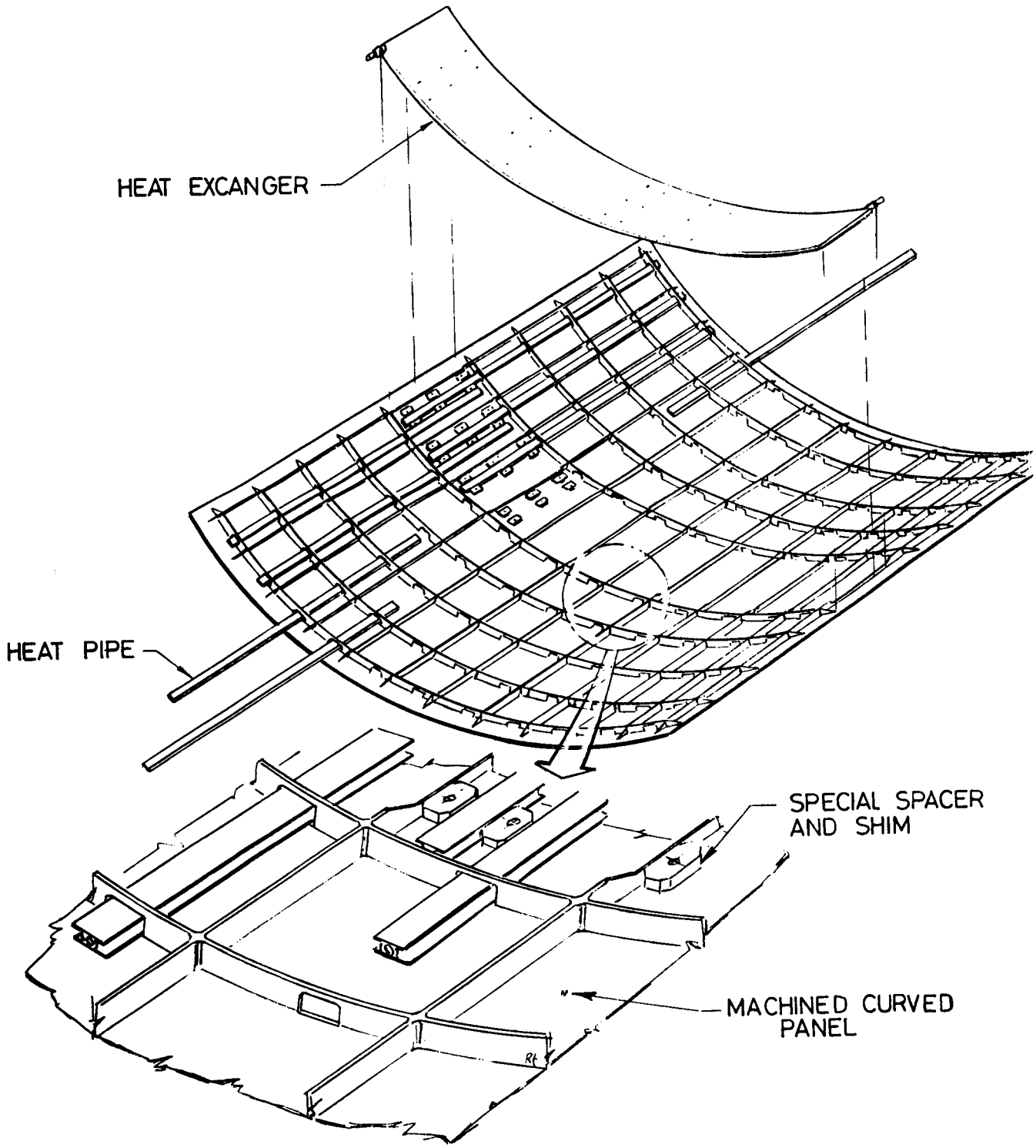

Figure 7. Hybrid radiator concept

MOBILE TEST FIXTURE SYSTEM FOR USE IN A THERMAL VACUUM FACILITY

Ronald C. Weber, Robert E. Stoyer and Warren A. Carpenter

CBI Na-Con, Inc.

ABSTRACT

CBI constructed a turnkey thermal vacuum facility for Rockwell International. A key component of this facility is a mobile test fixture system which allows production line type testing of Navstar satellites. Five major subsystems are integrated into the mobile test fixture concept which minimizes turn around time between tests. All spacecraft intrumentation, wiring and computer aided checkout is performed outside of the chamber while other satellites are under thermal vacuum test within the chamber. The system is currently in use performing as expected.

INTRODUCTION

Rockwell International was awarded a contract to provide 28 Navstar satellites in the final phase of the Navstar program. The delivery schedule is such that one large thermal vacuum facility is required with a very high degree of utilization. One of the key components of the facility, to minimize spacecraft turn around time, is the mobile test fixture and transporter system as specified by Rockwell and designed and constructed by CBI. This paper describes a system which integrates five major subsystems including the transporters, multiplexers, a thermal shrouded test fixture, a thermal isolation system and an internal utility distribution system into a mobile test fixture system. See Fig. 1 and Fig. 2.

This concept allows the spacecraft to be mounted on the test fixture outside of the chamber. Instrumentation and computer checkout of the spacecraft and its instrumentation is accomplished at this station. The spacecraft, which is still mated to the test fixture, is then moved into the chamber using an air transporter system. The spacecraft then requires the connection of only two plug-in instrumentation cables and a minimum of other utilities prior to the start of thermal vacuum testing. No vertical lifts or rehandling of the satellite are required after attachment to the test fixture in the assembly area.

TRANSPORTER

The chamber has a truncated door which eliminates a pit and other floor discontinuities thus maximizing the useable floor space around the chamber as shown in Fig. 3. The absence of a door pit or slot also eliminates the need for a pit elevator or bridge. The use of a truncated door, however, results in a nine inch step up into the chamber. This elevation change is accommodated by using a two tier piggy-backed transporter system as shown in Fig. 4. The lower transporter, which remains outside of the chamber, is nine inches high and is designed to allow the upper transporter, test fixture and spacecraft to float onto the flat 20' x 30' floor section of the shroud. Both of the transporters are provided with an air bearing movement system to minimize shock transmission to the spacecraft and to allow hand movement around the lab. The lower transporter is capable of being used as a general facility cart when the test fixture is not being moved.

MULTIPLEXERS

The second key subsystem is the utilization of commercially available multiplexers mounted in the test fixture for use during pretest outside of the chamber and during the thermal vacuum testing inside the chamber. Four Hewlett Packard model No. 3498 multiplexers are mounted within each of the two test fixtures as shown in Fig. 5. This concept was inspired by Don Glover and first used by Boude Moore at McDonnell Douglas. The multiplexers were modified by CBI and extensively tested successfully by Don Glover of Rockwell.

Disassembly of the multiplexers is required to remove non-vacuum compatible frame materials. The multiplexers also require active heating to operate in the 80 K, high vacuum environment. The multiplexers are mounted between 3/8" thick aluminum plates painted to achieve an emissivity of 0.9. Each plate is equipped with a 120 watt cartridge heater for the thermal conditioning. These heaters are designed to be powered by computer controlled, time proportioning power supplies. Rockwell technicians found that simple on-off thermostat control of the heater provides adequate temperature regulation so that the computer controlled power supplies can be used for other functions. Vacuum compatability also requires that the multiplexer cabling be supplied with teflon insulated wire.

The use of the multiplexers on the test fixtures allows Rockwell to instrument and wire the spacecraft with up to 800 data channels prior to spacecraft entry into the chamber. This means that wiring and an extensive pre-test program can be accomplished while another spacecraft is still under test within the chamber. The only instrumentation wiring that must be completed within the chamber is the connection of two plug-in cables to the test fixture multiplexers from the computer control and data acquisition system which is located outside of the chamber. The 800 channel capability of the multiplexers provides Rockwell with a 50% redundancy to enhance reliability.

Two similar multiplexers are located on fixed mounts within the vacuum chamber for transmission of all chamber instrumentation. These units are provided to minimize wiring and feedthru costs and to maximize the flexibility to alter instrumentation for any individual test that may be required. These multiplexers are also thermally conditioned to operate in the thermal vacuum environment.

Rockwell International conducted an extensive test program to ensure that the multiplexers were suitable for operation over the entire operational range of the chamber. The multiplexers were even operated throughout the corona discharge pressure range to ensure that the units would provide a continuous link with the spacecraft. The highest voltage encountered in the multiplexer was the 110 V power supply.

CBI supplied a networked computer system and software for facility control, data acquisition, data manipulation and display. This system consists of four HP 1000 series computers including two model A600 computers and two model A900 computers. The system also includes tape, hard disk memory storage, video control stations and hard copy printing and plotting capability. The computer system allows simultaneous control and data acquisition for the chamber and its related systems as well as for a spacecraft under test within the chamber and a spacecraft under pre-test or post-test

checkout outside of the chamber. The computer system along with the multiplexers installed on the test fixture almost completely eliminates in-chamber hook-up and check out of the spacecraft environmental support systems.

TEST FIXTURE THERMAL SHROUDS

The third significant feature of the test fixture system is the thermal shrouds on each test fixture as shown in Fig. 6. The thermal shrouds thermally screen the spacecraft from the test fixture and are designed to thermally approximate the operational characteristics of the chamber thermal wall in the LN_2 and GN_2 modes of operation. These shroud circuits are temperature controlled by the internal utilities system.

The use of thermal shrouds on the test fixture eliminates any radiation from warm test fixture structural elements thus minimizing the time required for the spacecraft to reach thermal equilibrium. The thermal shrouds on the test fixture also eliminate heat loads from the multiplexers and their heaters.

INTERNAL UTILITIES SYSTEM

The fourth subsystem of the mobile test fixture system is an internal utilities system. This system provides liquid and gaseous nitrogen supply and return connections and electrical feedthrus for fast and convenient hook-up. These utility connections are located in the area below the flat thermal wall floor. This area below the floor is an ideal location because connections can be made to fluid manifolds and electrical feedthrus without interference from a shroud which is installed very close to the chamber shell. Normal access to the area below the shroud floor is a hatch through the floor.

Two fluid supply manifolds are provided within the chamber to thermally condition all auxiliary shroud circuits such as the test fixture shrouds, a decontamination plate or any thermal targets which may be required. One manifold provides four taps for LN_2 only. The other manifold provides 26 taps for either LN_2 or heated GN_2. The temperature of auxiliary shroud circuits is computer controlled using a thermocouple mounted on the auxiliary panel which operates a solenoid valve located in a discharge manifold vessel. The discharge manifold vessel is installed within the chamber. The system is shown schematically in Fig. 7.

The discharge manifold vessel is installed within the vacuum chamber for a number of reasons. The first is that the vessel does not require thermal insulation if it is located within the chamber due to the insulating effect of the vacuum. The second reason is that only one six inch bayonet type chamber penetration is required for GN_2 discharge instead of twenty four ½" diameter penetrations that would be required for individual circuits. This vessel is shown in Fig. 8.

Twenty four individual circuits penetrate the valve box through twelve Conflat type ports. The circuits then discharge through Magnatrol solenoid valves which are located within the discharge manifold vessel. GN_2 is then vented out of the chamber and building through the six inch diameter vent line. Any liquid nitrogen carryover is allowed to vaporize within the vessel. Each individual circuit is connected using Cajon VCR fittings. Individual circuits are capped when not in use. The Cajon fittings proved to be very reliable in high vacuum, cryogenic service. The Conflat flanges are provided to allow access for maintenance to each pair of Magnatrol valves.

The solenoid valves used in the discharge manifold vessel must operate in a cryogenic condition and may even be submerged in LN_2 in the event of a thermal control failure. CBI, therefore, tested three brands of solenoid valves. The tests were conducted at CBI's Plainfield, Illinois research facility and were conducted to determine which solenoid valve could operate properly if submerged in LN_2. It was found that only the Magnetrol valve would perform properly under these conditions.

All instrumentation and electrical feedthrus for the chamber are located in three 48" ϕ pods installed on the bottom of the chamber. Each of the pods is provided with six 12" ϕ instrumentation ports. These ports have hinged quick opening blind flanges which can be adapted for almost any feedthru requirement. The design includes a full opening (48" ϕ) bottom hatch which allows the technician to work on the outside or inside connections at chest level. See Fig. 9.

Computer controlled power supplies were provided as part of the internal utilities system. The power supplies were prewired into the chamber using feedthrus located in the 48" ϕ instrumentation pods and prewired into the computer system with process variable feedback returning to the computer through the multiplexers. The power supplies consist of 20 autoranging D.C. units which are capable of 0-10 AMPS, 0-60 volts and up to 200 watts; 40 A.C. time proportioning units capable of 110 V and 40 AMPS; as well as 18 low voltage D.C. units. PID and RAMP control is available for each of the units with simple fill in the blanks type programming.

THERMAL CONTROL OF SPACECRAFT SUPPORT RING

The fifth subsystem consists of active thermal control for the spacecraft support ring of the test fixture. See Fig. 10. The temperature of the support ring is controlled to minimize conductive heat transfer between the spacecraft and support ring thus simulating a free flying spacecraft.

Thermal control of the support ring is provided by multiple 50 watt cartridge heaters attached to the support ring. The cartridge heaters are computer controlled using a differential temperature type thermocouple circuit which is attached to the support ring and the spacecraft. Any temperature difference between the support ring and the spacecraft activates the heaters. Active cooling of the support ring is not required because of the test cycle parameters and the thermal conditions within the spacecraft.

CONCLUSION

In the past, the majority of thermal vacuum facilities have been constructed with little regard to test turn around time. However, close consideration to the requirements of production line type testing as exhibited by Rockwell International has allowed CBI to design a facility with many innovative features, expressly designed for rapid turn around.

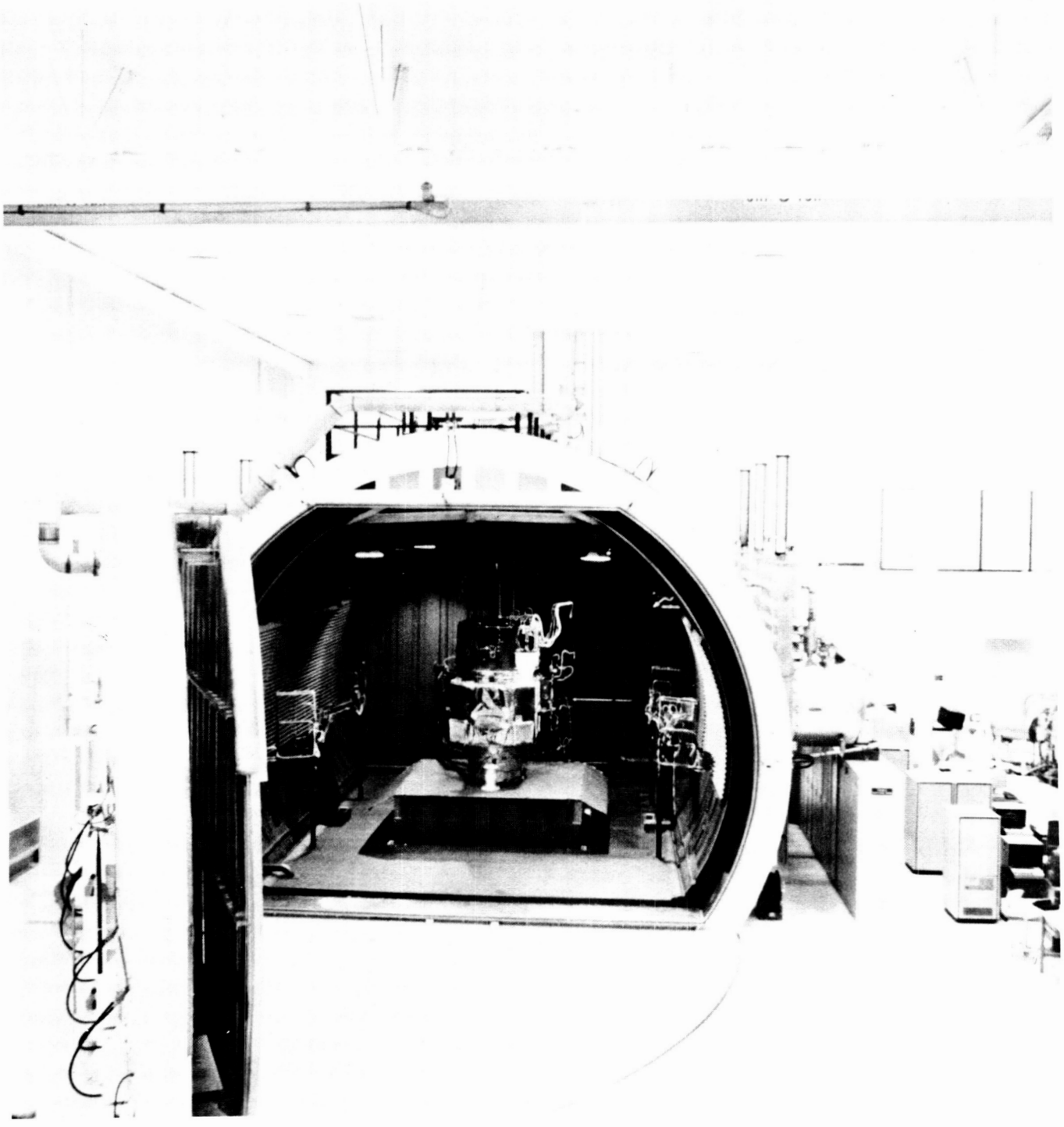

Figure 1. Facility overview

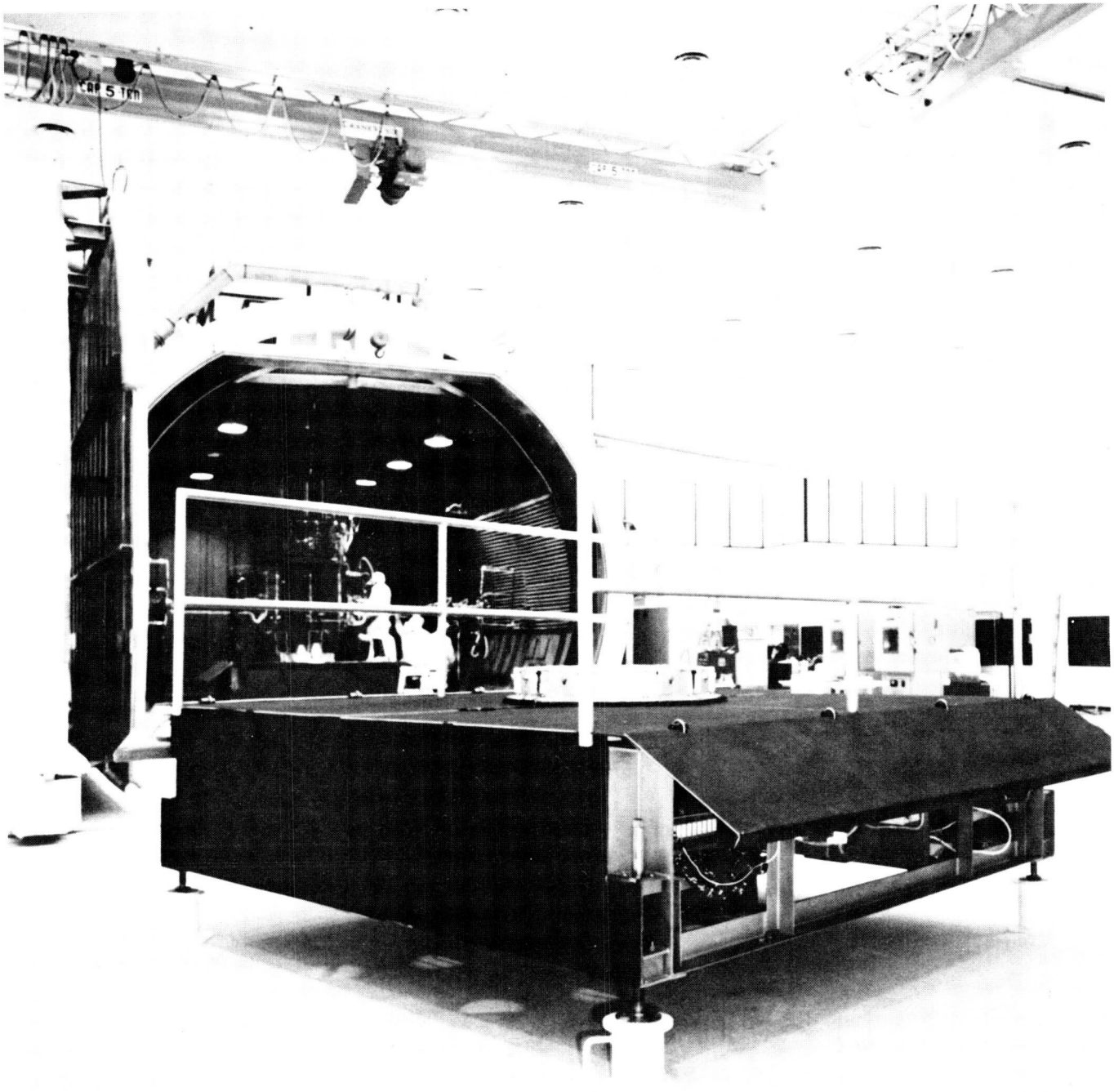

Figure 2. Test fixture

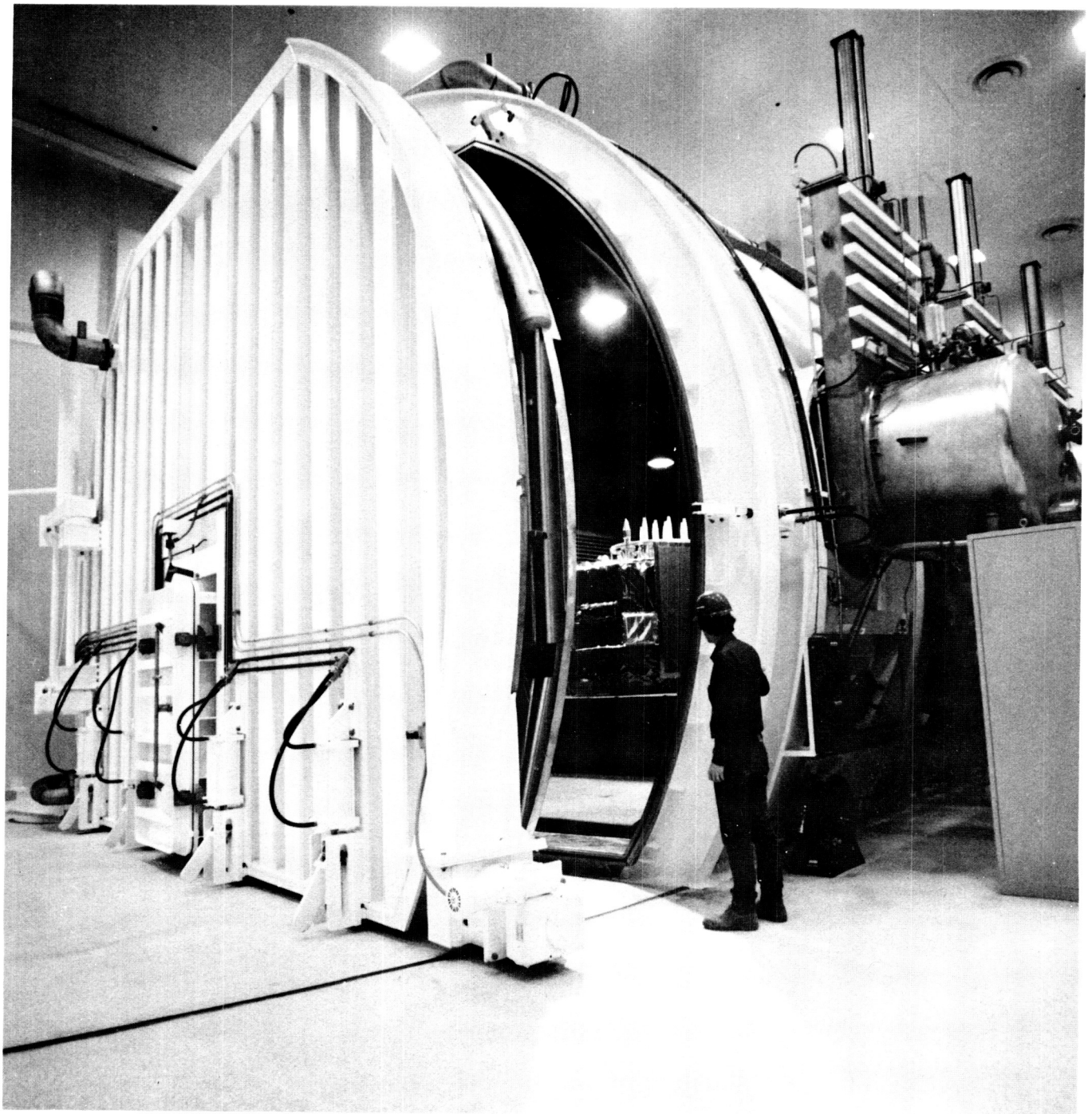

Figure 3. Truncated chamber door

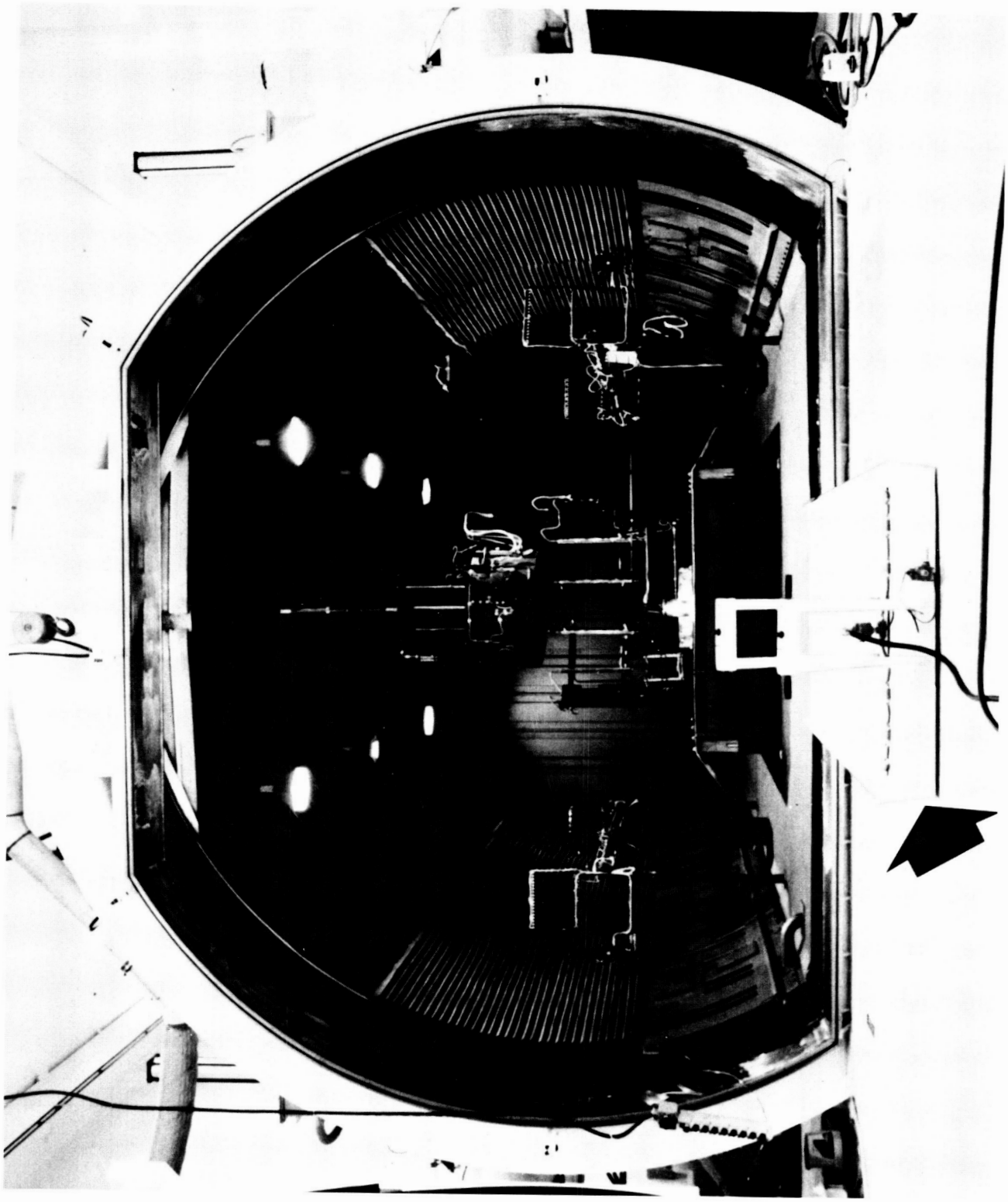

Figure 4. Transporter

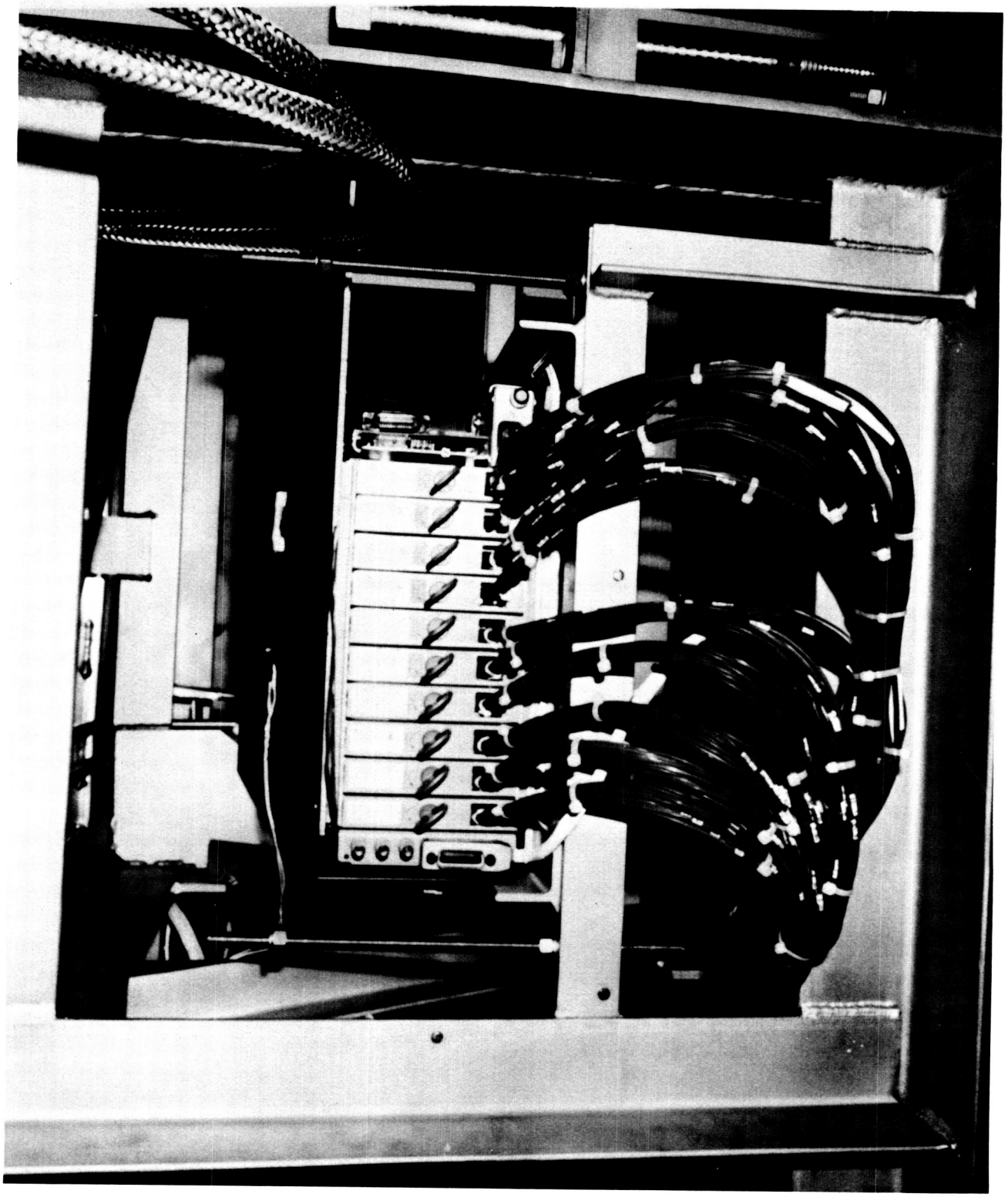

Figure 5. Test fixture multiplexers

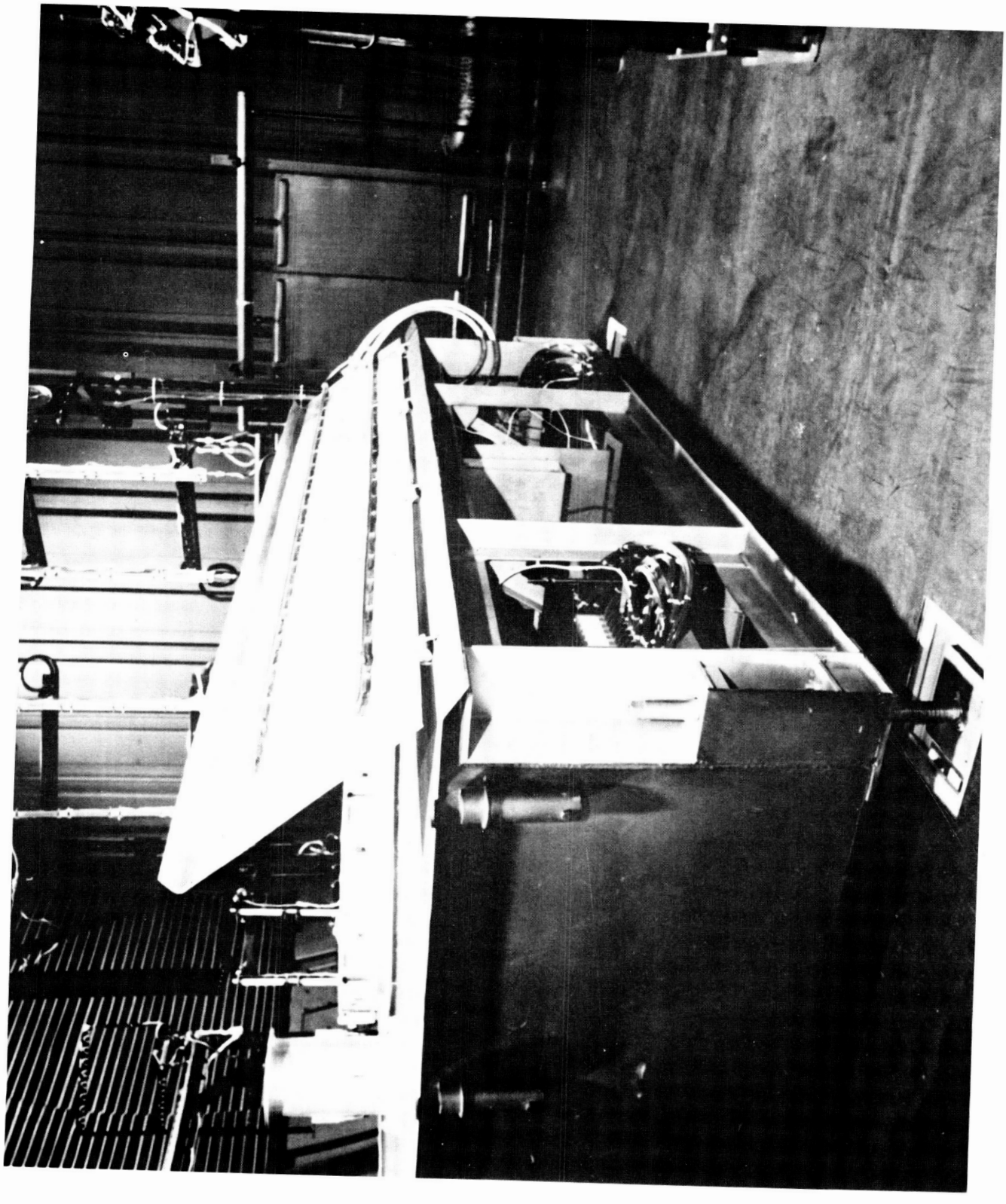

Figure 6. Test fixture thermal shroud panels

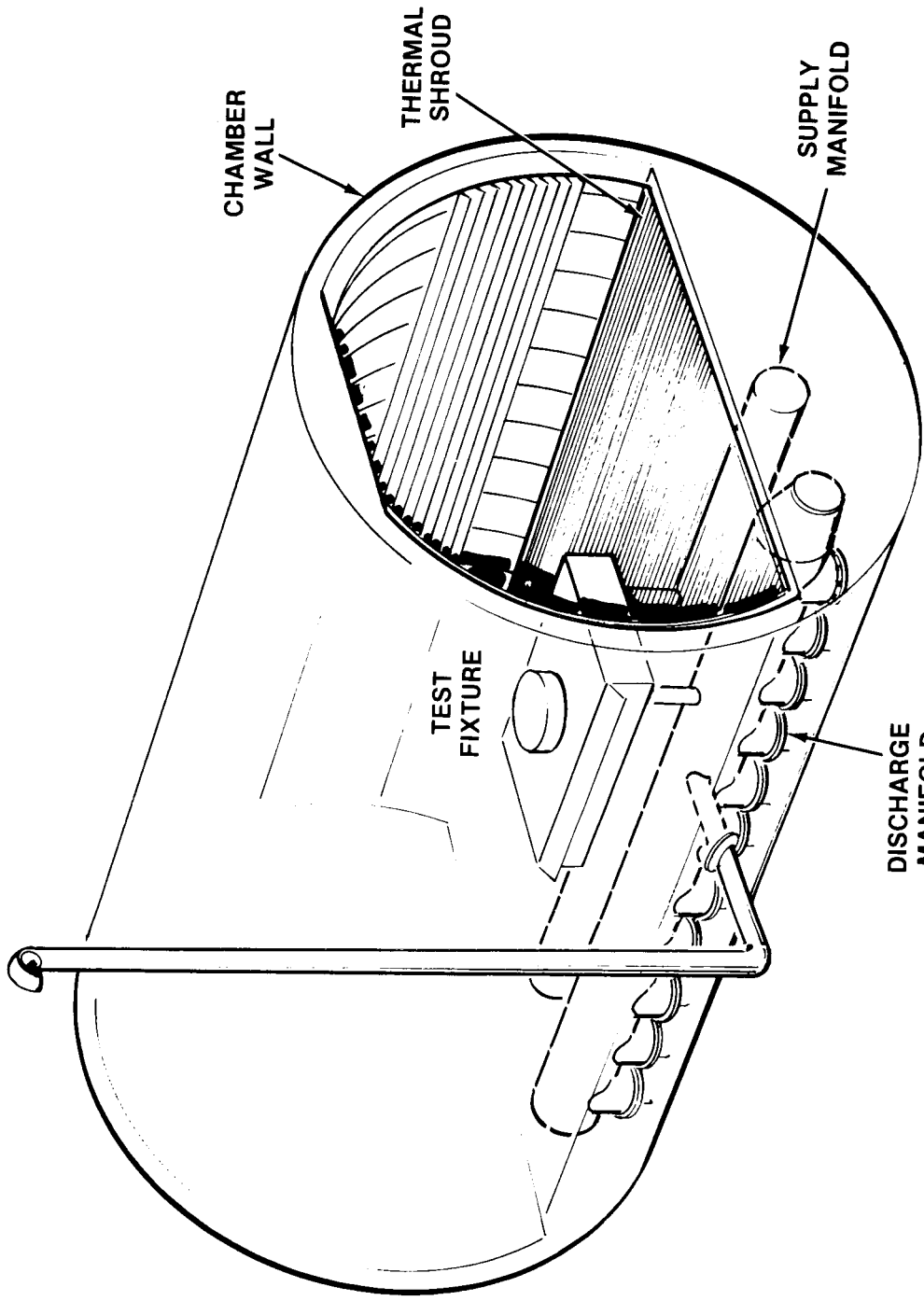

Figure 7. Internal utilities schematic

Figure 8. Discharge manifold vessel

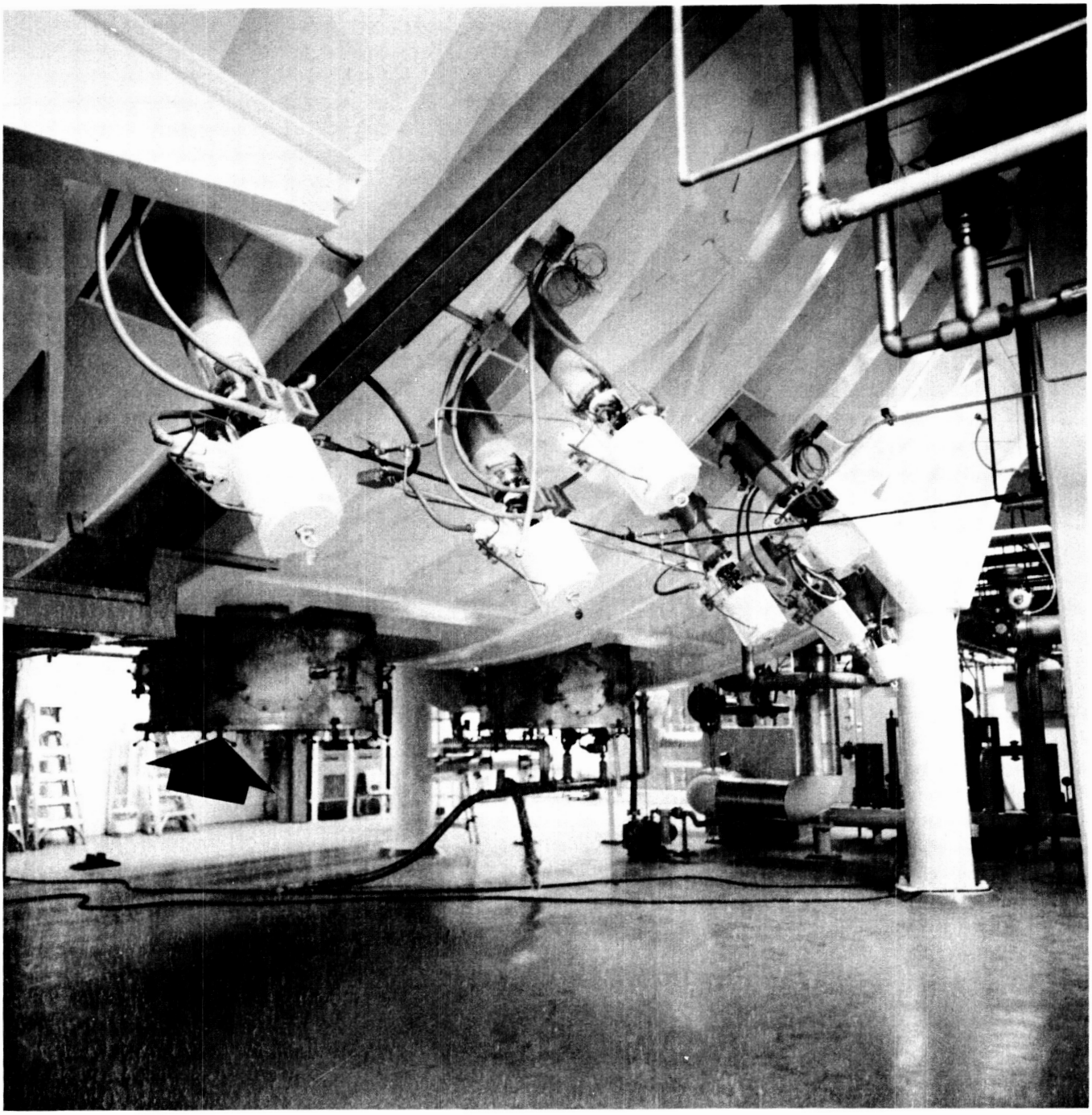

Figure 9. Instrumentation pods

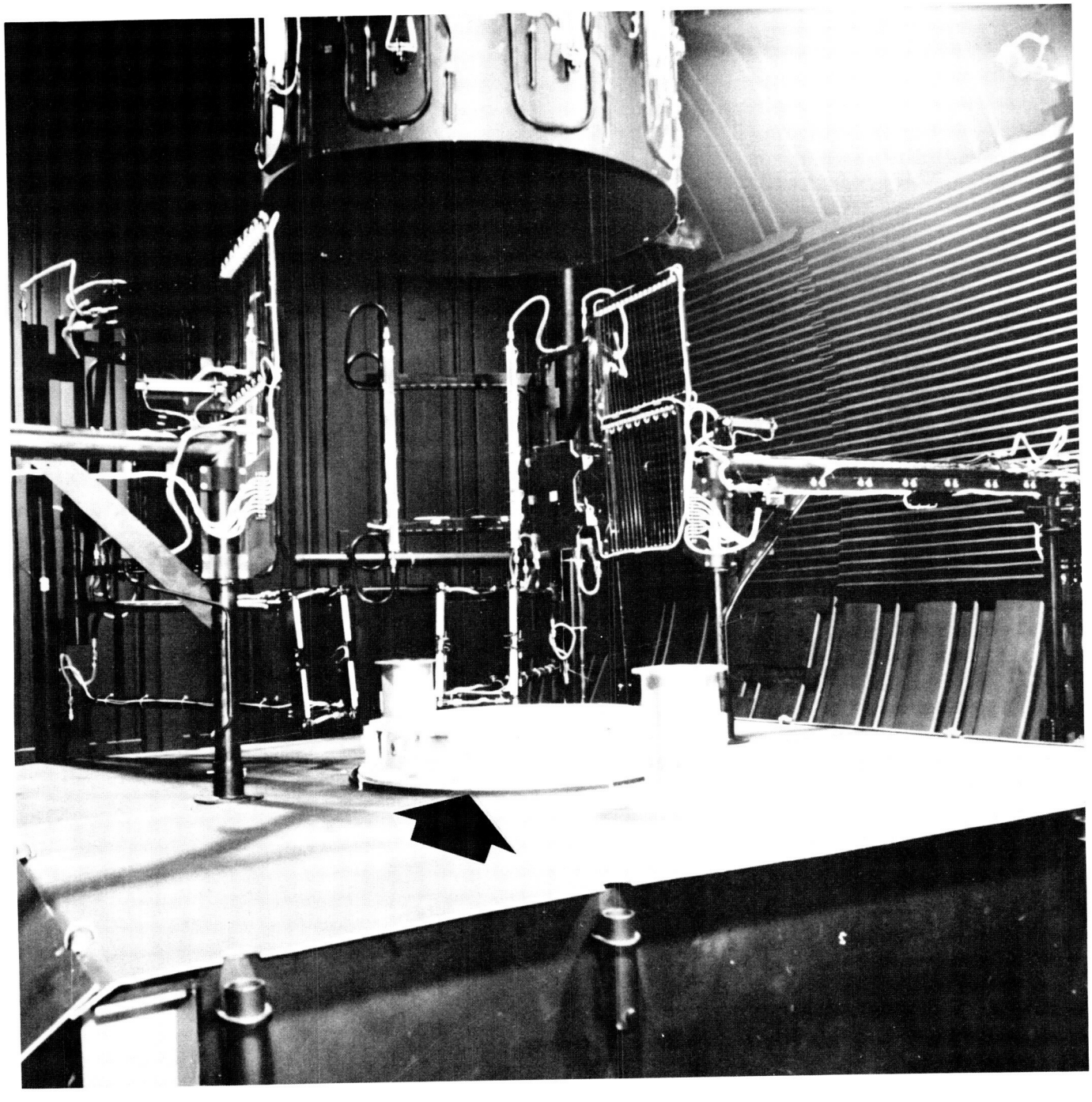

Figure 10. Space craft support ring

MOVING THE FACTORY INTO ORBIT

Robert Dannenfelser, Jr.
Reliance Electric Company

ABSTRACT

Prompted by attention focused on the Space Shuttle Program's cost and safety problems and the publicity surrounding the intended U.S.Spacestation, it seems timely to investigate the status of those efforts being made to use space as a commercial manufacturing environment.

INTRODUCTION

Orbital manufacturing requires identifying those products suitable for the space environment; the best type of production platform; the most economical launch and service arrangements; the technologies in use today that show the greatest promise for transplant to orbital application and perhaps most importantly, an evaluation of the economic impact to a nation that participates in this venture or so declines.

It should be noted that all of the written material researched for this paper was produced prior to January 28, 1986. The events of that infamous day make much of what was written seem particularly rosy in its forecasts, particularly in terms of delivering equipment into orbit, i.e. everything to be done via the Space Shuttle. The questions surfacing in the media regarding America's direction in its space program are part of this paper's topic; their final resolution should not be considered a prerequisite to making hard decisions by the U.S. industrial sector, as they will not be for our industrial competitors around the world.

MAKING THINGS THAT ARE OUT OF THIS WORLD

There are projections that by the year 2000, a new industry will exist with sales between $15 and $100 billion(1). Its factories will produce products to help people live longer, healthier lives; put more powerful electronic devices in home and industry, make critical mechanical devices work better and last longer and affect other areas of our lives that few people have even thought of yet! It will be pollution free, environmentally safe and its growth will spur other industries to develop complimentary "spin-off" products. This sparkplug of 21st century tecnnology is space manufacturing.

The space environment, for all its hostility and the difficulty of getting there, presents unique conditions that cannot be reproduced anywhere on earth. Its three major conditions are microgravity, vacuum isolation and extreme temperatures. Solar panels can be made very large and increasingly efficient solar cells can produce large quantities of "free" power to keep orbital factories going. Table I below details those materials for proposed space manufacture that take advantage of these particular conditions.

Table I
Feature/Product Benefit Relationships

Microgravity/ Freedom from Vibration	- Pharmaceuticals (electrophoresis) - Pure crystal and film growth - Containerless material processing
Vacuum Isolation	- recombitent DNA research (safety considerations) - contamination free environment for many different processes
Extreme Temperatures	- metalurgical alloy processes - crystal growth - molecular physics research

All of these products have in common that they are small, difficult or impossible to produce in quantity on earth and often for reasons of human safety, require expensive manufacturing facilities on earth. The space environment suites their special manufacturing requirements to a "T".

THE SHAPE OF THINGS TO COME

Discussing an Orbiting Manufacturing Facility is a little like talking about cars; it's a generic term. Different types fit different needs. To date, experiments have been conducted aboard the Space Shuttle, the ESA Spacelab that rides in the shuttle

payload bay and even as far back as Skylab in the American space program. The Soviet Union has been conducting material processing experiments for 10 years on Salyut space stations and to date has performed over 1500, while the U.S. has done about 100 (2). These facilities have been small, experimental devices not designed to produce sufficient quantity of product to allow for commercialization. These one-shot manufacturing sessions have also been limited by the length of the shot, at least in the case of the U.S. space program. Shuttle missions last only as long as a week, insufficient time to fine tune a process or produce economic quantities of a product. What the Soviets may have actually done is unknown, but Salyut crews have been in space for many months at a time, overcoming the drawbacks we've had to face.

James Samuels, First VP of Research at the financial firm Shearson Lehman Brothers in New York City has stated: "What's lacking in materials processing in space is the factory. Experiments on the Shuttle are of small magnitude, producing only small quantities of material. Until a large enough space facility to produce large enough quantities of materials is available, it's difficult to see how materials processing in space could be an ongoing business (3)." Lately, the trend seems to be focusing on the proposed U.S. Spacestation as the means for any future space activity. A Stamford University researcher, pushing for increased commercial interest in space, observed: "It seems odd that we're working on (building) unmanned factories on Earth while saying we need people for manufacturing in space (4)." A material scientist at 3M Company's R&D group views the proposed Spacestation as designed for R&D only, using space as an environment for doing science *FT1.* Others agree that NASA should focus its efforts and attention on exploration and basic research and development. Another important consideration is the very high cost of putting and keeping men in space, considerably higher then automated spacecraft. This combination of requirements and restrictions seems to be driving the need for advanced free-flying platforms, and not too surprisingly that is the direction both ESA and a private American firm are leaning. Originally scheduled for launch in 1987, EURECA (for EUropean REusable CArrier) is an extension and enhancement of the SPAS (Shuttle PAllete Satellite) system put into orbit and retrieved on STS-7 in June 1983 (5). The EURECA satellite would stay in orbit about six months after being placed there by the Shuttle, and would thus be retrieved after spending that time in materials processing. More ambitious is the Industrial Space Facility as designed and built by Space Industries Inc.. This vehicle also would be placed in orbit by the Shuttle, but unlike EURECA, it is fully enclosed and pressurized for human occupation. Once checked out and set-up, the mission specialist will leave, the ISF will be detached from the Shuttle and left as an automated free flyer. It will be visited by future shuttle flights which will attach new supply modules, recover processed material, make any specialist-required adjustments or repairs and then be left again to do more processing (6).

The vehicle is still being developed with a launch schedule for the early 1990's. Time to make modifications due to relevant launch vehicle costs and availability considerations is soon running out. What can be done here to "boost" the economics of space processing?

GETTING THERE IS HALF THE CHALLENGE

Of immediate concern to everyone involved with American space exploration and use is the current (8/1/86) unavailability of any launch vehicle deemed safe and operational. The consecutive failures of the Space Shuttle, the Air Force Titan 34D and NASA's Delta launch vehicle have sent many, both in the U.S. and abroad, rethinking their strategy for the use of space. The realization that once the Shuttle does become reoperational it will be largely dedicated to military payloads for almost two years has stunned the civilian space community. A great deal of evaluation is still going on for the when-and-where to use the Shuttle versus expendible launch vehicles. In addition, the questions are raised about a private contractor going into the space launching business by renting NASA's existing facilities. Along these lines, it's been proposed that the enhanced Titan 34D7, which is being built for the Air Force, be made available to private purchasers with all the line start-up and development costs being paid by the Air Force. The noteworthy feature of the Titan 34D7 is that its payload configuration and capability closely match that of the Shuttle. In the free market's hands, the "business" of launching business satellites, whether communication or manufacturing, would become more price competitive with French Ariane, especially the Ariane III which has a larger payload capability similar to the Titan 34D7. Also to be considered is the up-and-coming space launch capability of the Japanese and the Chinese. Even the Soviet Union is loosening up its bonds of secrecy to court its substantial launch capability to the world market. Run as a business venture, launch costs could begin to drop from the $5000 per pound they are now with the Shuttle toward the long dreamed of $100 per pound predicted in the mid-1970's. If costs could be substantially reduced, the number of products that may be economically manufactured in orbit could easily triple *FTZ*. Under such a coherent industrial space policy, only scientific satellites and the Spacestation itself need be placed in orbit by the Shuttle. Both military and industrial satellites would be launched by mass-produced, expendable launch vehicles. The Shuttle's ongoing use would be the servicing, repair and/or recovery of satellites already in orbit when the need for manned observation and activity could not be replaced by automation.

MAKING (THINGS) DO (MORE)

The Factory of the Future is a term that's been used in the Instrumentation & Control marketplace for 5 or so years now here on earth. It describes a workplace that is sparsely populated by human workers but rather is highly automated, very precise in the quality of its products, capable of adapting to changing environmental considerations and requiring only routine servicing by its human operators. This goal has been the driver for bringing new technology to market and generating spinoff products into many other markets. For example, the development of the microprocessor has meant that large complex electronic measurement and control products have been reduced in size and cost with corresponding increases in features and operating life. As the demand for greater sophistication in microprocessors grew, new uses were found for the older micros; now microwave ovens, televisions, VCR's and sewing machines have benefitted from capabilities that were once available only in industrial devices. As more uses were sought for these advanced microprocessors, a whole industry sprang up around "personal computers". The list of such products goes on.
The microprocessor of 8 years ago is growing into the microcomputer of today, and it along with several other state-of-the-art manufacturing trends would be most applicable to the needs of a space manufacturing system. The microcomputer is the cornerstone to the world of miniaturization needed to package a complex factory into 2500 cubic feet, or less. Figure I shows a currently available industrial controller with I/O interface modules to the process itself. Such a device, occupying but 0.25 cubic feet could control an entire process at a cost of under $5000 (7).

Knowing how to respond to modified production procedures, changing environmental considerations or unscheduled equipment shutdowns is typically a "man's" job. But there won't be any men in free-flying manufacturing facilities like those described earlier. Having the "smarts' to deal with changing conditions is no longer only in the realm of human operators, but is becoming available in artificial intelligence, or "Expert" control products. Figure II shows a device for controlling a process loop that, instead of solving a conventional second order equation to adjust a final control element, uses over 200 IF/THEN rules to establish pattern recognition techniques for individual loop control. This product represents the first such device in the industrial marketplace that has taken the fledgling science of Artificial Intelligence from the chessboard onto the shop floor (8).

Another recently introduced industrial product is a certain type of I/O device that can be programmed to be either an input or an output. The electronics on board the device are capable of either driving or receiving current, unique in the industry.

In addition, the device has built in diagnostics that report back to the central controller the nature of any failures that occur in the device (9). An extension of this technology could allow for a central controller on a free-flying station to reconfigure the instrumentation on board in event of a failure, so continuous processing would not be interrupted. The final new "technology" to be discussed here is not a piece of hardware at all, but rather a design philosophy that works by using all of the above technologies to some degree, coupled with mechanical robotics. It's call Flexible Manufacturing Systems. What it says is, instead of designing a production line to mass produce a single part or item, put small, intelligent, reconfigurable controllers at each station along the line; give each station the ability to do many different things; even give the line itself the ability to redirect the flow of material from start to finished product, skipping stations not needed to make product X, returning several times if required for product Y. This method of built-in flexibility eliminates the need for any retooling to make changes in a product, or to go from one product to another. The result is a production facility that can make small runs of a given part, or even just one unit of a given part, and most importantly, be competitive with large, dedicated production lines. Such a situation can be found at a Rockwell International plant making parts for the B-1B bomber. Flexible Manufacturing has started to find a niche in what are traditionally viewed as machine tool industries, i.e. industries where things are machined, not where stuff is processed. In the process industries, the term batch processing describes the condition where a given amount of product A (cookies) is produced, then equipment is reset (cleaned), reprogrammed (new receipe) and another product is produced (muffins). Much attention has been paid to batch processing in recent years as two diverse technologies, discrete and continuous control, have started overlapping. Control systems touted as Batch Controllers have come to market. At present, batch control devices remain more than anything else a single box with two, still separate technologies shoe-horned inside. This brings up the final point to be made in the case of space manufacturing.

THE GIVE AND TAKE

"The frontier of space should be a driver for new technology" is the first thing I was told by one space manufacturing advocate *FT3*. It certainly is for weapons technology as being developed for the Strategic Defense Initiative (SDI or Star Wars research as it's more commonly referenced). The field of space manufacturing would also be a driver for reusable, transportable technology here on Earth; not to mention the day to day benefits of products actually made in orbit. In the earlier days of the space program, spinoff products were easily identified by their use in the space program. Teflon and Velcro will be forever immortalized for bringing the space age into the home more so than televised lift-offs!

The color camera, smaller than a shoe-box, used on the moon by Apollo 12 astronauts cost tens of thousands of dollars. Today anyone can film their kids splashing in a pool with a color video camera that costs about $600 and is functionally the same thing. Redundant computers on the Space Shuttle, and the voting algorithms in software that make them work together, have been transported to industrial controllers over the last few years: the calculated mean time between failures (MTBF) - over 300 years. Even the solar cells used to power communications satellites now show up on watches and calculators.

Consider a few of the products that could be readily made in quantity in space and some specific applications: composite alloys could be perfectly manufactured that have an operational life expectancy many times that of any earth-manufactured. How much more valuable will the machines incorporating these be? In space, gallium-arsenide crystals can be grown that can be used for denser and faster micro-chips. With the extremely competitive nature of the world computer industry, what impact would it have for the company that had a computer with orders of magnitude greater speed, memory and operating life versus any of its competitors? Of most serious concern, what if these products were only available from the Japanese, the Germans or the Soviet Union? What can happen if technology transfers do not take place from Space to Earth is pointed up by this example. The Soviet space program has perfected for several years now sending Progress robot resupply ships to automatically dock with orbiting Salyut space stations; no mean feat! Yet, when they experienced the problem at the Chernobyl nuclear plant earlier this year, the Soviets borrowed a robot from West Germany to go inside the damaged plant to observe its condition. The need to go to an outside source for such technology is evidence of the failure in the Soviet economic system to promote the transfer of technology from one segment of its economy to another. The U.S. is not free from guilt here either. Witness the video technology described earlier: perfected by a need in the U.S. space program 16 years ago, advanced video equipment used in this country today is almost exclusively made overseas. Consider this scenario: super-dense galium-arsenide computer chips become commercially available through an orbiting manufacturing facility. They are then etched with not one, but three complete microcomputers complete with enough permanent memory to contain a complete redundant (voting) operating system. The resultant product would be a microcomputer with an operating life of not thousands of hours, but hundreds of years, and would fit in the palm of your hand! Such a device implanted in control and measuring equipment here on earth could revolutionize the reliability aspect of industrial products. And if all such available products say "made in Japan" the U.S. instrumentation industry could be in big trouble.

The initial product, made in space, forged together with the technology used to build space capable hardware would produce an end result that would stand in a class by itself, unreproducible, since the heart of the device is a substance that's available in only one place.

To catch up would require years of effort while revenues were being lost to this unique competitor.
Space based industry will be a new way of life so says Dr Roald Zagdeev of the Soviet space program (10). It will be so for everyone as the next century dawns--it will be for good or bad based on decisions made by U.S. companies, the U.S. government and other interests around the world. These decisions are being made now, with billions of future dollars riding on them.

CONCLUSION

The methods are still under development, the costs need to come down and interest needs to be rekindled in light of recent failures of launch vehicles, but space manufacturing is an enterprise on the near horizon that those closest to it are sure will be worth billions of dollars by the end of this century. Viewed as a technology driver, it appears to be the greatest non-military effort for its world-wide participants to sharpen their competitive edge in many fields of science and engineering. It is a swinging door for industry, allowing advanced production schemes to be enhanced and used "up-there" while transporting what's developed into spinoff products "down-here". Though any financial rewards must be considered long term at this point, it appears that short-sightedness on any nation's part could easily lock it out of marketplaces yet to be tapped 10,15 and 20 years from now. For the benefit of the future U.S. economy, a coherent industrial policy for the use of space, from launch vehicles to licensing agreement, needs to developed.

REFERENCES

1. The Great Space Race - PBS broadcast Spring 1986

2. The Great Space Race - PBS broadcast Spring 1986

3. Space World June 1986 Article: Rx for the 1990's
by Bridget Minty Register

4. Stanford News Release of 5/12/86

5. Dedicated Reusable Space Platforms--A New Economic Tool for Space Research and Applications by D.E. Koelle and W. Kleinau as published in the Proceedings of an American Astronautical Society Conference held March ,1984 at the Goddard Space Flight Center.

6. Industrial Space Facility Program Space Industries Inc.

7. duTec Stack 65 programmable control system. duTec Company Jackson, MI.

8. The Foxboro Company EXACT Controller. The Foxboro Company Foxboro, MA.

9. General Electric Series 6 Genius I/O. The General Electric Company Charlottesville, VA.

10. Interview with Prof. Von Eshleman Stanford University

11. The Great Space Race PBS broadcast Spring 1986

FOOTNOTES

1. Interview with Dr.Chris Chow 3M Company R&D Group

2. Interview with Prof. Gayton Germain Stanford University. Instructor:Commercial Development in Orbit.

3. Interview with Prof. Von Eshleman. Stanford University.

BIBLIOGRAPHY

1. Space World Magazine, June, 1986.
Article: Rx for the 1990's by Bridget Minty Register.

2. Space Commerce - Free Enterprise on the High Frontier by Nathan C. Goldman. Ballinger Publishing, Cambridge, MA 1985.

3. Stanford News, release of 5/12/86. Stanford University News Service, Stanford, CA.

4. Specification document, Stack 65 programmable control system. duTec, Jackson, MI July 1986.

5. Industrial Space Facility Program description. Space Industries, Inc. Webster, TX July 1986.

6. Permanent Presence - Making It Work; the 22nd Goddard Memorial Symposium Proceedings. Published by the American Astronomical Society, San Diego, CA; Article: Dedicated Reusable Space Platforms - A New Economic Tool for Space Research and Applications by D.E. Koelle and W. Kleinau March, 1984.

7. Microgravity Science and Applications Program Tasks compiled by Elizabeth Pentecost, NASA, Washington, D.C., Technical Memorandum 87568, May, 1985.

8. Second Symposium on Space Industrialization, Proceedings NASA Conference Publication 2313, February, 1984.

9. The Soviet Year in Space, 1985 by Nicholas L. Johnson Teledyne Brown Engineering, Colorado Springs, CO.

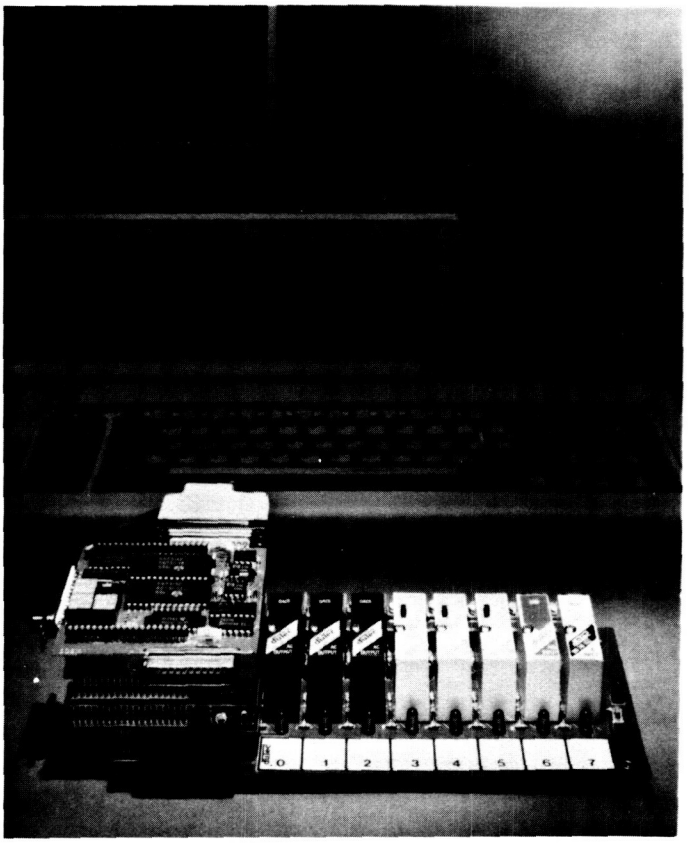

Figure 1. Programmable controller for process applications from duTec (courtesy of duTec Company)

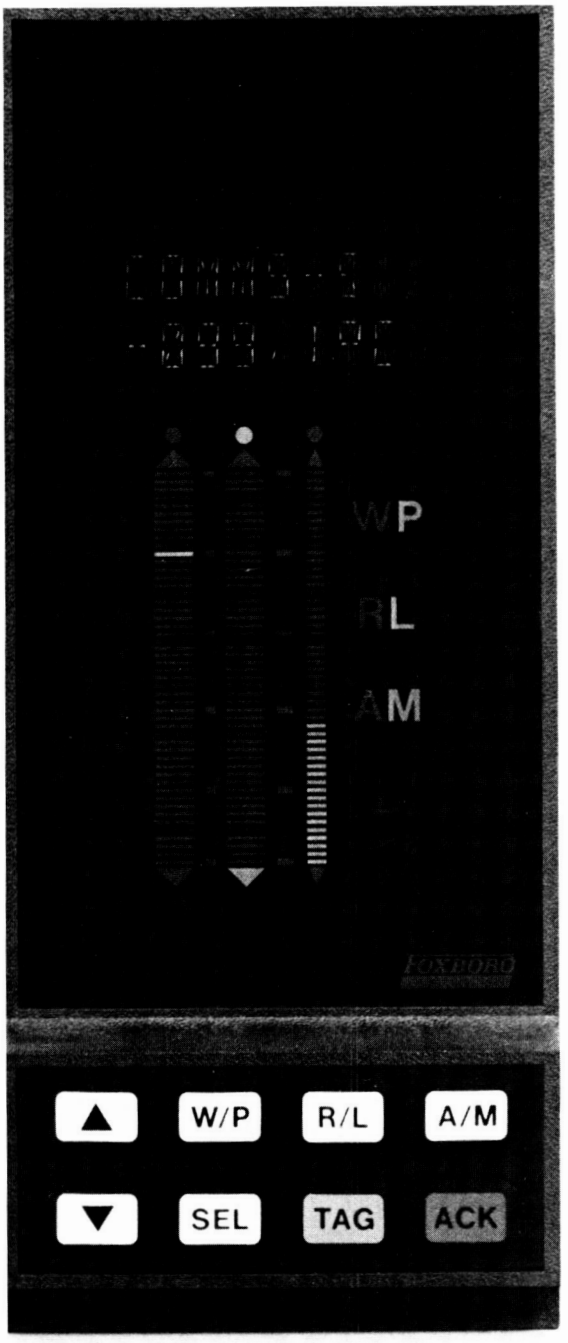

Figure 2. Single loop process controller with artificial intelligence algorithms for closed loop control. (courtesy the Foxboro Co.)

SURVEILLANCE SYSTEMS TEST AND EVALUATION FACILITIES

Jere J. Matty
Arnold Engineering Development Center/DOTF

Ronald Dawbarn
Calspan Corporation

ABSTRACT

In January of 1983, a team was formed by AEDC to explore test methodologies and test facility concepts required to meet the needs of future space-based surveillance systems. This team was composed of members from the Air Force and Calspan/AEDC Division and involved a contract with the Ralph M. Parsons Company who subcontracted to TRW Space and Technology Group, JAYCOR, Pittsburgh Des Moines Corporation, and Cryogenic Vacuum Incorporated. The output of this study was a road map of test methodologies and test facilities that will aid the development of this country's critical space-based sensor assets. This paper is a condensation of those results.

INTRODUCTION

In May of 1984 the Air Force Systems Command designated AEDC as the Center of Expertise for space environment-simulation testing. In this capacity, the Center is to provide the test and evaluation expertise in several assigned functional areas, including space sensors. The test and evaluation of such systems is particularly challenging when one considers that they must be able to operate in a thermonuclear environment against extremely large numbers of targets. This presents a unique problem for the test and evaluation of such systems. For example, in the development cycle for a new aircraft, engines and airframes are first thoroughly ground tested; then the assembled aircraft is subjected to an extensive flight test program. This eventually includes intensive operational testing prior to theater deployment.

Certainly no one would recommend going directly from component ground test to system deployment. The situation that faces the space-based sensor developer is an inability to test his system in orbit against a realistic attack scenario including the thermonuclear environment. This means that the "flight and operational" testing must be performed in ground test facilities. The simplistic approach to adequate ground testing is to try to simultaneously capture the entire operational scenario in a ground test environment. This is analogous to a flight of a full-scale aircraft in a wind tunnel at the proper altitude, air temperature, Mach and Reynolds numbers. The test methodology that has developed in the ground testing of spacecraft has shown that there are ways to "take the problem apart," i.e., determine where to substitute simulation for duplication and still obtain useful data. This development of a test methodology in the space-based sensor arena is presently in the early stages. The following paragraphs outline an approach which addresses some of the applicable methodology issues and the test facilities that result.

PERFORMANCE TESTING LEVELS

Although a space-based surveillance satellite has many components, the prime focus of this paper is the surveillance sensor. It can be divided into four major

elements: the focal plane array, cryocooler, signal processor, and telescope (see Fig. 1). The initial performance level test deals strictly with the focal plane array and progresses to the entire payload.

FOCAL PLANE ARRAY (FPA) LEVEL

The first level of testing to be performed on the sensor involves the FPA. There are three discrete parts to this level of testing: functional validation, characterization with a single point source, and characterization with a dual point source.

FPA Functional Validation

The goals of this level of FPA testing are to establish a common Air Force FPA test facility to eliminate differences among basic focal plane evaluations performed in the manufacturers' plants. Simple, flooded, focal plane testing will be conducted from 10^{-16} to 10^{-10} W/pixel in AEDC's Component Checkout Chamber (C^3) as shown in Fig. 2. The C^3 is a 1.2-meter-diameter bell jar and will be configured with a retractable mount for the focal plane to ensure a high test article throughput. The variable intensity blackbody source was developed by AEDC and has been calibrated by the National Bureau of Standards. The data from such tests will be computer-based for ease of access and analysis.

FPA Characterization with Single Point Source

The FPAs that show promise after the functional validation phase of testing will be tested at this level with blackbody flooding and the use of a single point source (see Fig. 3). At this level the FPA response to a simulated target and background can be evaluated along with spectral discrimination and crosstalk. Six orders of magnitude will again be available for the single point source. The point source will be scanned over the FPA through a combination of mirror and blackbody source motions controlled remotely during the test.

FPA Characterization with Dual Point Source

Again, the best FPAs from the previous test will be advanced to the dual target testing. At this point, through the use of beam splitter or dual projector technology, two targets will be provided to the FPA (see Fig. 4). Each will be controllable for conducting target tracking/crossing studies. All of the above tests are envisioned as being conducted with the FPA cooled by the test facility refrigeration machines. The next level of testing includes the flight cryocoolers.

FOCAL PLANE ARRAY/CRYOCOOLER LEVEL

At this point, the FPA has been tested as much as practical as a single unit. The major issues now involve the interface problems between the FPA and flight cryocooler, i.e., vibration, thermal uniformity, and thermal switching. Some of the

tests previously performed in the C^3 will be repeated with the flight cryocooler in place of the facility refrigeration devices. Basic cryocooler life testing, requiring only vacuum conditions, can be performed in the 2- by 2-meter chamber shown in Fig. 5.

FPA/CRYOCOOLER/SIGNAL PROCESSOR LEVEL

At this level, the addition of the signal processor requires the testing of ability to interpret complex scenes, i.e., more than two targets. Such tests will be performed to investigate the system's ability to discriminate among targets as well as perform kill assessments. This can be accomplished using relatively small chamber optics due to the absence of the sensor telescope (see Fig. 6). This test methodology makes use of projection rather than solid-state technology to produce the complex scene. AEDC has carried out extensive studies in the area of scene generation, and we believe the most promising techniques for producing Long Wave Infrared (LWIR) scenes to be solid-state thermal emitters and projection systems using scanning mirrors.

The basic advantage of solid-state scene generation is the potential for large numbers of targets. However, this technology is still developmental and may have serious limitations in providing wide dynamic range and spectral fidelity.

AEDC has used direct projection of targets from blackbody sources rather successfully in our aerospace chamber 7V. This technology is being improved through the use of mixing/integrating spheres to produce spectrally accurate targets for use in discrimination/kill assessment testing. AEDC is also developing a mechanical mirror scanning system designed to project spectrally accurate, blackbody targets in a cryogenic environment. Modules of four independently controllable target generators are in the prototype stages and are undergoing test at AEDC. Groups of these projectors may be assembled as shown in Fig. 7 to produce large numbers of targets.

The methodology and test facilities required to evaluate space sensor hardness has also been investigated at the Center. Although this topic is the subject for another paper, the results of our work have indicated the need for pilot X-ray and large X-ray test facilities for evaluating the hardness of the FPA/cryocooler/signal processor combinations (see Figs. 8 and 9). These facilities would be capable of producing full-threat-level-X-ray fluence levels and dose rates of the appropriate spectra to evaluate sensor performance.

FPA/CRYOCOOLER/SIGNAL PROCESSOR/TELESCOPE

Finally, the sensor will be fully assembled and tested for optical performance through the addition of the satellite telescope. At this level of testing, the sensor aperture diameter sizes the facility. The broad categories for sensor testing at this level are optical alignment, focus, radiometric throughput, and off-axis rejection (OAR). AEDC has performed sensor performance testing at this level in the aerospace chamber 7V for sensors with entrance aperture sizes less than one-half-meter diameter. OAR testing for sensors of the same class are carried out in the Mark I aerospace chamber as shown in Fig. 10.

One-Meter-Class Sensors

For sensors with entrance apertures in the one-meter class, the Mark I aerospace chamber would have to be modified as shown in Fig. 11 with the addition of a 20-K cryoliner, cryo-optics, and source generation device to conduct performance testing. Traditional OAR testing for sensors of this class will require either very large facilities or the use of a new test methodology. One such OAR methodology is under investigation at AEDC. The traditional OAR testing is conducted in such a manner that the length of the required test facility is a function of the test article entrance aperture and the OAR angle (see Fig. 12). This results in unacceptable facility sizes for sensors in the one-meter class. An alternate approach would be to map the sensor entrance aperture with a collimated test beam (see Fig. 13). This technique decouples the facility length from the test article entrance diameter. Such a technique will allow OAR testing of one-meter-class sensors in the Mark I chamber.

2- to 3-Meter-Class Sensors

Finally, as sensors move into the 2- to 3-meter entrance aperture range, a new facility will be required. The concept definition of this facility was the primary focus of the Center's contract with the Ralph M. Parsons Company. The facility is conceived as being a very large vacuum chamber (40 meters in diameter by 65 meters long) in which is mounted a high-performance optical bench. This facility would include cryopanel modules capable of rapid buildup/removal to ensure maximum facility flexibility with minimum operating costs. Figure 14 shows the SPACE facility configuration for OAR and mission performance of 2- to 3-meter-class space-based sensors. The dual antechamber design and multiple buildup bays ensure the maximum throughput for the facility; i.e., the tests are built up on carts and then injected into the facility. This facility will become a part of the AEDC space test complex as a national asset.

CONCLUSION

AEDC is continuing to update and modify plans to provide required test support in the space-based sensor arena. This country's future may well hinge upon our present and future role in space, and AEDC will continue to develop the test methodologies and facilities required to take us there successfully.

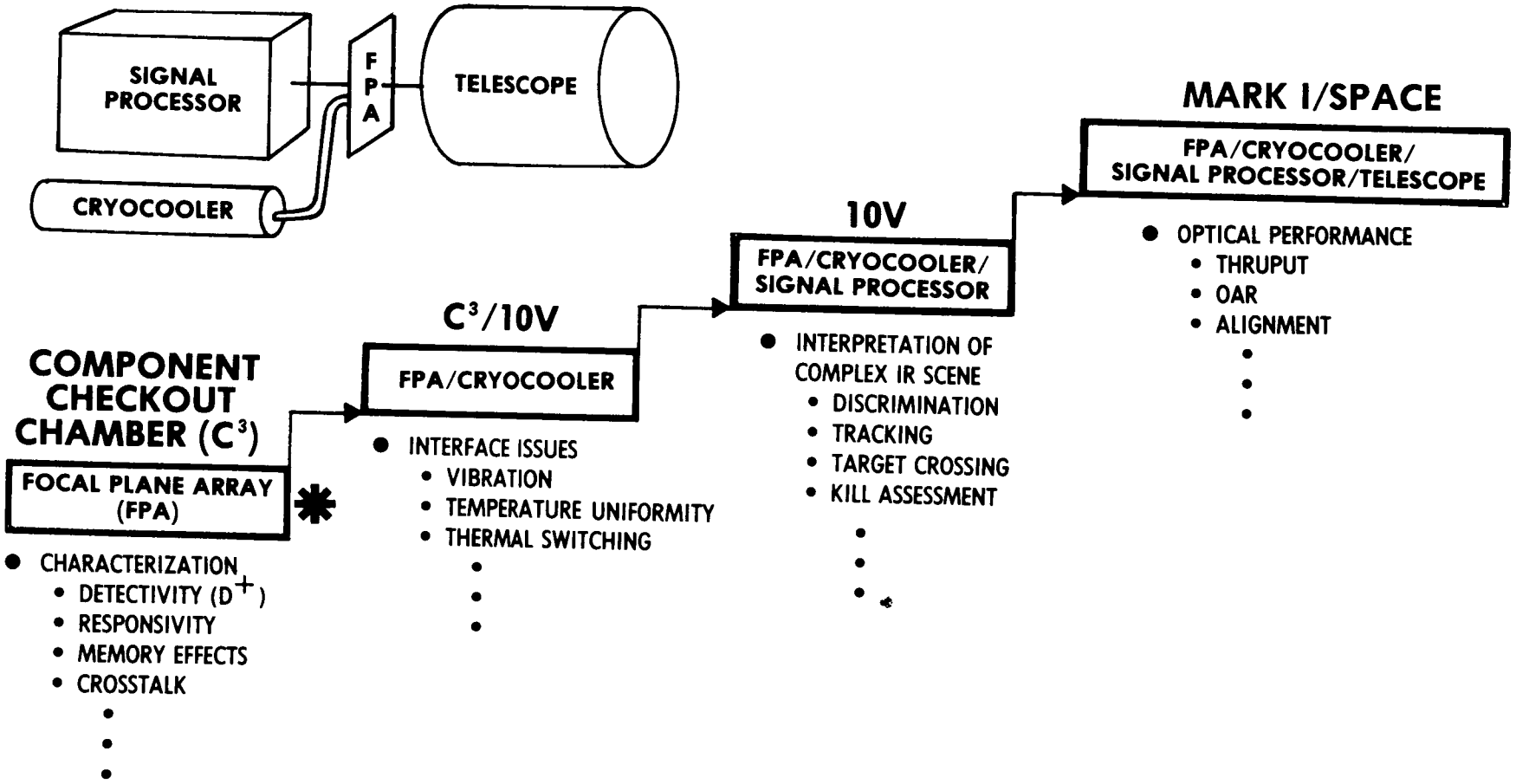

Figure 1. Surveillance system performance testing levels

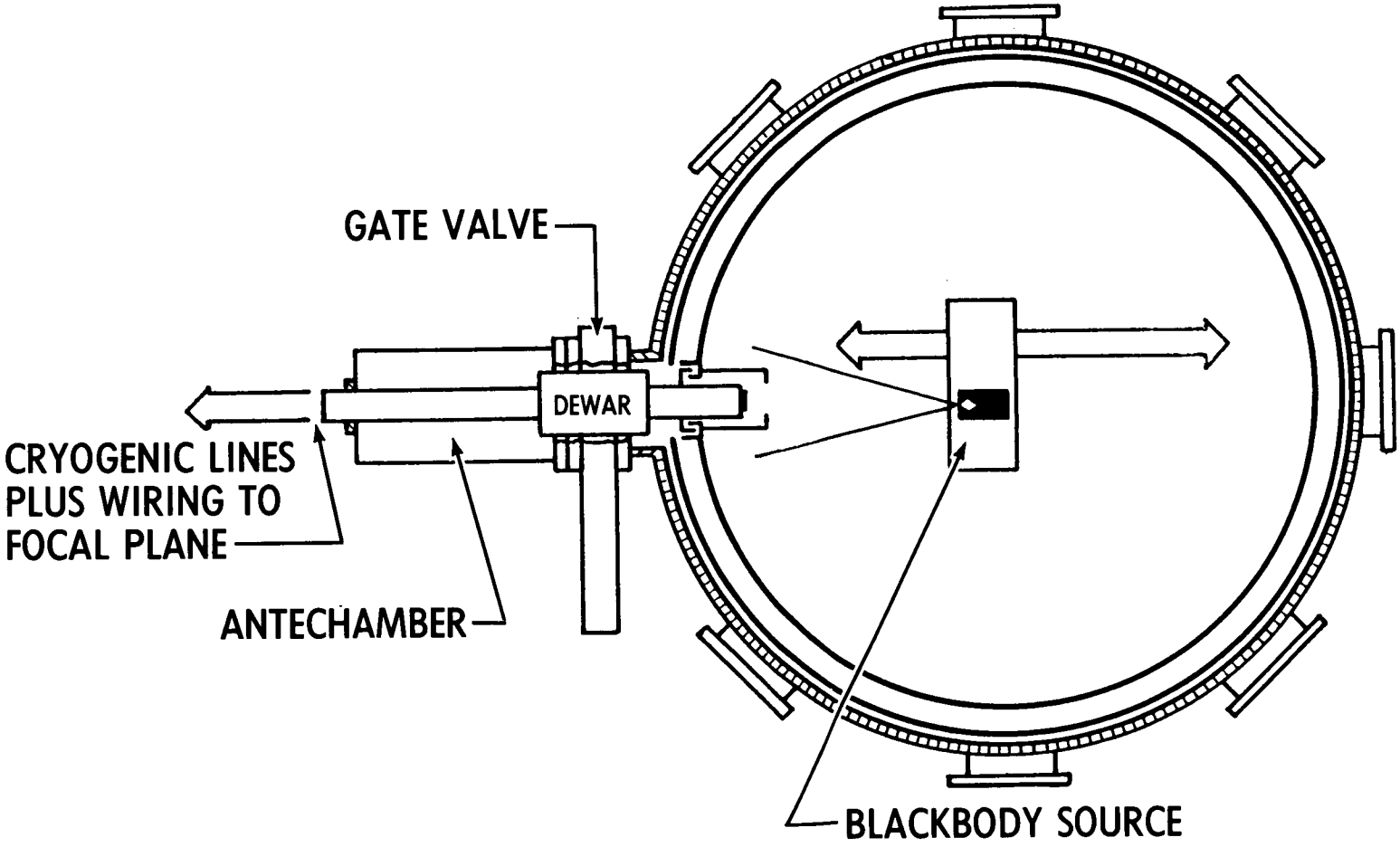

Figure 2. FPA functional validation test in AEDC component checkout chamber

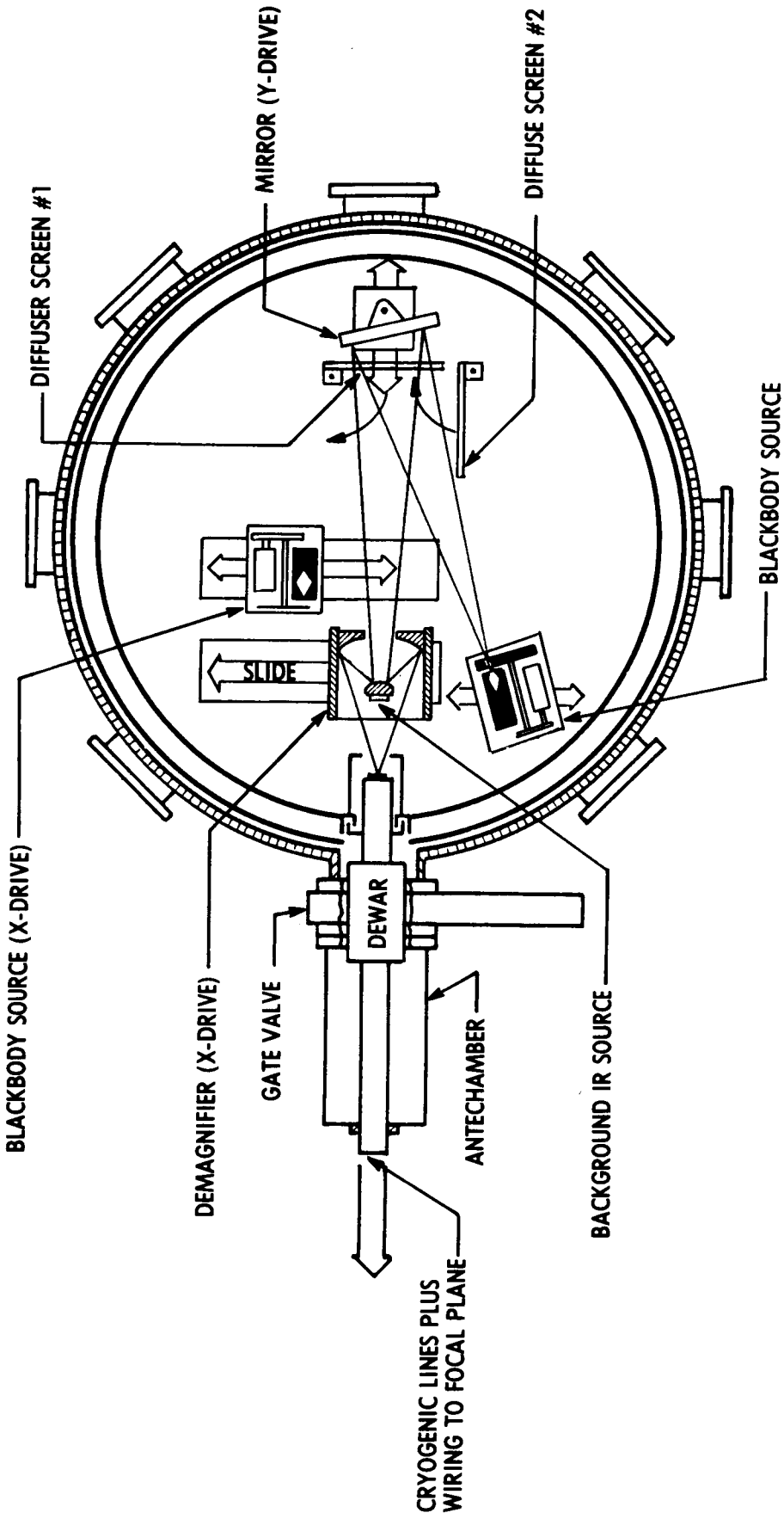

Figure 3. FPA characterization with single point source in AEDC component checkout chamber

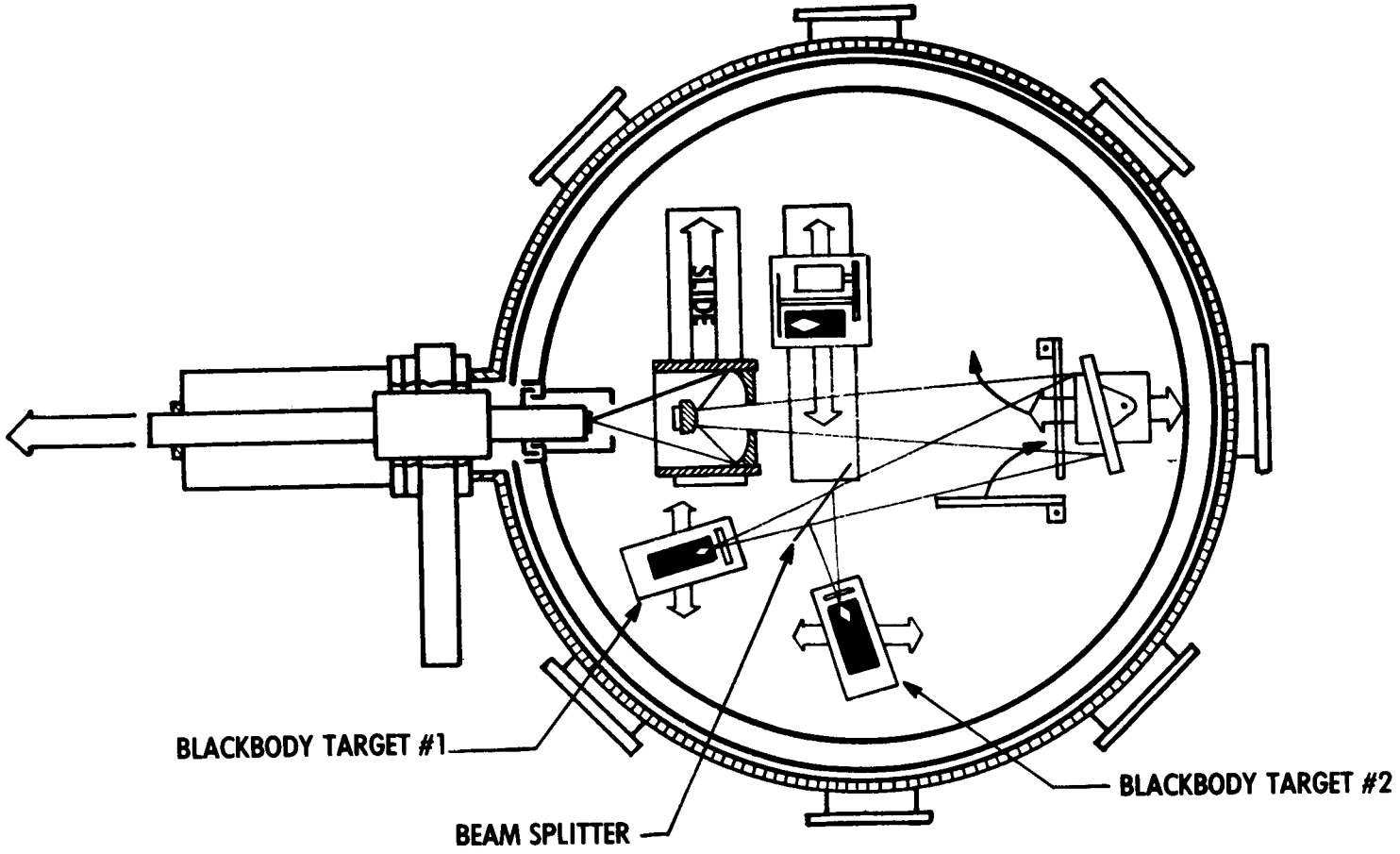

Figure 4. FPA characterization with dual point source in AEDC component checkout chamber

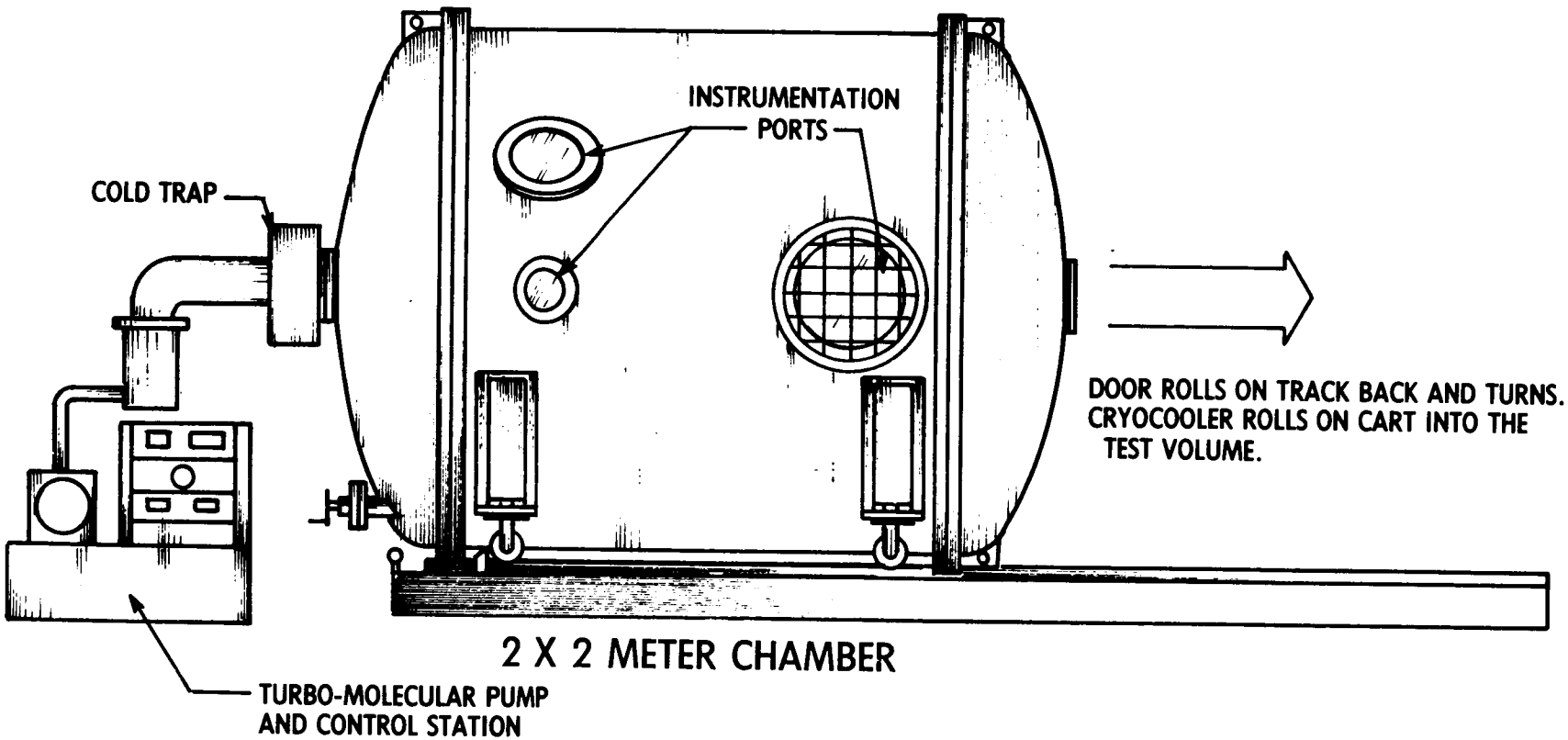

Figure 5. Sensor cryocooler life testing at AEDC

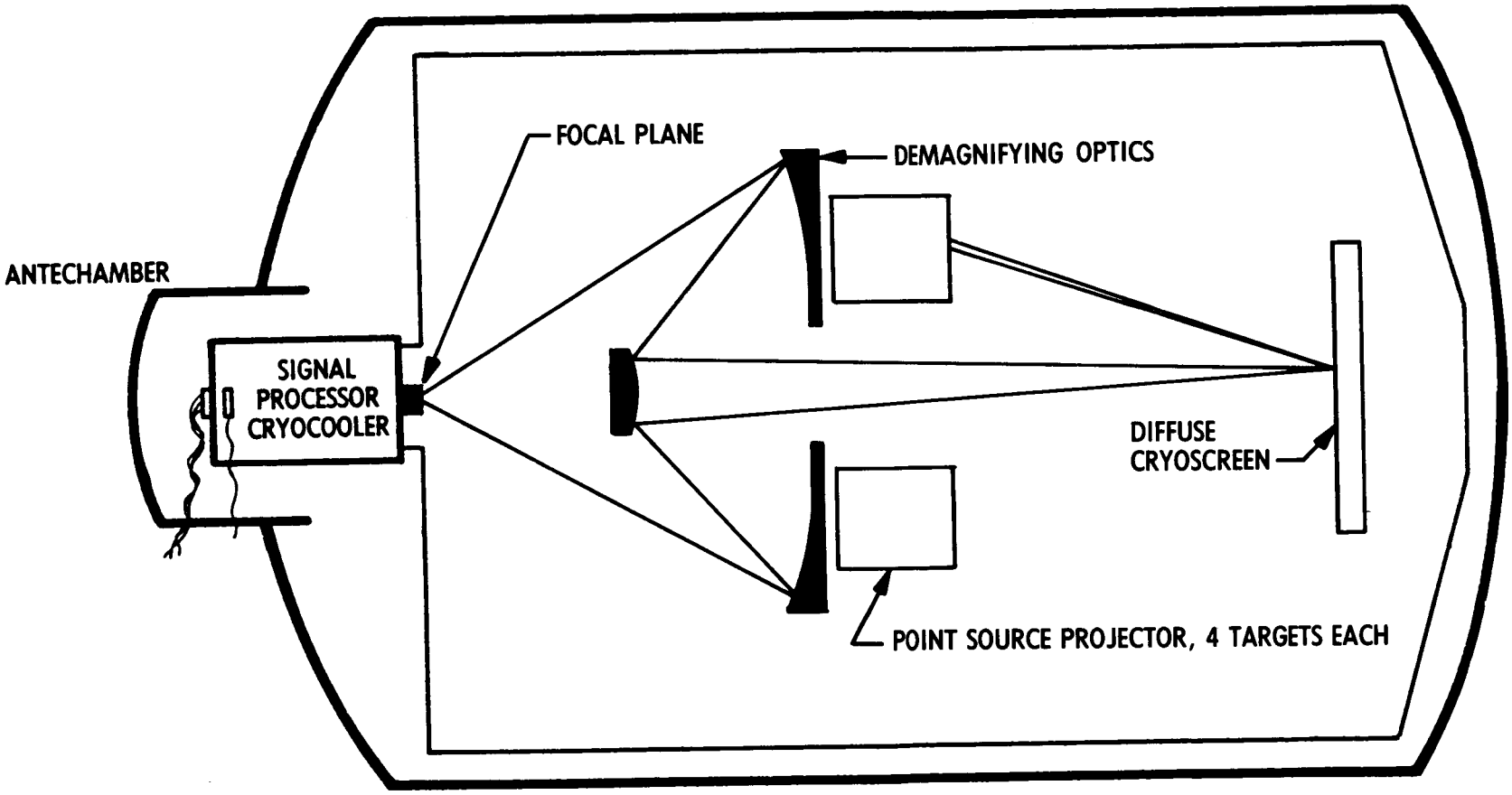

Figure 6. Complex scene projection layout

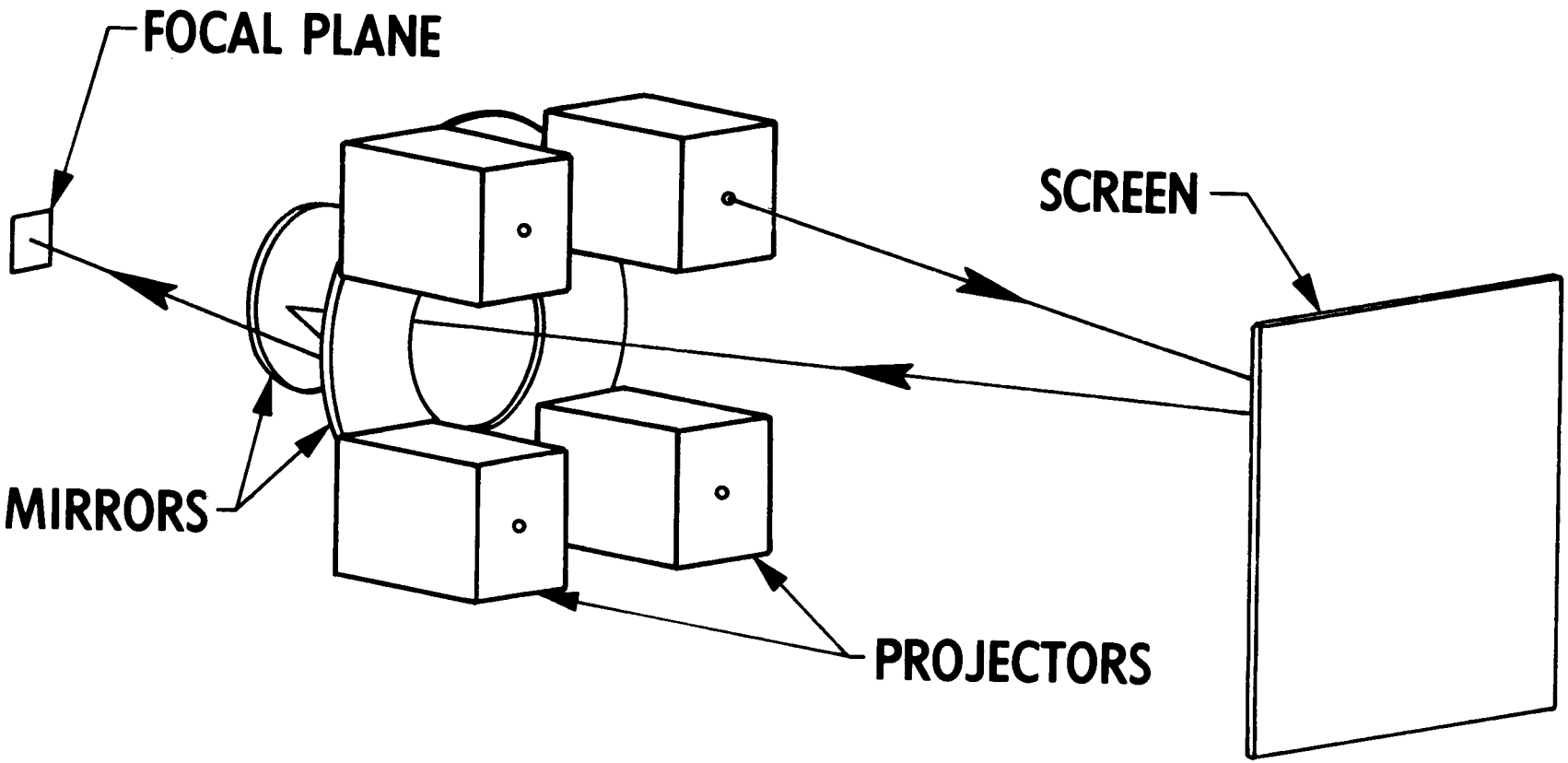

Figure 7. Target generator follow on

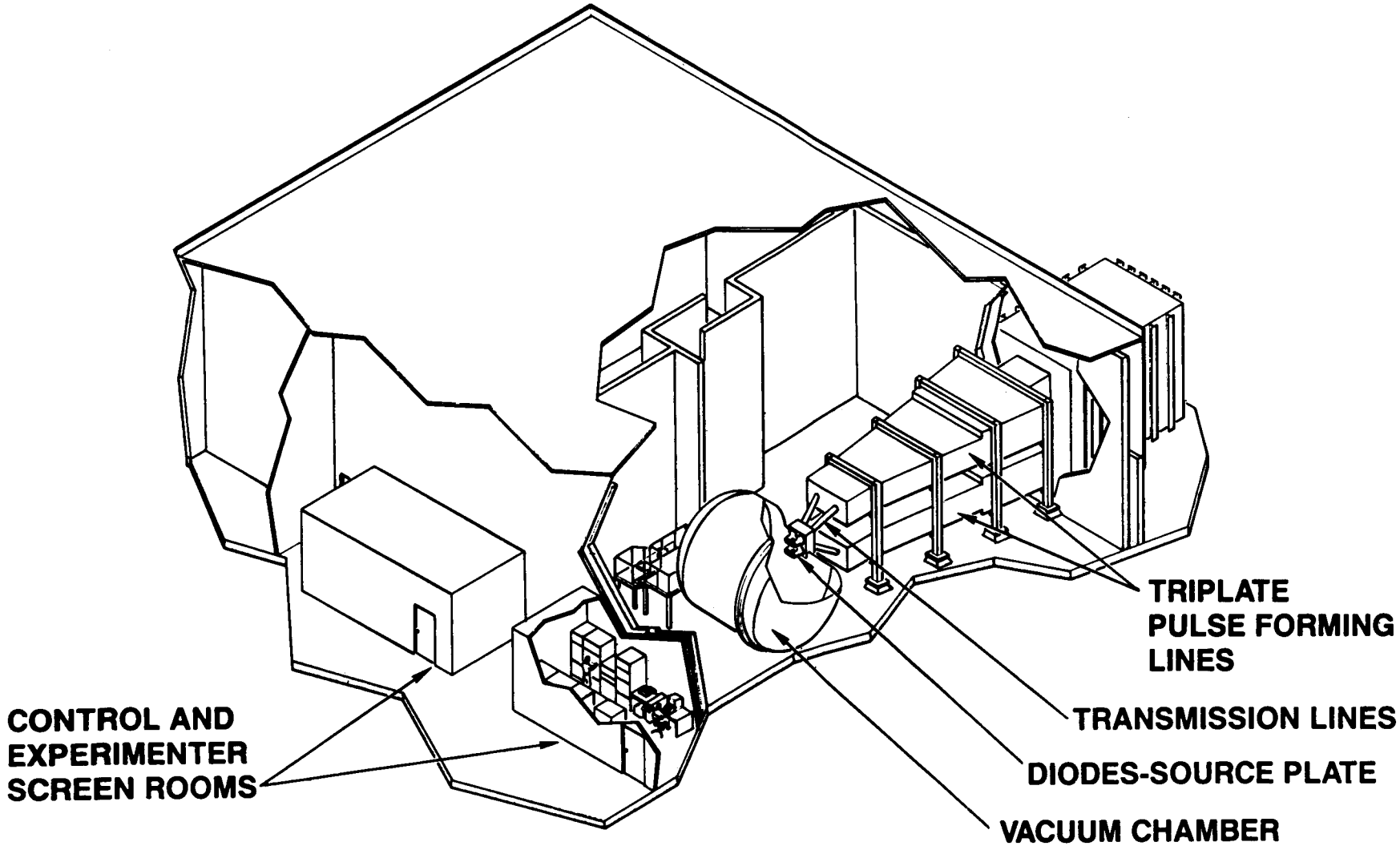

Figure 8. AEDC pilot x-ray facility

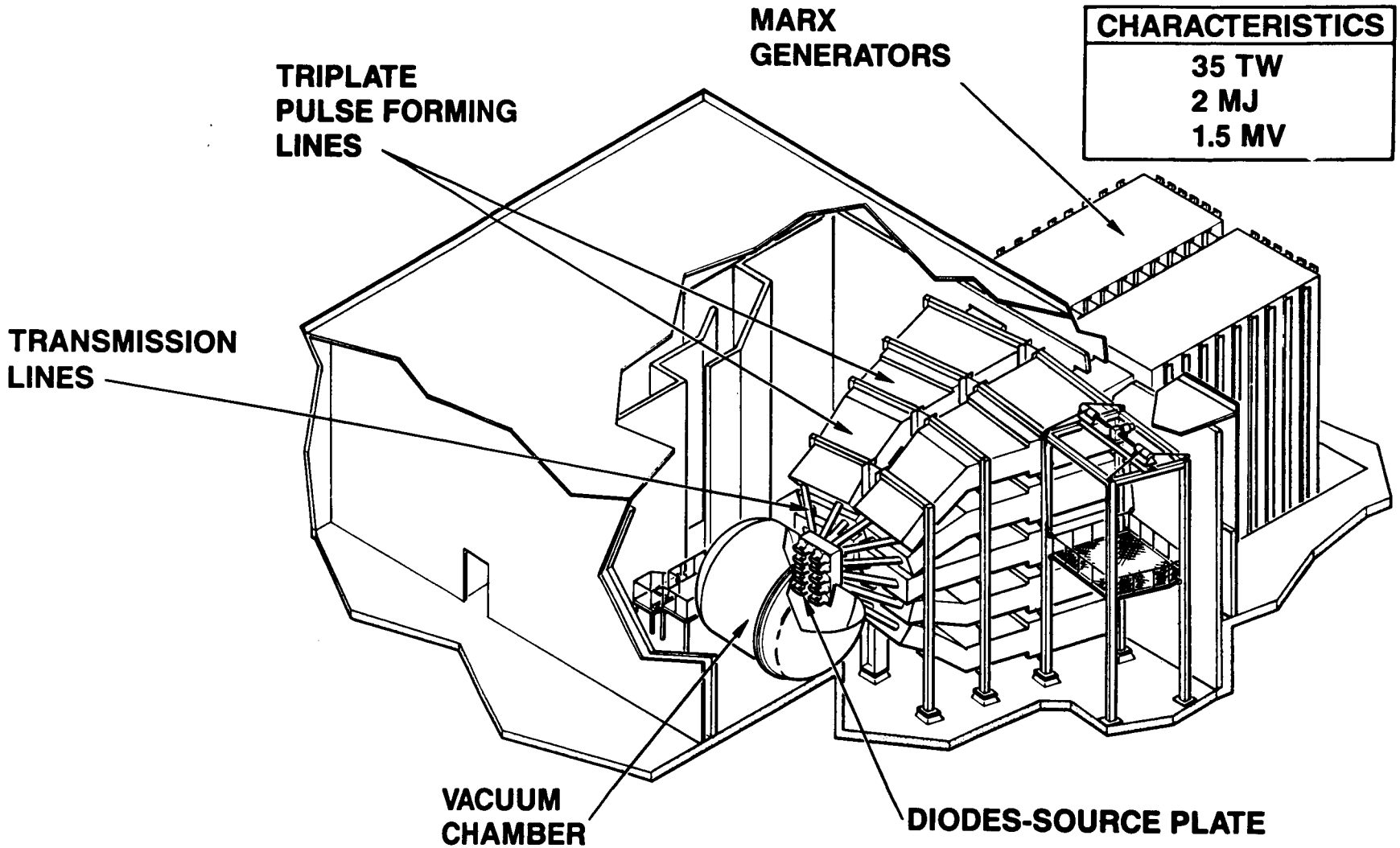

Figure 9. AEDC modular x-ray facility

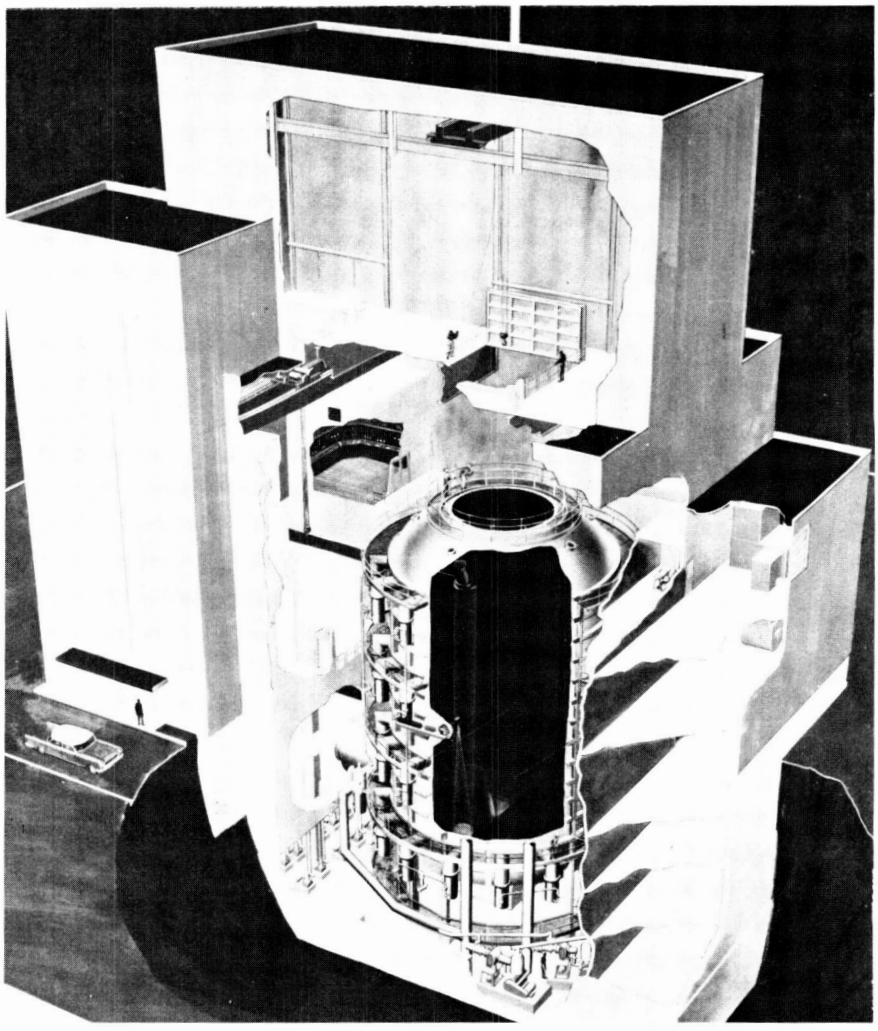

Figure 10. Small sensor off-axis-rejection testing in AEDC aerospace chamber mark I

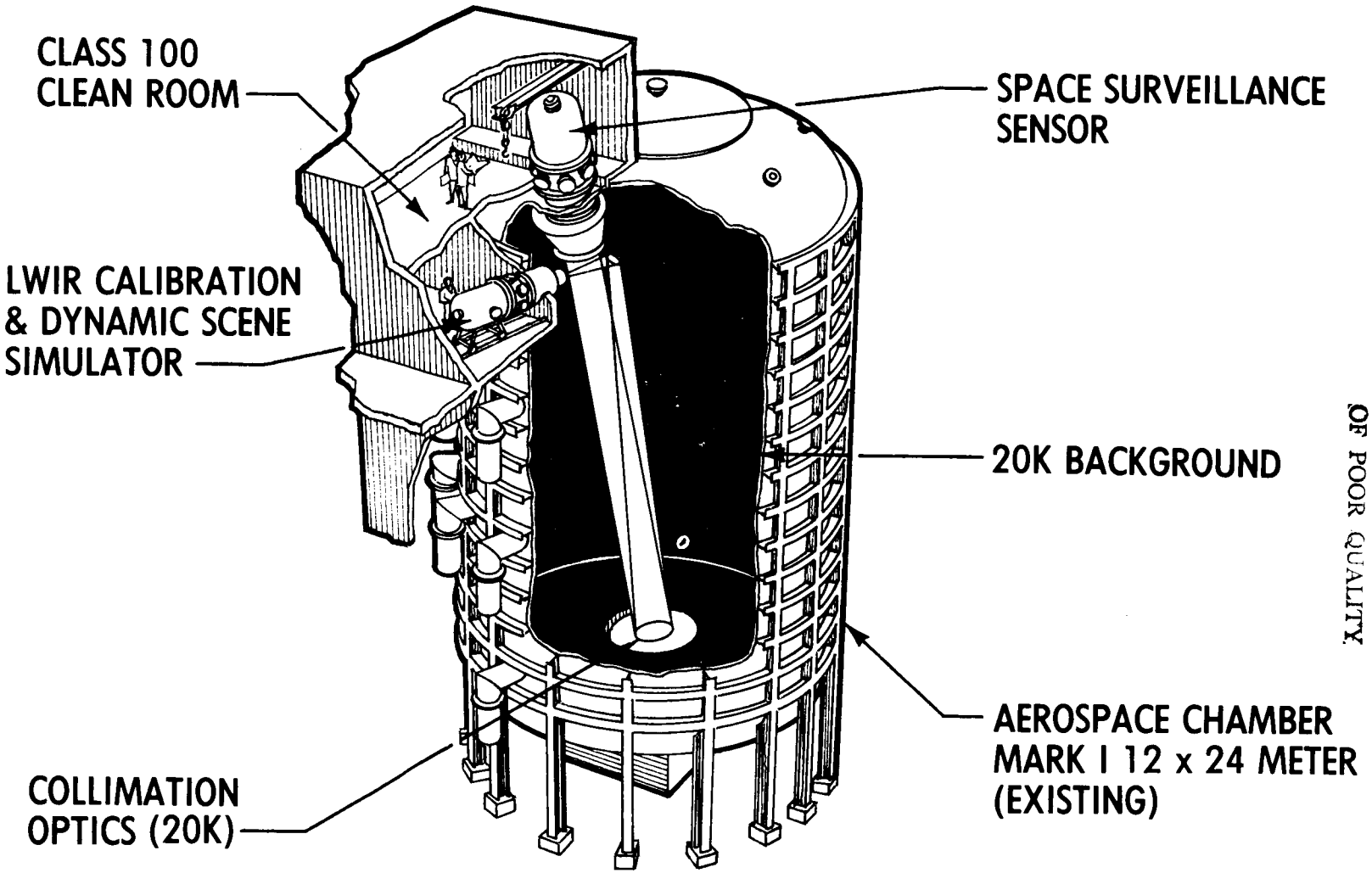

Figure 11. Concept for 1-meter class sensor testing in AEDC aerospace chamber mark I

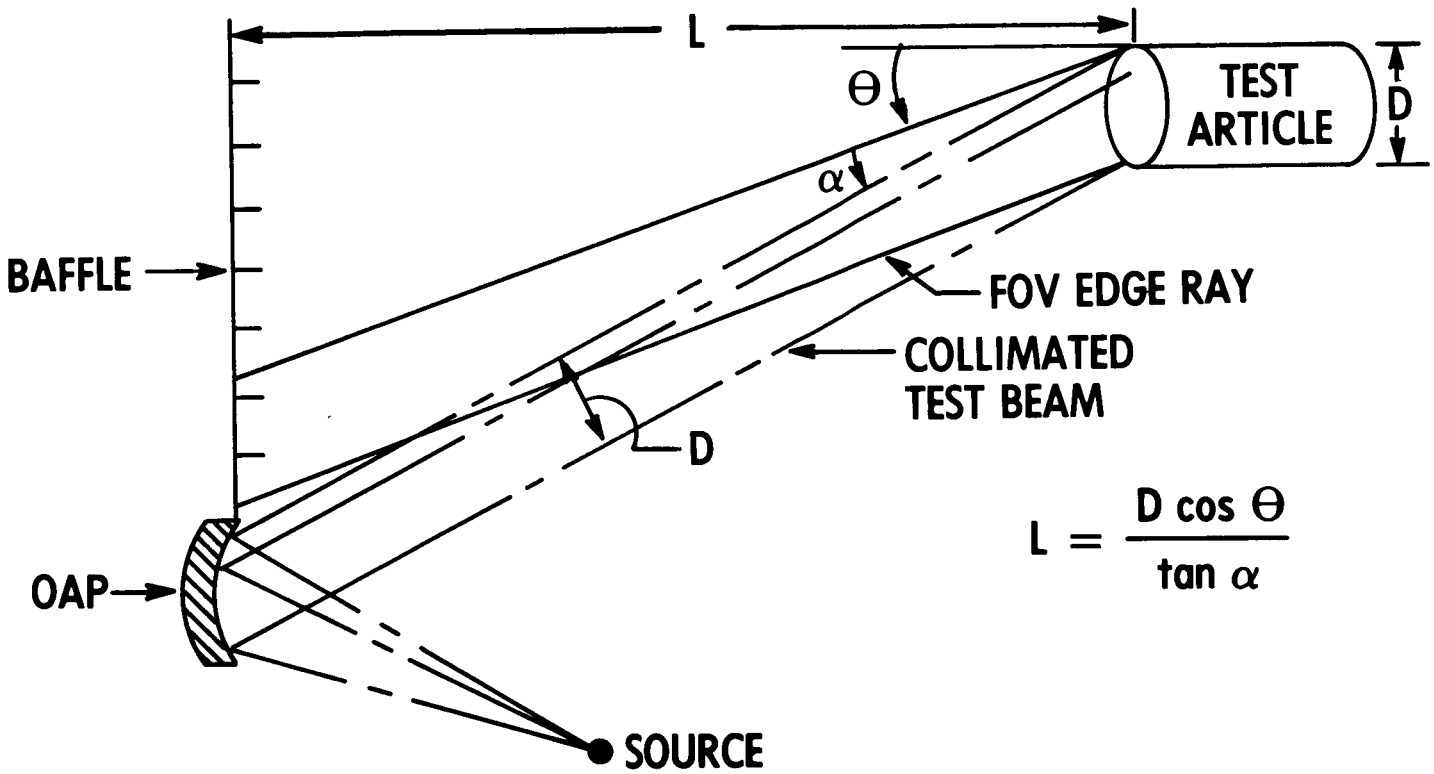

- FACILITY LENGTH IS PROPORTIONAL TO TEST ARTICLE DIAMETER FOR FULL APERTURE OR SUBAPERTURE TEST BEAMS

Figure 12. Traditional off-axis-rejection geometry

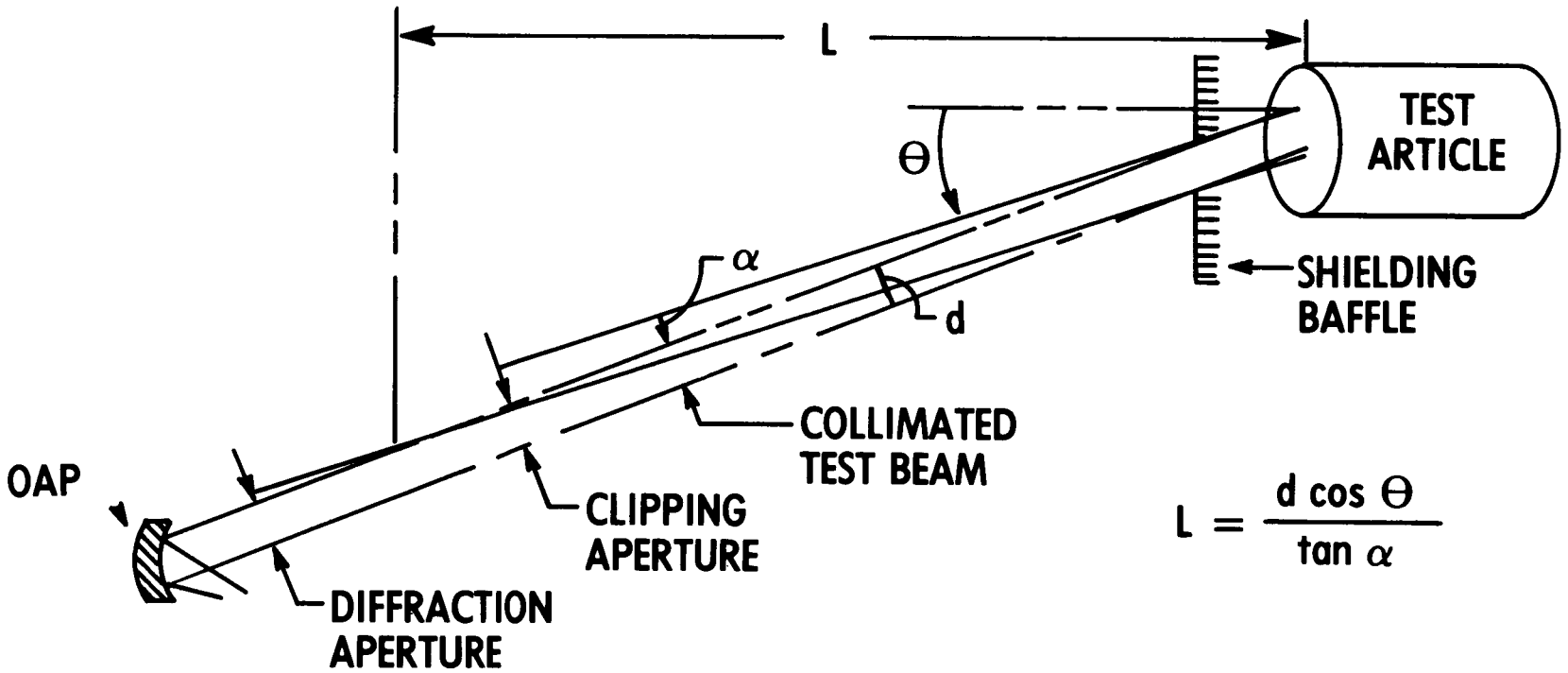

- FACILITY LENGTH PROPORTIONAL TO TEST BEAM DIAMETER

Figure 13. Alternate off-axis-rejection geometry

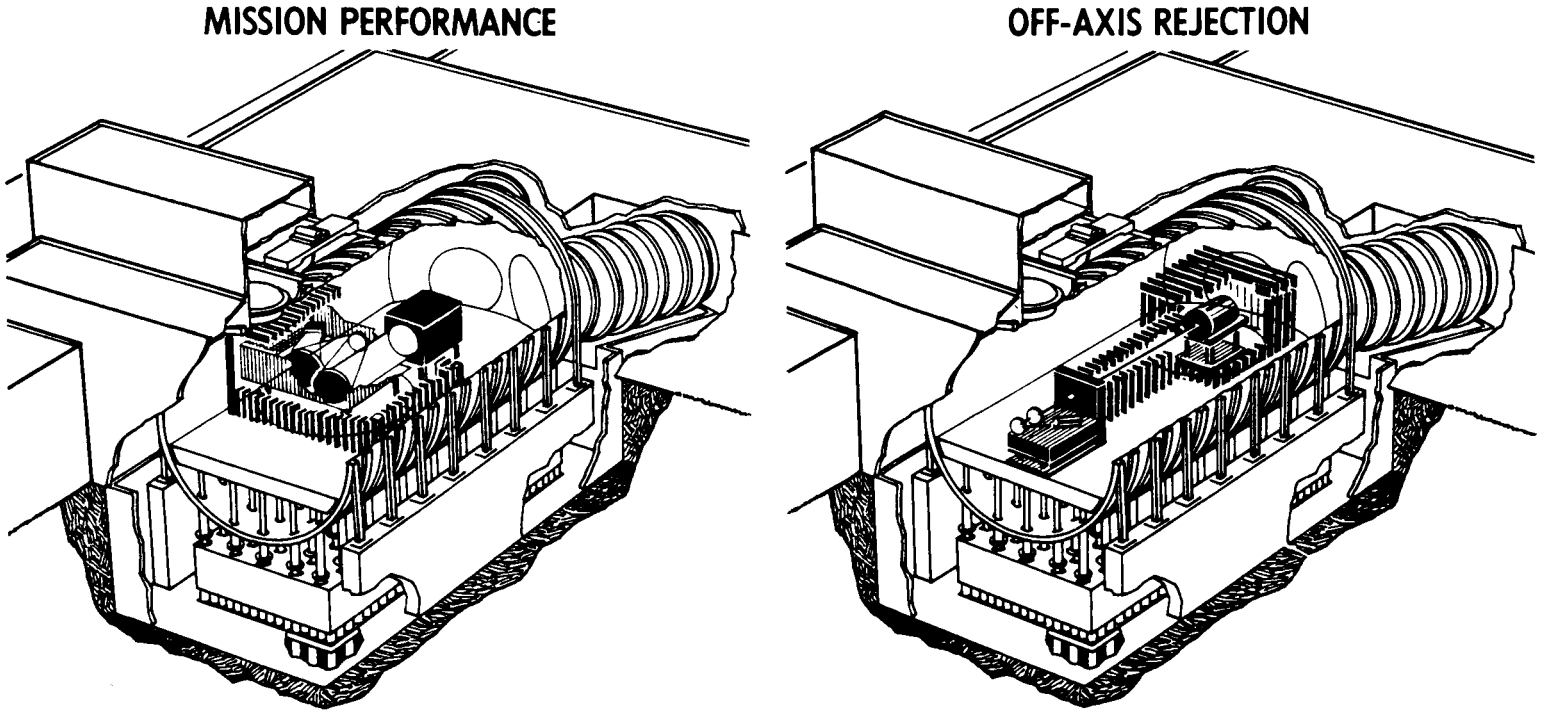

Figure 14. 2- to 3-meter sensor testing in AEDC space facility

MATHEMATICAL MODELLING OF SOLAR ULTRAVIOLET RADIATION INDUCED OPTICAL DEGRADATION IN ANODIZED ALUMINUM

John D. Ruley

University of Dayton Research Institute
300 College Park Ave.
Dayton, Ohio 45469

ABSTRACT

In the design of spacecraft for proper thermal balance, accurate information on the long-term optical behavior of the spacecraft outer skin materials is necessary. This paper presents a phenomenological model for such behavior, explains the underlying principles involved, and gives some examples of the model's fit to actual measurements under simulated earth-orbit conditions. The paper concludes with some comments on applicability of the model to materials testing and thermal modelling.

INTRODUCTION

Since the early 1960's, a considerable body of data has been acquired on the performance of Alzak[1] anodized aluminum under simulated space radiation conditions. This material has generally poor space stability, but is unique in that it demonstrates a consistent, repeatable deterioration in optical properties when exposed to ultraviolet radiation in vacuum[2]. This characteristic makes it an ideal reference material for validation of space simulation facility performance.

In 1981, major modifications to the AFWAL/ML[3] SCEPTRE (Space Combined Effects Primary Test Research Equipment) began, with a goal of raising the then-inadequate (.2 UV sun) simulated solar intensity to a useful (>1.0 sun) level, and .1 mil Alzak was decided upon as a control material. By 1985, this effort had been concluded, which provided a unique opportunity to examine Alzak behavior under simulated solar UV intensities in the range 0-1 sun. Examination of the historical record provided further information from an earlier work[4] which has extended this data set to 3 suns (SCEPTRE data at >1 sun intensity has been in a combined UV/electron environment). Thus, data is available for an extremely wide intensity range under known conditions with a known material.

---

*Research performed under Air Force Contract No. F33615-84-C-5130, University of Dayton Research Institute

[1]A product of Alcoa Corporation

[2]"Proceedings of the International Symposium on Solar Radiation Simulation" - IES/ASTM, January 1965, pps. 115-122.

[3]Air Force Wright Aeronautical Laboratories/Materials Laboratory

[4]"Effects of Vacuum-Ultraviolet Environment on Optical Properties of Bright Anodized aluminum Temperature Control Coatings," AFML-TR-67-421, J. H. Weaver, AFML, May 1968.

The desire to understand the material behavior arises from the need for space simulation testing to be conducted under accelerated conditions, i.e. at intensities greater than those experienced in the actual flight environment. Testing is usually conducted at intensities for 2-10 suns, and then "scaled" by multiplying the test time against the intensity to yield what is presumed to be a useful dose measurement, generally called "Equivalent Sun-Hours" or ESH. The unstated assumption in such scaling is that of Reciprocity - that a reciprocal relationship exists between the intensity and the time constant for material damage, with no significant deviation in total damage to the material.

The SCEPTRE tests of Alzak do not bear out this assumption. While data from individual test runs can be nicely fitted to a "french curve" asymptotic trace (Figure 1), when the data is expressed in terms of the total dose in ESH, any such relationship disappears (Figure 2). This suggests that a more complicated relationship between time, intensity, and damage occurs.

It is the intent of this paper to express, as completely as possible, that relationship.

DERIVATION OF THE MATH MODEL

Consider a monomolecular layer of Alzak containing some number N_o of possible sites for color center formation. Figure 3 illustrates the behavior of such a layer when exposed to ionizing radiation at an intensity of 3 ionizing photons/unit area/unit time. One photon interacts with a site, forming a color center. Another photon interacts with an existing color center - and has no effect. The last photon passes through the layer without effect, presumably to create a color center deeper in the material.

Our objective is to derive an equation which will define the concentration of color centers in this layer as a function of time.

$$\frac{d}{dt}\left(\frac{N(t)}{N_o}\right) = \sigma\left(\frac{N_o - N(t)}{N_o}\right) I_o \tag{1}$$

this equation is satisfied by N(t) defined as

$$N(t) = N_o\ (1-e^{-t/\tau})\ ;\ \tau = \frac{1}{\sigma I_o} \tag{2}$$

which may be divided through by N_o to yield the concentration of color centers as a function of time

$$\frac{N(t)}{N_o} = 1-e^{-t/\tau} \tag{3}$$

The observable value related to the concentration of color centers is the solar absorptance ($\alpha_s(t)$), which may be found by

$$\alpha_s(t) = \alpha_o(N_o - N(t)) + \alpha_1(N(t)) \tag{4}$$

Subtraction of the initial value yields the change in solar absorptance as a function of time

$$\Delta\alpha_s(t) = \alpha_s(t)-\alpha_o = \alpha_1(1-e^{-t/\tau}) \tag{5}$$

Now this model is very interesting, despite its flaws, since this is the model implied by the assumption of linear reciprocity stated in the introduction. Indeed, a 100 hour exposure to radiation at 2 UV sun intensity should, according to this model, have exactly the same effect as 200 hours of exposure at 1 UV sun.

Attempting to fit the observed data to this model yields Figure 4. Clearly the model fails - and the most obvious way in which it could fail is by assuming that all the damage occurs in a single monolayer of material.

Therefore, let us consider a multi-layer model.

Figure 5 illustrates such a model, which is essentially a stack of monolayers as defined in Figure 3, viewed from the side. Again, we see three incident photons. One forms a color center in layer one, one impacts an existing center without effect, and the third passes through to create a new center in layer 2. The difference between this case and the monolayer case is now clear - at heightened intensities, damage will be done deeper in the material, so the total saturation value for color center concentration (and, by inference, solar absorptance) will be higher.

The model is described by

$$\frac{\partial}{\partial t}\Big|_x \left(\frac{N(x,t)}{N_o}\right) = \sigma\left(\frac{N_o-N(x,t)}{N_o}\right) I(x) \;;\; I(x)=I_o e^{-ax} \tag{6}$$

which is satisfied by

$$N(x,t) = N_o(1-e^{-t/\tau(x)}) \;;\; \tau(x) = \frac{1}{\sigma I(x)} \tag{7}$$

Dividing through by N_o yields the Color Center Concentration

$$\frac{N(x,t)}{N_o} = 1-e^{-t/\tau(x)} \tag{8}$$

This completes the derivation of the model, but does not yield an observable quantity. To get an observable ($\alpha_s(t)$) from this, we again apply Equation (4), noting this time that we must integrate over the thickness of the material, which leads to

$$\frac{\alpha_s(t) = \alpha_o \int_o^{D'} [N_o-N(x,t)]dx+\alpha_1 \int_o^{D} N(x,t)dx}{\int_o^{D^*} N_o\, dx} \tag{9}$$

rearranging terms, and integrating the simpler ones yields

$$\frac{\alpha_s(t) = \alpha_o N_o D+(\alpha_1-\alpha_0) \int_o^{D} N_o(1-e^{-\sigma t I_o e^{-ax}})dx}{N_o D} \tag{10}$$

This cannot be analytically solved for all time, but it can be solved for the trivial case of t=0 (yielding α_o, as expected), and for the limit as time goes to infinity. This last yields

$$\lim_{t\to\infty} [\alpha_s(t)] = \frac{\alpha_o N_o D+(\alpha_1-\alpha_0)N_o d_1}{N_o D} \tag{11}$$

Where we note that at depths greater than d_1, no color centers are formed, so the integral range for the N(x,t) term is thus restricted. Cancelling the N_o's yields

$$\lim_{t\to\infty} [\alpha_s(t)] = \alpha_o+(\alpha_1-\alpha_0)\frac{d_1}{D} \tag{12}$$

And subtraction of the α_0 yields

$$\Delta\alpha_s = \alpha_s-\alpha_0 = (\alpha_1-\alpha_0)\frac{d_1}{D} \tag{13}$$

Which expresses the total change in absorptance over infinite time. It merely remains to find the maximum depth of damage d . We do this by applying Beer's Law to compute the intensity at the maximum depth.

$$I(x)\Big|_{x=d_1} = I(d_1) = I_o e^{-ad_1} \tag{14}$$

Taking the log of both sides, noting that the threshold intensity at the depth of maximum damage must be a constant (since at greater depths it is quantum-mechanically improbable that there will be any effect) and solving for d_1 yields

$$d_1 = A\ \ln(I_o) + B \tag{15}$$

where A and B are arbitrary constants. Substituting this back into Equation (12) and combining constants yields

$$\lim_{t\to\infty} \Delta\alpha_s(t) = (\alpha_1-\alpha_0)(A\ \ln(I_o)+B)/D \tag{16}$$
$$= A\ \ln(I_o)+B$$

We now make the assumption that the complete, time-dependent equation can be separated into static and dynamic components, of which Equation (16) is the static component

$$\Delta\alpha_s(t) = [\Delta\alpha(t)]_{t=\infty} f(t) \tag{17}$$
$$= (A\ \ln(I_o)+B)f(t)$$

Inspection of Equation (10) yields the dynamic (time-dependent) component

$$f(t) = K\int_o^{d_1}\left[1-e^{-t/\tau(x)}\right]dx;\ \ \tau(x) = \sigma t_o e^{-ax} \tag{18}$$

Which has no analytical solution. We approximate this function by converting it to series form

$$f(t) \cong K \sum_{i=1}^{n} (1-e^{-t/\tau(x)})\Delta x \; ; \; x=\Delta x(i-1); \quad \tau(x)=\sigma I_o e^{-a\Delta x(i-1)} \tag{19}$$

And then note that the most significant term is the first, due to the nature of the exponential component. Truncation of all terms for i>1 yields

$$f(t) \cong K(1-e^{-t/\tau}) \; ; \; \tau = \frac{1}{\sigma I_o} \tag{20}$$

where K is an arbitrary constant. Substitution back into Equation (17), and combination of the constants finally yields

$$\Delta\alpha_s(t) = [\Delta\alpha_s(t)]_\infty \, f(t) = a_1(I_o)(1-e^{-t/\tau(I_o)})$$

$$\tau(I_o) = \frac{1}{\sigma I_o} = \frac{k}{I_o}$$

$$a_1(I_o) = A \ln(I_o)+B$$

$$\text{where } \sigma,A,B = \text{constant} \tag{21}$$

Which represents an approximate expression for the observable variable - the change in solar absorptance.

TESTING THE MODEL AGAINST REALITY

Figures 6 and 7 illustrate that, indeed, τ is inversely proportional to intensity, and a_1 is linear with the log of the intensity. Simple least-squares fitting produces the constants in question, thus

$$\tau = 95.0/I$$

$$a_1 = .008 \log(I) + .042$$

(or k=95, A=.008, B=.042 in the nomenclature of Eq. (21)

Substituting these into Equation (21) and plotting for the actual test intensities of .2, .5, 1.0, and 3.0 suns yields Figure 8 - which shows that the equation does indeed fit the data to within the illustrated error limit of $\pm.005$ in α_s.

This data fit is far too close to be fortuitous - if this model is not accurate, it is at least much closer than the naive model illustrated in Figure 4.

CONCLUSION - IMPLICATIONS ARISING FROM THE MODEL

Given that Equation (21) provides a working approximation to material behavior in this case, we are left with several interesting questions:

1 - Does the model apply to other materials?

We do not know. Existing SCEPTRE data sets for materials other than Alzak encompass at best two exposure intensities, which is insufficient to validate linearity of a_1 and τ. However, if an iterative solution for a_1 and τ is tolerated, every data set we have, for organic and inorganic paints, OSR's, etc. can be fitted to Equation (8). This procedure yields a resultant function which is valid only at the intensity for which data is available, but it is nonetheless encouraging.

2 - Does the model apply to other radiation environments?

Again, insufficient data prevents us from making a definitive answer, but the iterative procedure mentioned above has so far been successful at producing a fit to within experimental error limits for all SCEPTRE UV/vacuum and UV/vacuum/electron tests.

3 - Assuming that the model is (at least approximately) valid, what does it say about present-day accelerated testing of spacecraft materials for space stability?

The model has several implications for accelerated testing, well expressed by comparing Figures 4 and 8. The assumption that test results can be corrected for varying intensity by scaling the time axis is clearly false. It does appear, however, that testing at accelerated intensities represents a "safe worst case", since the saturation value is always higher for higher intensity.

Perhaps the most important implications are for intercomparison of ground-based simulation data to flight test results. When those of us in the simulation community speak of a "UV-sun" we mean an equivalent UV intensity to that from the sun, assuming a view factor of 1.0 = with the specimen normal to the incident light ray. In the real environment, for most any condition, view factor considerations will lead to a time-averaged intensity of less than .5 UV-suns for a real spacecraft on-orbit. If the simulation testing has been conducted at 2 suns, then the acceleration factor will be 4, not 2 as is often claimed. Given the intensity dependent nature of Equation (21), this suggests that such comparisons need to be examined very carefully - and leads one to question exactly what is meant if ground test results at high acceleration factors do indeed match flight test data. Given the prediction that tests at accelerated intensity will always yield more damage than a lower intensity, one is left to wonder which non-modeled component of the flight environment is responsible for the implied additional damage, and which materials are susceptible to its effects.

If Equation (21) does prove applicable to other materials and other environments, then it may become possible to answer some of these questions, and to put modern ground-based space environmental effects testing on a more sound theoretical footing. In this regard, it should be noted that the models defined by Equations (1) - (21) are in fact special cases of a model defined by Equation (22),

$$\frac{\partial}{\partial t}\left[\frac{N(x,t)}{N_o}\right] = \sigma(x,t)\left[\frac{N_o - N(x,t)}{N_o}\right] I(x,t) \qquad (22)$$

In which both the incident radiation intensity and the cross-section are defined as functions of both depth and time. If solutions - whether exact or approximate - can be found for this model, then it may well prove possible to generalize the work described herein to more complex systems and conditions.

REFERENCES

1. "Proceedings of the International Symposium on Solar Radiation Simulation," IES/ASTM, January 1965.

2. "Effects of Vacuum-Ultraviolet Environment on Optical Properties of Bright Anodized Aluminum Temperature Control Coatings," AFML-TR-67-42), J. H. Weaver, AFML, May 1968.

SYMBOLS

t	time (hrs)
$N(t)$	number of cells in a given monolayer changed up to time=t
N_o	number of cells per monolayer
$N(t)_{total}$	total number of cells changed at time=t
α_s	solar absorptance (absorptance units)
α_o	initial solar absorptance (absorptance units)
α_1	final solar absorptance (absorptance units)
σ	radiation effectiveness cross-section (fraction)
k, A, B, a_1	arbitrary constants
τ	time constant (hrs)
I_o	surface radiation intensity
I_i	radiation intensity at layer i
n	number of layers to which radiation penetrates
i	index of a given layer
Δd	thickness of a single layer of material
d_1	maximum depth to which radiation penetrates
a	optical density of material at radiation wavelength
D	total thickness of material

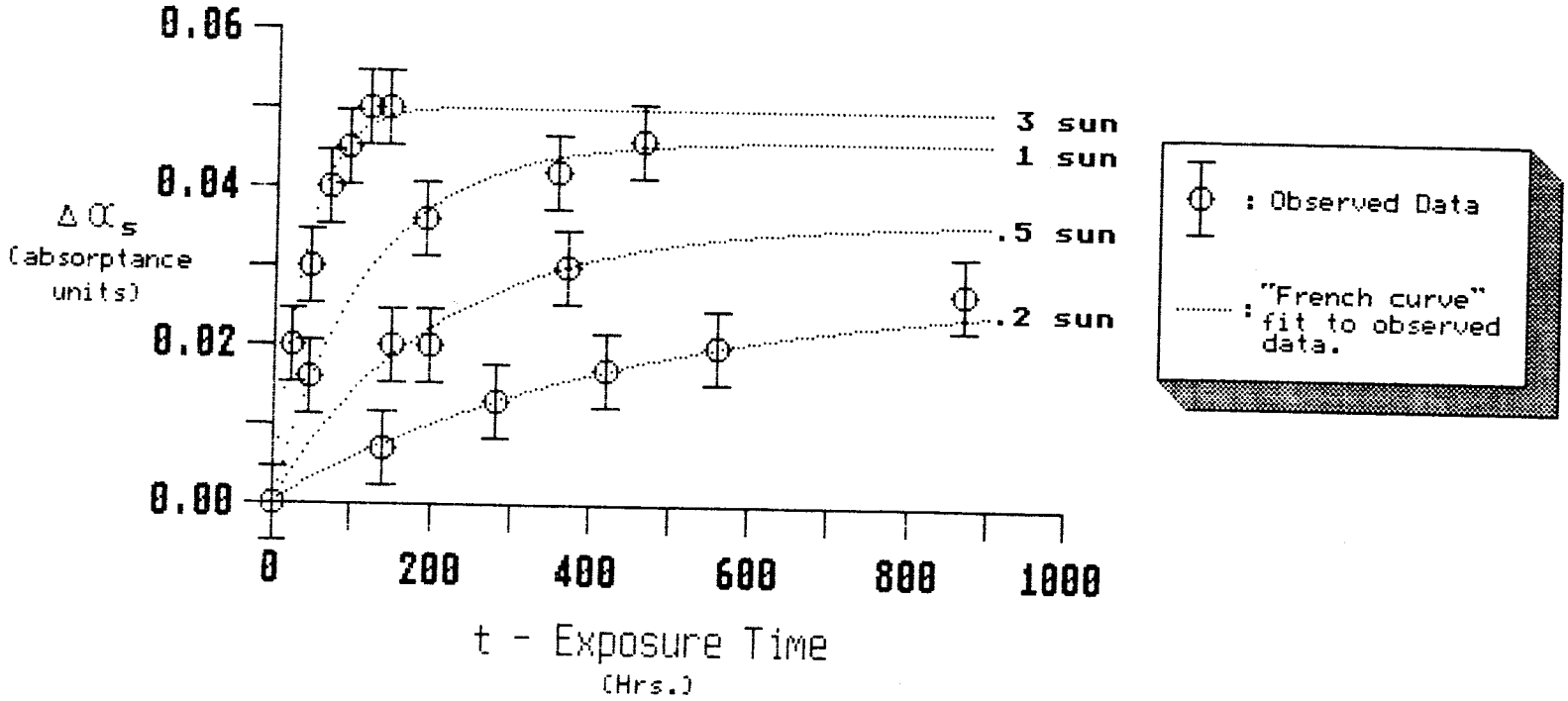

Figure 1. Alzak data for various intensities

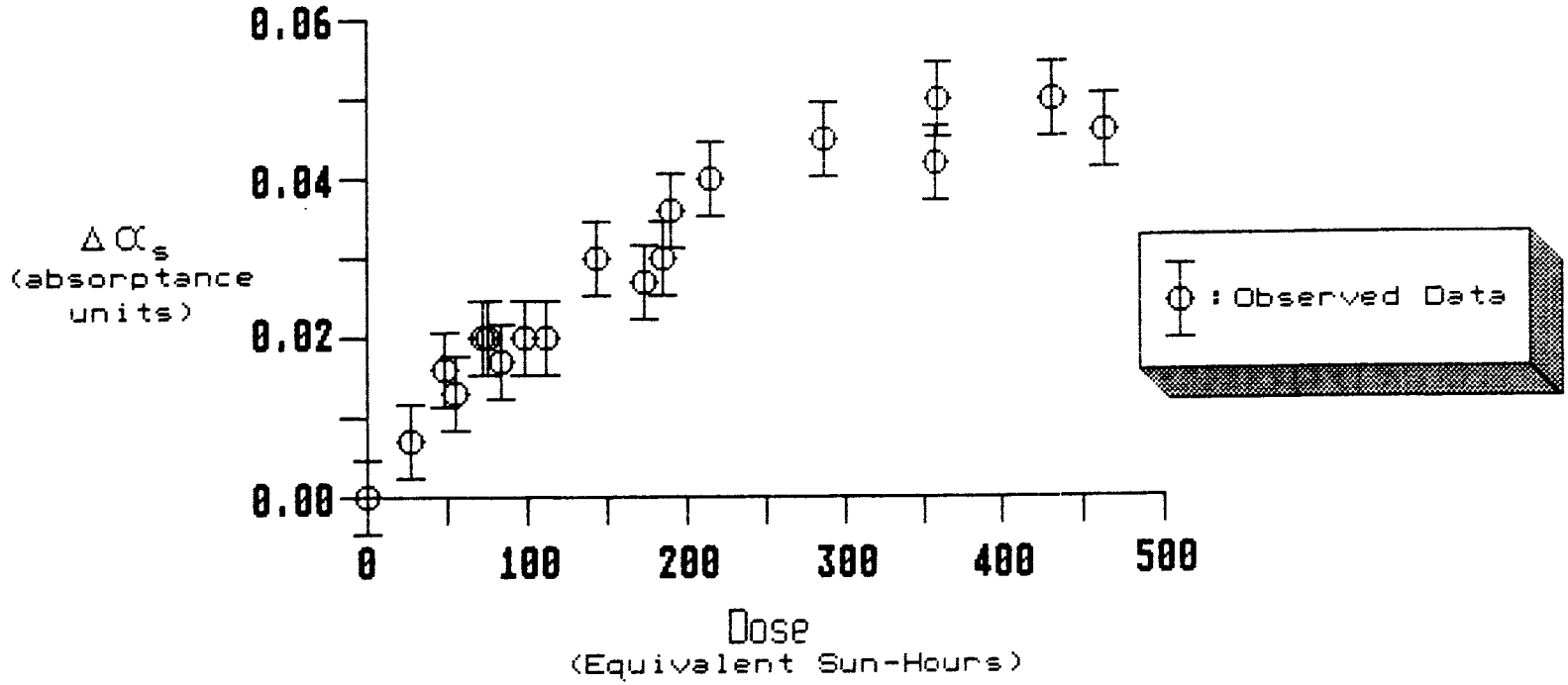

Figure 2. Degredation vs. dose - no simple relationship

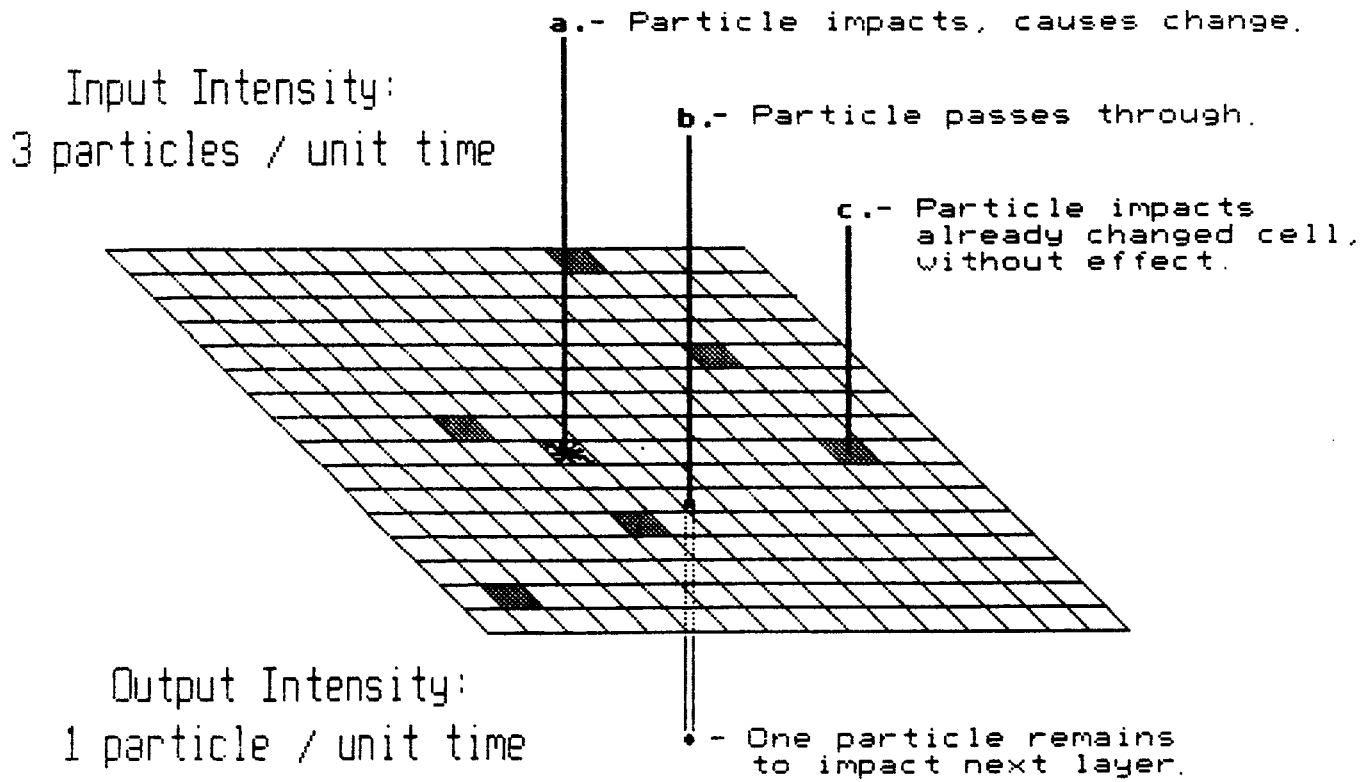

Figure 3. Degradation phenomena in one monolayer

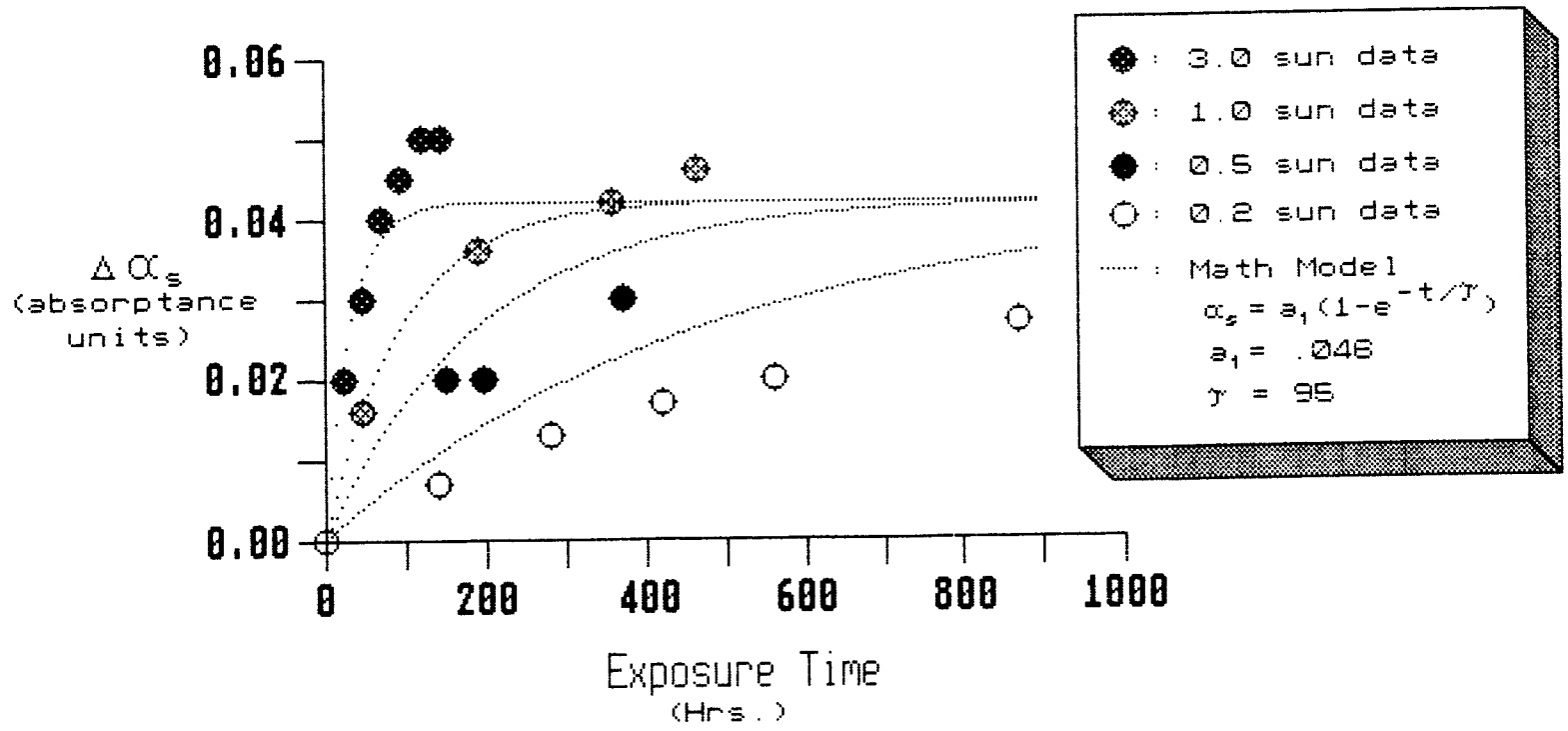

Figure 4. ''Naive'' monolayer math model

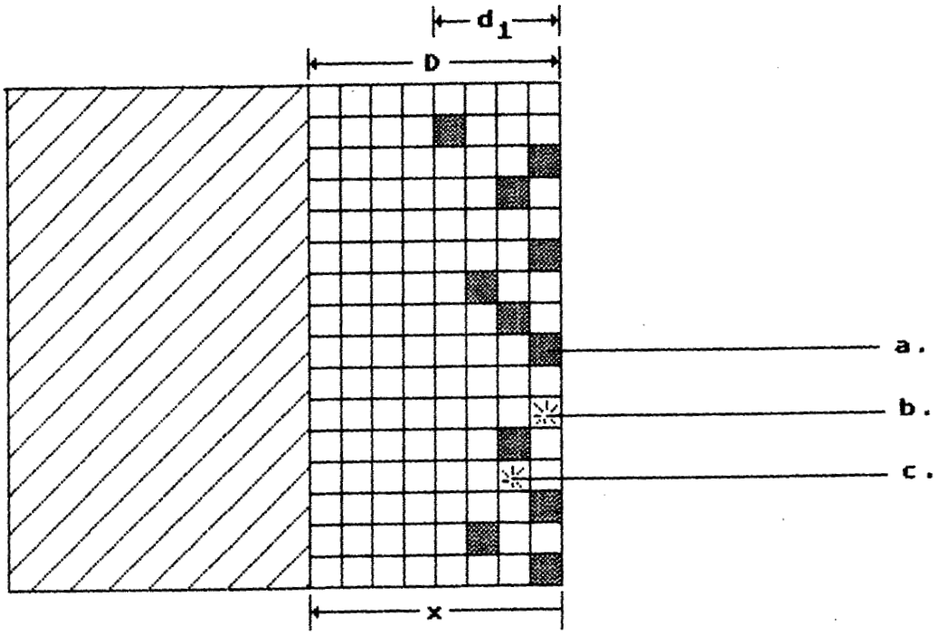

$$\text{Model:}\quad \left.\frac{\partial}{\partial t}\right|_x \frac{N(x,t)}{N_o} = \sigma \frac{N_o - N(x,t)}{N_o} I(x)$$

Figure 5. Color center generation in depth

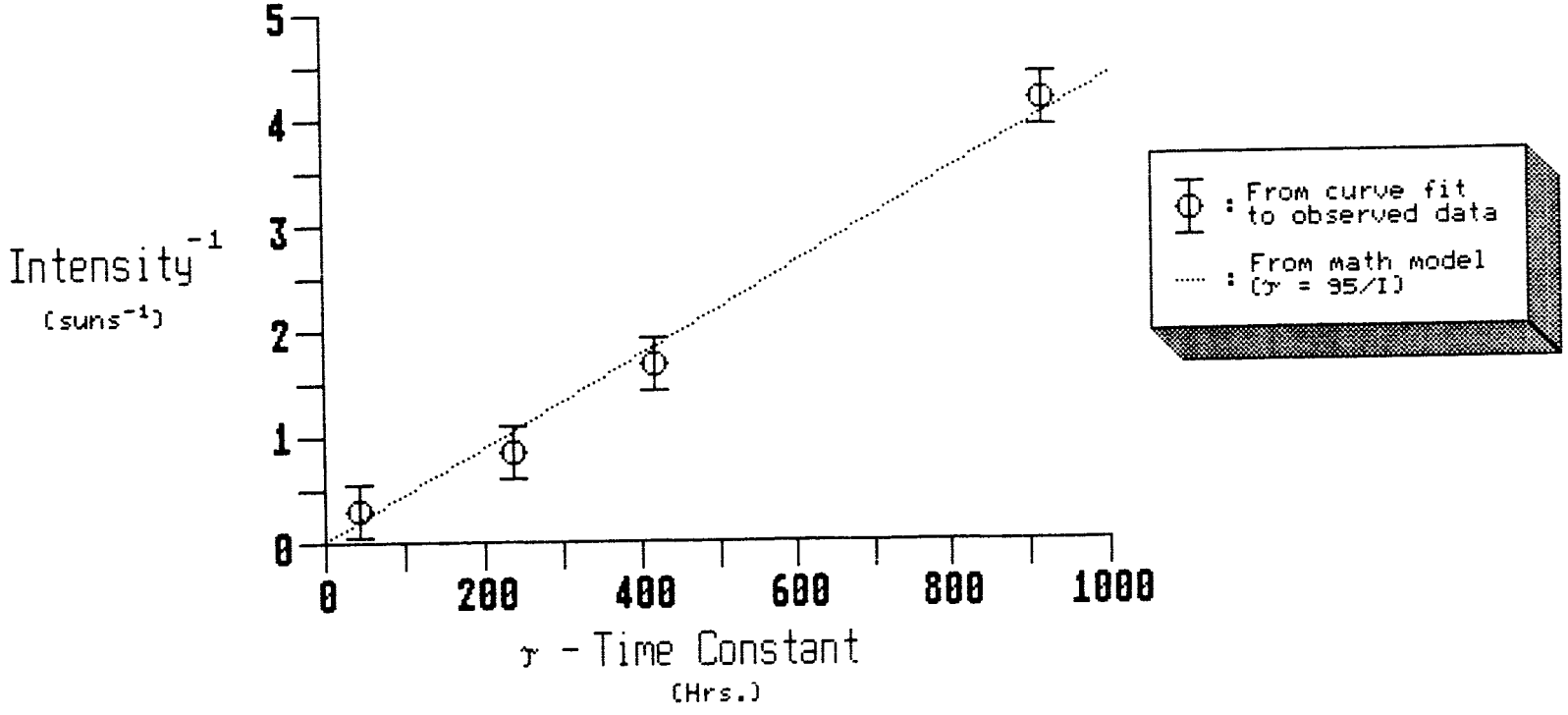

Figure 6. Inverse linearity of τ with intensity

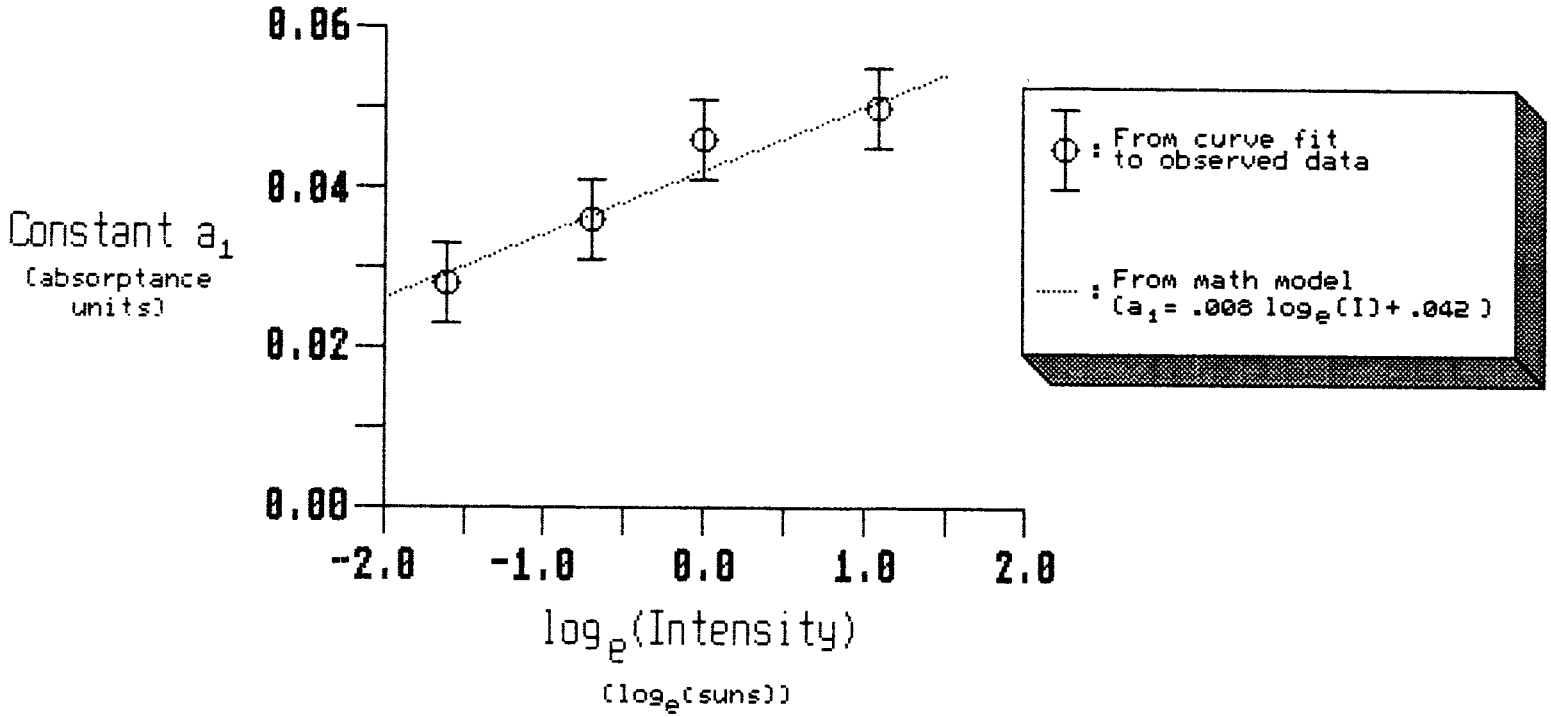

Figure 7. Linearity of a_1 with $\log_e$ (intensity)

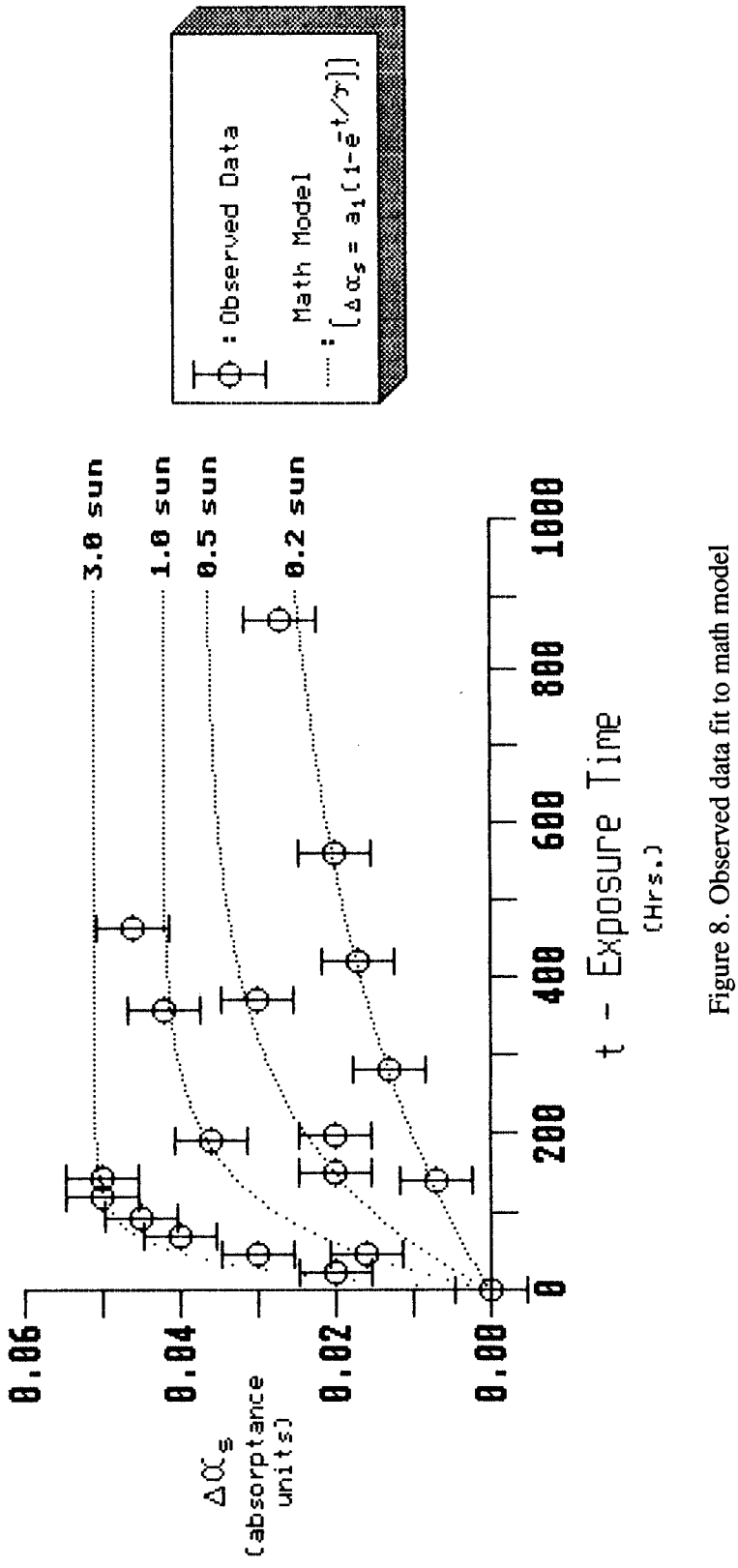

Figure 8. Observed data fit to math model

HIGH INTENSITY 5 eV O-ATOM EXPOSURE FACILITY FOR MATERIAL DEGRADATION STUDIES

J. B. Cross, L. H. Spangler, M. A. Hoffbauer, and F. A. Archuleta
Los Alamos National Laboratory
Chemistry Division
Los Alamos, NM 87545

Lubert Leger and James Visentine
Lyndon B. Johnson Space Center
Houston, TX 77058

Don E. Hunton
Air Force Geophysics Laboratory
Hanscom Air Force Base, MA 01731

ABSTRACT

An atomic oxygen exposure facility has been developed for studies of material degradation. The goal of these studies is to provide design criteria and information for the manufacture of long life (20 to 30 years) construction materials for use in low earth orbit. The studies that are being undertaken using the facility will provide (1) absolute reaction cross sections for use in engineering design problems, (2) formulations of reaction mechanisms for use in selection of suitable existing materials and design of new more resistant ones, and (3) calibration of flight hardware (mass spectrometers, etc.) in order to directly relate experiments performed in low earth orbit to ground based investigations.

The facility consists of (1) a cw laser sustained discharge source of O-atoms having a variable energy upto 5 eV and an intensity of between 10^{15} -10^{17} O-atoms s^{-1} cm^{-2}, (2) an atomic beam formation and diagnostics system consisting of various stages of differential pumping, a mass spectrometer detector and a time-of-flight analyzer, (3) a spinning rotor viscometer for absolute O-atom flux measurements, and (4) provision for using the system for calibration of actual flight instruments.

INTRODUCTION

The exterior surfaces of spacecraft operating in the low earth orbit (LEO) environment are bombarded with oxygen atoms at an average rate of 10^{15} s^{-1} cm^{-2} and with a collision energy of 5 eV caused by the spacecraft's 8 km/s orbital velocity. In addition to this very reactive species, N_2 (11.5 eV collision energy) and N-atoms are present and collide with these surfaces at fluxes 0.3 and 10^{-3} that of atomic oxygen, respectively.

The reactivities of spacecraft surfaces with the LEO environment which is used to predict surface recession for Space Station materials have been derived by exposing these materials during Shuttle flights of limited duration and low atomic oxygen fluence. These in-flight investigations are important, but the Shuttle is limited in its usefulness in evaluating coating life. For example, even during conditions of maximum solar activity, a 7-day mission at an altitude of 222 km would result in an atomic oxygen fluence of only 1.3×10^{21} atom/cm^2, assuming maximum (normal incidence) exposure. Yet fluences for long-duration missions, such as Space Station, will be in the range of 10^{22} - 10^{23} atom/cm^2. Therefore, ground based studies must be conducted to determine the validity of extrapolation to high fluence conditions using reactivities derived from low fluence exposures. To aid in these investigations, a number of atomic oxygen simulation facilities are being developed using various techniques to accurately simulate the LEO environment. The particular facility described here will be used to study: material interaction rates as a function of time, the interaction mechanisms leading to surface recession, the full life (10^{22}-10^{23} atom/cm^2) effects of atomic oxygen on exposed surfaces and protective coatings, and scattering angular distributions and O-atom energy loss both of which will be important parameters in computer modeling of Space Station interaction with the LEO environment. The facility is designed to produce a beam of neutral atomic oxygen at energy levels typical of orbital conditions (5 eV). In addition, it is designed to be capable of producing fluxes in the range of 10^{16}-10^{17} atom/s-cm^2, in order to study reactivities at typical Space Station fluences within reasonable periods of time. Assuming an incident flux as high as 5×10^{16} atom/s-cm^2, materials must be exposed for approximately 50 hours to obtain fluence levels typical of Space Station solar inertial surfaces.

The simulation of the LEO environment has focused on the development of intense sources of O-atoms in the energy range of 2 to 10 eV. The limitations of many of these sources can be traced to reactions of the species with the production apparatus and the characteristics of the production methods. For example the source developed by Knuth[1] has been used for the production of atomic oxygen[2] but due to reactions with the electrodes, the oxygen is admitted downstream of the discharge region resulting in a maximum kinetic energy of about 1 eV and an intensity of 3×10^{17} s^{-1} sr^{-1}. Radio frequency discharges[3,4] have been used to produce oxygen atoms with kinetic energies of 0.1 to 1.0 eV and intensities of 10^{17-18} s^{-1} sr^{-1}. The production of high mass kinetic energy species is accomplished by seeding and heating in helium[5] expansions but low mass species (<20 amu) are limited to roughly 1 to 2 eV in kinetic energy using this technique. Charge exchange methods excel at energies >100 eV but suffer from space charge limitations[6] below 10 eV producing beam intensities orders-of-magnitude less than the previously mentioned techniques. Due to the low duty cycle of pulsed beams, techniques using pulsed laser breakdown require peak intensities of 10^3 to 10^4 that of cw beams in order to effectively equal cw time averaged intensities. The plasmas mentioned above are produced by electric fields having a range of frequencies from constant (dc arcs), <1 kHz (ac arcs), 20 to 50 MHz (inductive coupling), and 2.5 GHz (microwaves). These sources require some physical device to support the plasma. Direct current arcs require electrodes, rf plasmas require an induction coil, and microwaves require a resonator or waveguide. Because

rf and microwave source heating occurs by direct plasma-electric field interactions characterized by large absorption coefficients with the outer layers of the plasma, these modes of plasma production are characterized by low power density (<200 W cm^{-3}), modest temperatures (<8000 K except for dc arcs - 20,000 K). Power inputs ranging from 15 kW for dc arcs to 100's of watts for rf and microwave sources are required.

LASER SUSTAINED PLASMAS

In the early 1970's, it was hypothesized[7,8] and then demonstrated that a free-standing continuous discharge could be produced by focusing the output of a sufficiently powerful cw-CO_2 laser in inert[9] and molecular[10] gases at one atmosphere or above. The discharge resides near the focus of the laser and operates above the plasma frequency at 30 THz where the electric fields interact with individual electrons and ions to heat the plasma via free-free transitions (inverse Bremsstrahlung).[11] The laser power maintenance threshold depends upon the type of gas, the total pressure, whether the laser beam is horizontal or vertical (convection sweeps the hot gas out of the laser focal volume), the focusability or coherence of the laser beam, and the optical quality of the lens system. For example our work uses a 1-in. focal length ZnSe miniscus AR coated lens operated in the horizontal position with a transverse flow 1.5 kW CO_2 laser. The gases xenon, argon, and neon require 50, 300, and 1300 W, respectively for maintenance of the discharge. Because the focused power of the cw laser is in the range 10^6 to 10^7 W cm^{-2}, several orders of magnitude smaller than typical breakdown thresholds, a high energy external spark is needed to initiate the discharge. This can be provided by a conventional spark[12] or as in this work a pulsed CO_2 laser. The primary advantages of the laser sustained discharge in creating energetic atomic beams are the high temperatures produced by the high power densities (10^4 W-cm^{-3}), the ability to sustain the discharge independent of nozzle material, and low total input power. Preliminary results using xenon have been reported in ref. 12.

SOURCE CONSTRUCTION AND OPERATION

A cross-sectional view of the source is shown in figure 1 and consists of two portions, the lens holder and nozzle holder. The 1-in.-diam ZnSe AR coated miniscus lens is clamped to the end of a water-cooled copper tube. Indium gaskets are used to cushion and seal the lens as well as to provide maximum heat transfer to the copper. A threaded copper clamping ring is tightened onto the lens while heating the lens, holder, and indium to 50 to 70°C. This procedure provides excellent sealing of the lens onto the indium. The nozzle holder is made entirely of copper with all joints being welded rather than brazed. The nozzle body is made from a 3.2-mm platinum rod 3.2-mm long drilled to within 0.76 mm of one end to a diameter of 2.39 mm. The nozzle body is brazed into the end of the nozzle holder and the 0.2-mm- diam nozzle is then electron discharged machined through the 0.76-mm wall. A 3-mm-thick copper wall separates the platinum nozzle from the water cooling jacket. A double viton O-ring is used to seal the lens and nozzle holders and to locate the lens concentric with the nozzle.

Figure 2 shows the source mounted in the molecular beam scattering apparatus and aligned with both the plasma sustaining cw (maximum power 1.8 kW) and plasma initiating pulsed (0.5 J) CO_2 lasers. The output of the cw laser traverses the length of a 3.2-m laser table and is reflected back and turned 45° to enter the source assembly. Both copper turning mirrors (M1 and M2) are water cooled. The pulsed laser beam is placed nearly coaxial to the cw beam using the set of copper coated glass mirrors (M3, M4, and M5). Initial alignment of the cw, pulsed, and HeNe laser beams is accomplished by burning a pinhole in a 0.1-mm-thick nickel foil using the cw laser and then adjusting the pulsed laser turning mirrors to place it through the same hole. The cw CO_2 laser is then turned off, the mirror M6 placed in the path of the cw beam, and the HeNe laser is aligned to pass through the pinhole.

Final alignment of the cw laser beam with the nozzle is accomplished through operation of the source with argon and optimizing the time-of-flight distributions for maximum velocity by moving the discharge radially using the final turning mirrors M1 and M2 and axially by movement of the ZnSe lens. After initiating and aligning the discharge using argon, other gases are mixed with the argon to obtain radical species with velocities <5 km/s. If velocities greater than 5 km/s are desired, the argon is replaced with neon yielding velocities <10 km/s.

BEAM CHARACTERIZATION

Beam characteristics are depicted in the TOF distributions of figures 3, 4, and 5. The time-of-flight (TOF) analyzer used for these studies consisted of a 12.5-cm-diam disk rotated at 310 Hz with 8 equally spaced 1-mm slots located on its circumference. The TOF analyzer is calibrated using low pressure (200 torr) room temperature expansions of neon, argon, and krypton gases. The ion energy in the quadrupole mass spectrometer detector[12] was found to be 10 eV (25-cm path length) and the neutral flight path length was 19.5 cm. The entrance to the detector was a round 0.152-mm-diam hole. Slots (0.2-mm wide) below each 1-mm slot are used to obtain timing signals from a light bulb and photocell detector. This timing signal was used to control a 256 channel multichannel scaler having a 2-μs dwell time/channel which was used to record the time-of-flight (TOF) spectra. The TOF spectra shown have not been corrected for ion flight times, timing mark offset (12 μs), or instrumental broadening. The reported velocities were obtained by correcting for ion flight times and timing mark offsets but not instrumental broadening.

The calculation of molecular dissociation follows that of Lee,[3]

$$R = N_0/N_{0_2} \tag{1}$$

$$= (x_D/x_{0_2})/\eta\ (x_{0_2}/x_0)(I_0-\eta\ I_{0_2})/I_{0_2}$$

$$\%\ \text{dissociation} = R/(R+2) \tag{2}$$

where I_0 and I_{0_2} are the experimentally observed number density signals at mass 16 and 32 with the discharge on, η is the ratio of number densities of mass 16 and 32 with the discharge off, x_D is the dissociative ionization cross section of O_2 to form O^+, $x_D = 0.88$ A^2, and x_i are the ionization cross sections which we have taken to be,

$$x_{0_2} = 1.52 \text{ Å}, \text{ and } x_0 = 1.15 \text{ } A^2 \quad .$$

Figure 3 shows argon TOF distributions with the discharge off and on. The velocities with the discharge on were calculated to be 4.2 km/s for argon and 6.9 km/s for neon with the discharge slightly backed away from the nozzle. Our previous work[12] with xenon predicted that the argon and neon velocities would be 3.6 km/s and 6 km/s, respectively, indicating that a crude estimate of other gas velocities (V_m) can be obtained using the formula[12]

$$V_m = V_{Ar}(40/m)^{1/2} \ (T_m/T_{Ar})^{1/2} \qquad (3)$$

where m is the mass of the carrier gas, the subscript Ar refers to argon, and T_m is the plasma spectroscopic temperature of the carrier gas.[10]

Figures 4 and 5 show TOF spectra for mass 16 and 32 with oxygen mixtures of 40% and 49%, respectively. Essentially 100% dissociation of O_2 into O-atoms was observed with the 40% oxygen argon mixture while a 49% mixture produces 98% dissociation indicating that increasing amounts of oxygen may produce recombination within the nozzle.

The extent of dissociation is highly dependent upon the placement of the discharge within the nozzle; small changes in the radial or axial position can easily produce ratios of O-atoms to O_2 of 50%. Figure 6 shows the effect that a 0.5-mm axial change in the discharge placement in the nozzle has on the gas velocity distribution. As the discharge is moved farther into the nozzle the velocity distribution becomes broader and peaked at higher velocities. The plasma acts as a plug when placed in the nozzle and the initial density (10^{20} cm^{-3}) drops by a factor of roughly 100 to values of 10^{18} to 10^{17} cm^{-3} due to the high temperature of the plasma. At the higher plasma temperature a decrease in the total collision cross section would also be expected.[13] This creates a condition in which the nozzle is operating at a Knudsen number close to unity or in the transition region between hydrodynamic and free molecular flow thus causing a broadening of the velocity distribution. The higher peak velocities are observed because cooler boundary layers in front of the discharge are reduced in intensity.

O-ATOM EXPOSURE FACILITY

Figure 7 shows a diagram of the O-atom beam exposure facility. The beam source is pumped by a 2000 l/s diffusion pump while the two downstream differential pumping chambers are pumped with 500 l/s turbomolecular pumps. The

scattering chamber is equipped with a 1500 l/s turbomolecular pump. A water cooled boron nitride skimmer is used to extract the O-atoms from the expansion and to isolate the nozzle chamber from the first differential pumping stage. A remotely operated straight-through valve on the nozzle chamber allows that chamber to be vented for nozzle replacement without venting the remaining apparatus.

A rotatable quadrupole mass spectrometer detector employing a Brink[14] type ionizer is shown along with the time-of-flight chopper. The three-stage, differentially pumped detector has an angular resolution of 1° and a detection sensitivity of 10^{-4}, i.e., one ion is produced for every 10,000 neutrals entering the ionizer.

The port opposite the nozzle source houses a spinning rotor viscometer[15] and calibrated leak which are used for absolute measurements of beam flux. In addition hardware exists for coupling flight mass spectrometers to the system for calibration. The flux (Q) entering the mass spectrometer is calculated from the equation

$$Q = \rho \cdot S$$

where ρ is the absolute number density measured by the calibrated spinning rotor gauge while S is the calculated effusive conductance out the entrance aperture slit of area A_0

$$S = \frac{1}{4} \cdot A_0 \cdot \sqrt{\frac{8\ kT}{\pi m}}$$

where k = Boltzmann's constant (1.38×10^{-16} ergs molecule^{-1} K^{-1}), T is the wall temperature (Kelvin), and m is the mass of a molecule (grams). Mass spectrometer measurements of O-atoms are then related to this flux Q. Figure 8 shows some representative mass spectra taken with a flight instrument provided by the Air Force Geophysics Laboratory. The primary background is water vapor (10^{-8} torr) and N_2. Lower pressures can be obtained through the use of a liquid nitrogen cryoshroud and mild heating (100°C) of the system.

GAS-SURFACE SCATTERING

Initial results of gas scattering from an uncharacterized nickel surface are presented in figures 9 and 10. The molecular beam apparatus described in ref. 12 was used along with a pseudorandom sequence TOF chopper. The TOF detector is operated at 400 Hz with the multichannel scaler operating with a dwell time/channel of 10 μs. Angular distributions were obtained by modulating the direct beam at 400 Hz with a tuning fork chopper while data was accumulated with a phase locked pulse counter. The TOF chopper was kept in operation during angular distribution measurements. Counting times of 2 min/angle were used for angular distributions and 5 min/angle for TOF acquisition. These initial experiments focused on large incident angle (70°) scattering because of the ease of observing both the direct and scattered beams. The discharge source was operated with a 50% mixture of oxygen and argon with

the axial position of the discharge slightly back of the nozzle (velocity was not optimized). Figure 9 shows strong specular scattering of atomic oxygen over the angular range accessible to the detector indicating predominantly direct scattering with surface residence times on the order of the collision time. Figure 10 shows TOF spectra taken at the specular angle 70° and at 80° from the surface normal for both atomic and molecular oxygen. The data of figure 10 when converted to translational energy indicates that approximately 1/2 the initial beam energy was lost to the solid. The surface was not characterized but most likely consisted of nickel oxide with overlayers of O_2. Further experiments are in progress to obtain angular distributions near the surface normal to determine the extent of energy accommodation and to fully characterize the surface.

CONCLUSION

An O-atom exposure facility has been described which consists of (1) a cw laser sustained discharge source of O-atoms having a variable energy up to 5 eV and an intensity of between 10^{15}-10^{17} O-atoms s^{-1} cm^{-2}, (2) an atomic beam formation and diagnostics system consisting of various stages of differential pumping, mass spectrometer detector and time-of-flight analyzer, (3) a spinning rotor viscometer for absolute O-atom flux measurements, and (4) provision for using the system for calibration of flight instruments.

A new beam source has been described that uses a laser sustained plasma technique for producing high intensity ($>10^{18}$ s^{-1} sr^{-1}) and high translational energy (>2 eV) beams. Data indicates that beam temperatures near the plasma spectroscopic temperature can be obtained and that data from one gas can be used to predict results from others. Atomic oxygen beam energies of 2.5 to 3 eV have been produced with intensities of $\sim 4 \times 10^{18}$ s^{-1} sr^{-1}. Measurements have been taken that show the instrument capable of measuring both the extent of energy equilibration produced by high velocity collisions with engineering type surfaces and nonreactive scattering angular distributions of O-atoms. This type of information along with reaction cross sections will provide the data base for computer modeling of Space Station interactions with LEO environment.

REFERENCES

1. Knuth, E. L.; Winicur, D. H.: J. Chem. Phys. 46 (1967) 4318). Knuth, E. L.; Rodgers, W. E.; Young, W. S.: An Arc Heater for Supersonic Molecular Beams, Rev. Sci. Instr. 40 (1969) 1346.

2. Silver, J. A.; Freedman, A.; Kolb, C. E.; Rahbee, A.; Dolan, C. P.: Supersonic Nozzle Beam Source of Atomic Oxygen Produced by Electric Discharge Heating; Rev. Sci. Instr. 53 (1982) 1714.

3. Lee, Y. T.; Ng, C. Y.; Buss, R. J.; Sibener, S. J.: Development of a Supersonic $O(^3P_J)$, $O(^1D_2)$ Atomic Oxygen Nozzle Beam Source, Rev. Sci. Instr. 51 (1980) 167.

4. Grice, R.; Gorry, P. A.: Microwave Discharge Source for the Production of Supersonic Atom and Free Radical Beams, J. Phys. E12 (1979) 857.

5. Campargue, R.: Progress in Overexpanded Supersonic Jets and Skimmed Molecular Beams in Free-Jet Zones of Silence; J. Phys. Chem. 88 (1984) 4466.

6. Ardenne, M. V.: Tabellen der Elektronenphysik, Ionenphysik and Ubermikroskopie., Veb Deutscher Verlag Der Wissenschafter, Berlin (1956), pg. 507.

7. Razier, Y. P.: The Feasibility of an Optical Plasmatron and It's Power Requirements; ZhETF Pis. Red. 11 (1970) 195 [JETP Lett. 11 (1970) 120].

8. Razier, Y. P.: Subsonic Propagation of a Light Spark and Threshold Conditions for Maintenance of a Plasma by Radiation; Zh. Eksp. Teor. Fiz. 58 (1970) 2127 [Sov. Phys. JETP, 31 (1970) 1148].

9. Razier, Y. P.: Laser Induced Discharge Phenomena. Consultants Bureau, New York (1977).

10. Kozlov, G. I.; Kuznetsov, V. A.; Nasyukov, V. A.: Sustained Optical Discharge in Molecular Gases; Zh. Tekh. Fiz., 49 (1979) 2304 [Sov. Phys. Tech. 49 (1979) 1283].

11. Hughes, T. P.: Plasmas and Laser Light. John Wiley, New York (1975).

12. Cross, J. B.; Cremers, D. A.: High Kinetic Energy (1-10 eV) Laser Sustained Neutral Atom Beam Source; Nuc. Instr. and Methods, B13 (1986) 658.

13. Levine, R. D. and Bernstein, R.B.: Molecular Reaction Dynamics; Oxford University Press, New York (1974), p. 25.

14. Brink, G. O., Rev. Sci. Instrum., 37, 857 (1966).

15. Femerey, J. K.; J. Vac. Sci. Technol., 9, 108 (1972).

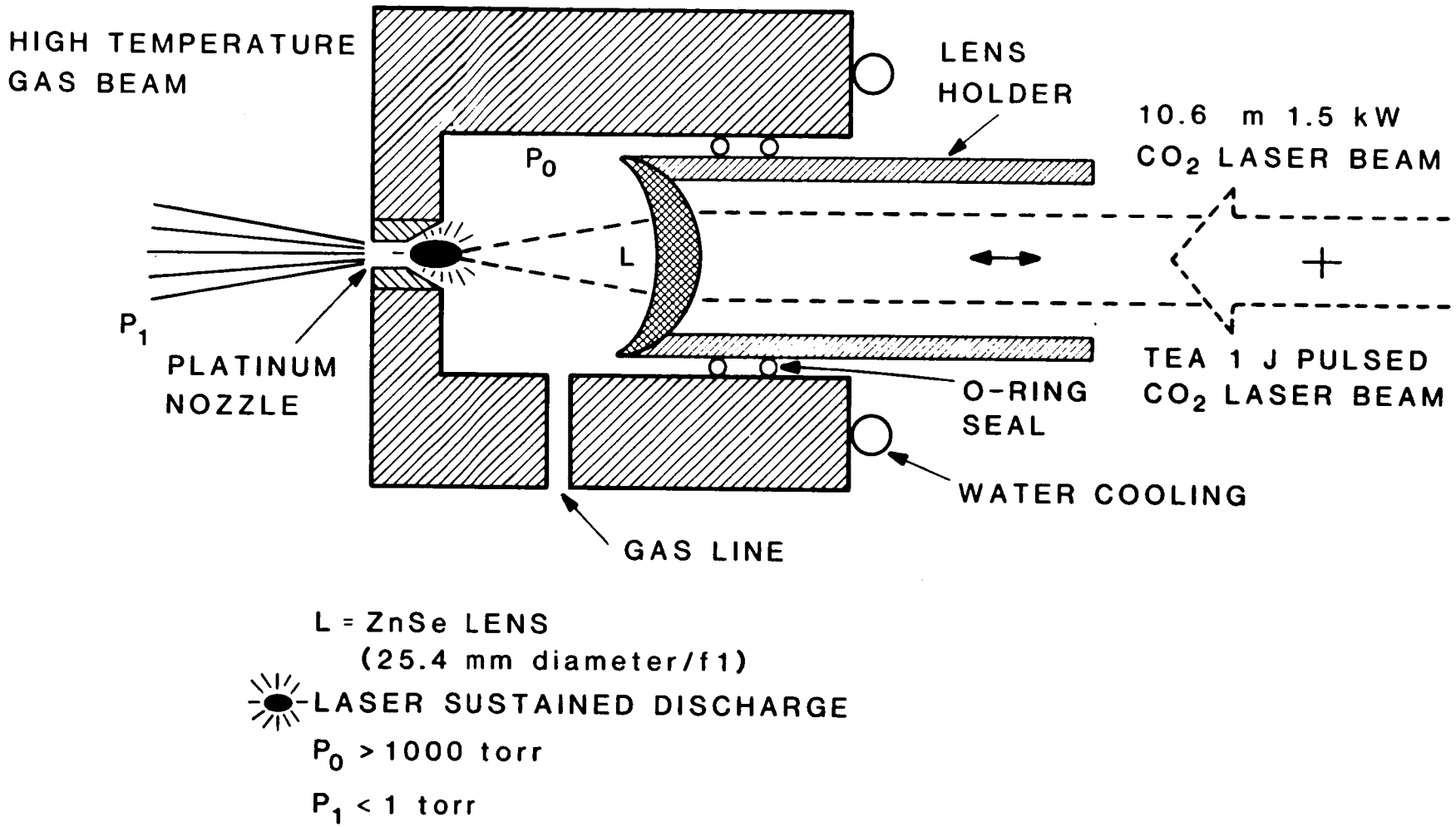

Figure 1. Laser sustained discharge atomic beam source: discharge is initiated using a pulsed (0.5 J) TEA CO_2 laser and sustained with a 1.5-kW CO_2 laser.

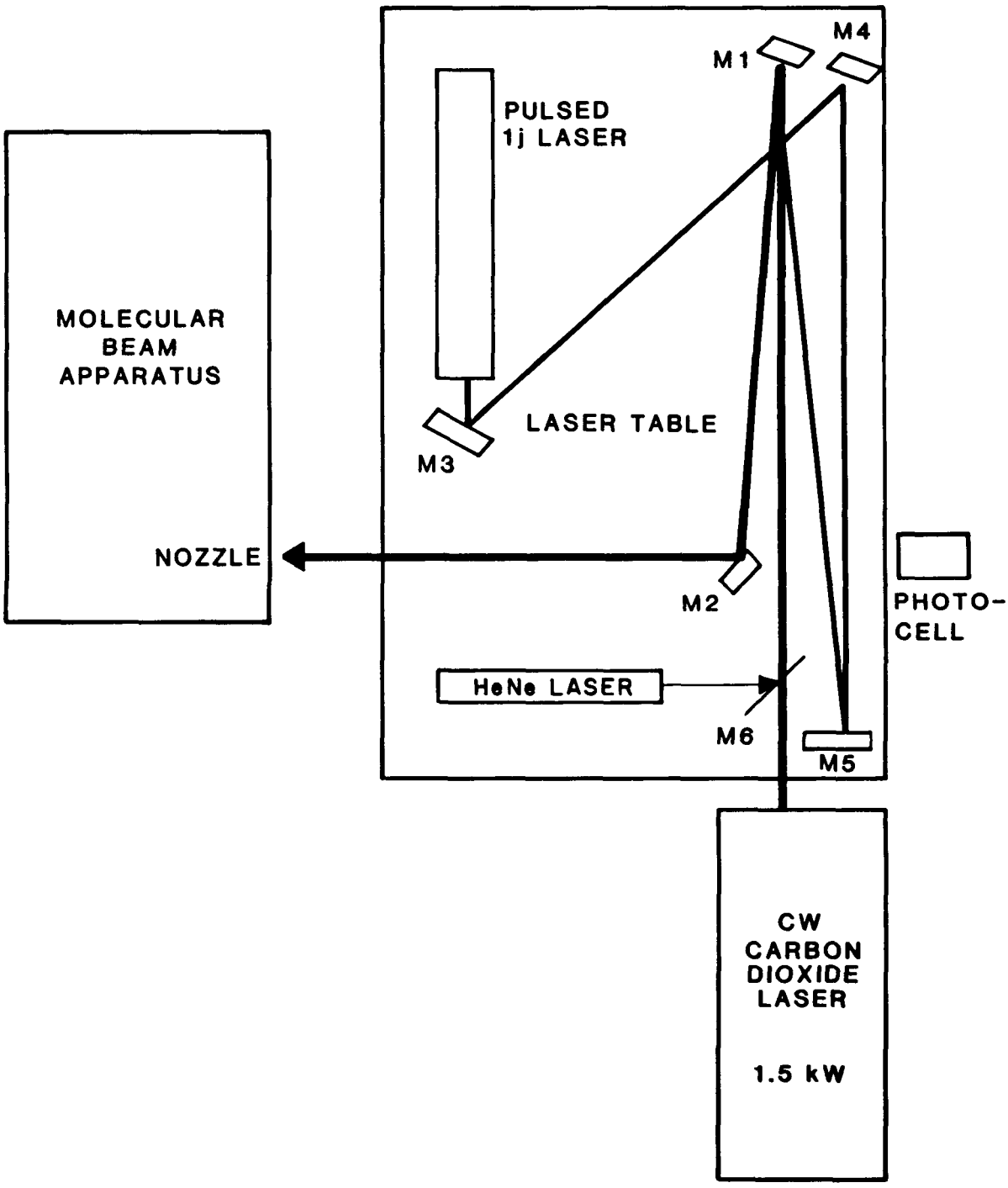

Figure 2. Alignment of pulsed and cw CO_2 lasers with nozzle. The 5-cm-diam water cooled mirrors M1 and M2 are used to align both the pulsed and cw lasers with the nozzle. Mirrors M3, M4, and M5 are used to align the pulsed laser with the cw laser. Mirror M6 employs a kinematic magnetic mount to place the HeNe laser beam co-axial to the cw laser beam. When operating the cw laser the mirror M6 is removed. The photocell detects the plasma light emitted from the nozzle assembly and interrupts the cw laser operation if the plasma is extinguished.

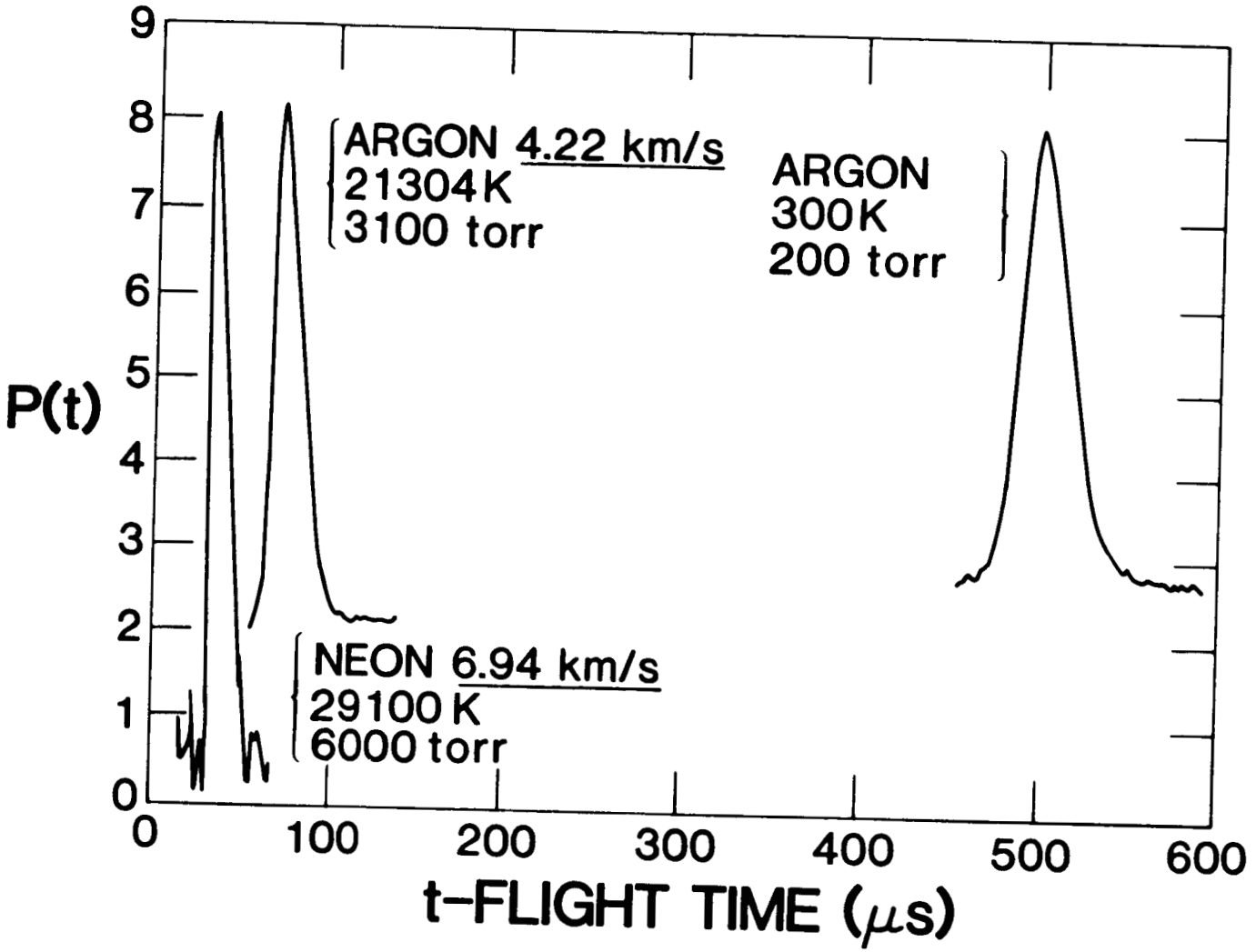

Figure 3. Argon and neon time-of-flight distributions. Flight times have not been corrected for timing mark offset or detector ion flight times.

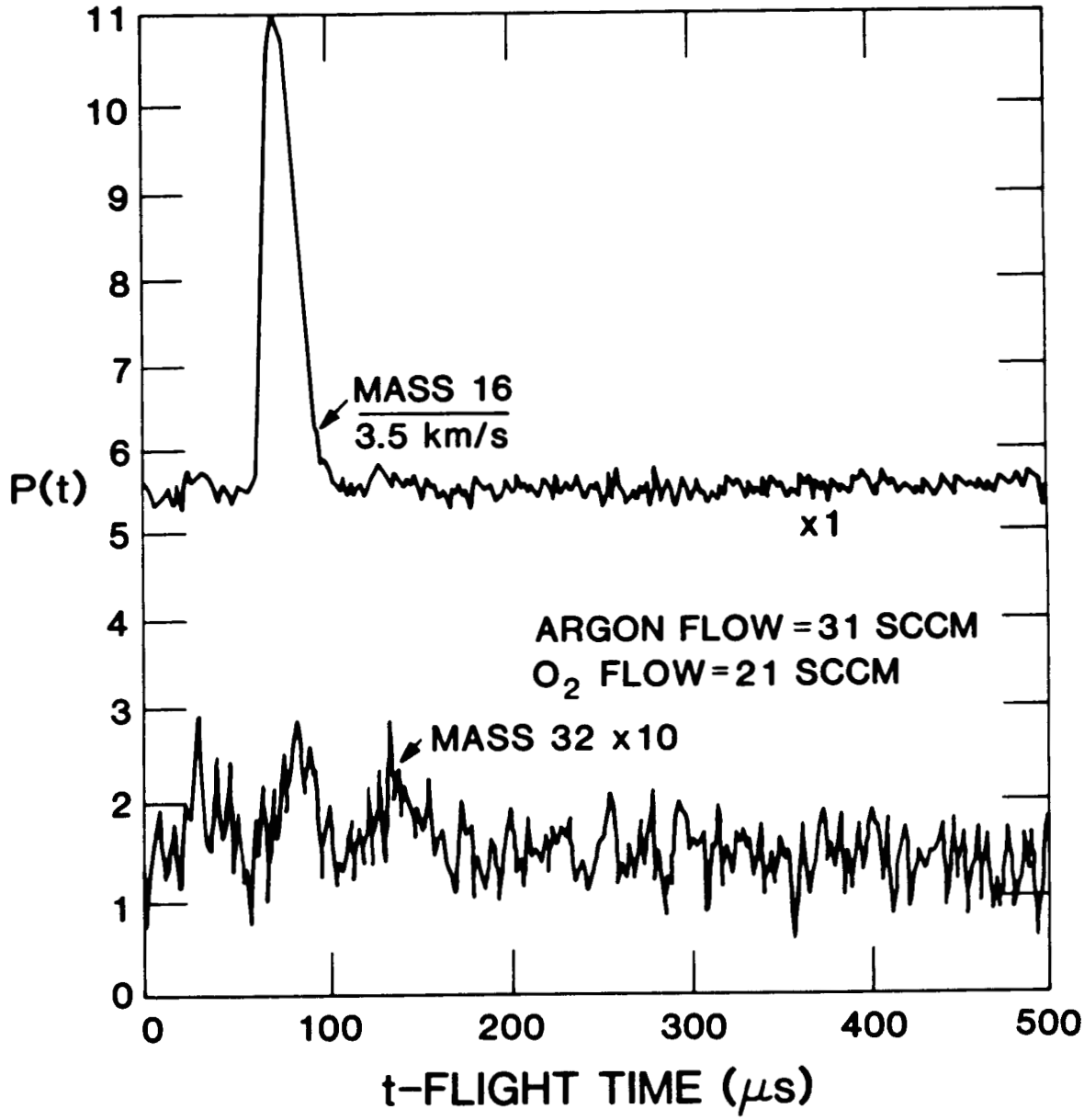

Figure 4. TOF Distribution of mass 16 and 32 using 40% O_2, 60% argon mixture.

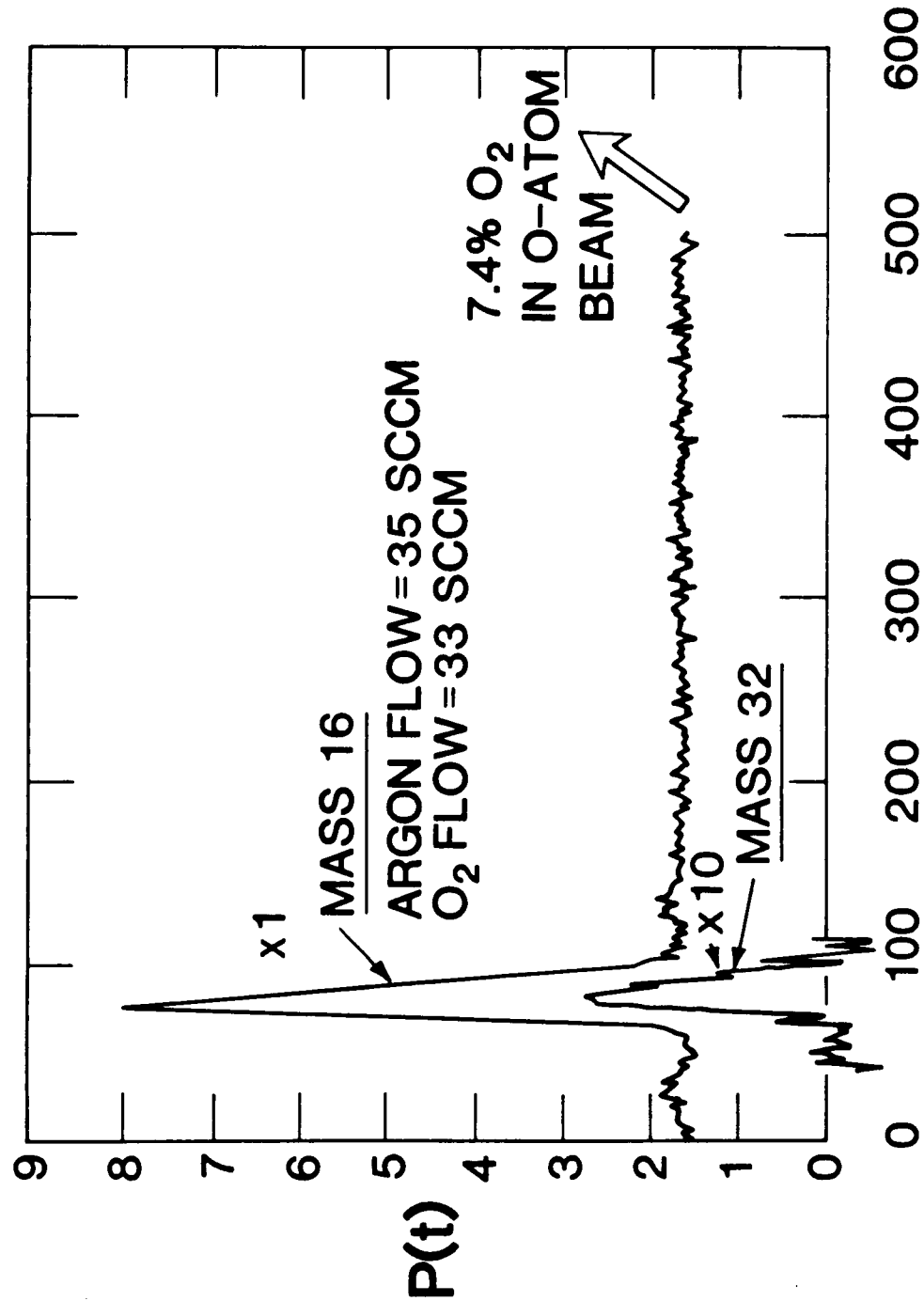

Figure 5. TOF distribution of mass 16 and 32 using 49% O_2, 51% argon mixture.

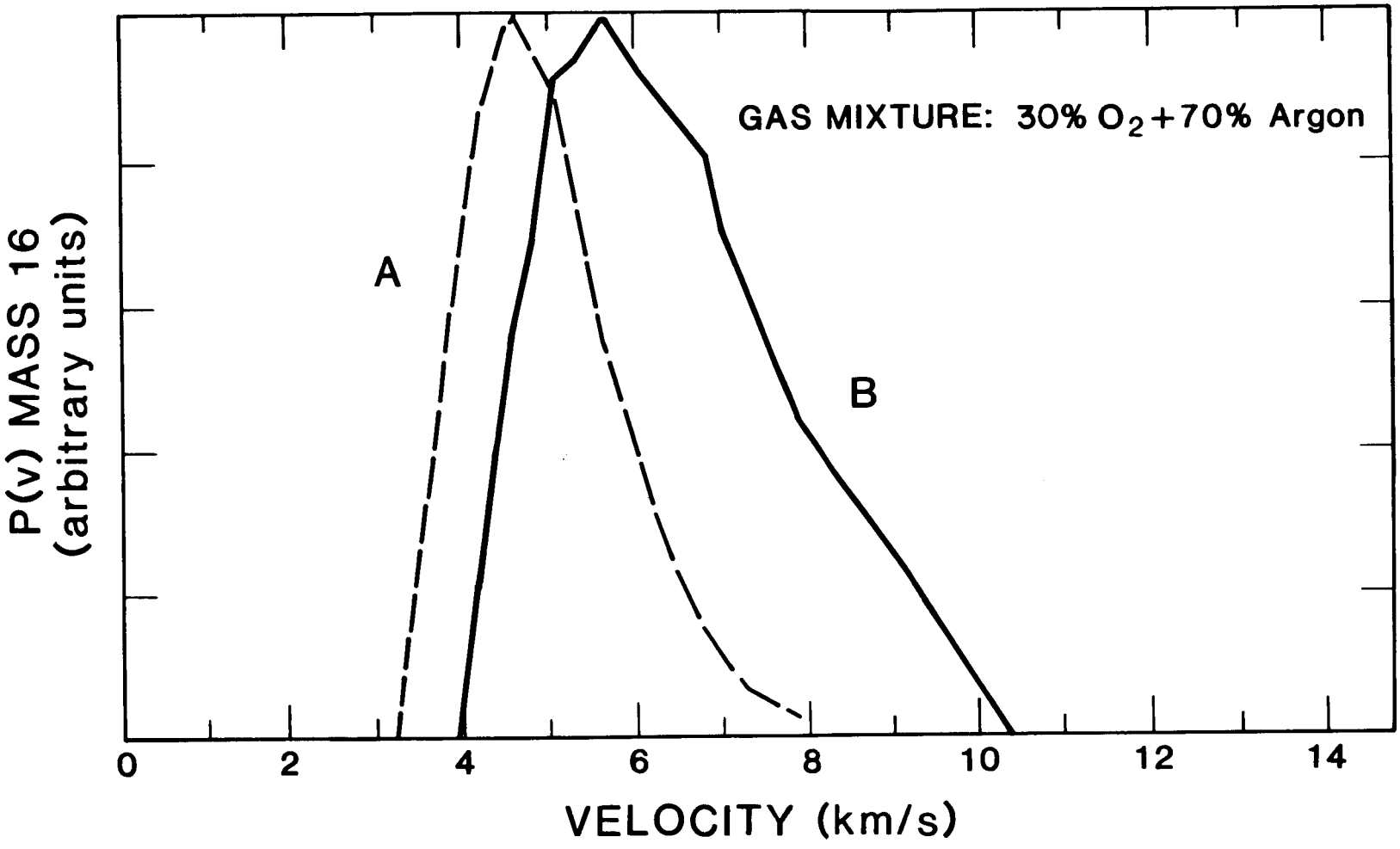

Figure 6. TOF distributions of mass 16 using a 30% O_2, 70% argon mixture. Distribution A was taken with the plasma at the entrance to the nozzle while distribution B was taken with the plasma moved 0.5 mm farther into the nozzle.

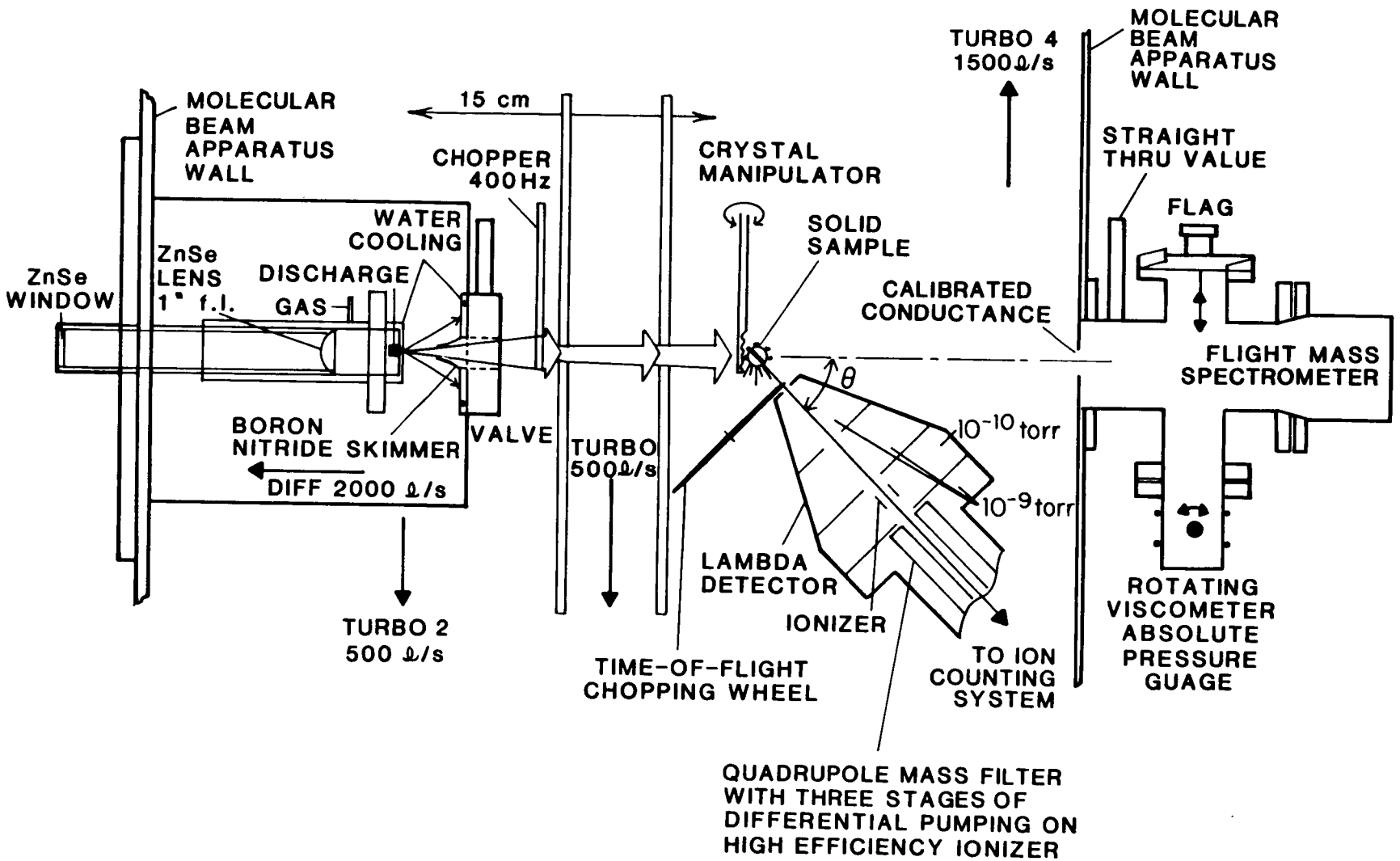

Figure 7. Los Alamos molecular beam dynamics apparatus: shows the central portion of the instrument including the molecular beam source, and movable detector. The detector is an electron bombardment ionizer-quadrupole mass spectrometer suspended from the rotatable lid of the main vacuum chamber and is used for the measurement of angular distributions. Also shown is a time-of-flight chopping wheel that provides 50% transmission efficiency using cross correlation techniques. Pumping of the system is accomplished by a 1500 1/s turbo on the scattering chamber, a 500 1/s turbo on the differential pumping chambers, a 2000 ℓ/s diffusion pump on the nozzle source and ion pumps on the detector.

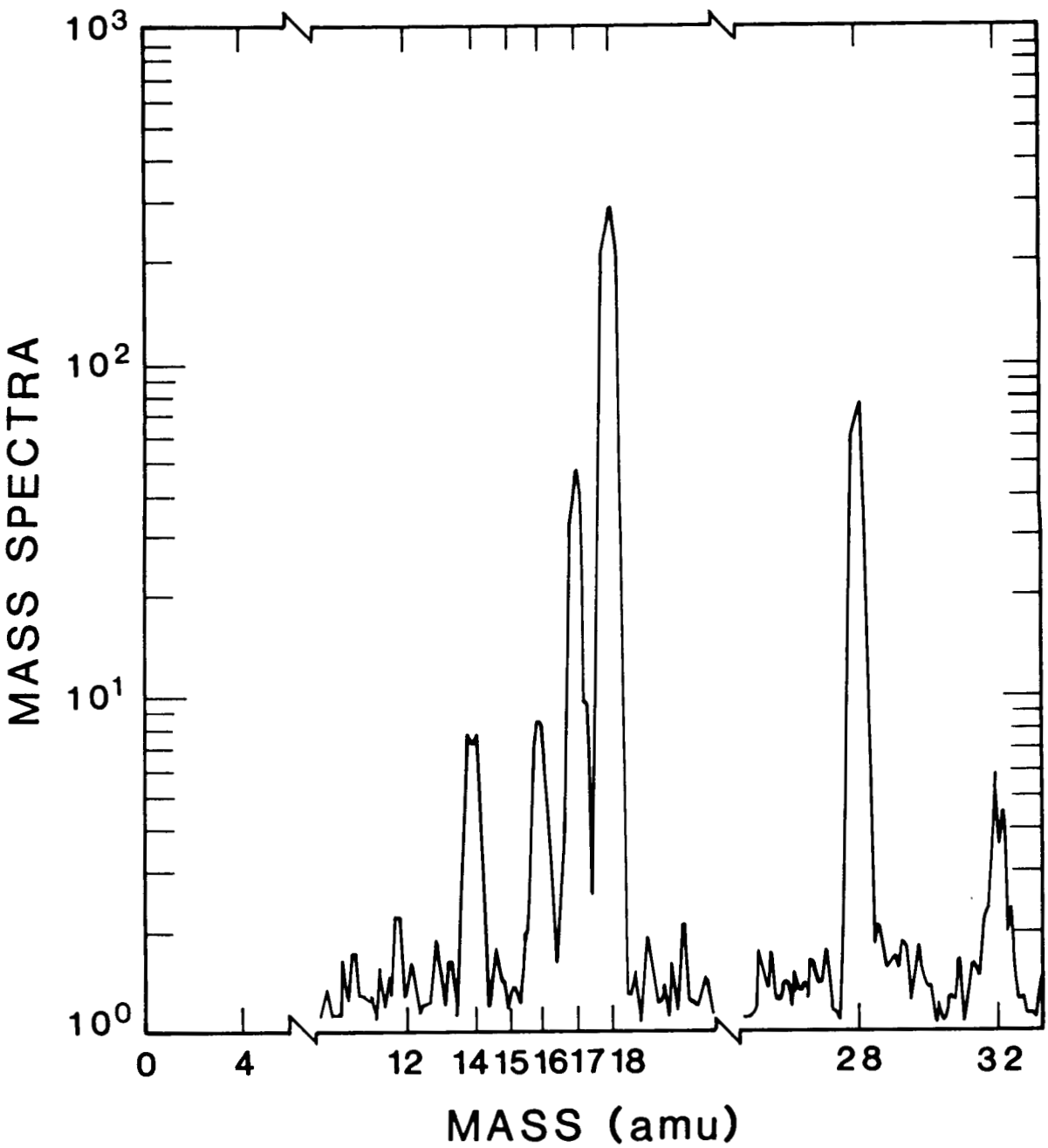

Figure 8. Background (3 x 10^{-7} torr) mass spectra taken with the AFGL flight mass spectrometer.

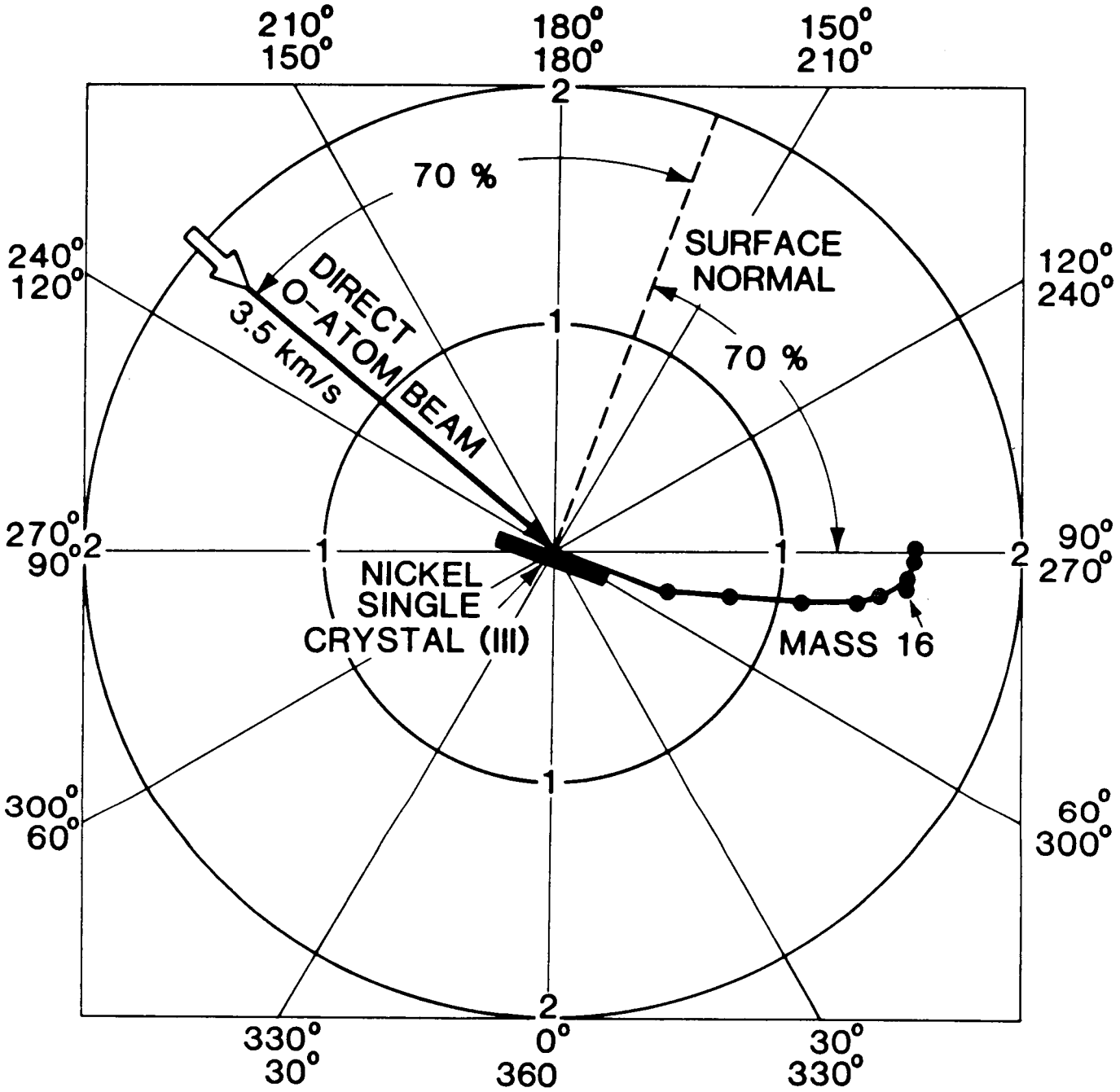

Figure 9. Angular distribution of O-atoms scattered from uncharacterized nickel crystal. Error bars on data points are the size of the plotting symbol. Surface temperature was 300 K.

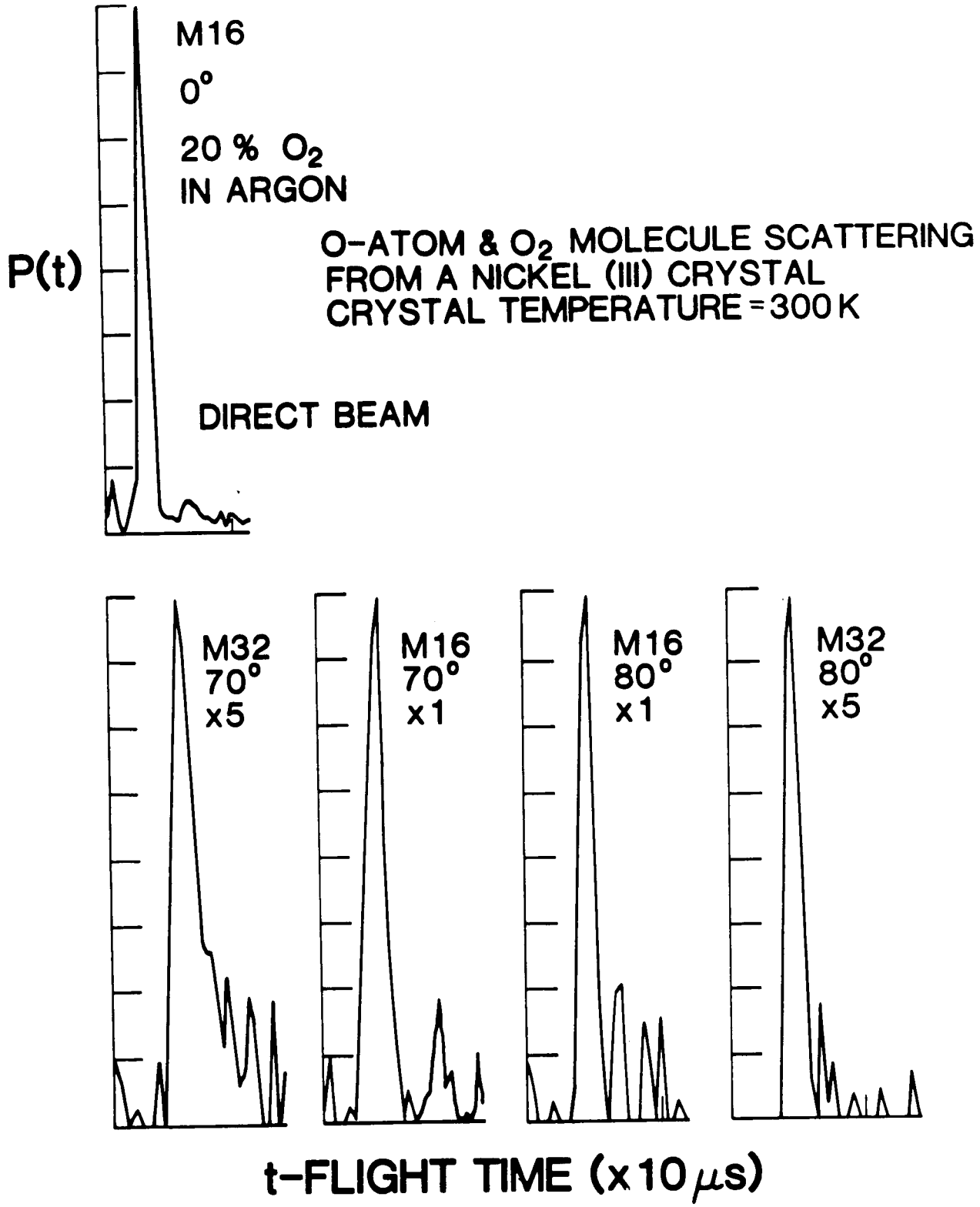

Figure 10. TOF distributions at 70 and 80° from surface normal. The mass 16 distribution when converted to energy indicates roughly 50% of the energy was transferred to the solid.

RAPID TOXICITY DETECTION IN WATER QUALITY CONTROL UTILIZING AUTOMATED MULTISPECIES BIOMONITORING FOR PERMANENT SPACE STATIONS

E. L. Morgan
Tennessee Technological University

R. C. Young
The Advent Group, Inc.

M. D. Smith
U.S. Tennessee Valley Authority

K. W. Eagleson
Department of Natural Resources and Human Development

ABSTRACT

Automated biomonitoring may provide real-time physiological response information as a result of cause/effect relationships between developing toxicity and representative aquatic animals. However, since the reliability of using information from a single-species or from selected water quality measures may be subject to question when viewed in light of developing toxicity, we developed a computer-assisted multiple species biosensing system for water quality monitoring. Because fish have typically been used in earth-based applications of automated biomonitoring and are assumed to be difficult to maintain in near zero gravity, emphasis was placed on developing methods for detecting species-specific bioelectric potentials induced by unrestrained mussels and other sedentary invertebrates. A specially designed differential amplifier was constructed for measuring signals induced by various activities from not only fish but invertebrate subjects. Specific responses were detected as discrete analog signals, each sign wave converted to a digital voltage, and filed in computer storage. A management program provided various means for data gathering, filing, and retrieval.

The objective of this study was to evaluate proposed design characteristics and applications of automated biomonitoring devices for real-time toxicity detection in water quality control on-board permanent space stations. Simulated tests in downlinking transmissions of automated biomonitoring data to earth-receiving stations were simulated using satellite data transmissions from remote earth-based stations.

INTRODUCTION

Computer-assisted automated biomonitoring systems used to detect developing toxicity in water quality surveillance programs have typically relied upon a single species, the fish, as the test subject. In a review by Cairns and

van der Schalie (ref. 1), representative early warning biological monitoring systems employing fish as biosensors and several innovative systems designed to measure invertebrate responses to water quality change were evaluated. From those described for detecting aquatic invertebrate movement activities, several devices were identified which included remote probe configurations for receiving action potentials generated when the animal's body integument changed positions (ref. 2). Applying similar techniques for water pollution monitoring, Idonlboye-obu (ref. 3) established a bioassay procedure where marine decapod action potentials could be detected under increasing exposure to toxic hydrocarbons. Incorporating a computer for data management, Macioroaski, et al. (ref. 4) evaluated crayfish abdominal movements as a measure of increasing water toxicity to aquatic animals.

Although automated biomonitoring devices may prove effective in detecting developing toxicity in certain specific applications, it seems unreasonable to expect a single-species or animal group to be universally responsive to the wide variety of pollutants which might contaminate space station water supplies. Recognizing the complex matrix of abiotic and biotic interrelationships and the episodic character of many closed water supply systems, the relative toxicity of certain substances may be modulated either through attenuating or amplifying processes. Therefore, to account for possible toxic modulatory effects and the bias of depending on a single-species for judging toxicity, the development of an automated multiple-species biological monitoring system employing groups of different types of aquatic animals representing various trophic levels could prove helpful to space station water management and quality control programs. The initial research and design for an automated multispecies biosensing device coupled with physical sensors capable of simultaneously deriving biotic response data and physical parameters has been discussed by Morgan and Young (ref. 5) and Morgan, Young, and Crane (ref. 6).

In meeting the objective of developing a computer-assisted multispecies biological monitoring system capable of giving an early warning of developing toxicity in water supplies, emphasis was placed on the following: (1) extending system versatility by developing techniques for detecting responses from a variety of aquatic invertebrates occupying different trophic levels, (2) developing a universal differential amplifier capable of detecting bioelectric responses from an array of different aquatic animals, (3) expanding amplifier and register interface units from groups of discrete in-put channels and coupling these with IBM-PC based systems, and (4) integrating these components and in-putting biological response information into a data collection platform for simulating downlinking to earth-based receiving stations.

SYSTEM DESIGN

BIOLOGICAL CONSIDERATION

Crucial to this effort was the observation that various unrestrained aquatic animals induce bioelectric signals into the surrounding water which can be recorded as rhythmic analogue signals representative of specific movement activities, i.e. gill beats, heart rates, etc. Utilizing appropriate techniques

and accompanying electronics, changes in bioelectric responses may be detected and processed with respect to possible water quality induced stress to the animal.

HOLDING CHAMBERS FOR ANIMALS

Design characteristics and specific configurations used for fish, mussel, and burrowing mayfly nymph maintenance while monitoring have been discussed previously (ref. 4, 5). In summary, housing individual free-swimming fish chambers consisted of PVC plastic tubes equipped with a pair of probe-antennae. Probes were designed to receive bioelectric potentials induced by each gill ventilatory response and were connected to appropriate electronics for detection. (Figure 1). Burrowing mayfly nymph chambers consisted of selected lengths of tygon or plastic tubing of various diameters, each configured with a set of micro-antennae. Once the nymph was established within the artificial tube chamber, bioelectric signals generated by the rhythmic peristaltic oscillation of its paired abdominal gills were easily detected by accompanying electronics.

Mussel myoelectric events were readily monitored by micro-probe antennae which were located between the mantle tissue and the inner valve of the animal. Caution was taken not to insert these into the tissue. Combined with gill action, foot muscle, and abductor muscle events, bioelectric responses generated by peristaltic contractions of the heart could be selected for and recorded.

A multiple species complement was realized by simultaneously monitoring groups of bluegill sunfish, heelsplitter mussel, and burrowing mayfly nymph artificial tube chambers. Artificial tube chambers containing individual nymphs were positioned in a subcontainer which was floated at the surface of the tank holding the mussels and fish chambers. Groups of four free-swimming individuals from each species were isolated from each other and electrodes connected to individual channels for data entry to the minicomputer.

COMPUTER-ASSISTED AUTOMATED MONITORING

Differential d. c. amplifiers were constructed that meet requirements for a wide range of water quality conditions and were flexible enough to detect weak bioelectric events from various aquatic animals (ref. 5). One amplifier was used for each animal and the gain and filter set to read the specific analog frequencies. Undesirable high frequencies were filtered at the initial stages of amplification. Amplifiers were interfaced to an IBM-PC compatible having various peripherals, including tape backup and modem. Analog response signals were digitized and stored in registers until inputed to the computer for filing on disk. The complete automated computer-assisted biomonitoring system (ACABS) was an updated version of the automated fish respiration monitoring system (AFIRMS), which was fabricated by the Data Services Branch, TVA (ref. 6).

SYSTEM TESTING

PREPARING ANIMALS FOR MONITORING

Using a continuous monitoring configuration, fish were individually isolated in plastic tube chambers which were placed in glass aquaria equipped with flow-through water exchange. Mussels were positioned on gravel substrates within the aquaria. Because mayfly nymphs displayed a tendency to abort artificial burrows made of tygon tubes, they were further isolated by placing an individual tube chamber housing a single nymph in a screen-bottomed plastic cylinder. This isolation cylinder was then submerged in the aquaria. Test subjects were allowed to acclimate for a week or more in isolation while receiving once-through lake water and prevailing photoperiods. Animals received food while acclimating to ambient conditions but not during test treatments.

BENCH TESTING MONITOR

Preliminary testing was done by selecting groups of acclimated individuals from each of three groups, i.e., bluegill, burrowing mayfly nymph, and heel-splitter mussel and continuously monitoring their bioelectric frequencies for a one- to three-day reference period. Then, two individuals from each group were selected as controls for a one-day treatment interval which followed. A one-day treatment was designed to simulate an acidic water supply where a pH depression between 5.5 and 4.5 was gradually achieved over several hours period. The initial ambient pH value ranged from 7 to 8. Treatment solutions were batch mixed lake water and were administered by interrupting reference lake water flows and allowing treatments to gradually replace ambient reference flows. Explosure to maximum pH depress persisted for 6 to 12 hours when reference lakewater was again delivered without altering flow rates. Following the acid exposure treatment, reference ambient conditions were reached within several hours while test subjects were continually monitored for the remaining few days of the recovery period.

Prior to acid treatments, a time-rated data base of bioelectric responses was developed from test fish maintained under ambient once-through lake water flows. This data base was then used as a reference for comparing changing stressful responses induced by acid water exposures (Figure 2).

DATA CAPTURE VIA SATELLITE

Referred to as a remote data collection platform (CDP), this self-contained computer which functions as a d. c. powered central controller and processor in conjunction with various communication modeules was used to simulate data capture via satellite downlinking. Features include expandable PROM/RAM memory, a programmable calendar/alarm clock, an S-34 controller port, RS-232 operator port, and being supported by the S-FORTH operating system.

Breathing events generated by individually monitored fish, for example, were received by the DCP in digital form. The data were held for a pretest monitoring interval by interface registers prior to submission to the DCP. Data presented to the DCP were transmitted to the NOAA-Geostationary Operational Environmental Satellite (GOES) six times daily. Broadcast data received by GOES were then retransmitted to a receiving station for processing (Figure 3). Depending on monitoring needs, simultaneous transmission of water quality parameters included: temperature, dissolved oxygen (DO), hydrogen ion concentration (pH), specific conductance, and oxidation-reduction (redox) potential. Physical sensors were positioned in-stream alongside fish-holding chambers.

PROPOSED WATER SOURCE TOXICITY TESTING

Coupled with existing methods for biological and chemical water quality testing of space station water supplies, automated biosensing may have merit as an early warning to developing problems. Such a protocol would eliminate the inherent weaknesses of relying on chemical/physical measures alone. Unlike most other biological test systems, the automated biomonitoring approach provides real-time detection of developing toxicity, continuously (ref. 1, 6).

CONCLUSION

Through previous studies using remote biosensing devices for water quality monitoring, a series of technical questions have surfaced which will require attention should automated biomonitoring be considered as part of an early detection to developing toxicity in water sources on permanent space stations. Specifically, even though fish have been used for more than a decade as test subjects in earth-based automated biomonitoring systems, little information is available on the effect of near zero gravity on fish breathing responses, much less that of other aquatic animals. Other concerns include: (1) To what extent will aquatic animals accommodate to sustained low gravity? (2) Will test animals need induced gravity in order to function appropriately? (3) How often will test subjects need to be fed or replaced? (4) What type holding chamber designs need testing? (5) Are automated multispecies biosensing devices appropriate for space station monitoring?

Realizing these needs and gaining insight through previous studies, reasonable answers to these questions will be forthcoming. Given the advanced state of technology, the primary concerns and areas requiring additional research deal almost entirely with those of a biological nature.

REFERENCES

1. Cairns, J., Jr.; and van der Schalie, W. H.: Biological Monitoring, Part I. Early Warning Systems. Water Research, Vol. 14, 1980, pp. 1179-1196.

2. Camougis, G.: Recording Bioelectric Potentials from Aquatic Animals. Turtox News, Vol. 38, 1960, pp. 156-167.

3. Idonlboye-obu, B.: Recording Bioelectric Action Potentials of Marine Decapod Crustacea by Remote Electrodes: A Bioassay Procedure for Monitoring Hydrocarbon Pollution. Environ. Pollut., Vol. 12, 1977, pp. 159-166.

4. Macriorowski, A. F.; Cairns, J., Jr.; Benfield, E. F.: Laboratory Simulation of an In-Plant Biomonitoring System Using Crayfish Activity Rhythms to Detect Cadmium Induced Toxic Stress. 25th Annual Meet. North Amer. Benthological Soc., Roanoke, VA, April 6-8 (Abstract), 1977.

5. Morgan, E. L.; and Young, R. C.: Automated Fish Respiratory Monitoring System for Stream Acidification Episode Assessment. Verh. Internat. Verein. Limnol., Vol. 22, Part 3, 1984, pp. 1432-1435.

6. Morgan, E. L.; Young, R. C.; and Crane, C.: Automated Multi-Species Biomonitoring Employing Fish and Aquatic Invertebrates of Various Trophic Levels. Freshwater Biological Monitoring, Pergamon Press, Oxford, England, 1984, pp. 75-80.

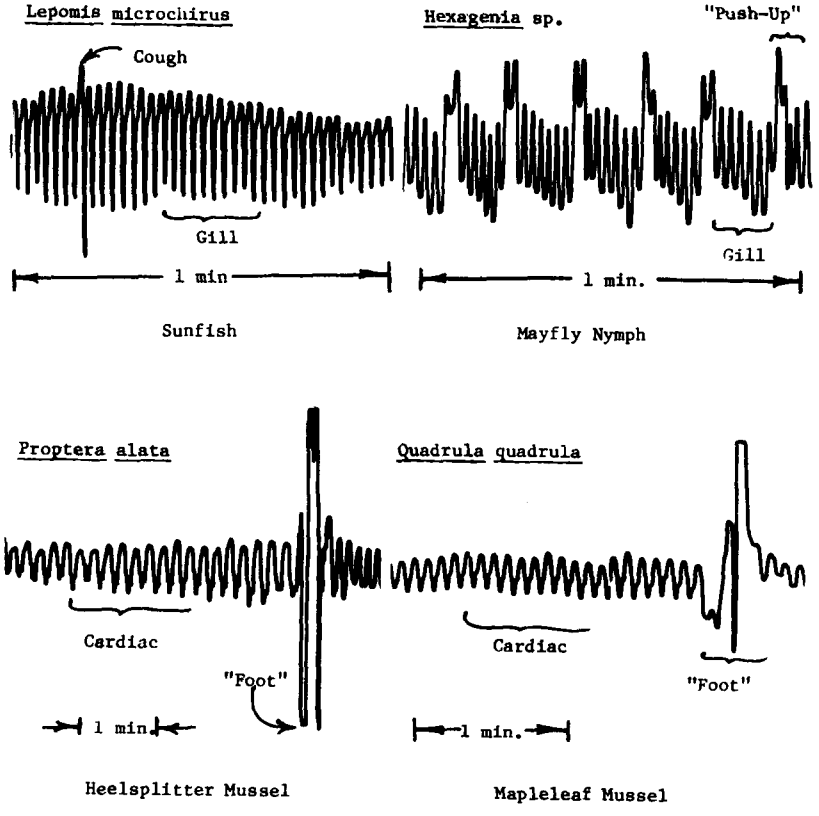

FIGURE 1. REPRESENTATIVE PHYSIOLOGICAL RESPONSES MONITORED UNDER AMBIENT WATER QUALITY EXPOSURES BY AUTOMATED MULTISPECIES BIOSENSOR AT REMOTE STREAMSIDE STATION, CENTER HILL LAKE, TENNESSEE

REFERENCE

Frequency Distribution

Group	Freq	%Freq	Cum.Freq.	%Cum.Freq.	Midpoint	Histogram
1	4	0.4	4	0.4	10.27E+00	:*
2	23	2.2	27	2.6	12.20E+00	:***
3	29	2.8	56	5.4	14.14E+00	:****
4	36	3.5	92	8.8	16.07E+00	:*****
5	60	5.8	152	14.6	18.01E+00	:*********
6	113	10.9	265	25.5	19.94E+00	:**********
7	154	14.8	419	40.3	21.88E+00	:**********
8	158	15.2	577	55.5	23.81E+00	:**********
9	131	12.6	708	68.1	25.75E+00	:**********
10	110	10.6	818	78.7	27.68E+00	:**********
11	90	8.7	908	87.3	29.62E+00	:**********
12	56	5.4	964	92.7	31.55E+00	:********
13	33	3.2	997	95.9	33.49E+00	:*****
14	20	1.9	1017	97.8	35.42E+00	:***
15	5	0.5	1022	98.3	37.36E+00	:*
16	9	0.9	1031	99.1	39.29E+00	:*
17	3	0.3	1034	99.4	41.23E+00	:
18	3	0.3	1037	99.7	43.16E+00	:
19	0	0.0	1037	99.7	45.10E+00	:
20	2	0.2	1039	99.9	47.03E+00	:

TEST

Group	Freq	%Freq	Cum.Freq.	%Cum.Freq.	Midpoint	Histogram
1	24	5.3	24	5.3	16.78E-01	:********
2	11	2.4	35	7.8	50.33E-01	:****
3	9	2.0	44	9.8	83.87E-01	:***
4	9	2.0	53	11.8	11.74E+00	:***
5	8	1.8	61	13.6	15.10E+00	:***
6	10	2.2	71	15.8	18.45E+00	:***
7	7	1.6	78	17.4	21.81E+00	:**
8	18	4.0	96	21.4	25.16E+00	:******
9	53	11.8	149	33.2	28.52E+00	:**********
10	60	13.4	209	46.5	31.87E+00	:**********
11	48	10.7	257	57.2	35.23E+00	:**********
12	58	12.9	315	70.2	38.58E+00	:**********
13	50	11.1	365	81.3	41.94E+00	:**********
14	36	8.0	401	89.3	45.29E+00	:**********
15	16	3.6	417	92.9	48.65E+00	:*****
16	13	2.9	430	95.8	52.00E+00	:****
17	14	3.1	444	98.9	55.36E+00	:*****
18	4	0.9	448	99.8	58.71E+00	:*
19	0	0.0	448	99.8	62.07E+00	:
20	1	0.2	449	100.0	65.42E+00	:

Fisher's Least Significant Difference Test

LSD	Difference	Test Result
.816044	8.504669	SIGNIFICANT

FIGURE 2. BREATHING RESPONSE OF BLUEGILL SUNFISH SUBJECTED TO SUBTLE ACIDIFICATION

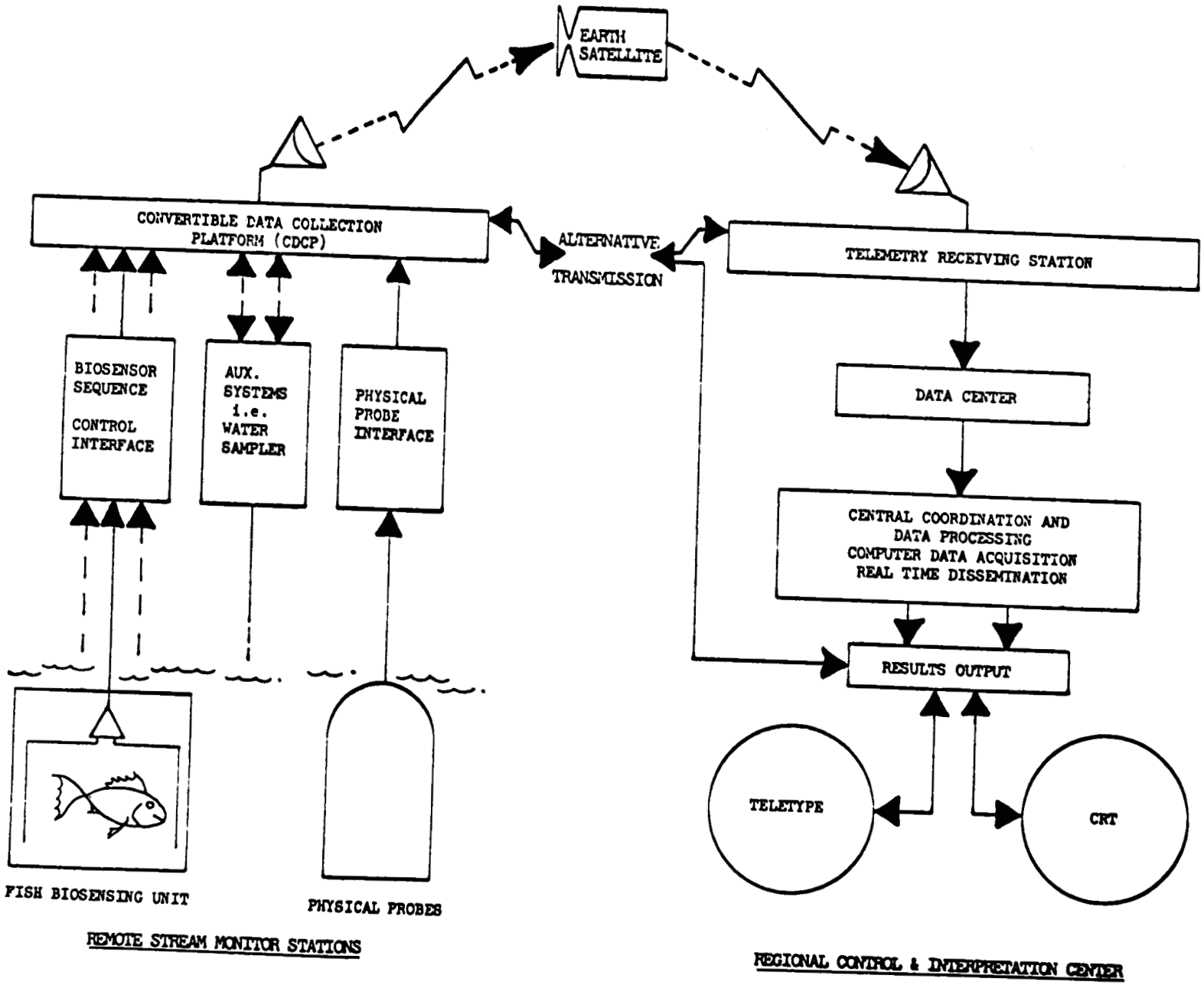

FIGURE 3. CONFIGURATION FOR SATELLITE DATA TRANSMISSION FROM REMOTE BIOMONITOR

CHARACTERISTICS AND PERFORMANCE OF THE ESTEC LARGE SPACE SIMULATOR CRYOGENIC SYSTEM

H. Amlinger
Leybold Heraeus, Hanau, Germany

S. J. Bosma
ESA/ESTEC, Noordwijk, The Netherlands

ABSTRACT

With a solar beam of 6 meters, the Large Space Simulator (LSS) at ESTEC, The Netherlands, is one of the world's largest solar simulation facilities (ref. 1).

The design of the LSS cryogenics system, however, provides the facility with the intended flexibility to serve for a variety of thermal test configurations, in addition to solar simulation and mechanical tests. The operational concept of the cryogenics system foresees in automated control of more than 20 modes of operation.

The liquid nitrogen (LN_2) cool-down and circulation circuit as well as the gaseous nitrogen (GN_2) warm-up circuit are completely separated and have individual control of system parameters. Both, the main chamber shroud elements (C1) and the auxiliary chamber (C2) baffle shrouds, can be operated independently or in combination.

Furthermore, it is possible to perform vacuum thermal cycling tests (VTC) by controlling the C1 shroud at temperature levels variable between 100°K and 373°K. The paper presents the final concept and performance characteristics of the LSS cryogenic system.

INTRODUCTION

The performance of the cryogenic system is based on the final acceptance test of the complete LSS facility, performed at ESTEC in April 1986.

The acceptance test involved both solar simulation at the specified 1.8 kW/m^2 radiation level and vacuum temperature cycling during continuous operation of the facility for 400 hours in various configurations. The LSS motion system, which is subject to another procurement contract, will be delivered in 1987 and as a result is not included in the cryogenic test configuration.

TEST ANALYSIS CONCEPT

The standard housekeeping data of the cryogenics system involves a variety of 60 sensors to measure system parameters as flow, level, pressure and temperature. More than 100 dedicated thermo-couples were applied to measure shroud temperatures during the acceptance test.

The data measured by the programmable logic controller (PLC) as well as the PLC status information, was sent to the LSS facility data handling system. The LSS facility data handling provided the following support functions:

- Presentation of data, temperatures, flows, pressure, etc.
- Presentation of system status, valve positions, on/off alarm status, interlocks.
- Presentation of graphs/sensors versus time print-outs, etc.
- Warning and alarm messages.
- Recording of data for problem investigation.
- Recording of data for test reporting.

These features provided high flexibility in adjusting system operations, short fault identification times and analysis of system performance.

Figure 1 shows a typical cool-down and warm-up curve.

THE LIQUID NITROGEN CIRCULATION CONCEPT

For the LN_2 circulation a closed loop pressurised system has been selected, because this concept represents the thermodynamically most suitable system for cooling large shrouds with low operation and investment cost.

In the closed loop pressurised system, the pressure of the liquid nitrogen is increased in the recirculating pump only to the extent needed for overcoming the flow losses in the shroud circuit. The necessary increase in the boiling temperature of the liquid nitrogen in front of the shrouds is achieved by raising the pressure level of the entire circuit so much above normal atmospheric pressure, that liquid nitrogen is available for all operating steps with high heat load.

The liquid nitrogen which is heated up in the shrouds, is cooled again in a heat exchanger and is subsequently immediately pumped back through the shrouds panels by the recirculating pump. The recirculated liquid nitrogen from the shrouds is cooled in the heat exchanger by liquid nitrogen which boils under atmospheric pressure.

In order to build up the necessary positive pressure in the circuit in front of the recirculating pump and for compensating the volume changes resulting from temperature changes, the circuit is connected to a partially nitrogen-filled expansion vessel at the point of lowest pressure in the system.

After the entire system, incl. the shrouds, has been cooled down to the boiling temperature of nitrogen, which occurs at atmospheric pressure, the circuit is raised to the necessary positive pressure by evaporating nitrogen with a reboiler heat exchanger in the expansion vessel. The desired pressure is built up in the expansion vessel by providing a nitrogen gas cushion above the liquid, which is pressure regulated by a closed loop control system.

In the LN_2 circulation mode, after the nitrogen has been cooled and equilibrium has been reached, no evaporation of the recirculated nitrogen occurs in the closed loop system. In contrast to the open pressurised system, the energy for increasing the boiling pressure must be supplied only once when the system is taken into operation.

Since, during this process, the recirculating pump sucks in liquid nitrogen, which is already at a correspondingly high pressure (high NPSH), the risk of cavitation in the recirculating pump, which can occur in the open systems, is eliminated.

The LN_2 inlet temperature of the shrouds is appr. 78°K and the outlet temperature about 83°K. To avoid local boiling of LN_2, the selected system pressure is 8 bar which corresponds with a boiling temperature of 100°K.

The system pressure is controlled by a pressure controller. If deviations from the adjusted setpoint occur, either vaporised N_2 is generated to the expansion vessel or released to the atmosphere if the adjusted pressure is exceeded.

The shrouds in C1 and C2 are subdivided into various circuits (see figure 2); each of them is equipped with flow and temperature measuring control units, installed in the circuit outlet line. By this means, it is possible to adjust individual flow rates, so that an equal temperature difference is provided over each shroud circuit.

The LN_2 nitrogen reboiler has a temperature difference of appr. 5°K between inlet and outlet and is cooled by evaporating LN_2.

THE GASEOUS NITROGEN CIRCULATION CONCEPT

The GN_2 system circulates gaseous nitrogen over the shrouds of the main chamber and auxiliary chamber by means of a rotary piston blower. The suction-side of the blower is protected by a water bath / heat exchanger, which provides either cooling or heating of the incoming gaseous nitrogen to maintain the specified blower temperature limitations.

On the pressure side of the blower, an additional heater is used during the warm-up mode to heat up the shrouds to any temperature level between 273°K and 373°K. A smaller dimension blower / heat exchanger combination is used to maintain the main chamber shrouds at ambient temperature, while the auxiliary chamber shrouds C2 are warmed-up with GN_2.

The GN_2 circuit has alarm and control functions of main system parameters, which are independent of the LN_2 system. Furthermore, each shroud circuit has a separate set of isolation and control valves for LN_2 and GN_2 circulation, so that a wide variety of operational modes is feasible.

VACUUM TEMPERATURE CYCLING MODE

The VTC mode envisages cooling and heating of the main chamber shrouds over a specified temperature range of 173°K to 373°K with a speed of 1°K/min. The VTC mode has been implemented by the addition of a LN_2 injection system into the GN_2 circuit.

A temperature controller works in split range technique and activates either the LN_2 injection valve or the GN_2 heater according to the shroud temperature set-point. A counter flow heat exchanger has been included in the GN_2 circuit to economise the LN_2 consumption.

CRYOGENIC SYSTEM PERFORMANCE

LN_2 COOL-DOWN AND CIRCULATION MODES

Table 1 lists a comparison of the design baseline to the actual system performance, which proves that the requirements have been adequately met. The cool-down / circulation mode is performed and controlled fully automatically by the programmable logic control (PLC).

The maximum temperature increase over the shrouds following switch-on of the sun simulator to the specified 1.8 kW/m^2 solar intensity was measured at 3°K in the 400 hours test configuration. As a result, the LN_2 flow rates through the individual shroud circuits do not have to be modified in dependence of solar intensity levels, providing again a relaxation of pre-test activities.

The flow rate requirements which are shown in table 2 can be met by one LN_2 circulation pump. The second circulation pump is completely redundant and improves significantly the LSS overall reliability. The cryogenic system has been designed and tested for a system pressure of 8 bar, the specified solar intensity level of 1.8 kW/m^2 was, however, accomodated by the shrouds at only 4 bar.

Both, the margin in system pressure and the heat load contingency of 45 kW, will allow thermal and solar simulation tests at higher than specified heat loads and solar intensity levels.

Furthermore, the LN_2 boil-off mode has been implemented. This mode is selected if, due to a malfunction, LN_2 circulation is not feasible. The system is depressurised and the shrouds are operated in a conventional LN_2 boil-off to ambient pressure. LN_2 level in each shroud and refilling is controlled by the PLC automatically. The 400 hours test demonstrated that trouble-shooting of instrumentation and pumps in the circulation system will be feasible without breaking chamber vacuum or draining the shroud circuits by selecting the boil-off mode.

LN_2 DRAINING AND GN_2 WARM-UP MODES

The temperature/time requirements are well within the specification. Typical warm-up times are:

C1/C2 2.5 hours from 100°K to 300°K

C1/C2 6 hours from 100°K to 373°K

These warm-up times are achieved with limited GN_2 inlet temperatures to the shrouds (45°C as compared to an achievable setting of 120°C) and reduced system pressure (4 bar as compared to a design pressure of 6 bar). The contractual requirements are:

- Warm-up of both C1 and C2 shrouds from 100°K to 373°K within 12 hours.
- Warm-up of either C1 or C2 shroud from 100°K to 373°K within 8 hours.
- Temperature stability at 300°K and 373°K shall be ± 10°K.

These specifications have been met with considerable margin to allow the system to be tuned to customer requirements. In fact, any temperature level between 273°K and 373°K can be obtained and controlled during warm-up mode. The warm-up time will now depend on customer allowed temperature gradients over the shrouds, and times as short as 1 hour are feasible.

VTC MODE

Table 3 lists the VTC performance characteristics.

Although the actual performance showed some deviations to the design baseline, the extension of the temperature range down to 105°K is considered a substantial asset in view of the tendency of present customer requirements towards lower temperature limits. The installation of the counterflow heat exchanger introduces a significant reduction in LN_2 consumption; some examples are shown in table 4.

Finally, the VTC mode has many control parameters which require additional tuning. Continued testing during 1986 will provide an optimum VTC performance, which has again the potential to be adapted to customer requirements.

SHROUD PERFORMANCE

In the past, most of the space simulators have been equipped with Al-shrouds due to their good thermal conductivity, low weight and lower cost. Recently, Al-shrouds in service have experienced thermal vacuum cracks and new cracks have appeared during each thermal vacuum test.

The stainless steel shrouds incorporated in the LSS cryogenics system demonstrated excellent performance during various warm-up and LN_2 cool-down / circulation phases. The specified leak tightness, being:

- Individual leak rate $<10^{-4}$ mbar l/s.
- Integral leak rate $<10^{-3}$ mbar l/s.

Typical leak rates were better than 10^{-6} mbar l/s. The shroud design in the main chamber is self supporting, avoiding mechanical stress due to temperature gradients between shroud and chamber. The number of dismountable couplings is restricted to a minimum. Both factors increase shroud leak integrity and reliability.

The installation of the majority of internal pipes and headers on the shroud inner chamber side, as well as the baffle principle in the auxiliary chamber, allow easy maintenance and repair. The disadvantage of the moderate thermal conductivity and the higher weight of the stainless steel shrouds is compensated by the improved reliability and maintainability in particular with respect to leak tightness.

Also the baffle principle has demonstrated the advantages of free access to chamber walls to build-up platforms for facility maintenance and cleaning.

CONCLUSIONS

The LSS cryogenics system has proven its operational capabilities under simulated heat load conditions and provides sufficient margin for future elevated requirements.

The high level of instrumentation and operational sophistication allows facility operations with minimum staff. The acceptance test proved that nominal operating pressures can be lower than the design parameters, providing increased system safety and reliability. The ease of access for repair and the incorporated reduncancy will limit system down-time. Finally, the system design resulted in a low consumption of LN_2, which is an important factor in keeping the operational costs at a low level.

REFERENCES

1. Brinkmann, P.W., October 1985, Main Characteristics of the Large Space Simulator (LSS) at ESA/ESTEC, NASA CP 2340, proceeding of the 13th Space Simulation Conference, Orlando, Florida.

TABLE 1: LN_2 COOL-DOWN AND CIRCULATION MODE PERFORMANCE

PARAMETER	DESIGN	ACTUAL
Total heat load at 1.8 kW/m^2 solar power	135 kW	125 kW
System contingency	35 kW	45 kW
LN_2 consumption		
Cool-down	20 m^3	17 m^3
LN_2 circulation with 1.8 kW/m^2	4.5 m^3/h	2.7 m^3/h
LN_2 circulation without sun	2.8 m^3/h	1.8 m^3/h
System pressure to avoid LN_2 vaporisation	8 bar	down to 2 bar
Temperature increase over LN_2 circuit	5°K	3°K
LN_2 flow	72 m^3/h	82 m^3/h
Shroud temperature	100°K	100°K
Cool-down time	within 2 hours	within 2 hours

TABLE 2: SHROUD LN_2 FLOW RATE REQUIREMENTS

SHROUD CIRCUIT		SHROUD SURFACE (M^2)	FLOW RATE (M^3/H)	
			DESIGN *	ACTUAL
Top shroud	C1-1	71	4	8
Bottom shroud	C1-2	67	4	7
Lower cylinder	C1-3	90	18	19
Upper cylinder	C1-4	110	18	21
5 meter door	C1-5	31	8	9
8 meter nozzle and spout	C2-1	84	10	8
Baffle shrouds	C2-2	103	10	11
TOTAL	C1/C2	594	72	78 **

* Based on thermodynamic analysis of shroud circuits at 1.8 kW/m^3 solar intensity level.

** The difference between the sum of individual flow rates and the LN_2 pump capacity is due to a LN_2 by-pass line.

TABLE 3: VTC MODE PERFORMANCE

PARAMETER	DESIGN	ACTUAL
Cl temperature levels variable between	173°K - 373°K	105°K - 373°K
Rate of change of shroud temperatures	1°K/min. 173°K - 373°K	1°K/min. 105°K - 353°K 5°K/min. 353°K - 373°K
Temperature distribution at stabilised temperature	± 5°K	± 10°K

TABLE 4: VTC HEAT EXCHANGER ECONOMY

CASE	LIQUID NITROGEN CONSUMPTION (KG/H)	
	WITHOUT HEAT EXCHANGER	WITH HEAT EXCHANGER
173°K constant	2165	450
173°K cooling, 1°K/min.	3753	1858
273°K constant	572	245
273°K cooling, 1°K/min.	1629	1294

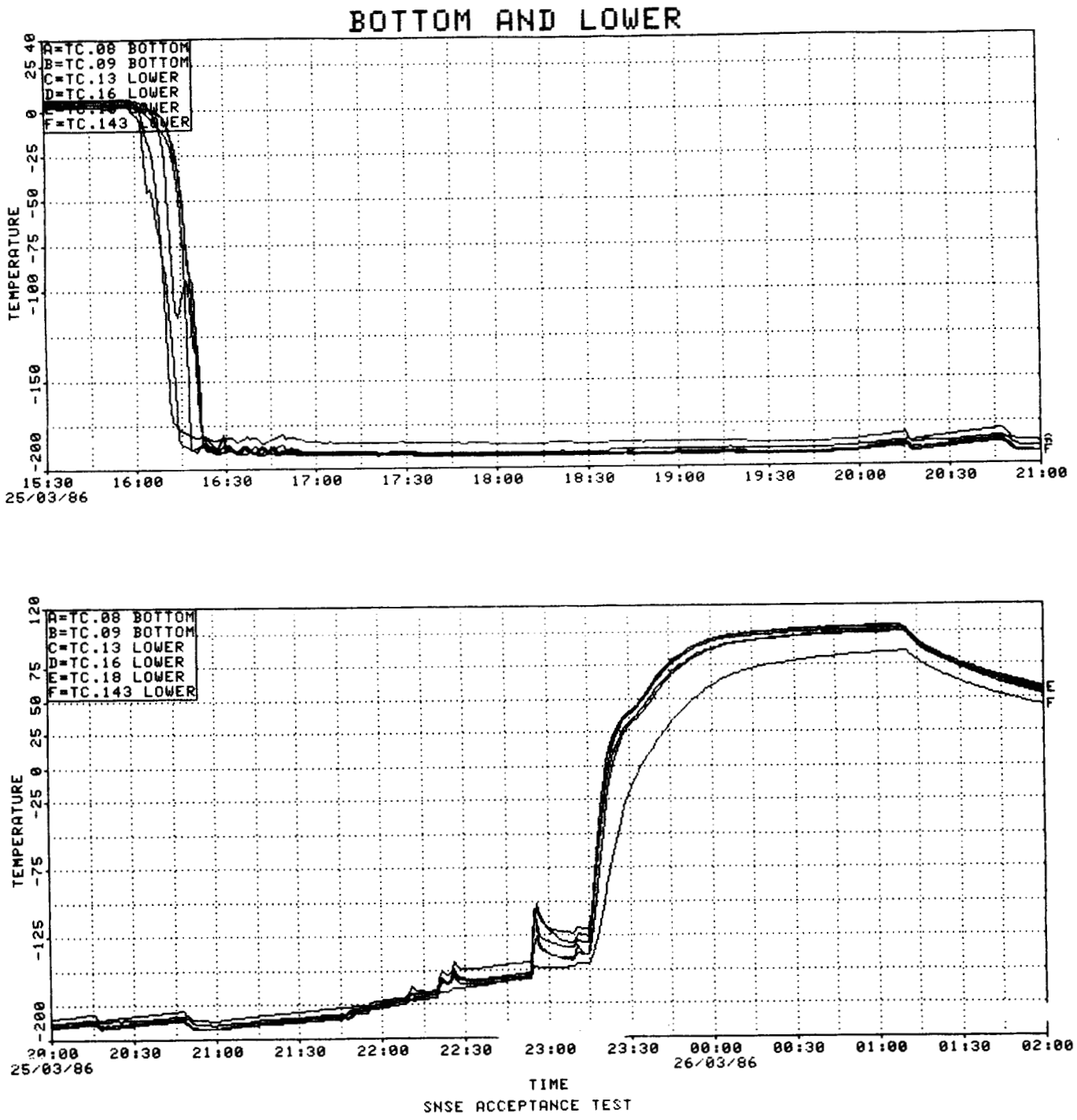

Figure 1. Typical cool-down and warm-up curve of a shroud

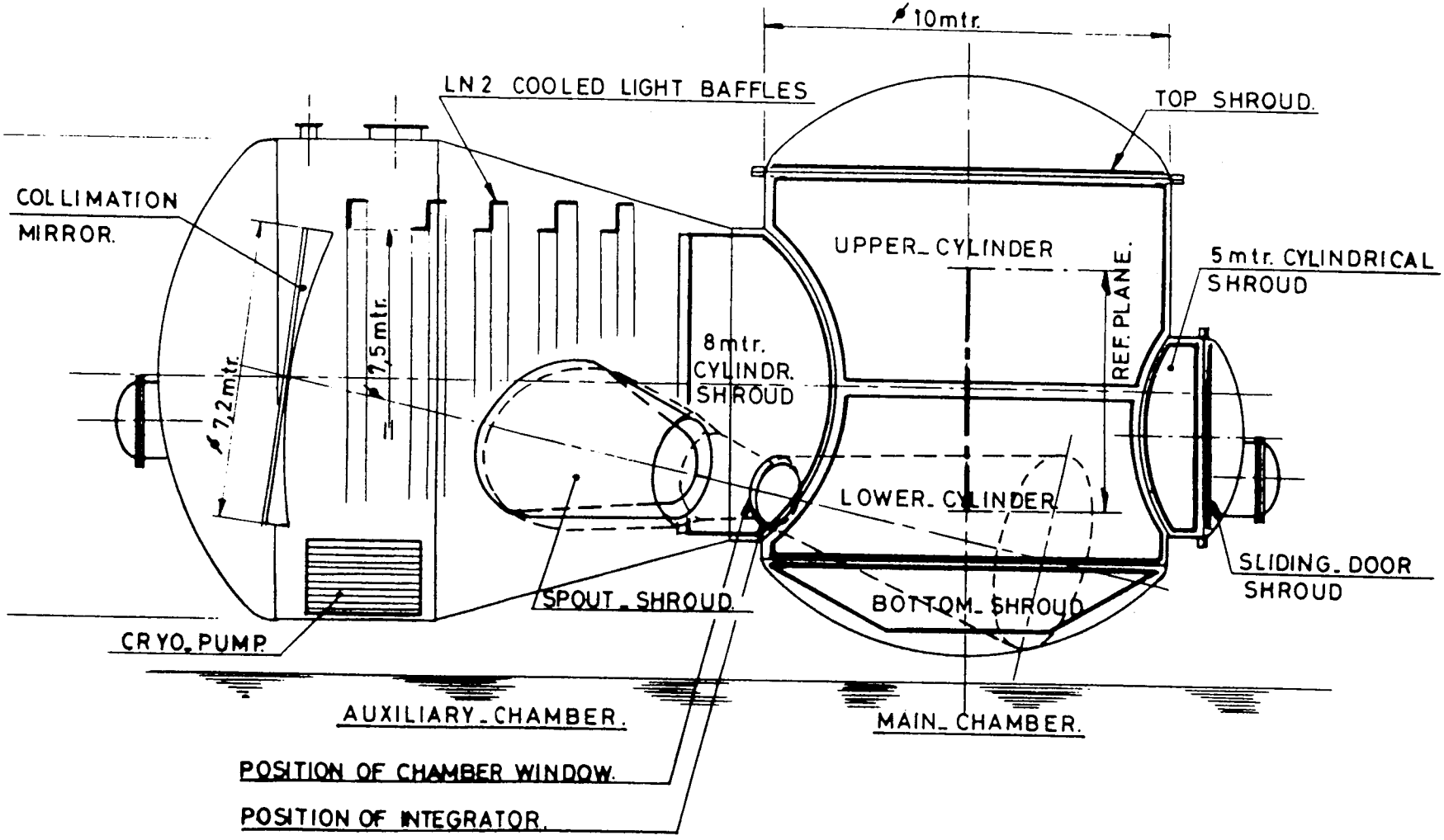

Figure 2. Layout of shroud elements

N88-10850

TEST OF THE HIPPARCOS PAYLOAD IN THE LIEGE VACUUM FACILITY FOCAL

C. Jamar, A. Cucchiard, J. Jamar, D. Macau-Hercot
- 1 AL Space, University of Liége

J. P. Camus, D. Dubet, J. P. Macau
S. A. Espace Hipparcos Project

ABSTRACT

The Liége thermal vacuum optial bench (FOCAL) has been used to control the mechanical stability of the structure of the ESA HIPPARCOS astrometry payload.

The payload is designed to measure angles of .001 arcsec between stars during 2.5 years and this accuracy can only be reached with an extreme stability of the device. The structure of the payload is made of carbon fiber; it is thermally stabilised with an accuracy of .01°C.

The principle of the HIPPARCOS payload will be described. Some dimensions are particularly critical: the angle between two mirrors sticked to each other (beam combiner), this angle has to stay stable to 0.001 arcsec during the satellite lifetime,, the length between this beam combiner and a grid at 1400 mm in front of it is also critical: the distance must be constant within 10 nm, etc...

The methods of measurement make use of the interferometry between reflective surfaces, of variation of polarimetry for the torsion of the structure and of supercentroiding on a linear CCD for the measurement of the angle between the two mirrors of the beam combiner.

During the test, the payload is enclosed in a shell made of shrouds having a geometry close to the shading structure of the spacecraft. The shroud temperatures are defined by the conditions in orbit, eg. the spacecraft is spinning in front of the sun with a period of 2 hours and the temperature of the shrouds is cycled around the payload with a 2 hours period.

In order to avoid disturbances by vibrations, the payload is put on an adapter interfaced with the optical bench and the seismic block; the shrouds are supported by a carrier with no direct interface with the table. This method avoids perturbances brought up by the cooling fluid of the shrouds.

THE COMBINED RELEASE AND RADIATION EFFECTS SATELLITE, A JOINT NASA/DOD PROGRAM

D. J. Berrier
The Aerospace Corporation

ABSTRACT

A permanent presence in space requires a clear understanding of the space environment and its effects (1). This environment consists of complicated and variable plasmas and fields that have significant effects on space systems and on man in space. The Combined Release and Radiation Effects Satellite (CRRES) has been developed to help clarify the space environment picture.

INTRODUCTION

CRRES is a two-phase joint USAF/NASA program consisting of a low earth orbit phase (LEO) and geosynchronous transfer orbit (GTO) phase (2). The program offices for the CRRES are at USAF/SD and NASA headquarters. At USAF/SD, The Aerospace Corporation provides technical review for the SD Program Office. NASA Marshall Space Flight Center (MSFC) has the responsibility to acquire the CRRES and has a contract with Ball Aerospace Systems Division (BASD) for design, development, integration, and test of the CRRES (see Figure 1). In addition, MSFC has management responsibility for the NASA experiment program in LEO and GTO.

The 360 km circular 28.5 degree inclined low earth orbit phase will last 45 to 90 days and will be managed by NASA (see Figures 2 and 3). During this phase, active experiments will consist of tracer chemicals that will be released over ground observation sites. Their interaction with the ionosphere, atmosphere, and earth's magnetic field, enhanced by orbital kinetic energy, will be monitored by passive CRRES-mounted instruments and ground-based instruments. The CRRES-mounted instruments, developed by the Naval Research Laboratory, will also monitor the near-earth environment under steadystate conditions, i.e., when no chemical releases occur. The intent of ionospheric monitoring of chemical releases and steady-state conditions is to improve knowledge of coupling of the upper atmosphere with the ionosphere, the structures irregularity, the chemistries and other conditions of the ionosphere that affect communications.

The geosynchronous transfer orbit phase will last three to five years and will be managed by the U.S. Air Force. The 400 x 36,800 km, 18 degree inclination orbit will be achieved using a modified Minuteman III third-stage solid rocket motor, which will be jettisoned after the burn is completed. This orbit will cause the CRRES to transition through the earth's inner and outer radiation belts approximately every ten hours and encounter variable plasmas and fields from near earth to geosynchronous altitudes in a nearly infinite number of orientations. During this orbital phase, the variable intensity and

composition of the radiation belts plasma and fields will be accurately measured and mapped. Over 50 instruments will be used to perform this task, including instruments to measure magnetic and electric fields, particles, waves, total radiation dose, cosmic rays, heavy ions, low/medium/ high energy electrons and their pitch angles, and the effects of tracer chemicals. See Figure 4.

The CRRES geosynchronous transfer orbit instruments have been developed by several agencies. The Air Force Geophysics Laboratory in Bedford, Massachusetts, is responsible for the Space Radiation Experiment, which consists of five deployable booms and 28 electronics units including a set of state-of-the-art microelectronics to be exposed and correlated to space radiation. The Office of Naval Research, Washington, D.C., has sponsored the Energetic Particles and Ion Composition Experiment, developed by the Lockheed Palo Alto Research Laboratory, and the Isotopes in Solar Flares Experiment, developed by the University of Chicago.

In addition, an experimental set of new type gallium arsenide solar panels will be onboard CRRES, to determine their radiation hardness, thermal annealing, and high efficiency power generation characteristics in the space environment. This experiment will operate during both phases of the mission and has been developed by the Air Force Aero-Propulsion Laboratory, Air Force Wright Aeronautical Laboratories, WrightPatterson Air Force Base, Ohio.

CRRES launch will be on the Shuttle and is scheduled for mid-1989 from Kennedy Space Center. Data will be recovered and processed through 1994 and beyond. These data will give us a much clearer picture of the space environment and its effects, and help assure a permanent presence in space.

CRRES MISSION DATA

Engineering, modeling, and science data obtained by CRRES will improve understanding of the geospace environment and its effects.

Engineering data will chronicle environmental effects on advanced solid-state microelectronics and other materials, such as gallium arsenide solar cells and dielectrics.

Modeling and science data will be collected to significantly improve the existing radiation belt model by refining existing data and by filling gaps in existing models. Better equatorial data above 8000 km altitude, higher energies and more accurate angular distribution data will be obtained. Additional science data will improve understanding of geospace dynamics. This includes particle acceleration and transport, particle sources and losses, and magnetic storm effects (3).

ENGINEERING DATA

The CRRES microelectronics experiment will provide data to improve satellite survivability and reliability in the space radiation environment. It

will measure effects of long-term total radiation dose degradation and short-term radiation soft error, or single event upset (bit-flip) rates, on over 300 representative advanced microelectronics parts and compare these effects to radiation content and orbit position. Total radiation dose effects on microelectronics devices limit satellite operational lifetime and therefore increase costs, and soft error (bitflip) rates limit on-orbit system reliability. Also, performance of these 60 types of microelectronics test devices will be correlated with the radiation environment data from onboard instruments so that the adequacy of existing microelectronics ground test radiation simulation programs can be determined.

A functional duplicate of the spaceborne microelectronics package will be used for ground test so that deficiencies in ground test simulation programs can be identified and existing ground test simulations can be improved, during and after the CRRES mission. The microelectronics experiment is part of the Air Force Geophysics Laboratory group of Spacerad instruments (4).

Another engineering data experiment is the Air Force Aero-Propulsion Laboratory's High Efficiency Solar Panel experiment. Gallium arsenide cells have been shown in the laboratory to have beginning of life electrical power generation efficiencies as high as 18 percent, as compared to 14.6 percent for silicon cells. To date, silicon has been the commonly used material for spacecraft solar cells. It has also been shown in the laboratory that gallium arsenide is nearly three times as efficient as silicon at high temperatures, and is also more efficient at end of life, after exposure to high electron radiation flux.

The laboratory environment cannot simulate all space radiation events simultaneously, and thus there is a question about the accuracy of the laboratory data on gallium arsenide solar cell radiation damage. Measurements of different types of gallium arsenide solar cells, along with the measurements of the radiation in space, will provide highly accurate engineering data for the design of space solar cell panels. The effect of annealing the space radiation damage in gallium arsenide solar cells will also be studied. This will be accomplished by running the cells at an elevated temperature and evaluating their degradation. Different types of panel fabrication technology will be used to remove this source of data bias from the experiment. Welded and soldered solar cell strings of the same type will be used, for example, to remove the possibility of getting erroneous data caused by the use of improper interconnects (5).

A third engineering data experiment is the Air Force Geophysics Laboratory's Internal Discharge Monitor, which will detect, analyze and record internal electrical discharges on 16 typical spacecraft materials in the measured space environment (4). These electrical discharges are due to charge buildup in dielectrics, which is caused by penetrating radiation.

RADIATION BELT MODELING AND SCIENCE DATA

The increasing demands for space systems electronics capability, reliability and lifetime, and for operability in a hostile environment require

more accurate modeling of the geospace environment. The biological effects on man of long-duration exposure to the space environment will become even more important with the advent of the space station.

The CRRES will use the most complete set to date of accurate cross-calibrated extended-range instruments, to provide improved particle type modeling and wave modeling over the 3- to 5-year term. In addition, CRRES will give a better understanding of geospace dynamics such that process ordering algorithms can be derived to improve our ability to predict geospace dynamics. (4)

CRRES experiments will provide much of the data missing in existing radiation belt data models including energetic heavy ion measurements at low altitudes; very high energy electrons greater than 5 MeV throughout the orbit and very high energy protons from 50 to greater than 300 MeV below 10,000 km. Dosimeters will measure true dose under controlled shielding conditions (3).

The CRRES particle detectors are all cross-calibrated and cover with high accuracy the full range of geospace energies for electrons, protons, and ions. The total energy spectrum covers from 10 ev to above 9 Gev (4).

Field and wave experiments include accurate 3-axis fluxgate and search coil magnetometers mounted on a 6-meter boom, which cover the frequency range from dc to 10 kHz, a passive plasma sounder with 100 M tip-to-tip wire booms, which covers the E-field from 5.6 Hz to 400 kHz; and a microprocessor-controlled thermal plasma probe with 100 M tip-to-tip booms and spherical probes, that covers the thermal plasma range to 10 EV and the E-field from dc to 1 kHz (4).

In the low earth orbit phase of the CRRES mission, the Naval Research Laboratory's Low Altitude Satellite Study of Ionospheric Irregularities will be operated in three primary modes: a low data rate (16 kbps) mode to provide survey measurements of the nightside ionosphere, an intermediate/high rate (64/256 kbps) mode in the region of high probability for the occurrence of spread-F irregularities, and a high rate (256 kbps) mode centered about the chemical releases. This set of Naval Research Laboratory instruments includes pulsed plasma probes for measuring electron density fluctuations, temperature, mean-ion-mass fluctuations, and spacecraft potential. Also included is a quadrupole ion mass spectrometer to measure positive and negative ion composition and density fluctuations; and a VLF wave analyzer to measure the E-field spectrum from dc to 100 kHz and B-field spectrum from 1 Hz to 100 kHz (5). These instruments will collect data at low altitude (360 km) and complement the previously discussed wave and particle experiments, which will be used in the geosynchronous transfer orbit.

The NASA Marshall Space Flight Center will be conducting chemical release experiments in low earth orbit and out to geosynchronous altitude. These experiments will also help clarify the geospace environment picture. Their objectives include tracing low-latitude electric fields and studying ion transport along magnetic flux lines. Artificial ionospheric instabilities will also be induced chemically and ground-to-satellite communications effects will

be studied. Attempts will be made to induce holes in the ionosphere and to use those holes to focus HF radio waves. The effects of heating ion clouds using ground-based HF transmitters will also be studied. Operation of the Naval Research Lab's low altitude instruments onboard CRRES will be coordinated with all low earth orbit chemical release experiments.

Additional NASA chemical release experiments will include performing Alfen wave dynamics critical velocity experiments on ions at orbital velocity and studying ion cloud dynamics under divergent magnetic field strengths in both CRRES orbits. Also, artificially perturbing high energy trapped particle populations by injecting Li seeding plasma in the geosynchronous transfer orbit will add to our understanding of the effects of extreme radiation at synchronous altitudes (7).

SUMMARY AND CONCLUSION

The CRRES mission has been carefully planned to help clarify the geospace environment picture and its effects on space hardware, communications and on man. CRRES instruments have been selected for synergism, accuracy, and applicability, and will be cross-calibrated for consistency. They will provide data to fill the gaps in geospace modeling data already obtained, and will update and correct existing models. The chemical release experiments and low altitude instruments will clarify the character of the ionosphere in low earth orbit and the high altitude chemical release experiments will improve knowledge of how trapped particle populations behave out as far as synchronous altitudes. The ionospheric studies will lead to significantly improved earth-space intercommunications.

REFERENCES

1. H. Garrett and S. Worden, Capt USAF Space Division, "The Space Environment, Friend or Foe?" (1984).

2. CRRES System Description Handbook, Rev. A, Ball Aerospace Systems Division, NASA/MSFC, (2 April 1985).

3. F. Djuth, "CRRES Mission Data and Inclination Change," The Aerospace Corporation (2 February 1984).

4. E. G. Mullen, "Spacerad Overview," Air Force Geophysics Laboratory (7 April 1986).

5. T. M. Trumble, "Space Applications of GaAs Solar Cells," Air Force Wright Aeronautical Laboratory (27 November 1982).

6. E. Szuszczewicz, "LASSII/CRRES Experiment Requirements Document," Naval Research Laboratory (11 February 1983).

7. D. Reasoner, "CRRES Chemical Release Mission Scientific Objectives," NASA Marshall Space Flight Center (1 November 1984).

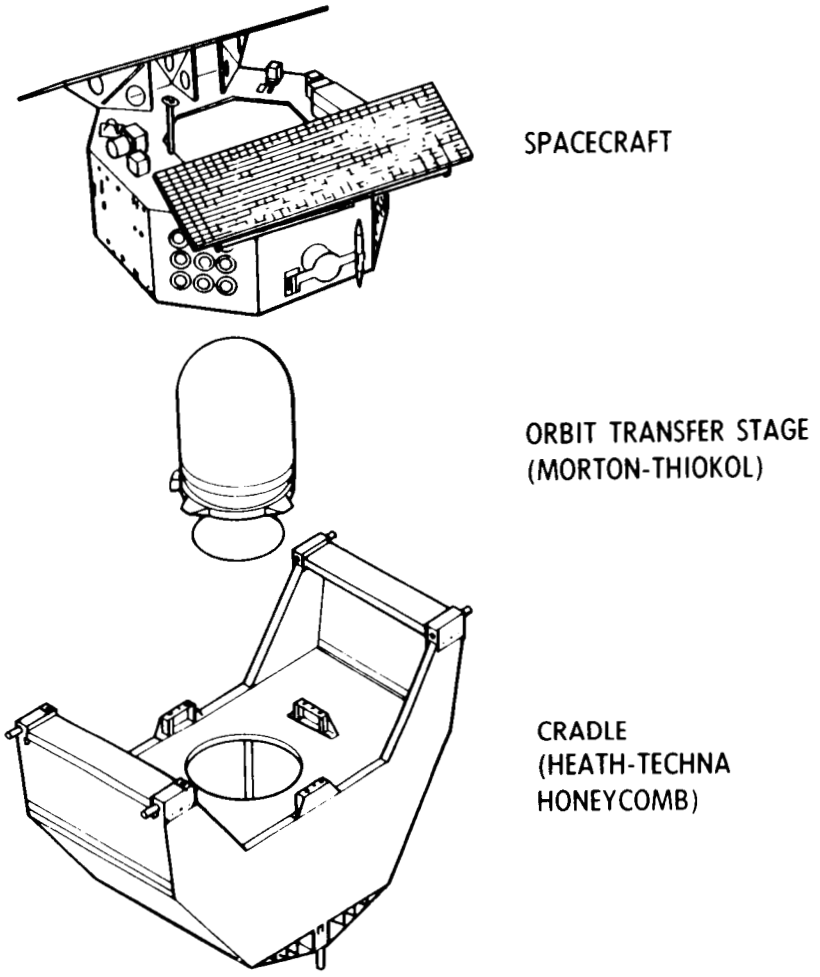

Figure 1. CRRES system

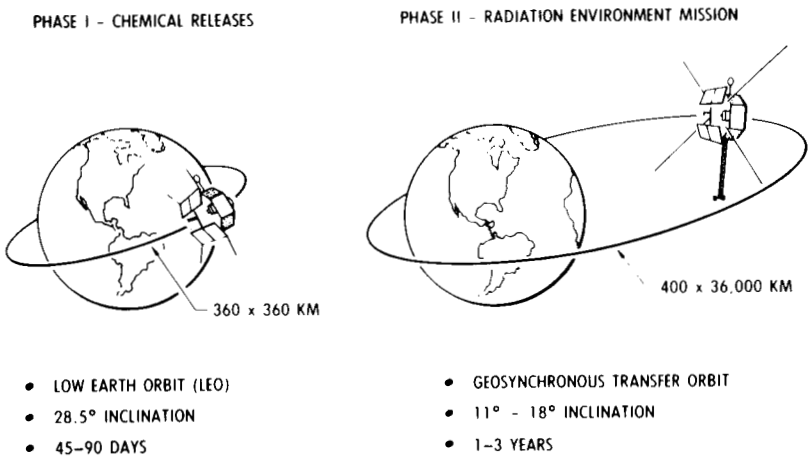

Figure 2. Combined release & radiation effects satellite (CRRES) two-phase mission

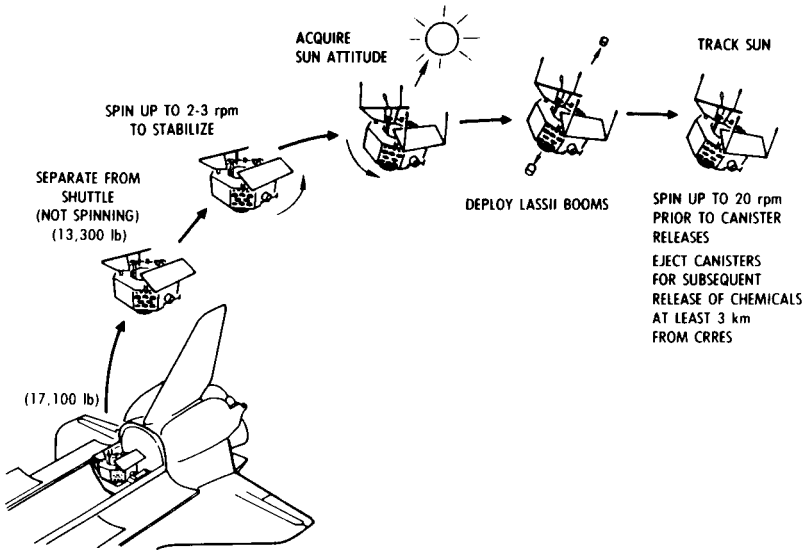

Figure 3. CRRES deployment and low earth orbit operations

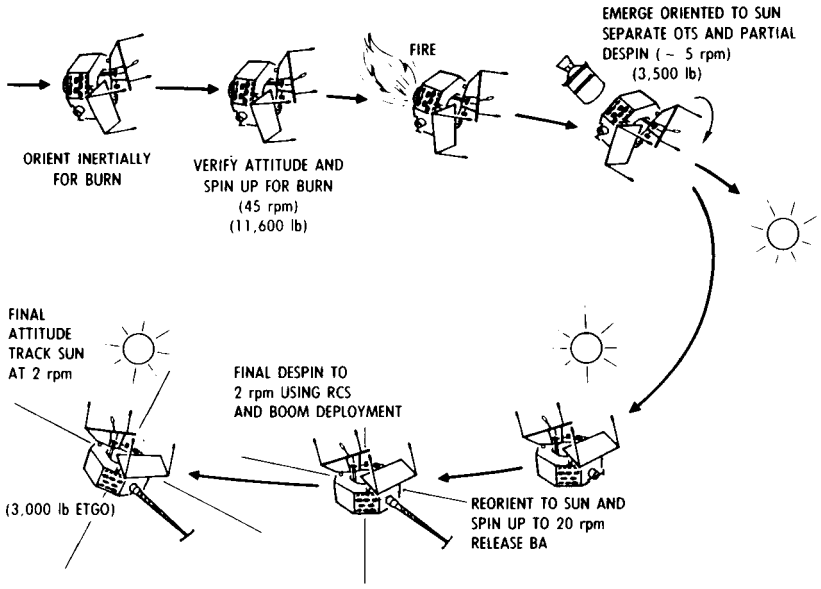

Figure 4. CRRES geosynchronous transfer orbit insertion and operations

N88-10852

DESIGN CONCEPTS TO IMPROVE HIGH PERFORMANCE SOLAR SIMULATOR

Dr. H. J. Juranek
Carl Zeiss, Oberkochen, Germany

Dr. H. U. Frey
IABG. Munich, Germany

ABSTRACT

In the early eighties ESTEC wanted to start a new large space simulation chamber, its main characteristics were already published (ref. 1). An important part of it was the solar simulator. Compared to the already existing large facilities in the US there were many features and requirements which were changed or tightened. This because of several reasons; roughly they can be divided into two categories: Reasons which give the benefit to the customer and others which give the benefit to ESTEC respectively directly to the operation team.

The main requirements of interest concern:

- the chamber, i.e. the solar beam (it was required to be parallel and horizontal) and the test volume,
- the intensity range,
- the uniformity of the intensity in the reference plane and in the remaining volume,
- the collimation angle,
- the stability of the solar beam,
- the reliability of the facility,
- the efficiency,
- last not least the safety standard and the ease of maintenance.

This paper treats the proceeding and the ideas to raise the well known off-axis concept of solar simulators to this level.

INTRODUCTION

Based on the ESTEC requirements concerning the efficiency, the collimation angle, the light distribution, and the boundary conditions of the existing building, a detailed mathematical study on the basic ray trace parameters was performed. Fig. 1 defines the meaning of the ray trace parameters and table I shows the qualitative impact, specially of the diameter of the integrator, the

projection distance (which is coupled to the throw distance) and the off-axis angle, on the performance parameters. Table 1 clearly shows that there is no straight way to achieve an absolute optimum for every one of these performance parameters in question because a measure which has a positive impact on one parameter influences the next to the negative side. So what one had to do is to choose the design parameters for the best compromise, which still meets the original basic requirements of the ESTEC.

In parallel to these calculations the mathematical shape of the reflector had to be performed to make sure that the integrator size, the efficiency, and the projection distance can be met. Table II shows the original requirements of ESTEC as well as the final outcome as the result of the negotiated compromise. Fig. 1 gives the remaining geometrical data which were of importance for the vessel design and the civil engineering. After having fixed these basic data the vessel design and the civil engineering could nearly independently proceed.

Separately we developed the detailed concepts of the sun simulator components which are discussed below and which are important to achieve the goal.

THE LAMP MODULE CONCEPT

Looking at the intensity distributions of a Xenon arc (ref. 2) one easily notices the high brightness of the arc at the cathode. This means that the light generated by this part must not be wasted, which in return means that the reflector has to surround the arc as far as possible, the hole for the rod of the Xenon bulb must be as small as possible. This of course means that it would not be possible to withdraw the bulb through the reflector. So there are only two ways out: 1: To assemble and to disassemble the Xenon bulb from the outside of the lamp array or 2: to withdraw the Xenon lamp together with the reflector. Because of reasons of ease of maintenance and of safety it was decided to follow the second solution. Of course now it is only logical to withdraw the whole lamp fixture, together with the Xenon lamp and the reflector. This unit is called lamp module. It is shown in Fig. 2. Apart from the ignition device the lamp module contains a sensitive alignment possibility for the arc. By detailed calculations it turned out that efficiency and symmetry of the reflector light distribution is severely affected as soon as the arc is not in its optimum optical position.

Fig. 3 shows the measured difference between an aligned and misaligned arc. In addition it shows the difference in efficiency. Thus the module concept stands for

- ease of maintenance
- good light output
- symmetrical light distribution because of the possibility of alignment
- safety.

THE REFLECTOR CONCEPT

Normally one uses ellipsoids to solve tasks of this kind. The disadvantage of mathematical ellipsoids is their low efficiency for extended light sources and the fact that they produce light distributions with sharp peaks with very steep gradients. Yet the proper mixing function of the typical insect-eye-integrator is only guaranteed if the intensity per lens channel can be assumed to be a constant. Thus a lot of mathematical effort was put into broadening the light distribution in the field lenses plane.

The goal of the mathematical analysis was fourfold:

- To collect a maximum of light of the arc in the usable area of the collector.
- To radiate as much as possible of this collected light into the field lens stop, whereas this stop was limited by the collimation angle and the projection distance.
- To fit the distribution in the integrator plane as far as possible into a rectangular profile.
- To design the light pencil of the reflector to a small divergence. Which means that the reflector diameter is close to the integrator diameter.

Fig. 3b shows a comparison between the calculated light distribution and a measured one.

In addition the reflector concept includes a reflection coating which guarantees high efficiency during a long time. Here Carl Zeiss did not choose a simple Al-layer but an Al/SiO_2-layer. The quartz layer prevents the reflector from quick degradation. It maintains its high average reflectivity of about 85 % for years. Whereas a pure Al-coating very quickly drops down to less than 70 %. The reflector concept stands for

- good efficiency
- little degradation
- broad light distribution in the field lens plane.

THE INTEGRATOR CONCEPT

Looking into the collimation mirror of an off-axis system one can notice that the tank window picture is subject to an elliptical distortion. Detailed ray tracing calculations confirm that the cut view through the beam perpendicular to the chamber axis is an ellipse. The ratio of this ellipse is given by the following formula

$$\frac{1 - T\left(\frac{2\cos\alpha}{r} - \frac{1}{p}\right)}{1 - T\left(\frac{2}{r\cos\alpha} - \frac{1}{p}\right)}$$

where
T = Throw distance
p = projection distance
T = Target distance
α = off-axis angle

Normally the customer has no benefit of an elliptically shaped beam. The power outside the inscribed largest circle of this ellipse is lost and cannot be included into the efficiency. In the case of the ESTEC - simulator the above ratio is 7,5 % which is a non negligible quantity.

Remembering that the field lenses of the integrator are imaged into the reference plane it is evident to compensate this distortion by a counter elliptical shape of the field lenses. If the optical workshop is equipped with modern numerically controlled optical machinery, the costs of the respective lenses are comparable to normal circular ones.

In designing the remaining lens parameters, i.e. the radii and the thicknesses, all mathematical effort is put into achieving a sharp light distribution in the test plane. This because of two reasons:

1. Every light pencil outside the specified area is wasted power and does not contribute to the efficiency.

2. These "light tails" could hit the shroud system which would demand an additional cooling.

Fig. 4 compares the precalculated light distribution to the measured one in the test plane. Of course the calculated graph takes into account the 55 light channels of the integrator.

Very important mathematical and experimental investigations were done on the thermal loads on the lenses and window. These studies showed that the temperatures of these items can be held below reasonable values, provided the water cooling of the mounts and the gas-stream cooling in the window - integrator area are appropriately designed. It could be shown that these temperatures are to be expected below 370 ^{o}C which means that a Mg F_2 - coating on the lenses and the window became possible. Such a layer improves the reflectivity from 3,5 % to 1,5 % per surface.

Thus the main goal in designing the integrator was to achieve a high light uniformity and a high efficiency.

THE WINDOW CONCEPT (INCL. MOUNT)

To a smaller extent this concept is an efficiency concept too. Yet this is covered by the note that it became possible to coat it, so the same effect as for the lenses is reached.

However, the window concept is mainly a safety concept. One has to face the following facts:

1. The loads on the window are due to the atmospheric pressure and due to the thermal load

2. The diameter of the window for the LSS came out to 1080 mm which means that it is the largest quartz window of the world.

3. Quartz is a brittle material the strength of which mainly depends on its surface finishing. Even small surface cracks could cause a catastrophe.

In the first step the temperature in the window was calculated based on the amount of light to be absorbed due to the well known material absorption curves and based on a cooling concept, the mode of which takes into account three processes: radiation (in the direction to the chamber, shrouds, and projection lenses), conduction (in the material), convection (transition from the glass to the GN_2). Fig. 5 shows the worst case temperature distribution and in part b the resulting stresses in the materials due to this temperature distribution and an atmospheric pressure of 1.0 bar.

A second step was to test different surface finishing methods and to determine by experiment the stress intensity factors of the respective finishing methods on this material. In dependence of the applied stress and the present length of the cracks those factors govern the crack propagation velocity. Which means that they contain the information which says when a certain crack will result into the failure of the window.

Applying crack propagation theory (ref. 3...7) in the reverse way one can check by a proof test whether a certain item would resist to a given stress for a demanded lifetime (for example 5000 hrs operational time). In practice this means the window is exposed to definite stresses - at every point of the window they are always higher than during actual operation - their exact figure is determined by a crack propagation calculation which takes into account the demanded lifetime. The test equipment which was chosen by us is a pressure vessel as shown in fig. 6. The proof test has to be repeated after the qualification period.

The safety concept includes the design of the window mount. To avoid stresses specially in the area of the edges a belt-mount was chosen similar to those mounts which are normally used for performing interferometric measurements on big optical items. A rough idea of such a mount is given by fig. 8. So the window concept stands for efficiency but mainly for safety.

THE COLLIMATION MIRROR CONCEPT

Due to our good experiences with smaller facilities, for example IABG/-Munich, we followed a concept of a segmented type mirror.

The ESTEC mirror is constructed out of 121 hexagonal segments each of which is GN_2 - cooled (see fig. 9). A special structure was designed to fix the segments via three alignment bolts and one load carrying bolt in a fixed position.

The GN_2 cooling has certain advantages compared to a fluid cooling (in case of failure). For example there is no danger of contaminating a satellite and there is no danger of freezing. The homogeneity of the temperature distribution achieved by this cooling turned out to be perfect. During the acceptance tests of the ESTEC - facility the measured temperature difference between two arbitrary points of the mirror was less than 2 ^{o}C (vertical) and less than 0,5 ^{o}C in horizontal direction. This shows that such a segmented mirror can be ideally temperature controlled, which is a precondition for a stable beam during the whole test. Yet the main arguments which show the advantages of a segmented mirror type are:

- The segments can be coated with high performance layers such as Al/SiO_2. The quartz protection guarantees a high efficiency over years of operation. Contrary to this a full size mirror can only be coated with a simple Al-layer because to our knowledge there are no facilities in the world of that size to do multi-layer coating.

- If one decides to go for a metal mirror the segments can be made out of rolled material whereas big size blanks would usually be castings. Cast aluminum would result in rather poor optical surfaces because of pinholes which cannot be avoided.

- A segmented mirror can be repaired.

- And last not least a segmented mirror type can be easily designed for later enlargement.

Thus the mirror concept stands for long term efficiency and high ease of operation.

THE POWER SUPPLY AND CONTROL CONCEPT

One important feature of a modern solar simulator is the power supply and control.

The assignment of the power supply is to ignite the Xenon lamps and to supply the D.C. within the required ripplefree standard (see table II). The design of the rectifiers was based on well known principles of high power electronics in using the thyristor technique and fitting common marketable components to an optimum solution of the problem. Fig. 7 shows the quality of the D.C.

The assignment of the control is to stabilize the light intensity to a given set level during a solar simulation test. Specially the control has to compensate a lamp failure of a lamp within less than 1 sec without remarkable overshoot (see fig. 7).

A special feature is the "SUMMARY CONTROL". Here only an arbitrary subset of lamps is operated within the control loop, whereas the remaining lamps are operated on constant current conditions. It is within the duty of those lamps

which are included in the summary control to compensate variations of the other lamps or to compensate lamp failures.

The whole solar simulator is safeguarded by a programmable logical control (PLC), SIEMENS type S 105. The PLC does the interlocking by continuously checking the incoming data from the various units, i.e. rectifiers, lamphouse etc. (see fig. 10).

CONCLUSION

By improving several important components of the well known off-axis solar simulator system a considerable step forward was made. Specially the careful mathematical studies on the optics and the thermal side of the problem lead to a highly efficient system with low operational costs and a high reliability. The actual performance of the simulator is significantly better than the specified one, and in particular the efficiency is outstanding. No more than 12 lamps operating at 18 kW are required to obtain one Solar Constant in the 6 m beam.

One of the main conclusions is that contrary to the time the project was started we now know that using sophisticated optics even larger facilities of high performance can be designed without leaving the proven off-axis concept and using a spherical mirror. Vice versa, using high performance optics is a mean to reduce costs at a given size of the beam, because the number of lamps is one of the most cost driving factors in constructing a solar simulator.

REFERENCES

1. Brinkmann, P. W., October 1985, Main Characteristics of the Large Space Simulator (LSS) at ESA/ESTEC, NASA CP-2340, Proceedings of the 13th Space Simulation Conference, Orlando, Florida

2. Thouret, W.E., Leyden, J., Strauss, H.S., Shaffer, G., Kee, H.; October 1972, 20 to 30 kW Xenon Compact Arc Lamps for Searchlights and Solar Simulators, Journal of IES

3. Davidge, R.W. et al (1973): Strength-probability-time (SPT) relationships in ceramics.
J. of Mt. Sci. 8 (1973), 1699-1705

4. Evans, A.G. and Wiederhorn, S.M. (1974): Proof testing of ceramic materials - an analytical basis for failure prediction.
Intern. J. Fracture 10 (1974), 379-392

5. Exner, G. (1983): Erlaubte Biegespannung in Glasbauteilen im Dauerlastfall. Glast. Ber. 56 (1983), 299-312

6. Kerkhof, F., Richter, H. and Stahn, D. (1981): Festigkeit von Glas. Zur Abhaengigkeit von Belastungsdauer und -verlauf.

7. Scheidler, H. (1977): Verletzlichkeit und technische Festigkeit von Glas. Glast. Ber. 50 (1977), 214-222

TABLE I

Impact on / Measure	Cost of chamber cooling system	Collimation angle	Efficiency	Intensity distribution
Enlargement of integrator diameter	raising investment (lowering operation cost)	negative impact	improvement	positive impact if collectors properly adapted
Enlargement of the projection distance which implicates enlargement of throw distance	cost driving	positive impact	reducing	positive impact
Enlargement of the off-axis angle	cost reducing	negative impact	neutral	negative impact

TABLE II: THE BASIC ESTEC REQUIREMENTS AND THEIR REAL OUTCOME

Requirement	contractual	outcome
Collimation angle	$\pm 2^{o}$	$1,9^{o}$
Test volume	Ø 6 m x 5 m	6,05 m x 6 m
Intensity range	0.65...2,7 kW/m²	0.1...3.5 kW/m²
Variation of the intensity in the test plane	± 4 %	± 3%
Variation in the remaining test volume	± 6 %	± 4 %
efficiency	> 12 %	> 18 %
ripple of the intensity p.t.p	0.5 %	0.5 %
Stability during 400 hrs	0.5 %	less 0.5 %
In case of a lamp failure: reaction time for the control to reachieve the old intensity level:	5 sec	0,2 sec
Redundancy	A failure of 2 lamps must not have an impact on the shape of the intensity distribution	7 lamps less do not affect the shape of the intensity distribution
Reproducibility	± 1 % of the intensity distribution profile during 400 hrs	less 1 %

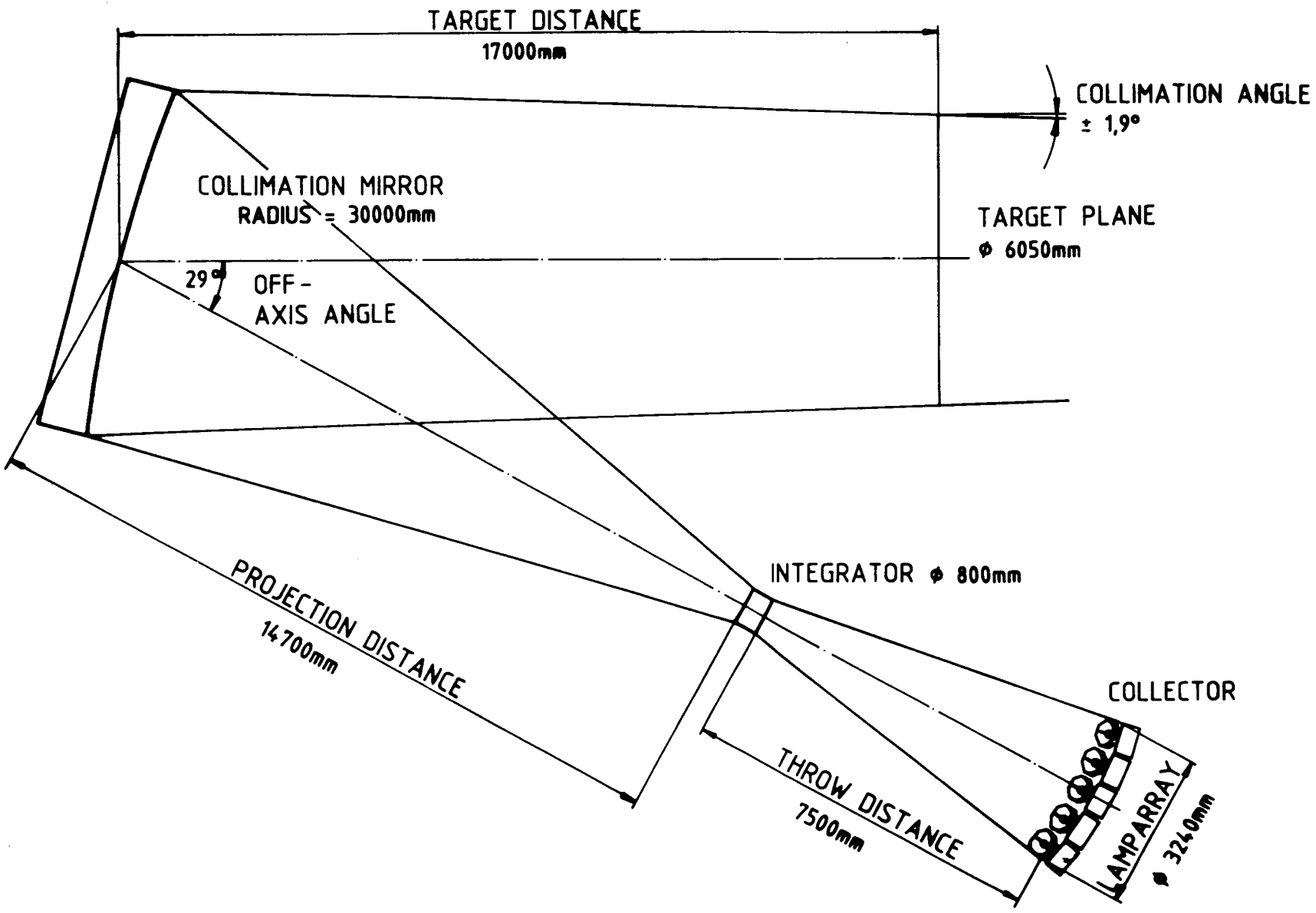

Figure 1. Optical ray trace and basic design data

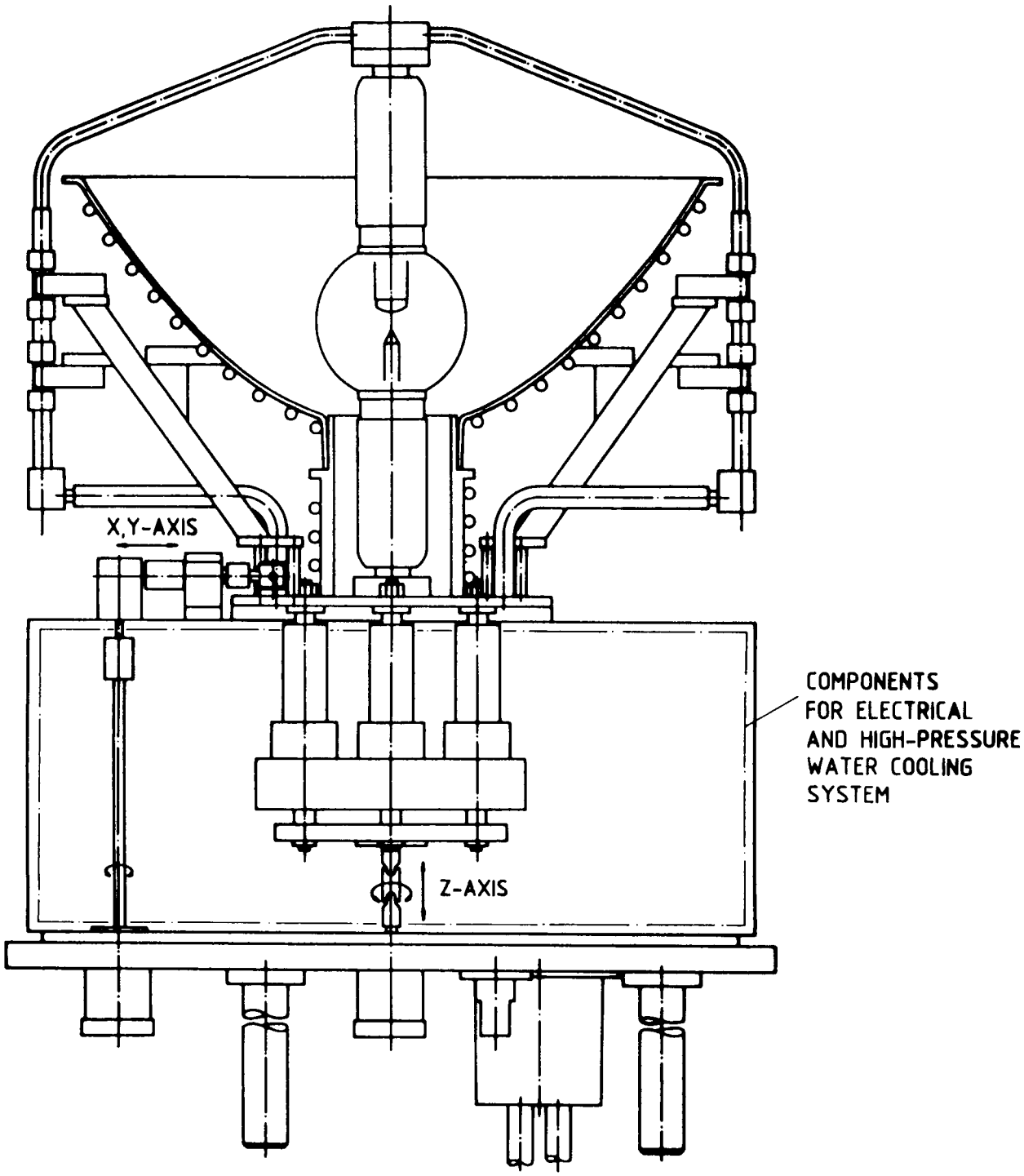

Figure 2. Lamp module design

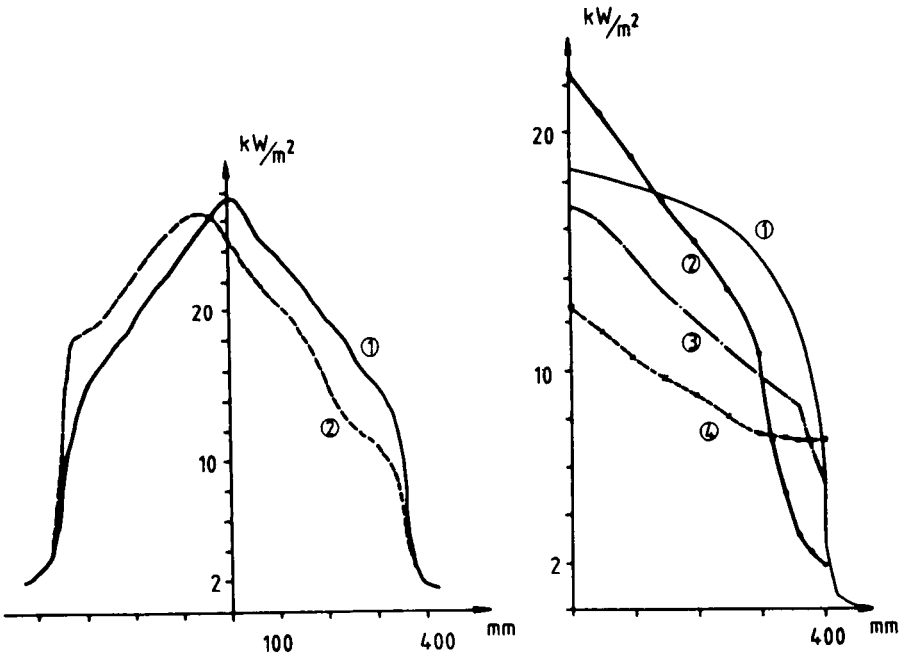

FIG. 3a:
① CORRECTLY ALIGNED ARC
② MISALIGNED ARC

FIG. 3b:
① THEORETICAL GRAPH
② ③ ④ MEASURED GRAPH IN DIFFERENT Z-POSITIONS

Figure 3. Light distribution in the integrator plane

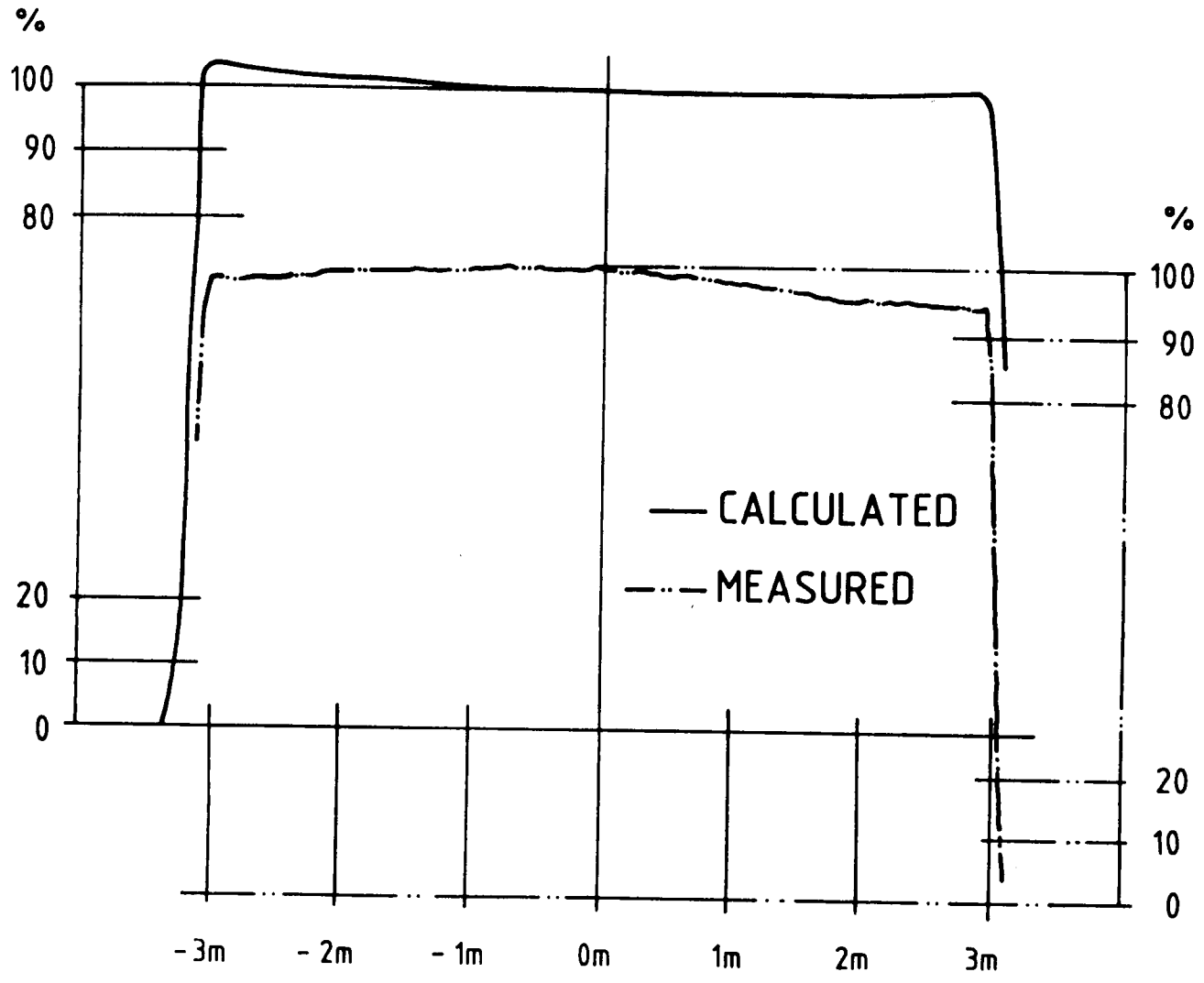

Figure 4. Light distribution in the reference plane

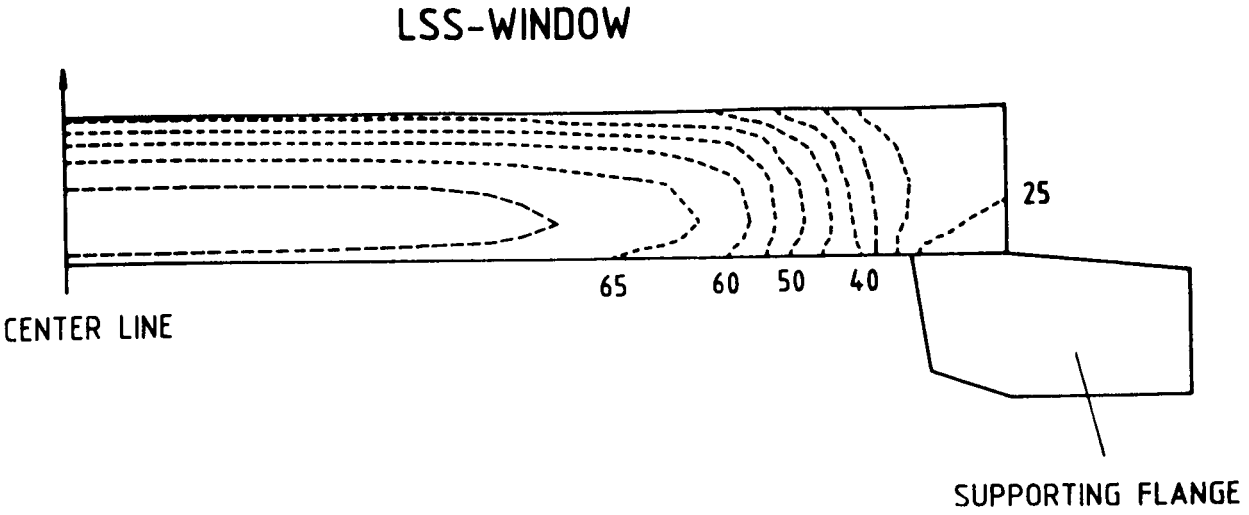

Figure 5a. Temperasture distribution [°C] in the window

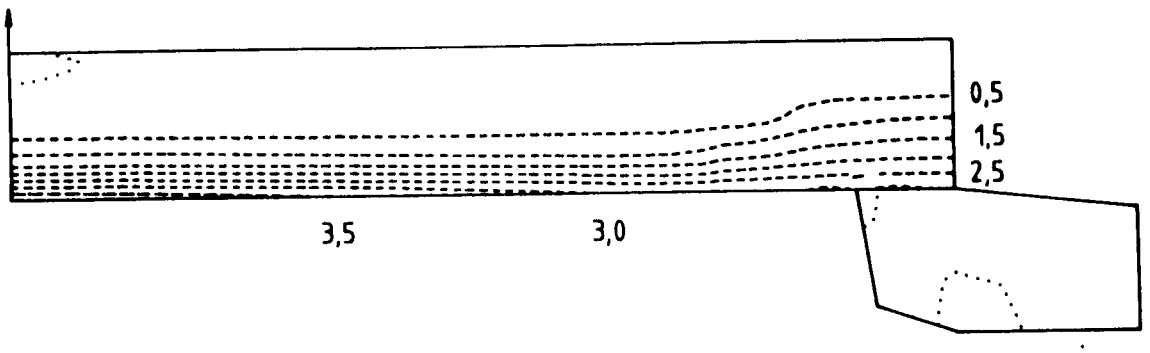

Figure 5b. Stress distribution [MPa] in the window

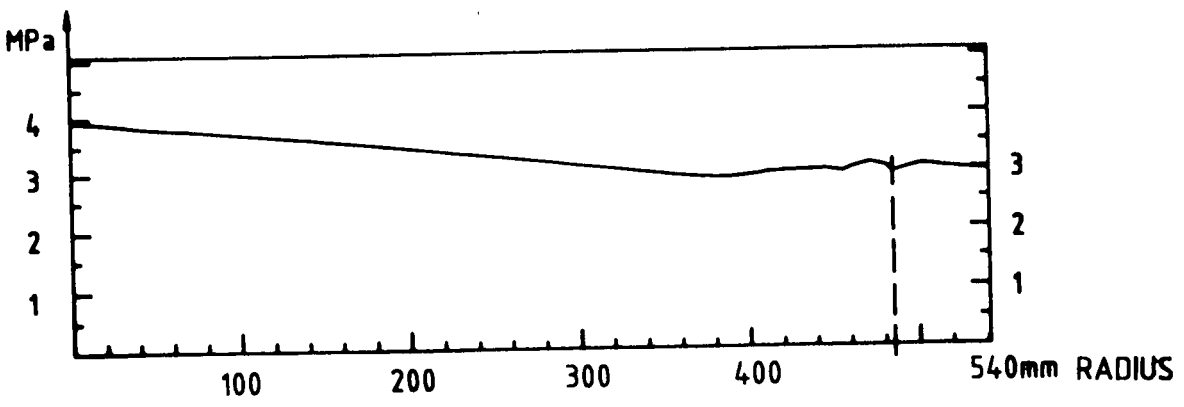

Figure 5c. Stress distribution on the window surface

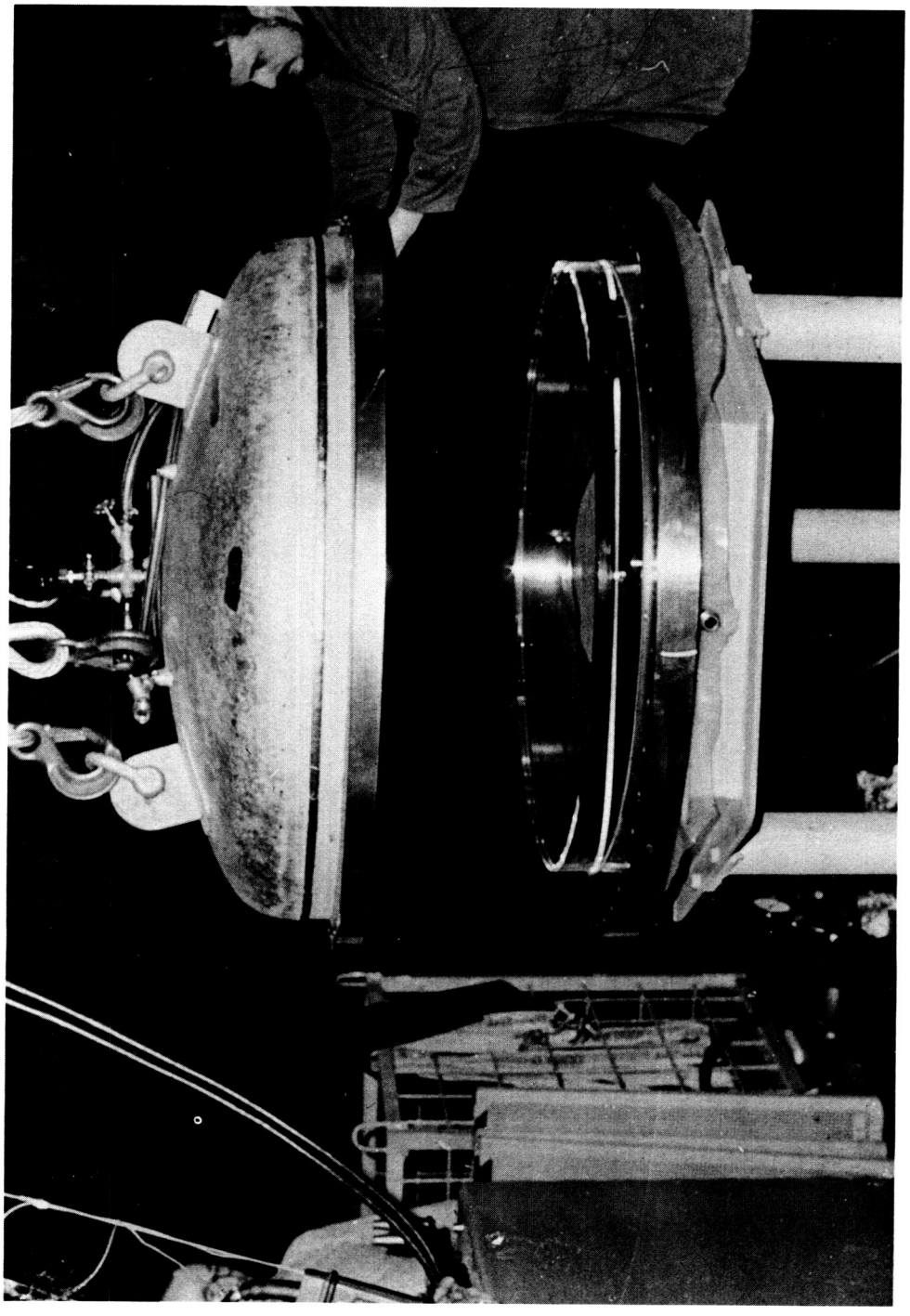

Figure 6. Proof test device

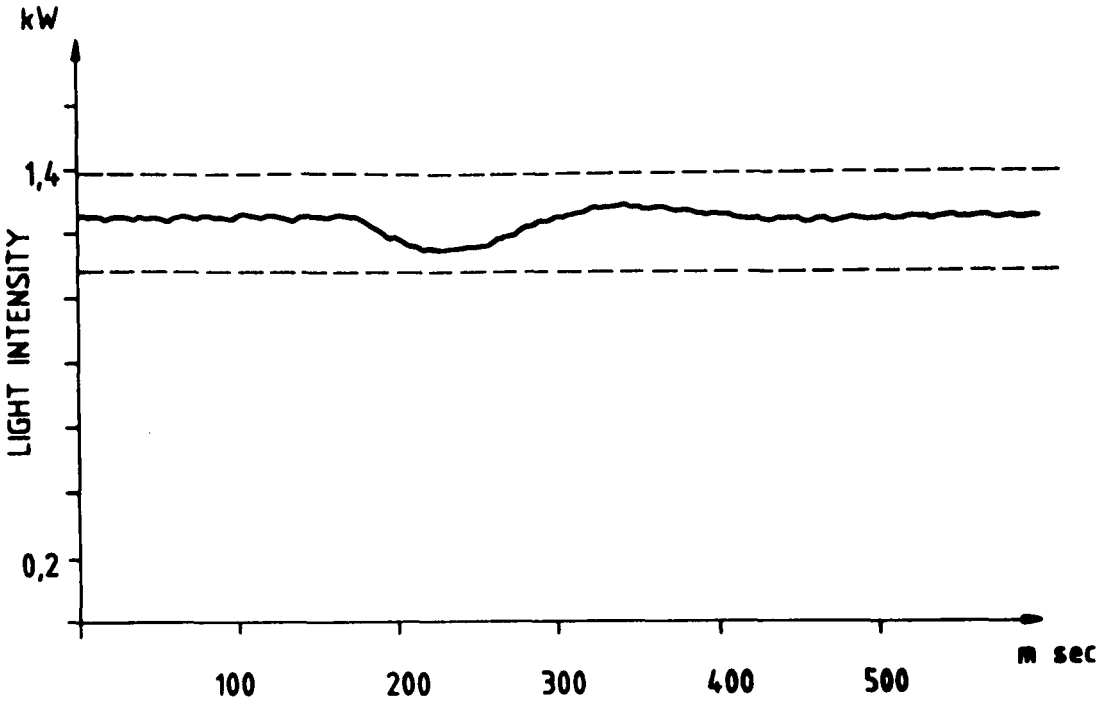

Figure 7a. Reaction of the summary control in case of a failure of 2 lamps

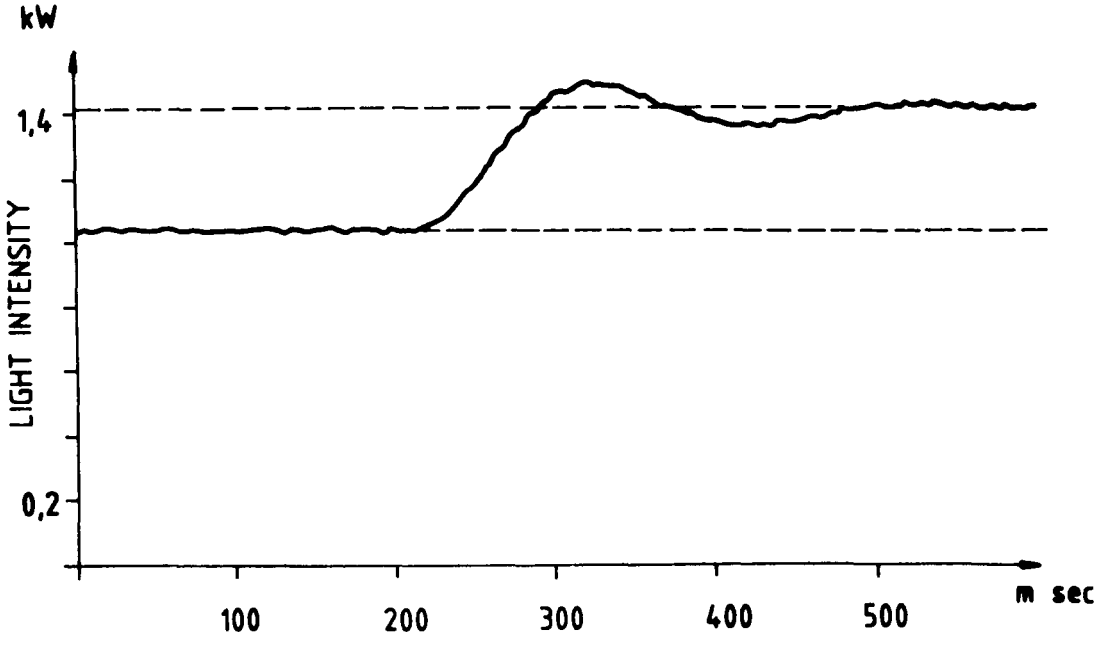

Figure 7b. Control behavior when changing power level

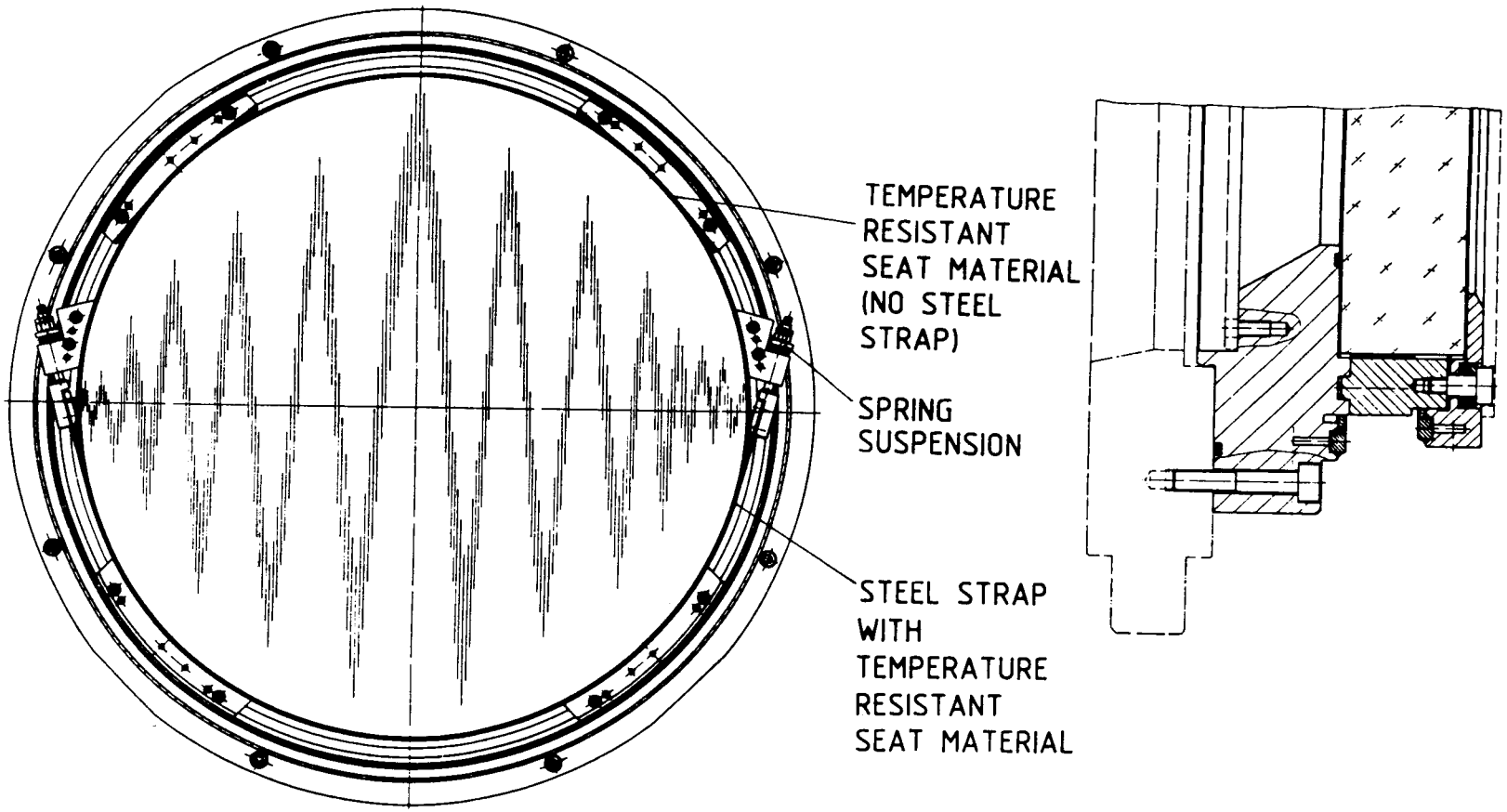

Figure 8. Design principle for the belt mount of the window

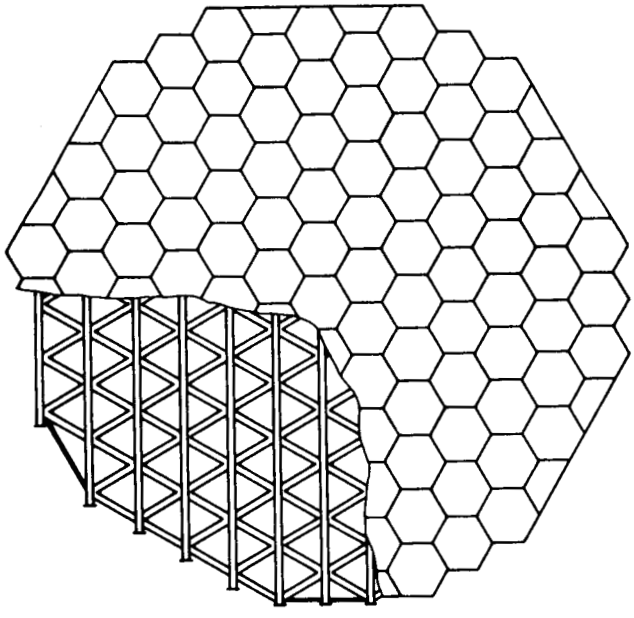

Figure 9. Design concept for the segmented collimation mirror

EVALUATION AND CERTIFICATION OF HEATER ASSEMBLIES DEVELOPED FOR THERMAL VACUUM ACCEPTANCE TESTING

J. E. Allen
Rockwell International Corporation

ABSTRACT

Preparation of Rockwell International's Thermal Vacuum Chamber for acceptance testing of a mass produced satellite required the development of unique quartz lamp and hot wire heater assemblies. Testing performed on the basic elements of these heaters is described, as is the final testing done to certify that the heater assemblies meet the thermal requirements for acceptance testing. The methods and procedures of thermal mapping used during the development and final certification of these heater assemblies are presented.

The absence of a definitive standard for determining flux distribution and heating boundaries for heaters of this type required the development of a test plan incorporating several thermal mapping techniques. These techniques include the measurement of heat flux using a multiple calorimeter array for both vacuum and ambient test conditions, and a photographic method for detecting heating boundaries. The test plan and thermal mapping techniques are discussed.

THERMAL TESTING BY INTERNAL IR HEATING OF THE FEP MODULE*

D. M. Nathanson, R. A. Efromson, E. I. Lee
M.I.T. Lincoln Laboratory

ABSTRACT

A spacecraft module, to be integrated with the FLTSATCOM spacecraft, was tested in a simulated orbit environment separate from the host spacecraft. Thermal-vacuum testing of the module was accomplished using internal IR heating rather than conventional external heat sources. For this configuration, the technique produced boundary conditions sufficiently similar to the average steady-state conditions expected for flight to enable verification of system performance and thermal design details.

INTRODUCTION

An EHF module and antenna system built at MIT Lincoln Laboratory will be integrated with each TRW FLTSATCOM Flight 7 and 8 spacecraft. The module will be attached to the aft end of the spacecraft and the antenna system will be included at the forward end. Together these are known as FLTSAT EHF Package (FEP). The FEP arrangement is shown in Fig. 1. The spacecraft will be in a near-geosynchronous orbit.

The EHF module forms a hexagon, 2.3 m (7.5 ft) across the flats, 1.2 m (4 ft) on a side and 36 cm (14 in.) tall. It consists of an aluminum frame, supporting 6 honeycomb panels, on the inside of which are mounted electronic components. The outsides of the panels are covered with second-surface mirrors and will have multilayer-insulation blankets to form the mirror apertures.

The EHF module is to be thermally isolated to minimize impact on FLTSAT-COM. Low-conductivity attachments are to be used between the EHF module and spacecraft module. An insulation blanket will span the area between the sections. The thermal-insulation arrangement used at the aft end of previous FLTSATCOM spacecraft will be transferred to the aft end of the EHF module.

The system was to be thoroughly tested at Lincoln Laboratory prior to delivery. The EHF module was to be tested, separate from the host spacecraft, to boundary conditions similar to those expected for flight. The thermal performance of the electronic systems in vacuum could then be verified along with the performance of the exterior blankets and radiating surfaces. Geometric constraints of the thermal-vacuum facility precluded the use of solar simulation or external IR sources. The module could only be tested in a stationary position with minimal clearance between panel faces and the liquid-nitrogen-cooled shroud. The flight antenna system was tested separately but back-up antenna positioners

* This work was sponsord by the Department of the Air Force. The views expressed are those of the authors and do not reflect the official policy or position of the U. S. Government.

and receivers were included within the module for test purposes.

The most practical test method was to introduce IR radiation from inside the module. Heated panels, in the form of a central hexagon, were positioned in the area normally occupied by the FLTSAT apogee kick motor (AKM). Studies using a mathematical model of the test configuration indicated that boundary conditions sufficiently similar to flight conditions could be produced to test the performance of the system and verify the spacecraft thermal design.

TEST CONFIGURATION

The thermal-vacuum test facility is shown schematically in Fig. 2 with the module installed on the transporter. The vacuum chamber had a 2.4 m (8 ft) inside diameter and was 8.2 m (27 ft) long. The transporter rolled in for installation and the track, external to the tank, was removed. With the module installed, the North panel had approximately 18 cm (7 in.) clearance to the cold wall. The South panel opposite had more clearance because of the shape of the vacuum chamber.

The EHF module was thermally isolated from the transporter by supports incorporating fiberglass insulators and 10-W guard heaters. Some components of the antenna system and a vacuum gauge were also mounted on the transporter inside the module. The interface with the host spacecraft was not simulated. A top view of the setup is shown in Fig. 3.

The introduction of heat to the interior of the EHF module was accomplished using the smaller hexagonal structure mounted inside. This central hexagon was as tall as the module and 0.6 m (2 ft) on a side, roughly the size of the AKM. The faces were 0.16-cm (1/16 in.)-thick aluminum, painted flat black, and were thermally isolated from each other and the support structure. Each face was equipped with heaters and was separately controllable. This design was particularly appropriate because the central hexagon occupied the space normally occupied by the spacecraft motor and central support column.

The entire module was covered with multilayer-insulation blankets leaving only the mirror radiating apertures. The top and bottom openings, between the module and the central hexagon and within the central hexagon, were closed out. Blankets were also included inside the central hexagon, between the panels and their support frame.

MATHEMATICAL MODEL

A mathematical model of the flight configuration was developed for use with the Lincoln Laboratory Transient Thermal Analyzer, a network-analog, finite-differencing computer program. Model detail included box power dissipation and weight data, mirror and insulation-blanket definition on radiator panels, interfaces with the FLTSATCOM spacecraft module, aft-end solar heating, and orbital environments.

The flight mathematical model was revised to describe the test configuration. Only the parts of the EHF package included in the test were included in

the mathematical model. The solar arrays and attachments to the rest of the spacecraft were not included while the receiver front-ends and linear actuators were. The exterior node representing space was replaced with one representing the vacuum-chamber cold wall. Its temperature was increased to -180°C and its area was reduced to account for the proximity of the shroud. The cylindrical blanket surrounding the AKM was replaced by the central hexagon panels. These six nodes were given mass and input power. There was no sun loading.

A partial hexagon model was used for early verification of the computer analysis developed for the panels on the EHF module. A separate mathematical model was derived to provide predictions with which to compare results. Test detail and emphasis were concentrated on panels where high-power-density boxes were located. The North and South panels (panels 2 and 5), where thermal doublers were used, were tested separately. The outside face of the North panel contained film heaters beneath the silvered Teflon* tape used to simulate mirrors. These heaters produced boundary conditions consistent with solar heating on the North panel at end-of-life (EOL) summer solstice. The results of these tests correlated well with the mathematical model. Details of the math model derived for the test were incorporated into the flight model for use as a design tool and for flight predictions.

Boundary conditions for the flight system test could then be chosen to produce module temperatures similar to those expected in orbit. Initially power levels for the heated control panels were estimated by conducting a detailed accounting of average solar heating on panels and insulation, and comparing the results with the test configuration. Net heat losses through all insulation blankets facing the cold shroud were considered in the overall accounting, and the net power levels were adjusted to compensate for these losses. The power levels were then fine-tuned to produce temperature distributions which were similar to the various average steady-state conditions expected for flight.

TEST PROCEDURE

A dry-run thermal-vacuum test using an engineering model was conducted in February 1986. The engineering model is shown in Fig. 4 in the test configuration but without any blankets installed. Thermal-insulation blankets to be used in the test were first fitted to the engineering model and installed on the flight module after the dry run. The engineering model was instrumented and data were taken to test the control concept and verify a mathematical model of the test setup, particularly with respect to the central hexagon and the module's proximity to the cold wall. Three states resembling those of the flight system test were examined: simulated vacuum-bake, power-up, and beginning-of-life (BOL) equinox average.

The thermal-vacuum test of the flight EHF module was conducted in April 1986. Figure 5 shows the flight module in the test configuration. Functional tests were conducted under boundary conditions controlled with the central hexagon. Orbital average conditions of BOL equinox, EOL summer and winter

*Teflon: polytetrafluoroethylene resin manufactured by E. I. du Pont de Nemours & Co., Inc.

solstice, and BOL cold turn-on were simulated. The range of temperatures was roughly -20° to 50°C.

Preceding the start of testing, the vacuum chamber was pumped down without liquid nitrogen in the cold wall. The central hexagon was used at this time to heat one panel selectively in order to provide a preconditioning vacuum-bake environment. At the end of testing, during purge of the cold wall, heat from the central hexagon maintained module temperatures without power to the module. Under these conditions the flexibility of local control was beneficial.

Only steady-state equilibrium conditions were examined. Equilibrium was defined for the engineering-model test as no temperature change greater than 1°C in one hour. This was revised to 1°C in two hours for the flight-system test.

TEST RESULTS

Most of the temperatures measured in the engineering-model test were within 2°C of mathematical-model calculations. Details of the test setup, including the central hexagon and the vacuum-chamber cold wall, were modeled to sufficient accuracy.

In the flight EHF-module test, the majority of measured temperatures were within 5°C of predictions. Some of the highest and lowest power boxes exhibited the largest discrepancies, approaching 7°C, but in favorable directions. A high-power box was cooler than expected because of a lack of model detail defining the location of the highest power sections. Some low-power boxes were sensitive to ohmic heating of the wiring harness, which lined the perimeter of the structure, and were warmer than expected.

Panel-temperature distributions were close to those expected for average steady-state conditions in orbit. The Table lists some representative measured temperatures and mathematical-model estimates for the test arrangement. Corresponding estimates for average orbital conditions are also listed for comparison. No changes were made to the existing panel-insulation layout or mirror-aperture areas.

It is particularly noteworthy that temperature gradients produced at high-power-density boxes were similar to those expected in flight. One unit on the South panel dissipated almost 50 W. The temperature difference between the box sidewall and the panel mounting area was estimated to be 7°C for EOL winter conditions. A corresponding gradient of 8°C was produced in the EOL winter test. The internal IR heating technique did reproduce this type of temperature distribution.

CONCLUSIONS

In this configuration, the method of control worked as intended. The central hexagon supplied heat from inside the module to produce boundary conditions similar to those expected in flight. The technique provided flexibility for temperature control during various phases of vacuum-chamber operation. Internal IR radiation was a viable option for testing.

COMPARISON OF REPRESENTATIVE PREDICTED AND MEASURED
EHF MODULE TEMPERATURES

	BOL Equinox Average Temperature (°C)		
	Test Mathematical Model Prediction	Test Measurement	Flight Mathematical Model Prediction
Panel 1			
Component	23	22	23
Panel	19	17	18
Panel 2			
Component	22	18	21
Panel	13	10	15
Panel 3			
Component	12	11	13
Panel	8	--	8
Panel 4			
Component	23	21	19
Panel	14	18	12
Panel 5			
Component	34	33	30
Panel	27	24	24
Panel 6			
Component	19	17	17
Panel	16	17	14

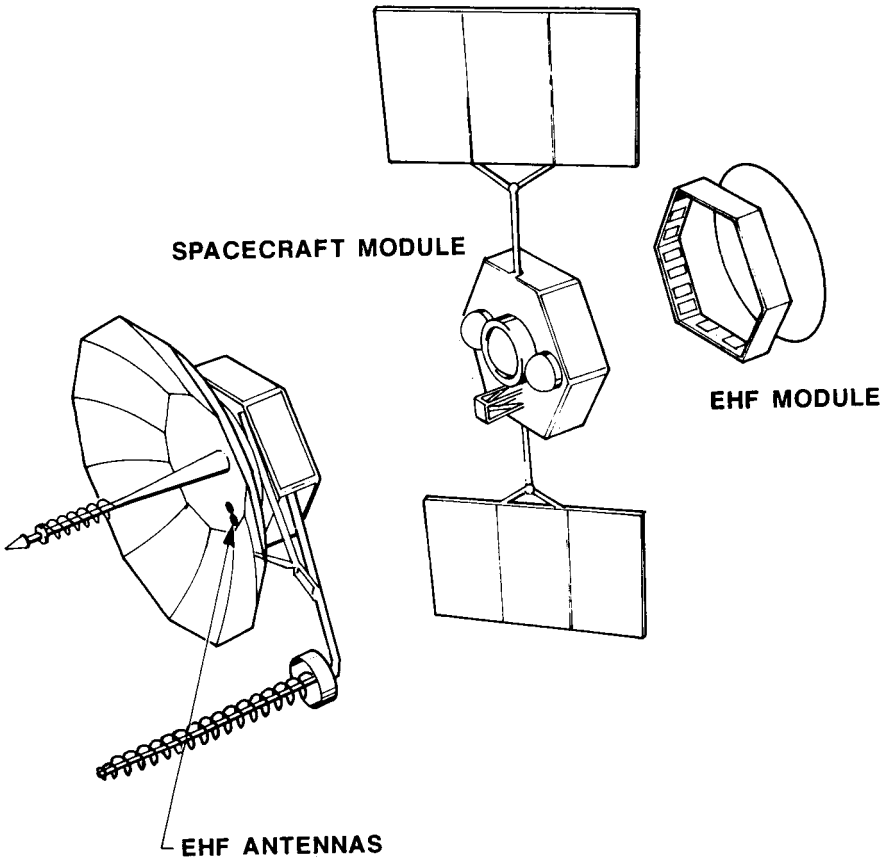

Figure 1. FEP arrangement

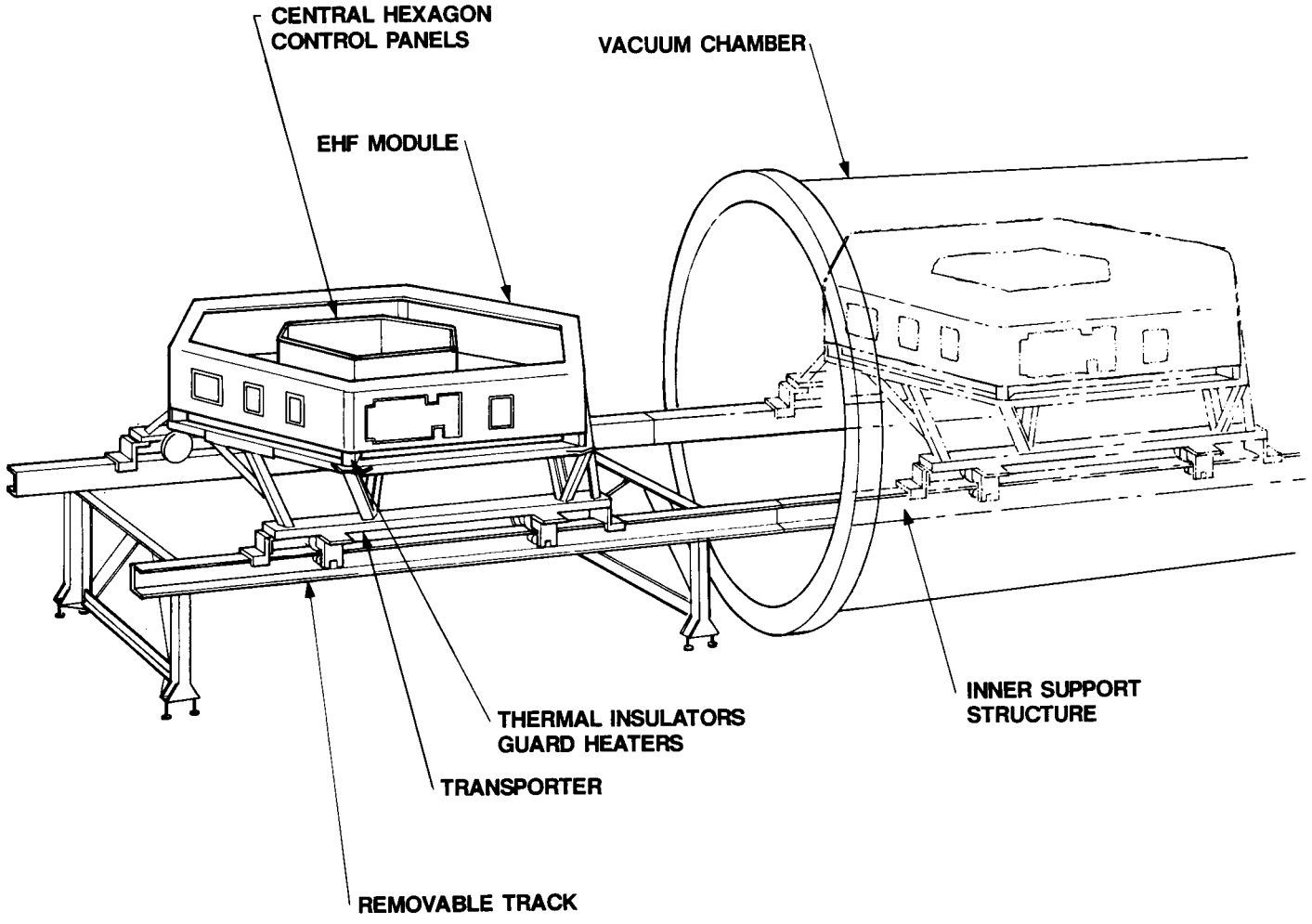

Figure 2. EHF module thermal-vacuum test configuration

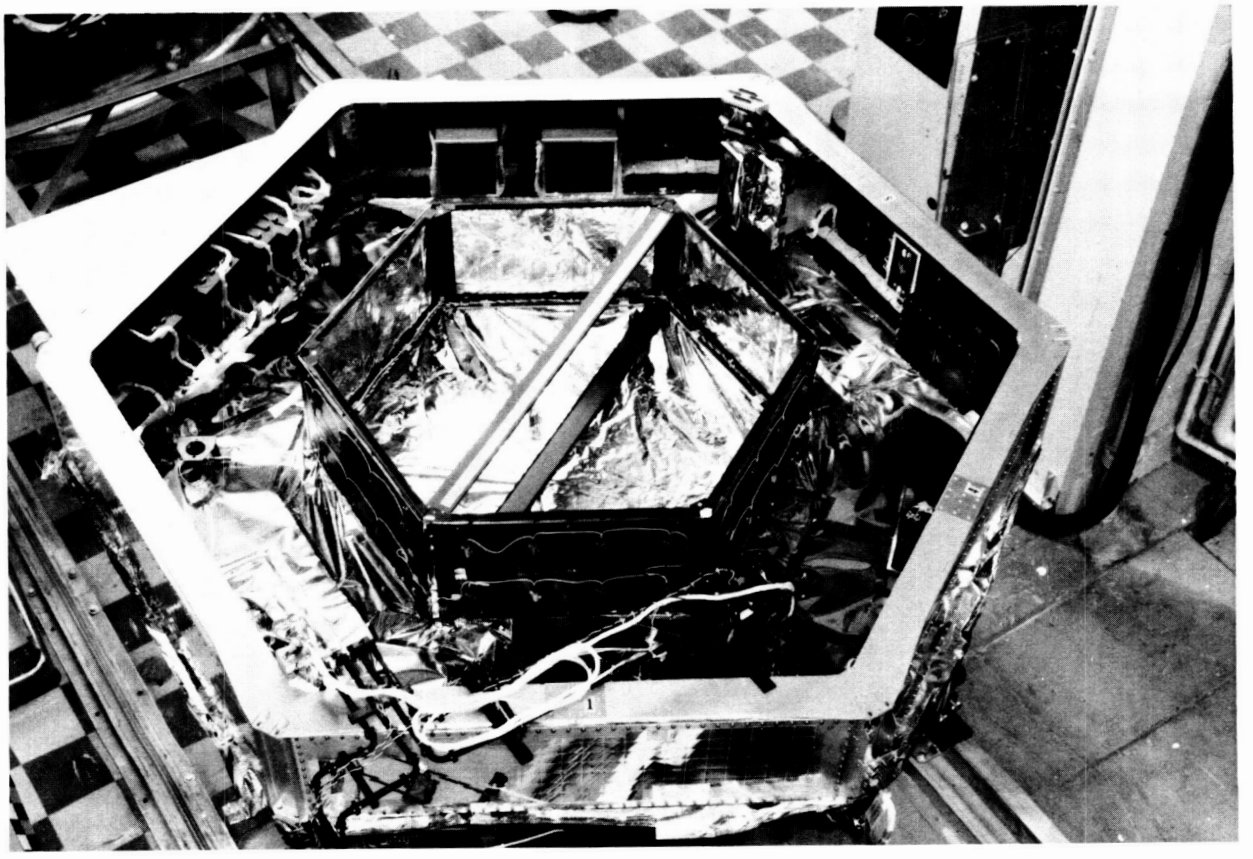

Figure 3. EHF module and central hexagon, top and panel blankets removed

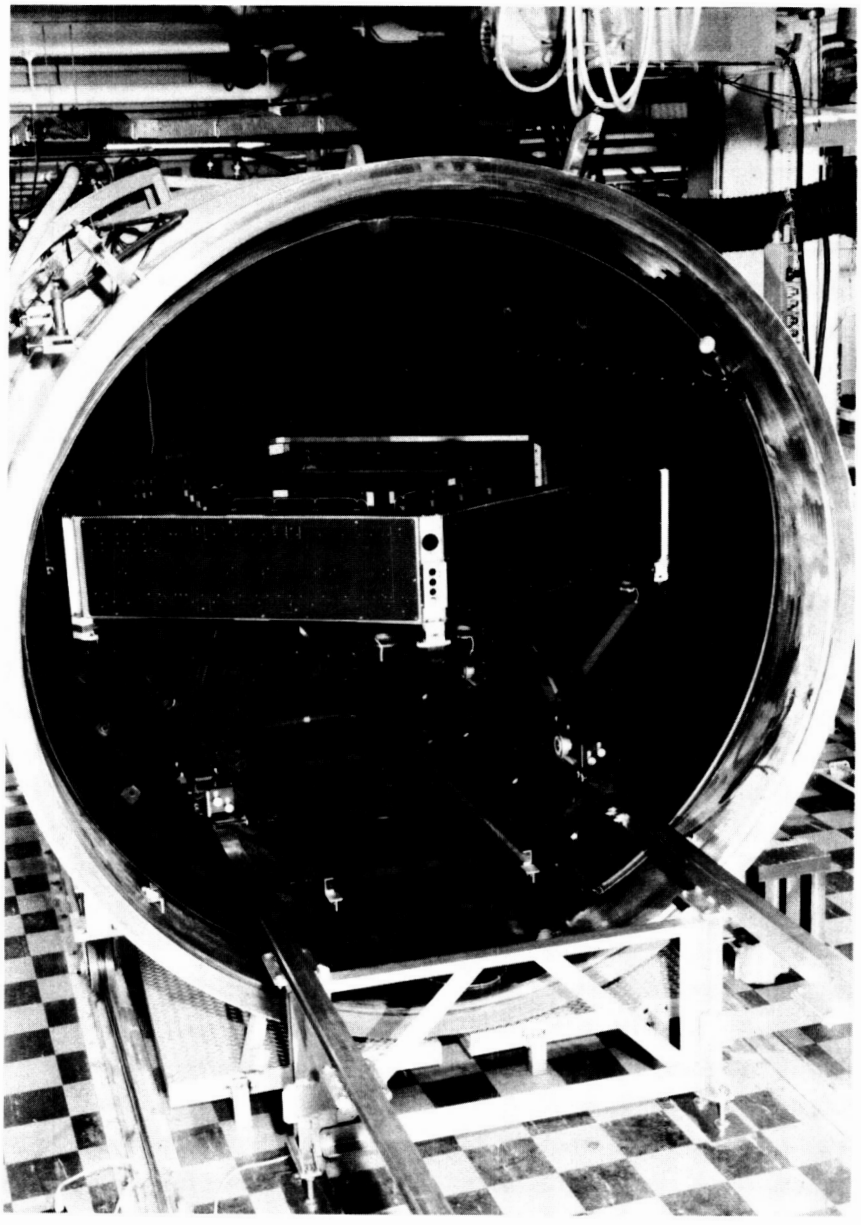

Figure 4. Engineering model in thermal-vacuum test configuration without insulation blankets.

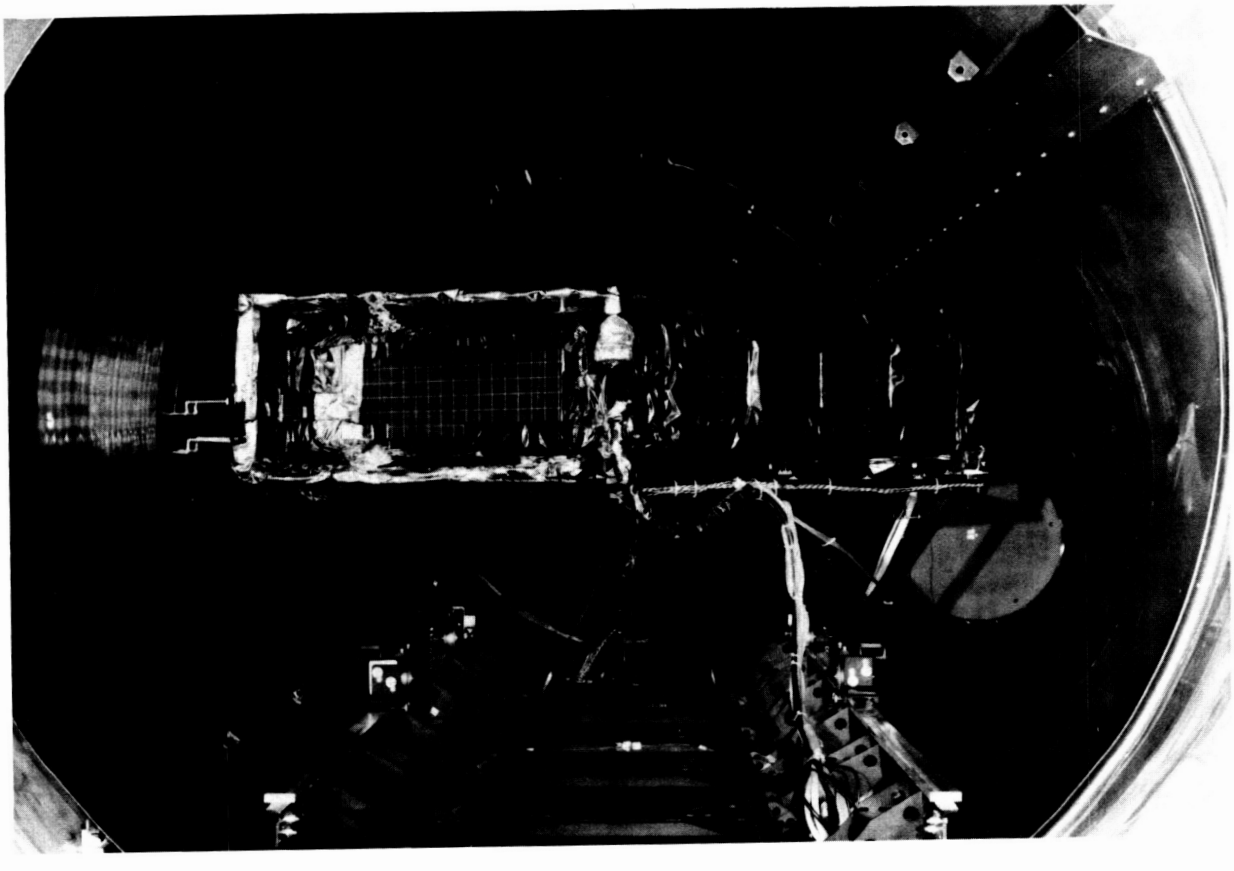

Figure 5. EHF module in thermal-vacuum test

S26-14
102860

N88-10855

A NEW TYPE OF LAMP AND REFLECTOR FOR I.R. SIMULATION

BY G. SÄNGER,

ESA/ESTEC, NOORDWIJK, THE NETHERLANDS.

E 688 9472

ABSTRACT

The lamps and reflectors used for I.R. Simulation tests at ESTEC did not allow to predict the intensity for test condition with the desired accuracy. This was due to:

- poor reproducibility of the polar diagrams
- unknown contribution of the radiation in the long wavelength range in vacuum
- imperfection in quartz bulb and misalignment of the lamp in the reflector

When using a 1000W coiled spiral type quartz lamp with a diffuse reflector these short comings are overcome and due to the good reproducibility an overall accuracy within ± 2% should be obtained.

1. SCOPE

The I.R. simulation (IRSIM) plays a major role in spacecraft testing and considering the ambitious programs both in USA and Western Europe the requirements for such tests will be even more stringent in the future.

At ESTEC numerous IRSIM tests were performed, among them the solar panel tests of Intelsat V and VI; though these tests were all successfully, there was often considerable effort required to estimate the intensity of the the I.R. lamps with the desired accuracy for the test condition. Since in addition "Testing for a permanent presence in Space" requires:

- o long term tests (mainly IRSIM)
- o numerous thermal cyclings (also mainly IRSIM)
- o high accuracy (Solar Simulation but also IRSIM)

we felt that some improvement was necessary for IRSIM tests (1).

Of most concern was a more precise prediction of the intensity for the test conditions and as main shortcomings were identified:

- o the polar radiation characteristics of the individual lamps + reflectors differ considerably (in order to simplify the computations for the thermal analysis nearly identical polar diagrams are desired).

- o intensity distribution measurements under test conditions (that is at low I.R. background and under vacuum) are expensive and complicated. Therefore, these measurements are performed at ambient and extrapolated for vacuum and low I.R. background.

- o for the extrapolation for test conditions, however, a good knowledge of the lamp data and lamp parameters is required (the data given by the producer are often idealised, in addition not much is known for non-standard use).

It is purpose of these investigations to find the main characteristics and properties of the lamps (+ reflectors), their shortcomings and if possible an improvement. Measurements were performed on prospective candidates, that is:

500 W lamp
500 W lamp with metallic reflector
500 W lamp with reflecting white strip
1000 W lamp
1000 W lamp with reflecting white strip
1000 W lamp with diffuse reflector

2. GENERAL CONSIDERATIONS

When using a quartz lamp one has to consider for more precise measurements not only the filament as radiator but also the quartz bulb, because it is getting rather hot. For the condition given here in connection with reflecting mirrors this implies - due to the focussing effect of the reflector - that not

only the intensity but also the intensity distribution and the spectrum might change when going from ambient to vacuum.

In order to estimate this effect, the relevant data of the lamps shall be measured and defined first.

2.1 Energy balance of a lamp

For steady state conditions obviously the following equations are valid:

1. $I_t = I_e + I_{conv} + I_{abs}$

2. $I_t = \varepsilon_f \cdot F_f \cdot \sigma \cdot T^4 + \varepsilon_b \cdot F_b \cdot \sigma \cdot (T_b^4 - T_a^4) + C_{ba} \cdot (T_b - T_a)$

3. $C_{fb} \cdot (T_f - T_b) + \alpha_b \cdot F_b \cdot \varepsilon T^4$
$= \alpha_f \cdot F_f \cdot \sigma \cdot T_b^4 + \varepsilon_b \cdot F_b \cdot \sigma \cdot (T_b^4 - T_a^4) + C_{ba} \cdot (T_b - T_a)$

I_t - total energy of lamp (produced in filament)

I_e - emitted energy of filament directly to ambient (thus not absorbed by bulb)

I_{conv} - energy transferred from filament to bulb by convection

I_{abs} - energy of filament absorbed by bulb (bulb is in the long wavelength range opaque)

T_a - ambient temperature (300°K)

T_f, T_b - temperatures of filament and bulb

C_{fb} - conductivity factor for heat transfer filament-bulb (W/°K)

C_{ba} - conductivity factor for heat transfer bulb-ambient (W/°K)

F_f, F_b - effective surfaces of filament and bulb

$\varepsilon_{f,\,b}$ - emittance of filament, bulb

$\alpha_{f,b}$ - absorptance of filament, bulb

σ - Stefan Boltzmann constant $5.6686 \cdot 10^{-12}$ [w/cm^2. °K^4]

V, A - indicates the operation of the lamp under vacuum or ambient.

- The first equation means that the energy of the filament is emitted to ambient and a part also transferred to the bulb both by convection and absorbed radiation.

- The second equation considers that the total intesity is transmitted to ambient by the filament radiation (first term), by the bulb radiation (second term) and the energy transferred to the ambient atmosphere by convection (third term)- which is of course zero when operating the lamp under vacuum.

- The third equation gives the energy balance of the bulb, the left hand side represents the energy input from filament (both by the filament radiation and by convective heat transfer filament-bulb by the gas in the lamp) and the terms on the right hand side express where the energy is going to (back radiation to filament, radiation to ambient and heat transfer to ambient by convection).

When these factors are known the behaviour of the lamps may be estimated also for non standard conditions.

2.2 1000W lamp

The 1000W lamp was recommended as spectral radiation standard due to its high stability, high colour temperature and ease of handling (2). First quartz iodine lamps were produced which showed within the spectral range (0.25 - 2.5μ) a smooth curve; the quartz halogene (bromium) lamps show at high resolution small peaks at 308, 309, 393, 395, 586, 587 and 668 nm which, however, may be completely neglected for thermal radiation measurements. The spectrum agrees with that of a black body within the measuring accuracy (± 3%).

The filament is a coiled spiral (also named coiled coil) of tungsten wire ($\sim$ 0.3mm ø); the piral is $\sim$ 1.3mm ø and roled up to 11 coils of 5. mm outer ø. Considering the gap between the windings of the spiral one will find for the tungsten wire a length of $\sim$ 1.0m (length of the spiral $\sim$ 160mm with $\sim$ 260 windings of $\sim$ 1.3mm ø). The total surface of this wire is $\sim$ 9cm^2.

For the overall emittance follows then with:

$$I = 1000W = \varepsilon \cdot F \cdot \sigma \cdot T^4$$

where $F = 9\ cm^2$
$T = 3200\ °K.$

for $\varepsilon = 0.19.$

This value is lower than given for tungsten (fig. 1) at this temperature, which is - of course - due to the blockage of the emitting surface. When, however, approximating the emitting filament by a cylinder of 0.5cm ø and 2.3cm length (giving an emitting surface of ~3.6cm^2) one will find for ε = 0,467 which is higher than given and can be attributed to the fact that the surface is rough and no longer smooth for this approximation (3).

The bulb has a surface of 18.8cm^2 (1.5cm ø x 3.9cm length, approximated by a cylinder) and absorbs the light beyond ~ 4μ with a transient range of $\Delta\lambda$ = 1.5μ (Fig. 2). Measurements with and without quartz plate should eliminate the radiation of the bulb itself (see however annex) (4).

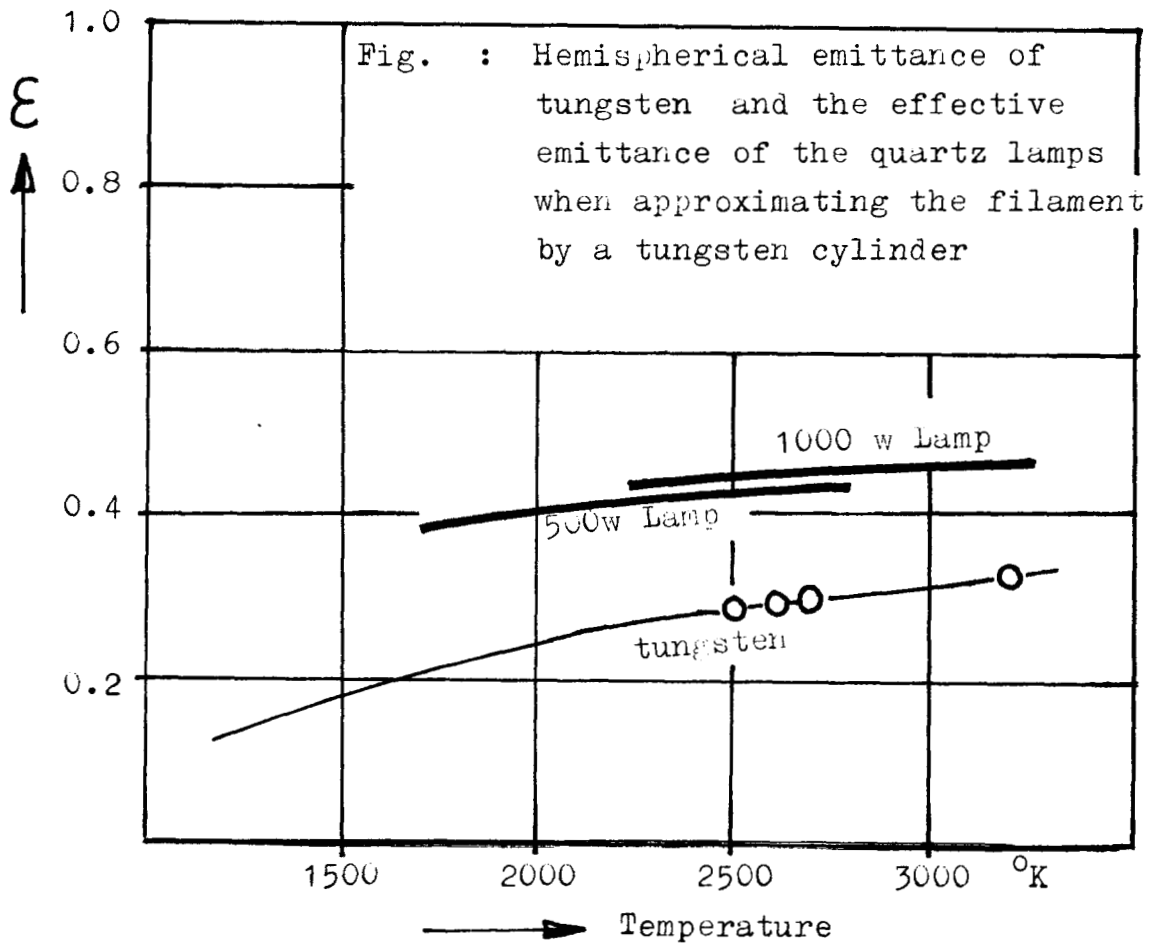

Fig. : Hemispherical emittance of tungsten and the effective emittance of the quartz lamps when approximating the filament by a tungsten cylinder

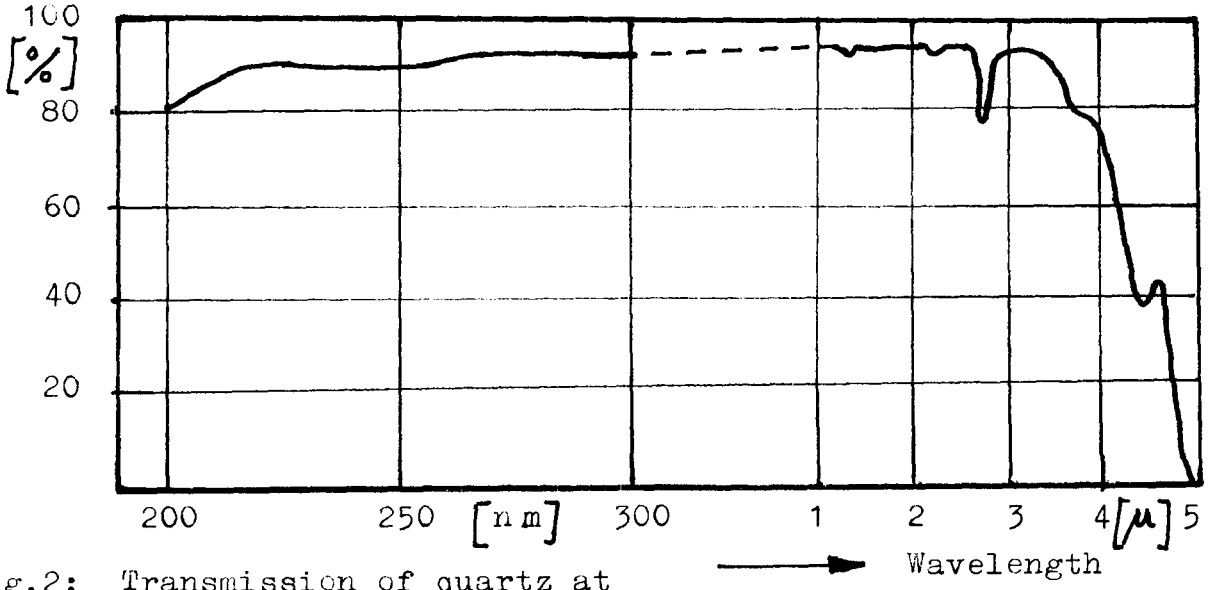

Fig.2: Transmission of quartz at ambient temperature (type Homosil, Herasil, 1mm thick)

Of course one has to consider for such measurements the surface reflection (2x) according to Maxwell relation:

$$R = \left(\frac{n - 1}{n + 1}\right)^2$$ (n refraction index here = 1.45, or 6,8 %)

When the radiation intensity of the bulb is known one can estimate the bulb temperature considering the effective emittance (Fig. 3).

2.3 500W lamp

The bulb itself is cylinder of 9.5mm ø and 14cm long giving a surface of 4.2cm^2. The wire is ~0.25mm in ø and the length of the filament spiral is 12cm; considering the windings (~380) the total length of the wire is thus ~1m and the overall surface is ~ 8cm^2.

When assuming the filament temperature given by the producer to 2500°K it would require an effective emittance of ε = 0.28 which it too high for this configuration.

Actually a similar value should apply as that found for the 1000W lamp although, the simpler arrangement (simple stretched spiral and not a coiled one) will cause a lower blockage, however this effect should not exceed 10%. It is though that ε = 0.21 is a good value leading to a filament temperature of 2685°K - and this value will be used in this report. When approximating the spiral-filament by a cylinder of ~1mm ø and 12 cm length the effective overall emittance is ε = 0.447.

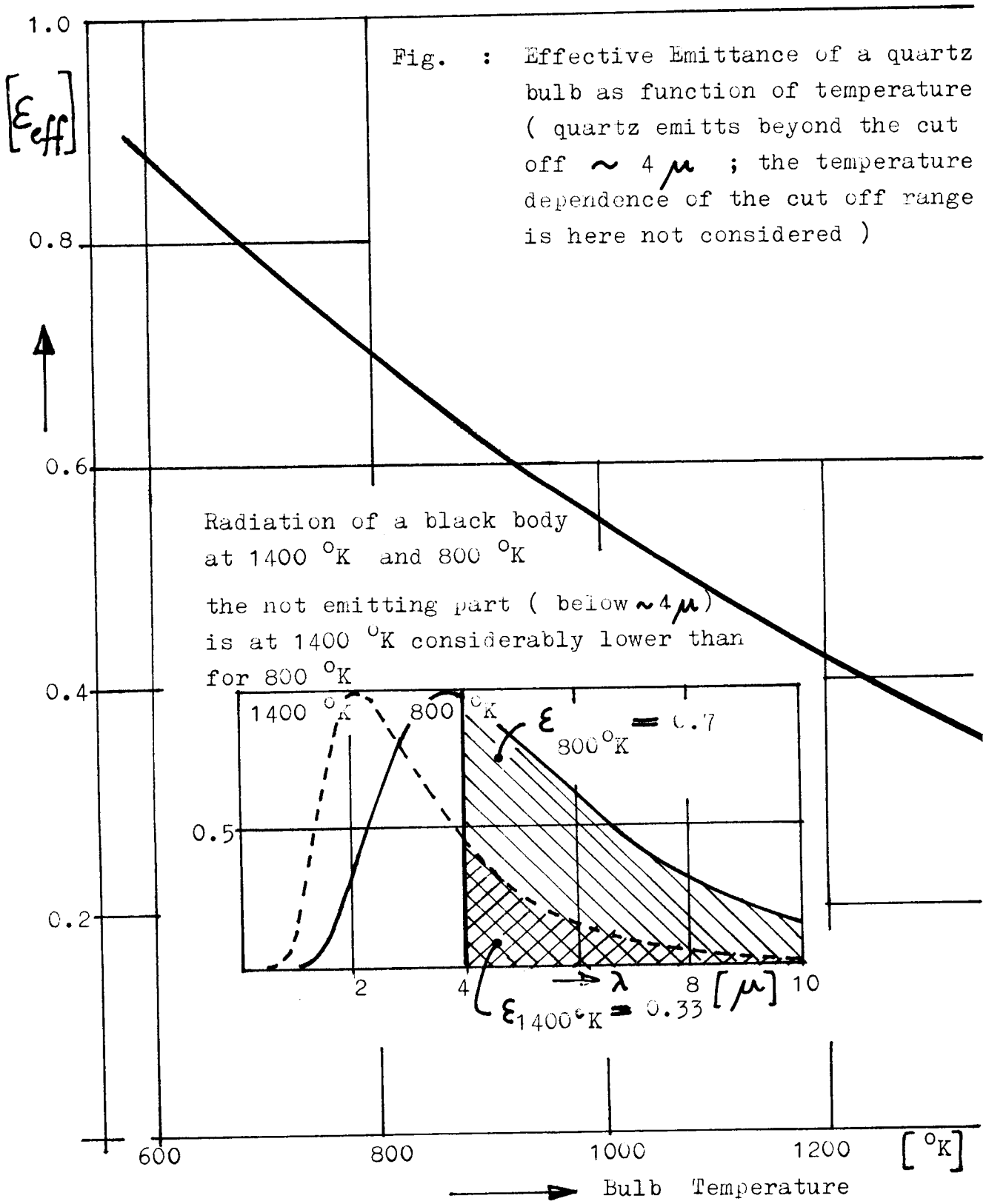

Fig. : Effective Emittance of a quartz bulb as function of temperature (quartz emitts beyond the cut off ~ 4 μ ; the temperature dependence of the cut off range is here not considered)

3. ARRANGEMENT FOR MEASURING THE LAMP DATA

The lamps were investigated for nominal power level (100%) down to 50% power level (lower levels than this are considered not realistic).

In principle it would have been sufficient to perform measurements:

- with and without quartz plate to separate the radiation coming from filament and from bulb (see however annex).
- under vacuum (or better the ratio ambient-vacuum) to eliminate the convective cooling by ambient air.

In order to reduce the experimental uncertainties and to gain as much information as possible, additional runs were performed. Since no CaF_2 window with high transmittance in the I.R. range (7μ) was available, a quartz window had to be used.

The measurements were performed with the following objectives and conditions:

1. In order to guarantee utmost reproducibility for all measurements constant current setting was applied; (simultaneously the voltage was measured for additional check).

2. The total intensity was measured inside the vacuum chamber by means of a water cooled Hycal sensor (without window).

3. In order to eliminate I.R. absorption by water vapour in natural air also measurements were performed at dry GN_2 atmosphere. (5, 6).

4. For rough information about the spectral distribution, the following were used:

   - a solar cell for the short wave length range (till 1.1μ)
   - a glass plate for the range till 2.7μ.
   - a quartz plate for the range till 4μ.

5. A Reeder thermopile was placed close to the quartz window to get an indication of scattered light (mainly I.R.).

6. At some distance, where stray light is expected to be negligible a K + Z - thermopile was installed for additional indication and cross check.

7. For studying the filament itself a parabolic mirror was used to focus the filament image onto Reed thermopile(s).

The experimental mock up is shown in fig. 4.

Fig.4: Experimental mock up for the measurements at ambient and under vacuum (eliminating the cooling effect of air and estimating the temperatures of bulb and filament). For assessment of the absorption effect of water vapor - assuming 65 % relative humidity - also measurements under dry GN_2 atmosphere were performed.

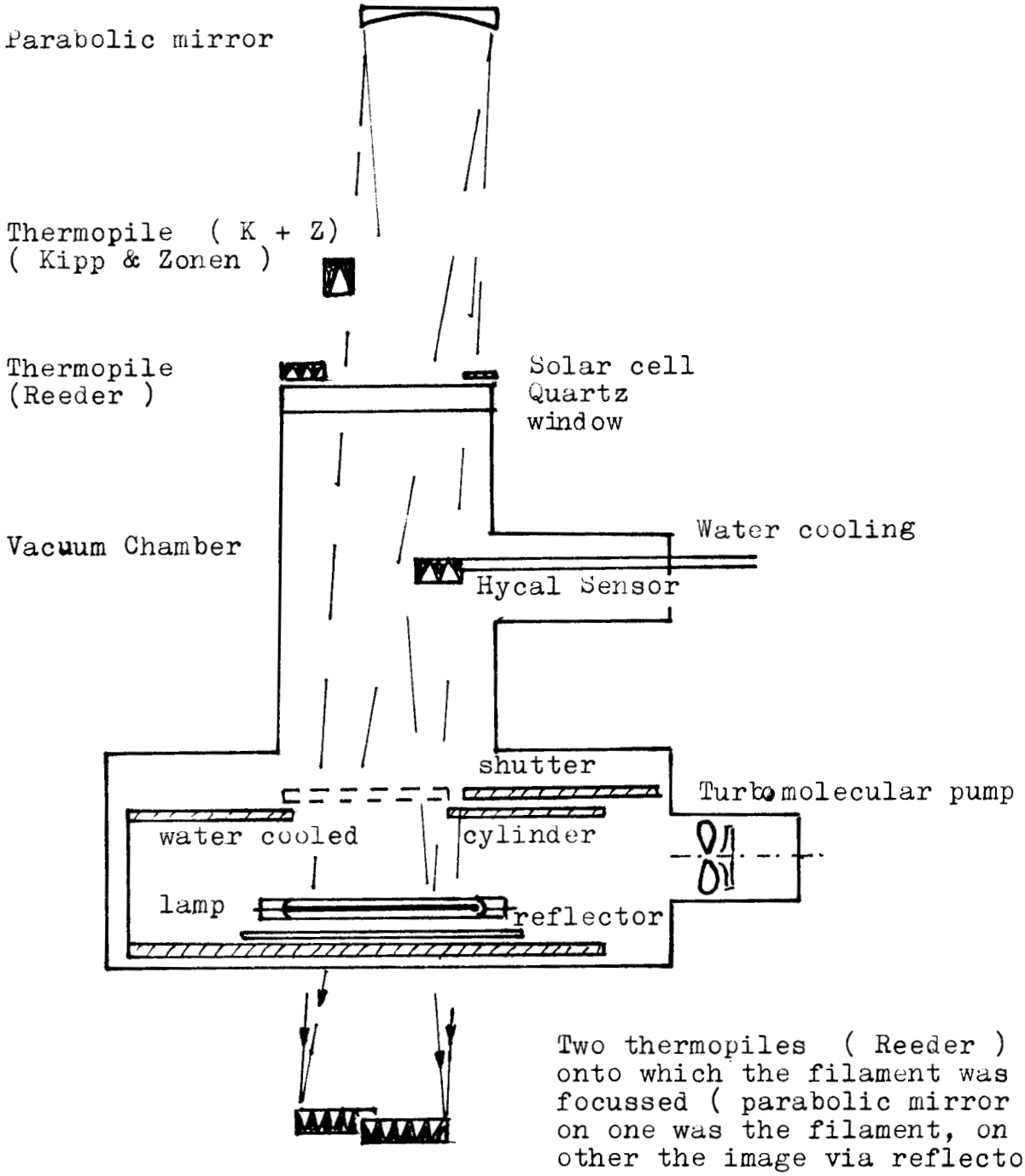

4. EVALUATION OF THE MEASUREMENTS

The measurements allow to calculate the unknown factors for the 1000W and the 500W lamp.

4.1 Heat loss to ambient air by convection

Obviously the cooling effect of the ambient air is eliminated when measuring under vacuum:

$$I_t = I_a + C_{ab} (T_b - T_a), \text{ or}$$

$$\frac{I_a}{I_t} = 1 - C_{ab} (Tb - T_q) \cdot \frac{1}{I_t}$$

The ratio of the output of the lamps as measured with the Hycal sensor in air and vacuum is given in Fig. 5. During these measurements it was observed that the power remained rather constant, the small correction will be considered in § 4.2.

Fig. 5: Ratio of the output of the lamps obtained at ambient and under vacuum for the 500 w lamp and the 1000 w lamp; both lamps without reflector. (measured with the Hycal sensor, no window)

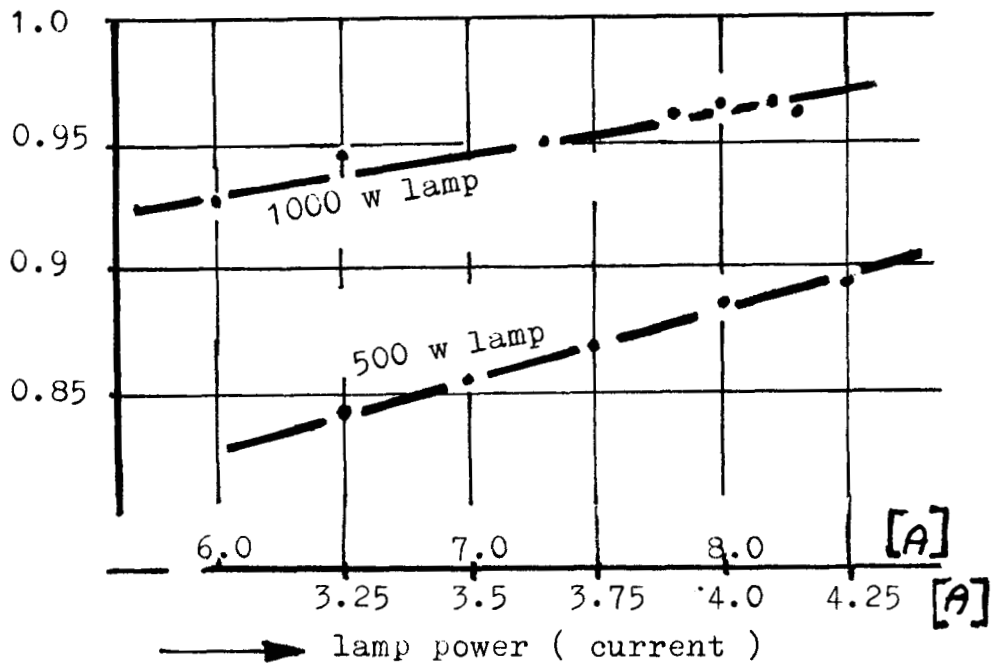

Measurements with and without quartz plate - as already mentioned - were performed in order to eliminate the radiation of the bulb itself from which the bulb temperatures are found when considering:

$$\frac{\text{signal with quartz plate*}}{\text{signal without quartz plate}} = \frac{\varepsilon_f \cdot F_f \cdot \sigma \cdot T_f^4 - \varepsilon_b \cdot F_b \cdot \sigma \cdot (T_b^4 - T_a^4)}{\varepsilon \cdot {}_fF_f \cdot \sigma \cdot T_f^4}$$

(* corrected for surface reflections)

The emitted and absorbed energy is given for different lamp power in Fig. 6 a, b for the 500W lamp, and in fig. 7 a, b for the 1000W lamp.

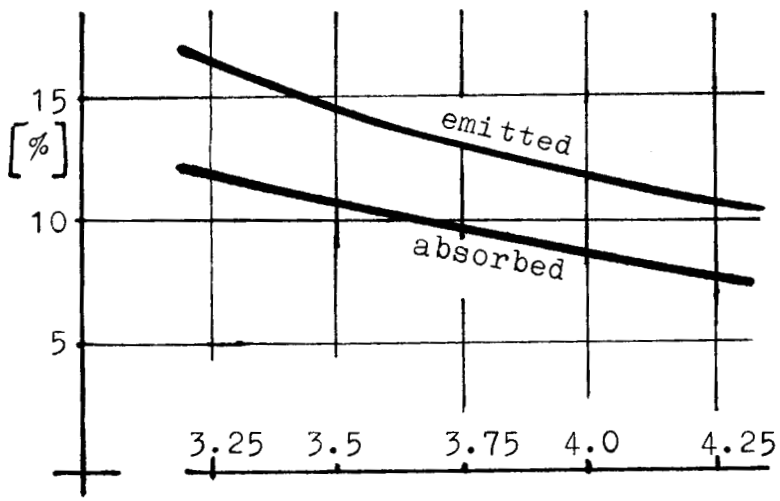

Fig. 6a : The emitted and absorbed energy of a quartz bulb (500 w) decreases compared with the total lamp output for high power level (at ambient)

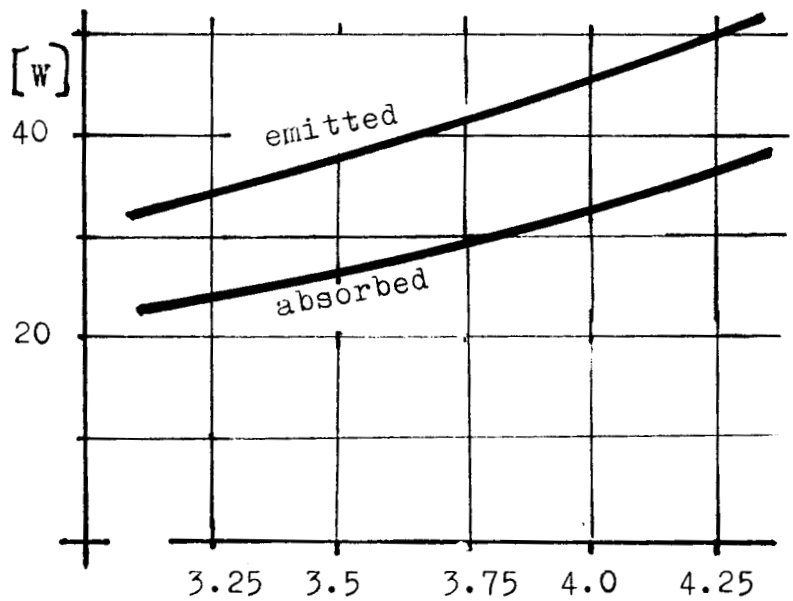

Fig. 6b : The emitted (and absorbed) energy of a 500 w lamp is 50 w at ambient and nominal power; the difference between absorbed and emitted energy is due to convective heat transfere filament-bulb

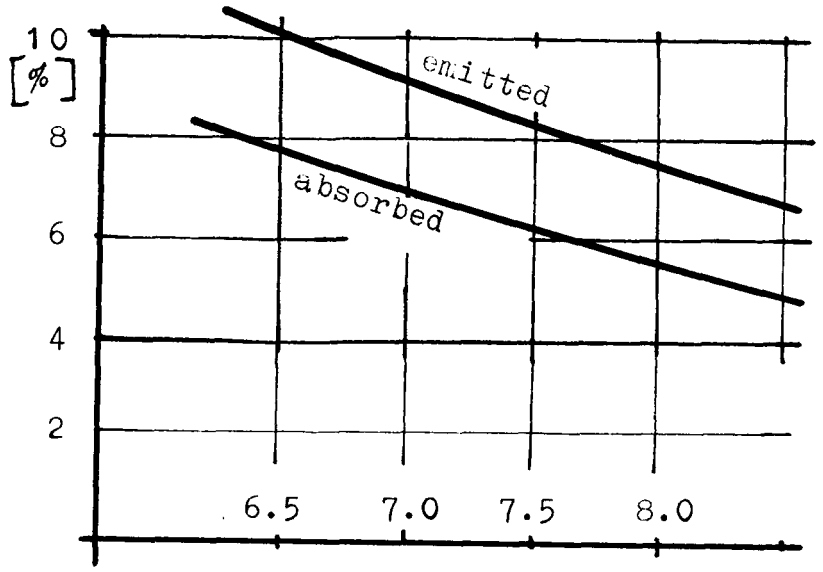

Fig. 7a :
The percentage of emitted and absorbed energy of a 1000 w lamp is considerably lower than found for the 500 w lamp.

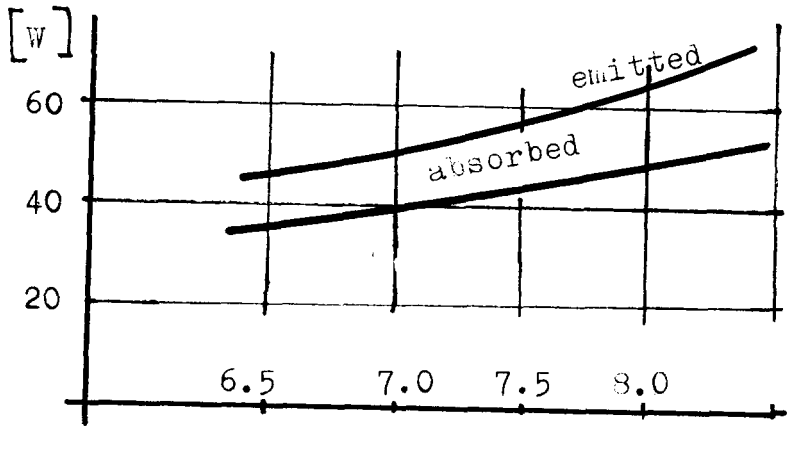

Fig. 7b :
The emitted and absorbed energy of the 1000 w lamp is only 35 % nigher than found for the 500 w lamp.

For simplicity T_a was not considered here; in worst case it will contribute only ~5% of the bulb radiation which is again only 20% of the total lamp radiation, hence it will be not more than 1%, of the total lamp intesity; for nominal power and for the 1000W lamp the error will be always negligible.

For these data, the bulb temperature T_b for both ambient and vacuum may be calculated; since ε_b, however, also depends on temperature (fig. 3) an iteration procedure had to be applied (fig. 8).

The conductivity factor C_{ba} of the heatflow from bulb to ambient air reamins - as to be expected - constant (fig. 9). One may assume that the cooling of the bulb by ambient air is in first approximation proportional to the bulb surface, and when comparing the 1000W lamp and the 500W lamp it agrees within ± 5% with their surface ratio. (Of course this is no longer valid in case the lamps are cooled e.g. by a fan).

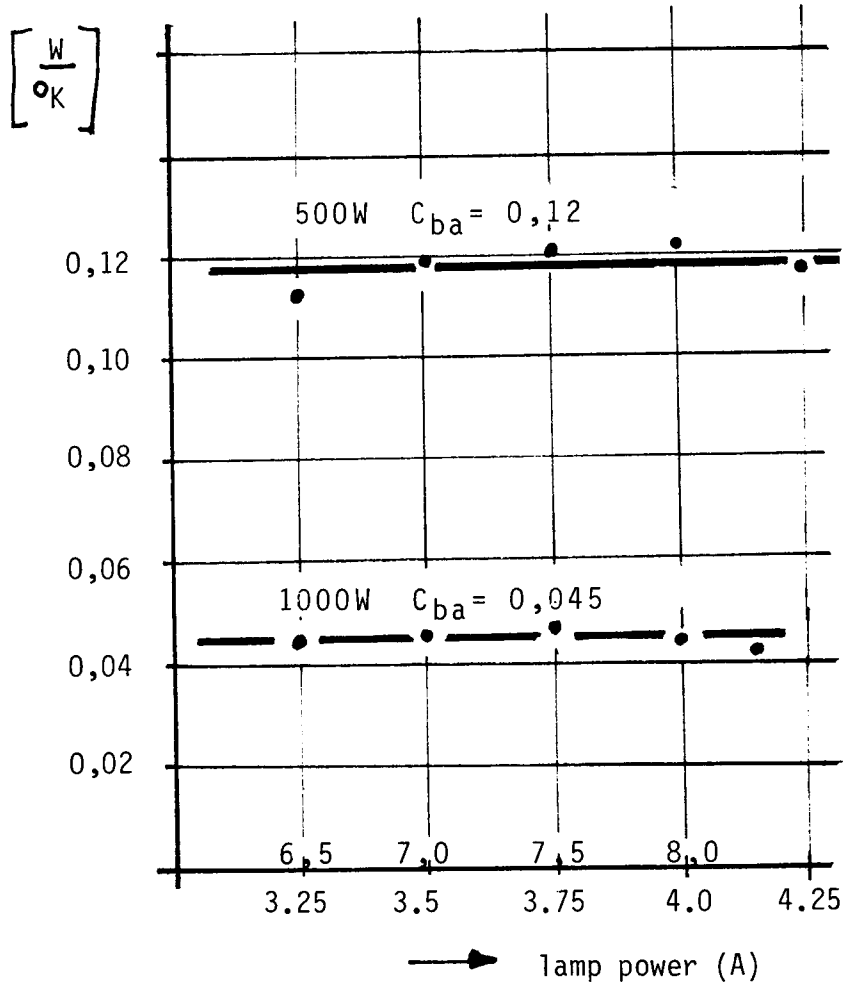

Fig. 9: Conductivity factor for heat transfer bulb-ambient

$(H_{ba} = C_{ba} (T_b - T_a)$

for a 500W lamp and a 1000W lamp.

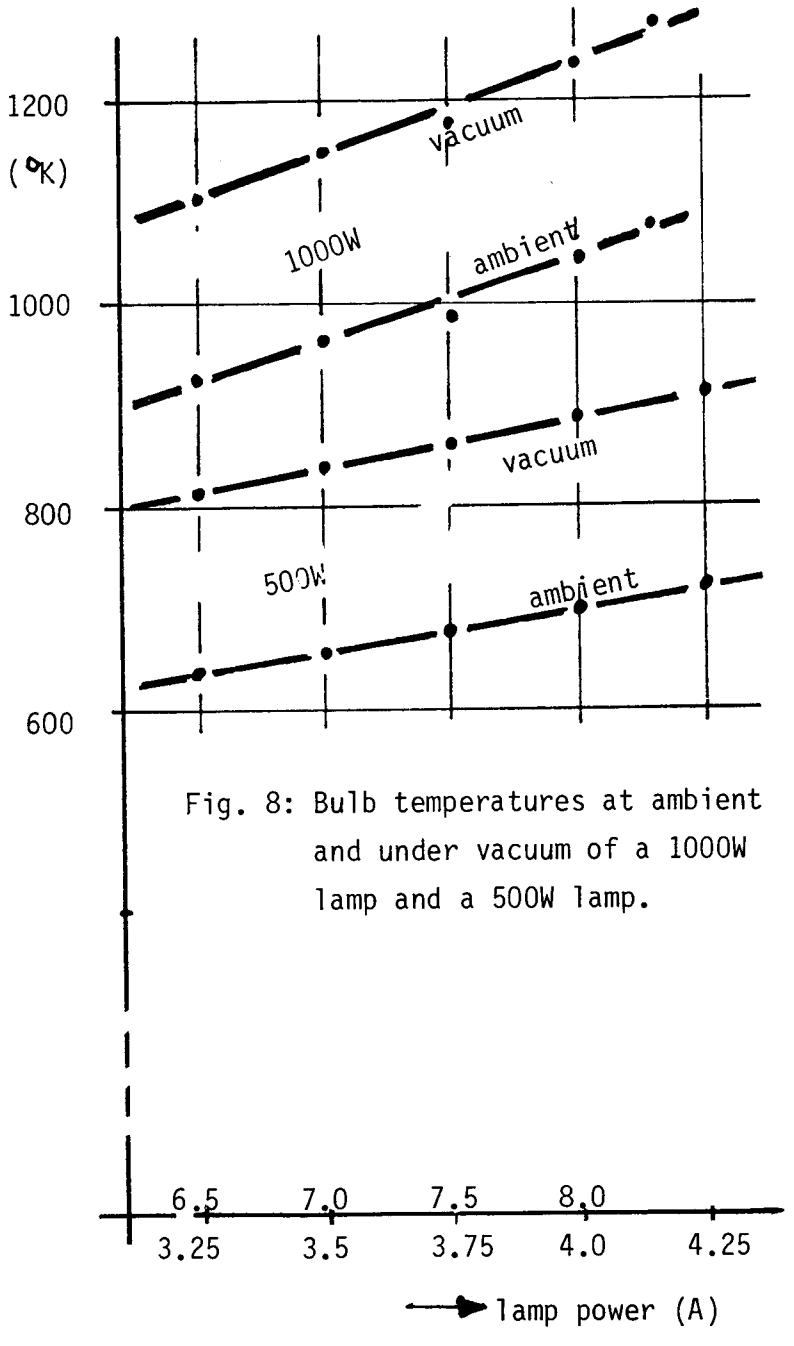

Fig. 8: Bulb temperatures at ambient and under vacuum of a 1000W lamp and a 500W lamp.

4.2 Heat transfer from filament to bulb

Since the boundary conditions of the lamps are know the inner parameters may be studied here - referring to the second equation - in particular:

- o the absorbed radiation energy by the bulb due to the opaqueness beyond 4μ.
- o the conductivity constant C_{fb}.
- o the back radiation bulb-filament.

The percentage of absorbed radiation by the bulb is increasing for lower filament temperatures due to the shift to longer wavelengths. (Fig. 10). When considering the back radiation bulb-filament one should know the effective absorptance for the configuration given (coiled spiral) as function of the temperature. It is assumed that the in first approximation the ratio of the effective absorptances at the temperatures T_1 and T_2 is the same as the ratio of the absorptances of tungsten for the same temperatures, or:

$$\frac{\alpha_{eff}\ (T_1)}{\alpha_{eff}\ (T_2)} = \frac{\alpha_{tungst}\ (T_1)}{\alpha_{tungst}\ (T_2)}$$

For nominal power (T = 3200°K) both effective absorptance ($\alpha = \varepsilon = 0.467$) and absorptance of tungsten ($\alpha = \varepsilon = 0,31$) is given.

The conductivity constant for the convective heat transfer of the gas in the lamp depends on the molecular velocity of the gas, which again depends on the root of the temperature.

It is:

$$C_{gas} = A \cdot n \cdot \bar{v} \cdot \bar{l} \cdot \frac{S_h}{N_l}$$

$\bar{v}$ - mean molecular velocity
$\bar{l}$ - mean free path
A - form factor
S_h - specific heat
N_l - Avogadro's Number
n - density

Here is only $\bar{v}$ a function of temperature (even $\bar{l}$ is temperature independent). Hence follows:

$$C_{gas} = \text{const} \sqrt{\frac{T}{T_o}}$$

Since C_{fb} increases with temperature, it compensates partly the influence of decreasing temperature difference ($T_{fil} - T_{bulb}$) when going from ambient to vacuum; in addition the back-radiation of the bulb will increase as well (T^4) and the decreasing emissivity ε_b of quartz is also partly compensated in this case by the increasing effective absorptance $\alpha_f = \varepsilon_f$.

Both effects have the consequence that the filament temperature - and hence the electrical power of the lamp when operated on constant current setting - will remain nearly constant when going from ambient to vacuum (difference $\sim$ 1%).

This result also means that no remarkable influence is to be expected when lamps without reflector are operated in a chamber with warm or cooled (LN_2) shrouds.

4.3 Discussion of the results for nude lamps

The measurements performed on nude lamps allow the following conclusions:

- When going from ambient to vacuum the additional heat input may easily be considered. (5 - 10% for the 1000W lamp and 10 - 17% for the 500W lamp).
- The lamps may be operated nearly at nominal power level with warm or cooled (LN_2) shrouds also under vacuum).
- In order to reduce the contribution of the bulb radiation the lamps should be operated nearly at nominal power level (e.g. it is better to use a few lamps at high power than numerous lamps at low power).

5. LAMPS WITH REFLECTOR

Naturally for IRSIM tests the radiation of the lamps to the rare side (to the shrouds) should be reduced as much as possible which means a reflector should be used. Commercially available were two types of lamp + reflector.

5.1 Lamp with reflecting white strip

The lamps with reflecting white strip (actually a TiO coating on the rare side of the quartz bulb) have the advantage that lamp and reflector are one radiation unit and thus simpler. The transparancy of the reflecting strip was however still $\sim$ 30% and that was considered too high; these lamps were therefore rejected for IRSIM test. The polar diagrams are shown in fig. 11.

5.2 Lamp with metallic reflector

The lamps provided with a metallic reflector showed no radiation to the back and were therefore chosen for IRSIM tests. Though all the IRSIM tests at ESTEC were performed with this type of lamp + reflector with good success, there is a disadvantage which cannot be overlooked: the polar radiation characteristics differ for the individual lamps considerably (see fig. 12).

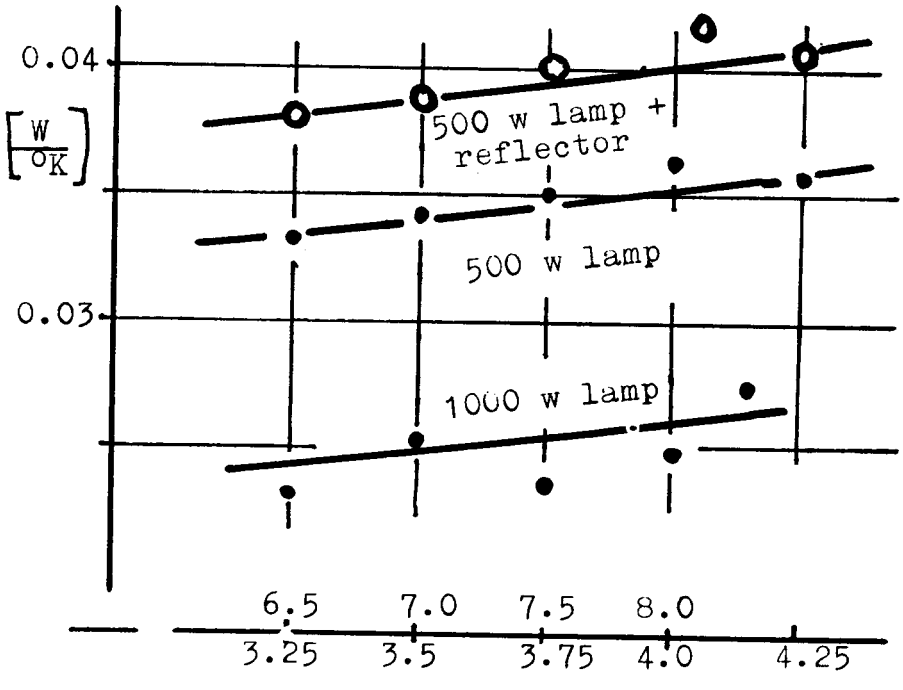

Fig. 10 :

Conductivity factor for the heat flow from filament to bulb; an estimation is also given for the 500 w lamp with reflactor

Fig. 11 :
Polar radiation diagram for 500 w lamps with reflecting white strip (TiO).

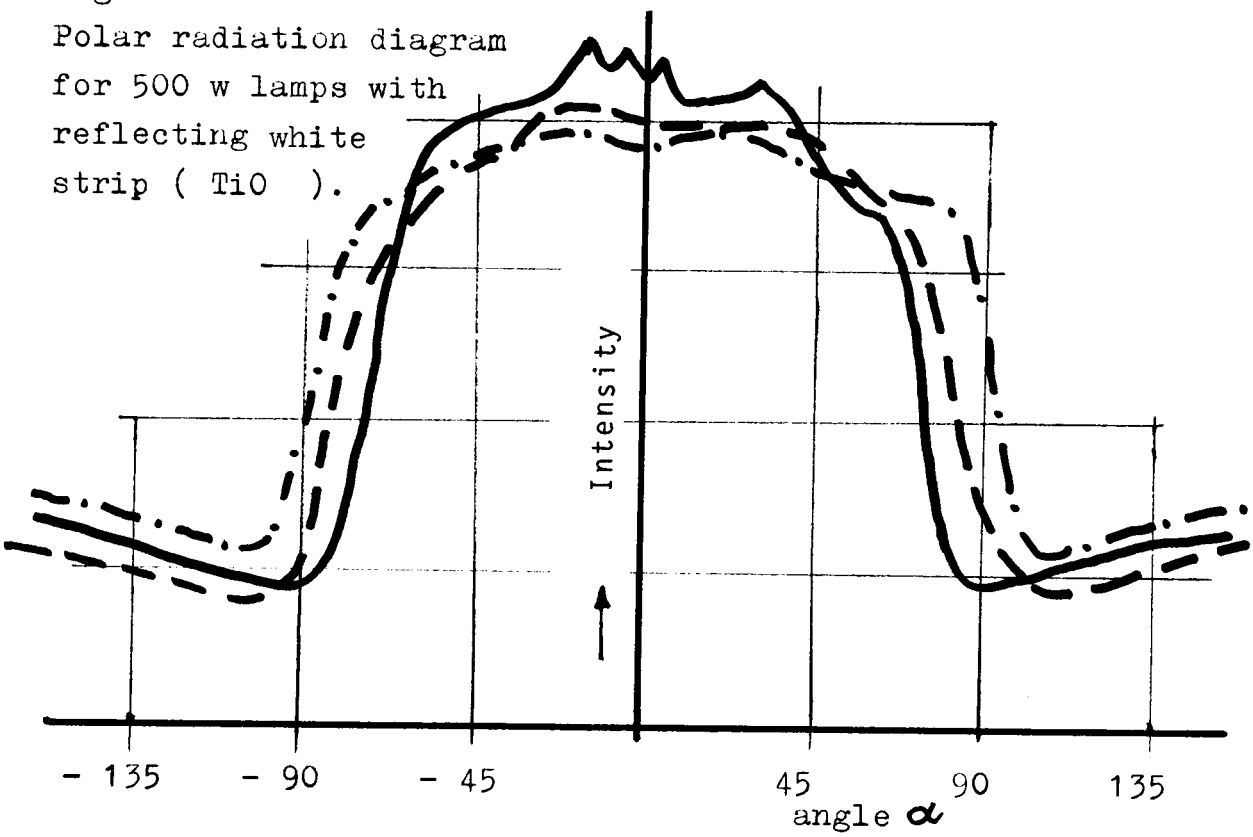

Fig. 12: Some polar diagrams of 500W lamps with metallic reflector.

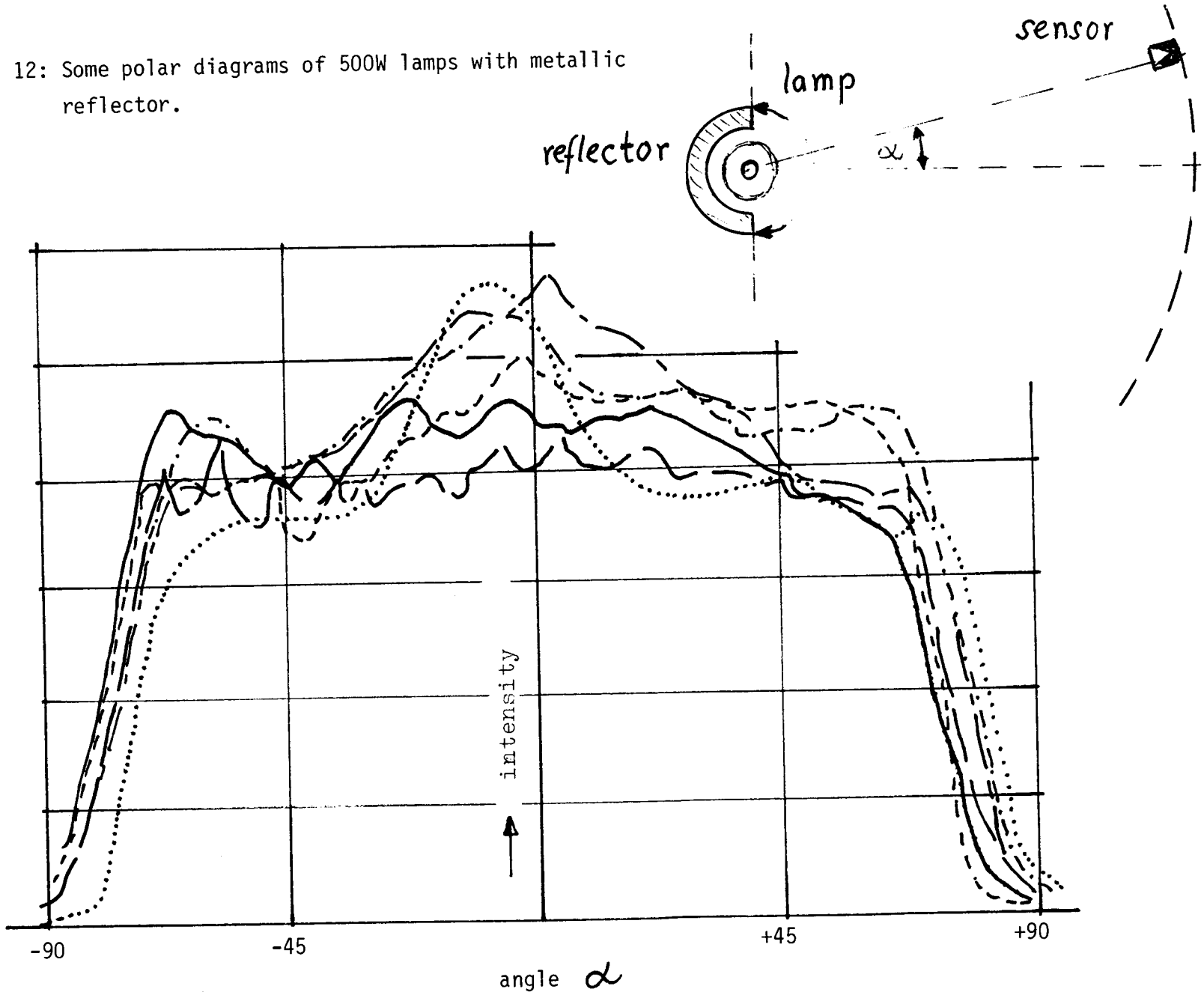

5.3 Discussion of the results of the polar diagrams

The polar diagrams of both types, show sharp peaks and valleys being superimposed to a more smooth slope. Since even nude lamps show occassionally these sharp peaks they are obviously due to imperfections of the quartz bulb itself (actually due to bubbles in the quartz, acting as focussing or defocussing lens). The irregularities showing the more smooth slope are due to imperfections of the reflector and/or misalignment of the filament in the reflector. In order to overcome these shortcomings one should:

- o use a lamp with larger filament diameter so that the peaks are more spread out and furthermore
- o use a diffuse reflector.

Both requirements may be met when using a 1000W quartz lamp (coiled spiral filament) with e.g. MgO coating on the rare side (7). The 1000W lamp has in addition the advantage that the radiation of the bulb itself is relatively low in comparison with the filament intensity. Unfortunately lamps with coated MgO back are delicate to handle because the MgO layer shows poor adherence. Numerous attemps with other coatings were performed (8, 9) and the investigations are still in progress, at present, however, as the most practical solution is considered a 1000W lamp in combination with a small stainless steel reflector coated with MgO.

6. 1000W LAMP WITH MgO COATED REFLECTOR

Reflector + lamp are shown in fig. 13. The reflecting surface was coated with MgO smoke; since here the coating was on an inner surface the poor adherence of the MgO did not affect the handling seriously.

6.1 Polar diagrams

As already mentioned it is highly desirable for the analysis to have for all lamp-reflector units an identical polar diagram. Even for a diffuse reflector a fair adjustment of the lamp is necessary in order to achieve reproducible polar diagrams. Since the position of the filament in the quartz bulb varies from lamp to lamp each filament had to be positioned to the centre line of the reflector individually by bending slightly the lamp holder.

For the NOSAT-IRSIM test 20 lamp + reflector units were prepared. For a complete analysis is of course necessary to know the radiation characteristics for the hemispherical space. Therefore for each lamp the polar diagrams were measured for: 90° (≙ lamp vertical), for the tilted positions 75°, 60°, 45°, 30°, 15° and for 0° (lamp horizontally, the filament is in the measuring plane). For the 0° position both the light intensity coming from the filament and that coming via the reflector should follow the cosine distribution; (except around 10° ± 4° - the inclination angle of the spirals of the filament - a somewhat lower intensity is found because of the higher blockage effect for the back part of the filament). The result is shown in fig. 14.

Fig. 13:

Lamp in a reflector (MgO coated; this reflector has a low blockage factor.

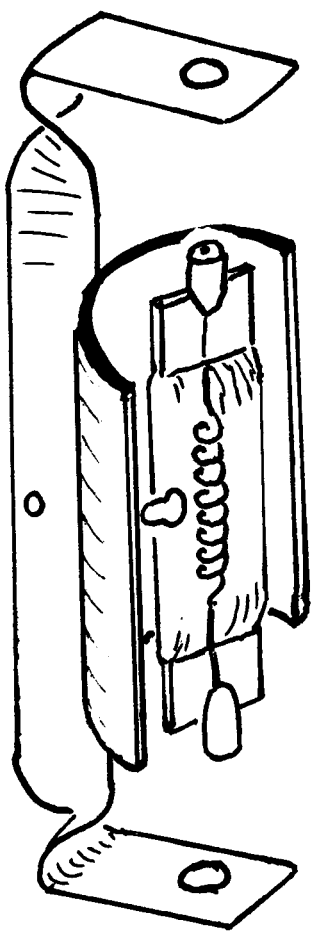

Fig.: 14

Polar diagrams of 1000W lamps with MgO coated reflector (hemispherical space) mean spread of 20 individual units.

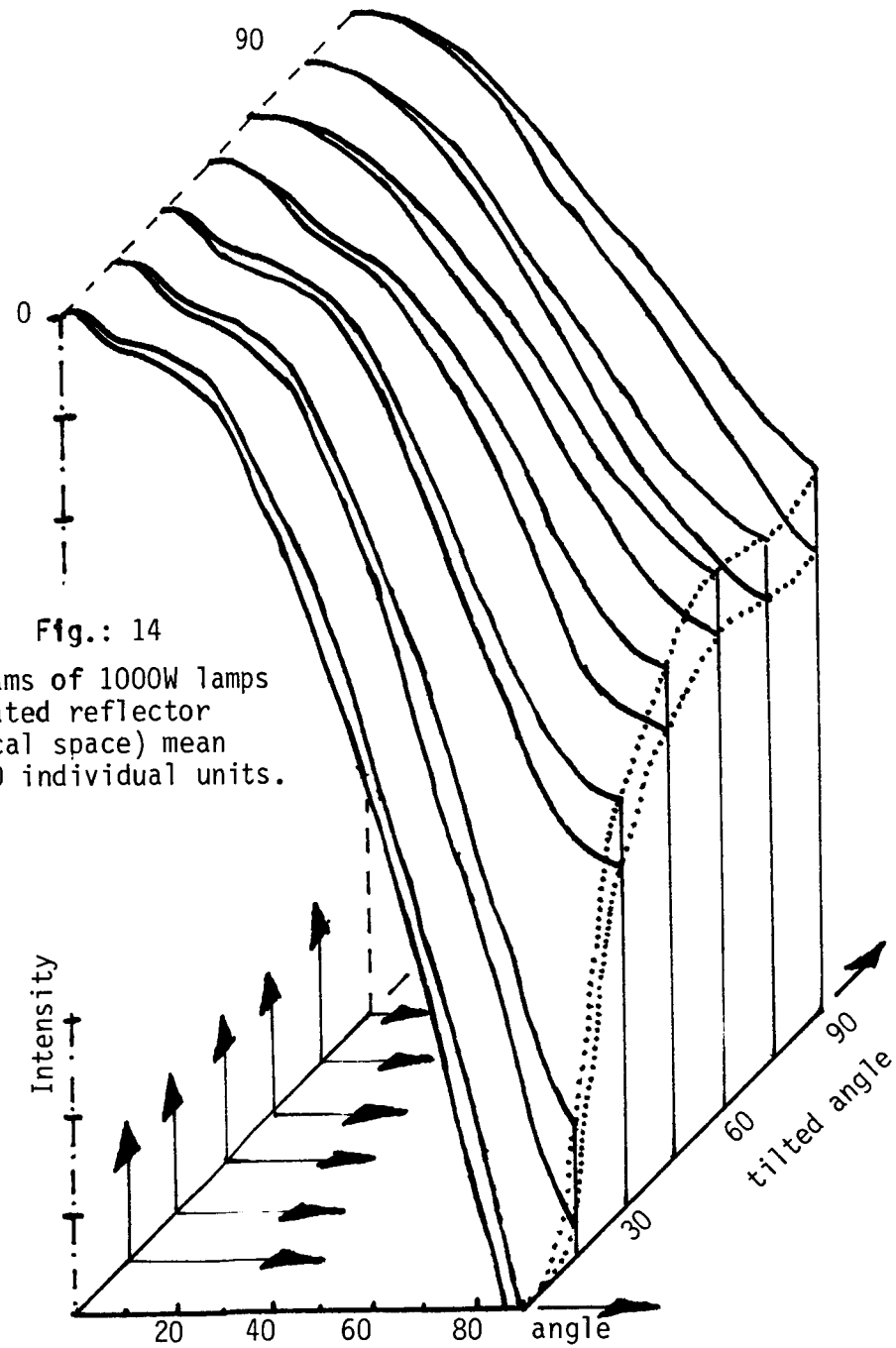

For the 90° position (lamp axis perpendicular to measuring plane) only the light intensity via the reflector should obey in first approximation the cosine law; that from the filament directly should be independant from the angle; hence for the angular intensity distribution one should in first approximation expect a cosine superimposed to an independent value. For the tilted lamp positions one should of course expect a gradual change between these two polar radiation diagrams.

Naturally the total light output for the same power setting varies for the individual lamps slightly ($\sim \pm$ 1%). It is, however, easy to adapt the lamp power for each lamp such that the same maximum intensity - perpendicular to lamp + reflector - is achieved and to normalise in this way the polar diagrams. This was done for these lamps; the lamp current varied between 7.78 and 7.95 A. The scatter for the individual lamps is indicated.

6.2 I.R. contribution when going from ambient to vacuum

As already mentioned it is common practice to measure the intensity of a lamp array at ambient and to extrapolate or calculate the intensity for vacuum conditions. Previous measurement on the 500W lamp showed for the intensity obtained at ambient and under vacuum the ratio 0.9 for nominal power level which decreased with decreasing power level and for 50% power level 0.84 was found; for the lamps with metallic reflector approximately the same ratio was found. Therefore also for the 1000W lamp with reflector a similar ratio is expected as found for the nude lamps (fig. 15). That actually a slightly higher effect was found is possibly due to the diffuse reflector. Irrespective, however, the cooling effect is also here only halve the value found for the 500W lamp + reflector.

The temperature of the reflector itself was measured (see fig. 16) and for nominal power only 270°C were measured; no problems are anticipated concerning heat input onto uncooled shrouds and structure when calibrating the lamp array at ambient.

6.3 Experience on 1000W lamp + reflector

As described in §4.3 the vacuum has little effect on the filament temperature. The reflector, however, blocks off nearly halve the radiation, hence a stronger influence is to be expected. Since for the 1000W lamp bulb and specially the filament temperatures are considerably higher than found for the 500W lamp the reliability had to be checked. Several lamps were tested for $\sim$ 400 h at nominal power - and occasionally even a few percent higher. All lamps survived, only on one lamp the filament sunk slightly down with the consequence that due to the dense filament spirals the quartz bulb reached the softening temperature on the reflector side and formed a small bubble. Long term tests are not yet performed at reduced power level; however at 90% power the filament temperature would be reduced by Δ T = $\sim$ 85°K and at 80% even by 180°K so one may conclude that long test periods may be performed in case the lamp power is restricted to $\sim$80% of nominal power.

Fig. 15: Ratio of the output of a 1000 w lamp and a 500 w lamp with reflector obtained at ambient and under vacuum

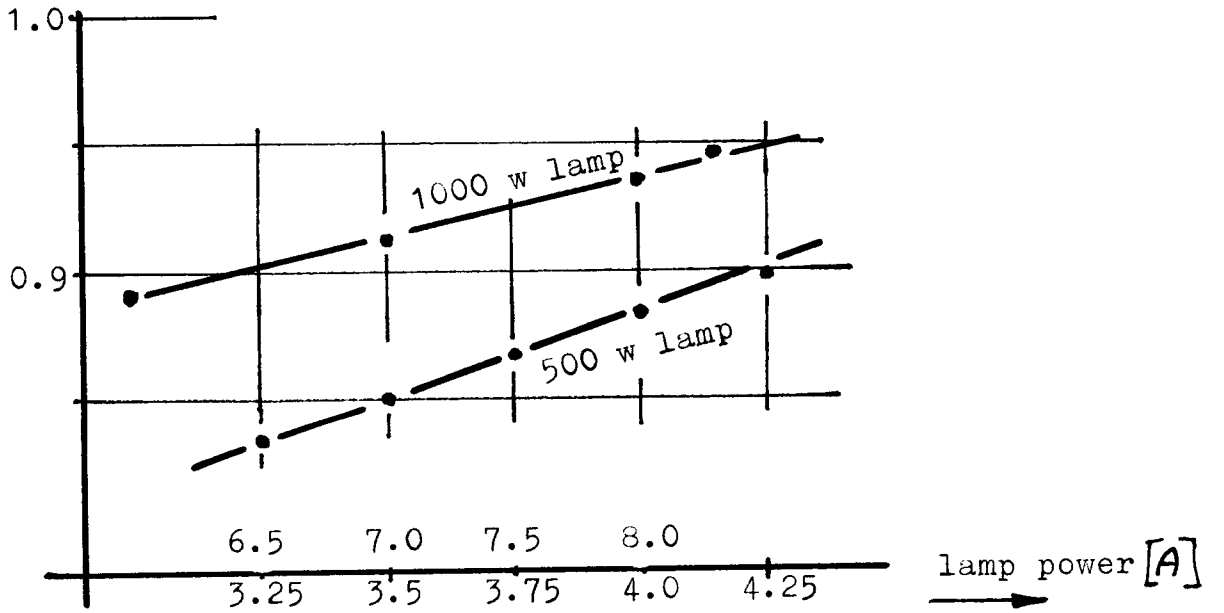

Fig. 16: Temperature of the MgO coated reflector of a 1000 w lamp as function of lamp power

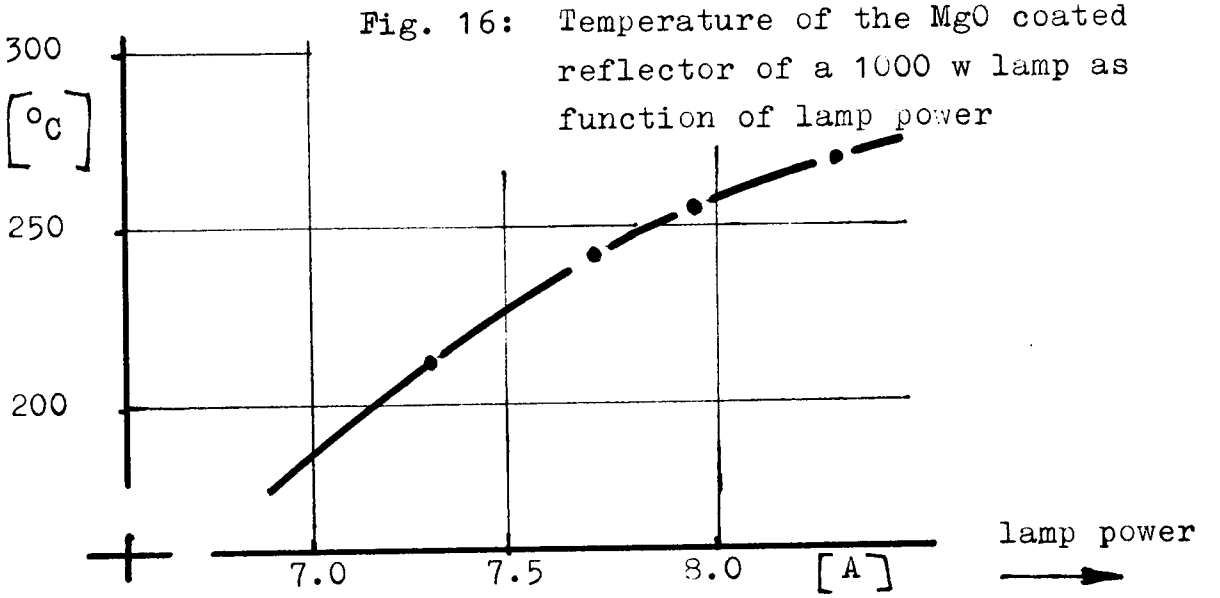

The reflectors survived the test as well though here by protective coating with a noble metal improvements are feasible.

7. DISCUSSION AND EXPECTED ACCURACY OF THE 1000W LAMP + MgO REFLECTOR

Previous investigations showed that a good solution is obtained for the lamp array given in fig. 17 and when the mutual distance of the lamps is approximately the same as to the test plane. In the following for this configuration reproducibility, intensity distribution and accuracy shall be discussed. (10).

7.1 Reproducibility

Referring to the polar diagrams and the scatter in intensity given in fig. 14 the achievable reproducibility was calculated for the central point (perpendicular to the central lamp); it is assumed that this represents the reproducibility of the whole lamp array. The calculated contribution to the total intensity of the individual array parts (central lamp, 1. lamp square, 2. lamp square, 3. lamp square) is shown in fig. 18, and for the overall reproducibility follows 0.5%. Not incluced is here a geometrical misalignment of the lamps; irrespective, however, it is considered that an overall reproducibility of within ± 0.5% should be achieved.

7.2 Intensity distribution

In figs 19, 20 the calculated intensity distribution for the Y-axis is given for the distance to the test plane 30, 50, 70 and 90cm; the mutual distance of the lamps was always 70cm. It demonstrates that also for this polar diagram for ~70cm distance (~ same distance of the lamps) an optimum is achieved; larger distances cause mainly a sharper fall off towards the corner. The intensity drop between the lamps is only ± 2%.

7.3 Expected accuracy of the intensity for test conditions

When calibrating a lamp array at ambient and extrapolating for vacuum the following uncertainties and corrections are to be considered; for lamp power was assumed 75% of nominal power (~ 7.5 A).

1.	Accuracy of primary standard fluxmeter	:	± 1%
2.	Reproducibility of lamp array	:	± 0.5%
3.	Contribution of bulb when going into vacuum (no longer air cooling) + 7%	:	± 0.2%
4.	I.R. absorption by water vapour + 1%	:	± 0.2%
5.	Correction for higher filament temperature under vacuum (in case lamps are operated at constant current) + 2%	:	± 0.2%

The overall accuracy is still within ± 1.5%.

Fig. 17:

Lamp array of 49 lamps schematic.

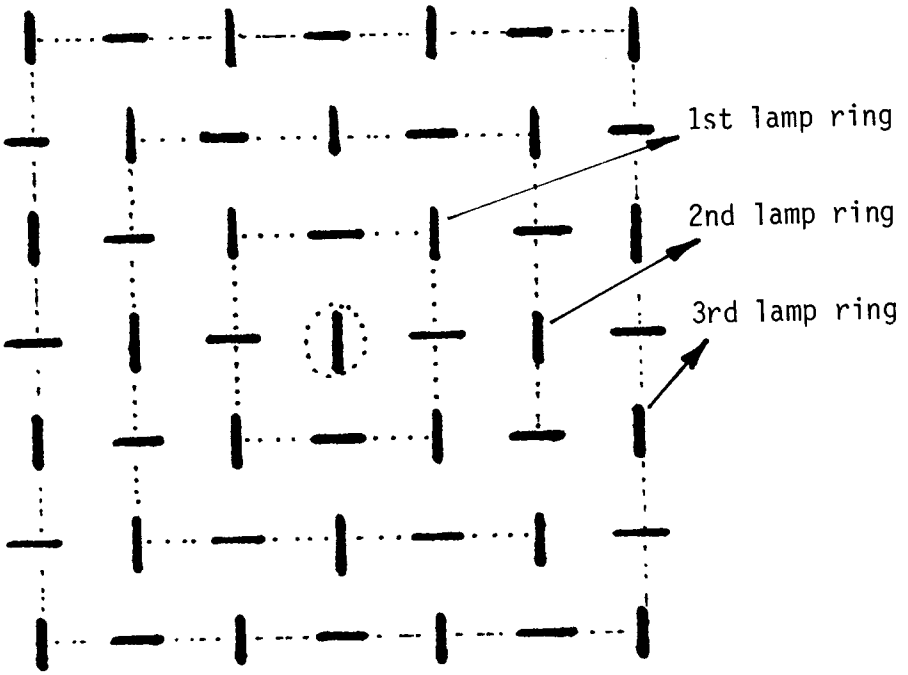

Fig. 18:

Calculated intensity at the central point (opposite central lamp).
Contribution of the individual lamp rings.
The calculated scatter of the intensity for the individual lamp rings is given below.
It is below 1% for the worst case.

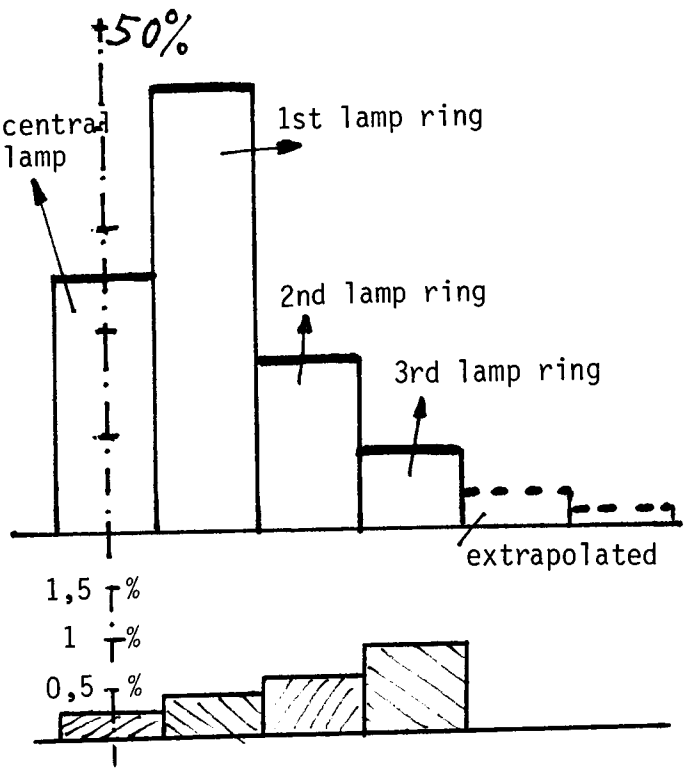

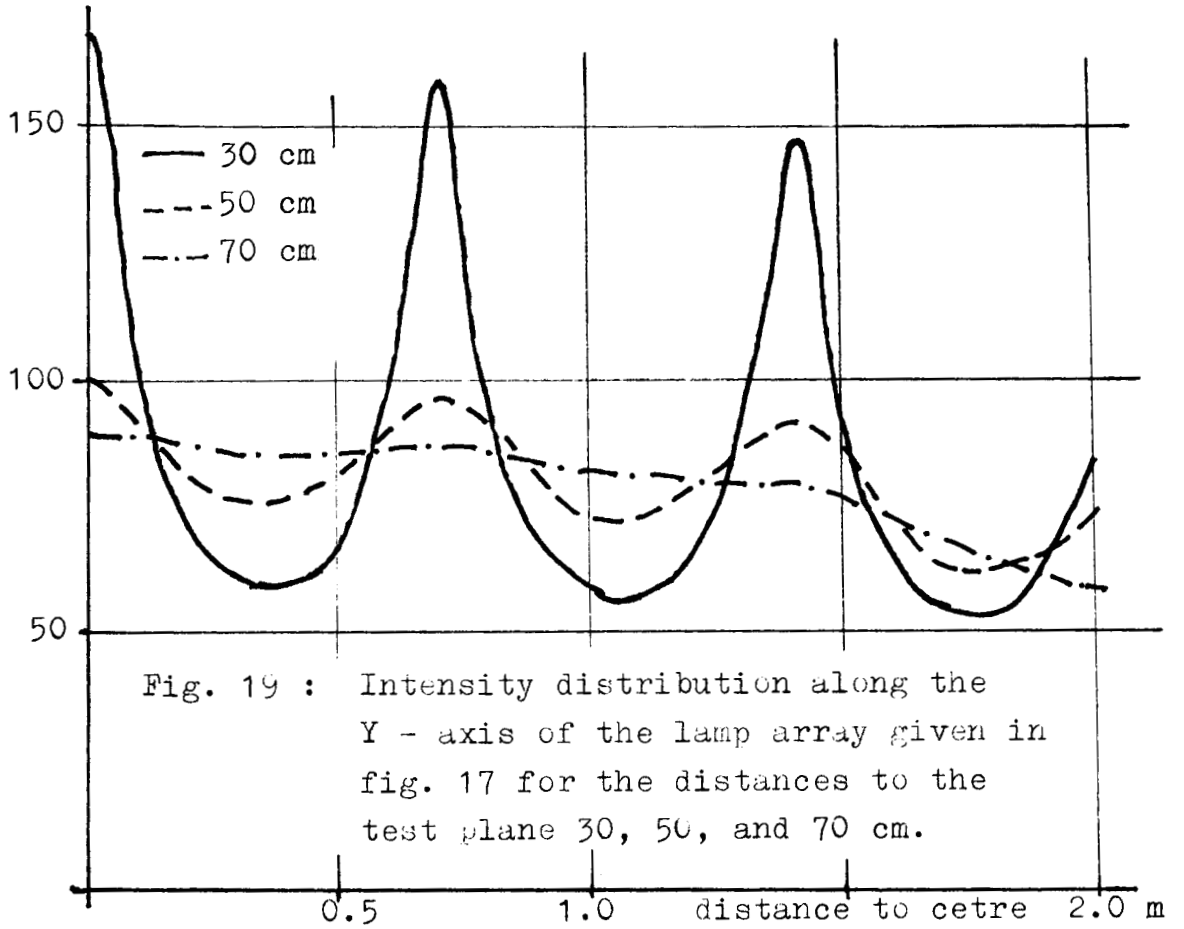

Fig. 19 : Intensity distribution along the Y - axis of the lamp array given in fig. 17 for the distances to the test plane 30, 50, and 70 cm.

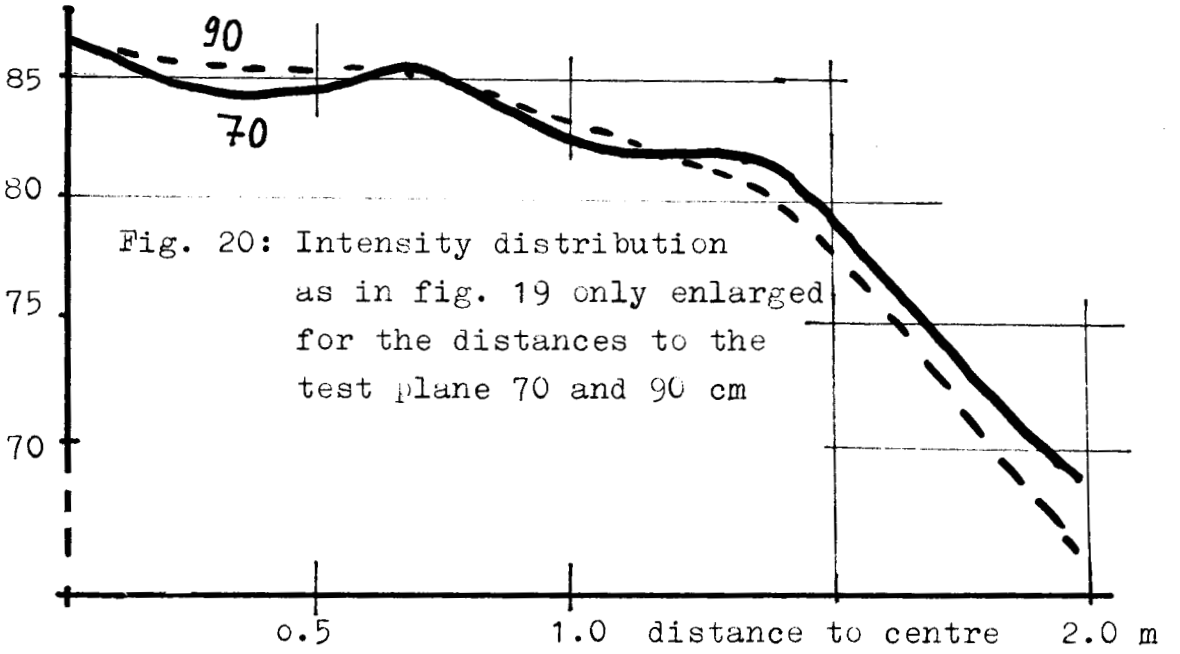

Fig. 20: Intensity distribution as in fig. 19 only enlarged for the distances to the test plane 70 and 90 cm

REFERENCES

1. Y. Chaouat & J.B. Walker

"Surface Property measurements for Spacecraft Thermal Balance Testing", Environmental & Thermal Control systems for Space Vehicles International Symposium, Toulouse, France, 4-7 October 1983.

2. R. Stair, R.G. Johnston and E.W. Halbach

Journal of Research of the NBS Vol. 64A, No 4 July-August 1960.
"Standard of Spectral Radiance for the Region of 0.25 - 2.6 ".

3,4 "Thermal Radiative Properties"
Thermophysical properties of Matter IFI/Plenum, New York - Washington 1970.

5. G. Sänger, W.A. Shickle

"Influence of the I.R. Absorption on the measurements of simulated Solar Radiation".
ESRO TN-94, Sept. 1969.

6. G. Bauer

"Strahlungsmessungen im optischen Bereich".
Friedrich Viehweg & Sohn, Braunschweig 1962.

7. 32nd meeting aof the "Working Group for Space Simulation", Seal Beach, California, Sept. 1985.

8. Y. Chaouat, ESTEC private communication.

9. De Jonge, Fa. Michael Holland Chroome, Amsterdam, private communication.

10. R.P. Rogers, ESTEC, private communication.

ANNEX

The absorption of the quartz bulb of a lamp was measured by means of a monochromator. One lamp 1000W was placed before the entrance slit of the monochromator (filament off axis) and the light of a second 1000W lamp was focussed onto the monochromator slit, passing the bulb (only) of the first lamp. The quartz was heated up by operating this first lamp at the power level concerned, and the ratio to the transmittance at ambient (no lamp power) is measured.

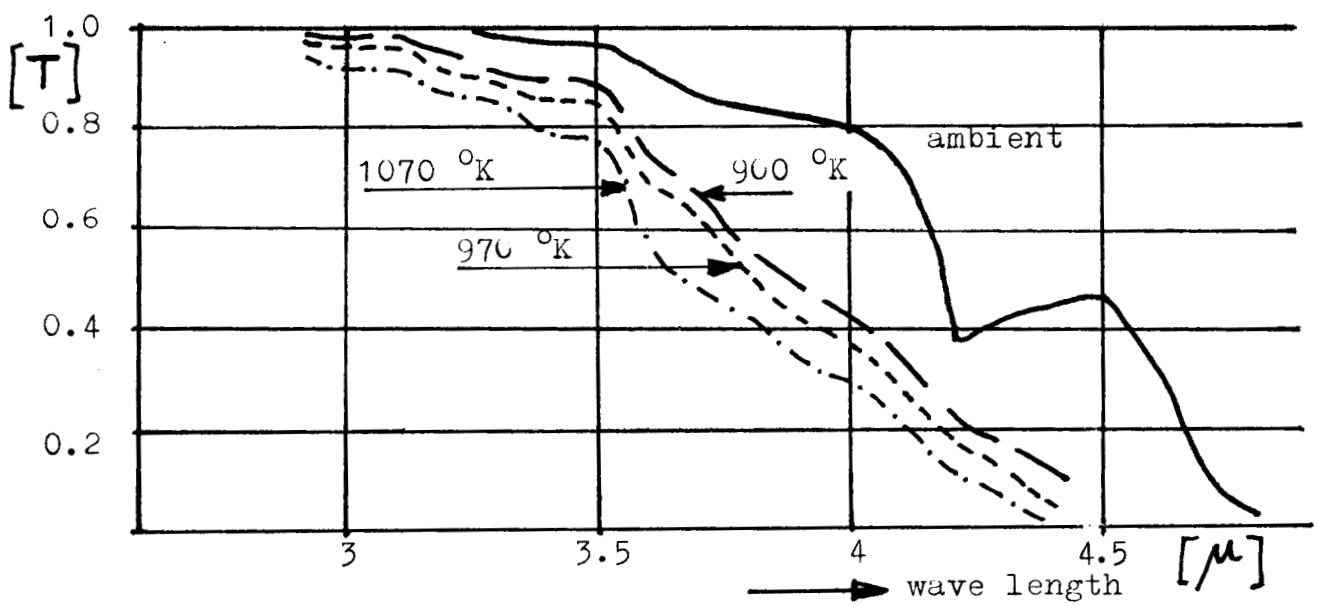

Fig. : Transmission of quartz around the cut off range (3 ÷ 5 μ) at ambient and at the operational temperatures of the quartz lamp (1000 w Lamp) operated at 8.30; 7.0; and 6.0 Amp. The surface reflection is not considered.

EVALUATION OF THE INFRARED TEST METHOD FOR THE OLYMPUS THERMAL BALANCE TESTS

M. Donato, D. St-Pierre, J. Green
Spar Aerospace Limited, Ste-Anne-de-Bellevue, Quebec, Canada

M. Reeves
David Florida Laboratory, Ottawa, Ontario, Canada

ABSTRACT

The present work reports on the performance of the infrared (IR) rig used for the thermal balance testing of the Olympus S/C thermal model. Included in this evaluation are the rig effects themselves, the IRFLUX computer code used to predict the radiation inputs, the Monitored Background Radiometers (MBR's) developed to measure the absorbed radiation flux intensity, the UTR (Uniform Temperature Reference) based temperature measurement system and the DPS data acquisition system.

The IR rig description and design has been reported in a previous paper (1). The logistics for the preparation and running of the rig and facilities are going to be detailed and compared to those for a Solar Simulation facility.

A preliminary set of verification tests were performed on a 1 m x 1 m zone to access the performance of the IR lamps, calrods, MBR's and aluminized baffles. The results were used, in part, to obtain some empirical data required for the IRFLUX code. This data included lamp and calrod characteristics, the absorptance function for various surface types, and the baffle reflectivities.

The MBR's were coated and calibrated with the same surface finishes as found in the S/C zones. Two different geometries were used; a round radiometer for all kapton surfaces (black paint, ITO) and a square MBR design for SSM's and white painted carbon fiber surfaces. Because eighty MBR's were used for the test, a mounting technique which did not interfere with the S/C surfaces was devised.

The temperature measurement system was based on UTR's located inside the chamber such that all feedthroughs were copper-copper. This system was devised to achieve a temperature measurement accuracy of $\pm$ 0.2 C for the over 900 thermocouples used in the tests. A primary and secondary real time data acquisition system were linked in order to provide continuous monitoring of all channels based on a two minute time scan.

The Olympus Thermal Model tests were divided in five phases: equinox, eclipse, sun off full power calibration, winter solstice and summer solstice. A detailed analysis for each S/C zone was performed to separate the effects of rig, shroud, the interaction of other S/C zones and the IR source radiation. For all tests phases the temperatures of the baffles, lamp and calrod supports, and major rig members were recorded. The radiation flux intensity on the S/C zones arising from the various rig elements was measured and compared with direct calculations and with pretest predictions.

(1) Design of an Orbital Heating Simulator Using IR Techniques by Donato et al, 13th Space Simulation Conference, 1984.

TRANSIENT MODELING OF THE THERMOHYDRAULIC BEHAVIOR OF HIGH TEMPERATURE HEAT PIPES FOR SPACE REACTOR APPLICATIONS*

Michael L. Hall and Joseph M. Doster
Nuclear Engineering Department
North Carolina State University

ABSTRACT

Many proposed space reactor designs employ heat pipes as a means of conveying heat. Previous researchers have been concerned with steady state operation, but the transient operation is of interest in space reactor applications due to the necessity of remote startup and shutdown. A model is being developed to study the dynamic behavior of high temperature heat pipes during startup, shutdown and normal operation under space environments. Model development and preliminary results for a hypothetical design of the system are presented.

INTRODUCTION

HEAT PIPE DESCRIPTION

A heat pipe is an effective means of transferring heat from one location to another without pumps or moving parts. It consists of a closed system filled with a working fluid. One section of the pipe is placed in a heat source, causing the working fluid to evaporate and the resultant vapor to expand into the remainder of the heat pipe. A different section of the heat pipe is placed in a heat sink, causing the working fluid to condense. The liquid is then conveyed back to the evaporator section by capillary action through a wick structure (see figure 1). The primary heat transfer is due to the latent heat of the working fluid, which results in a nearly isothermal system. The large heat transfer with the accompanying small change in temperature makes the heat pipe equivalent to a structure with a very high thermal conductivity.

DESIGN CONSIDERATIONS FOR SPACE REACTOR USE

Many of the current space based reactor designs for both civilian and military applications employ heat pipes as a means of conveying heat (ref. 1). In these designs, thermal radiation is the principal means for rejecting waste heat from the reactor system, making it desirable to operate at high temperatures.

*The research was performed under appointment to the Nuclear Engineering, Health Physics, and Radioactive Waste Management Fellowships program administered by Oak Ridge Associated Universities for the U. S. Department of Energy.

Lithium is generally the working fluid of choice as it undergoes a liquid-vapor transformation at the preferred operating temperature. There are, however, problems inherent to the choice of a liquid metal as the working fluid. The reactor assembly will have to be launched into orbit, presumably in a cold state with the lithium solid. Therefore, the conditions under which the heat pipe will be self-priming from a frozen state are of great interest. A similar problem is that of restarting the heat pipe after it has been shut down and allowed to solidify; the difference between this problem and the former one being the initial distribution of the solid lithium. An additional concern, particularly in military applications, is the ability of the system to handle extreme bursts of heat input concentrated at a particular location such as might be expected if the satellite were the subject of a military attack.

PURPOSE OF THIS WORK

The steady state behavior of heat pipes has been studied by other researchers (refs. 2,3,4). However, the nature of the previously mentioned processes of remote startup, restart, and reaction to threats necessitates an accurate, detailed transient model of the heat pipe operation. This paper covers the development of a model of the vapor core region of the heat pipe which is part of a larger model of the entire heat pipe thermal response. Other transient heat pipe modeling has been done, including a thermal model of a low temperature heat pipe by Chang and Colwell (ref. 5) which does not include the hydraulic behavior modeled in this paper. Another notable effort involves a modification of the ATHENA code to model an entire space reactor system (ref. 6). This paper differs from the ATHENA code modification in its modeling of diffusion, which the ATHENA code does not treat. In addition, future plans for the model presented in this paper include the modeling of startup from a frozen state.

MODEL DEVELOPMENT

CORE MODEL

The vapor core is modeled using the area averaged Navier-Stokes equations in one dimension, which take into account the effects of mass, energy and momentum transfer. The core model is single phase (gaseous), but contains two components: lithium gas and a noncondensible vapor. The differential form of the equation set used is:

Mixture Continuity Equation

$$\frac{\partial \rho_m}{\partial t} + \frac{\partial}{\partial z}(\rho_m V_m) = \Gamma + \frac{\partial}{\partial z}\left[\rho_m (D_N - D_g)\frac{\partial X_N}{\partial z}\right]$$

Noncondensible Continuity Equation

$$\frac{\partial \rho_N}{\partial t} + \frac{\partial}{\partial z}(\rho_N V_m) = \frac{\partial}{\partial z}\left[[\rho_m D_N]\frac{\partial X_N}{\partial z}\right]$$

Mixture Internal Energy Equation

$$\frac{\partial (\rho u)_m}{\partial t} + \frac{\partial}{\partial z}\left[(\rho u)_m V_m\right] = -P_m \frac{\partial V_m}{\partial z} + \Gamma h_g^{pc} - H(\frac{2}{r})(T_m - T_w) + \frac{\partial}{\partial z}\left[\rho_m \{D_N h_N - D_g h_g\}\frac{\partial X_N}{\partial z}\right]$$

Mixture Momentum Equation

$$\rho_m \frac{\partial V_m}{\partial t} + \rho_m V_m \frac{\partial V_m}{\partial z} = -\frac{\partial P_m}{\partial z} - \frac{f_m \rho_m}{2D_h} V_m \left|V_m\right| + \rho_m g$$

State Equation

$$\rho_m = \rho_m (P_m, (\rho u)_m, \rho_N)$$

This equation set presupposes the thermal equilibrium of the lithium gas and the noncondensible, making a second internal energy equation unnecessary. The gases are assumed to have the same convective velocity, eliminating the need for a second momentum equation. However, differing diffusive velocities are allowed with the inclusion of concentration driven mass diffusion (ref. 7). Evaporation and condensation provide mass and energy transfer to and from the liquid wick section. Condensation is assumed to occur only at the liquid-vapor interface, and not by liquid droplet formation in the vapor core. The evaporation rate is given by the following relation:

$$\Gamma = (\frac{2}{r})(\frac{M_g}{2\pi R T_w})^{1/2}[P_{sat}(T_w) - P_g]$$

Convective energy loss to the wick surface is included, but thermal conduction is not included in the model at present. The body forces are assumed zero for a space based system.

This system of coupled nonlinear partial differential equations is solved using a finite difference method. First, the equations are differenced spatially, using a staggered mesh in which the fluid properties are evaluated at the cell centers and velocities are evaluated at cell boundaries. When it is necessary to evaluate a fluid property at a cell boundary, the variable is "donored" (symbolized by a dot over the variable) by setting it equal to the closest "upstream" cell center value, where "upstream" is determined by the velocity at that location. For example, the donored density is defined as:

$$\dot{\rho}_{i+1/2} = \begin{cases} \rho_i & \text{if } V_{i+1/2} > 0 \\ \rho_{i+1} & \text{if } V_{i+1/2} < 0 \end{cases}$$

The equations are differenced temporally using a semi-implicit discretization which maintains a linear system in the new time variables while adding increased stability over a fully explicit method. In the semi-implicit method, the velocities in the convective terms and the pressures in the momentum equation are evaluated at the new time step. Finally, the state equation is differenced separately by expanding it about the present time step in a Taylor's series, truncating the series after the linear terms and evaluating the truncated series at the new time step. The final discretized system is:

Mixture Continuity Equation

$$\frac{\rho_{m,i}^{N+1} - \rho_{m,i}^{N}}{\Delta t} + \frac{\dot{\rho}_m^N V_m^{N+1}\Big|_{i+\frac{1}{2}} - \dot{\rho}_m^N V_m^{N+1}\Big|_{i-\frac{1}{2}}}{\Delta z_i} = \Gamma_i^N + \frac{1}{\Delta z_i}\left[\dot{\rho}_m^N (D_N - D_g)\Big|_{i+\frac{1}{2}} \left(\frac{X_{N,i+1}^N - X_{N,i}^N}{\Delta z_{i+\frac{1}{2}}}\right) - \dot{\rho}_m^N (D_N - D_g)\Big|_{i-\frac{1}{2}} \left(\frac{X_{N,i}^N - X_{N,i-1}^N}{\Delta z_{i-\frac{1}{2}}}\right)\right]$$

Noncondensible Continuity Equation

$$\frac{\rho_{N,i}^{N+1} - \rho_{N,i}^{N}}{\Delta t} + \frac{\dot{\rho}_N V_m^{N+1}\Big|_{i+\frac{1}{2}} - \dot{\rho}_m^N V_m^{N+1}\Big|_{i-\frac{1}{2}}}{\Delta z_i} = \frac{1}{\Delta z_i}\left[\dot{\rho}_m^N D_N\Big|_{i+\frac{1}{2}} \left(\frac{X_{N,i+1}^N - X_{N,i}^N}{\Delta z_{i+\frac{1}{2}}}\right) - \dot{\rho}_m^N D_N\Big|_{i-\frac{1}{2}} \left(\frac{X_{N,i}^N - Z_{N,i-1}^N}{\Delta z_{i-\frac{1}{2}}}\right)\right]$$

Mixture Internal Energy Equation

$$\frac{(\rho u)_{m,i}^{N+1} - (\rho u)_{m,i}^{N}}{\Delta t} + \frac{(\dot{\rho} u)_m^N V_m^{N+1}\Big|_{i+\frac{1}{2}} - (\dot{\rho} u)_m^N V_m^{N+1}\Big|_{i-\frac{1}{2}}}{\Delta z_i} = -\frac{P_m^N (V_{m,i+\frac{1}{2}}^N - V_{m,i-\frac{1}{2}}^N)}{\Delta z_i}$$

$$+ \Gamma_i^N h_g^{pc} - H\left(\frac{2}{r}\right)(T_{m,i}^N - T_{m,i}^N) + \frac{1}{\Delta z_i}\left[\dot{\rho}_m^N (D_N h_N - D_g h_g)\Big|_{i+\frac{1}{2}} \left(\frac{X_{N,i+1}^N - X_{N,i}^N}{\Delta z_{i+\frac{1}{2}}}\right) - \dot{\rho}_m^N (D_N h_N - D_g h_g)\Big|_{i-\frac{1}{2}} \left(\frac{X_{N,i}^N - X_{N,i-1}^N}{\Delta z_{i-\frac{1}{2}}}\right)\right]$$

Mixture Momentum Equation

$$\frac{\dot{\rho}^{N}_{m,i+\frac{1}{2}}}{\Delta t}\left(V^{N+1}_{m,i+\frac{1}{2}}-V^{N}_{m,i+\frac{1}{2}}\right) + \dot{\rho}^{N}_{m,i+\frac{1}{2}}\left(V_m\frac{\partial V_m}{\partial z}\right)\Bigg|^{N}_{i+\frac{1}{2}} = -\left(\frac{P^{N+1}_{m,i+1}-P^{N+1}_{m,i}}{\Delta z_{i+\frac{1}{2}}}\right)$$

$$-\left(\frac{f^{N}_{m}\dot{\rho}^{N}_{m}}{2D_h}\,V^{N+1}_{m}\left|V^{N}_{m}\right|\right)_{i+\frac{1}{2}} + \dot{\rho}^{N}_{m,i+\frac{1}{2}}g$$

State Equation

$$\rho^{N+1}_{m,i} = \rho^{N}_{m,i} + \left(P^{N+1}_{m,i}-P^{N}_{m,i}\right)\frac{\partial \rho_m}{\partial P_m}\Bigg|^{N}_{i} + \left\{(\rho u)^{N+1}_{m,i} - (\rho u)^{N}_{m,i}\right\}\frac{\partial \rho_m}{\partial (\rho u)_m}\Bigg|^{N}_{i}$$

$$+ \left(\rho^{N+1}_{N,i}-\rho^{N}_{N,i}\right)\frac{\partial \rho_m}{\partial \rho_N}\Bigg|^{N}_{i}$$

These equations, along with a similar momentum equation evaluated at $i-\frac{1}{2}$, constitute a linear algebraic system of six equations in eight variables

$$\left(\rho^{N+1}_{m,i},\ \rho^{N+1}_{N,i},\ (\rho u)^{N+1}_{m,i},\ V^{N+1}_{m,i+\frac{1}{2}},\ V^{N+1}_{m,i-\frac{1}{2}},\ P^{N+1}_{m,i-1},\ P^{N+1}_{m,i},\ P^{N+1}_{m,i+1}\right)$$

Algebraic manipulation is used to reduce this to a single equation in three variables

$$\left(P^{N+1}_{m,i+1},\ P^{N+1}_{m,i},\ P^{N+1}_{m,i-1}\right)$$

This single equation is then applied at every node in the physical system to be modeled, resulting in a matrix equation with a tridiagonal structure. The matrix equation is easily solved by a forward-backward sweep (Thomas algorithm) to yield the pressure distribution at the new time step. Back substitution into the discretized equation set then yields the remainder of the variables at the new time step. This method of discretization is similar to the methods used in the TRAC and RELAP computer codes (refs. 8,9).

This finite difference method necessitates limits on the time step size in order to assure stability and accuracy. The Courant limit, which specifies that a fluid element cannot be transferred more than one cell during a time step, is:

$$\Delta t < \min_i \left|\frac{\Delta z_{i+\frac{1}{2}}}{V_{m,i+\frac{1}{2}}}\right|$$

The time step must also satisfy a diffusive Fourier modulus criterion:

$$\frac{1}{2} > \max_i \left|\frac{D_{N,i}\Delta t}{(\Delta z_i)^2}\right| \quad \text{and} \quad \frac{1}{2} > \max_i \left|\frac{(D_{N,i}-D_{g,i})\Delta t}{(\Delta z_i)^2}\right|$$

The error inherent to truncating the state equation series expansion, referred to as density truncation error, is controlled by decreasing the time step when

the error exceeds a user specified value:

$$\max_i \left| \frac{\rho_{m,i}^{N+1} - \rho_m(P_{m,i}^{N+1}, (\rho u)_{m,i}^{N+1}, \rho_{N,1}^{N+1})}{\rho_{m,i}^{N+1}} \right| < E_{max}$$

WALL/WICK MODEL

In the current work, the wall and the wick of the heat pipe are modeled simplistically. A detailed thermohydraulic model of the wick is under development. The primary reasons for including a model of the wall and the wick are: to provide a wall temperature for calculating evaporation rates and convective heat losses for the core model; and to connect the core model with boundary conditions exterior to the heat pipe. Currently, the wall and the wick are modeled as a single entity, using a lumped parameters approach which assumes a constant temperature throughout the wall and the wick at any particular axial node. The mechanisms of heat transfer available to the wall/wick are: exterior heat input, exterior radiative heat loss, convection to the core gas and evaporation at the core-wick interface. The heat balance equation for the wall/wick is then:

$$q''_{in} - \varepsilon\sigma T_w^4 + H(T_m - T_w) - (\frac{r}{2})\Gamma h_{fg} = \frac{m_w C_p}{A_s} \frac{dT_w}{dt}$$

After the core model is updated to the new time step, the wall temperature is up-dated by implicitly differencing this equation and solving the resultant nonlinear equation for the wall temperature by a Newton-Raphson rootfinding technique at every axial location. Exterior boundary conditions vary along the length of the heat pipe. In the evaporator section, a total net heat flux into the heat pipe is specified. In the adiabatic section of the heat pipe, all heat loss mechanisms are set to zero. Radiation is the only means of heat loss assumed in the condensing end of the heat pipe.

RESULTS

MODEL CONDITIONS

The model has been applied to a 2.0m heat pipe that consists of an evaporator section of $z\varepsilon[0,.3]$, an adiabatic section for $z\varepsilon[.3,1.5]$, and a condenser section for $z\varepsilon[1.5,2]$. These sections are used only to determine which boundary conditions to apply: heat input, zero heat flux, or heat output. A starting temperature of 700K is used. The heat pipe is operated at 15kW throughput for 20s in order to heat it up and then the power is dropped to the desired operating condition of 1.184kW. A heat pipe of this design would normally operate at 15kW and 1500K, but the highest throughput the model will allow with an operating temperature of 1500K is 1.184kW if the only means of heat loss is radiative cooling. Initially, the heat pipe is filled with a noncondensible gas (air) at a pressure of 250Pa.

ANALYTICAL STEADY STATE RESULTS

Most of the steady state heat pipe analysis has been based on Cotter's early work (ref.3). These analyses have been primarily concerned with pointing out limits to the heat transfer capability of the heat pipe in the form of sonic, boiling, wicking, and entrainment limits. Of greater importance to this work is the application of Cotter's theory to predict pressure, temperature, and velocity distributions inside the heat pipe's vapor core. Cotter's theory assumes that the temperature distribution is simply a constant value. The velocity distribution, assuming constant heat addition in the evaporator and constant heat rejection in the condenser, linearly increases from zero to Q_t/h_{fg} in the evaporator, remains constant through the adiabatic section, and then linearly decreases to zero again in the condenser. The predicted steady state pressure distribution is more complicated and is presented in Figure 2, as calculated by the HTPIPE code (ref. 4).

EXPERIMENTAL STARTUP OBSERVATIONS

In his later work, Cotter describes three basic modes of heat pipe startup that have been observed experimentally (ref. 10). The first mode, a uniform startup, occurs when the vapor density is high, and there is continuum flow throughout the heat pipe. A second, frontal startup mode is observed when the vapor density is so low that free molecular flow effects are important. This mode has a continuum to free molecular flow transition region that moves down the length of the heat pipe and causes the progressing, frontal temperature distribution. The third startup mode is also frontal, caused now by the presence of a noncondensible gas. This gas is swept out of the evaporator section and forms a plug that is compressed into the condenser end. The interface between the two gases is sharply defined and the temperature change across this front is more abrupt than that of the second startup mode.

MODEL RESULTS

The heat pipe was modeled for a period of greater than six minutes model time. The work was done in FORTRAN on a VAX-11/750 and required approximately 36 hours of CPU time. Results from the first 20 seconds (startup results) and from the state of the model at 360 seconds (when many of the primary fluctuations have died out and the model is approaching steady state) are presented.

Wall temperature increases evenly across the evaporator section during startup, with the rest of the heat pipe following behind (Figure 3). The step changes in temperature at the end of the evaporator are due to the simplistic wall/wick model where axial heat transfer has been neglected. The adiabatic and condenser wall sections are heated by condensation and convection from the central gas core. The mixture temperature generally follows the wall temperature (Figure 4). However, the sharp temperature changes present in the wall are not present in the core because of the convective transport of the hot gas. The frontal startup shown in the model resembles a combination of the second and third startup modes observed by Cotter, which should be expected due to the presence of the

noncondensible and the low vapor densities. At 16 seconds, both the mixture and wall temperatures have assumed flat profiles.

The lithium gas pressure increases with time as the wall temperature increases and condensation is inhibited (Figure 5). The lithium gas produced in the evaporator section travels down the heat pipe, pushing the noncondensible gas ahead of it (Figure 6). By 16 seconds, the noncondensible has been packed into the end of the condenser with the lithium occupying the remainder of the heat pipe. The moving noncondensible-lithium interface is sharply defined, as observed by Cotter. The total pressure remains relatively flat throughout the startup transient.

The mixture velocity exhibits a maximum during the startup of the heat pipe (Figure 7), with the distribution peaking at the end of the evaporator section. The magnitude of the peak increases quickly to its maximum value at 4 seconds, and then decreases slowly as lithium gas is transported further down the heat pipe before condensing. The maximum value of 700 m/s is much larger than steady state values of around 10 m/s.

The evaporation rate during startup increases rapidly to a rather constant value in the evaporator section (Figure 8). Note that the 1-second line is approximately at zero: an evaporation rate above that line indicates net evaporation, while an evaporation rate below that line indicates condensation. Due to the relatively cold wall temperature beyond the evaporator section, the lithium gas begins condensing as soon as it leaves the evaporator, with the effective condensing length of the heat pipe increasing with time. Condensation increases when the gas reaches the condenser section, which is radiatively cooled.

After 360 seconds of model time both the wall and the mixture temperature show a drop of less than 20 degrees from the evaporator to the condenser (Figures 9,10), not including the plug of noncondensible gas in the condenser end. The temperature variations in this plug of gas are due to relatively poor low velocity heat transport of the noncondensible as compared to condensation, and the lack of conduction in the core model which would reduce the 40 degree temperature gradient. The pressure distributions show that the noncondensible has been compacted into the condenser end (Figure 11). Mixture pressure is very flat, but does have some variation which has been magnified greatly in Figure 12. This distribution has the same general shape as the steady state distribution calculated from the HTPIPE code (Figure 2).

The mixture velocity distribution at 360 seconds consists of three linear sections (Figure 13). The evaporator section is linearly increasing, which coincides with Cotter's theory on steady state heat pipe behavior. The condenser section is linearly decreasing in velocity, which also agrees with Cotter's theory. However, the velocity profile in the adiabatic section is not flat, as Cotter's theory predicts, but rather decreases linearly with a different slope from the condenser region. The reason for this behavior can be seen in the evaporation rate (Figure 14). The evaporation rate is constant in both the evaporator and condenser section, as Cotter assumes, but has a nonzero value in the adiabatic section. The nearly constant condensation rate in the adiabatic section causes the velocity in that section to resemble the linearly decreasing velocity of the condenser. Condensation in the adiabatic section indicates that the system has not fully achieved a steady state condition.

Diffusion was taken out of the model in order to determine its effect on heat

pipe performance. Figures 15 through 20 (in which diffusion has been neglected) correspond to Figures 3 through 8. There is little difference between the sets of plots, indicating that diffusion does not affect the heat pipe performance during this transient.

SUMMARY

A transient model of the vapor core of high temperature heat pipes has been developed. Model trends show good agreement with both analytical steady state calculations and experimentally observed startup behavior. Diffusion does not have a large effect on heat pipe performance for this particular transient. Investigation into the transient conditions during which diffusion has a more prominent effect is planned. Future modeling efforts will include a thermohydraulic model of the wick region with provisions for startup from a solid state and conduction in the vapor core.

SYMBOLS

A_s - surface area of the liquid-vapor interface (m^2)
c_p - specific heat (J/kg·K)
D - mass diffusion coefficient (m^2/s)
D_h - hydraulic diameter (m)
E_{max} - maximum tolerable error
f - friction factor
g - acceleration due to gravity (m/s^2)
H - heat transfer coefficient ($J/m^2 \cdot K$)
h - enthalpy (J/kg)
h_{fg} - latent heat of evaporation (J/kg)
h_g^{pc} - enthalpy of the lithium gas upon changing phase (J/kg)
M - molecular weight (kg/kg·mole)
m - mass (kg)
P - pressure (Pa)
Q_t - total heat throughput (W)
q''_{in} - heat flux incident on the heat pipe (W/m^2)
R - gas constant (J/kg·mole·K)
r - inner wick radius (m)
T - temperature (K)
t - time (s)
u - internal energy (J/kg)
V - velocity (m/s)
X - mass fraction
z - axial distance (m)

Greek Letters:

Γ - evaporation rate ($kg/m^3 \cdot s$)
Δ - difference between two values, e.g. $\Delta X_i = X_{i+1/2} - X_{i-1/2}$, $\Delta X_{i+1/2} = X_{i+1} - X_i$
ε - emissivity
ρ - density (kg/m^3)

σ - Stefan-Boltzmann constant ($J/m^2 \cdot s \cdot K^4$)

Subscripts:

g - lithium gas
i - spatial node
m - mixture
N - noncondensible gas
sat - vapor-wick saturation value
w - wick/wall

Superscript:

N - time step

REFERENCES

1. Jay E. Boudreau and David Buden, "A New Generation of Reactors for Space Power," Symposium on Advanced Reactor Systems, Washington, DC, 1982.

2. P. D. Dunn and D. A. Reay, Heat Pipes (Pergamon Press, Ltd., Oxford, NY, 1976).

3. T. P. Cotter, "Theory of Heat Pipes," LA-3246-MS, 1965.

4. F. C. Prenger, Jr., "Heat Pipe Computer Program (HTPIPE) User's Manual," LA-8101-M, 1979.

5. W. S. Chang and Gene T. Colwell, "Mathematical Modeling of the Transient Operating Characteristics of a Low-Tempeature Heat Pipe," submitted to Numerical Heat Transfer.

6. C. D. Fletcher and H. Chow, "Simulation of the General Electric SP-100 Space Reactor Concept Using the ATHENA Computer Code," submitted to the Third Symposium on Space Nuclear Power Systems, January 1986.

7. R. B. Bird, W. E. Stewart, and E. N. Lightfoot, Transport Phenomena (John Wiley and Sons, Inc., New York, 1960).

8. "TRAC-P1A/MOD1--An Advanced Best-Estimate Computer Program for Pressurized Water Reactor Loss-of-Coolant Accident Analysis," Los Alamos National Laboratory report.

9. V. H. Ransom, et al., RELAP5/MOD2 Code Manual, Volume 1: Code Structure, System Models and Solution Methods, EGG-SAAM-6377, April 1984.

10. T. P. Cotter, "Heat Pipe Startup Dynamics," Thermionic Conversion Specialist Conference, Palo Alto, CA, 1967.

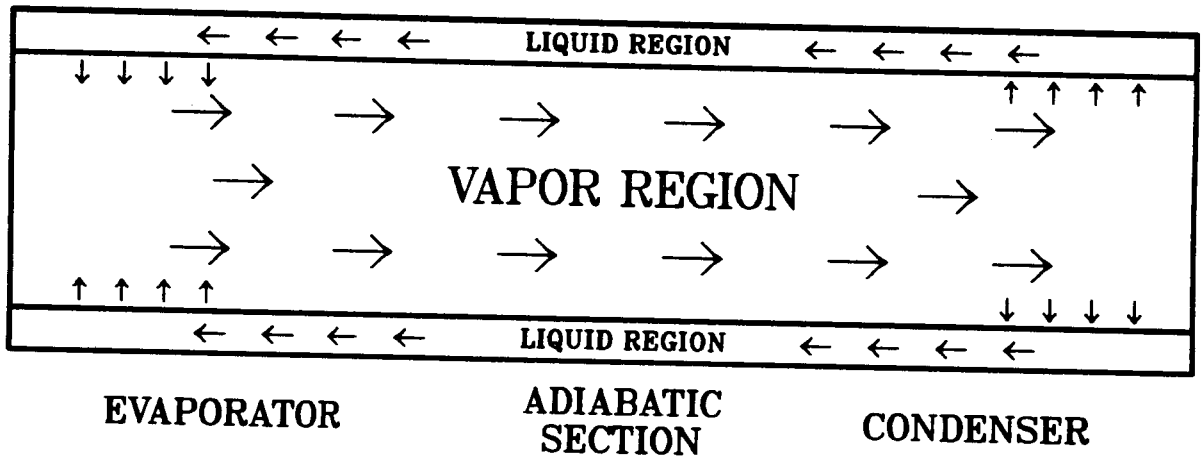

Figure 1. Heat pipe schematic diagram

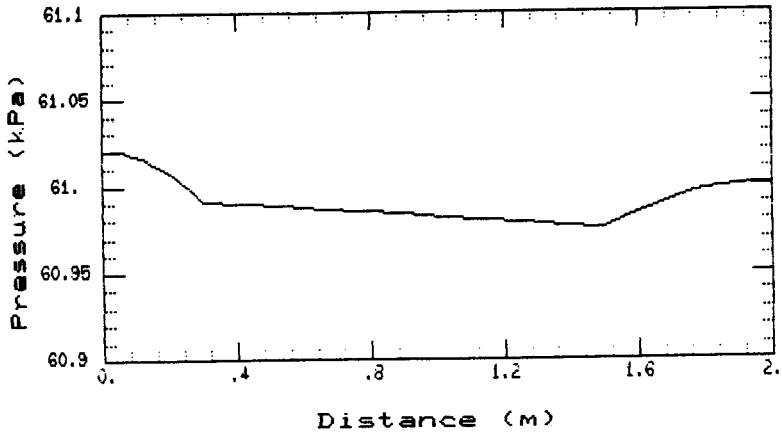

Figure 2. Steady state pressure profile (HTPIPE)

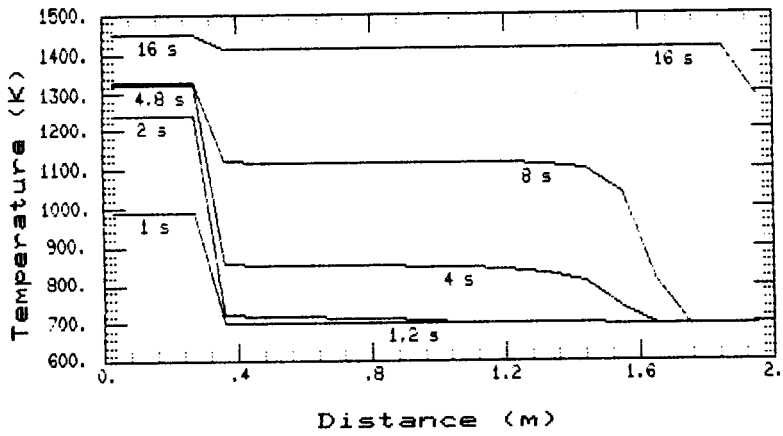

Figure 3. Wall temperature (startup)

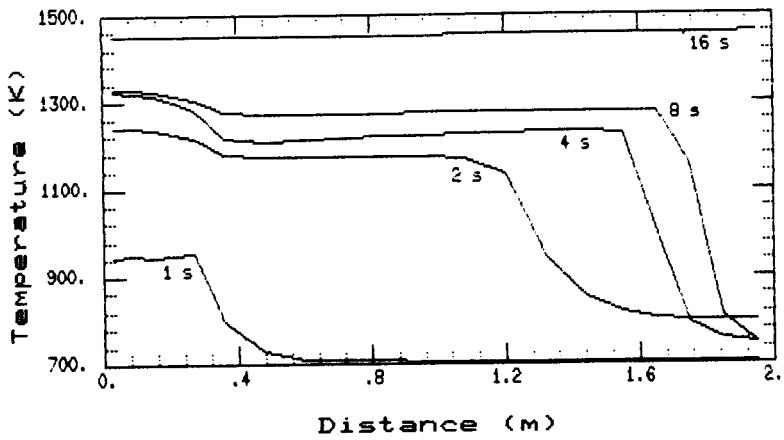

Figure 4. Mixture temperature (startup)

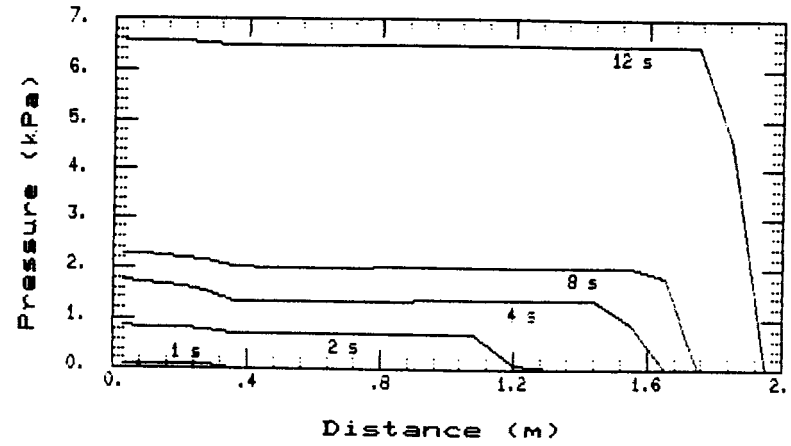

Figure 5. Lithium gas pressure (startup)

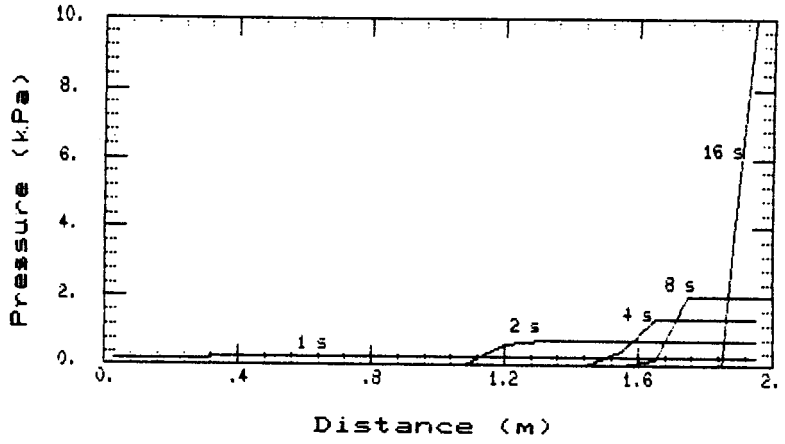

Figure 6. Noncondensible pressure (startup)

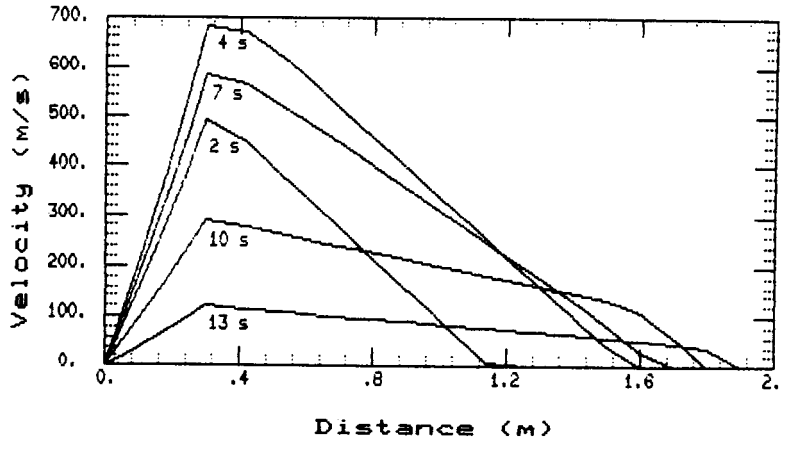

Figure 7. Mixture velocity (startup)

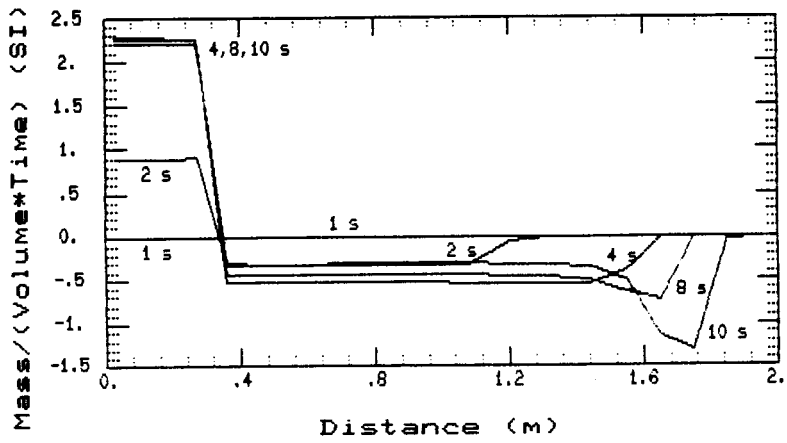

Figure 8. Evaporation rate (startup)

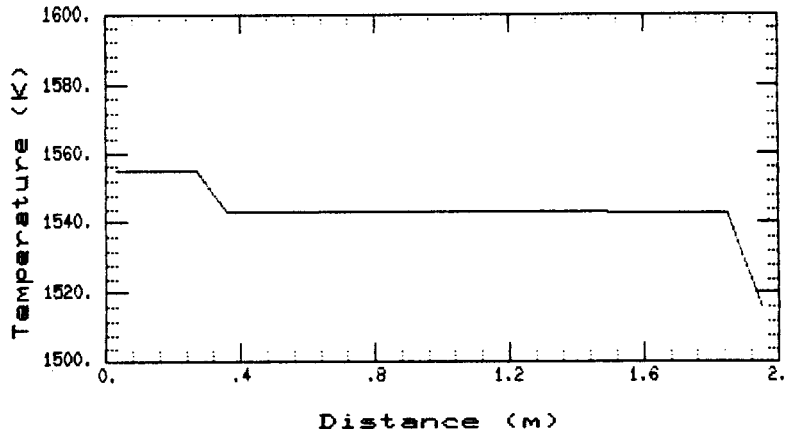

Figure 9. Wall temperature (360 seconds)

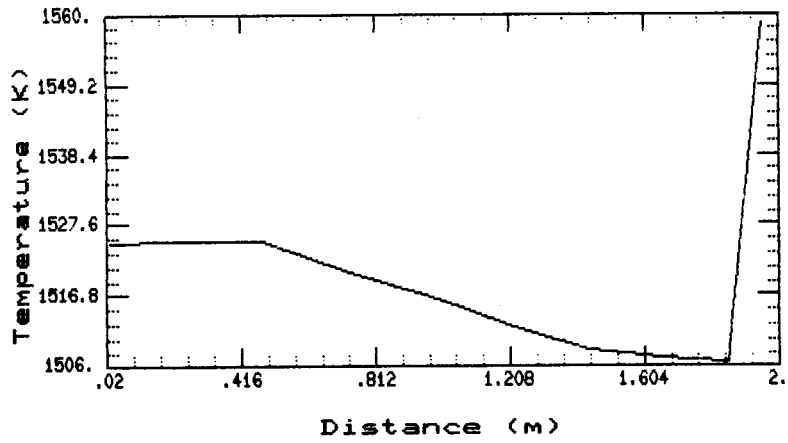

Figure 10. Mixture temperature (360 seconds)

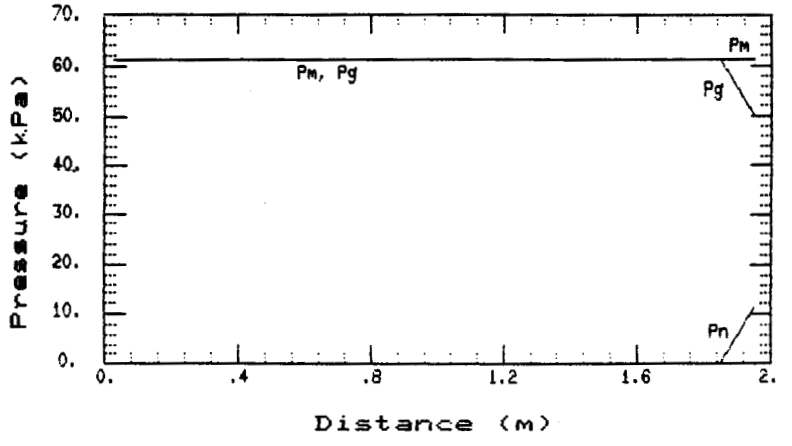

Figure 11. Pressures (360 seconds)

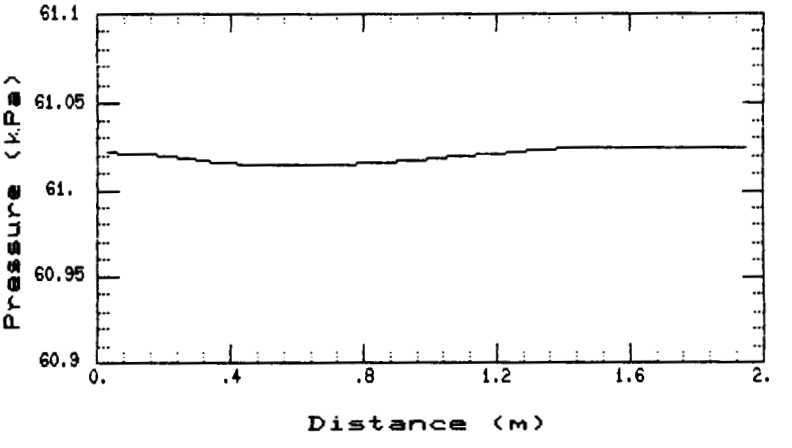

Figure 12. Mixture pressure (360 seconds)

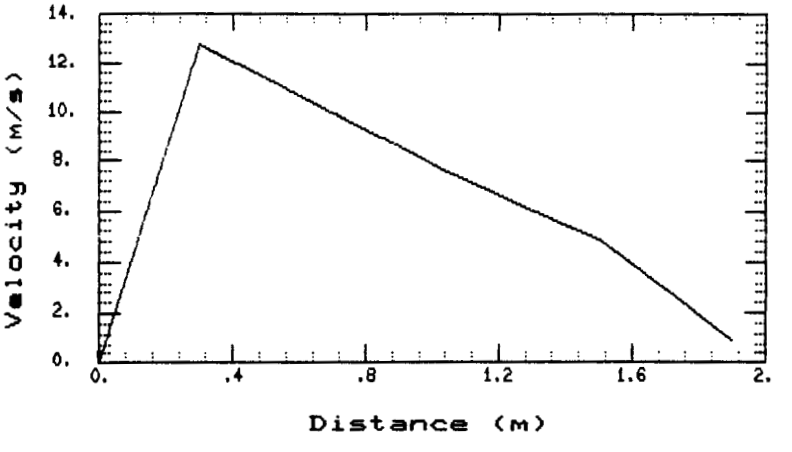

Figure 13. Mixture velocity (360 seconds)

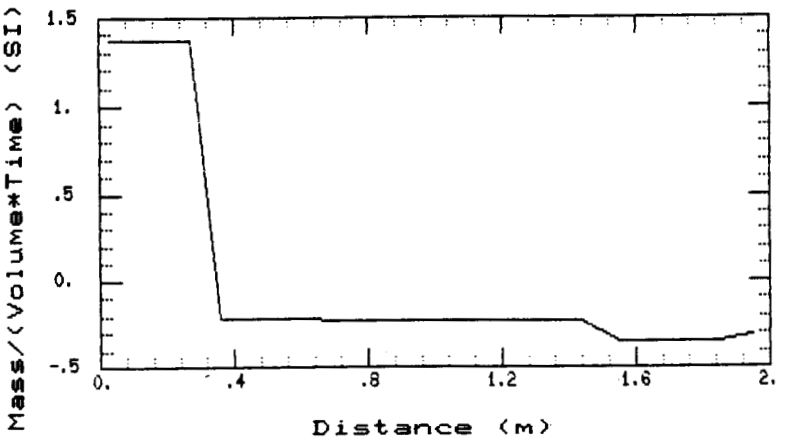

Figure 14. Evaporation rate (360 seconds)

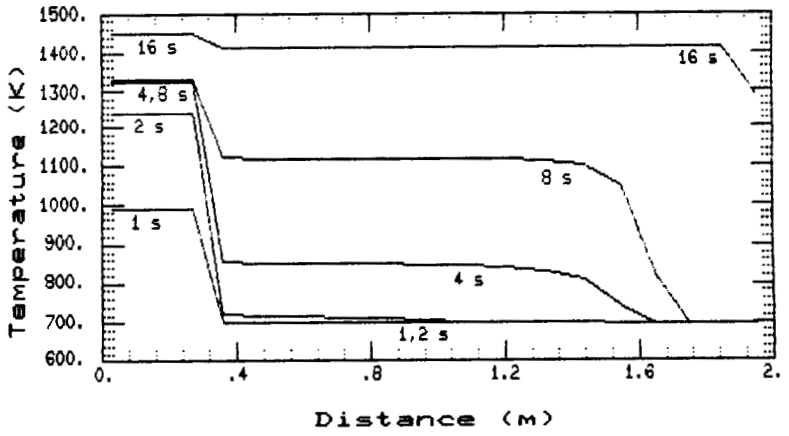

Figure 15. Wall temperature (startup, no diff)

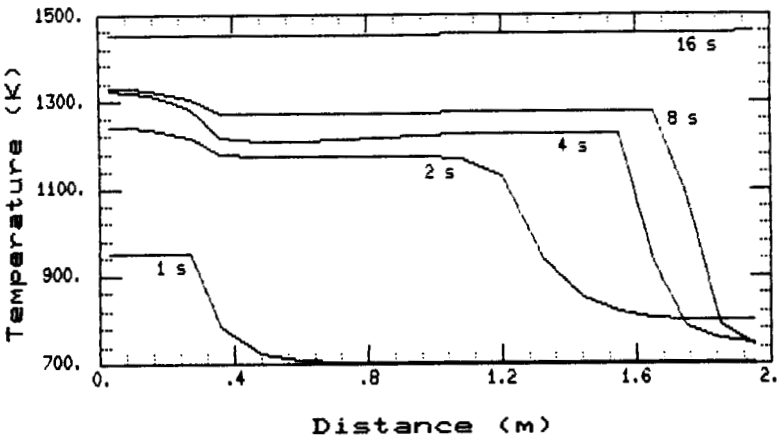

Figure 16. Mixture temperature (startup, no diff)

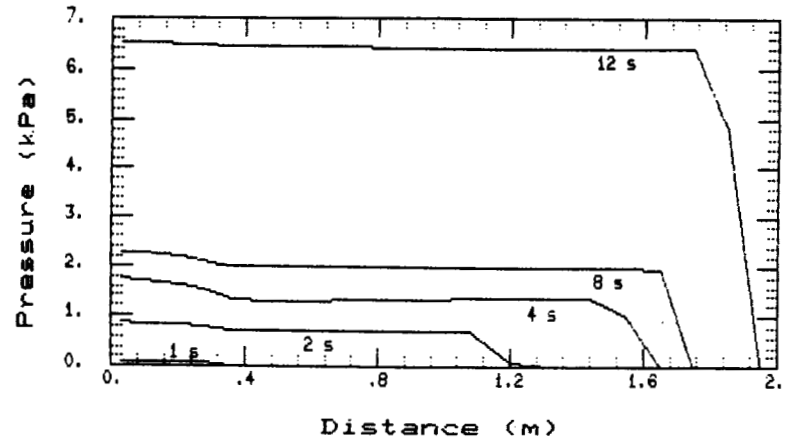

Figure 17. Lithium gas press. (startup, no diff)

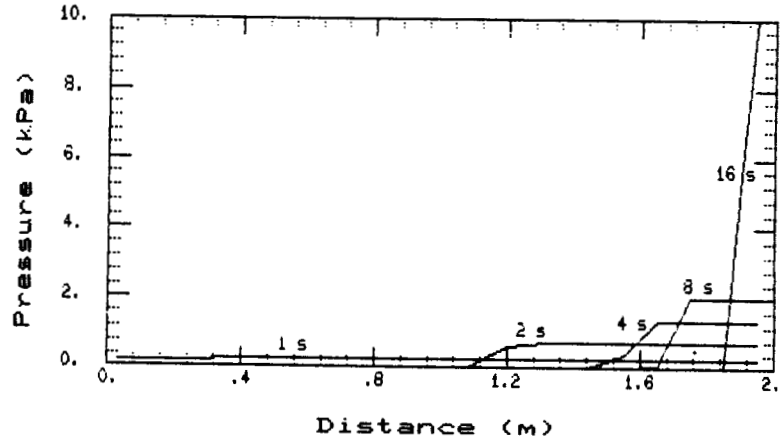

Figure 18. Noncondensible press. (startup, no diff)

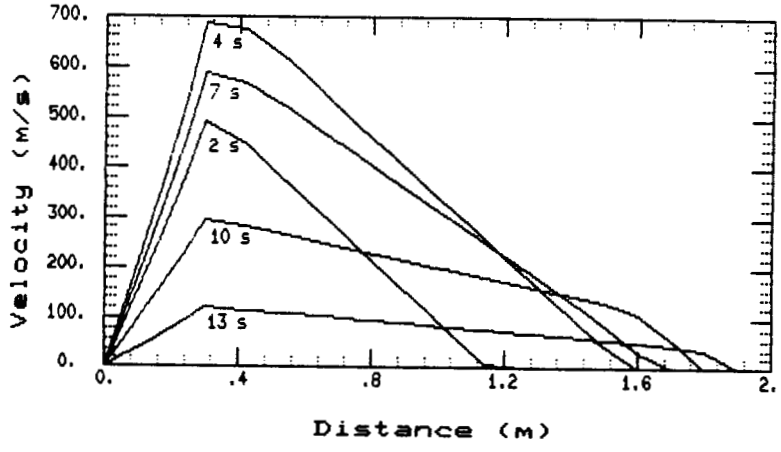

Figure 19. Mixture velocity (startup, no diff)

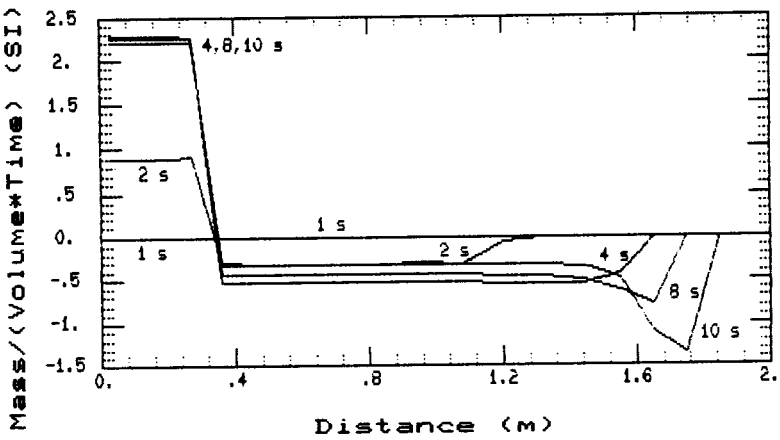

Figure 20. Evaporation rate (startup, no diff)

APPLICATIONS OF HEAT PIPES TO COOL PWBS AND HYBRID MICROCIRCUITS

by

DR. K. S. SEKHON, SENIOR SCIENTIST
Hughes Aircraft Company
Fullerton, California

ABSTRACT

Increases in microcircuit power density and closer packing of chips in hybrid packages to meet high-frequency or high-speed circuit requirements has resulted in higher component temperatures, which results in reduced reliability performance. Improved thermal management techniques, such as heat pipe cooling, must be used to lower component temperatures. This paper describes some of the advanced thermal management techniques, developed at Hughes, to reduce operating junction temperature under extreme environmental temperature conditions. Heat pipes in electronic component packaging provide many advantages over conventional cooling methods by reducing component temperatures, eliminating hot spots, and providing design flexibility. We are beginning to find heat pipes cooling components inside hermetically sealed enclosures, removing heat from flat packs, serving as an isothermal mounting plate for an amplifier on a spacecraft, or doubler as a structural member and thermal conductor to cool a solid-state module. Developments are even under way to integrate heat pipes into circuit cards, and to build heat pipes into power transistors. Heat pipes in actual electronic packaging applications, and those under development, will be discussed. Performance characteristics of heat pipes will be given, and examples of how thermal problems in electronic packaging were solved through the use of heat pipes will be described.

Heat pipes were incorporated in the high power transistors and successfully tested under power levels as high as 40 watts. Several prototypes were subjected to 1,000 hour testing at high temperature. Chemical compatibility of the heat pipe fluid with the semiconductor chips was tested by immersing uncapped transistors in the fluid and operating them at high power over an extended period of time. Electrical effects of the wick and fluid on the high frequency operation of the transistors were also determined as a part of this study. During this study, transistor junction temperature was determined both by measuring electrical properties and by infrared microscope techniques. A major breakthrough in this work has been the development of the Hughes high performance Powder Wick (U.S. Patent 4,047,198) concept, which can be applied to the transistor chip by mass production methods. The Powder Wick has much higher performance than the fiber bundle wicks used in the earlier study and is electrically compatible with the microwave transistors.

Heat Pipe for PWB was invented (U.S. Patent #4,11,8,756) and developed at Hughes Aircraft Company, Fullerton, California. This heat pipe, which accommodates 50 DIP devices was designed to fit into existing Hughes equipments which use aluminum or copper thermal mounting plates for

conduction cooling of circuit card components. The circuit card heat pipe shell is made of beryllium copper. This material was selected for its high yield strength, high thermal conductivity and ease of manufacture. Use of beryllium copper results in a rugged heat pipe not requiring special handling and without sacrifice of thermal conductivity. Beryllium copper is easily fabricated and can be joined by brazing, soldering, or welding. The circuit card heat pipe uses stainless steel screen wicks in the evaporator and condenser in combination with sintered-fiber stainless steel artery wicks. The thin screen wicks provide a short heat transfer path from the shell of the heat pipe to the vapor space, providing a low thermal resistance and resulting in a low temperature drop. Since the thin, tightly woven mesh will have a high resistance to liquid flow, the artery wick is utilized to provide a low resistance path for fluid flow. The artery wick is a sintered-fiber metal with an open structure for fluid flow but with a pore size consistently with capillary pumping requirements. Methanol was selected as the heat pipe fluid for the circuit card heat pipe because it has a high surface tension, high latent heat of vaporization, and low viscosity. In addition, it has a relatively high vapor pressure at the operating temperature which minimizes problems with sonic velocity, entrainment, or any inert gases in the heat pipe. Compatibility of heat pipe fluid and materials is essential to reliable heat pipe operation. Incompatibility between the fluid and the wick and shell materials may lead to heat pipe failure from a number of causes. Selection of all material used was based on experimental life test data developed by Hughes and data from the technical literature on heat pipes. The results illustrate that thermal resistance on the PWB can be reduced to one half by utilizing circuit card Heat Pipe. Test data will be presented in this paper.

INTRODUCTION

A heat pipe may be defined as any device that transfers heat by evaporation of liquid from heated areas and condensation on cooler areas, with continuous return of the condensation to the heated area by capillary action. The simplest form of heat pipe consists of a sealed tube lined with a wick which is wet with a suitable volatile liquid. No gas other than the pure vapor of the liquid is present. If flow of the vapor through the tube is not at too high a velocity, pressure will be nearly uniform throughout the vapor space. The temperature along the wick surface will then be essentially constant at the equilibrium temperature for the liquid-vapor interface at the given pressure.

Addition of heat any point along the tube wall will cause the temperature all along the wall to rise through local evaporation and condensation on all cooler areas. Regions of the pipe where heat is introduced into the system are evaporator sections, and those where heat removal takes place are condenser sections. The mechanisms affecting the flow of heat axially along the pipe are all extremely rapid and the adjustment o temperature consequently occurs almost instantaneously. The primary thermal resistance of the pipe is usually caused by the conduction of heat through the tube wall and wick structure.

The most important non-electrical parameter in the prediction of electronic system reliability is the maximum operating junction temperature of the system semiconductor devices. The maximum junction temperature of the device may be computed from equation (1) as follows:

$$T_{jmax} = T_a + Q_{chip}\,(\theta_{jc} + \theta_{ca}) + (Q_{sub} - Q_{chip})\theta_{ca} \qquad (1)$$

Where

T_{jmax} = junction temperature of hottest chip

T_a = ambient air temperature

Q_{chip} = power dissipation in the hottest chip

Q_{sub} = total power dissipation on the package

θ_{jc} = thermal resistance from junction to case for the hottest chip (internal thermal resistance)

θ_{ca} = thermal resistance from case to ambient or ultimate sink (external thermal resistance)

It can be seen from equation (1) that the only thermal variables which play an important role in thermal packaging are θ_{jc} and θ_{ca}. At Hughes-Fullerton, a number of studies have been conducted over the past ten years to develop heat pipes to minimize θ_{jc} and θ_{ca}. They included three different studies on the development of heat pipes for Standard Electronics Modules and circuit cards. These studies demonstrate the application of heat pipes to enhance the reliability of electronic components by reducing their operating junction temperatures. This paper will also include the results of Independent Research and Development in the development of heat pipe for microcircuits. Reductions in junction temperatures up to 50°C have been achieved by incorporating heat pipe concept in a standard package.

The reliability of a semiconductor device is a function of its normalized junction temperature. The normalized junction temperature is given by:

$$T_n = \frac{T_j - T_s}{T_{jmax} - T_s} \qquad (2)$$

Where

T_n = normalized operating junction temperature

T_j = junction temperature (collector junction for transistors)

T_s = temperature at which power derating begins (usually 25°C)

T_{jmax} = maximum rated junction temperature determined from the device specification

At Hughes-Fullerton, a number of studies have been conducted to develop heat pipes to minimize θ_{jc} and θ_{ca}. This paper summarizes the results of these studies.

HEAT PIPE DEVELOPMENT TO REDUCE THERMAL RESISTANCE

In the cooling of high power solid state devices, such as power transistors, the overall thermal resistance from the device junction to the surrounding ambient environment may be considered in terms of a series of thermal resistances. In devices designed for higher operating frequencies, the internal resistance from junction to case will establish the limits of device performance.

Changes in chip design, to limit collector-to-base capacitance and to distribute the power dissipation more uniformly over the chip surface, have raised the upper frequency limits for high power transistors by allowing the thermal dissipation area to approach the total chip area. Current trends in transistor design involve the use of overly emitter electrode construction and built-in diode compensation to permit higher power and higher temperature operation. The particular techniques used vary widely from manufacturer to manufacturer, even for what is nominally the same transistor. However, all of the techniques used involve distribution of the transistor junction over the surface of the chip while controlling the collector-to-base capacitance. This generally means placing limits on the chip size which, in turn, causes thermal limits on device performance. Elimination of this frequency power limit within the restrictions of present chip design required application of heat pipe cooling methods directly at the chip surface to provide a mechanism for minimization of temperature irregularities over the chip surface and reduction of the junction-to-case thermal resistance. The objective of the program was the development and demonstration of heat pipe techniques for power transistors operating in the VHF range with dissipation power of 25 watts or more. Program goals were to reduce θ_{jc} by 33% at a given power level over conventionally packaged devices without significant change in electrical characteristics.

The most fundamental capability offered by heat pipes to the cooling of electronic components is the achievement of extremely high values of thermal conductance. Heat pipes have an additional advantage as thermal conductors in that they may utilize non-metallic, non-electrically conductive materials in order to maintain electrical isolation while retaining high thermal conductance. Another useful characteristic is the capability for acceptance of widely varying thermal fluxes without variation in temperature. Power density variation of 10 to 1 is possible in the evaporator area of a heat pipe without appreciable variation of evaporator surface temperature. This insensitivity to local variations to input power may be exploited in the reduction of local temperature variation or hot spotting.

Of the various characteristics of heat pipes, the one of most concern in power transistor cooling applications will be the high limiting values of local heat. The wick surface nearest the junction of the transistor will be exposed to extremely high values of heat flux. As the heat input in this evaporator section of the heat pipe is increased, the temperature at the liquid-wick-wall interface will rise to the point where nucleate boiling occurs in the adjacent liquid. The heat pipe will continue to operate if the capillary and buoyancy forces are great enough to cause convection of the vapor bubbles through the wick and into the vapor core. The high limiting values of local heat flux permit application of heat pipes to solid state device cooling. A schematic of a heat pipe configuration for the above-described application is shown in Figure 1.

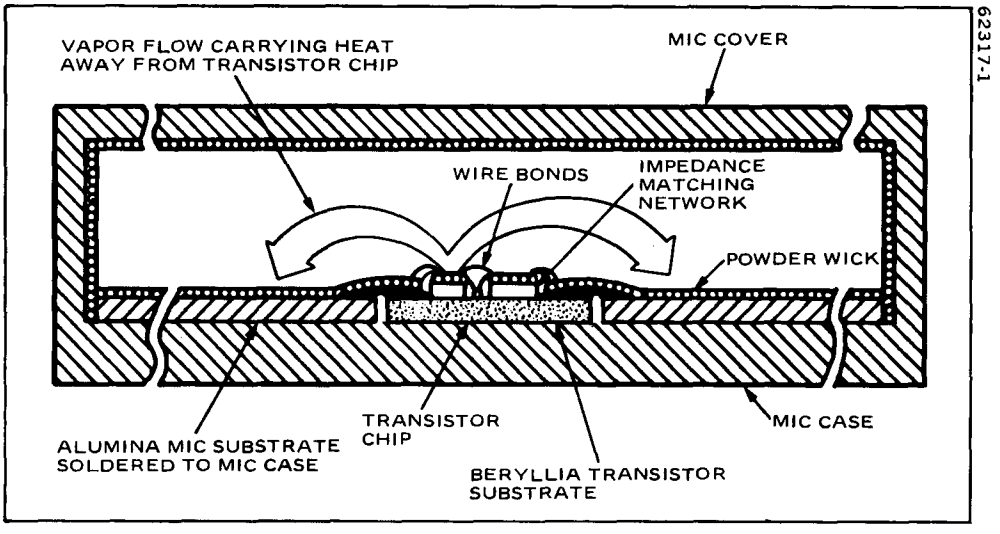

Figure 1. Section of Heat Pipe Cooled MIC RF Transistor. Heat is absorbed by the evaporating heat pipe fluid and carried to the alumina substrate where it is released by the condensing fluid and transferred through MIC case to the heat sink.

A glass fiber (Refrasil) wick was used in the heat pipe tests. The wick consists of fiber glass stand bundles 0.01 cm (0.004 inches) in diameter spaced 0.041 cm (0.02 inches) apart over the chip surface. The open configuration was chosen because of the high heat flux density at the chip surface and low thermal conductivity of the dielectrical wick material. The individual strand bundles served as a means of transferring fluid from the region alongside the chip which served as a condenser when the device was base cooled to the chip surface. Surface forces distributed the fluid over the chip surface providing a flow distribution to the largest part of the chip surface while maintaining a minimum thermal path to the vapor space.

Work to date has demonstrated the feasibility of the Hughes approach by: 1) significantly lowering the junction temperature of RF transistors by heat pipe cooling; 2) demonstrating heat pipe cooling at high junction power

density; 3) demonstrating that the electrical performance of the transistors was not affected by the heat pipe fluid and wick materials used; and 4) development of a high performance powder wick concept which can be applied to RF power transistors on a production basis. (See Figures 2 and 3.)

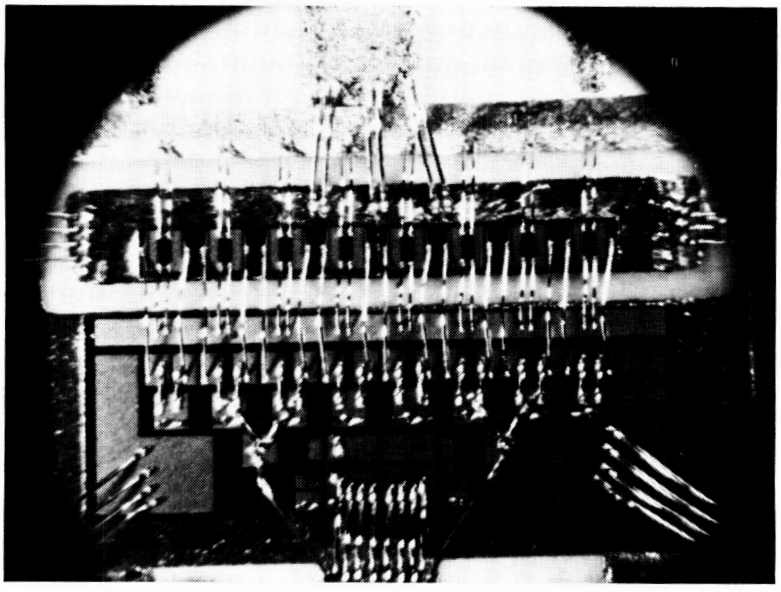

Figure 2. Multicell RF Power Transistor. Typical microwave bipolar power transistors are too complex to incorporate conventional heat pipe wick construction.

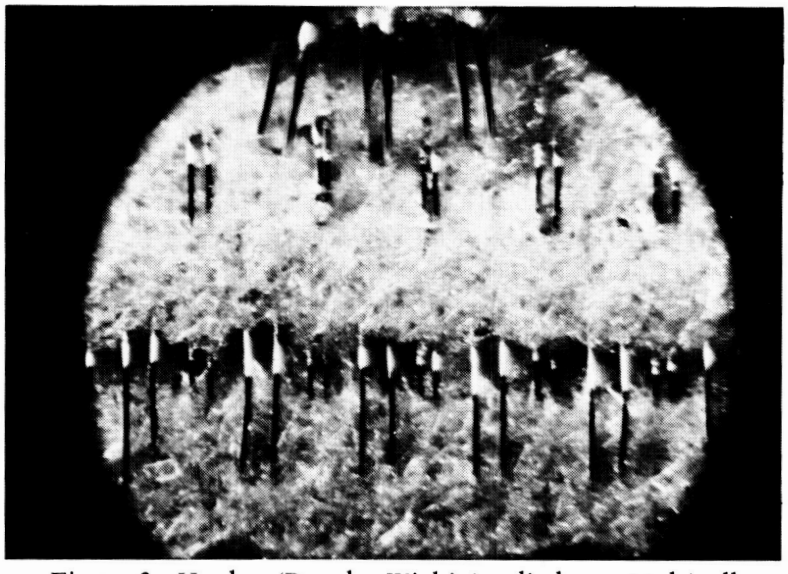

Figure 3. Hughes 'Powder Wick' Applied to a Multicell Transistor. The 'Powder Wick', designed to give high fluid flow and heat transfer performance, is applied without disturbing the transistor bond wires.

Reduction in thermal excursion during high power applications has two obvious benefits: either (1) increased reliability, or (2) increased power output for the same peak junction temperature and associated reliability. This phenomenon is basically true regardless of the type of solid state power generating device employed or the chosen frequency of operation. Figure 4 demonstrates transistor junction temperature reductions of up to 60°C or (alternatively) 33 percent higher power levels with the same junction temperature with the application of heat pipe cooling. The transistor was eutectically bonded to provide good heat transfer across the bond.

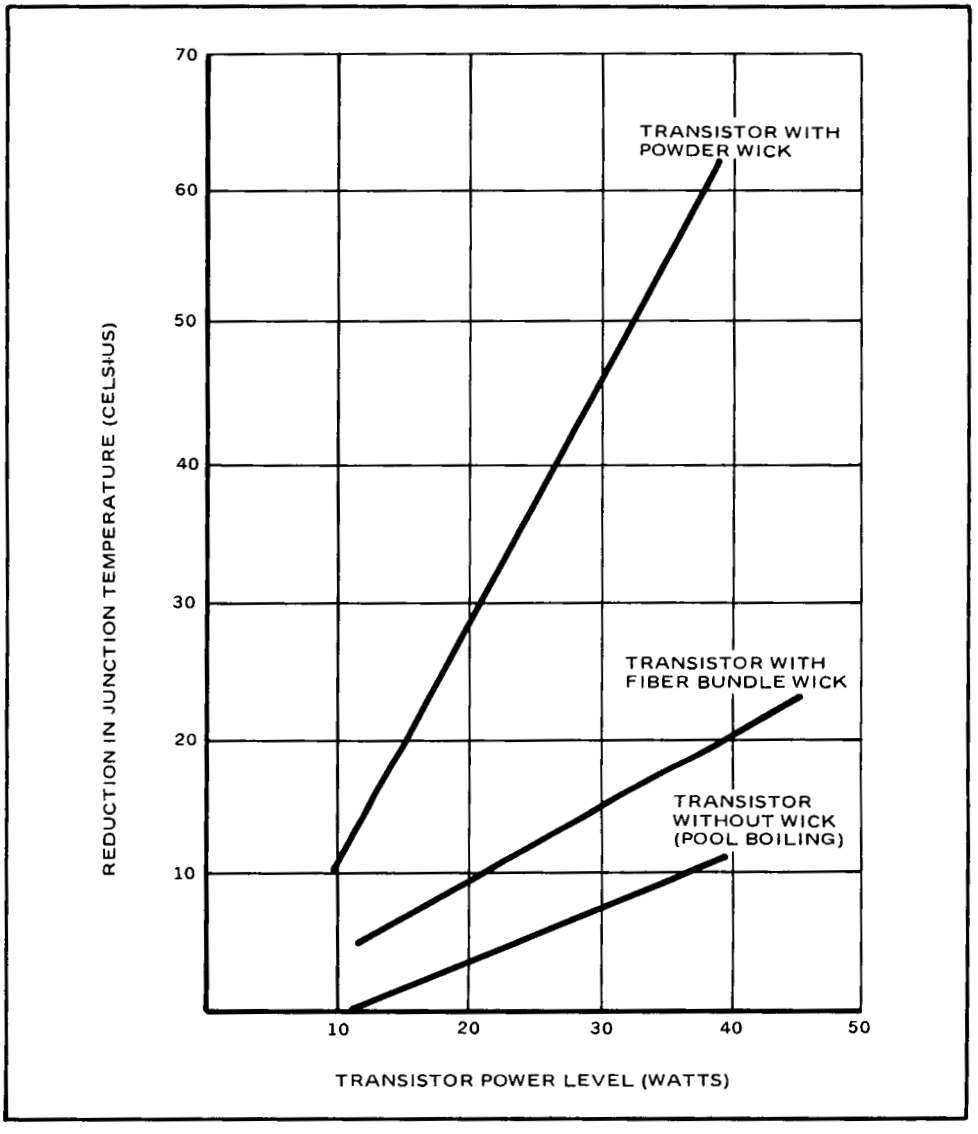

Figure 4. RF Power Transistor Temperature Characteristic. Junction temperatures are compared for a transistor (TRW-2N5071) with and without the application of a heat pipe.

Advanced model of a circuit card heat pipe, developed by Hughes, is shown in Figure 5. This heat pipe, which accommodates 50 DIP devices was designed to fit into existing Hughes equipments which use aluminum or copper thermal mounting plates for conduction cooling of circuit card components. The circuit card heat pipe shell is made of beryllium copper. This material was selected for its high yield strength, high thermal conductivity and ease of manufacture. It is also corrosion resistant and compatible with the heat pipe fluid. Use of beryllium copper results in a rugged heat pipe not requiring special handling and without sacrifice of thermal conductivity. Beryllium copper is easily fabricated and can be joined by brazing, soldering, or welding.

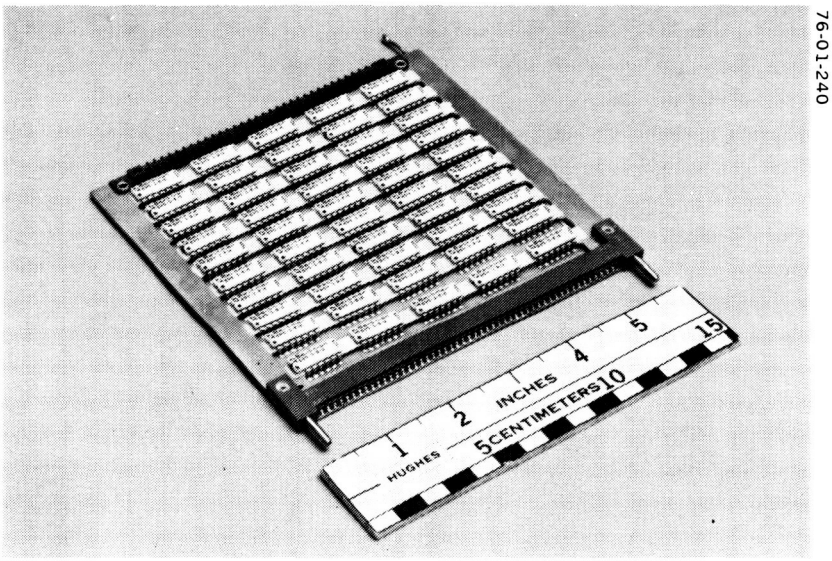

Figure 5. DIP Circuit Card with Heat Pipe Thermal Mounting Plate. The heat pipe is designed to accommodate up to 50 DIPs and has a very high heat transfer capability.

The circuit card heat pipe uses stainless steel screen wicks in the evaporator and condenser in combination with sintered-fiber stainless steel artery wicks. The thin screen wicks provide a short heat transfer path from the shell of the heat pipe to the vapor space, providing a low thermal resistance and resulting in a low temperature drop. Since the thin, tightly woven mesh will have a high resistance to liquid flow, the artery wick is utilized to provide a low-resistance path for fluid flow. The artery wick is a sintered-fiber metal with an open structure for fluid flow but with a pore size consistent with capillary pumping requirements.

Methanol was selected as the heat pipe fluid for the circuit card heat pipe because it has a high surface tension, high latent heat of vaporization, and low viscosity. In addition, it has a relatively high vapor pressure at the operating temperature which minimizes problems with sonic velocity, entrainment, or any inert gases in the heat pipe.

The experimental results of testing the heat pipe with a 30 watt load are shown in Figure 6, where a comparison is made with analytical data for similar metallic thermal mounting plates. The data demonstrates the superior performance of the heat pipe in lowering both the maximum component mounting surface temperature and the temperature gradient between components.

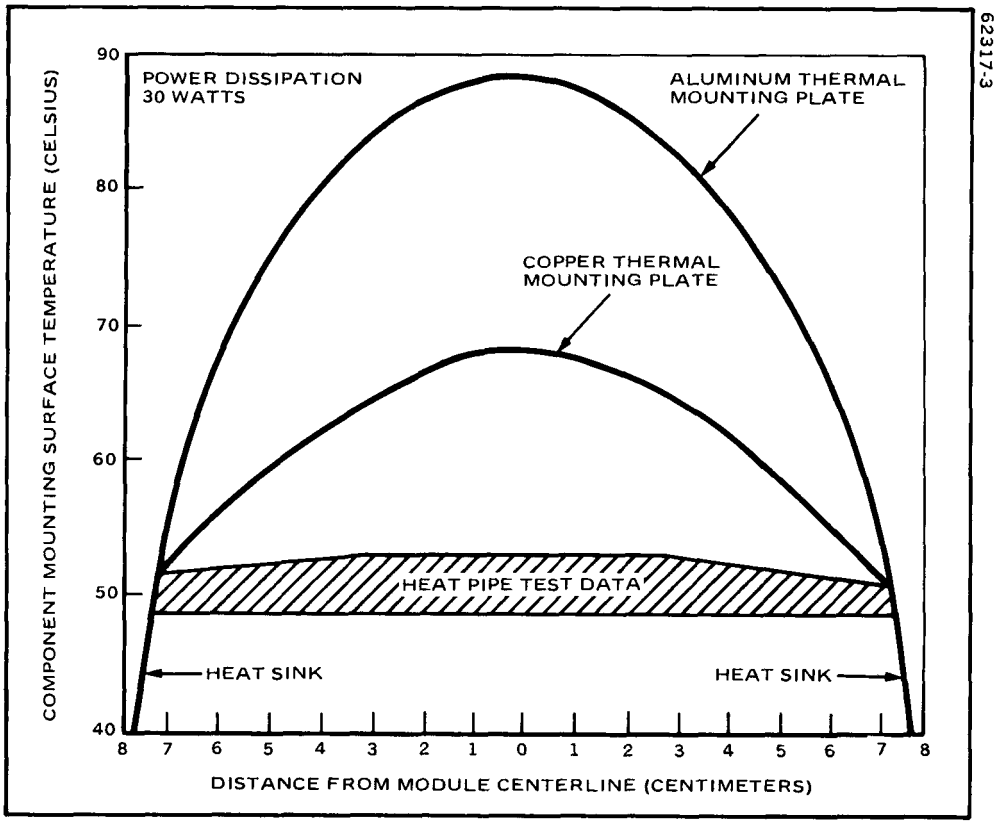

Figure 6. Performance Comparison of Heat Pipe Thermal Mounting Plate with Copper and Aluminum Thermal Mounting Plates. Heat pipe thermal mounting plate shows markedly superior performance.

In addition to thermal testing, the circuit card was qualified for use on jet aircraft by being tested to random vibration per MIL-STD-810C, Method 514.2, Procedure 1A Modified, and Shock per MIL-STD-810C, Method 516.2, Procedure 1. The circuit card was operational during the vibration testing and no degradation of performance was observed. No degradation of performance was noted following the shock testing.

CONCLUSIONS

Heat pipes have been successfully used in several applications in packaging electronic components. New developments with heat pipe devices show even more promise to improve electronic component performance. The design data and device technology are sufficiently reduced to practice. In many instances, electronic package designs are limited only by the

imagination and ingenuity of the packaging engineer. As with any device, the heat pipe will not solve all problems; but if the packaging engineer understands heat pipes and their limitations, and considers operating conditions and subsystem and system requirements, heat pipes can solve many complicated thermal problems, and can remove limitations that are imposed by conventional designs.

REFERENCES

1. Sekhon, K.S., "Heat Pipe Applications to Control Electronics Temperature in Radars," IEEE 1977 Mechanical Engineering in Radar Symposium, November 1977.

2. Cotter, T.P., "Theory of Heat Pipe," LA-3246-ms, March 1965.

3. Sekhon, K.S., Nelson, L.A. and Fritz, J.E., "Improved MIC Performance through Internal Heat Pipe Cooling," National Electronic Packaging and Production Conference, March 1977 and May 1977.

4. Sekhon, K.S., and Basiulis, A., "Heat Pipe in Electronic Component Packaging," National Electronic Packaging and Production Conference, March 1977 and May 1977.

5. Harbough, W. and Eastman, G.Y., "Experimental Operation of Constant Temperature Heat Pipes," Fifth Intersociety Energy Conversion Engineering Conference, Las Vegas, Nevada, September 1970.

6. Dunn, P. and Reay, D.1A., "Cooling of Electronic Components," Heat Pipes, Pergammon Press, Ltd., 1976, pp 235, 241.

7. Coolings, J.R. and Harwell, "Rassar Array Comes of Age," Microwaves, August, 1972.

8. Nelson, L.A. and Sekhon, K.S., "Development of Heat Pipes for SEM-1A Module," Report No. 0252-1, December 1976.

9. "Thermal Control of Power Supplies with Electronic Packaging Techniques," Final Report MCR-75-389, Martin Marietta, Denver, Colorado, 1975.

10. Ruttner, L.E. and Sekhon, K.S., "Development of Heat Pipe for SEM-2A Module," Report No. 0300-1.

11. Nelson, L.A., "Application of Heat Pipes and Phase Change Devices for Cooling of Electronic Equipment," Nepcon Central, Chicago, Illinois, October 1974.

12. Gianetti, R.J., Merrigan, M.A., and Nelson, L.A., "Thermal Control of Airborne Electronic Equipment," AFFDL-TR-73-12.

13. Merrigan, M.A., "Investigation of Novel Heat Removal Techniques for Power Transistors," Report No. ECOM-0021-F.

SPACE STATION CONTAMINATION CONSIDERATIONS

L. Leger, H. Ehlers and S. Jacobs
NASA Johnson Space Center
Houston, Texas 77058

ABSTRACT

A base for the conduct of low-Earth orbital activities will be provided with the establishment of Space Station in the early 1990's. The Station core structure is large, approximately 100 meters in its major dimensions, and will support a variety of activities such as platform servicing, orbital transfer vehicle servicing, satellite servicing, material processing and life sciences studies. It will also serve as an observing platform for astronomy and Earth observation. All of these activities must be compatible if the Station is to be most useful. This compatibility is provided through the development of a requirement set which considers the needs of all the users involved.

One area being covered in this requirement set addresses the external induced environment generated by Space Station activity or more specifically by gases, particles, and light background. These contaminant species must be controlled if sensitive systems, such as solar energy collectors or science experiments exposed to the external environment are to function properly. The requirements, which will be discussed in detail, generally set limits on the level of gas species, matter deposited on surfaces and light background levels over the various spectral regions. They also address environment monitoring and contamination controls during manufacturing. Limits on effluent release and system leakages are in turn derived from these requirements. Overall, the process provides an optimum balance between laboratory/environmental life control system fluid management problems and contamination sensitive external systems.

Once requirements are established, Space Station contamination performance, which is analytically assessed, can be compared with needs, and design trades can be directed to optimum system design. Performance studies conducted to date indicate that the core Station can provide an adequate environment for astronomy measurements if contamination effects are considered early in design. Results of these studies and associated design solutions which define the preliminary Space Station environment will be presented.

CONTAMINATION CONTROL CONCEPTS FOR SPACE STATION CUSTOMER SERVICING

K. A. Maruya, L. E. Ryan, L. A. Rosales,
and E. H. Medler
TRW, Inc.

ABSTRACT

The customer servicing operations envisioned for Space Station, which include instrument repair, orbital replacement unit (ORU) changeout, and fluid replenishment for free flying and attached payloads, are expected to create requirements for a unique contamination control subsystem for the customer servicing facility (CSF). Both the core Space Station (SS) and CSF users present unique requirements/sensitivities, not all of which are currently defined with common criteria. Preliminary results from an assessment of the effects of the CSF-induced contamination environment are reported. Strategies for a comprehensive contamination control approach and a description of specific hardware devices and their applicability are discussed.

INTRODUCTION AND SUMMARY

The servicing operation is baselined to include capabilities for repair, replacement, replenishment, and refurbishment of potential users and/or user hardware. These users can be either free flying (FF) or station-attached payloads, and as a group, will present various degrees of sensitivity to contamination. For example, observatories such as the Hubble Space Telescope (HST), the Space Infrared Telescope Facility (SIRTF), and the Advanced X-Ray Astrophysics Facility (AXAF) are generally classified as extremely sensitive to molecular and/or particulate contaminants whereas other users such as the Gamma Ray Observatory (GRO) are considered to be less sensitive.

Due to the multipurpose function of the CSF, many sources of contamination can be introduced into the servicing area. Leaks from fluid replenishment subsystem components, extravehicular activities (EVA), outgassing from CSF materials of construction, and particulate generation and shedding from mechanisms and surfaces subjected to impacts or loads, can directly influence the contamination environment within the CSF. In addition, sources originating from the exterior of the CSF -- STS PRCS and VRCS bipropellant exhaust products, pressurized module waste product dumping and outgassing, atomic oxygen, and micrometeoroids -- can also compromise the cleanliness and affect the mechanical/thermal/optical properties of critical user payload surfaces.

In order to predict the degree of control needed to meet user requirements, an investigation was undertaken whereby major sources of contamination were identified, and their generation, transport, deposition, and ultimate effects characterized based on preliminary design information. EVA/EMU (Extravehicular Mobility Unit) water emissions, structural support member outgassing, and nominal liquid propellant leaks resulted in unacceptable levels of molecular

contaminant film accretion and CSF ambient pressures for a tightly sealed enclosure with no contaminant collection or control. A neutral particulate analysis, which considered the dislodgement of particles from CSF interior surfaces as a result of a sudden impact force, resulted in the emission of relatively large particles (>50 microns) but low overall obscuration of user payload surfaces. A study addressing particle charging effects indicated a small degree of charging within the CSF and a significant reduction in particle migration/collection time if electrostatic particle collection methods could be employed.

Because of these preliminary modeling results, a contamination control subsytem concept was created to provide a means for maintaining the CSF within core SS and user specifications. The conceptual design consisted of candidate hardware components divided into four groups according to their function: (1) measurement/monitoring/alarm, (2) collection and control, (3) treatment/storage/disposal, and (4) cleaning and refurbishment. Actual sizing of the components was not performed at this time; however, qualitative trades were made for each class of hardware components, comparing factors such as collection or measurement efficiency, power/facilities requirements, reliability, and technology development requirements.

BACKGROUND INFORMATION

CONFIGURATION

The generic conceptual design of the CSF is illustrated in figure 1. This representation shows the basic rectangular box configuration of the servicing bay enclosure (SBE) attached to the station keel and supported by additional structural members. The dimensions of the enclosure are nominally 10.7 m (35 ft) square (in width and depth) and 27.4 m (90 ft) long. Figure 2 shows a retracted view of the facility revealing much of the servicing specific hardware and mechanisms currently baselined. The servicing mission must provide for manipulation and accommodation of both large and small users, housing of support equipment for (1) EVA (work stations, tools, etc), (2) thermal control subsystem hardware, (3) fluids handling subsystem equipment, (4) communications, data handling, and power distribution components, and (5) any contamination control devices deemed necessary for the resident user. The present baseline is that the CSF volume will remain unpressurized.

In relation to the core SS (dual keel configuration), the CSF is located in the +z half attached to one of the dual keels with its "top" located near the upper boom and, when extended (or "closed"), stretches some 27.4 m (90 ft) in the -z direction. This position is illustrated in figure 3. Placement of the CSF is important in that other SS elements -- habitable modules, subsystem components (thermal, structural, power, attitude and control, etc.), STS docking port, and Orbital Maneuvering Vehicle (OMV) docking and/or storage locations -- as well as direct line-of-sight to the RAM direction (atomic oxygen flux) and micrometeoroids can all have significant impact on the contamination environment within the CSF volume.

THERMAL AND ORBITAL ENVIRONMENTAL FACTORS

The proposed SS low earth orbit (LEO) will be at 28.5° inclination at an altitude of 460 km. Initial deployment and operating capability is expected to occur in the early to mid-1990s. Atomic oxygen (AO), ultraviolet (UV) and ionizing radiation, micrometeoroid impacts, and core SS surface charging can affect the behavior of any contamination sources present. Table I summarizes expected values for relevant environmental parameters (ref. 1). Materials compatibility and long-term stability should be considered as major issues for the maintenance of a suitable CSF environment.

Outer surfaces of the CSF are expected to vary in a cyclic manner between 200 K (-100° F) and 339 K (+150° F). Depending on its thermal mass, each component within the CSF will experience temperature fluctuations within this range. At least two sides of the SBE will attain the temperature extremes for a given cycle. The CSF thermal control system, consisting of an active thermal loop, cold plates, radiators, heaters, and the enclosure itself, will be operational to ensure that user thermal constraints are met and maintained.

SERVICING SCENARIOS AND TIMELINING

A mission list, which is shown in table II, commits the occupancy of the CSF for a range of 38 to 90 days per year; an option to close the facility during STS docking and departure would add an additional 8 days per year. EVA manpower requirements for servicing operations have been estimated at approximately 200 man-hours per year.

Specific mission scenarios and time-sequencing have been developed for certain initial operating capability (IOC) missions, but will vary according to the degree and type of servicing needed. However, common or generic operations have been identified, namely, OMV and remote manipulator system (RMS) type maneuvering and manipulation, followed by SBE extension ("closing of the CSF") and a host of probable servicing operations including mechanical/electrical interfacing, ORU replacement, EVA assisted refurbishment of damaged equipment, testing, verification, and checkout procedures, and final demating of the user payload. Elapsed time for servicing can range from 5 to 28 days or more; HST and GRO have been tentatively scheduled for 14 days each.

DEFINITION OF REQUIREMENTS

In lieu of common contamination control criteria not presently defined for all Space Station elements, a combination of space-measurable and earth-based requirements have been circulated within the program customer and contractor community. A major goal of the contamination control effort appears to be the standardization of molecular, particulate, and other pertinent environmental parameter requirements to facilitate interfacing between station elements. Relevant to customer servicing are (1) user payload requirements and sensitivities, and (2) core Space Station requirements.

USER REQUIREMENTS AND SENSITIVITIES

Requirements of this type have been seen to take on various forms -- contamination deposition rates, thicknesses, surface obscuration, "airborne" particulate servicing environment per FED-STD-209B, and surface cleanliness levels per MIL-STD-1246A. Functional performance requirements based on end-of-life goals have also been encountered. The heterogeneity of user sensitivities and omission of contamination budgets for servicing operations create additional confusion to the task of defining maximum acceptable limits as a result of servicing. A review of the various requirements summarized in table III indicates that extremely low levels of contaminaton can result in unacceptable degradation to the critical systems. A total accumulation of 20 angstroms of molecular contamination was allocated for HST optical surfaces (ref. 2), very little to none of which was budgeted for on-orbit operations such as servicing at the CSF. In general, particulate levels are not well defined. Particle concentrations can however, be expressed equivalently by FED-STD-209B guidelines taking into account that smaller particles (5 microns or less) will not settle by gravitational forces.

Maximum pressure requirements have been included to prevent failure of high voltage electronics as a result of exceeding critical pressures (e.g., exceeding the "Paschen pressure" for traveling wave tube assemblies (TWTAs) can result in arcing and subsequent system failure).

CORE SPACE STATION REQUIREMENTS

A preliminary set of core SS requirements has been circulated among program contributors. The set included criteria for (1) materials selection, (2) initial station hardware surface cleanliness, (3) background spectral irradiance, (4) molecular column density (MCD), (5) particulate background, and (6) molecular deposition accretion rates. External (unpressurized) and internal (pressurized) servicing requirements were outlined as well as provisions for monitoring and verification.

CONTAMINATION ENVIRONMENT MODELING AND ANALYSIS

In an attempt to provide a theoretical basis substantiating the need for a comprehensive conceptual design for contamination control, a preliminary analysis was performed predicting the contamination environment associated with the CSF interior and its potential effects on user payloads. A flow chart representation of the analysis, as seen in figure 4, indicates the basic data input and output information associated with the task. The results of the modeling effort, although preliminary, were beneficial in defining meaningful requirements in addition to providing baseline rationale for creating a distinct subsystem for contamination control.

CASE STUDY DESCRIPTION

The analysis focused on the servicing of an observatory class vehicle (HST) contained within the enclosed CSF. Simplifying assumptions were made to impart conservativeness and thereby create a "worst-case" scenario. Figure 5 illustrates HST secured in the CSF with the SBE in the retracted position. When closed, the SBE was assumed to prevent infiltration of contamination from the exterior; conversely, all internally generated contamination was not allowed to escape by "venting or leaking."

CONTAMINATION SOURCE IDENTIFICATION

Major sources of molecular contamination were identified and incorporated into the model based upon quantity, generation potential, relative effects, and availability of reliable data. Both permanent and intermittent/periodic sources were considered.

Particulate sources generated within the CSF were thought to be the result of several phenomena. Dislodgement and redistribution of existing surface particulate contamination, sloughing, flaking, or friction generated wear, and even impact-induced particle generation from both CSF materials of construction and EVA/EMU sources, were considered potential particulate cleanliness concerns. As experimental data on particle generation characteristics were found to be extremely limited, mechanisms based on theory were developed and generation data computed and input into the model.

A list of all sources considered, classified as either molecular or particulate, is shown in table IV. The current space suit and EMU are prone to particle generation from the outer layers of the thermal micrometeroid garment (TMG) and emit water and carbon dioxide continuously during EVA. Generation potential was defined in terms of outgassing rate test data* and customer/contractor supplied EMU emission rates.

DESCRIPTION OF MODEL

The molecular transport model employed was based on a simplified conservation of mass/kinetic theory of gases approach. The results were compared and verified (with very good agreement) by results obtained from a time-dependent, three-dimensional direct-simulation Monte Carlo solution. Generation and deposition rates were both considered as strong functions of surface temperature (ref. 3). Deposition thicknesses for both user payload interior and exterior surfaces were computed as were partial pressures resulting from each source.

An attempt to characterize the particulate contamination environment included (1) a charging effects analysis, and (2) a neutral particle dislodgement/redistribution analysis. The charging effects investigation was undertaken to determine whether surface charge would play a significant role in particle

*JSC and TRW outgassing data.

adhesion and transport. The charged particle current densities existing at the proposed SS orbit altitude (460 km) and magneto-induced potential across the entire facility were analyzed and the influence of charging on neutral particles was estimated. Data supporting the feasibility of electrostatic collection of particles were also presented.

DISCUSSION OF RESULTS

A summary of the results for all molecular contaminants considered is presented in table V. Graphite-epoxy outgassing was predicted to result in a deposition thickness greater than 750 angstroms assuming 10% permanent sticking or residence of available outgassing products on HST Optical Telescope Assembly (OTA) surfaces. This conservative prediction, which exceeds the 5-year on-orbit budget of 20 angstroms by a factor of 35, can be attributed to the very large quantity of exposed graphite-epoxy (see table IV) in addition to its relatively high outgassing rate. The assumption of water being the major outgassing constituent of graphite-epoxy would greatly reduce the predicted thickness for HST; however, unprotected cryo-cooled surfaces (e.g., SIRTF optics) would experience the conservative or "worst case" deposition levels. The beta cloth enclosure material clearly contributes insignificant molecular contamination levels.

Figure 6 illustrates pressurization characteristics of the CSF from (a) beta-cloth outgassing and (b) EMU emissions during a normal 6-hr EVA shift, as a result of the simplified gas and Monte Carlo modeling techniques. It is apparent that EMU water emissions will "pressurize" the CSF even with substantial trap or vent area. Liquid hydrazine leaks can also result in elevated, however brief, internal CSF pressures.

The particle dislodgement/redistribution analysis resulted in very low obscuration of HST interior and exterior surfaces. A worst case prediction of less than 0.1% obscuration appears well below the 5% obscuration budget allocated for the OTA components as reported by MSFC personnel. The obscuration values were based upon dislodgement data of the type shown in table VI, a summary of data for the stated impact velocity, initial surface cleanliness, and beta cloth panel size.

The preliminary results obtained in the particle charging analysis indicated that the CSF surfaces will probably be only weakly charged due to the low charging level expected; particulates will most likely have to be charged in order to rapidly collect them using electrostatic techniques. The magnitude of the particulate attachment forces will have to be assessed in order to determine the effectiveness of direct neutralization of charged surfaces.

CONCEPTUAL SUBSYSTEM DESIGN

SUBSYSTEM DEFINITION

Both customer and contractor program documents have identified key functional requirements for the CSF contamination control subsystem (CCS). The top priority

would obviously be to control all forms of contamination within the facility "to enable servicing of observatory class satellites and instruments with sensitive surfaces and systems." To accomplish this, provisions must be made for (1) measurement/monitoring of the internal contamination environment, (2) collection and disposal as appropriate to maintain acceptable levels, and (3) cleaning, refurbishment and cleanliness verification of components in need of such action. Part (2) of the functional requirement also implies that core SS requirements are met.

METHODS OF ACCOMPLISHMENT

Due to the abundance of contamination sources and their complexity of interactions associated with the overall environment, realization of these functional goals would require a comprehensive subsystem approach to the problem beginning with the design phase and continuing through the mission phase by considering operational alternatives which minimize the possibility of compromising servicing users. This subsystem approach can be divided into three general categories--design, operational, and hardware implementation controls.

The most important control associated with design efforts is the careful selection of hardware configurations and their materials of construction. This is true of the core Station as well as the CSF. Low outgassing and low particle generating or shedding materials are obviously preferred; special criteria may be in order for very large surfaces (such as the SBE). Also, cleanliness levels during ground processing and transport should be maintained to prevent additional contamination accumulation.

The design of a self-contained, low contamination generation potential EMU and space suit would reduce the significant contribution expected from the present system: in fact, a self-contained EMU is expected for IOC missions. In addition, the development and implementation of robotic capability would eliminate the "human" influence altogether.

Suspected temporal variations in the contamination environment due to intermittent and periodic sources suggest that judicious planning of highly contaminating events can reduce the chance of contaminating the CSF interior and/or its resident user. Closure of the CSF during events such as shuttle docking/departure, pressurized module dumping (especially modules which vent high molecular weight constituents), and other possible instances where the potential for contamination of the CSF is high, should be scheduled to prevent contamination of resident users and internal CSF surfaces. Periodic maintenance of the CSF itself may be required to reinstate its surfaces to an "acceptably clean" level.

The third category suggests the selection and implementation of contamination control devices dedicated to the CSF for the purposes of meeting the three functional provisions as stated previously.

SUBSYSTEM CANDIDATE HARDWARE AND TRADE ANALYSIS

In the interest of controlling both molecular and particulate forms of contamination, a comprehensive "shopping list" of control devices was created and is shown in the block diagram of figure 7. For the conceptual design phase, this shopping list acts as a collection of possibilities -- developed, flight proven, or strictly conceptual -- from which devices or combinations thereof could be selected to meet individual user requirements. The candidate hardware systems are subdivided into four groups as described in the following qualitative trade analysis.

Monitoring/Measurement System

As previously mentioned, translation of earth based monitoring criteria into space-applicable terms has not been well defined. Moreover, the measurement of contaminant species -- molecular or particulate -- with good spatial resolution in the CSF volume is thought to be a very difficult problem due to the low pressures involved. The devices shown in the measurement/monitoring block of figure 7, mass spectrometer/residual gas analyzer, ionization (pressure) gauge, and quartz crystal microbalance (QCM), have been developed to provide valuable information on the identification, concentration, and deposition rates of molecular species, and have been flown with reasonable degrees of success. Further investigation into the applicability of these devices for the CSF would be required prior to final hardware selection.

Representative and reliable measurement techniques of the particulate environment have not been identified to date. Light scattering and bright light illumination devices are possible real time monitoring methods, however, one would require extensive technology development and the other suffers from limited resolution. Cumulative monitoring using witness samples and subsequent counting, sizing, or other quantification of particulate levels and their effects can be implemented if pressurized evaluation laboratory space were made available.

Collection and Control System

Contamination which contributes to an unacceptably high level within the CSF requires some mitigating activity to attain the desired environment. Collection and/or control hardware can range from very basic and simple passive devices to very complex and expensive systems. Obviously, the most cost-effective solution is preferred so long as the environment is "within specification" and does not experience excursions from specified levels for extended periods of time.

Molecular contamination such as outgassing products, small hydrazine leaks ($\leq$1 cc), material processing product venting, and water dumps can, in theory, be collected using (1) cold plates, (2) sorption surfaces or beds, or (3) they can be controlled passively through the use of shields, baffles, and covers. Redirection of contamination is not considered an ultimate collection method, however, and further treatment or disposal would be required. Inert gas purges may be possible for very small unpressurized volumes; in most situations, creation of enough gas

molecule collisions would constitute a major drawback for this method. Condensation of outgassing products and other high molecular weight species can be efficient at moderate temperatures (200 K to 300 K), however, water, hydrazine, and compounds with condensation temperatures below 200 K would require active cryogenic surfaces for efficient and predictable collection. Table VII summarizes key trade issues for these devices. Heaters may be used to prevent deposition onto a critical surface by decreasing the sticking probability of impinging contaminant molecules.

The particle charging analysis concluded that electrostatic collection of particles ranging in size between 10 and 500 microns was feasible inside the CSF. Inducement of surface charge on the particles and placement of oppositely biased collector surfaces (usually in plate form) would be required. Modeling results have indicated that a 15-fold reduction in the time required for a negatively charged particle to arrive at a neutral surface (2.5 hr) could be expected if the surface were biased (10 min for a +100 V plate). Filtration or associated techniques that rely on entrapment or inertial impaction typically require a controlled, directional flow of the gas to be cleansed.

Treatment/Storage/Disposal System

A nonventing CSF complicates the disposal of collected or redirected contamination, and creates the need for an independent system which will determine their ultimate fate. To date, nonline-of-sight venting paths are by far the most cost-effective and universally accepted method for expelling gaseous products for the majority of space vehicles. However, the unique environment of the Space Station and its many contamination control concerns dictate that this method may not be acceptable. This would then call for an alternate approach such as encapsulation and sealing of contaminants in containers and subsequent transport to an appropriate "waste holding area." Reduction of voluminous or large amounts of contamination may be considered to reduce spatial requirements for temporary storage.

An alternative to simple venting or storage of higher molecular weight or chemically reactive species is to breakdown their structure by physical/chemical methods. Media containing catalysts, reactants, or adsorption materials can result in conversion of such species to reaction products with lower condensation temperatures (such as water and carbon dioxide), and hence lower sticking probability on surfaces maintained at or near ambient temperatures.

Cleaning and Refurbishment

Studies have been performed to simulate atomic oxygen (AO) erosion for the removal of carbonaceous material from critical surfaces.* Other suggested methods include dry wiping by astronauts to remove particulate contamination and the use of high energy plasma electrons for molecular film cleaning. Methods that rely on EVA assistance are not recommended for sensitive components because of the molecular emissions and particulate generation potential associated with

*Perkin Elmer and General Electric studies.

the current EVA/EMU design. Robotic manipulation of cleaning equipment would virtually eliminate contamination introduced as a result of the cleaning process. In any event, surface cleanliness verification techniques applicable to the CSF environment would be needed if cleaning of surfaces with very low contamination budgets is performed.

CONCLUSION

The complex Space Station environment and the preliminary requirements for customer servicing of contamination-sensitive users and the core SS present unique contamination control concerns. Preliminary analysis has indicated the need for a comprehensive "subsystem" approach to address these concerns. In the area of requirements, criteria applicable to the unpressurized CSF environment are sorely needed; interfacing of servicing, user, and core SS requirements should also be accomplished stressing maximum commonality of criteria. Although the large size and the operations (EVA, moving mechanisms) associated with the multipurpose function CSF can result in an unfavorable contamination environment for sensitive users, preliminary design solutions have been identified. The evolution of the contamination control subsystem concept will depend upon careful CSF and core SS design considerations, coordination of operations between Space Station elements, and the development of a technically efficient and cost-effective contamination monitoring, collection, and disposal flight hardware system.

ACKNOWLEDGEMENTS

Additional contributors to the work described in this paper were R. D. McGregor (Molecular Transport Analysis), E. Y. Wong (Neutral Particle Analysis), and D. A. Brent (Particle Charging Effects Analysis), all of TRW, Inc., Redondo Beach, CA.

REFERENCES

1. Durcanin, J. T: Surface Material Behavior in Low Earth Orbit, RCA Astro Technology Report, November 1985.

2. Carr, J: Contamination Sensitivities for HST, AXAF, and SIRTF. ORI PIR No. 23, April 1986.

3. Scialdone, J. J: An Estimate of the Outgassing of Space Payloads, Their Internal Pressures, Contaminations, and Gaseous Influences on the Environment. AIAA No. 85-0957, June 1985.

TABLE I. SUMMARY OF SPACE STATION LEO ENVIRONMENTAL CONDITIONS

Environmental Parameter	Quantitative Description
Orbital characteristics	460 km altitude 28.5^{o} inclination
Atomic oxygen fluence (1)	
-RAM Directed	2.0×10^{21} atoms/cm^2-yr
-Non-RAM	2.5×10^{20} atoms/cm^2-yr
Solar UV radiation	
-Near (0.2-0.4 microns)	123 W/m^2
-Vacuum (<0.2 microns)	3 W/m^2
Debris flux, F (2)	Log F = -2.52 Log D - 5.46 (3)

(1) Normal solar activity assumed
(2) Debris at 500 km altitude
(3) D = diameter of debris (cm)

TABLE II. MISSION LIST FOR CUSTOMER SERVICING

Mission Designation	Mission Name	User Type (1)
SAAX 0004	SIRTF	FF
SAAX 0012	HST	FF
SAAX 0013	GRO	FF
SAAX 0016	Small Solar Physics (SMM MOD)	FF
SAAX 0017	AXAF	FF
SAAX 0022	Spartan Platform No. 1	FF
SAAX 0031	Hitchhiker No. 1	ATT
SAAX 0207	Solar Terrestrial Observatory (STO)	ATT
SAAX 0250	Hitchhiker No. 4 (ERBE) (2)	ATT

(1) FF - free flyer; ATT - station attached
(2) ERBE -Earth Radiation Budget Experiment

TABLE III. SUMMARY OF REQUIREMENTS FOR KEY SERVICING USER PAYLOADS

Vehicle	Type	Contamination Requirements/Sensitivities	
		Molecular	Particulate
HST	FF	- < 20 Å per 5 yr on-orbit (2) - 15 PPM HCs max (3) < 10E -5 torr amb pressure	- Class 100 through Class 100K (OTA exposure dependent) - Optics extremely sensitive
AXAF (1)	FF	- Sensitive to HC deposition - < 10E -5 torr amb pressure	- Class 100 through 1000 (aperture open) - Class 10K (aperture closed)
SIRTF (1)	FF	- Mat'l outgassing rate <3.0 E-7 gm/cm^2/hr - MCD < 10E+11 molec/cm^2	- Class 300 for servicing
ASO/SOT	ATT	< 10 Å on mirrors	- Class 10K for instrument repair
STO	ATT	- Sensitive to H_2 and O_2	- None identified

(1) Payloads contain cryogenic surfaces
(2) No specific budget or allotment for servicing per MSFC
(3) HC - hydrocarbons

TABLE IV. LIST OF SOURCES CONSIDERED FOR INTERNAL SOURCE CONTAMINATION ANALYSIS

Material	Application	Quantity	Source Type (1)
Beta cloth	Enclosure material	15,000 ft^2(2)	M/P
Graphite epoxy	Support structure	5,000 lbs ($\sim$ 18,000 ft^2)	M
Electronic boxes	---	TBD	M
Wire insulation	---	TBD	M
Lubricants	Track/rail, motor drives	TBD	M/P
Hydrazine	Refueling	1 cm^3/disconnect	M
EVA/EMU	Servicing/maintenance	0.1 gm H_2O/sec activity 31.5 cm^3 air/min TBD particulate	M/P

(1) M - molecular; P - particulate
(2) Based upon 10.7 x 10.7 x 27.4 m (35 x 35 x 90 ft) CSF configuration

TABLE V. SUMMARY OF MOLECULAR TRANSPORT DEPOSITION AND PRESSURIZATION ANALYSIS FOR HST SERVICING

Contaminant Source	Contamination Parameter	
	Deposition Thickness On OTA Surfaces (angstroms)	CSF Internal Pressure (torr)
EMU water dump (1)	(2)	$\frac{7 \times 10^{-4}}{\text{Trap area } (M^2)}$
EMU air leakage (1)	(3)	$\frac{1.1 \times 10^{-5}}{\text{Trap area } (M^2)}$
Hydrazine spill (1 cm^3)	(4)	1×10^{-4} (5)
Graphite-epoxy outgassing (6)	770	3.5×10^{-7}
Beta-cloth outgassing (6)	< 1	3.2×10^{-11}

(1) Based on current EMU design; IOC available waste collection unit for current EMU would eliminate source and subsequent deposition
(2) Extremely high on cold surfaces
(3) Very high on cryogenic surfaces without moderate venting or trapping
(4) Highly dependent on areas of cold surfaces
(5) Instantaneous pressure, dissipates rapidly
(6) Based on 14-day servicing mission

TABLE VI. RESULTS OF PARTICLE DISLODGEMENT ANALYSIS

0 Input Parameters: Impact Velocity - 60 cm/sec
Initial Surface Cleanliness - Level 750
Per MIL-STD-1246A
Beta-Cloth Panel Area - 150 ft^2

Particle Size Range (Mean Particle Dia in Microns)	NP_i (1) ($No./ft^2$)	Fraction Dislodged	NP_d (2) ($No./ft^2$)	TNP_d (3) (No.)
50-100 (75)	73,900	0.15	11,085	1.66E+6
100-200 (150)	5,700	0.75	4,275	6.41E+5
200-300 (250)	332	0.96	319	4.78E+4
300-400 (350)	54	0.99	53	8.02E+3
400-500 (450)	8	1.0	8	1.20E+3
500-700 (625)	5	1.0	5	7.50E+2
750 (750)	1	1.0	1	1.50E+2

(1) NP_i - Initial surface particulate level

(2) NP_d - Number of particles dislodged per unit area of beta-cloth

(3) TNP_d - Total number of particles dislodged per beta-cloth panel

TABLE VII. QUALITATIVE TRADE ANALYSIS FOR MOLECULAR CONTAMINANT COLLECTION DEVICES

Collector/Control Device Type	Advantages	Disadvantages
Cold Plate	Very high capacity Nonselective adsorption Current technology available	Large surface areas required Large facilities requirement (power, cryogen supply) Reliability concerns
Adsorption Media	Minimum facilities required Lightweight Regeneration possible	Low capacity Efficiencies varies with contaminant concentration May generate particles
Inert Gas Purge with Filtration	Technology available Effective for suitable geometry Makes use of existing user purge hardware	Large gas volumes required CSF plumbing required Limited applicability
Passive Devices (shields, vents, baffles)	Very low cost Flight proven	Not an ultimate destruction method Devices may be large

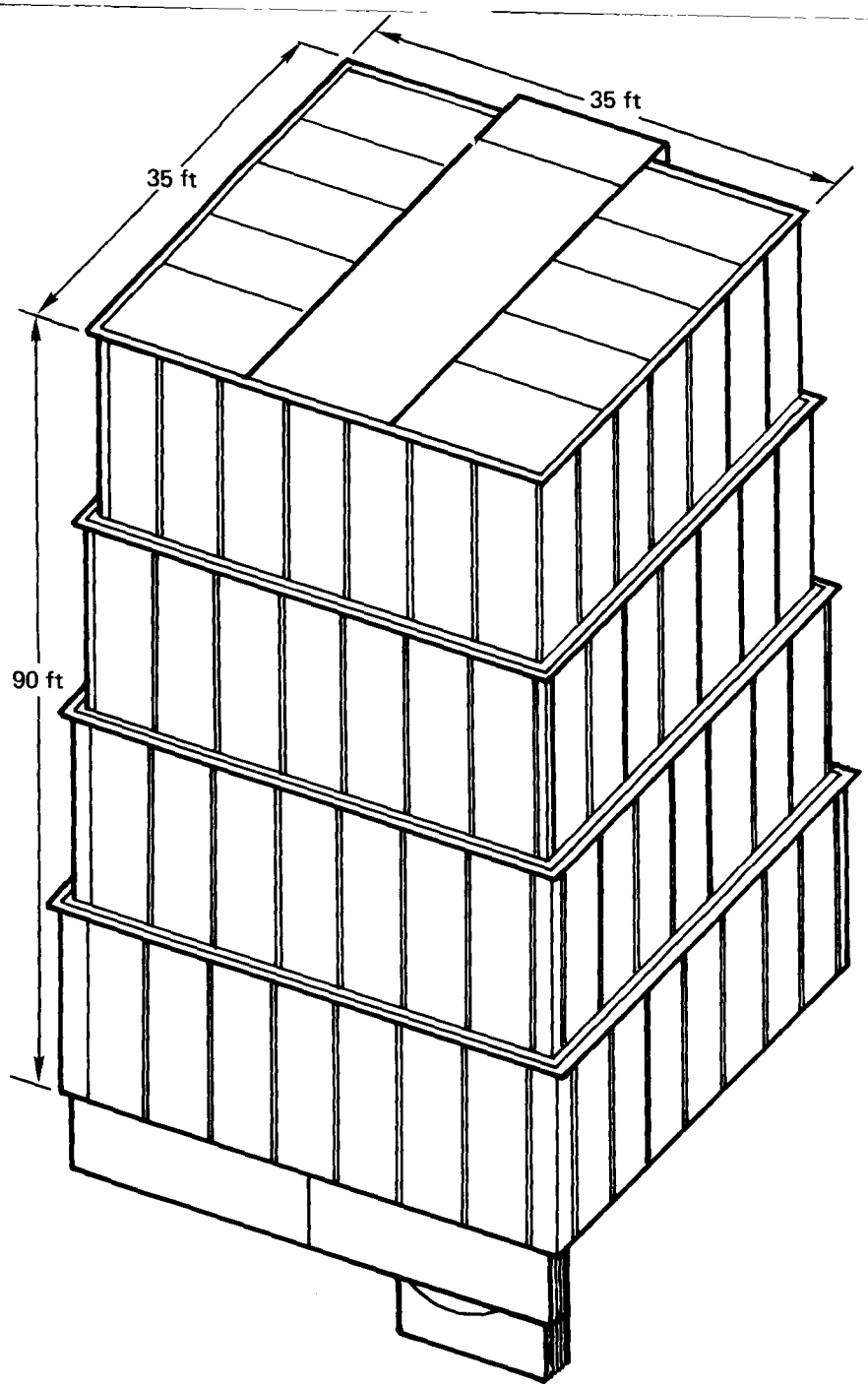

FIGURE 1. CSF -- EXTENDED MODE

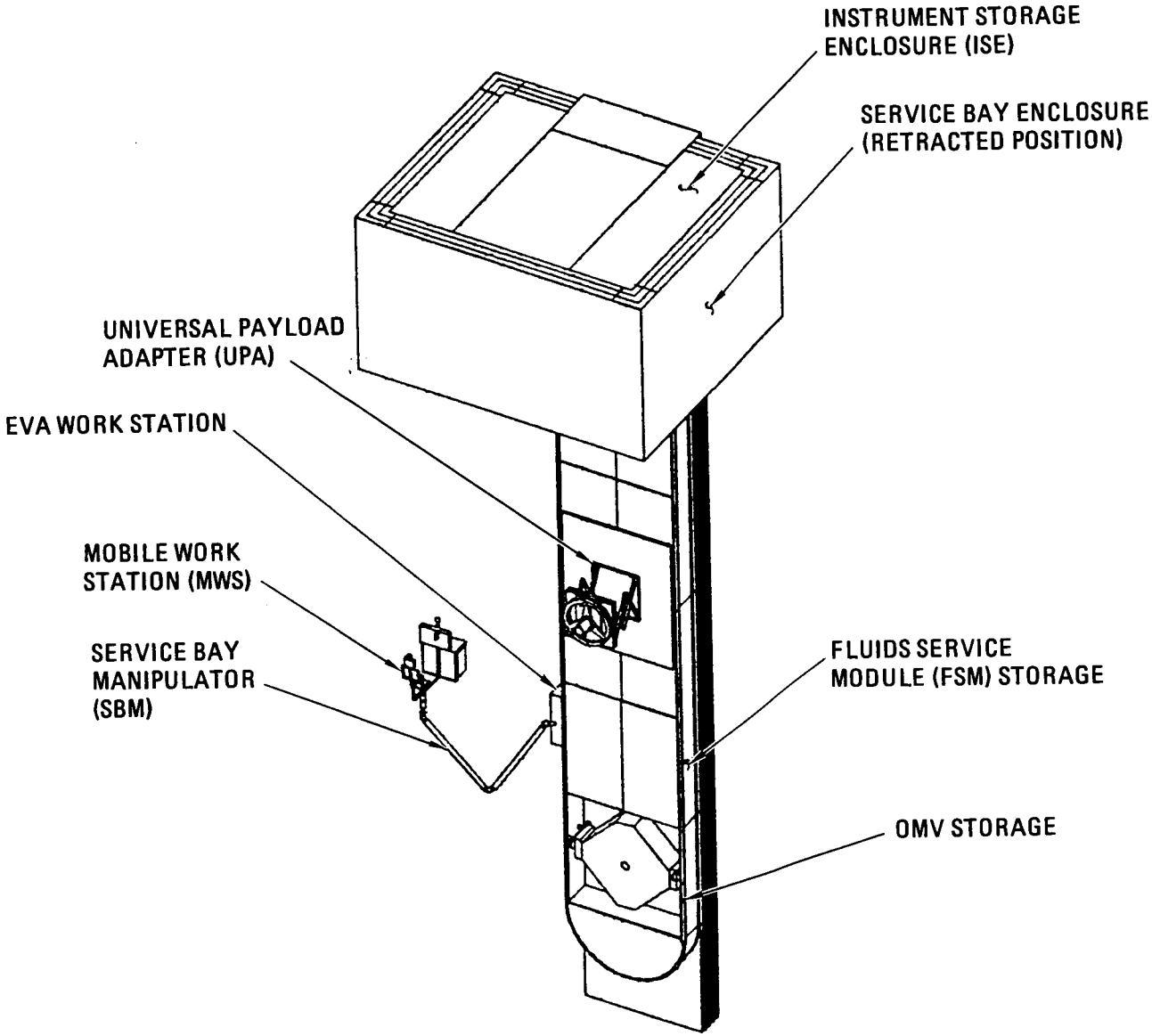

FIGURE 2. CSF RETRACTED MODE SHOWING VARIOUS SERVICING MECHANISMS

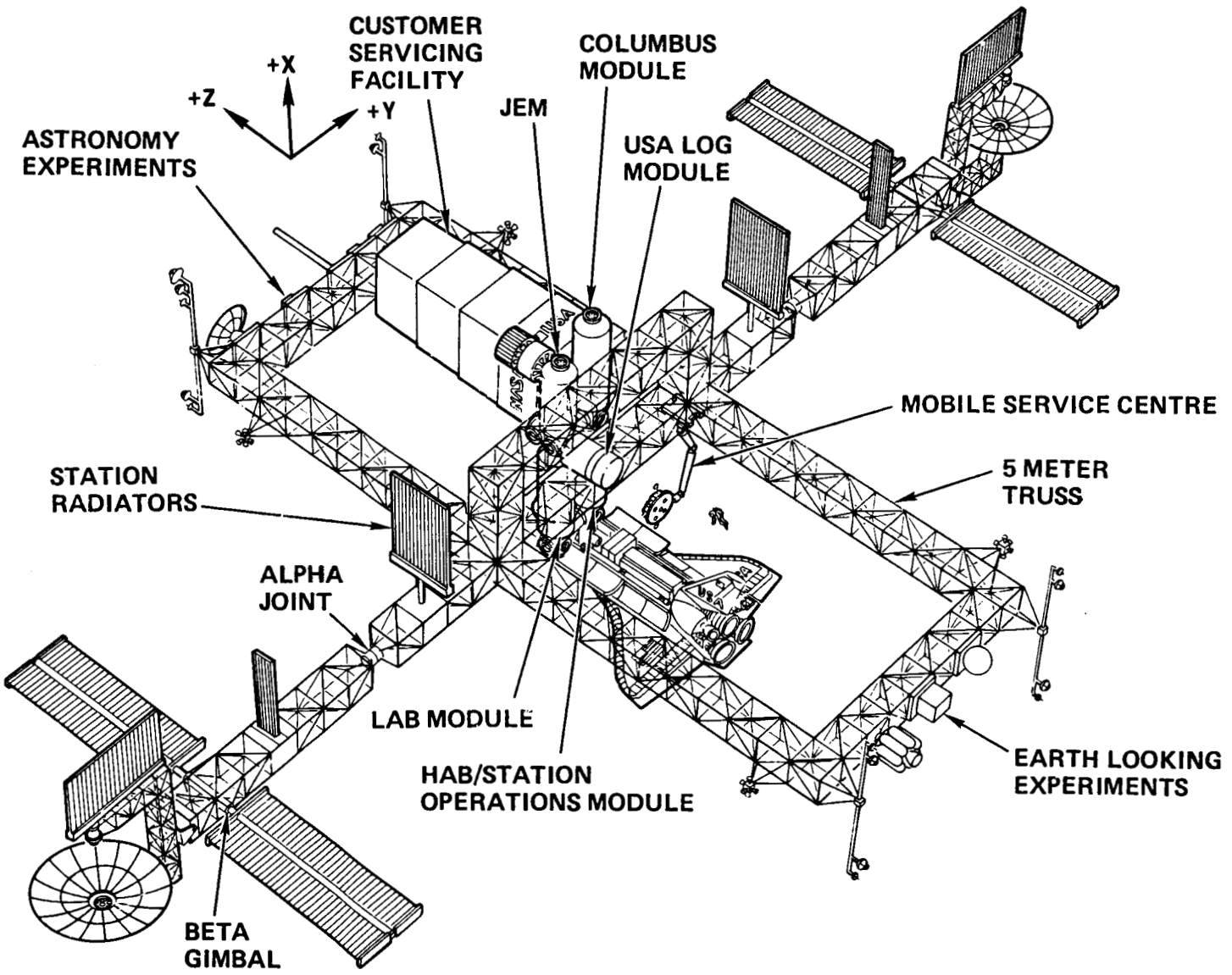

FIGURE 3. SPACE STATION DUAL KEEL CONFIGURATION

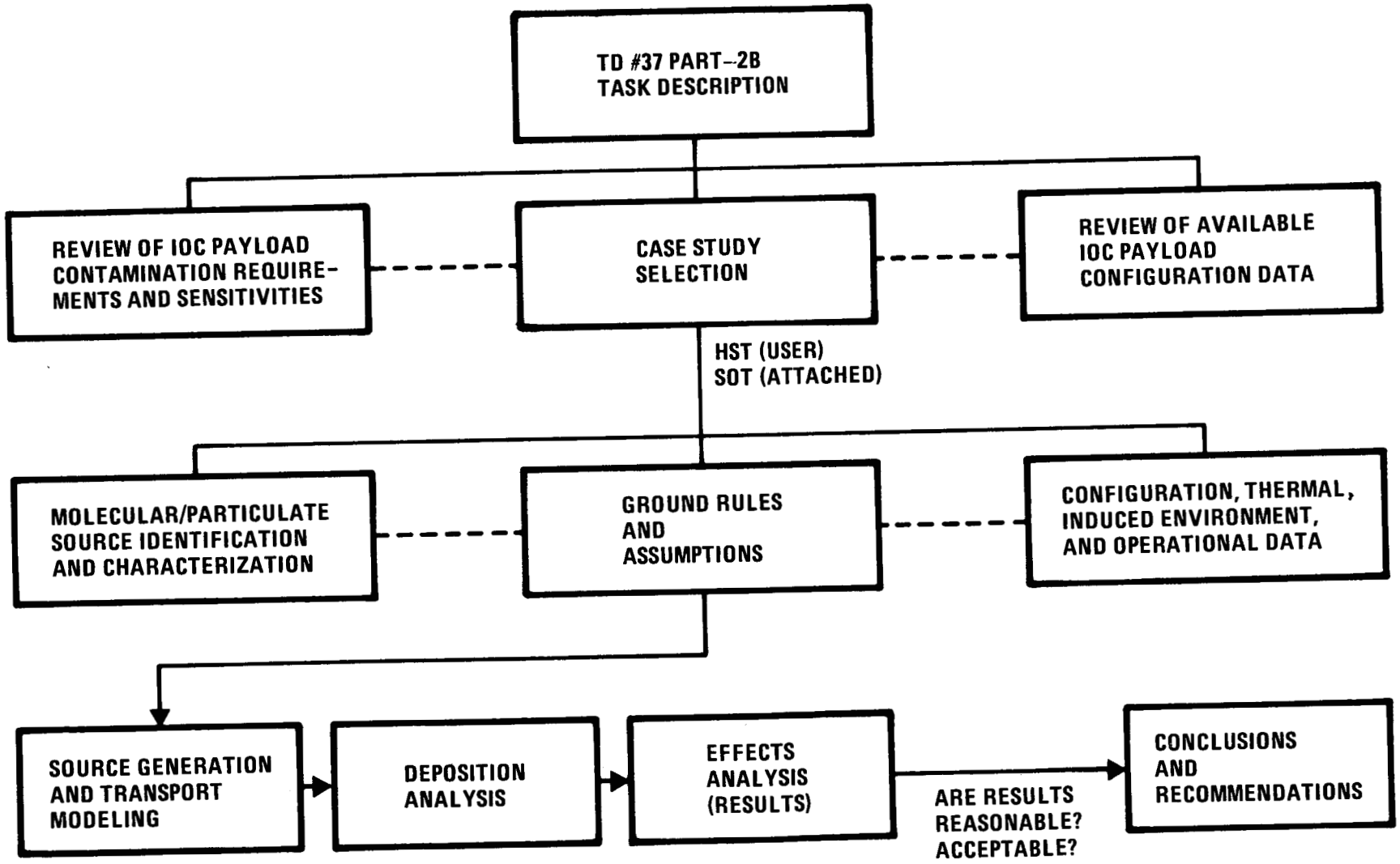

FIGURE 4. FLOW DIAGRAM OF SERVICING AREA CONTAMINATION ANALYSIS -- INTERNAL SOURCES

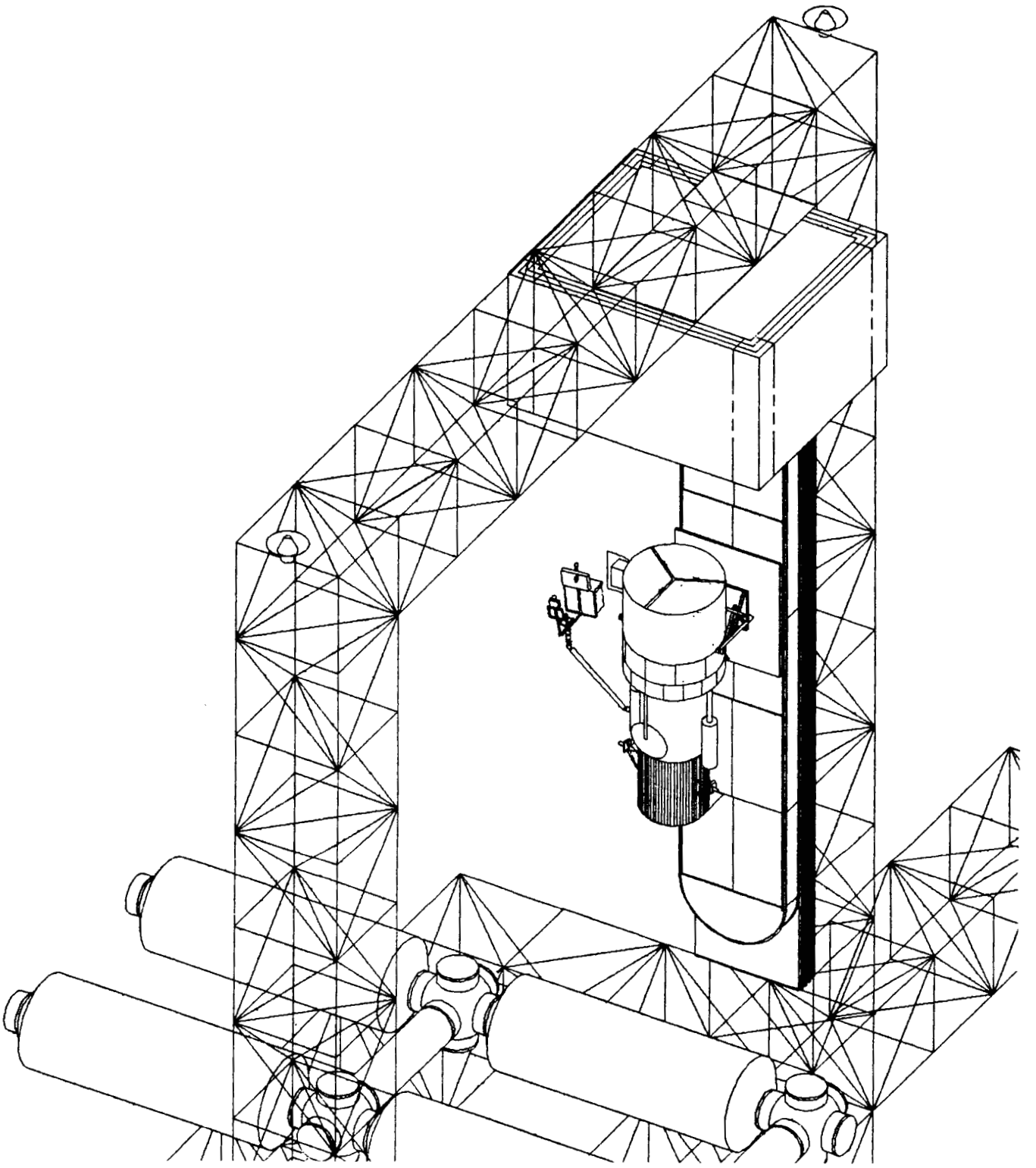

FIGURE 5. SERVICING HST IN THE CSF

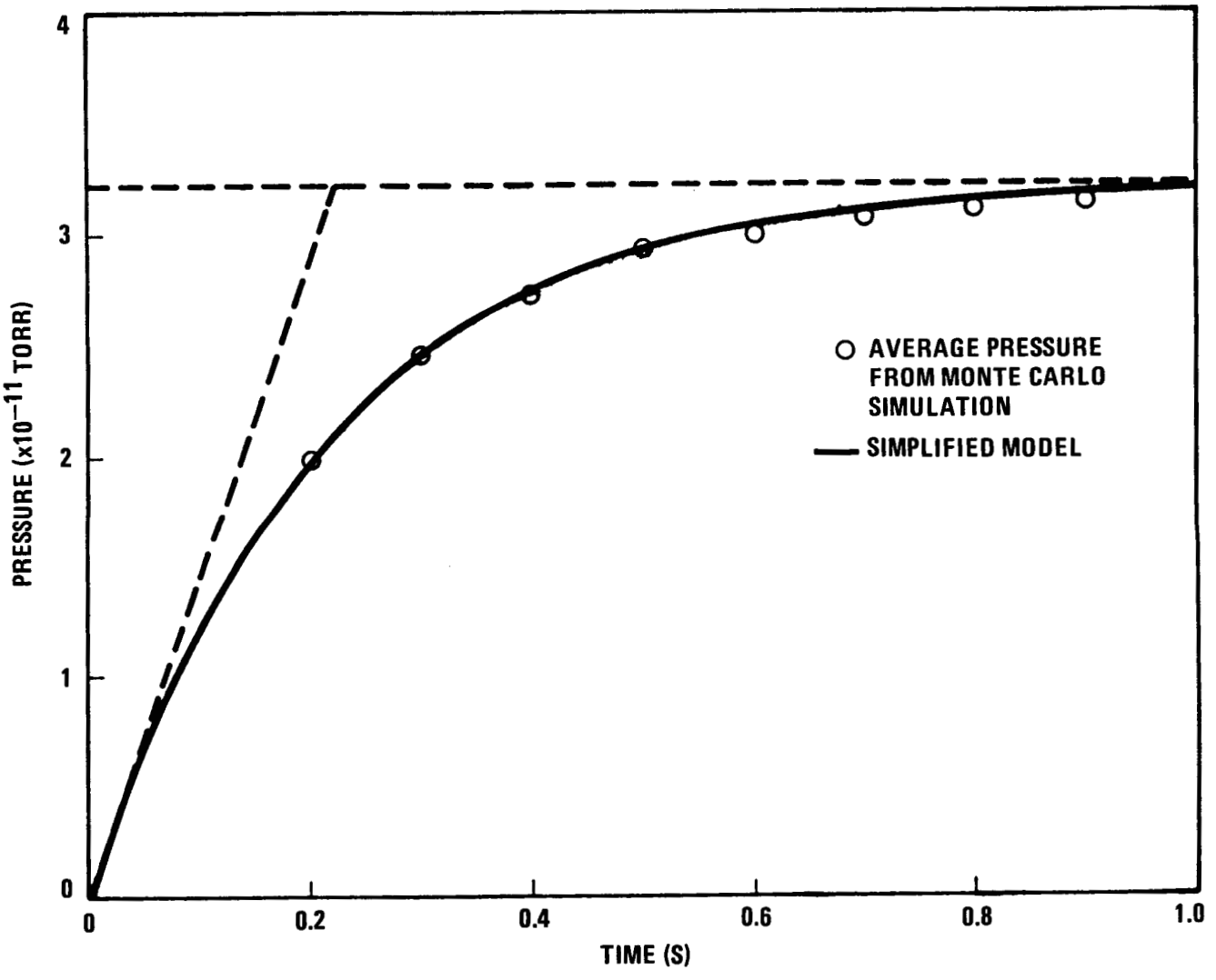

FIGURE 6a. TRANSIENT PRESSURIZATION OF CSF BY BETA-CLOTH OUTGASSING

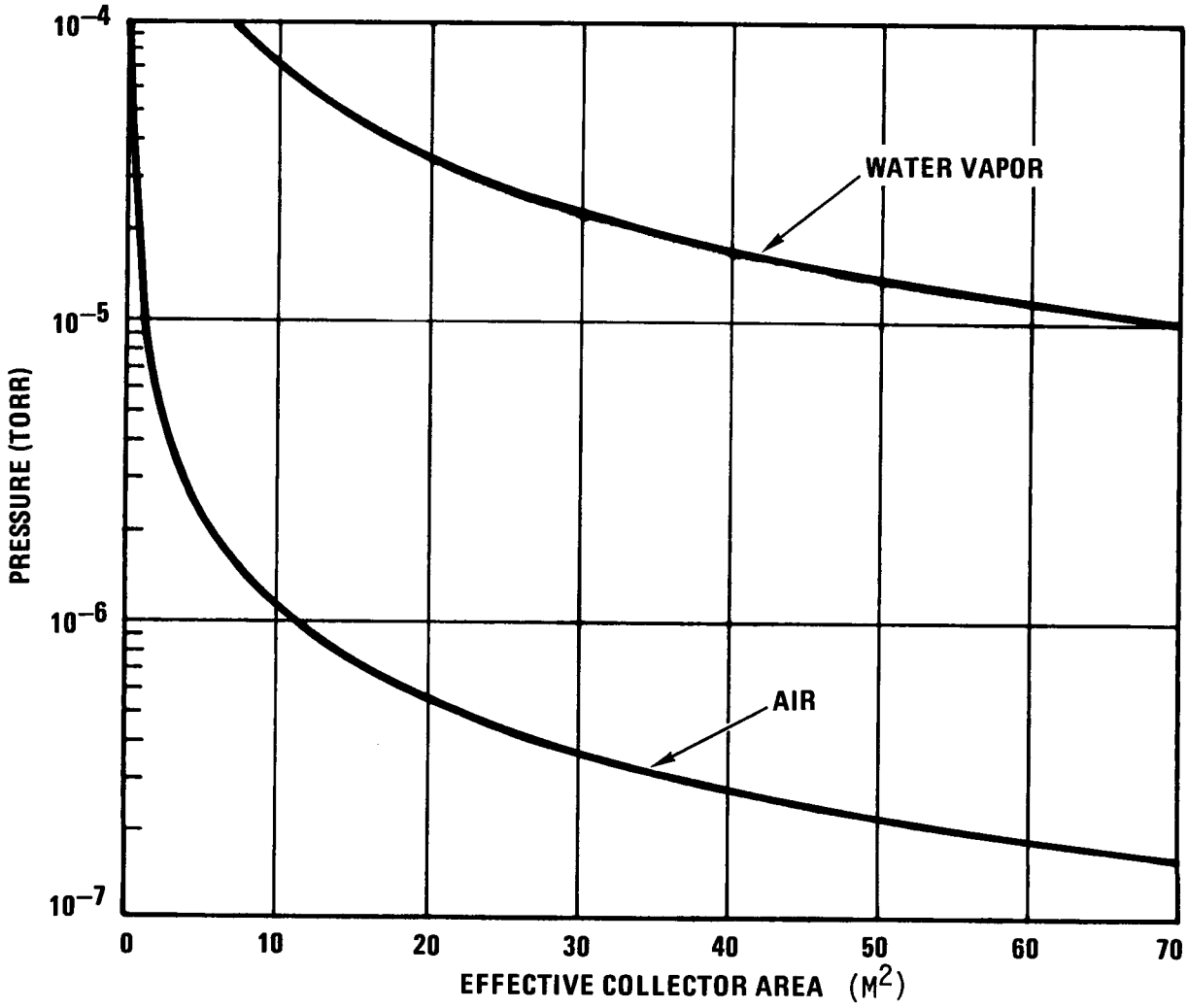

FIGURE 6b. CSF PRESSURIZATION FROM EMU WITH ACTIVE COLLECTION

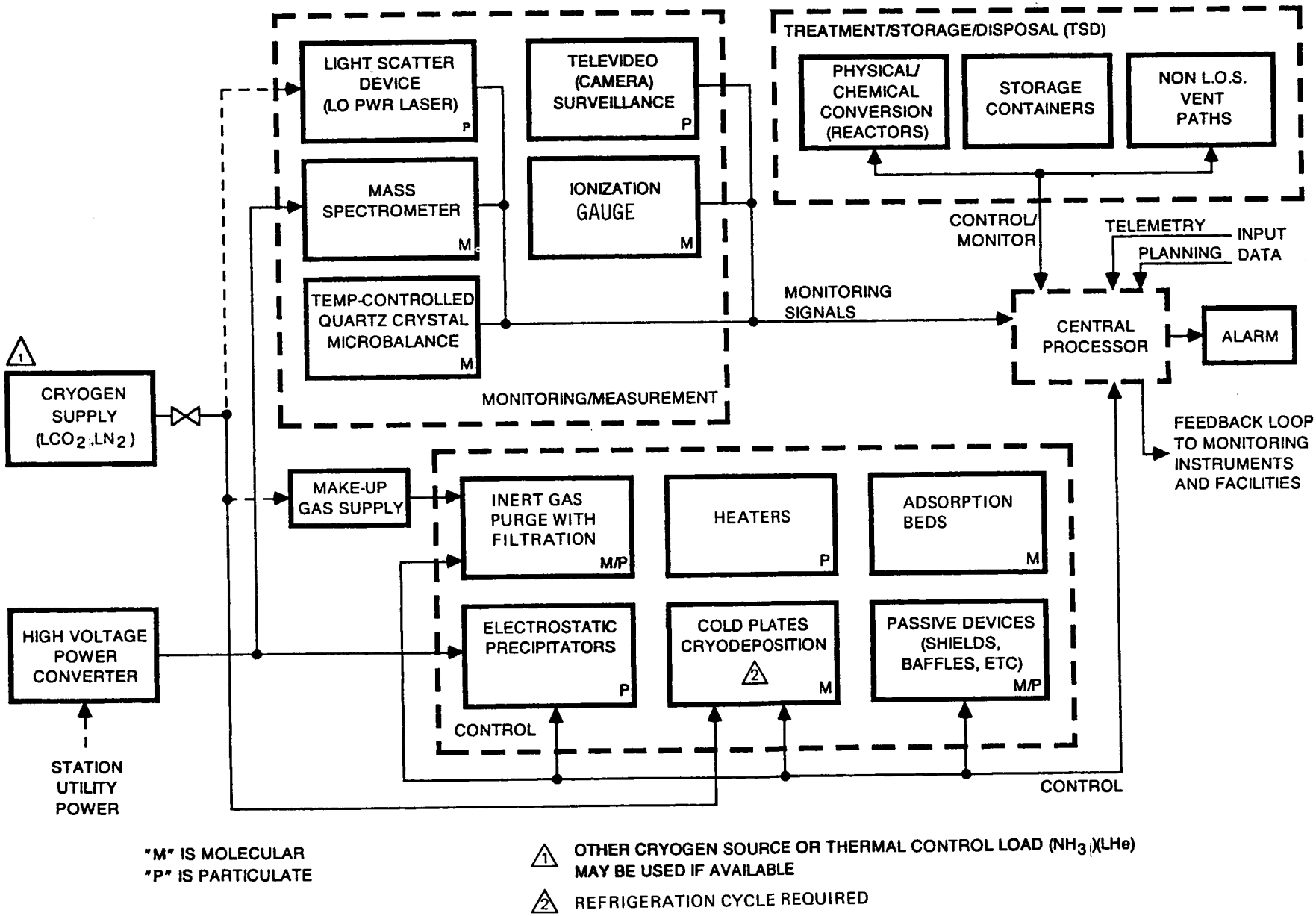

FIGURE 7. BLOCK DIAGRAM OF PROPOSED HARDWARE FOR CSF CONTAMINATION CONTROL SUBSYSTEM

SCENE SIMULATION FOR PASSIVE IR SYSTEMS*

Capt J. D. Holt, USAF

R. Dawbarn and A. B. Bailey
Calspan Corporation

ABSTRACT

The development of large mosaic detector arrays will allow for the construction of staring LWIR sensors which can observe large fields-of-view instantaneously and continuously. In order to evaluate and exercise these new systems it will be necessary to provide simulated scenes of many moving targets against an infrared clutter background. At the AEDC as part of our ongoing efforts to provide a test capability in this area of sensor evaluation, we are monitoring the development of a number of simulator technologies which have the potential for providing a multiple target test capability. However, since at this time there is not a system available for use within a cryo-cooled vacuum environment, we are currently developing a projector/screen system for use at the AEDC in an attempt to provide the needed test capability.

This system is comprised of a mechanical scanner, a diffuse screen, and a miniature blackbody. A prototype of the mechanical scanner, which is comprised of four independently driven scanners, has been designed, fabricated, and evaluated under room and cryogenic vacuum conditions. A large diffuse screen has been constructed and tested for structural integrity under cryogenic/vacuum thermal cycling. Constructional techniques have been developed for the fabrication of miniature high-temperature blackbody sources. Finally, a concept has been developed to use this miniature blackbody to produce a spectrally tailorable source.

INTRODUCTION

The role of satellite-borne long wavelength infrared (LWIR) systems is rapidly changing from passive early warning of an offensive missile launch to that of a major segment of an active defense-in-depth (DID) network. Projected satellite systems will perform many tasks including early-warning, destruction of boost-phase vehicle, tracking of those rockets which leak through, mid-phase discrimination of active reentry vehicles (RVs), and subsequent destruction and handover to ground-based systems for the final defense leg.

No one type of sensor system can be expected to perform all of the detecting, tracking, and discriminating functions which will be required. At the present time it is not known which of the various systems may be located on common satellite

---

*The research reported herein was performed by the Arnold Engineering Development Center (AEDC), Air Force Systems Command. Work and analysis for this research were done by personnel of the AEDC Director of Technology, Deputy for Operations, and Calspan Corporation/AEDC Division, operating contractor for the AEDC aerospace dynamics test facilities. Further reproduction is authorized to satisfy needs of the U. S. Government.

platforms or which may be on multiple smaller satellites. It is obvious, however, that the future test facilities needed to evaluate and test these systems prior to deployment must provide infrared targets and scenes which can reproduce scenarios typical of the most stressing offensive attack which can be envisioned.

It is the purpose of the present report to give a brief summary of multiple target simulation requirements and describe the status of a source projection target system.

REQUIREMENTS FOR TESTING IR SENSORS

The field-of-view (FOV) of infrared (IR) sensor systems can be divided into three types: the space background, the earth limb, and the earth surface. Each of these fields-of-view consists of a background contribution and a set of targets, and in each case the targets move relative to the background. In some instances the targets may be colder than the background, thus producing a negative contrast target.

Sensors confined to looking above the earth limb will see targets against a background of stars. These stars, along with the targets, will appear as point sources at the focal plane of the sensor and will be the least complex scene required. The types of objects could range from reentry vehicles (RV), decoys and spent rocket casings to plumes from final deployment and dispersion thrusters. Such plumes and intentionally deployed particle clouds could reach sufficient size as to appear as extended sources--illuminating several adjacent pixels on the mosaic array in the detector focal planes.

A simulated target scenario for sensor systems will thus require an overall background at 20 K to simulate the space environment. It should include a pattern of stars which can be swept across the field-of-view. The rate at which the stars move across the background will depend on the particular orbit and viewing attitude of the sensor. Superimposed on this scene will be the targets and objects of the simulated attack force. While these objects all move in the same general direction some allowance must be made for individually tailored trajectories. Discrimination between targets and decoys in this exoatmospheric phase of the trajectory will most likely rely on target signatures. Therefore, a test simulator should have the capability of producing targets and objects with sufficient spectral structure for the sensor to exercise its discrimination algorithms. The possibility of a blooming target to simulate plumes and particle clouds would also be desirable.

The earth limb field-of-view requires all of the previously noted simulations plus a superimposed extended source over an extensive portion of the imaged scene. This extended source could have significant structure depending on the atmospheric conditions. Periods of intense solar activity can result in auroral events with significant radiation in wavelengths to which the IR systems are sensitive. This structure can last from seconds to several minutes; thus an additional simulation requirement is a superimposed IR background which has a structured intensity that can be varied with time.

The requirements for an earth-looking FOV simulator are so different from those previously described that it is probable that completely different concepts and technologies will be needed to produce it. The emitted and reflected radiation from the earth surface and clouds will provide a complex, structured background.

Exoatmospheric objects such as satellites, RVs, and decoys can be cooler than this background and can present a negative contrast. Objects reentering the atmosphere will experience aerothermal heating, and thus their radiant energy can be expected to increase by several orders of magnitude as they are being tracked. Objects within the atmosphere, such as aircraft, cruise missiles, and ships, will have positive signatures; however, these will be modified by atmospheric absorption. This absorption will vary depending on the pathlength of the radiation through the atmosphere which will be a function of the viewing angle of the satellite system.

The ability to test surveillance sensor systems hinges on the development of new target simulation techniques. It is unlikely that a single scene generator will be able to provide the variety of scenarios required for the evaluation of the various types of sensors which are being proposed for future surveillance and defense systems.

TEST METHODOLOGY

Surveillance systems using staring mosaic arrays are expected to have large aperture optical telescopes with a wide field-of-view. This presents a particular problem for a ground test facility which must provide a simulated IR scene at an effective infinite distance. The prime technology barrier is the large mirrors needed to provide the collimated radiation. A test methodology has been proposed which circumvents the problems associated with the large chamber optics.

In this evaluation sequence, the mission/scenario testing is accomplished on the sensor focal plane before assembly in the telescope system. The test must provide an IR scene generator and a set of optical mirrors to focus this scene on the mosaic array. This testing can provide an evaluation of the optical performance of the focal plane and the data processing capability of the associated computer system and its algorithms.

A subsequent test program is conducted with the telescope assembled. In this test a collimating mirror is required; however, it can be limited in size to the entrance aperture of the test system. This test becomes one of integration, optical alignment, telescope throughput, off-axis rejection, and radiometric calibration, all of which can be accomplished by mapping the field-of-view with calibrated IR sources.

Two types of test facilities are required. The first is a focal plane array (FPA) facility that provides radiometric calibration and also produces dynamic IR scenes to test the detector system's ability to detect, sort, and track objects. The second facility requires a collimation system that can illuminate the full aperture of the sensor telescope. The mirrors required for such a facility need to be approximately 20-percent larger than the entrance aperture of the test article. Full-aperture illumination would preserve the diffraction-limited resolution of the sensor telescope and would also permit total FOV tests by using a scanning and focal plane mapping technique.

In the present paper our concern is with the development of a system to produce dynamic IR scenes for the FPA facility.

REVIEW OF TARGET SIMULATOR CONCEPTS

Multiple target simulator concepts fall into two general categories. Those systems in the first category compose the scene from a mosaic of discrete elements and can be further grouped as IR emitters or IR modulators, figs. 1a, 1b, and figs. 1c-1e, respectively. Illumination by a wide-beam IR source is required for all of these systems, i.e., figs. 1a-1e. The second category is comprised of what are classed as analog systems, c.f., figs. 1f and 1g.

Some examples of the concepts that have been, or are currently being evaluated are listed in table I. Our assessment of the state-of-the-art with regard to the scene simulators that are being developed for use with warm backgrounds has indicated that some of these may be capable of adaptation for use in a cryogenically cooled vacuum environment. However, the unavailability of a multiple target simulator to provide a mix of spectrally differing targets with independent control of intensity in a cryo-cooled vacuum environment provided the impetus for the cryogenic projector system currently being developed at the AEDC.

CRYOGENIC MULTIPLE TARGET SYSTEM

Components for the projection screen multiple target system are shown in fig. 2. The sources are miniature IR emitters which in the prototype will be designed as blackbody cavities. In future versions the spectral output of the sources will be tailored to simulate specific target signatures. The projection optics are duplicated for each source and consist of a set of cryogenically cooled (20-K) mirrors driven by mechanical actuators. The choice of mirror driver is determined by the type of target motion to be simulated. The mechanical scanner currently under development is geared toward slow-moving targets at large distances. The screen is a cryogenically cooled reflective surface which is diffuse to IR radiation. The number of moving targets which might be projected simultaneously with this system is limited by the degree of miniaturization which can be accomplished in the sources and scanners. The clutter background can be projected from a single still-frame projector. Recent development efforts have been directed toward constructing and testing the projection screen, developing and testing the scanner system, and developing the technology required to produce a high-temperature miniaturized blackbody source.

MINIATURE BLACKBODY SOURCE

It was recognized early in the development process that currently available blackbody sources were too large for use in a multiple target system. These conventional blackbody sources are composed of an isothermal cavity whose walls have an emissivity close to unity and an area much larger than the emitting orifice. The requirement to operate the source within a vacuum/cryogenic environment complicates the design of a miniature blackbody (MBB) since: (1) The need to operate within a 20-K enclosure results in strong thermal gradients between the MBB and its support structure. This complicates the problem of providing an isothermal cavity and results in an increased design effort to minimize heat loss from the cavity; (2) Outgassing from components used in the manufacture of conventional blackbody sources can contaminate sensitive optical components located within the cryogenic/vacuum environment. As a result of the need to minimize these heat loss and contamination effects it is not appropriate to use construction techniques that have been used successfully for blackbody sources operating at ambient conditions. It has been

determined that the multiple target system will require a contamination-free MBB operating at temperatures up to 600 K. This operational requirement places severe restrictions upon the materials used for construction and necessitates improved thermal isolation.

A schematic of an AEDC MBB is presented in fig. 3. The core of the blackbody is made of aluminum. A dual acme thread is cut in the outer surface to accommodate the heater wire (fig. 4). The dual thread permits both ends of the heater wire to exit at the rear of the core. Prior to winding the insulated heater wire on the core, the ends of the constantan heater which are to be used as the electrical supply leads are stripped and electroplated with copper. This adds power leads to the heater without any welded or soldered connections. The insulated section of the heater wire is wound on the threaded portion of the heater core and attached to it in such a manner that good thermal contact is established between the heater wire and the core. The heated core is mounted in the MBB assembly via a ceramic tube (fig. 3), and the heater leads pass through two passageways down the length of this tube.

Work continues in the area of embedding temperature sensors in the body of the core. The current technique under investigation is potting the ceramic-coated platinum sensors into the core using a curable ceramic cement. Initial work has indicated reasonably successful bonding to the anodized core holes.

SPECTRAL SOURCES

One method for discriminating between RVs and decoys is by comparing the spectral signatures of the objects in the FOV of the sensor. This can be accomplished by using bandpass filters at the detectors. Some systems use two color bands and others three. A simplified example of discrimination between an RV and an identically shaped decoy might consist of determining the temperature difference between them. One would expect that during the mid-course flight that the massive RV would retain its basic temperature while the low mass decoy would drop in temperature as they both radiated heat. The absolute radiant energy received by a sensor could not be relied on to distinguish the difference since the view angle and aspect angle of each object could be quite different. However, the ratio of the energy received in two appropriately chosen bands could be used to identify the RV as the warmer object. Evaluation of the ability of dual- and tri-color sensors to discriminate between targets and decoys in a ground test facility requires spectrally tailored sources. This can be accomplished with blackbody sources using spectral filters.

A schematic of a method for producing a spectrally tailored source is shown in fig. 5. The concept is shown for a two-color system although it can be extended for a tri-color source. The radiation is produced by two blackbody sources. In front of each blackbody is a bandpass filter corresponding to the bandpass filters of the sensor to be tested. The relative intensity of the radiation to be included in each band is set by adjusting either the blackbody temperature or the orifice size to the mixing integrating sphere. The total intensity of the radiation is set by choice of orifice size between the mixing sphere and the attenuating sphere.

PROJECTION SCREENS

Earlier studies have indicated that gold-coated grit-epoxy surfaces hold promise as being capable of operating at cryogenic temperatures with acceptable diffuse reflecting characteristics. Recent studies have shown that such surfaces can

survive repeated cycling from 20 to 300 K. However, some bidirectional reflectivity distribution function (BRDF) measurements with a grit screen have shown that for small illuminated areas of the screen it does not diffuse tightly focused coherent radiation. For larger areas of illumination, acceptable diffuse reflection characteristics were obtained. From considerations of these data and BRDF measurements obtained with other materials, there are indications that acceptable diffuse characteristics can be obtained with materials that diffuse focused IR radiation with internal body-reflection properties. The gold-coated grit-epoxy surfaces are surface diffusers, i.e., the incident radiation does not penetrate into the body of the material. Surface diffusers were chosen because they had a better chance of surviving the vacuum cryogenic conditions. Examples of body diffusers are compressed salt powders in which radiation actually enters the material, undergoes multiple reflections in the crystalline structure, and is reemitted in a diffuse manner. However, compressed salt powders have obvious limitations when considered for use in a cryogenic/vacuum contamination-free environment. A suitable body diffuser target projection screen could possibly be made of a thin sheet of germanium, a crystalline, IR transmitting material used frequently as a vacuum chamber window. Radiation incident upon the rough face of the germanium would be partially scattered and reflected in a random distribution pattern while the remainder of the radiation would be transmitted into the material where it would undergo multiple scattering from the internal crystalline structure, reflect off the plated back surface, and be reemitted at the rough surface. Some inherent blooming of the target will occur in this (and any) body diffuser.

MECHANICAL ACTUATOR

A mechanically scanned mirror system can provide a state-of-the-art dynamic target generator for objects which move across the FOV of the sensor at slow angular rates. A typical scenario might suppose a sensor viewing a target traveling at 17,000 nmi/hr at a distance of 5,000 nmi. The angular velocity (assuming the object traveling normal to the line-of-sight) is approximately 1 mrad/sec. These rates can be provided by standard micrometer drives operating pivoted mirrors.

A gimbal system for pivoting a mirror flat both in the X and Y directions about a single point on its surface is shown in fig. 6. The friction-free X and Y pivots consist of Bendix flexures. The Bendix flexure has the advantage of rigid conductive paths through the device and thus provides for direct cooling of the mirror from the mounting block.

A prototype system using four such gimbaled mirrors assembled in a common unit is shown in fig. 7. The focused beam from four independent sources housed between the micrometer drives is folded onto the gimbaled mirrors via mirror flats on the underside of the cruciform central mounting block.

The Newport Research Corp. (NRC) micrometer drives (modified for vacuum use) have a 0.1-μm resolution which, when coupled to the 75-mm moment arm of the gimbal, provides a resolution of 1.3 μrad of the mirror or 2.6 μrad of the steered beam. The minimum and maximum micrometer drive speeds using the standard controller will provide beam slew rates from 1 to 10 mrad/sec.

A prototype of this actuator (fig. 8) has been constructed, and its performance has been evaluated at ambient conditions using an He/Ne laser as a radiation source. This evaluation has shown that multiple targets can be projected onto the screen and moved independently of each other in a controlled repeatable manner. A gimbaled

mirror driven by an NRC micrometer drive has been tested under cryogenic/vacuum conditions and has been found to operate in a controlled, repeatable manner.

CONCLUSION

An infrared multiple target/complex scene generator is a requirement for evaluation of sensor systems prior to deployment. Test facilities must provide the sensors with a range of realistic mission simulations to effectively determine the operating characteristics. Due to the diversity of mission requirements, no one simulation system can meet all the needs of the sensor testing community; therefore, a wide variety of approaches are currently under development. Most of the prototype multiple target simulators stress the ability to create a large number of discrete, precisely located sources with fixed spectral content and limited dynamic range. The AEDC simulation system emphasizes spectrally tailored, analog target images having wide dynamic range in a cryogenic environment. These attributes are definite requirements for testing space-viewing sensors. The system can produce a small number of targets, it is mechanically complex, and a diagnostic capability must coexist with it to determine the positional accuracy of the individual targets. All of these limitations can be dealt with in a manner which will not detrimentally affect the usefulness of the concept.

Table 1.
Evaluation of potential concepts for IR scene generators

Concept	Vacuum	Cryogenic	Independent Spectral Sources	Intensity & Spectral Independence	Number of Targets
Mosaic modulator	Yes	No	No	No	each pixel
Liquid crystal modulator	Yes	No	No	No	each pixel
Magneto-optic modulator	probably	No	No	No	each pixel
Deformable mirror	probably	No	No	No	each pixel
Thermal element array	Yes	Yes	Yes	No	each pixel
Laser Scanner	probably	probably	Yes	No	Scan limited
Membrane Converter	Yes	No	Yes	No	Source limited
Analog Projector	Yes	Yes	Yes	Yes	4 → 40

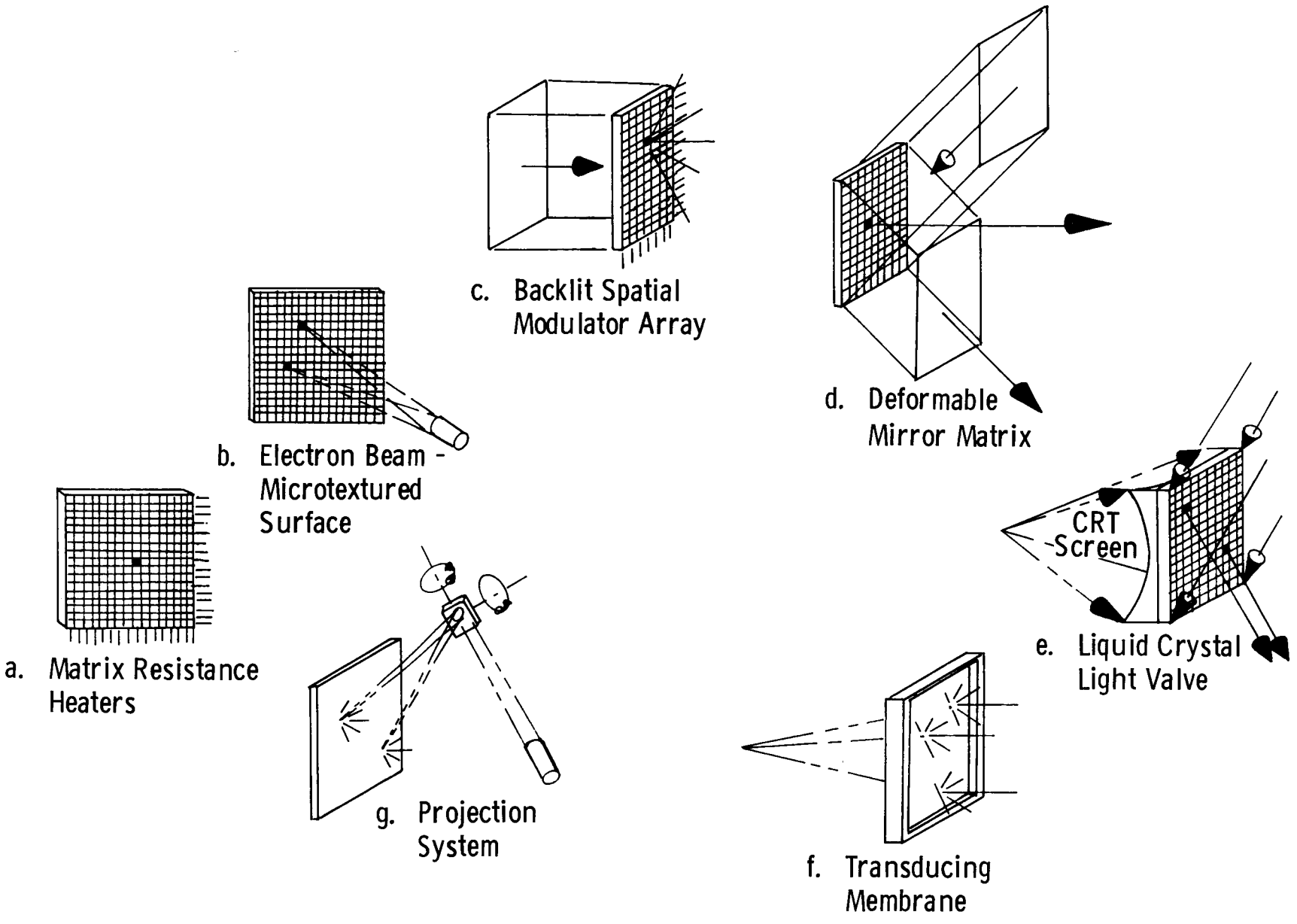

Figure 1. Organization of multiple target simulators

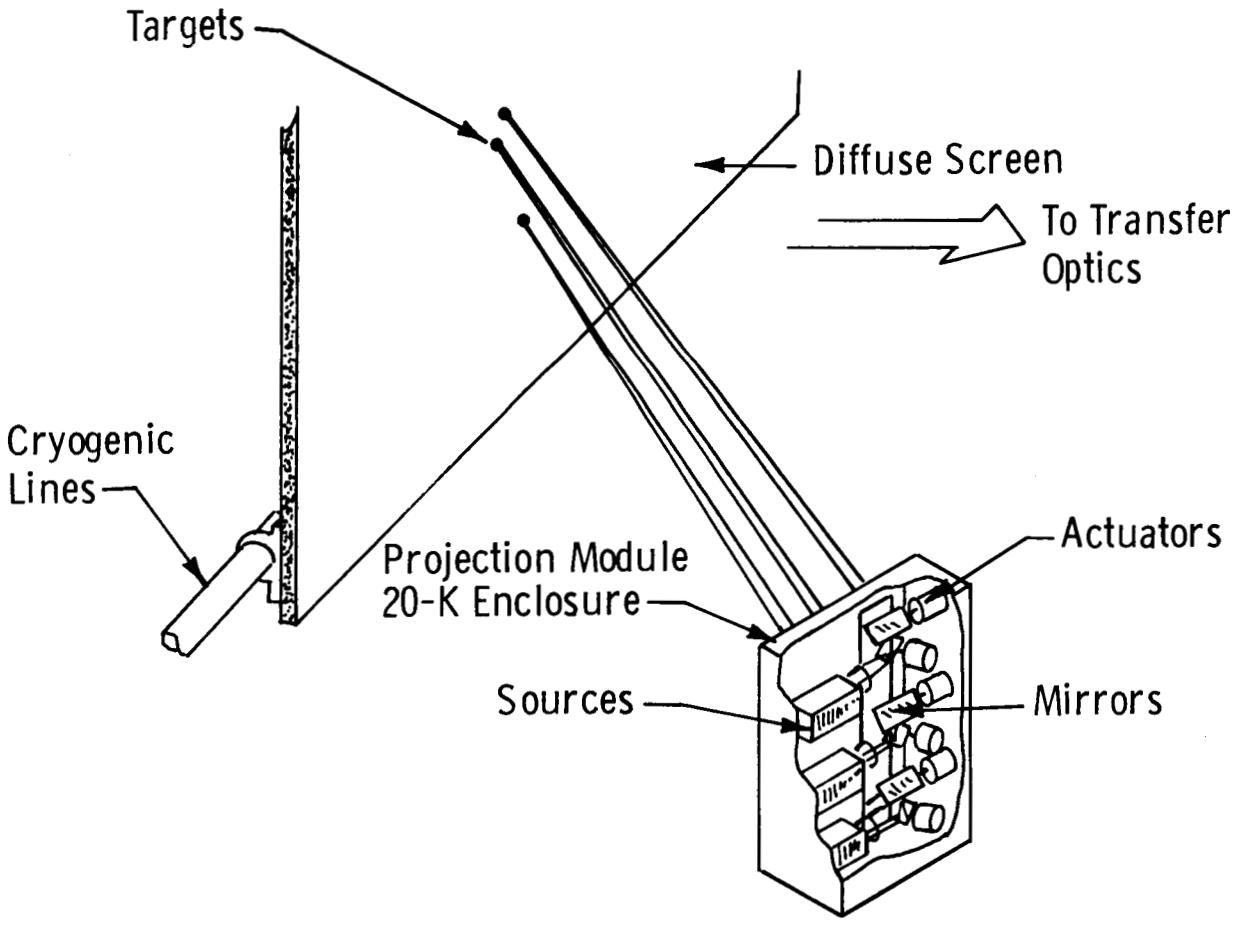

Figure 2. Multiple target projection system

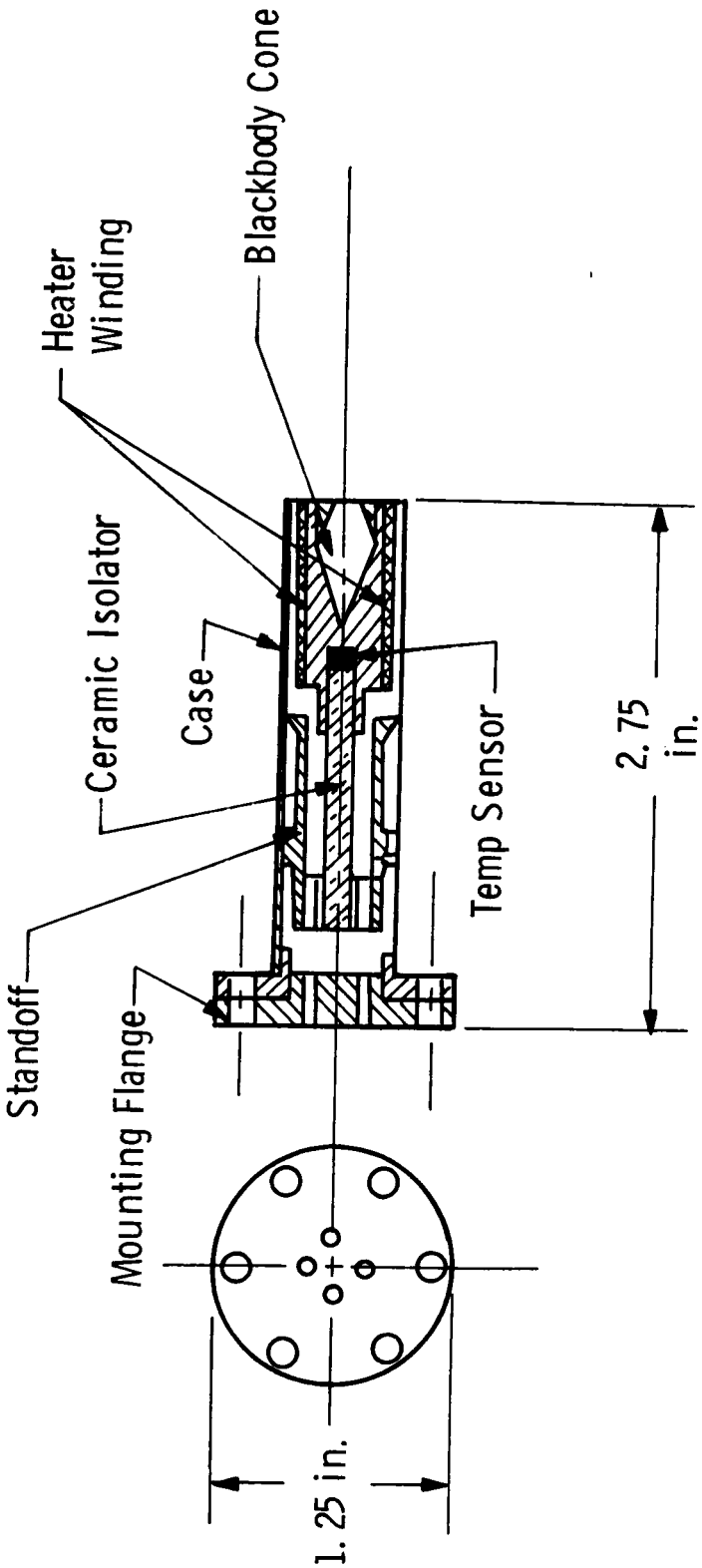

Figure 3. Miniature blackbody schematic

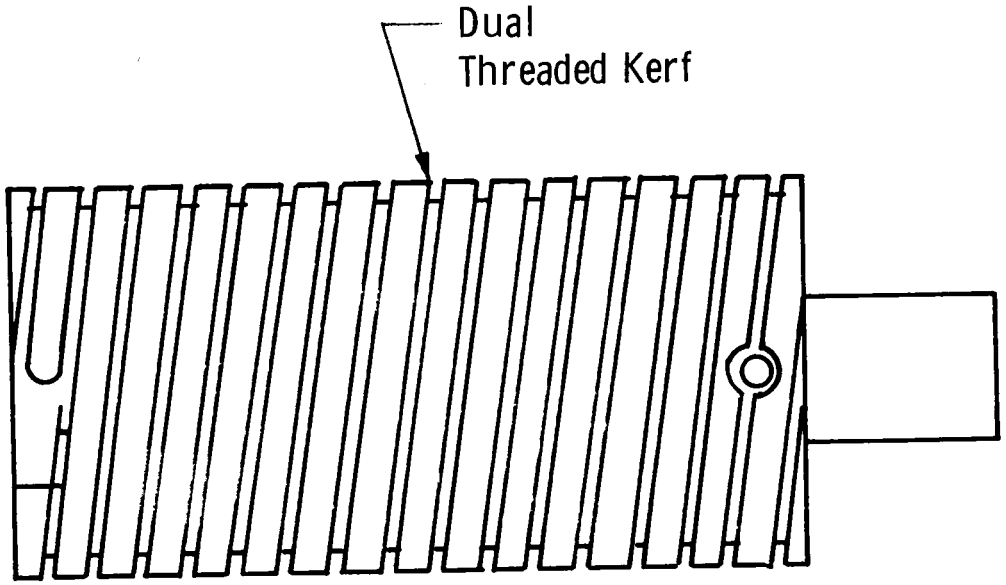

Figure 4. Heater core

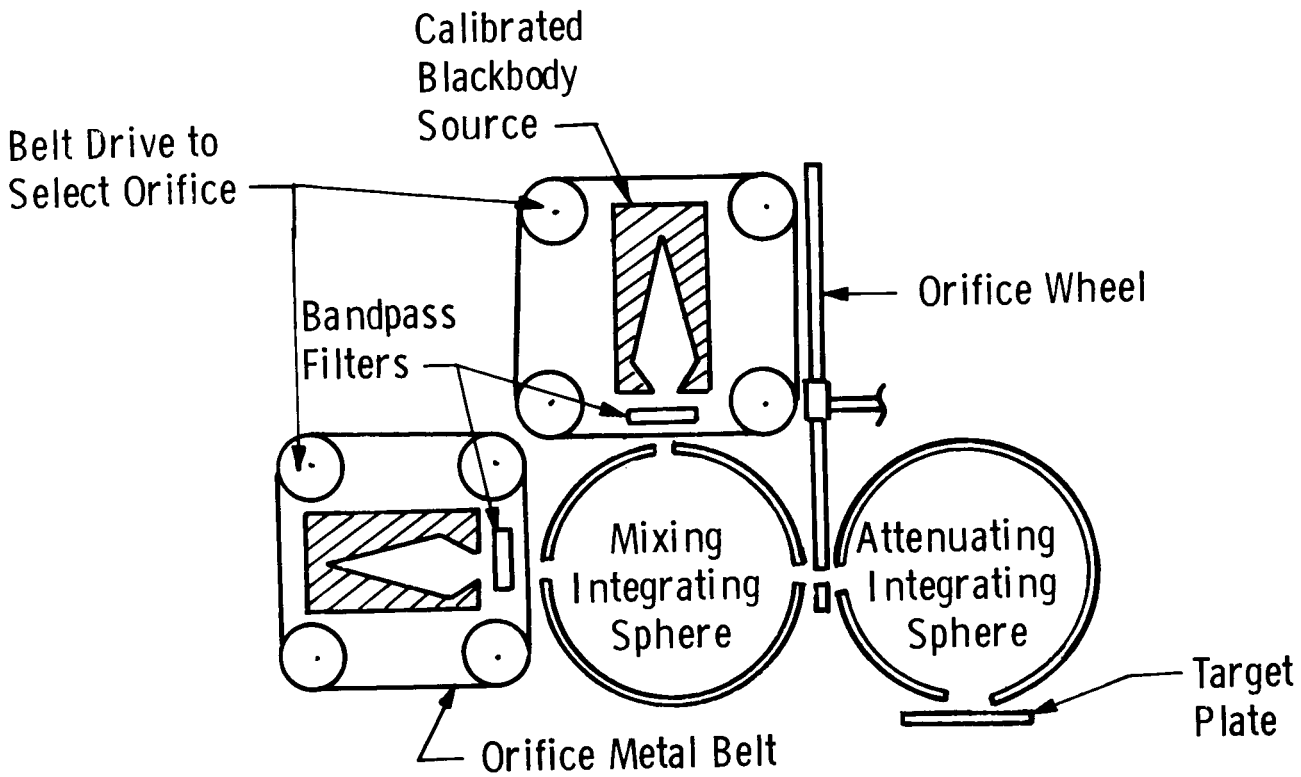

Figure 5. Spectrally tailored IR source

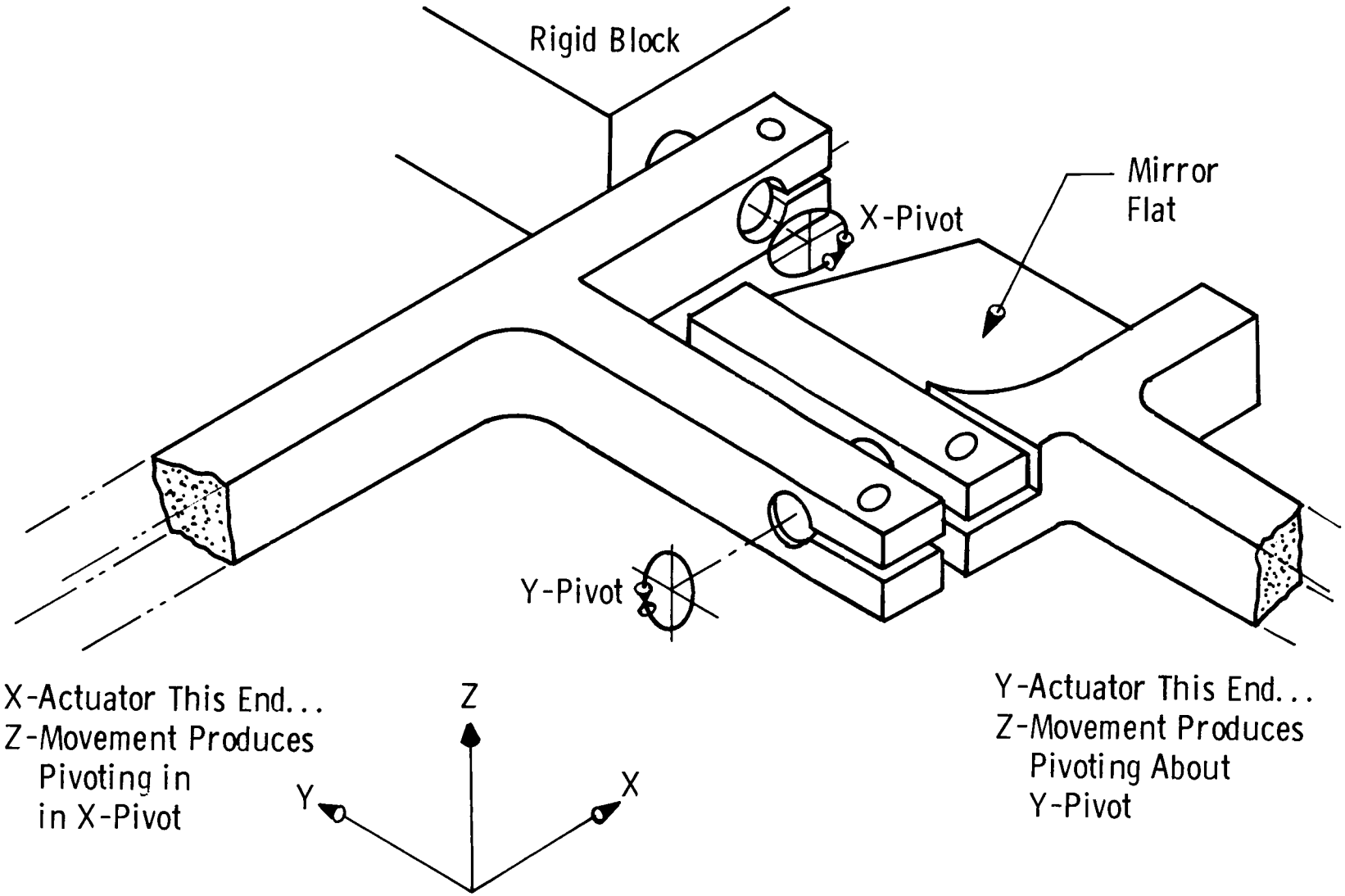

Figure 6. Pivoting flexure mount

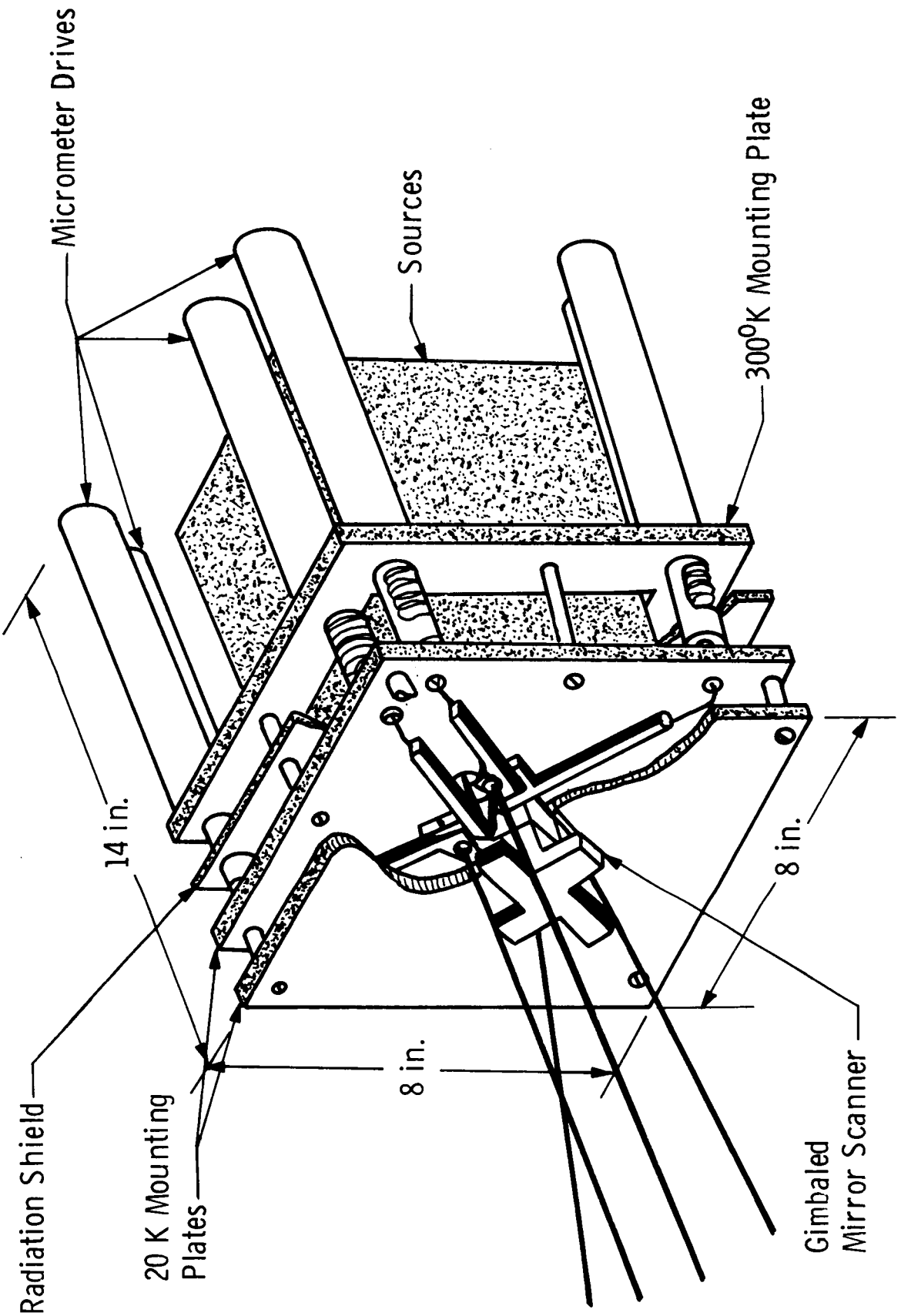

Figure 7. Mechanical mirror scanning system

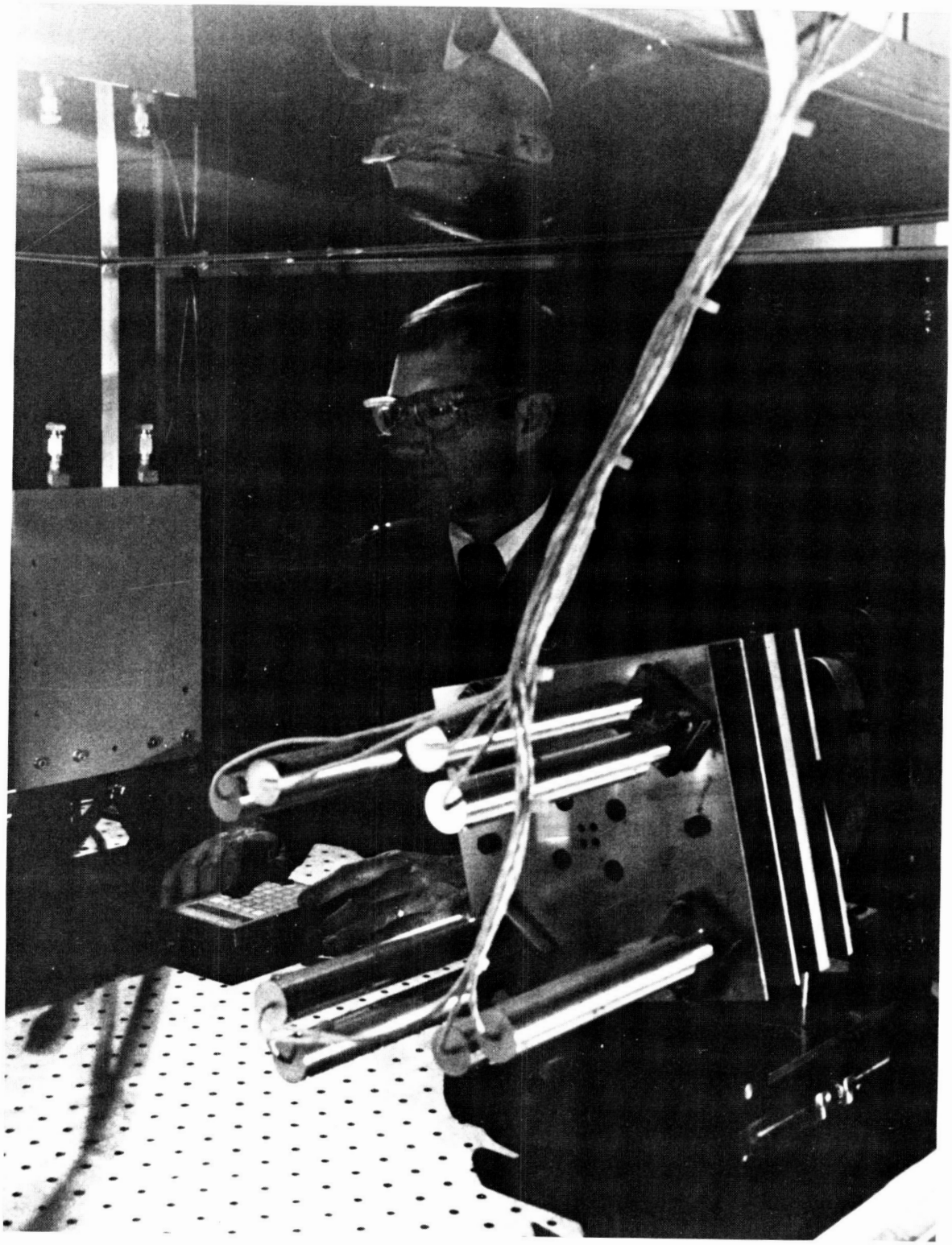

Figure 8. Photograph of mechanical mirror scanning system

SURFACE SCATTERING CHARACTERISTICS AND THE MEASUREMENT OF PARTICULATE CONTAMINATION

Paolo A. Carosso

TS Infosystems, Inc.

and

Nancy J. P. Carosso

NASA Goddard Space Flight Center

ABSTRACT

Surface scattering measurement techniques can be adopted for use in spacecraft contamination control programs. A witness mirror measurement program was developed and implemented for the NASA Cosmic Background Explorer (COBE) spacecraft. Scattering measurements were obtained before and after a qualification level vibration test for several COBE prototype instruments. The measurements indicate a significant amount of particle redistribution occurred during the vibration test. This paper summarizes the methodology used and the results obtained from this monitoring program.

INTRODUCTION

Contamination deposited on optical surfaces can greatly reduce instrument performance, therefore impairing the achievement of mission scientific goals. Particulates such as fibers, dust or remains of fabrication processes or chemical species, outgassed from a variety of materials or generated during virtually any mission phase and subsequently adsorbed or deposited on critical surfaces, degrade surface characteristics. Among the principal effects of the presence of contaminants are surface obscuration, scattering and absorption of incident radiation, loss of throughput, and increase of surface absorptivity. Particles in the instrument field of view have an obvious negative influence in the process of data collection.

The instruments installed on the Cosmic Background Explorer (COBE), are highly sensitive to contamination. It is therefore very important to keep under control the amount of contamination on all sensitive surfaces. Such an effort must be undertaken from the early fabrication, assembly and testing phases, and continue through all subsequent phases of the COBE mission. All requirements, procedures and monitoring plans necessary to achieve this goal are identified in the COBE Contamination Control Plan (CCP) [1].

The COBE CCP includes the implementation of a contamination monitoring program for the Thermal Structural Unit (TSU). The TSU is a set of prototype instruments which were used for test and demonstration. The COBE instruments are located in an element known as the Cryogenic Optical Assembly (COA). The TSU consisted of a prototype COA which contained a Diffuse Infrared Radiation Experiment (DIRBE) and a prototype Far Infrared Radiation Spectrometer (FIRAS), two of the most contamination-critical instruments on the COBE. Figure 1 depicts the COA with the two instruments. The primary objective of the contamination monitoring program was to monitor the presence of contaminants during all phases of the TSU testing.

This paper describes the results of the initial phase of the program developed to monitor contamination during the vibration test performed on the flight-like TSU integrated COA (Cryogenic Optical Assembly).

The vibration test was conducted March of 1985. The TSU COA was flight-like except there was no contamination cover over the DIRBE baffle aperture.

Prior to test, all TSU COA parts were cleaned to a level 100A per MIL STD 1246A [2], and assembled in a Class 10,000 clean tent. Surface cleanliness measurements taken before transportation to the vibration cell, revealed external COA surfaces to be level 200-300 per MIL STD 1246A. Prior to transport to the vibration test, the TSU was double bagged in cleaned RCAS 2400 bagging material.

The integrated flight-like TSU COA was originally instrumented with 15 contamination witness mirrors. Due to concerns about overstressing two of the DIRBE mirror mounts, two witness mirrors were taken off the TSU prior to the vibration test. The location of the witness mirrors are illustrated in Figure 1 .

The contamination witness mirror program consists of performing before and after testing characterization on each witness mirror, including:

1)- BRDF characterization;

2)- Surface cleanliness determination per ASTM F24-65 standard [3]; and

3)- Surface morphology examination by optical microscopy, with photographic documentation.

Bidirectional Reflectance Distribution Function (BRDF) measurement is a particularly interesting technique, as it provides information about the scattering properties of optical surfaces. The DIRBE performance requirement [1] is stated in terms of percent change of mirror BRDF.

BRDF measurements were performed on all witness mirrors before and after the vibration test. The comparison of these data show percent change in BRDF characteristics for the witness mirrors, which were exposed to the same contamination environment as the TSU COA surfaces.

RESULTS

BRDF CHARACTERIZATION

A complete description of the BRDF characterization technique adopted in this program is reported in Reference [4].

Each witness mirror was measured before and after the vibration test. In order to obtain a complete description of the mirror characteristics, three areas were measured on each mirror. The BRDF curves obtained for mirrors II, VI, are reported in Figures 2 to 13. In these figures, the curves labeled B1, B2 and B3 are relative to the mirror areas as measured before the vibration test. Analogously, curves A1, A2 and A3 refer to the after vibration test BRDF measurements. As it can be seen from the figures, the after test BRDF values are generally higher than the before test ones. The differences are certainly above the experimental error, and represent, therefore, an effect of the contamination accumulated on the mirrors during the vibration test. In some cases, the contamination effect is strong enough to cause dramatic changes in the BRDF values, up to two orders of magnitude

In general, as already mentioned, the BRDF values obtained in the after test measurements are higher in modulus. Also, the curves tend to level off at high scattering angles, which represents a diffuse scatter component due to the presence of contaminants. In other words, the specular behaviour typical of the clean mirror (straight BRDF line with negative slope), is poisoned by a component typical of a diffuse scatterer, in this case the contaminant particulates.

In Table 1, representative values of the BRDF curves are reported for each witness mirror. The BRDF values obtained at the scattering angles of 30 and 60 degrees on the central areas of each mirror were arbitrarily chosen to be representative comparison data. (curves #2 in the Figures). The percent change of BRDF based on these measurements are also reported in Table 1. It is noteworthy to remember at this time that the current DIRBE requirements allow a maximum of 50% BRDF change due to mirror contamination. The reported BRDF percent changes vary from 8% up to 600%, showing that, in some cases, a very significant amount of contamination occurred during the vibration test.

SURFACE CLEANLINESS LEVELS

The presence of contamination on the after test mirrors detected by the BRDF measurements is confirmed by the surface cleanliness level data, also reported in Table 1. In most cases, the after test cleanliness levels are higher (higher level of contamination) than the before test levels (which were levels 25-100 on the mirrors). Nine out of the twelve mirrors show an after test cleanliness level higher than the COA cleanliness requirement (level 300).

OPTICAL MICROSCOPY EXAMINATION

All witness mirrors were examined via optical microscopy to obtain a visual evaluation of the nature and morphology of contaminants and to evaluate the mirror cleanliness levels. Photographical records of contaminants were taken at magnifications varying between 45X and 100X. Cleanliness levels were obtained following the ASTM procedure [3].

In Table 2, the most interesting observed features are reported for each mirror. Fifteen mirrors were planned to be installed in the COBE TSU; Mirrors VII and IX were not installed because of potential stress on mirror mounts. Mirror XIV was not retrieved after the vibration test; it will be removed later in the program.

SUMMARY AND CONCLUSIONS

The data obtained from the contamination witness mirrors after the TSU COA first vibration test show that the TSU became significantly more contaminated during the course of the test. Because the TSU was bagged (except for the bottom of the bag which was taped to the attachment fixture in the vibration cell), the contamination could not have come from the vibration cell. It is deduced that the increase in contamination levels on the mirrors is a result of particle redistribution within and around the COA. In essence, the TSU COA was the source of contamination for itself. Unfortunately, because of TSU schedule constraints, some contamination control measures could not be implemented. For example, the FIRAS was not disassembled, cleaned, and reassembled in a clean room as originally planned; it was assembled 'dirty', and then cleaned as a completely assembled instrument, which is considered a substantially less effective cleaning method. Last minute drilling operations on the COA had to be performed in the COA clean room, and although measures were taken to clean-up any generated contamination, it is possible that some particulate matter was missed.

Particle redistribution on relatively "clean" hardware does occur. The result is further contamination of virtually all surfaces. The TSU COA vibration test witness mirror results presented in this report show that, on 9 out of 12 mirrors, contamination levels after the vibration test exceed the overall COA cleanliness requirement (level 300). And, specifically the DIRBE primary mirror, which has a cleanliness requirement of level 100, showed unacceptable increases in contamination (level 800 and level 1000 on the two witness mirrors located on the dummy primary in the TSU). Considering the BRDF data presented, one of the DIRBE primary witness mirrors had a 44% change in BRDF at 30 degrees, which falls close to the 50% requirement; and the other DIRBE primary witness mirror had a 77% change in BRDF, which exceeds the requirement.

FUTURE WORK

Using witness mirrors and the scattering measurement technique as a means to monitor contamination has proven to be an effective and useful tool. This technique can be used to monitor contamination in a number of different scenarios. For example, monitoring of cleanrooms and particle fallout, or monitoring of surface cleanliness during assembly, integration, test, transport etc., could be accomplished using this technique.

Table II. OPTICAL MICROSCOPY EXAMINATION DATA

Mirror # -	Location	- Contamination features
I	FIRAS PICKOFF MIRROR	Small particles observed. No large particles or fibers.
II	FIRAS PICKOFF MIRROR	Very large fibers observed, (1758X264 um, 1055X55 um, 530X70 um). Sharp edge metal particles present, 130X60 um. Several particulates up to ~100 um diam.
III	APCO	One large fiber (1385X176 um). Round particles up to ~180 um diam. in central area. Small dust particles elsewhere.
IV	APCO	Large metal particles with golden appearance, approximately round (198X176 um, 176X99 um).
V	APCO	One elongated fiber (circa 2000 um), metal particles (285X110), dust.
VI	DIRBE PRIMARY	Elongated fiber (770X33 um), smaller fibers, yellow-reddish particles (oxide like), 150 um max diam. Metal particles (probably Al). Several smaller dust particles.
VIII	APCO	Dust particles observed (240X110 um max).
X	APCO	Large fiber (505X420 um). Dust particles, max diam. circa 110 um.
XI	COA SIDE PANEL	Very elongated, folded fiber, 593X374 um. Round particulates up to circa 260 um.
XII	APCO	Fibers (530X310 um, 440X350 um). Possible ceramic-type particle with inclusions, 370X242 um.
XIII	DIRBE PRIMARY	Metal splinter (possibly Al) 950X130 um. Small diameter dust particles.
XV	COA SIDE PANEL	Dust particles observed on the whole surface.

REFERENCES

[1]- N.J.Pugel, "Cosmic Background Explorer Contamination Control Plan. Phase II", COBE-PL-732-1703-01, September 1984.

[2]- MIL-STD 1246A, "Product Cleanliness Levels and Contamination Control Plan".

[3]- ASTM Standard F24-65 (Reapproved 1983), "Measuring and Counting Particulate Contamination on Surfaces".

[4]- P.A.Carosso and N.J.P.Carosso, "The Role of Scattering Distribution Functions in Spacecraft Contamination Control Practices", Appl.Opt., Vol 25, page 1230, 1986.

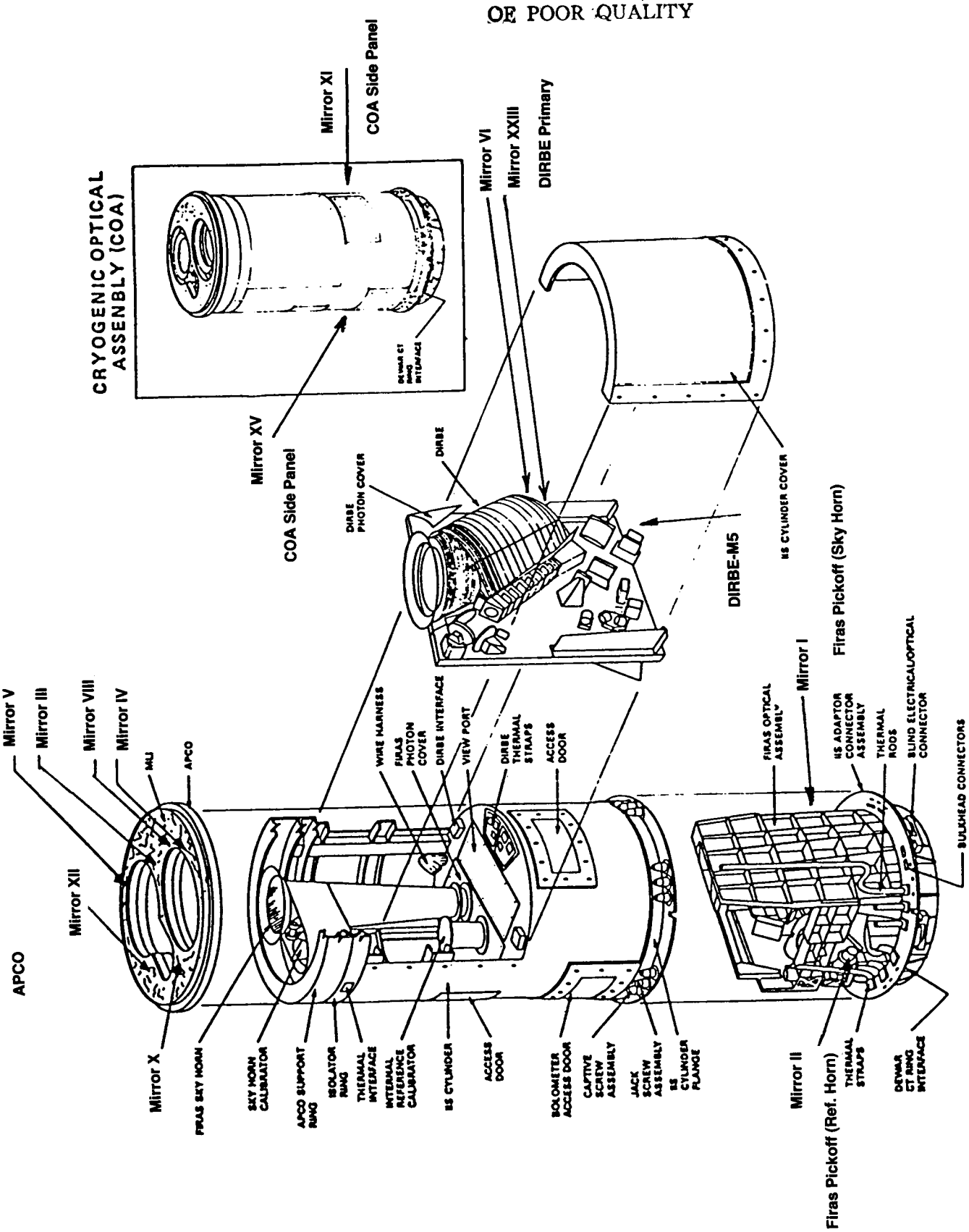

Figure 1. Witness mirrors location

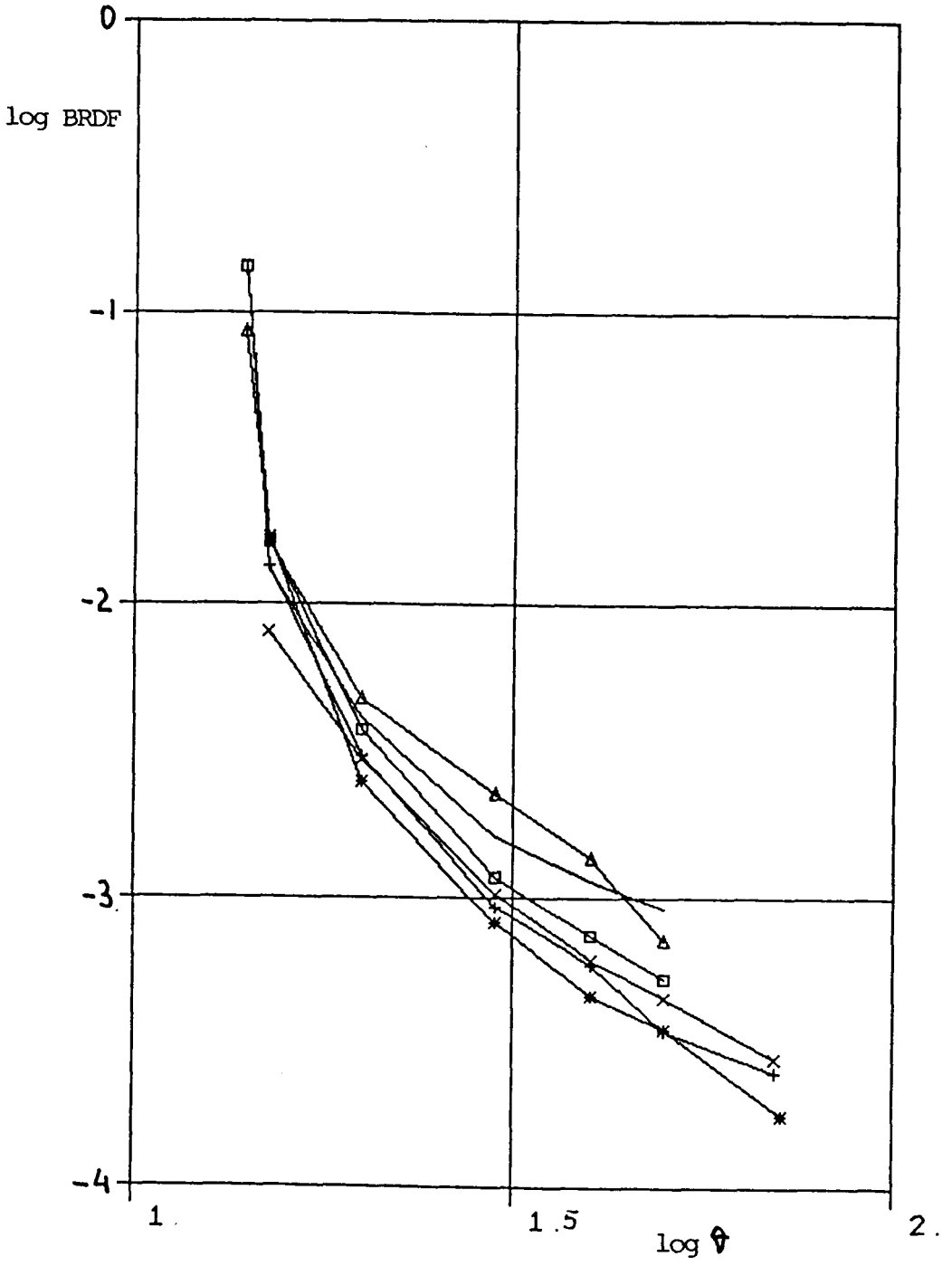

Figure 2. Mirror I

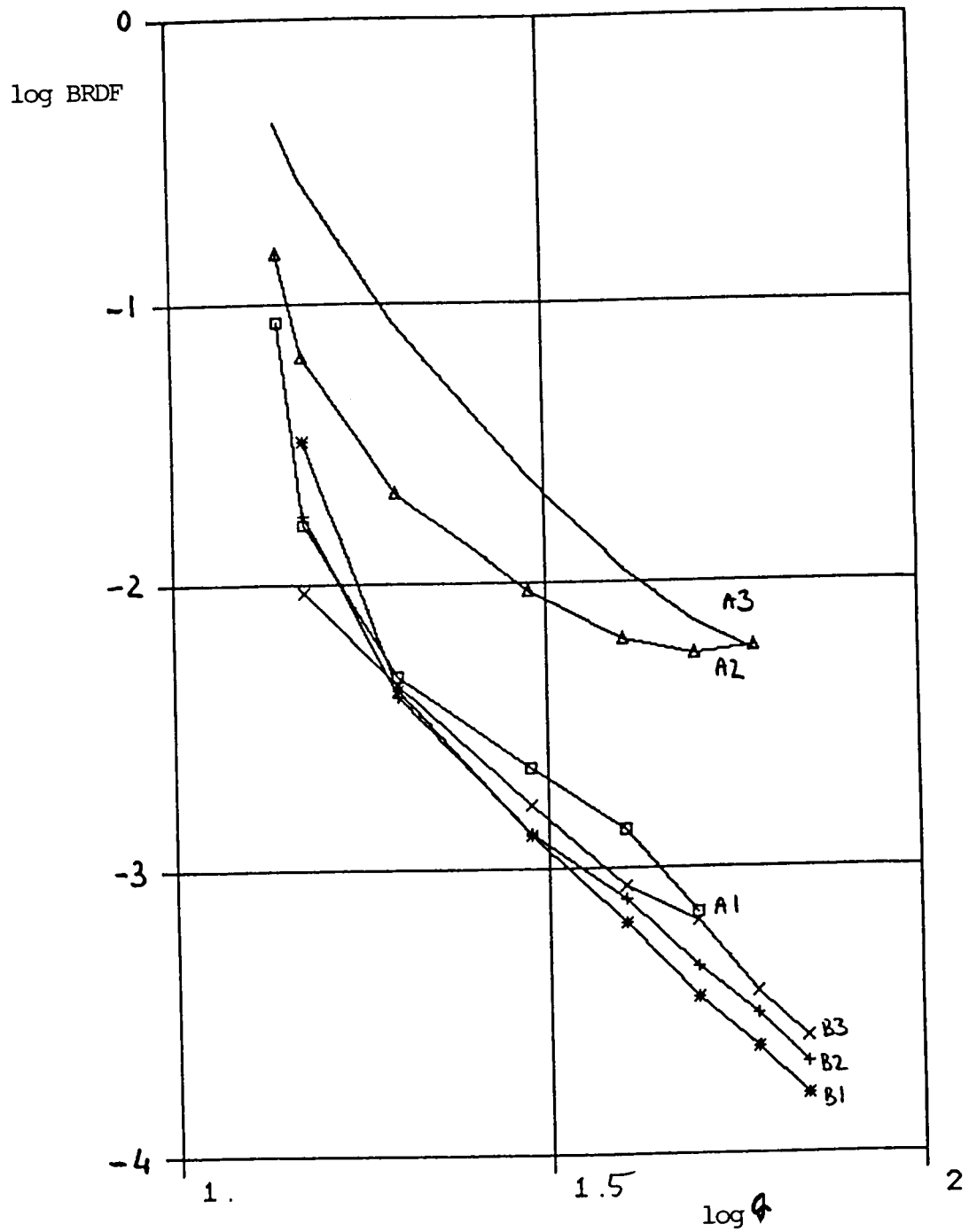

Figure 3. Mirror II

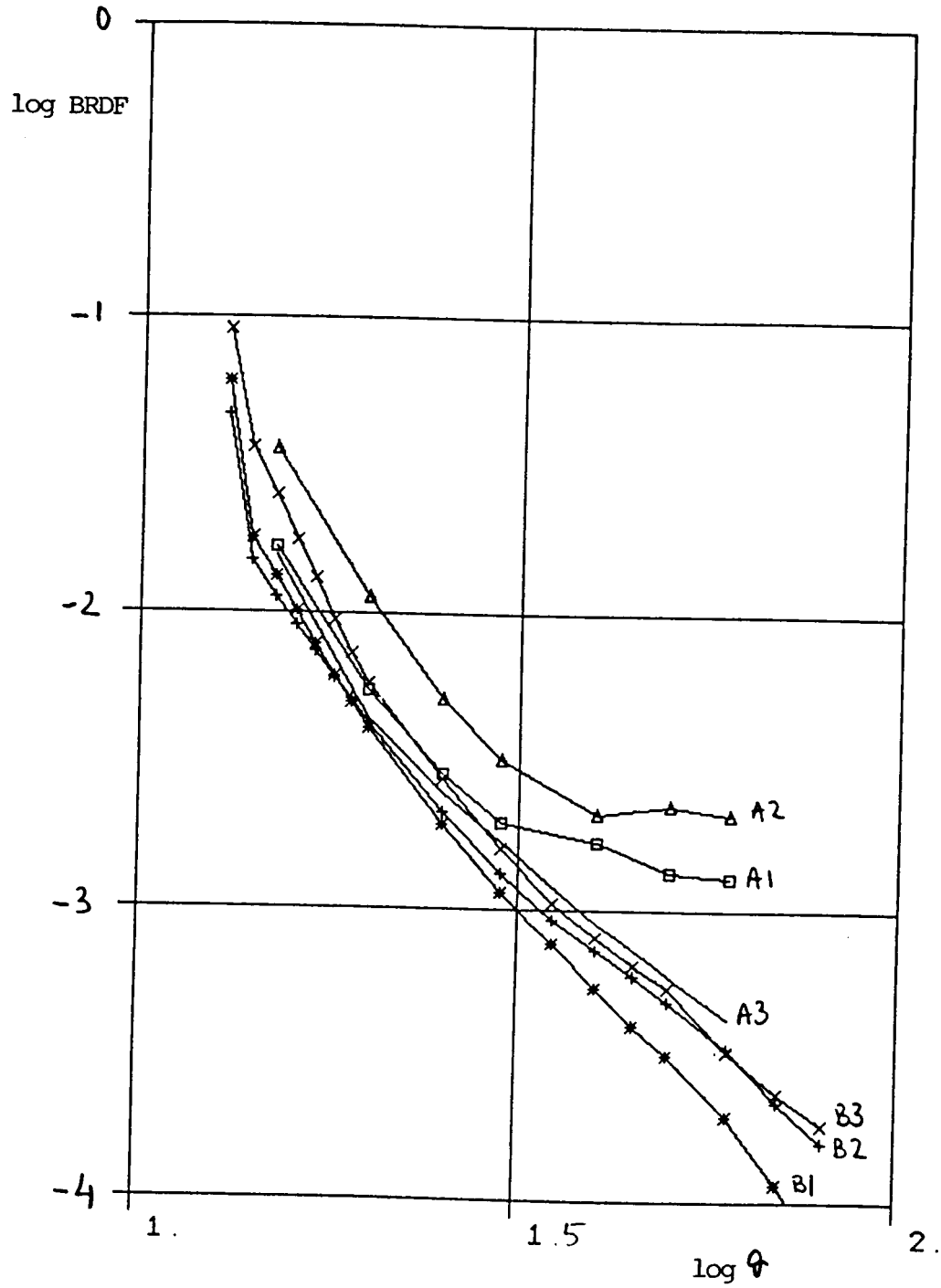

Figure 4. Mirror III

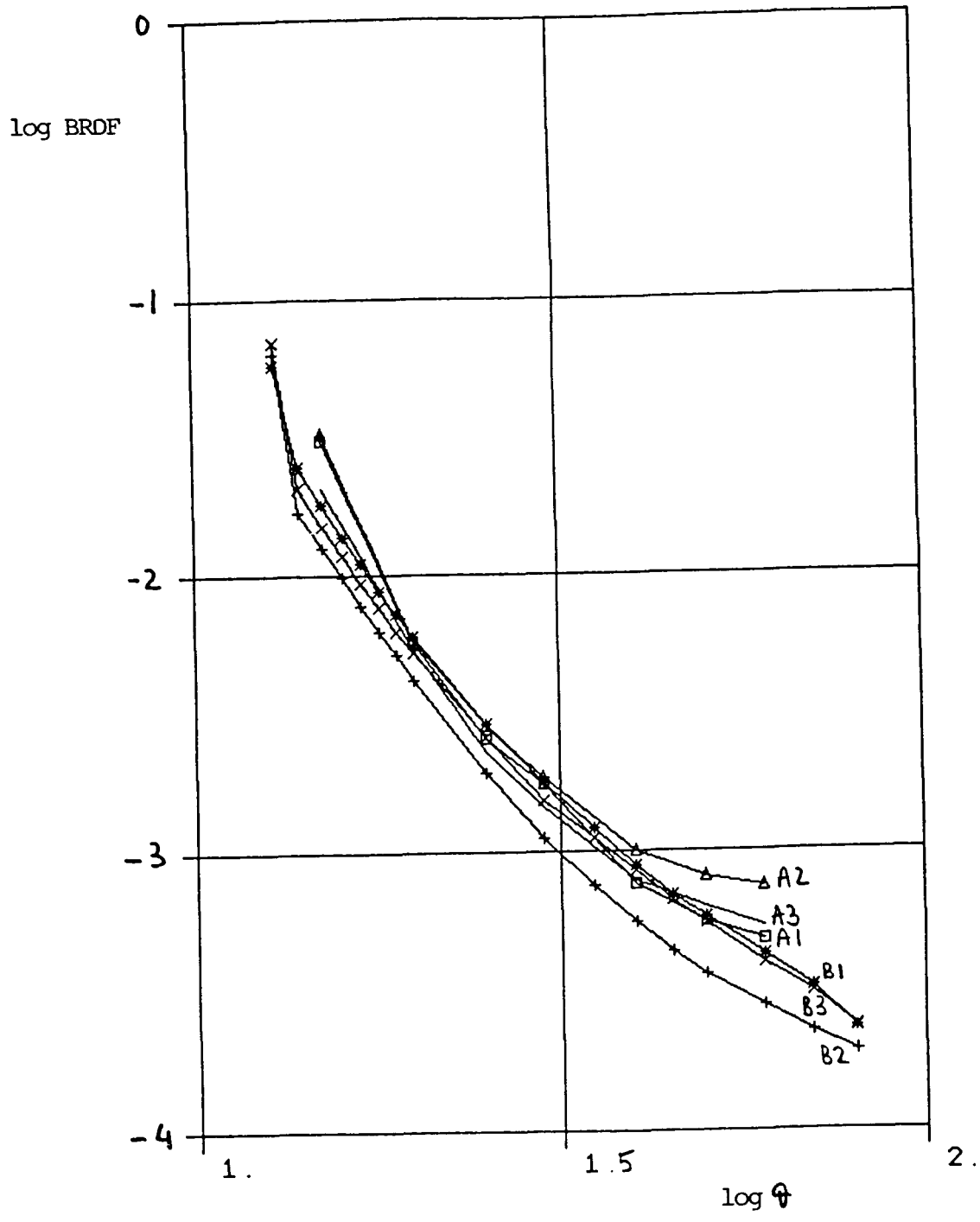

Figure 5. Mirror IV

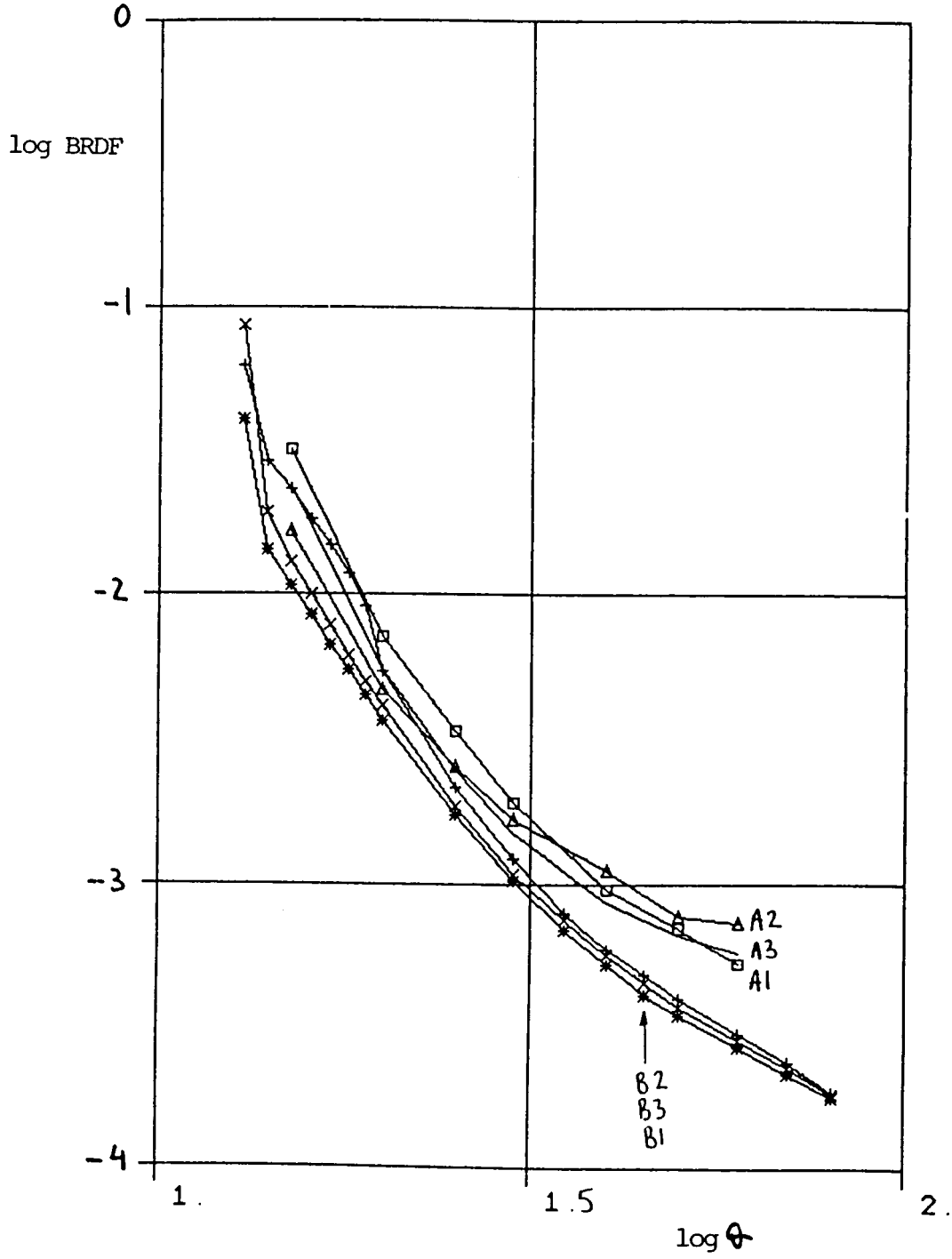

Figure 6. Mirror V

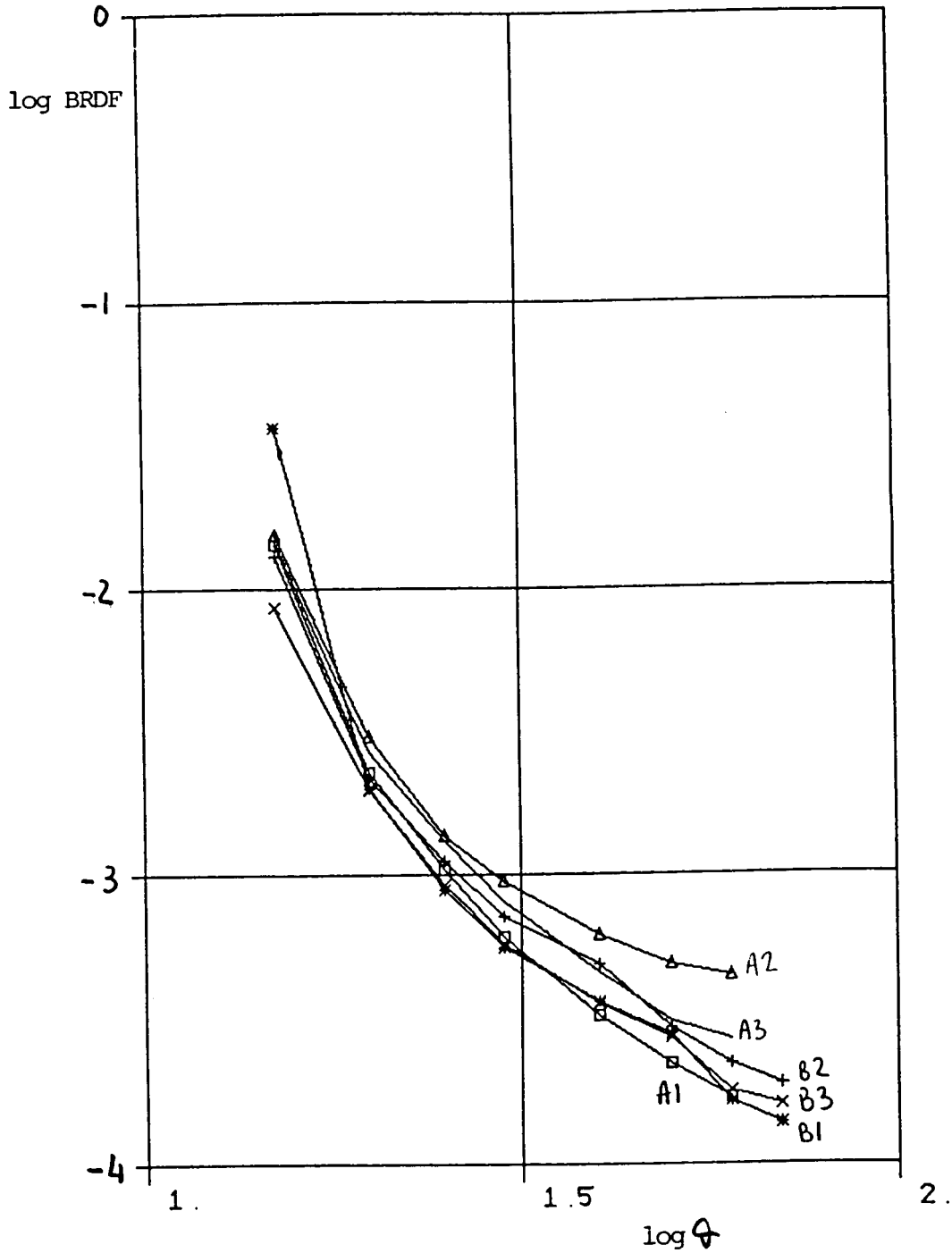

Figure 7. Mirror VI

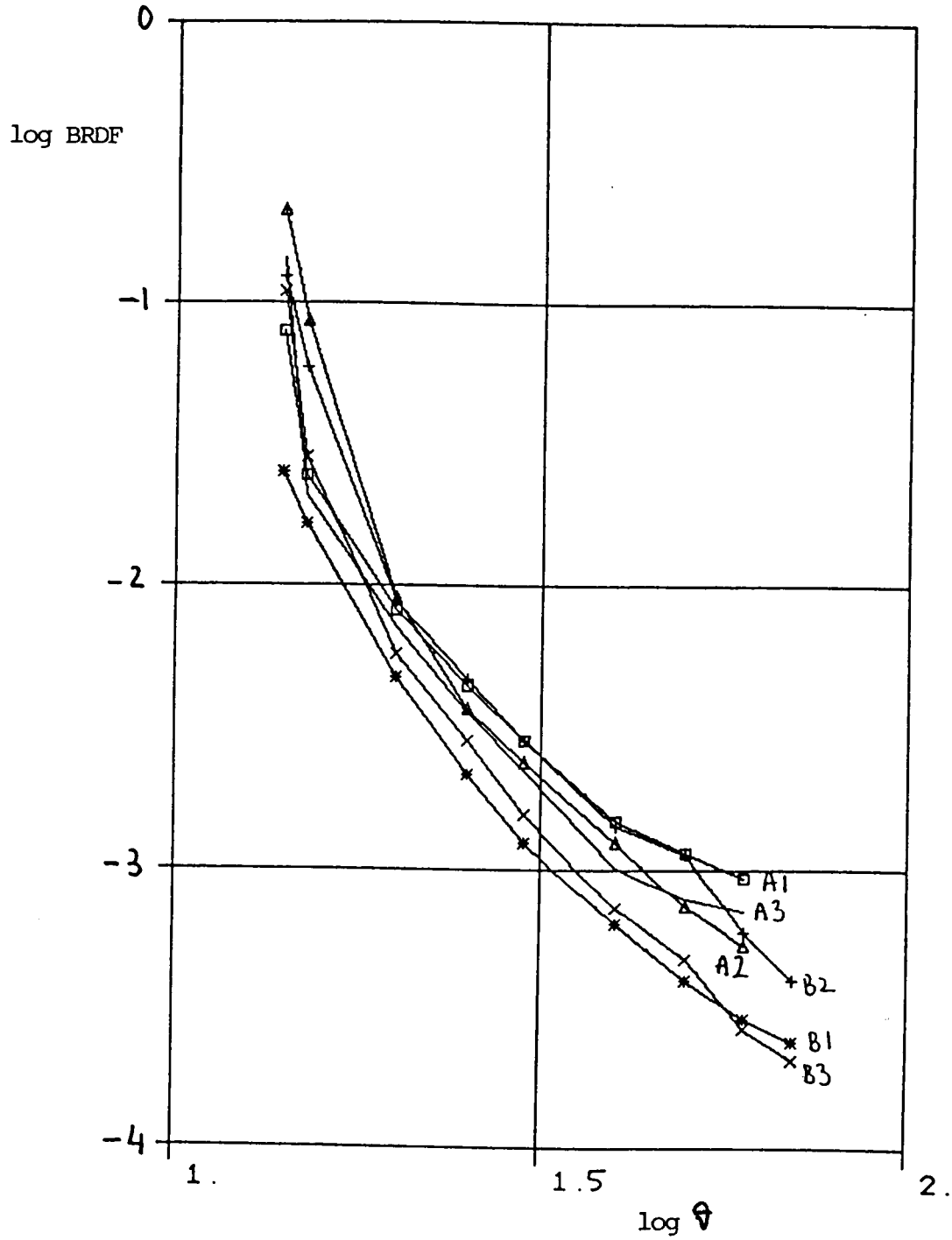

Figure 8. Mirror VIII

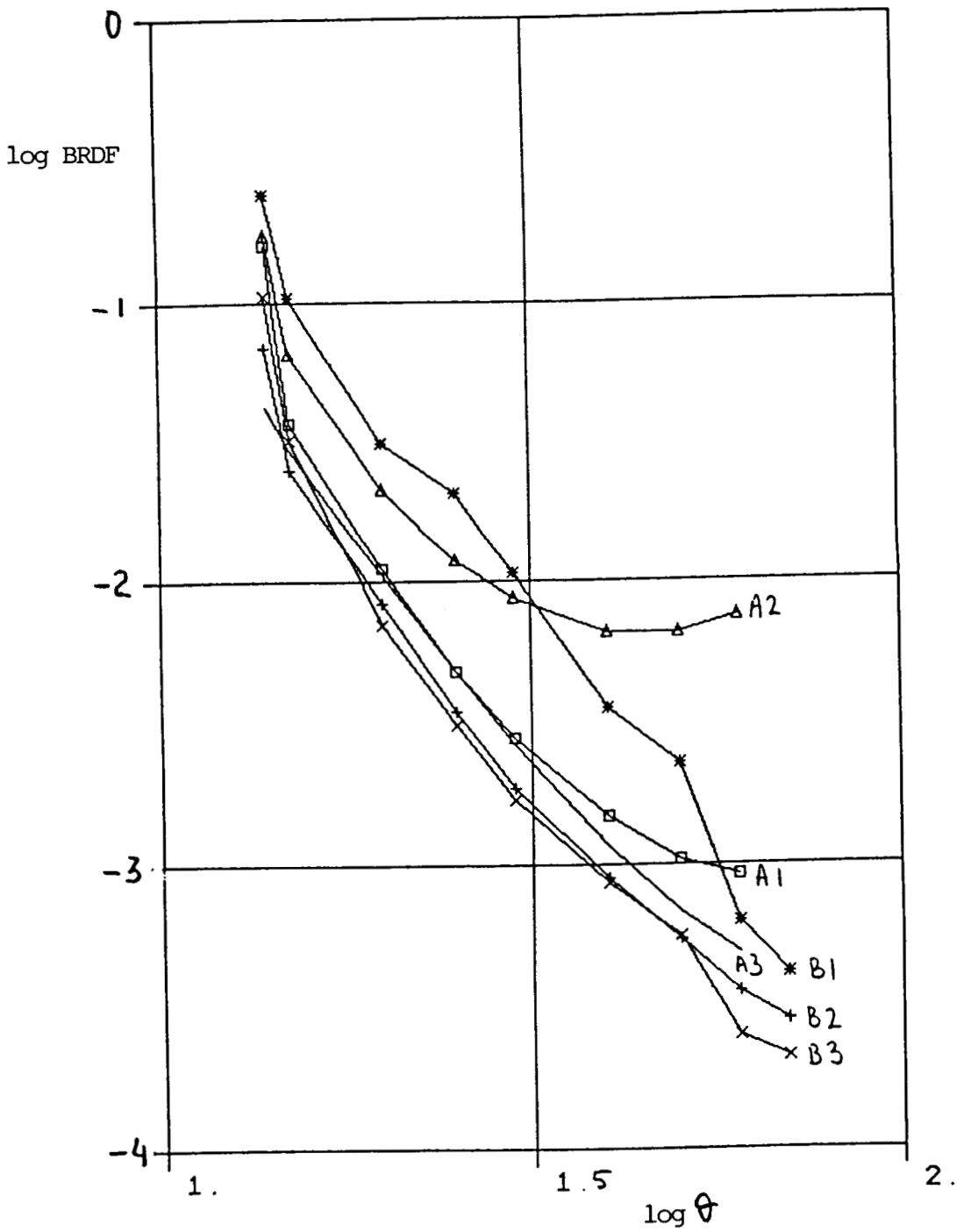

Figure 9. Mirror X

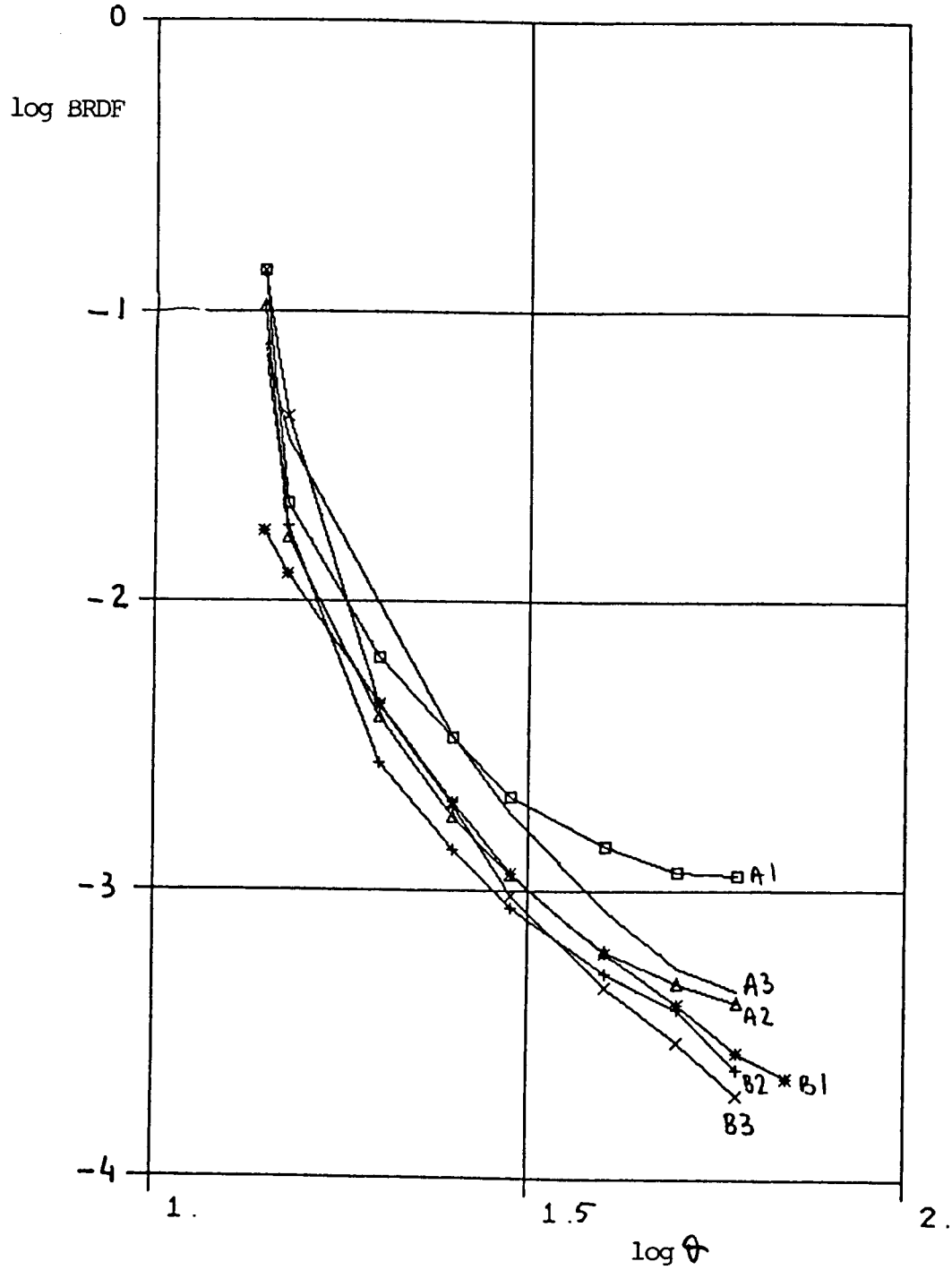

Figure 10. Mirror XI

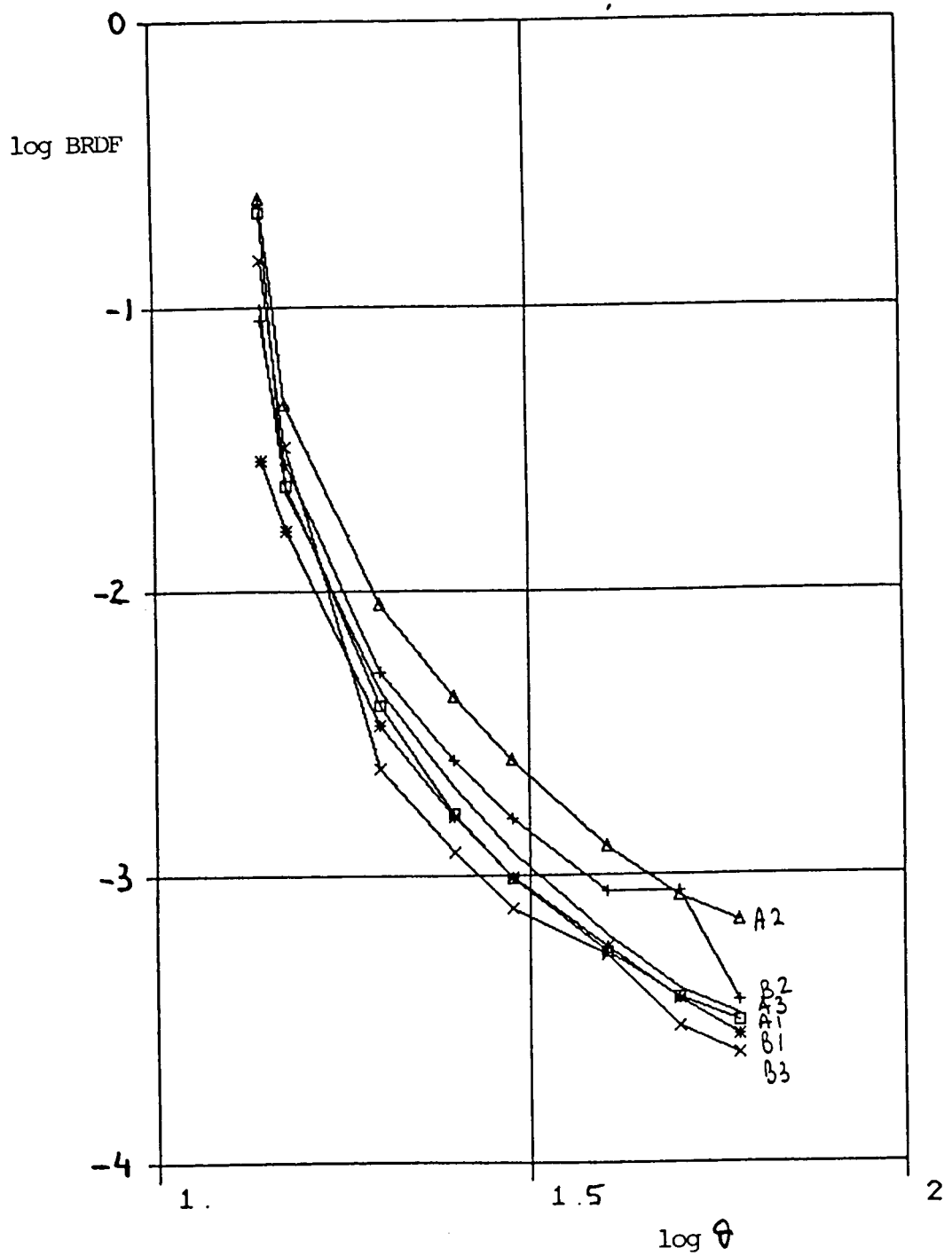

Figure 12. Mirror XIII

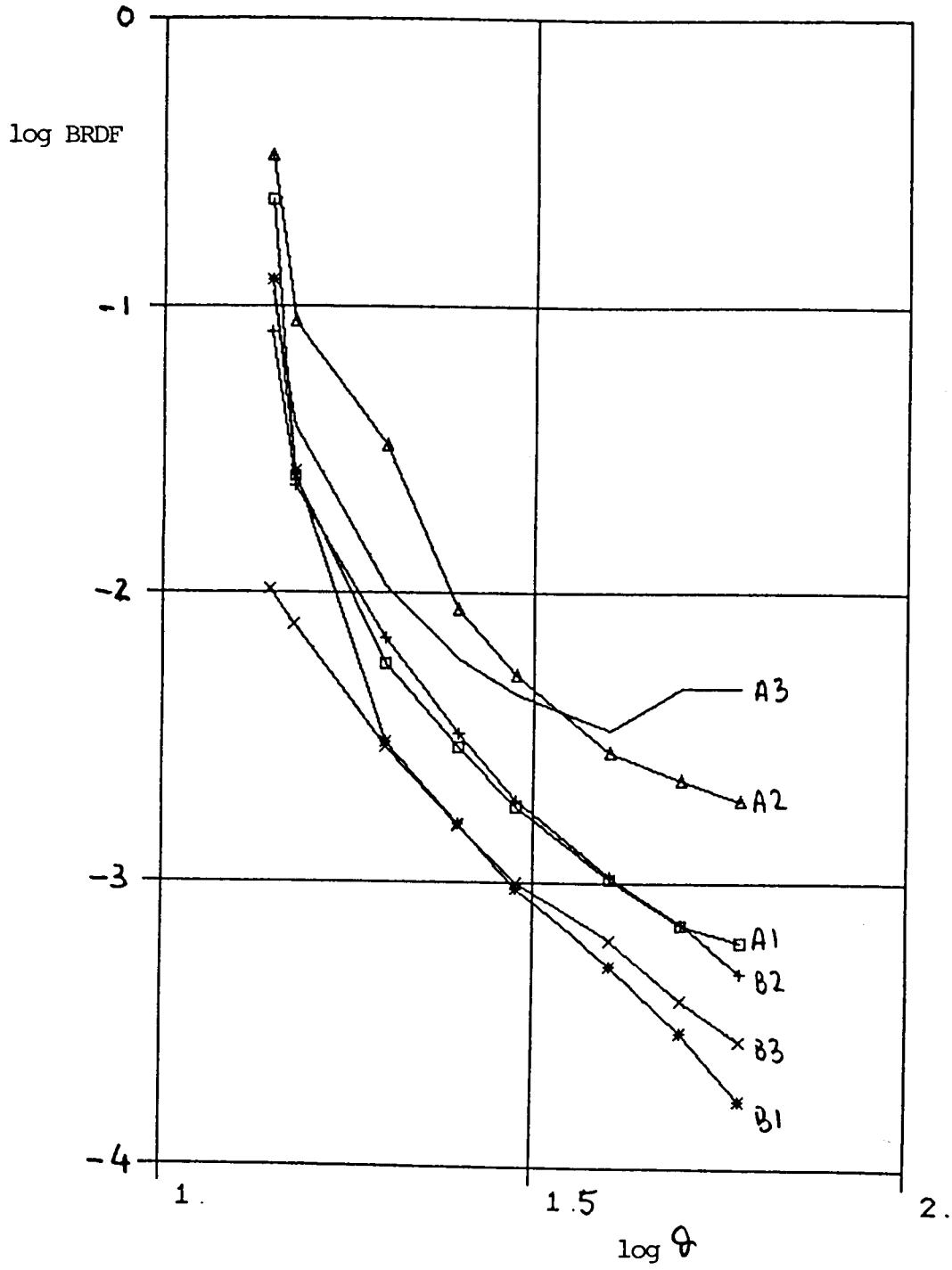

Figure 11. Mirror XII

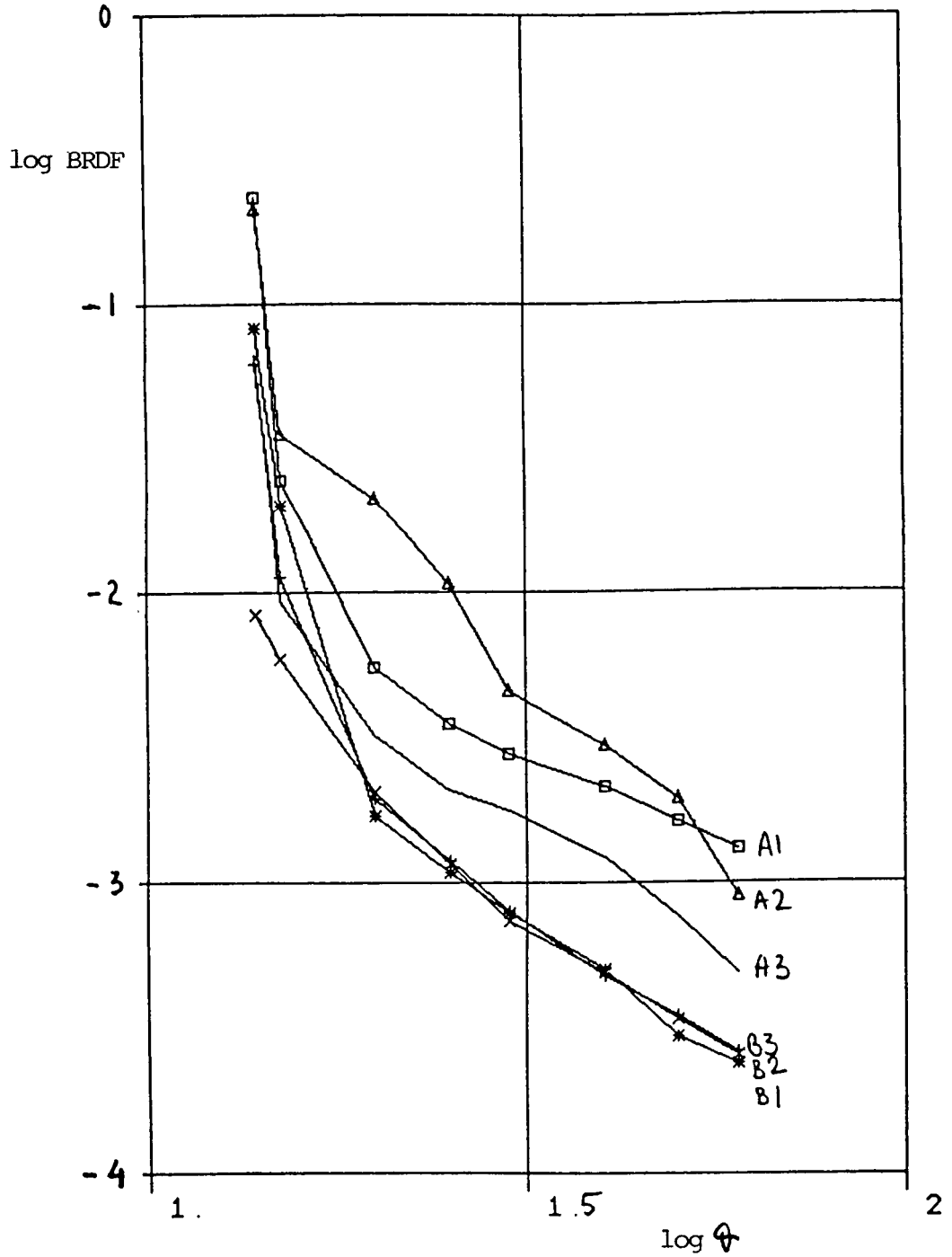

Figure 13. Mirror XV

LOW EXTRACTABLE WIPERS FOR CLEANING SPACE FLIGHT HARDWARE

Veronica Tijerina

Coventry Manufacturing Co., Inc.

and

Frederick C. Gross

NASA - Goddard Space Flight Center

ABSTRACT

There is a need for low extractable wipers for solvent cleaning of space flight hardware. Soxhlet extraction is the method utilized today by most NASA subcontractors, but there may be alternate methods to achieve the same results.

This paper will discuss the need for low NVR materials, the history of soxhlet extraction, and proposed alternate methods. The text will discuss different types of wipers, test methods, and current standards.

INTRODUCTION

Since the beginning of the space program there has been a need to clean space flight hardware with cloth wipers. In addition to using the wipers for cleaning, there was also a need to use them for collecting samples of contaminants from numerous sources in the space program. It was soon discovered that all commercial cleaning cloths (wipers) and swabs (mostly cotton) contained a wide variety and variable quantities of contaminants. These contaminants are now known as non-volatile residues (NVR's). Non-volatile residue is that quantity of molecular and particulate matter remaining, following the filtration of the solvent and evaporation of the solvent at the specified temperature. Types of NVR's include waxes, oils, grease, adhesives, and sizing compounds. When condensed, they have an oily resinous appearance.

NVR's from a wiper can be transferred to the hardware surface during a cleaning process. This is due to the fact that when exposed to a particular solvent, they are dissolved or dispersed. In this dissolved state the oils are easily transferred from the wiper to the hardware. It becomes obvious then that an item can be made no cleaner than the materials used to clean it. This applies to solvent cleanliness as well as material cleanliness. From these requirements, it may be concluded that the cleaning procedure used on the wipers is not an inconsequential matter. There are many methods of removing NVR's with great success; the most commonly used is soxhlet extraction. Soxhlet extraction utilizes a soxhlet apparatus to extract fatty or other materials with a volatile solvent. The only standard soxhlet extraction method that was found in the literature is ASTM D 1574 "Extractable Matter In Oven-Dried Wool" (ref.1). This method is, of course, not directly applicable to wipers.

The purpose of this paper is to present the methods used by different companies in extracting wipers to low NVR levels. Methods of NVR analysis are also discussed and the varying methods of gravimetric analysis are given in tabular form. It is hoped that the presentation of these various extraction and testing methods will precipitate a lively discussion that will result in the development of a standard method of testing NVR levels in wipers.

History of Soxhlet Extraction

Soxhlet extraction is named after its inventor, a German agricultural chemist, Franz von Soxhlet. A soxhlet extractor is an apparatus for use in extracting fatty or other material with a volatile solvent such as ether, alcohol, or benzene. It consists of a vertical glass cylindrical extraction tube that has both a siphon tube and a vapor tube. It is fitted at its upper end to a reflux condenser and at its lower end to a flask to allow the solvent to be distilled from the flask into the condenser. The solvent then flows back into the cylindrical tube and siphons over into the flask to be distilled again. See Figure 1.

Although many companies utilize soxhlet extraction for cleaning wipers, not all follow a standard procedure. Many of the companies use similar solvents, but the major differences are in the amount of time or number of cycles run. See Table I, "Soxhlet Extraction".

Soxhlet extraction has the advantages of requiring little attention once it is started, making use of a wide variety of solvents and continuously using hot, freshly distilled solvent for the cleaning action. There is very little solvent lost. Also, the desired NVR levels for wipers can be attained by subjecting the wipers to as many cycles as necessary. The disadvantages to using a soxhlet extractor include the long hours required for cycling, and the relatively small number of wipers that can be cleaned per batch.

The materials list and procedure used at Goddard Space Flight Center are given below. They represent the fundamentals for soxhlet extraction of wipers and swabs.

Materials and Equipment

- Polyester or cotton cleaning cloths (low linting)
- Reagent grade solvents such as ethanol, isopropanol, acetone, chloroform, trichlorotrifluoroethane
- Soxhlet extraction apparatus (available in a wide variety of sizes) which includes flask, extraction tube and water condenser
- Boiling chips or beads
- Glass fabric lined heating mantle
- Power regulator or variac for the mantle
- Rubber or plastic hose for water cooling lines
- Assorted clamps and ring stand

Procedure

1. Assemble the apparatus including the cooling water lines (make sure these are secured, wired or clamped).
2. Fill the flask about 2/3 with the solvent of choice.
3. Drop in 3 or 4 boiling aides.
4. Load the extraction tube with the swabs or cloths, not too tightly packed.
5. Fill the extraction tube about halfway to the siphon tube with the extracting solvent.
6. Assemble the apparatus and make sure the cooling water is flowing slowly.
7. Turn the power "on" and slowly increase until the boiling rate is steady and controlled.
8. Observe two or three siphoning cycles to make sure the system is working properly (make a note of the controller setting).
9. Allow the extraction to continue for 48 hours.
10. Turn off the power and allow to cool.
11. Remove the extracted material with clean, non-contaminating tongs or tweezers allowing the solvent to drain off.
12. Place in a clean pyrex or stainless steel beaker or tray.
13. Air dry in a hood or other well-ventilated, clean area.
14. Place in an oven at 100°C for about 1-2 hours, no odor of solvent should remain.
15. Store in a clean, dry, non-contaminating container or package until use.

The solvents most commonly used in extractions are methylene chloride, chloroform, isopropyl alcohol, ethanol, Freon TF, and a 3:1 mixture of 1,1,1-Trichloroethane and ethanol. Most contaminants found on assembled spacecrafts are removed by one or more of these solvents. If the cleaning cloths have been extracted by these solvents there should be a minimal chance of transference of contaminant. The wipers most commonly extracted and most commonly used in aerospace are cotton, polyester and nylon. As seen from the table, those companies which use the extracted wipers for sampling the hardware must attain lower cleanliness levels than for wipers used to clean.

A volume method of extraction has been developed by Coventry Manufacturing Company to increase the number of wipers cleaned per batch. Although the principles remain the same the process takes place on a much larger scale. Coventry Manufacturing uses a large rotating stainless steel drum to clean many wipers to acceptable cleanliness levels. The procedure is very similar to soxhlet extraction in that freshly distilled solvent is continuously being used. The difference is in the soak time. Each cycle lasts 10 minutes and is then repeated five times to achieve cleanliness levels of less than $5mg/ft^2$. These wipers are then made available to companies which utilize them for cleaning. If wipers are needed for sampling of hardware or other materials, lower cleanliness levels can be obtained by subjecting the wipers to additional cycles.

There is another known method of volume cleaning which is used by an aerospace company. Wipers are soaked for four hours in Freon PCA with ultrasonic agitation for three minutes every half hour. With this procedure wipers which originally contained $13mg/ft^2$ are extracted to levels of less than $3mg/ft^2$.

Non-volatile Residue Analysis

Once the wipers have been extracted or cleaned, remaining NVR levels must be verified. There are various NVR detection techniques which are commonly used in industry. The most common method is gravimetric analysis. See Table II.

General Procedure

1. The wiper to be analyzed is soaked in a particular solvent for a specified amount of time.
2. The wiper is then removed and the solvent is evaporated to dryness in a tared weighing dish.
3. The residues remaining after evaporation are then weighed and the weight recorded per area of wiper.

Although the standard method for NVR analysis is the ASTM F-331, (ref. 2), many companies use modified versions. The fundamental differences in gravimetric NVR analysis for 15 different companies are shown in Table III. Each company has modified the procedure according to their equipment on hand and their application.

Infrared Analysis of Non-volatile Residues

Once NVR's have been attained, they can then be analyzed by IR spectroscopy. The infrared portion of the electromagnetic spectrum represents a relatively small fraction of the total known radiation span. The area of major interest within the IR is a 2.5 to 25μ expanse. Examination of the absorption bands enables the type of contamination to be determined. The major contaminants found in wipers have been hydrocarbons, esters, and silicones. An IR spectrum is shown for each type of contaminant. See Tables IV thru VI.

CONCLUSION

This paper has discussed the general procedure and results of using a soxhlet extractor. With a soxhlet extractor aerospace specifications for wipers can be met. However, the expenses are high and the procedure time-consuming. A good alternative would be to consider commercially available wipers. However, these wipers would require monitoring of the extractable levels from batch to batch. A standardized test method for measuring extractables from wipers does not exist. Clearly, more work needs to be done in this area. Steps are being taken along these lines; the ASTM E-21 committee is in the process of standardizing a procedure for collecting NVR's deposited onto stainless steel plates in cleanrooms. Hopefully, considerations can someday be given to standardizing a test procedure for extractables from wipers.

REFERENCES

1. Standard Method of Test for Extractable Matter in Oven-Dried Wool. ASTM Designation: D1574-66

2. Standard Test Method for Nonvolatile Residue of Halogenated Solvent Extract from Aerospace Components (Using Rotary Flash Evaporator). ASTM Designation: F331-72.

3. Interim Federal Specification, Extraction Assembly NNN-E-00920b.

4. Contamination Control Technology. Cleaning Materials for Precision Precleaning and Use in Clean Rooms and Clean Work Stations. Military Handbook 406. p.95.

5. Product Cleanliness Levels and Contamination Control Program. Military Standard 1246A.

6. Recommended Practices for Wipers Used in Clean Rooms and Controlled Environments. RP-4 November 1984 Draft.

7. Beeson, D. Richard: IES Lecture Notes Tutorial II. Hardware Cleaning and Sampling for Cleanliness Verification.

Table 1
Soxhlet Extraction

AEROSPACE COMPANY	1	2	3	4	5	6	7
NUMBER OF WIPERS CLEANED PER BATCH	50	50	6-24	16-20	25	40-50	1500
SIZE OF WIPERS	100g of material	Various sizes	Various sizes	Various sizes	9" X 9"	9" X 9"	Various sizes
SOLVENT(S) USED	Methanol-150c Chloroform or MC-150c	50% Chloroform 50% IPA	Ethanol-25c MC-25c, Ethanol-25c, MC-25c	Predistilled 3:1 Mixture of Trichloroethane and Ethanol	Freon TF or IPA	3:1 Mixture of Trichloroethane and Ethanol	Freon TMC
AMOUNT OF SOLVENT USED	2 cycles worth	2.0 liters		7.2-12.0 liters			284 liters
TYPE OF WIPERS CLEANED	Cotton	Many types		Polyester		Polyester	Cotton or polyester
NUMBER OF CYCLES	300c	N/A	100c	N/A	3-4	N/A	5
HOURS OF RUN	N/A	At least 72	96	48-80	N/A	12-18	1
CLEANLINESS LEVEL ATTAINED	0.03 mg/ft^2	4.05mg/ft^2	$\leq$0.1 mg/ft^2	<0.5mg-0.1mg per wiper	<5mg/ft^2	<1.0mg/ft^2	<5mg/ft^2
APPLICATION	Subcontractor for aerospace companies	Subcontractor for aerospace companies	For sampling spacecraft surfaces	For sampling spacecraft hardware			Commercial wiper supplier

NOTES: Companies #1 & #7 are aerospace related companies
MC = Methylene Chloride
c = Cycles

Table II
Non-Volatile Residue Detection Techniques

TECHNIQUE	PRINCIPLE OF OPERATION	SENSITIVITY	TIME OF DETERMINATION	UNIT OF MEASUREMENT
Gravimetric	Weigh a container & evaporate a known quantity of solvent, reweigh the container, the gain is the NVR	*0.01 ppm by weight	From 0.75 to 8 hours	Milligrams per volume, converted to ppm by weight
Nephelometer	Solvent is made into an aerosol and sampled by light scattering photometer. When the NVR increases, the rate of evaporation is decreased resulting in larger aerosol droplets producing greater signal output	1 ppm	5 min.	ppm by weight or volume
Spectrophotometry	Absorption of electromagnetic radiation	1 ppm optimum	5 min. to 1 hour	percent transmittance converted to ppm or actual weight
Chromatography	Multitheoretical plate/distillation/ selective adsorbtion	1 ppm	5 min. to 1 hour	Retention volume and direct readout are difficult

*To our knowledge these low levels cannot be attained

Table III
Gravimetric Analysis

AEROSPACE COMPANY	1	2	3	4	5	6	7
SIZE AND NUMBER OF WIPERS TESTED		1	1		1 wiper 3" X 3"	1 wiper 4" X 6"	1 wiper 6" X 6"
APPARATUS USED FOR SOAK	Soxhlet extractor	Beaker-Flask with Condenser	600 - ml beaker	Soxhlet extractor	Beaker	Beaker	Beaker
NUMBER OF CYCLES IN SOXHLET EXTRACTOR	10						
SOLVENT(S) USED	Chloroform or methylene chloride	Acetone, IPA or Xylene	Freon 113	3:1 mixture of trichloroethane and ethanol	Ethanol	3:1 mixture of Trichloroethane and ethanol	Trichloroethane and 10% IPA
AMOUNT OF SOLVENT	2 cycles worth		500ml	2400ml	20-30ml		
TEMPERATURE OF SOAK		Boiling	RT (25°c)				RT (25°c)
TIME OF SOAK		10 min.	30 min.	16 hours	1 hour	2 hours	10 min.
OTHER						Agitate every 30 min. with clean forceps	
FIRST EVAPORATION IS SOLVENT FILTERED?		Yes	Yes	Yes			No
SIZE AND TYPE OF FILTER USED			.045µ				
METHOD OF EVAPORATION	Unknown	Vacuum flash evaporator	Boiling water bath	Rotary flash evaporator	Warm plate	Unknown	Oven or hot plate
TEMPERATURE OF EVAPORATION					38°C	35°-40°C	38°C
TIME OF EVAPORATION	2 hours						
SECOND EVAPORATION LAST FEW MILLILITERS EVAPORATED WITH (OR IN)	Heat lamp		Oven	Oven			
TEMPERATURE OF EVAPORATION			105°-110°C				
TIME OF EVAPORATION	1 hour		30 min.	1-1.5 hour			

Table III
Graviemetric Analysis (Continued)

GRAVIMETRIC ANALYSIS

AEROSPACE COMPANY	8	9	10	11	12	13	14	15
SIZE AND NUMBER OF WIPERS TESTED				2 Wipers 1 ft.2	1 Wiper 7" X 7"		100cm2	
APPARATUS USED FOR SOAK	500ml beaker	800ml beaker	Beaker	200ml beaker	Glass tray 3" X 8" X 8"	Flask		Flash evaporator flask
NUMBER OF CYCLES IN SOXHLET EXTRACTOR								
SOLVENT(S) USED	IPA, Freon, methylene chloride or 75% trichlor 25% ethanol			3:1 mixture of trichloroethane and ethanol	Freon TF or IPA	Freon, IPA or acetone	Spectroquality 2-propanol	Various reagent grade chemicals
AMOUNT OF SOLVENT	200ml	500ml		100ml	200ml			
TEMPERATURE OF SOAK					RT(25°C)	RT(25°C)	45°C	
TIME OF SOAK	1 Hour			5 Min.	10 Min.	1 Min.	30 Min.	500ml
OTHER	Ultrasonic agitation			Ultrasonic agitation		Shake or swirl		
FIRST EVAPORATION IS SOLVENT FILTERED?	Yes		Yes	Yes	Yes	Yes		
SIZE AND TYPE OF FILTER USED	41 Whatman		0.45-5.0	0.45 Nucleopore filter	0.45 Millipore filter	Whatman		
METHOD OF EVAPORATION	Heat lamp	Steam bath	Steam bath or hot plate	Oven with a vacuum	Hot plate	Oven	Steam bath	Rotary flash evaporator
TEMPERATURE OF EVAPORATION	RT (25°)			50°C				
TIME OF EVAPORATION								
SECOND EVAPORATION LAST FEW MILLILITERS EVAPORATED WITH (OR IN)	Heat lamp	Oven	Oven	2 Hours	20 Min.			
TEMPERATURE OF EVAPORATION		110°C	110°C					Oven
TIME OF EVAPORATION	Overnight	1.5 Hour	To dryness				105 to 110°C	1.5 Hour

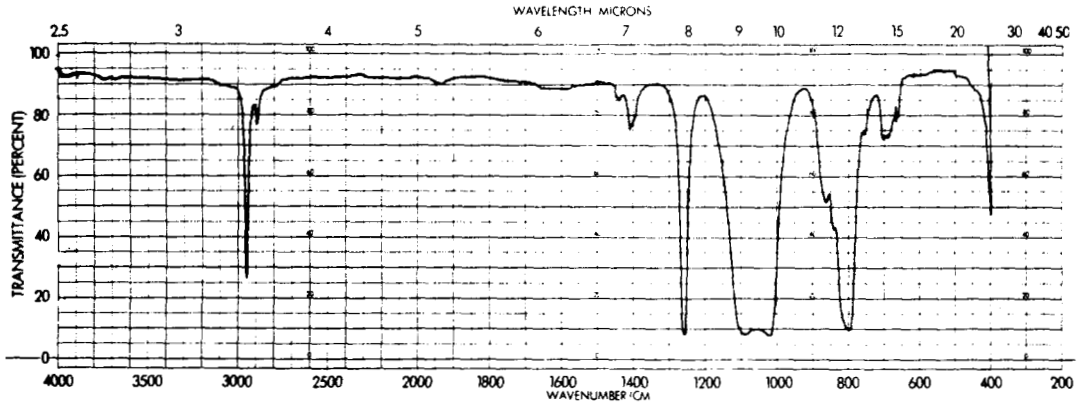

TABLE IV SILICONES

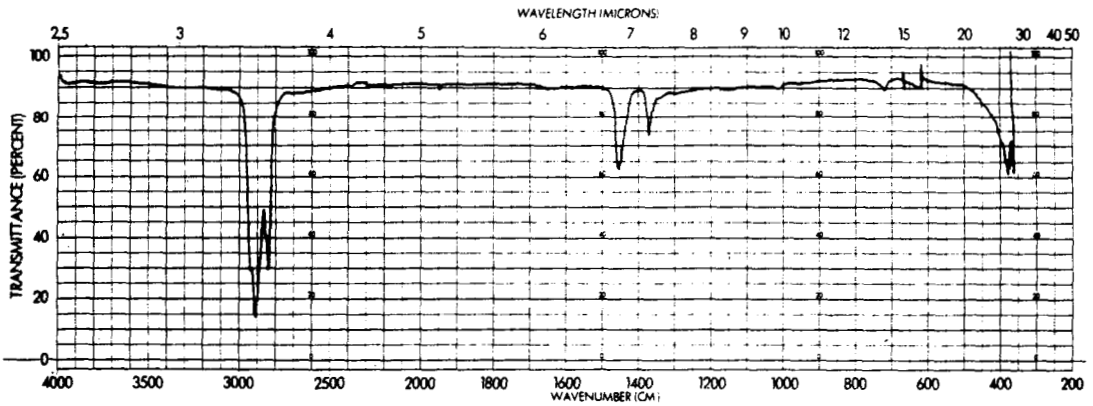

TABLE V HYDROCARBONS

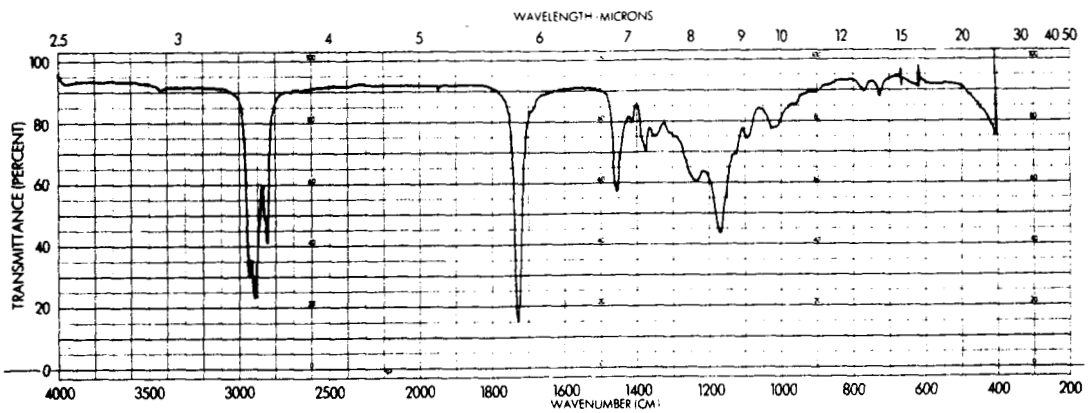

TABLE IV ESTERS

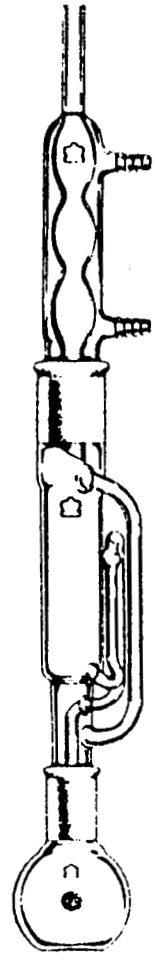

Figure 1. Soxhlet extraction apparatus

DESIGN, CONSTRUCTION, ACTIVATION, AND OPERATION OF A HIGH INTENSITY ACOUSTIC TEST CHAMBER

L. T. Kamel
Rockwell International Corporation

ABSTRACT

Rockwell International's Satellite Systems Division in Seal Beach recently completed a plant modernization program to support the mass production of 28 satellites. The modernization program consisted of multiple satellite integration and test stations and environmental test facilities, which included a high intensity acoustic test chamber, contained within a 50,000 square feet cleanroom. This paper discusses the design philosophy, construction, integration, and activation of the high intensity acoustic test chamber for production acceptance testing of satellites.

The 32,000 cubic-feet acoustic test cell consists of a steel reinforced concrete chamber with six electro-pneumatic noise generators. One of the innovative features of the chamber is a unique quarter horn assembly that acoustically couples the noise generators to the chamber. Design concepts, model testing, and evaluation results are presented in the paper. Considerations such as nitrogen versus compressed air source, digital closed loop spectrum control versus manual equalizers, and microprocessor based interlock systems are included in the discussion. Construction difficulties, anomalies encountered, and their resolution are also discussed. Results of the readiness demonstration testing are highlighted, and the paper concludes with illustrations and discussion of the first series of tests performed in the test cell.

A DIGITAL CONTROL SYSTEM FOR HIGH LEVEL ACOUSTIC NOISE GENERATION

By: John P. Lee, ORINCON Corporation, La Jolla, California
and
Jerry H. Bosco, Lockheed Missiles and Space Company, Sunnyvale, California

ABSTRACT

As part of a modernization of the Acoustic Test Facility at Lockheed Missiles and Space Company, Sunnyvale, a digital acoustic control system was designed and built by Spectral Dynamics Division of Scientific-Atlanta, Inc. [1] This paper discusses the requirements imposed by Lockheed on the control system, and the degree to which these requirements were met. Acceptance test results are discussed, as well as some of the features of the digital control system not found in traditional manual control systems.

INTRODUCTION

Lockheed's Large Vehicle Acoustic Test Facility provides the capability of subjecting space vehicles up to a size of 22 feet in diameter by 70 feet high to acoustic noise fields in excess of 150 decibels (re .00002 N/M**2). The facility has been in operation for eighteen years, using analog random noise generators and manually operated 1/3 octave filter banks to shape the sound spectrum in the test chamber. Three years ago a decision was made to modernize the facility, upgrading both the sound generation and analysis equipment. The new system would consist of two parts: a multi-channel, real-time data acquisition and analysis system and a digital acoustic noise generation and control system. There were no commercially available closed loop acoustic control systems on the market at that time, so Spectral Dynamics Division of Scientific-Atlanta was chosen to design and build one, based on their experience with building random vibration controllers for shaker tables. The result of this development, the SD1600 Acoustic Control System, is the topic of this paper. The task of building the data acquisition and analysis system was given to a group within Lockheed [2].

REQUIRED FEATURES

Lockheed's test laboratory and analytical group established a set of requirements for the acoustic control system which formed the basis for the development of the SD1600. These requirements, along with the final performance capabilities of the SD1600, will be discussed in this section. For each Lockheed requirement, a brief description of how the SD1600 meets (or fails to meet) this requirement is given.

General System Design Requirements:

1. The system should be software oriented rather than hardware oriented.

The SD1600 Acoustic Control System is based on a microprocessor. Test definition, operation, and control is software controlled.

2. An easy to use operator interface should be provided. It should be possible for less experienced workers to operate the equipment.

An interactive dialog provides an easy method for the user to enter test parameters such as the standard spectrum, pretest levels, test duration, microphone sensitivities, and graph labels. Once the test has been defined and the test definition saved on disk, the test may be run by simply pressing the start button. The SD1600 will automatically bring the test level through the user defined pretest levels up to full test. At each pretest level, the drive spectrum is automatically equalized to ensure that the response is within tolerance. In contrast, the previous manual system required a highly trained operator to equalize the spectrum by hand and provided very little protection against overtesting the specimen.

3. Built-in safety and reliability features to safeguard test specimens, test equipment and personnel.

The SD1600 has several built-in safety features to prevent accidental damage to test articles or test equipment. To protect against overtest, a hardware RMS meter is present to monitor the response signal and shut the test down very quickly if the level exceeds the abort limits. After measuring the response spectrum, the computer inside the SD1600 checks the level of each 1/3 octave band inside the frequency range of the test, and will abort the test if any band falls outside the abort limits.

Also, the operator may define a starting drive limit, which is used by the SD1600 as an upper bound to its drive signal when starting a test. If this limit is reached before sufficient response from the microphones is detected, the test is aborted, preventing overtest due to malfunctioning microphones and resulting loss of control signal.

In contrast to the automatic control system, the previous manual system relied on an operator to visually monitor a spectrum analyzer while the test was run, resulting in a less reliable and repeatable test run.

4. The new system should integrate easily with existing power amplifiers, transducers, microphones, and cables.

The SD1600 uses standard BNC cabling to connect to the existing power amplifiers and microphones. Amplifiers within the SD1600 will automatically compensate for differences in power amplifier and microphone sensitivities.

5. Acoustic controller should be able to be operated from its own front panel, or by commands sent from a host computer.

A great deal of effort was spent on the creation of a host computer interface which would allow a host computer (or remote terminal) to send commands and receive status reports from the SD1600. Using two character commands, the host computer can start or stop the test, step through the pretest levels, run the dialog, or request a graphic display of a response spectrum. The SD1600 sends status reports to the host when it changes pretest levels or stops, so that the host computer can monitor the progress of the test.

Specific Control Requirements:

1. The control system must be capable of creating drive signals for up to 3 non-overlapping transducer frequency ranges.

The SD1600 can be configured to drive up to 4 non-overlapping frequency ranges. The overall reference spectrum as defined by the user is automatically split up according to the cutoff frequencies which the user specifies for his transducers. Separate hardware in the SD1600 is used for creation of each of the drive signals, allowing the system to adapt to different power amplifier sensitivities.

2. It should be possible to control based on the average response of up to 16 microphones.

The SD1600 can accept up to 16 microphones for power spectrum averaging. The microphones don't have to have identical sensitivities, as the user can enter individual sensitivities when defining a test. However, for best performance, microphone sensitivities should be kept to within a few dB of each other.

3. The controller should be capable of equalizing at two pretest levels, -6.0 dB and -4.5 dB relative to full test level.

During the test definition dialog, the operator may define up to four pretest levels. Pretest level transitions can be done automatically by the SD1600, or the operator may manually step through the levels by toggling a switch on the front panel of the controller. Pretest levels may be set at any value between .1 dB and 60 dB below full test level.

4. At the -6 dB pretest level, equalization to within +-3 dB should be achieved in no more than 60 seconds for each 1/3 octave band between 25 hz and 2000 hz.

The process of reading in a response spectrum, correcting the drive spectrum, and sending an equalized drive signal to the transducers is

called an equalization loop. Typical equalization loop times for the SD1600 are between 12 and 18 seconds, depending on the bandwidth and number of degrees of freedom defined for the test. Thus, the 60 second requirement would allow at least 3 equalization attempts at the -6 dB level. When in the automatic mode of pretest level transitions, the SD1600 will make only 1 equalization attempt at each level. Test results show that equalization to within +-3 dB can be achieved easily with a single equalization pass.

5. At the -4.5 dB pretest level, equalization to within +-1.5 dB should be achieved in no more than 30 seconds for each 1/3 octave band between 25 hz and 2000 hz.

Again, the 30 second requirement is easily met by the SD1600, allowing up to 2 equalization loops at -4.5 dB. Experimental results at Lockheed show that the +-1.5 dB tolerances are just barely within the capability of the SD1600. A typical test will show most of the 1/3 octave bands to be in tolerance, with 1 or 2 bands (usually in the lower frequencies below 100 hz) at +-2.0 dB. The greater the nonlinearity of the transducers, the more difficult it is to achieve +-1.5 dB tolerances.

6. At full test level, equalization to within +-1.5 dB should be achieved in no more than 20 seconds for each 1/3 octave band between 50 and 2000 hz. At 25, 31.5, and 40 hz the tolerances are +3, -5 dB.

Recognizing the difficulty of equalizing the lower frequency bands at high levels, Lockheed permits a wider tolerance at 40 hz and below. The 20 second time requirement allows the SD1600 only 1 equalization attempt to get the response within tolerance. If the transducers were linear in their response to RMS changes, it would be necessary to equalize only once at the first pretest level. From then on, the response would be in tolerance at each pretest level and at full level. Unfortunately, typical transducers are not linear, especially at high levels. It is common for the transition from -4.5 dB to full test to result in a response which is about 1.0 or 1.5 dB low, if the full level is approaching the limits of the transducers and power amplifiers. The SD1600 will compensate for the undershoot in the first equalization pass, but again, due to non-linearities in the transducers, their will probably be a couple of bands out of tolerance at full level.

7. An automatic abort shall occur if the conditions specified in 4,5 and 6 cannot be achieved.

The control system will abort if any band in the measured response spectrum falls outside the specified abort limits.

8. If the response signal from any individual microphone drops below a specified number of dB below the nominal level, that microphone shall be discarded from the spectrum averaging. The test will continue, provided the number of remaining microphones is above the user defined minimum.

When gathering a response spectrum, the SD1600 multiplexes through the control microphones, adding each microphone's response to the running average. Before the response is added, however, its RMS level is compared with the reference level, and if the current microphone is too low, its response is discarded. From that point on, the test will continue (provided the number of remaining microphones is sufficient) without using the faulty microphone.

ACCEPTANCE TEST RESULTS

In June of 1986, tests were run in the large acoustic test chamber at Lockheed to determine the acceptability of the Spectral Dynamics system. Five tests were defined, ranging in overall level from 139.0 dB to 151.0 dB. The 139.0 dB test used a single transducer with a 20 hz cutoff frequency. The test was defined to drive frequencies between 25 and 400 hz. The remaining 4 tests used transducers in 3 frequency ranges. In each case we used 1 transducer with a lower cutoff of 20 hz. The drive signal for this horn had energy between 25 and 40 hz, inclusive. Up to 3 transducers were used to cover the 1/3 octave bands between 50 and 315 hz, and up to 4 transducers were used from 400 to 2000 hz.

The tests were defined to have 3 pretest levels at -9.0 dB, -6.0 dB, and -4.5 dB, with a start level of -12.0 dB. Full level test duration was set at 1 minute. An independent 1/3 octave analyzer was used to monitor the response at each pretest level and at the end of 20 seconds at full level.

For some of the tests, we found that the low frequency horn's start level was too low, making it impossible for the SD1600 to pull the initial drive signal up out of the ambient noise in the chamber. The low frequency horn's start level was modified to be -10.0 dB, leaving the others at -12.0 dB, and allowing the system to achieve a start level above the ambient noise level.

Test 1, whose standard spectrum appears in Fig. 1, proved to be the most difficult to run. This test was a high level test (151.0 dB) with a lot of power required in the low end. For this test, the response was well equalized at the -4.5 dB pretest level, but the transition to full level resulted in an undershoot of about 1.5 dB in the 1/3 octave bands below 125 hz. This was due to the fact that we were approaching the maximum capability of the transducers at this level. When the SD1600 equalized at full test level, it was able to bring the low end into tolerance, but as a result, harmonic distortion caused the high frequency portion of the spectrum to rise about 1.0 dB. After 1 minute at full level, the response spectrum was as shown in Fig. 2. For the most part, the response meets the +- 1.5 dB tolerance, with the exception of a couple of bands around 1250 hz, where the distortion caused by overdriving the low frequency horns resulted in exceeding the tolerances by 0.5 dB or so.

Test 3 proved to be more successful. Fig. 3 shows the response spectrum for the 144.2 dB test 3. All bands between 31 and 2000 hz

are equalized to within +-1.5 dB. The transition to full level from the -4.5 dB pretest level went smoothly, with no undershoot as was observed with Test 1.

As an illustration of the powerful display features of the SD1600, Fig. 4 shows a table of 1/3 octave bands, along with the response level and deviation from standard for each band for one of the stored responses from Test 3.

Another feature available with the SD1600 which is not generally available with manual control systems is the ability of the SD1600 to control and display spectrums in narrowband format. Using the narrowband format allows the operator to view the response spectrum calculated at up to 800 equally spaced frequencies across the bandwidth of the test. Fig. 5 shows a response spectrum displayed in narrowband format for test 3.

The other spectrums used for the acceptance test ran much like test 3. The SD1600 has about a 16 second equalization loop time, so the time constraints were met. Control accuracy was generally +-1.5 dB for the tests with overall level below 150 dB. The tests above 150 dB controlled to +-2.5 dB, although there were usually only one or two 1/3 octave bands outside the +-1.5 dB tolerances. In subsequent testing, we have found that by adjusting the crossover frequencies and the number of horns used for the test we can improve the performance of the high level tests.

CONCLUSIONS

The requirements for a digital control system for the Lockheed Acoustic Test Facility have, for the most part, been met by the Spectral Dynamics SD1600 Acoustic Control System. The system has proven to be easy to operate and reliable. It is estimated that at least $50,000 per year savings in nitrogen gas and payroll will result because of the speed and ease of use of the SD1600. The ability to control spectrums above 150 dB to +-1.5 dB tolerances remains questionable for the Lockheed facility at this time. Adjusting horn cutoff frequencies did result in improved control for the high level tests, so we hope that as experience in running the new control system increases, the performance at high test levels can be enhanced.

AUTHORS' BIOGRAPHIES

John Lee is a Principal Engineer at ORINCON Corporation. Before joining ORINCON, he was with Spectral Dynamics Division of Scientific-Atlanta in San Diego, where he participated in the development of the SD1600 Acoustic Control System. He received his M.S. degree in Electrical Engineering from Oregon State University in 1983 and his M.S. degree in Mathematics from University of Oregon in 1979.

Jerry Bosco heads the Engineering Operations Group of the Large

Vehicle Acoustic Test Facility at Lockheed Missiles and Space Company, Space Systems Division, Sunnyvale, California. He is a Group Engineer with a background of 30 years of acoustic test experience. For the past two years, Mr. Bosco has worked on the updating of two acoustic test facilities, the most recent one being the large and sophisticated facility described in the present paper. His BSEE degree was from Heald Engineering College of San Francisco and was followed by graduate study at the University of California extension in Southern California. Mr. Bosco has just completed chairing an acoustic seminar for the Annual Technical Meeting if the IES, and is a Senior Member of the IES and a member of the Acoustical Society of America.

REFERENCES

[1] Lee, John P., "High Intensity Acoustic Noise Generation Closed Loop System", Proceedings of the Institute of Environmental Sciences, 1986, pp 170-180.

[2] Smith, Strether, "Data Acquisition/Control/Analysis Systems for Large-Scale Acoustic Testing Facilities", Proceedings of the Institute of Environmental Sciences, 1986, pp 163-169.

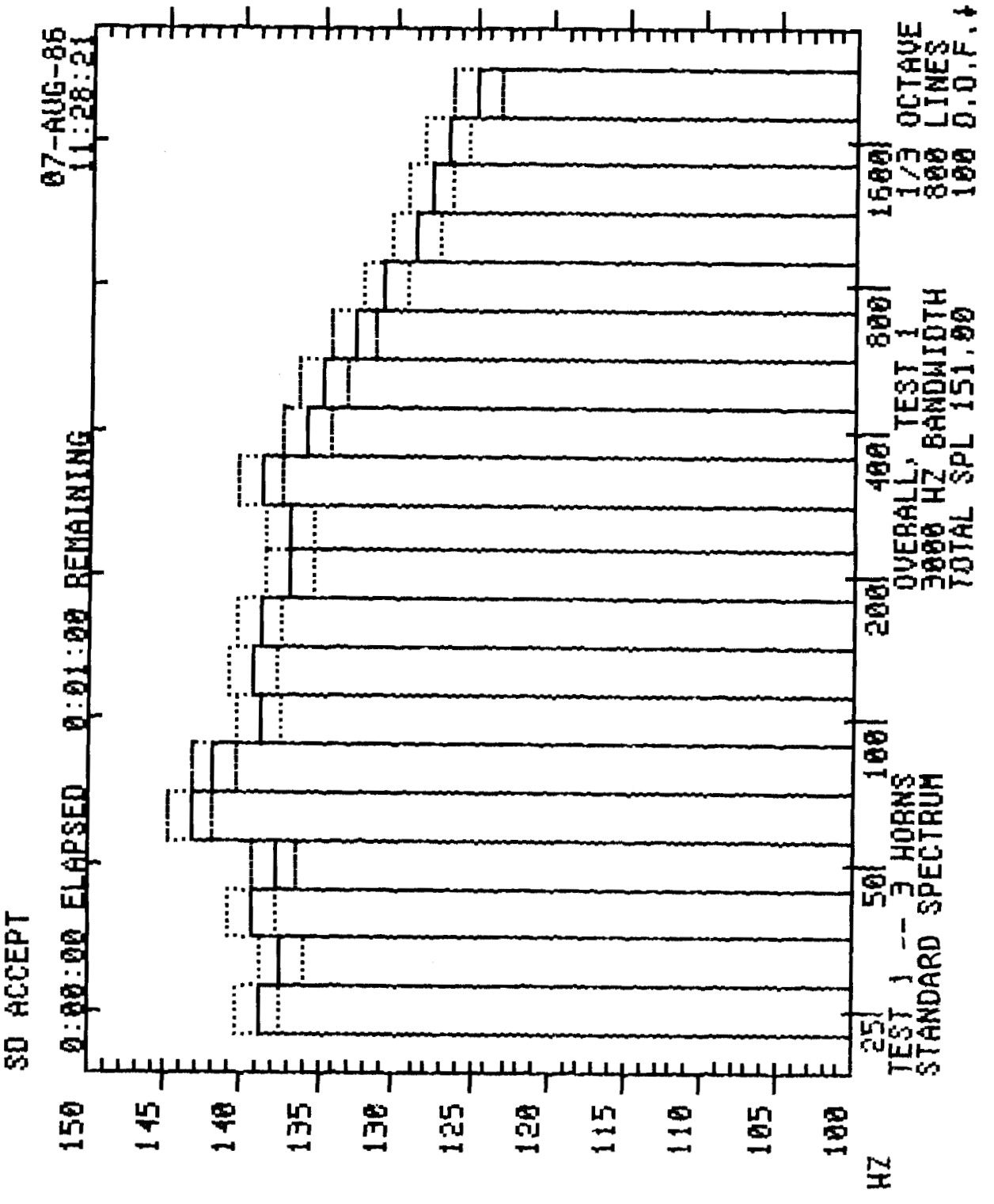

Figure 1. Standard spectrum

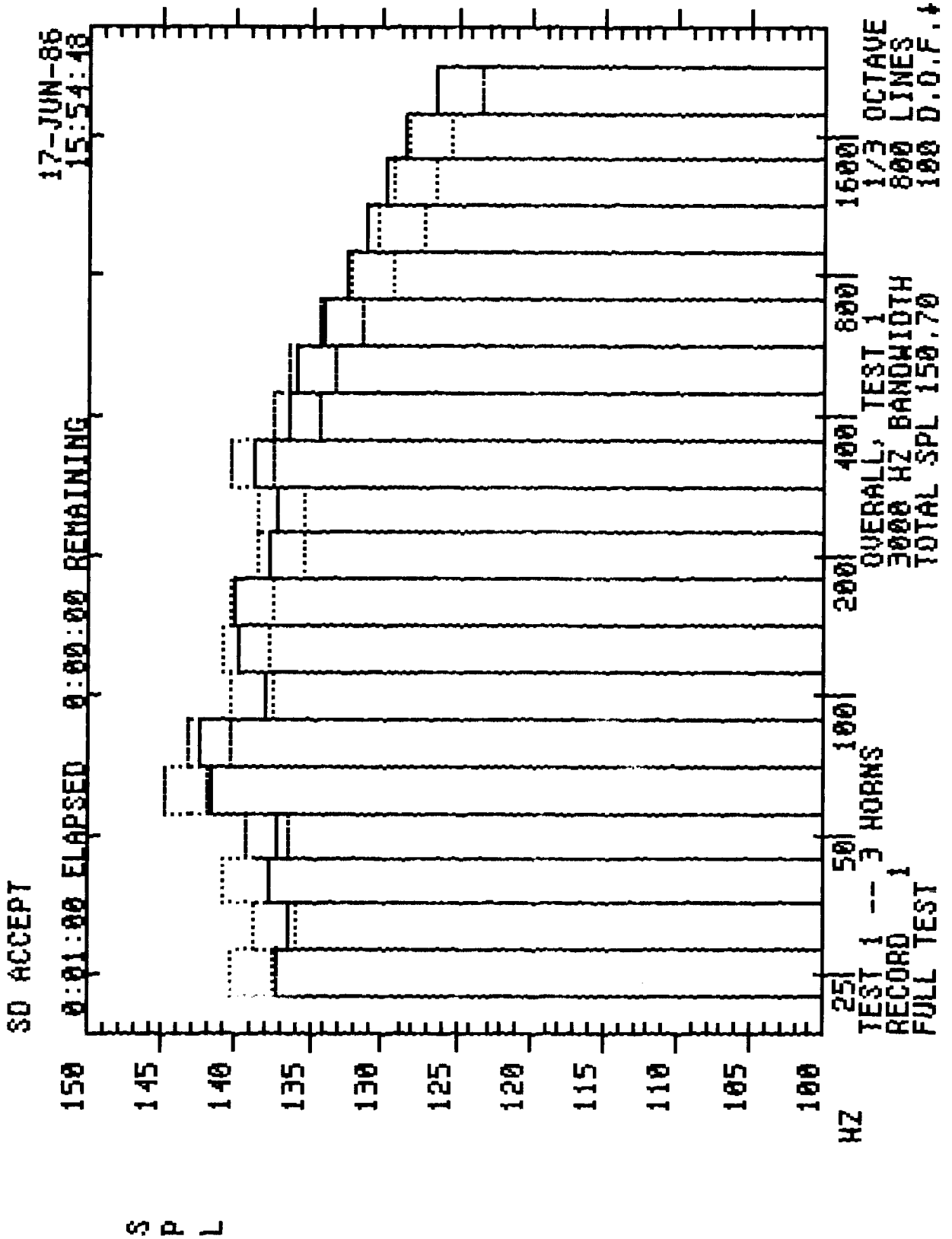

Figure 2. Response spectrum

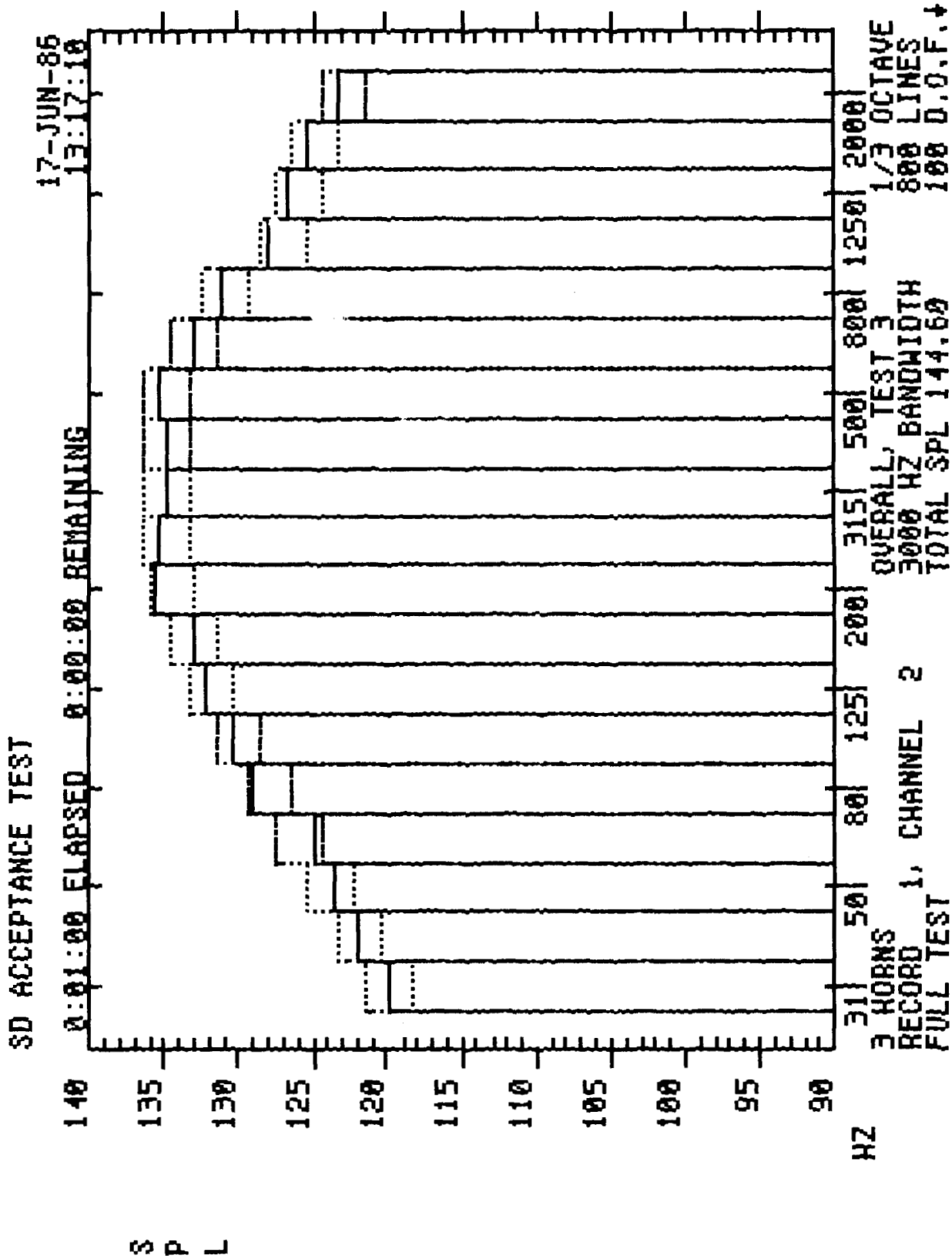

Figure 3. Response spectrum

TEST NUMBER 3 UNIT NUMBER 0 STORED RECORD # 1
OVERALL SPL 144.6 OVERALL RMS PASCALS 338.8 1/3 OCTAVE

FREQ	SPL	ERROR	FREQ	SPL	ERROR	FREQ	SPL	ERROR
31	119.9	-0.1	160	133.1	0.1	800	131.4	0.4
40	122.0	0.0	200	135.7	1.2	1000	128.2	1.2
50	123.6	-0.4	250	135.4	0.4	1250	126.9	0.9
63	124.9	-1.1	315	135.0	0.0	1600	125.5	0.5
80	129.2	1.2	400	135.0	0.0	2000	123.4	0.4
100	130.4	0.4	500	135.4	0.4			
125	132.4	0.4	630	133.2	0.2			

Figure 4. Response table

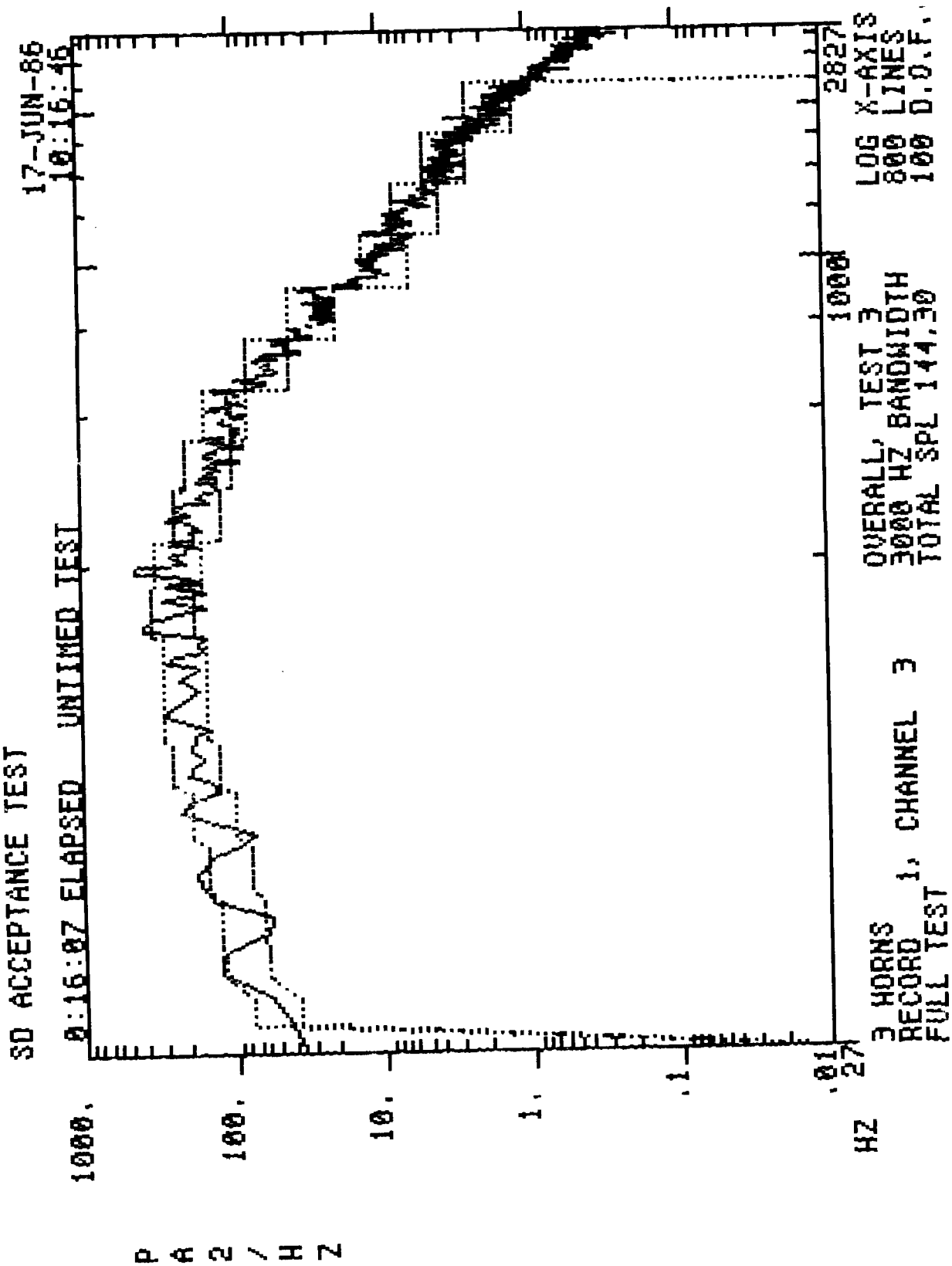

Figure 5. Narrowband response spectrum

BIBLIOGRAPHIC DATA SHEET

1. Report No.	2. Government Accession No.	3. Recipient's Catalog No.
NASA CP 2446		

4. Title and Subtitle	5. Report Date
Fourteenth Space Simulation Conference: Testing For A Permanent Presence In Space.	6. Performing Organization Code
7. Author(s) Joseph Stecher, Editor	8. Performing Organization Report No. 86B0561
9. Performing Organization Name and Address Goddard Space Flight Center Greenbelt, Maryland 20771	10. Work Unit No. 11. Contract or Grant No.
12. Sponsoring Agency Name and Address National Aeronautics and Space Administration Washington, D.C. 20546	13. Type of Report and Period Covered Conference Publication Nov 3 - 6, 1986 14. Sponsoring Agency Code

15. Supplementary Notes

16. Abstract

The Institute of Environmental Sciences Fourteenth Space Simulation Conference "Testing For A Permanent Presence In Space" provided participants a forum to acquire and exchange information on the State-of-the-Art in space simulation, test technology, thermal simulation and protection, contamination, and techniques of test measurements. The papers presented at this conference and the resulting discussions carried out the conference theme of "Testing For A Permanent Presence."

17. Key Words (Selected by Author(s))	18. Distribution Statement
Space Simulation Thermal Simulation Contamination Control Dynamic Testing	Unclassified-Unlimited Subject Category - 18

19. Security Classif. (of this report)	20. Security Classif. (of this page)	21. No. of Pages	22. Price*
Unclassified	Unclassified		

*For sale by the National Technical Information Service, Springfield, Virginia

GSFC 25-44 (10/77)